SEISMIC RETROFIT OF EXISTING STEEL TALL BUILDINGS WITH SUPPLEMENTAL DAMPING DEVICES

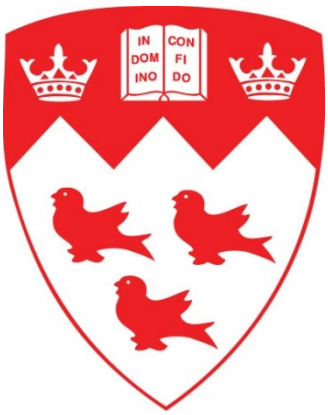

By

Sarven Akcelyan

Department of Civil Engineering and Applied Mechanics

McGill University

Montreal, Quebec, Canada

A thesis submitted to McGill University in partial fulfillment of the requirements of the degree of Doctor of Philosophy

ACKNOWLEDGEMENTS

Getting to this point was not easy; however I was not alone in this journey. There are many people to whom I am indebted for their support. First and foremost, I owe my deepest gratitude to my supervisor Prof. Dimitrios G. Lignos for his generous support through all these years. I was very eager to work on seismic protective systems and I would like to thank him for providing me this opportunity. It has been a great pleasure and privilege to work under his supervision. Our discussions have always been very enlightening. I have benefited from his guidance, encouragement, passion, kindness and patience and I wish to say a heartfelt thank you.

I also owe a debt of gratitude to Prof. Colin A. Rogers for his kind support during the last year of my doctoral studies. I would like to express my sincere thanks to Dr. Tsuyoshi Hikino, Prof. Masayoshi Nakashima, Prof. Kazuhiko Kasai and other researchers in the National Research Institute for Earth Science and Disaster Prevention (E-Defense) for conducting the experimental research and providing the experimental data for the needs of this research. I greatly appreciated the insightful discussions with Yusuke Suzuki, which helped me to understand Japanese journal papers. I am also thankful to Dr. Frank McKenna for his support in the *OpenSees* platform.

I acknowledge the Faculty of Engineering at McGill University (MEDA), the Natural Sciences and Engineering Research Council of Canada (NSERC) and Fonds de recherche du Québec -

Nature et technologies (FRQNT), for their financial support during my doctoral studies at McGill University.

In addition to the advanced knowledge in earthquake engineering, mastering the fundamentals in structural engineering was necessary for me to accomplish my doctoral research. Therefore, I would like to thank my professors at Istanbul Technical University, from where I received my bachelor's degree in Civil Engineering. I am also very grateful to my professors at University of Pavia (Rose School) and University of Patras. It was a great pleasure to learn earthquake engineering from world-class faculty members.

Without my friends, life as a PhD student would have been an even greater challenge. A special thanks to Evelina Violetta Nikolaidou for being always there. Thanks Cecile Yue Zhi for your great friendship through all these years. Thanks Shooka Karimpour for helping me and answering my endless questions about school and everyday life. Thanks Kunpeng Ji for being my office-mate till late hours. I will never forget your generous help during my miserable house moving experience. I am also very grateful to the people in our research group and in Office 275 for their friendship and for the wonderful times we shared.

Living in a new country far away from family was not easy. I owe a great debt of gratitude to Lusin, Hilda & Abraham Cakar and Tamar, Hagop & Arad Tchouldjian for being my second family and helping me immensely during my first year in Montreal.

Lastly, I would like to thank my family, my mother Ayda, my father Harutyun, my sister Selin and my grandmother Manisag for their unconditional love and support. I have no words to acknowledge the sacrifices you made for me. Especially, I am very grateful to my father Harutyun for his support through all my studies. I remember him carrying my backpack every

morning on the way to my primary school. Despite having financial challenges he managed to send me to an expensive high school. He was my main supporter when I decided to pursue graduate studies abroad. There is no doubt without his support all these would not have been possible. He has always been proud of me, but in reality I am more proud of him. And finally special thanks to my little nephew Luka. His lovely photos on my office desk were my greatest motivation.

ABSTRACT

A number of existing tall steel buildings in seismic regions may have potential deficiencies to seismic events with low probability of occurrence. This is attributed to the lack of knowledge in the seismic hazard, the absence of advanced dynamic analysis tools and capacity design principles at the time of construction. It is understood that the seismic performance of such buildings should be evaluated thoroughly such that effective retrofit solutions can be proposed. In this thesis, the emphasis is on the implementation of supplemental damping devices, particularly, nonlinear viscous damper (NVDs), oil dampers with relief valves (ODs) and buckling-restrained braces (BRBs).

In the context of performance based design there is an increased need to improve the reliability of state-of-art and simplified evaluation methods for tall buildings equipped with supplemental damping devices. This research presents enhanced models and algorithms for the numerical simulation of NVDs, ODs and BRBs within a nonlinear finite element program. Adaptive algorithms are implemented for computing high-precision solutions for nonlinear viscous and bilinear oil dampers with valve relief that are typically represented mathematically with a nonlinear Maxwell model. These algorithms possess excellent convergence characteristics for viscous dampers regardless of their velocity exponents and axial stiffness properties. Furthermore, a novel rate-dependent material model for BRBs and its calibration procedure with

experimental data is presented. The applicability and computational efficiency of the numerical models is demonstrated through a number of validation examples with data that involve component experimentation as well as the utilization of full-scale shake table tests of a 5-story steel building equipped with supplemental damping devices.

It is shown that regardless of the damper type, advanced or less sophisticated building models can satisfactorily predict the response of steel frame buildings with regular plan view, as long as the dampers are properly modeled. Based on a comparison of various engineering demand parameters (EDPs) with experimental data, it is shown that linear and nonlinear static procedures as per ASCE 41-13 may be unconservative for the evaluation of frame buildings with BRBs or NVDs, while the performance curves and P-Spectra methods provide more reliable predictions.

In order to enhance current design methods for dampers in tall buildings, a practical multi-degree-of-freedom (MDF) performance curves tool is developed. The advantage of this tool over currently used methods is that the designer can directly obtain story-based EDPs for a range of design solutions, which do not contain typical errors due to transformation, (i.e. SDF idealization, higher modes, flexural deformations, irregular damping distribution) and linearization. Guidance is provided on the construction of the MDF performance curves with simplified flexural shear beam models based on various damping properties and vertical damping distribution methods through a case study.

A comprehensive study related to the seismic performance assessment of a benchmark existing 40-story steel building with moment-resisting frames that represents typical 1970s construction in North America is presented. It is shown that the collapse risk of the benchmark building is high based on the regional seismic hazard. The main reasons are attributed to the development of

weak-story mechanisms due to seismic deficiencies of beam-to-column connections, high axial loads in columns and column splice fractures.

Supplemental damping provided by ODs is utilized to design an efficient seismic retrofit system for the 40-story steel building under consideration. Multiple retrofit solutions are designed based on three damping levels and vertical damping distributions, including a newly proposed damping distribution methodology. The proposed solutions are evaluated through rigorous nonlinear response history analysis. It is shown that the formation of local story collapse mechanisms can be prevented and the drift distribution can be controlled along the height of the building. The efficiency of vertical damping distribution methods varies with the level of the frame inelasticity.

RÉSUMÉ

De nombreux bâtiments en acier de grande hauteur existants peuvent avoir des défaillances structurelles à la suite de séismes présentant une faible probabilité d'occurrence. Ceci est dû au manque de connaissances de l'aléa sismique ainsi qu'à l'absence d'outils d'analyse dynamique avancés et des principes de conception par capacité lors de la construction de l'ouvrage. Il est entendu que la performance sismique de tels bâtiments doit être évaluée soigneusement afin de proposer des solutions de réhabilitation efficaces. Cette thèse met l'accent sur l'implémentation de systèmes d'amortissement complémentaires, en particulier des amortisseurs visqueux non-linéaires (ou NVD pour « nonlinear viscous dampers »), des amortisseurs hydrauliques à soupape (ou OD pour « oil dampers ») et des contreventements à diagonales confinées (ou BRB pour « buckling-restrained braces »).

Dans le cadre de la conception axée sur la performance, il est de plus en plus nécessaire d'améliorer la fiabilité des méthodes d'évaluation – simples ou sophistiquées – des bâtiments de grande hauteur équipés de dispositifs d'amortissement complémentaires. Ce travail de recherche présente des modèles et des algorithmes perfectionnés pour la simulation numérique de NVD, OD et BRB dans un programme d'analyse non-linéaire par éléments finis. Des algorithmes adaptatifs sont implémentés pour le calcul haute précision d'amortisseurs hydrauliques à soupape bilinéaires et visqueux non-linéaires qui sont traditionnellement représentés mathématiquement

par un modèle de Maxwell non-linéaire. Ces algorithmes possèdent des propriétés de convergence excellentes pour les amortisseurs visqueux quels que soient leurs exposants de vitesse et leurs propriétés de raideur axiale. De plus, pour les contreventements à diagonales confinées, un nouveau modèle de comportement – prenant en compte le taux de déformation du matériau – et sa procédure de calibration avec des données expérimentales sont présentés. Les possibilités d'application et la rapidité de calcul des modèles numériques sont démontrées à l'aide de plusieurs exemples de validation, avec des données provenant de tests de composant ainsi que l'utilisation de résultats obtenus avec une table vibrante pour un bâtiment en acier de cinq étages équipé de dispositifs d'amortissement complémentaires.

Il est montré que quel que soit le type d'amortisseur, des modèles plus ou moins sophistiqués de l'ouvrage peuvent prévoir de manière satisfaisante la réponse de bâtiments à charpente métallique réguliers en plan tant que les amortisseurs sont correctement modélisés. D'après une comparaison de plusieurs paramètres de demande sismique avec des données expérimentales, il est montré que les procédures d'analyse statique linéaire et non-linéaire employées par ASCE 41-13 peuvent sous-estimer les dommages lors de l'évaluation de bâtiments à ossature métallique comprenant des BRB ou des NVD, alors que les méthodes utilisant une courbe ou un spectre de performance donnent des prédictions plus fiables.

Afin d'améliorer les méthodes actuelles de conception des amortisseurs dans les bâtiments de grande hauteur, nous avons développé un outil pratique utilisant des courbes de performance pour des modèles à plusieurs degrés de liberté. L'avantage de cet outil, comparé aux méthodes actuelles, est que le concepteur peut obtenir directement les paramètres de demande sismique à chaque étage pour un ensemble de solutions structurelles, sans erreurs classiques dues à une transformation (concernant, par exemple, l'idéalisation du système par un modèle à un degré de

liberté, les modes supérieurs, la déformation en flexion du bâtiment, les irrégularités de distribution d'amortissement, etc.) ou à une linéarisation. Des conseils sont donnés, à l'aide d'une étude de cas, pour construire les courbes de performance pour des systèmes à plusieurs degrés de liberté avec des modèles simplifiés de poutre en flexion/cisaillement utilisant différentes caractéristiques d'amortissement et méthodes de distribution de l'amortissement vertical.

Nous présentons une étude détaillée de l'évaluation de la performance sismique d'un bâtiment de référence de quarante étages en acier avec des cadres rigides ductiles, existant, typique des constructions en Amérique du Nord dans les années 70. Nous montrons que le risque de ruine de ce bâtiment de référence, d'après l'aléa sismique de la région, est haut. Les principales raisons proviennent de la formation de mécanismes dits « d'étage faible », dus à des défaillances de connexions poutres-colonnes, à des charges axiales élevées dans les colonnes et à des fractures au niveau des raccordements de colonnes.

L'amortissement supplémentaire fourni par les amortisseurs hydrauliques est utilisé afin de concevoir un système de réhabilitation sismique efficace pour le bâtiment en acier de quarante étages en question. De nombreuses solutions de réhabilitation sont proposées, pour trois niveaux d'amortissement et de distributions de l'amortissement vertical, incluant une méthodologie de distribution de l'amortissement originale. Les solutions proposées sont évaluées au moyen d'analyses dynamiques non-linéaires rigoureuses. Nous montrons que la formation de mécanismes locaux de ruine d'un étage peut être évitée et que la distribution du déplacement latéral du bâtiment le long de sa hauteur peut être contrôlée. L'efficacité des méthodes de distribution de l'amortissement vertical varie avec le niveau d'endommagement plastique atteint par le portique.

PREFACE

In accordance with the "Guidelines for Thesis Preparation", this thesis is presented in a manuscript-based format. Authorships of the six articles are explained below.

Chapter 3:

Akcelyan, S., Lignos, D.G, Hikino, T. "Adaptive Numerical Method Algorithms for Nonlinear Viscous and Bilinear Oil Damper Models.", (submitted to journal).

- Numerical studies as well as writing of the manuscript were conducted by S. Akcelyan.
- Lignos, D.G., Hikino, T. provided supervision of the research and editing of the manuscript.

Chapter 4:

Akcelyan, S., Lignos, D.G. "Constitutive Model for Simulating the Loading-Rate Dependency of Buckling-Restrained Braces under Dynamic Excitations ", (submitted to journal).

- Numerical studies as well as writing of the manuscript were conducted by S. Akcelyan.
- Lignos, D.G., provided supervision of the research and editing of the manuscript.

Chapter 5:

Akcelyan, S., Lignos, D. G., Hikino, T., and Nakashima, M. (2016). "Evaluation of Simplified and State-of-the-Art Analysis Procedures for Steel Frame Buildings Equipped with Supplemental Damping Devices Based on E-Defense Full-Scale Shake Table Tests." *Journal of Structural Engineering,* 142(6).

- Numerical studies as well as writing of the manuscript were conducted by S. Akcelyan.
- Lignos, D.G., Hikino, T. and Nakashima, M. provided supervision of the research and editing of the manuscript.

Chapter 6:

Akcelyan, S., Lignos, D.G. "A Practical Design Method for Tall Buildings with Supplemental Damping Devices." (prepared for journal submission).

- Numerical studies as well as writing of the manuscript were conducted by S. Akcelyan.
- Lignos, D.G. provided supervision of the research and editing of the manuscript.

Chapter 7:

Akcelyan, S., Lignos, D.G. "Performance-Based Evaluation of a 1970s High-Rise Steel Frame Building". (prepared for journal submission).

- Numerical studies as well as writing of the manuscript were conducted by S. Akcelyan.
- Lignos, D.G. provided supervision of the research and editing of the manuscript.

Chapter 8:

Akcelyan, S., Lignos, D.G. "Seismic Retrofit of 1970s High-Rise Steel Frame Building with Supplemental Damping Devices". (prepared for journal submission).

- Numerical studies as well as writing of the manuscript were conducted by S. Akcelyan.
- Lignos, D.G. provided supervision of the research and editing of the manuscript.

The original scholarship and distinct contributions of this thesis are:

- Implementation of adaptive step-size algorithms for numerical models of nonlinear viscous dampers (NVDs) and oil dampers (ODs) within an open source finite element software, which is widely used by the earthquake engineering community.
- Development of a rate-dependent numerical model for buckling restrained braces.
- A comprehensive evaluation of current simplified and state-of-art assessment methods for steel structures equipped with BRBs and NVDs based on full-scale shake table tests of a five-story steel building.
- Development of a simplified multi-degree-of-freedom design and evaluation tool for tall buildings with supplemental damping devices.
- Seismic retrofit of a 1970s steel tall building with oil dampers with relief valve.

TABLE OF CONTENTS

LIST OF FIGURES

LIST OF TABLES

CHAPTER 1 : Introduction

1.1 Research Problem and Motivation

Urban centers and rapidly growing cities are characterized by tall buildings that contribute to the economic growth and sustainable development of societies. Although new buildings designed according to modern code provisions (AISC 2010c; IBC 2012; CSA 2014; NBCC 2015; AISC 2016) performed in a ductile manner in recent earthquakes, existing buildings designed before 1990s are relatively vulnerable to earthquake loading. Such buildings do not meet basic capacity design requirements, (e.g. strong column/weak beam ratio, panel zone strength requirements, prequalified beam-to-column connection detailing, column splicing detailing). Past earthquakes (e.g., Northridge 1994, Kobe 1995) caused severe damage in steel moment-resisting frames (MRFs) buildings (Nakashima et al. 2000). For instance, the 1994 Northridge earthquake highlighted several beam-to-column connection deficiencies (Bonowitz and Youssef 1995; FEMA 2000b). Similarly, column splices of existing steel frame buildings with partial joint penetration (PJP) weld joints are also viewed apprehensively. Past experimental studies indicated that column splices with PJP groove welds in thick assemblies subjected to cyclic loading do not behave in a ductile manner (Bruneau and Mahin 1990). Furthermore, panel zone design requirements have also been revised over the past few decades (FEMA 2000b). Studies by Krawinkler et al. (1975) illustrated that panel zone yielding could provide significant energy

dissipation to a steel MRF in a ductile manner. Thus, modern seismic provisions (AISC 2010c; CSA 2014) allow for controlled yielding in panel zones. More recent studies (Nakashima et al. 2007; Lignos et al. 2013; Elkady and Lignos 2014) suggest that the strong column/weak beam design requirements are not always sufficient to prevent soft story mechanisms at low probability of occurrence seismic intensities. This is due to the additional flexural demands from the composite action and the steel material cyclic hardening once beam yielding occurs.

Steel MRFs were widely used in high-rise buildings constructed between 1960 and 1990 in seismic areas, particularly those with above 35 stories (Almufti et al. 2012). Recent studies suggest that well-engineered tall buildings perform better than shorter ones during earthquakes (Naeim and Graves 2005). The advantage of tall buildings is that they are relatively flexible and earthquakes generally release less energy at the longer periods. However, as recently experienced in South Asia, Chile, and Japan the subduction zone earthquakes of magnitudes greater than eight are able to release significant energy at longer periods ranging from a few to 10 seconds. This generally coincides with the range of fundamental periods of flexible and/or tall buildings. Recent seismic hazard studies suggest that earthquakes of magnitude 9 could occur in the Cascadia subduction zone. The West Coast of North America including the Vancouver Island would experience such seismic events (Adams and Atkinson 2003). In such catastrophic event, the overall earthquake induced economic losses are expected to reach 75 billion dollars (AIR 2013). Notably, a recent experimental study of a prototype of a 21-story steel MRF designed in 1970s in Japan, demonstrated that tall buildings were expected to exhibit high cumulative plastic deformations in connections when subjected to long duration long-period ground motions (Chung et al. 2011). Fractures were observed at the bottom flange of the beams of the structure. Moreover, the composite action increased the strain demands at the bottom beam flange

appreciably. Other ground motion characteristics, such as near source and directivity effects have been found to be detrimental on the seismic response of tall buildings (Hall et al. 1995; Krishnan et al. 2006).

It is understood that there is an increasing need to investigate the seismic vulnerability of existing tall buildings in North America. In particular, several guidelines (FEMA 1997; ASCE/SEI 2014) have been published to assess and improve the seismic performance of existing steel buildings; however, as the majority of the construction worldwide consists of low and mid-rise buildings, most of these guidelines fail to address specific issues that may arise in the design and assessment of high-rise buildings. Several guidelines have been recently published (CTBUH 2008; PEER 2010; LATBSDC 2014) in order to provide reasonable performance objectives, design and evaluation recommendations for tall buildings. According to LATBSDC (2014) tall buildings are defined as those with height greater than 49m (160ft) above average adjacent ground surface. The same definition is adopted in this thesis.

Based on the aforementioned studies, seismic retrofit of existing tall buildings seems a rational approach in order to improve their seismic resilience. To this end, utilization of supplemental damping devices could be effective solution. Several types of passive control devices, such as metallic, viscous, oil, viscoelastic and friction dampers are commonly used to mitigate the seismic actions in tall buildings around the world (Christopoulos and Filiatrault 2006). These devices can protect structures by controlling story drifts, floor absolute accelerations and story shear forces along the height of a building. This was demonstrated in the recent 2011 Tohoku earthquake (Kasai et al. 2013b). Nevertheless, in existing tall buildings local upgrading may also be necessary. For instance, an experimental study carried out by Kyriakopoulos and Christopoulos (2013) indicated that a typical 1960s (Type 2) construction Canadian steel hospital

structure with perimeter MRFs could sustain story drifts up to 2% without dramatic connection failure. However, this may not be the case for other buildings, in which beam-to-column connections or other components may fail at relatively small drifts. Columns in tall buildings are typically exposed to high axial loads (Bech et al. 2015; Wang et al. 2017). The ASCE 41-13 (ASCE/SEI 2014) modeling guidelines treat such columns as force-controlled elements under the assumption that these columns cannot accommodate any plastic deformations. However, recent experimental studies with columns subjected to high axial loads contradict this assumption (Elkady and Lignos 2016; Lignos et al. 2016; Suzuki and Lignos 2016). Moreover, the moment demands in a column and subsequently in column splices are primarily obtained from elastic analysis; hence changes in the moment gradient due to inelastic behaviour of structural components is not considered. Therefore, we should first quantify the potential seismic deficiencies in existing tall buildings and then suggest a rational retrofit strategy.

A number of methods, such as the equivalent linear and nonlinear static methods, have been historically documented for evaluating the performance of existing structures. For tall buildings, the assumption of first mode dominated structure is not a valid one. According to ASCE (2010) and NBCC (2015) for regular structures exceeding 49m and 60m, respectively, dynamic analysis is required. For tall buildings equipped with supplemental damping devices, nonlinear response history analysis (NRHA) is recommended due to the nonlinear and/or rate-dependent response of dampers. Therefore, reliable damper numerical models as well as numerical solution algorithms are needed to assess the performance of the buildings with energy dissipation devices.

Although structural engineering analysis software is significantly improved throughout the past decades, the available damper models are still very limited in comparison with the vast number of dampers that have been developed. For instance, prior to this thesis there was no proper

damper model for nonlinear viscous dampers and bilinear oil dampers in the open-source simulation platform (*OpenSees*) (McKenna 1997), which is widely used within the earthquake engineering community. Instead, many researchers modeled nonlinear viscous dampers as a pure viscous model; therefore, the damper axial flexibility caused by the internal damper portion and supporting brace stiffness was neglected. The damper stiffness can heavily undermine the effectiveness of viscous dampers. Furthermore, if the damper stiffness is considered in the mathematical formulation of a damper, there is a need to improve the computational efficiency of the respective numerical solution algorithm. For instance, the numerical solution for the response of nonlinear viscous dampers with high axial stiffness and small velocity exponent typically require relatively small integration time steps (Oohara and Kasai 2002). If conventional fixed time-step numerical methods are utilized then a significant reduction in the global analysis time step is necessary. Therefore, the nonlinear response history analysis of tall buildings with supplemental damping devices becomes a challenging computational problem.

Similarly, better modeling approaches are needed for buckling-restrained braces. Buckling restrained braces (BRBs) dissipate energy through axial yielding of their steel core; therefore they are mainly considered as displacement-dependent dampers. These dampers, in case of low yield strength steel, they also accommodate velocity-dependent characteristics, due to the strain rate effects of the steel material and the unbonding material between the steel core and the restrainer, which amplifies the yield strength of the BRBs (Yamada et al. 2004). A simple way to consider rate-effects is amplifying the yield strength of the displacement-dependent steel material models (Yu et al. 2013). However, the amplification of the yield strength due to strain-rate effects is loading-history dependent; therefore more rigorous rate-dependent modeling approaches are required.

Commonly used simplified methods for the evaluation and design of buildings with supplemental damping devices have never been assessed with the utilization of full-scale experiments on buildings retrofitted with dampers. Static procedures are often employed for the seismic evaluation of steel buildings equipped with supplemental damping devices as discussed in ASCE 41-13 (ASCE/SEI 2014) and FEMA 274, 356 (FEMA 1997; 2000a).

Other challenges yet to be addressed in the design of supplemental damping devices in tall MRF buildings are the higher mode effects and the associated flexural deformation due to axial deformations of columns. Furthermore, the damper placement in existing tall buildings often causes irregularity in the vertical damping distribution. This distribution cannot be approximated with the classical damping assumption as it is typically recommended in ASCE 41-13 (ASCE/SEI 2014) and FEMA 274, 356 (FEMA 1997; 2000a). Therefore, the implementation of simplified methods in tall buildings with supplemental damping devices may lead to erroneous predictions of engineering demand parameters. More refined procedures are needed to improve the evaluation and the design methodologies for tall buildings equipped with supplemental damping devices.

It is recognized that in many cases yielding of the frame-system is inevitable in feasible retrofit solutions of the existing buildings. Thus, the frame nonlinearity adds another challenge in the design and evaluation of existing tall buildings with supplemental damping devices, particularly; this may significantly alter the efficiency of damping distribution methods. There is a number of studies, which explored the implementation of non-conventional retrofit techniques to pre-Northridge existing steel MRF tall buildings (Bjornsson 2014; Lai et al. 2015; Hutt et al. 2016). However, to the best of our knowledge there has not been a study conducted on the implementation of bilinear oil dampers. The advantage of such devices in retrofit configurations

is that they are able to cap the additional forces transferred to the framing members; therefore, the potential for a more economic retrofit is large.

1.2 Research Objectives

The aim of this thesis is to improve the seismic evaluation and assessment methodologies for existing tall buildings and suggest efficient retrofit techniques with innovative supplemental damping devices. The main research objectives of this research are summarized below,

- Development of computationally efficient numerical models and numerical solution algorithms for nonlinear viscous dampers and bilinear oil dampers.
- Development of rate-dependent numerical models for buckling-restrained braces.
- Evaluation and refinement of current simplified and state-of-art assessment methods for steel buildings equipped with supplemental damping devices.
- Improvement of simplified design and evaluation methods for tall buildings with supplemental damping devices.
- Seismic performance evaluation of existing pre-Northridge steel tall buildings and identification of structural deficiency indicators.
- Guidance for effective seismic retrofit strategies of existing tall buildings with supplemental damping devices.

1.3 Thesis Outline

Chapter 2 provides a fundamental background and literature review for the topics discussed in this thesis. These include fundamental characteristics of supplemental damping devices. A summary of damper modeling approaches used in past studies is also provided. Chapter 2 also includes a brief presentation of current simplified and state-of-art evaluation methods for

buildings with supplemental damping devices. A comprehensive summary of past research studies conducted on existing steel pre-Northridge MRF high-rise buildings in North America is presented. Finally, a review of seismic retrofit implementations for existing steel tall buildings is presented.

Chapter 3 discusses the numerical implementation of an improved adaptive algorithm for the numerical solution of the constitutive equation of nonlinear viscous and bilinear oil damper models subjected to random vibrations. In the damper mathematical formulation the damper axial stiffness is considered. The efficiency of the proposed algorithm is compared with that of traditional integration schemes employed for the numerical solution of initial value problems. The proposed numerical solution techniques are implemented in an open-source finite element simulation platform and are validated with full-scale experiments on damper elements and actual systems equipped with supplemental damping devices.

Chapter 4 presents a proposed mathematical model for BRBs that captures both displacement and velocity-dependent forces under dynamic excitations. The calibration process of the model is illustrated through an example that is applicable to any type of BRB. Furthermore, the model is validated with data from a full-scale shake table experiment of 5-story steel building equipped with BRBs. The proposed BRB model is implemented in an open-source finite element simulation platform.

Chapter 5 focuses on the evaluation of simplified assessment methods for steel frame buildings equipped with buckling-restrained braces (BRBs) and nonlinear viscous dampers (NVDs). This evaluation is based on full-scale experimental data from recent shake table tests that were conducted at the E-Defense facility in Japan. Guidance is provided on limitations of various

simplified methods depending on the supplemental damping device type. Several modeling approaches are also explored in different analysis platforms that are currently used by researchers and engineering practitioners. Guidance on the minimum level of sophistication for NRHA of steel frame buildings with BRBs and NVDs is also provided.

Chapter 6 proposes a simplified multi-degree-of-freedom (MDF) tool for the design of supplemental damping devices in tall buildings. To this end, first the concept of damper design and various vertical damping distributions is presented. The design method of dampers is based on the performance curves methodology developed by Kasai et al. (2008a). Guidelines on how to construct appropriate simplified models for tall buildings with dampers are proposed. In order to illustrate the proposed methodology, a case study, 40-story steel MRF building is utilized. Issues related to damping distributions, higher modes and global bending deformation are addressed. Finally, the MDF performance curves are constructed. Although the study focuses on bilinear oil dampers, the proposed methods can be easily implemented for other damper types.

Chapter 7 provides a detailed discussion regarding the global and local seismic deficiencies of existing steel tall buildings designed in 1970s. Particularly, issues related to capacity design requirements are addressed. To this end, a prototype 40-story steel MRF building representative of the tall building construction practice from 1970s is employed as a case study. To assess the seismic performance of the prototype tall building advanced nonlinear modeling techniques are utilized with the aim to provide guidelines for future retrofit solutions in existing tall buildings.

Chapter 8 presents seismic retrofit solutions for existing pre-Northridge steel tall buildings by means of utilizing supplemental damping devices. Oil dampers with valve relief are implemented to improve the performance of the prototype 40-story steel building discussed in Chapter 7.

Several retrofit schemes are discussed herein. To this end, MDF performance curves are utilized. A vertical damping distribution method is proposed, which provides an efficient retrofit solution for existing tall buildings, in which frame yielding is inevitable. Furthermore, detailed nonlinear response history analyses are conducted to observe the influence of the retrofit solution on the beams, columns and connections of the prototype steel MRF, particularly in comparison with the existing building.

Chapter 9 provides a summary and the main conclusions of this thesis. It summarizes the main findings of the research and its limitations as well as provides recommendations for future research related to the topic.

CHAPTER 2 : Literature Review

2.1 Introduction

This chapter presents a thorough literature review that begins with the essentials of supplemental damping devices (nonlinear viscous dampers, bilinear oil dampers and buckling-restrained braces) that are specifically employed as part of this thesis in Chapters 3 and 4. Numerical models that have been historically used to simulate the hysteretic response of these devices are presented. A review of the available simplified design and evaluation methodologies for buildings with energy dissipation devices that are commonly used today is presented. Finally, a review of past studies related to seismic retrofit of existing tall buildings is presented.

2.2 Supplemental Damping Devices

In the past three decades, various types of passive supplemental damping systems have been developed and utilized in frame buildings to control seismic and wind-induced vibrations (Constantinou and Symans 1993a; Soong and Dargush 1997; Christopoulos and Filiatrault 2006; Black and Makris 2007; Symans et al. 2008; Dong et al. 2015). This thesis focuses only on passive energy dissipation devices and the term supplemental damping systems refers to passive systems. Supplemental damping devices are mainly named after their energy dissipating mechanisms, such as yielding (i.e. metallic or hysteretic), friction or viscous/viscoelastic.

Dampers are also classified according to their rate-dependency, such as displacement-dependent and velocity-dependent. Three types of energy dissipation devices are discussed; nonlinear (fluid) viscous dampers, bilinear oil dampers and buckling-restrained braces (i.e., steel dampers).

2.2.1 Nonlinear (Fluid) Viscous Dampers

Figure 2.1 shows the typical construction of a fluid viscous damper with a double ended piston rod. Fluid viscous dampers contain a low viscosity fluid (e.g. silicon oil) and its flow through orifices leads to pressure differential across a piston head, which produces the damper force. The design of orifice dictates the relationship between the force and velocity. Thus, the general force-velocity relationship of nonlinear viscous models can mathematically be expressed as given in Equation 2.1 (Symans and Constantinou 1998),

$$F_d(t) = C_d \left|\dot{u}_d(t)\right|^{\alpha} \operatorname{sgn}\left(\dot{u}_d(t)\right) \tag{2.1}$$

in which, C_d is the damping coefficient and α is the velocity exponent that characterizes the viscous material; u_d and $\dot{u}_d$ are the displacement and velocity of the dashpot, respectively; and sgn represents the signum function. Thus, the peak force F_{d0} of a viscous damper under a harmonic displacement excitation that is described as $u_d(t) = u_{d0}\sin(\omega t)$, is as follows,

$$F_{d0} = C_d(\omega u_{d0})^{\alpha} \tag{2.2}$$

in which, u_{d0}; and ω are the peak displacement amplitude and the circular frequency of the sinusoidal excitation, respectively. Figure 2.2 shows the normalized force-velocity and normalized force-displacement relations of nonlinear viscous models with different α values. A typical Bernoullian cylindrical shaped orifice produces forces, which are proportional to the square of the velocity (i.e., $\alpha = 2$). Such dampers are utilized for shock wave absorption. For $\alpha = 1$, a viscous damper becomes linear while for $\alpha = 0$ the force-displacement hysteresis loop of a viscous damper becomes rectangular, which is typical for friction models (Pall and Marsh

1982). For seismic design applications of frame buildings, the capability of limiting the damper force output under high velocity pulses is often desirable. Therefore, for seismic applications, α should be selected such that $\alpha < 1$. For instance, velocity-dependent dampers, such as viscous dampers, are advantageous as the forces they develop are typically out-of-phase with displacement-induced forces within a frame building under earthquake loading (Constantinou et al. 1998). Recent earthquakes around the world have demonstrated the effectiveness of viscous dampers in response modification of conventional buildings to control structural and non-structural damage (Buchanan et al. 2011; Miranda et al. 2012; Kasai et al. 2013b). It is necessary to compute the energy dissipation of the damping devices to predict the supplemental damping that they can provide. In civil engineering design practice, earthquake-induced vibrations are usually simplified as harmonic motions. Thus, by integrating Equation 2.1 over the displacement of a steady-state harmonic motion per cycle the energy dissipation of purely nonlinear viscous models can be computed as follows (Constantinou and Symans 1993a),

$$E_{d,NL} = \lambda_{NL} F_{d0} u_{d0} \tag{2.3}$$

$$\lambda_{NL} = \frac{2^{\alpha+2} \Gamma^2 (1+\alpha/2)}{\Gamma(2+\alpha)} \tag{2.4}$$

in which, λ_{NL} relates to the velocity exponent; Γ represents the gamma function. Figure 2.3a illustrates the variation of λ_{NL} with different α values. If $\alpha = 0$, λ_{NL} becomes 4; for a linear viscous damper ($\alpha = 1$), λ_{NL} reduces to π. The greater the α the smaller the area of loop shown in Figure 2.2b.

Table 2.1 lists the structural applications of fluid viscous dampers in Canada from 1997 to 2016 based on the database of Taylor Devices Inc. (2017). According to this list, fluid viscous

dampers were implemented to mitigate seismic, wind, and human-induced vibrations in existing and new structures, such as bridges, reservoirs, stadium and airports.

2.2.2 Oil Dampers with Relief Valve (Bilinear Oil Dampers)

Linear viscous dampers produce forces that vary linearly with respect to the velocity demand. This implies that larger damper forces are generated if velocity demands exceed the expected ones. This may lead to more conservative design of non-dissipative members in line with the capacity-design philosophy. An alternative to overcome this challenge is the bilinear oil dampers. These dampers contain low viscosity oil with a relief mechanism, which suppresses the force after a certain limit (Ichihasi et al. 2000; Kasai and Nishimura 2004; Kasai et al. 2004c; Tsuyuki et al. 2004). Figure 2.4 illustrates the mechanism of a typical oil damper with relief valve (Yamamoto et al. 2016). For instance, the movement of the rod to the left leads the oil to flow from chamber A into chamber B through the valves. The pressure-adjusting valves regulate the differential pressure between two chambers. In oil dampers, the initial variation between pressure and flow rate is linear. At low flow rates only the pressure-adjusting valves open. The relief valves are activated by the high pressure in chamber A, once the flow rate exceeds a limit. This creates a bilinear relation between the damper force and velocity as shown in Figure 2.5a. Thus, the force produced by a bilinear viscous damper can be mathematically computed as follows,

$$F_d(t) = \begin{cases} C_d \acute{u}_d(t), & |F_d(t)| \le F_{dr} \\ \text{sgn}(\acute{u}_d(t)) F_{dr} + p(\acute{u}_d(t) - \acute{u}_{dr}), & |F_d(t)| > F_{dr} \end{cases} \tag{2.5}$$

in which, p is the post relief damping coefficient ratio; F_{dr} and $\acute{u}_{dr}$ are the relief force and velocity of the bilinear oil damper, respectively. The peak force F_{d0} of a bilinear viscous damper under sinusoidal displacement excitation $u_d(t) = u_{d0}\sin(\omega t)$ can be computed as follows,

$$F_{d0} = \left(p + \frac{1-p}{\mu_d} \right) C_d \omega u_{d0} \tag{2.6}$$

the peak damper velocity ratio, μ_d of a bilinear viscous damper, which is defined as the ratio of maximum velocity demand over the damper relief velocity can be computed as follows,

$$\mu_d = \frac{\acute{u}_{d0}}{\acute{u}_{dr}} = \frac{\omega u_{d0}}{\acute{u}_{dr}} \tag{2.7}$$

Figure 2.5b illustrates the hysteretic behaviour of a bilinear viscous damper under sinusoidal loading for different displacement amplitudes. In this figure, the x-axis has been normalized with respect to the peak displacement amplitude. The damper was designed for a peak damper velocity ratio, $\mu_d = 3$. The post-relief damping coefficient ratio was assumed to be $p = 0.1$. The displacement amplitudes were increased in three steps. During the first step the peak damper velocity was nearly equal to the damper relief velocity; therefore the hysteretic behaviour of the damper was identical to that of a linear viscous damper (Kasai et al. 2004c; Tsuyuki et al. 2004). Once the velocity demand exceeds the damper relief velocity, the relief mechanism is activated and the damping coefficient C_d suddenly drops as shown in Figure 2.5a.

Kasai and Nishimura (2004) suggested that the energy dissipation of purely bilinear viscous models (ODs ignoring the stiffness) under sinusoidal displacement can be computed as follows,

$$E_{d,BL} = \lambda'_{BL} C_d \omega u_{d0}^2 \tag{2.8}$$

$$\lambda'_{BL} = \left(2(1-p) \left(\frac{\sqrt{\mu_d^2 - 1}}{\mu_d^2} - \cos^{-1}\left(\frac{1}{\mu_d} \right) \right) + \pi \right) \tag{2.9}$$

As in case of NVDs, in order to compare the quality factor λ_{BL} of the force-displacement loop in terms of 4 units, one can rewrite Equation 2.8 in the following form,

$$E_{d,BL} = \lambda_{BL} F_{d0} u_{d0} \tag{2.10}$$

$$\lambda_{BL} = \frac{\lambda'_{BL}}{p + \frac{1-p}{\mu_d}} \tag{2.11}$$

Here F_{d0} is the peak force of the bilinear dashpot model, which can be computed by Equation 2.6; λ_{BL} is a quality factor of the loop related to the peak damper velocity ratio of the bilinear dashpot μ_d and the post relief damping coefficient ratio p. Referring to Figure 2.3b, λ_{BL} varies between π and 4. If μ_d is 1 the system is identical to a linear viscous damper, where λ_{BL} adopts its minimum value π. If p is 0 with the increase of the peak damper velocity ratio μ_d, the λ_{BL} approaches to 4. In case of practical p values, λ_{BL} reaches a peak value at a certain μ_d level and then it approaches back to π at large μ_d values.

2.2.3 Buckling-Restrained Braces (Yielding Devices)

Figure 2.6 illustrates a typical buckling restrained brace (BRB). The steel brace is composed of yielding (steel core) and non-yielding segments. In order to prevent buckling of the steel core a buckling-restrainer, a steel tube (typically HSS) filled with mortar surrounds the steel core. An unbonding material is applied to the restrained portion of the steel brace to prevent bonding and minimize the friction between mortar and steel brace. As buckling is restrained by the confinement provided by mortar the steel core can accommodate large compressive loads without buckling. Thus, steel core can yield in tension and compression. Unlike conventional braces, BRBs can dissipate a large amount of hysteretic energy.

Figure 2.7 shows the hysteretic behaviour of two nominally identical BRBs subjected to quasi-static and dynamic sinusoidal loading with constant peak displacement amplitudes, respectively (E-Defense 2008; Ooki et al. 2009). The quasi-static and dynamic tests were conducted with 0.05%/s and 2.0 Hz loading frequencies, respectively. Referring to Figure 2.7, the quasi-static test indicates a typical steel hysteretic behaviour with combined kinematic and isotropic material

hardening. Referring to Figure 2.7, the dynamic test shows significant amplification of the axial yield strength. Unlike the quasi-static test, the peak forces did not occur at peak displacements and the transition from loading to unloading (i.e., edges of hysteresis) was smooth. This is a clear evidence of the existence of viscoelastic forces. Kasai and Nishizawa (2010) demonstrated that these additional dynamic forces are generated by two distinct phenomena: (1) the strain-rate-dependent characteristics of low yield strength steel that is assigned to the steel core plate; (2) viscoelastic shear stresses on steel brace surface due to the interaction between the steel core, the unbounding material and the mortar. The latter is indicative of the abrupt increase of forces observed at the beginning of loading/unloading cycles. This results to the hardening behaviour of viscoelastic materials at high strain rate and large strains (Kasai et al. 2004b).

Since the earlier development of the first prototypes of buckling-restrained braces (BRBs) (Wakabayashi et al. 1973; Kimura et al. 1976; Watanabe et al. 1988), extensive experimental research has been conducted for their further implementation into the seismic design practice (Merritt et al. 2003a; 2003b; Black et al. 2004; Tremblay et al. 2006; Fahnestock et al. 2007; Tsai et al. 2008; Kasai and Matsuda 2014). In North America, buckling-restrained braces are considered as an alternative solution to conventional braces (Tremblay et al. 2006; Symans et al. 2008); lateral load resisting systems that employ BRBs are categorized as buckling-restrained braced frames (BRBFs) in North American seismic design specifications (CSA 2009; AISC 2010b). In Japan, BRBs are treated as yielding devices (i.e., steel dampers) and provide supplemental hysteretic energy to control lateral drift demands (Kasai et al. 2008b). It is common to employ low-yield point steel (σ_y = 100-225 MPa) in BRBs (Saeki et al. 1998). In this case, BRBs can provide supplement damping to a building at relatively small story drift ratios (Chen et al. 2001). The hysteretic behaviour of low-yield point steel shows significant dependency to

the loading-rate compared to mild steel (Yamada et al. 2004; Ooki et al. 2009; Kasai et al. 2010). In this case, the amplification of BRB forces due to strain-rate effects leads to higher demands on non-dissipative structural elements, such as connections, beams and columns. It should be stated that the use of low yield point steel is preferred in BRBs such that these devices can be effective in terms of providing additional lateral stiffness to the respective steel frame building in addition to strength.

2.3 Simulation Models for Supplemental Damping Devices

In the context of performance-based earthquake engineering reliable models are needed for simulating the nonlinear response of various structural components. This section presents currently available mathematical models that simulate the hysteretic behaviour of the three types of dampers under consideration.

2.3.1 Nonlinear (Fluid) Viscous Damper and Bilinear Oil Damper

In contrast with the idealized assumption of purely viscous dashpot models, viscous dampers show stiffness dependency characteristics that generally undermine the effectiveness of a viscous damper (Makris and Constantinou 1991). Based on prior experimental findings the hysteretic behaviour of a viscous damper is dependent on its axial stiffness as well as the frequency characteristics of the external applied force (Constantinou and Symans 1993a). In addition to axial stiffness of the metallic segments within the damper portion (cylinder), restoring forces are developed due to fluid compression. This effect can be minimized by the use of an accumulator or double ended piston rod as shown in Figure 2.1 (Constantinou and Symans 1993a; Symans et al. 2008). Typically the axial stiffness of the damper portions can be obtained empirically from experimental data as discussed in Makris and Constantinou (1991) and Kasai et al. (2004a; 2004b). Moreover, viscous dampers in frame buildings are typically installed with supporting

braces that consist of several components such as steel braces, clevises, brackets and gusset plates. These components provide additional axial flexibility to the damper and affect its behaviour. To this end, the Maxwell model (Maxwell 1867) has been found to be more appropriate to account for both the axial stiffness and frequency dependency of a viscous damper under dynamic loading (Makris and Constantinou 1991; Constantinou and Symans 1993a; Singh et al. 2003). In this case, a nonlinear dashpot and a linear spring are connected in series. The spring represents the axial stiffnesses of the damper portion and that of the various supporting components can be represented by an equivalent axial stiffness.

A number of researchers, have studied the effect of axial stiffness of viscous dampers on the seismic performance of frame buildings (Constantinou et al. 2001; Singh et al. 2003; Chen and Chai 2011; Liang et al. 2011; Londoño et al. 2013), but they mainly focused on linear viscous dampers. In the case of nonlinear viscous dampers, a common practice has been to neglect the damper axial stiffness (Pekcan et al. 1999; Ramirez et al. 2001; Lin and Chopra 2002; Hwang et al. 2008; Diotallevi et al. 2012). This is a convenient assumption because a closed-form analytical solution of the damper force can be computed when NRHA is employed. Recent shake table experiments of a full-scale 5-story steel frame building equipped with viscous dampers that were conducted at the world's largest shake table around the world (Ooki et al. 2009; Kasai and Matsuda 2014) demonstrated that the consideration of the damper axial stiffness is critical in order to accurately predict both local and global seismic demands of the test structure (Kasai et al. 2007; Kasai and Matsuda 2014). Furthermore, a blind analysis contest that was conducted to challenge the existing modeling capabilities for steel frame buildings equipped with various types of dampers demonstrated that in the case of viscous dampers incorporating the brace and damper axial stiffness improves the overall prediction accuracy by more than 20% compared to

the experimental data (Yu et al. 2013). Several researchers have proposed ways to account for the stiffness and frequency dependency of viscous dampers and to compute numerically their hysteretic response under random vibrations by employing the Maxwell model (Makris and Constantinou 1991; Constantinou and Symans 1993a; Reinhorn et al. 1995; Takahashi and Sekiguchi 2001; Oohara and Kasai 2002; Singh et al. 2003). Typical integration algorithms that have been employed to obtain numerically the viscous damper hysteretic response may require considerably small integration steps to overcome convergence problems (Oohara and Kasai 2002). In particular, numerical convergence may still be a challenge for frame buildings equipped with nonlinear viscous dampers with high axial stiffness and small velocity exponents (Oohara and Kasai 2002). This may be a fundamental constraint for the optimal seismic design and/or retrofit of frame buildings with nonlinear viscous dampers in which the locations as well as the damper sizes should be explicitly identified as part of the optimization problem (Lavan et al. 2008; Lavan and Avishur 2013). It is understood that improved integration algorithms should be utilized to reliably obtain the numerical solution of nonlinear viscous damper models. At the same time these algorithms should be computationally efficient when they are employed as part of NRHA of large-scale structural systems equipped with viscous dampers.

2.3.2 Buckling-Restrained Braces

Historically, BRBs have been modeled with bilinear elastoplastic models (Sabelli et al. 2003; Kiggins and Uang 2006). Others (Black et al. 2004; Yu et al. 2013) have utilized smooth hysteretic material models (Menegotto and Pinto 1973; Wen 1976) to simulate the Bauschinger effect as well as the combined kinematic/isotropic hardening that is typically evident in low yield stress point steel materials (Kanno 2016). Although the shear transfer of the steel core and mortar is minimized through the use of unbounding materials, recent experiments showed that the

compressive strength of BRBs is higher than the corresponding tensile strength due to the contact between the steel core and the mortar caused by the Poisson effect (Chen et al. 2001; Black et al. 2004; Tremblay et al. 2006). Therefore, Zona and Dall'Asta (2012) proposed a nonlinear asymmetric smooth hysteresis model to simulate the behaviour of BRBs. In a more recent study, Zsarnóczay (2013) modified the Menegotto-Pinto material model for the same purpose. A limiting feature of the aforementioned models is that they are not able to trace the steel material strain-rate dependency. The aforementioned models are only based on displacement-dependent constitutive relations. The dynamic force amplification due to strain-rate effects is typically captured through an adjustment of the steel core material yield strength such that the BRB hysteretic response of a certain loading frequency can be matched. This frequency is typically selected close to the fundamental frequency of the building under consideration (Yu et al. 2013). Although this approach is convenient, it requires the dynamic properties of the building *a priori*. In any case, such models are rate-independent; therefore, during the response history analysis the BRB force variation under different vibration frequencies is not captured. This could be a fundamental concern in tall buildings vibrating in higher modes. It is therefore understood that a reliable BRB model is needed that captures the strain-rate effects as part of its constitutive formulation. Yamada et al. (2004) found a nonlinear relation between the strain-rate and dynamic stress ratio based on a series of tests on BRBs fabricated with low yield point steel material (LYP100). They proposed a non-smooth hysteretic BRB model, which implicitly accounts for the strain-rate effects by amplifying the static stresses in the steel core with a dynamic stress ratio, which is a function of the strain rate. More recently, Kasai and Nishizawa (2010) tried to capture the velocity-dependent characteristics of low-yield strength point BRBs by explicitly considering the viscoelastic shear behaviour of the unbonding agent. An added

complexity in this case is how to provide rational input model parameters that reliably trace this behaviour.

2.4 Simplified Methods for Supplemental Damping Device Design

Several simplified assessment procedures have been developed for the seismic design and the performance evaluation of frame buildings equipped with supplemental damping devices. These methods include linear and nonlinear static procedures in accordance with ASCE 41-13 (ASCE/SEI 2014) and FEMA 274, 356, and 440 (FEMA 1997; 2000a; 2005) as well as performance curves (Kasai et al. 1998; Kasai and Ito 2005; Kasai et al. 2007), which are primarily based on linearization and transformation of frame buildings with dampers into equivalent linear single-degree-of-freedom (SDF) systems. More recently, a performance spectra (so-called P-Spectra) method (Guo and Christopoulos 2013a; 2013b) was proposed for the simplified design and retrofit of frame buildings with hysteretic and linear viscous/viscoelastic dampers. The P-Spectra method also provides an estimate of the expected residual deformations of a frame building with dampers. A brief summary of each simplified method is presented below.

2.4.1 ASCE 41-13 (ASCE/SEI 2014)

There are number of studies that shaped today's US standards for the design and evaluation methods for buildings with supplemental damping devices. Many of these studies were conducted by researchers at the University of New York at Buffalo (Constantinou et al. 1993; Makris et al. 1993; Reinhorn et al. 1995; Seleemah and Constantinou 1997; Soong and Dargush 1997; Constantinou et al. 1998; Symans and Constantinou 1998; Ramirez et al. 2001; Whittaker and Constantinou 2004; Symans et al. 2008). Whittaker et al. (1993) introduced the first guideline that was published by the Structural Engineers Association of Northern California

(SEAONC). In 1994, the Building Seismic Safety Council (BSSC 1995) published a draft guideline for the use of supplemental damping devices in new buildings. In 1997, FEMA 273 and 274 (FEMA 1997) reports were published, which provided comprehensive guideline for the use of supplemental damping devices for rehabilitation of buildings. More recently, FEMA 356 (FEMA 2000a) superseded FEMA 273 and 274 (FEMA 1997) reports and became a pre-standard for the seismic rehabilitation of existing buildings. Shortly thereafter, in 2001, based on the studies by Ramirez et al. (2001) BSSC published an improved NEHRP 2000 (FEMA 368) guideline (BSSC 2001) for the design of buildings with damping devices. In accordance with NEHRP 2000, Ramirez et al. (2001) developed the equivalent lateral force and response spectrum procedures for the design of buildings with yielding, viscoelastic, linear and nonlinear viscous dampers, in which the building nonlinear behaviour was incorporated. The methods were then validated with NRHA (Ramirez et al. 2003). Eventually, these pre-standard guidelines have been superseded by ASCE 41-13 (ASCE/SEI 2014) and ASCE 7-10 (ASCE 2010) for the implementation of supplemental damping devices in existing and new buildings, respectively.

The ASCE 41-13 (ASCE/SEI 2014) provisions are a seismic rehabilitation standard for existing buildings. There are four available procedures recommended for the evaluation of buildings with passive energy dissipation systems in ASCE 41-13 (ASCE/SEI 2014). These are (1) the linear static procedure; (2) the linear dynamic procedure; (3) the nonlinear static procedure; and (4) the nonlinear dynamic procedure. Linear procedures are only permitted if the framing system of building with supplemental damping devices is expected to remain within the elastic range for the selected hazard level. In this case, the effective damping ratio β_{eff} shall be less than 30% of the critical. Furthermore, the linear procedures are not permitted in cases where dampers are not present in all stories. In case that higher mode effects are significant, such as in tall buildings, a

linear dynamic procedure should be used, which is also known as response spectrum method. If yielding is expected in the retrofitted frame for the selected hazard level, nonlinear static procedure shall be used. In this case, the mathematical model of the building should account for the nonlinear behaviour of the framing system and dampers. If the higher mode effects are significant and/or dampers are not present in all stories, the nonlinear dynamic procedure should be utilized, which requires NRHA of the building model with dampers.

In this section, the main steps of the ASCE 41-13 (ASCE/SEI 2014) linear static procedure with emphasis on fluid viscous devices is presented. For instance, in an single-degree-of-freedom (SDF) system with an elastic frame and a supplementing damping device, assuming that the excitation frequency of the harmonic motion is the same as the equivalent frequency of the SDF system, the effective damping β_{eff} of the SDF system can be found as follows,

$$\beta_{eff} = \beta_0 + \beta_v = \beta_0 + \frac{W_d}{4\pi W_k} \tag{2.12}$$

in which, β_0 and β_v are the inherent and supplemental linear viscous damping respectively; W_d (or E_d) and W_k are the energy dissipated by the dampers and maximum strain energy in the frame, respectively. According to the linear static procedure in Section 14.3.1 of ASCE 41-13 (ASCE/SEI 2014) and Section C9.3.5.1 of FEMA 274 (FEMA 1997), the effective damping ratio of a multi-story building equipped with diagonal brace-type fluid viscous devices with same α can be computed as follows,

$$\beta_{eff} = \beta_0 + \frac{T_f^{2-\alpha}\lambda\sum_j C_{di,j}\left(\phi_{rj}\cos\theta_j\right)^{1+\alpha}}{\delta_t^{1-\alpha}\left(2\pi\right)^{3-\alpha}\sum_i\left(\frac{w_i}{g}\right)\phi_i^2} \tag{2.13}$$

in which, T_f is the fundamental period of the bare frame; λ is a function of velocity exponent α, which can be computed numerically or obtained from Table C9-4 of FEMA 274 (or in Equation

2.4); $C_{di,j}$ is the damping constant for device j; ϕ_i is the first mode displacement in floor i, which is normalized to the unity at roof level. ϕ_{rj} is the first mode relative displacement between ends of the device i in the horizontal direction; θ_j is the inclination angle of device j to the horizontal; δ_t is roof displacement; w_i is the seismic weight of floor level i; g is the gravitational acceleration. The target roof displacement δ_t can be obtained as follows,

$$\delta_t = \Gamma_f \phi_i S_d(T_f, \beta_{eff}) \tag{2.14}$$

in which, Γ_f is the mass participation factor; $S_d(T_f, \beta_{eff})$ is the damped spectral displacement at fundamental the period T_f. This displacement can be computed by multiplying the elastic 5% damped displacement spectra at the fundamental period of the building, $S_d(T_f, \beta_{5\%})$ with a modification factor B,

$$B = \frac{S_d(T_f, \beta_{eff})}{S_d(T_f, \beta_{5\%})} \tag{2.15}$$

Note that if NVDs are assumed as fluid viscous devices as in Equating 2.13 the effect of axial stiffness of NVDs is neglected. Although the stiffness effect of linear viscous dampers is well known (Constantinou et al. 1998), and accounted in simplified procedures (FEMA 1997; Constantinou et al. 2001), the stiffness of nonlinear viscous dampers is often neglected (Ramirez et al. 2001).

2.4.2 Performance Curves

A commonly used simplified design method for passive control devices is the so called "performance curves" (Kasai et al. 2008b). Performance curves are constructed by computing and plotting the dynamic peak responses of SDF shear systems with dampers by tuning the corresponding damper parameters. In theory, performance curves rely on the same principles of linearization methods as in ASCE 41-13 (ASCE/SEI 2014). However, the advantage of

performance curves is that the estimated damped system responses can readily be computed in terms of reduction factors for the given damper parameter. Thus, this method provides to a designer a simple graphical tool for selecting optimal properties of the desired damping system. Furthermore, effective damping and period formulations used in the linearization method account for the NVD's and OD's stiffness. Performance curves have been initially developed for yielding and viscous/viscoelastic devices (Fu and Kasai 1998; Kasai et al. 1998; Kasai and Ito 2005). More recently, they were extended to nonlinear viscous (fluid) dampers and oil dampers with relief valve (Kasai et al. 2007; Kasai et al. 2008a).

Performance curves are constructed by examining the dynamic response of SDF shear systems with dampers and utilizing linearization methods. Figure 2.8a shows the SDF response of a bilinear dashpot under sinusoidal dynamic excitation with a damping coefficient C_d, relief load F_{dr}, and post-relief damping coefficient ratio p. Figure 2.8b illustrates a bilinear oil damper as a Maxwell model by accounting for the combined damper axial stiffness, K_b^*, which includes the stiffness of the damper portion, K_d and that of the supporting brace, K_b. Finally, as a representative of a SDF building equipped with bilinear oil damper, Figure 2.8c illustrates a building equipped with oil dampers that is represented as a frame with elastic stiffness, K_f connected in parallel with a bilinear oil damper. The graphical definition of dynamic stiffnesses, such as loss (K_d'', K_a'', K'') and storage stiffnesses (K_d', K_a', K') of each case are illustrated. Not that the storage stiffness $K_d' = 0$ in the first case. Kasai et al. (2008a) compared the three systems above and computed the effect of K_d''/K_f and K_b/K_f ratios on the SDF system response. Based on this assessment they developed performance curves for bilinear oil dampers in terms of displacement-force reduction (R_d and R_a) with respect to undamped bare frame as shown in Figure 2.8b. The performance curves for bilinear oil dampers are constructed as a function of the

damper properties to be utilized. Therefore, engineering judgment is required initially to adequately estimate the damper properties to be used, which are mainly related to the fundamental period of the structure under consideration. These properties are the frame frequency, ω_f, the stiffness-to-damping coefficient ratio of the internal damper, β_k, the post-relief damping coefficient ratio, p and the peak damper velocity ratio μ_d.

Referring to Figure 2.8, the performance curves are constructed for $\omega_f/\beta_k = 0.33$, $p = 0.05$, $\mu_d = 2$. It is assumed that the fundamental period of the building lies within the constant pseudo-velocity spectrum region. Figure 2.8a illustrates the variation of the effective damping and effective period with respect to K_d''/K_f and K_b/K_f ratios. The higher the supporting brace stiffness of the damper (K_b) the higher the effective damping ratio becomes. This reduces the relative displacement and absolute acceleration demands. Referring to Figure 2.8a, if oil dampers are treated as fluid viscous devices (i.e., K_b and $\beta_k = \infty$) this assumption may significantly overestimate the supplemental damping. In reality the both K_b and K_d have a finite value and they can be computed based on available damper sizes. Furthermore, increasing K_d''/K_f may not be always beneficial. In an overly damped system story shear forces/ floor absolute accelerations as well as displacements may increase. Consequently, the key point in the damper design is the appropriate selection of K_d''/K_f and K_b/K_f ratios for the given building to achieve the desired performance objectives.

2.4.3 Performance-Spectra (P-Spectra)

More recently, performance spectra method was developed by Guo and Christopoulos (2013a) as extension of performance curves method to include the effect of nonlinearity of the frame to be retrofitted. The P-Spectra method was initially generated by obtaining the peak response quantities from NRHA of SDF systems with various damper properties. Later, by using

enhanced equivalent linearization methods, Guo and Christopoulos (2013b) developed a procedure for generating P-Spectra compatible with code-based uniform hazard spectra. In addition to response reduction predictions, the P-Spectra method provides estimation for the expected permanent deformations of a frame building with dampers.

2.5 Seismic Performance of Existing Tall Buildings

There are several existing steel tall buildings that were designed prior to 1990s (CTBUH 2016). In the West Coast of the US, steel moment-resisting frames (MRFs) were the most commonly used lateral load resisting system in high-rise buildings constructed between 1960 and 1990 in seismic areas, particularly those with above 35 stories (Almufti et al. 2012). These buildings do not meet today's basic capacity design principles. These include the strong column/weak beam ratio, panel zone strength requirements, prequalified beam-to-column connection detailing, as well as, column splicing detailing and weld deficiencies. The 1994 Northridge and 1995 Kobe earthquakes highlighted several deficiencies associated with the beam-to-column connection performance (Bonowitz and Youssef 1995; Mahin 1998; FEMA 2000b; Nakashima et al. 2000). Past experimental studies indicated that column splices with partial joint penetration (PJP) groove welds in thick assemblies compromise their behaviour under cyclic loading (Bruneau and Mahin 1990). Moreover, panel zone design requirements have also been revised over the past few decades (Krawinkler et al. 1975; FEMA 2000b).

Recent experimental and numerical studies (Nakashima et al. 2007; Lignos et al. 2013; Elkady and Lignos 2014) suggests that current strong column/weak beam design requirements are not sufficient to prevent soft story mechanisms at low probability of occurrence earthquakes. This is due to the additional flexural demands from the composite action and the steel material cyclic hardening.

Unlike what ASCE 41-13 (ASCE/SEI 2014) suggests, recent experimental studies (Elkady and Lignos 2016; Lignos et al. 2016; Suzuki and Lignos 2016) showed that seismically compact columns in steel frame buildings can accommodate appreciable plastic deformations without experiencing sudden loss of their axial load carrying capacity stability even under high axial loads. This is directly related to steel columns in bottom stories of tall buildings.

One of the earlier studies on the seismic evaluation of existing tall building prior to Northridge Earthquake were conducted by Anderson and Bertero (1989). This study was carried out to simulate the seismic response of an instrumented 42-story building located in San Francisco during the Loma-Prieta Earthquake. The building did not experience any damage. The 168 m (55 ft) tall office building with a rectangular 24 to 46 m (79 by 151 ft) floor plan was designed in 1972. The study reveals some of the typical design characteristics of tall buildings designed in this period. For instance, the lateral load consists of moment–resisting space frame. The beams were made up with rolled W sections and built-up members using A36 steel. Steel columns were made of welded box sections. In the bottom 33 floors the columns were fabricated from A572 Grade 42 steel, while in the upper floors A36 steel was used. The box sections varied from 51 by 51 cm (20 by 20 in.) to 66 by 66 cm (26 by 26 in.) with wall thickness ranging from 1.3 to 7.9 cm (1/2 to 3 1/8 in.). According to a three-dimensional simulation of the building the fundamental period of the building was found to be 5.8 sec. The response history analysis of the building model indicated that this building remained entirely linear elastic during the earthquake.

After the 1994 Northridge earthquake, many researchers studied multi-story pre-Northridge steel MRF buildings to assess their seismic vulnerability (Maison and Bonowitz 1999; Gupta and Krawinkler 2000; Luco and Cornell 2000; Lee and Foutch 2002). Most of these studies were conducted as part of the FEMA/SAC project. For instance, Maison and Bonowitz (1999)

presented a procedure for modeling, analysis and evaluation of existing steel MRF buildings with pre-Northridge connections by incorporating the knowledge gained from researches conducted aftermath of Northridge earthquake. Gupta and Krawinkler (2000) demonstrated a process to predict roof and story drift demands of frame structures by utilizing the spectral displacement at the fundamental structural period and incorporating the effects of higher modes, inelasticity, and P-delta. Luco and Cornell (2000) studied the effects of beam-to-column connection fractures on the story drift demands. To this end, sensitivity studies were carried out with various fracturing scenarios and parameters of brittle beam-to-column connections. Lee and Foutch (2002) conducted a comparative research on the performance evaluation of existing steel MRF buildings with brittle pre-Northridge beam-to-column connections, which were designed in accordance with the 1973, 1985, and 1994 UBC provisions.

More recently, Krishnan et al. (2006) assessed the seismic performance of two 18-story steel MRF buildings located in South California, which were designed in accordance with UBC 1982 (ICBO 1982) and UBC 1997. The seismic assessment of buildings was based on two possible earthquake scenarios expected in the region. The NRHA results indicated that the older building suffered severe damages and was likely to experience collapse. Although the newer building performed relatively better, it did not satisfy the life safety performance objective. Muto and Krishnan (2011) extended the work by Krishnan et al. (2006) by considering the effect of building orientations and different modeling approaches for beam-to-column connections to analyse the uncertainty in the performance of pre-Northridge beam-to-column connections.

The buildings in the aforementioned studies were not taller than 20 stories. Furthermore, the case study buildings were not space MRFs, which were often used in the design of tall buildings in 1970s in the West Coast of North America. More recently, Almufti et al. (2012) conducted a

seismic assessment on a prototype 40-story space MRF building, which was designed in accordance with UBC 1973 (ICBO 1973). A 3-dimensional nonlinear model of the building was developed to assess the performance of the building via NRHA. The study concluded that under a maximum considered earthquake (MCE) the building was expected to suffer severe structural and non-structural damage, exceed life safety limits or collapse. The authors stated that direct enhancement of structural deficiencies only would not be enough to improve the seismic performance and reduce transient and residual deformations dramatically. The study recommended exploring more efficient retrofit solutions, such as adding stiffness, supplemental damping or combination of these.

Bech et al. (2015) conducted a seismic assessment of three high-rise pre-Northridge existing steel MRF buildings in San Francisco, California. The aim of the study was to propose changes to steel column force-controlled evaluation criteria of ASCE 41-13 (ASCE/SEI 2014), which does not permit plastic deformation in columns with high axial loads by examining the demand on the columns in the existing buildings. For instance, among these buildings, 38-story building was designed in early 1970's. The natural periods of vibration were found to be 5.4 sec and 4.5 sec in both translational directions. The maximum compressive demand to capacity ratio (P_g/P_{cl}) of column due to gravity loads was 0.41. According to NRHA results, the building developed a weak story mechanism at about its mid-height. From the evaluation of demands in columns Bech et al. (2015) showed that columns in the existing buildings exhibited limited plastic rotation (<0.01rad) with axial demand to capacity ratio less than unity, which is an acceptable behaviour according to past experimental research conducted with columns under high axial loads. Thus, Bech et al. (2015) concluded that current ASCE 41-13 (ASCE/SEI 2014)

force-controlled criteria are too conservative and may lead to unnecessary and costly retrofit solutions.

More recently, Wang et al. (2017) carried out a seismic assessment of a 35-story existing pre-Northridge steel building, located in San Francisco, California. The building was designed in 1960s and its lateral force- resisting system consisted of space MRFs with a typical beam span of 9.15 or 9.35 m. Built-up box sections, H-sections and H-box sections were employed for the columns. The steel beams were made up with built-up and wide-flange sections. The building's fundamental natural periods were 4.70 sec, 4.53 sec and 4.15 sec in X-translational, Y-translational and torsional vibrations, respectively. The axial load demand to capacity ratio of columns was about 30 - 40% due to gravity loading. Tier-3 evaluation procedure was conducted as per ASCE 41-13 (ASCE/SEI 2014) via NRHA with two Basic Safety Earthquake Levels (BSE-1E and BSE-2E). According to this evaluation, the building was found seismically deficient, because the median peak story drift ratio was about 10% at both hazard as a result of side-sway mechanism occurred over the 4^{th} to 8^{th} stories. Furthermore, the lower half columns of the building experienced high compression forces. In exterior columns, the mean peak demand-capacity ratio reached up to unity. Similarly, tensile forces were large in these columns and resulted in widespread fractures of PJP splice weld connections.

2.6 Retrofit for Existing Tall Steel Moment-Resting Frame Buildings

In spite of the seismic deficiencies and damages observed in past earthquakes, many pre-Northridge steel buildings remained non-retrofitted due to financial challenges and reluctance of their owners (Bjornsson 2014). However, recent studies showed clearly the necessity of seismic upgrade for this type of buildings (Bech et al. 2015; Hutt et al. 2016; Wang et al. 2017).

Conventional upgrade techniques for tall buildings, such as stiffening (e.g., by adding steel braces), generally leads to an increase of the seismically-induced forces; often times the strengthening of framing members as well as the foundation is inevitable (Bjornsson 2014). Energy dissipation devices, such as velocity-dependent dampers may be effectively utilized in this case. For instance, fluid viscous dampers have been implemented in various buildings in North America (Constantinou et al. 1993; Symans and Constantinou 1998; Uriz and Whittaker 2001; Symans et al. 2008; Malley et al. 2011; Kyriakopoulos and Christopoulos 2013). As an alternative solution to fluid viscous dampers, oil dampers with relief valve have been widely used in several buildings in Japan. Recent shake-table tests indicated the effectiveness of such devices (Kasai and Matsuda 2014). In addition to this, tall buildings with oil dampers demonstrated a high seismic performance during the 2011 Tohoku earthquake in Japan (Kasai et al. 2013b).

Recent studies with seismically deficient existing tall buildings in the West Coast of US demonstrated the implementation of several retrofit solutions, such as conventional and buckling-restrained braces (Bjornsson 2014), nonlinear fluid viscous dampers (Lai et al. 2015), base isolation and elastic rocking wall spine (Hutt et al. 2016).

Bjornsson (2014) retrofitted a 20-story pre-Northridge steel case study building that was located in the greater Los Angeles metropolitan area with perimeter MRFs designed based on the 1994 Uniform Building Code. Bjornsson (2014) implemented multiple retrofit strategies to improve the seismic performance of the same building. Bjornsson (2014) added conventional or buckling-restrained steel braces to the existing building and following multiple retrofit schemes. This study indicated that the use of conventional or buckling-restrained steel braces effectively reduces the structural damage. It was noted that in the aftermath of a major earthquake it is not

clear if the damage induced to the conventional braces provide proper resistance in an aftershock.

Lai et al. (2015) proposed a retrofit strategy for a 35-story steel building (Wang et al. 2017) with fluid viscous dampers. Multiple conventional and non-conventional retrofit strategies were explored. For instance, before implementing fluid viscous dampers, the heavy exterior cladding that attracts seismic inertia forces were replaced with a lightweight curtain wall system and all the column splices were upgraded. For the damper placement, conventional damping distribution methods were utilized, namely a uniform, stiffness and shear force proportional. The amount of required damping was initially computed based on a targeting 1% peak roof drift ratio and a simple effective damping formulation given in Equation 2.13 was used, which neglects the effect of supporting stiffness and assumes that floor deformations are only attributed to shear deformations. Nevertheless, during the damper placement, the strategy proposed by Kasai et al. (2013a) were used to minimize the effect of flexural deformation on the damper efficiency. A sensitivity study with several supporting stiffness ratios and velocity exponents was implemented to find the optimal solution. The dampers were modeled by utilizing the *ViscousDamper* material, which is presented in Chapter 3 of this thesis. It was shown for brace stiffnesses larger than $2K_f$ the reduction in EDPs was not substantial. Therefore, considering the cost-benefit increasing the stiffness further was not found to be effective. The seismic performance assessment was carried out as per ASCE 41-13 at the BSE-1E and BSE-2E hazard levels. The outcome of the study showed that the retrofit reduces engineering demands parameters and number of connection fractures. However, to enable such mitigation large damper sizes were required. In order to reduce the damper sizes and for a more refined damper design and placement simplified optimization methods were later implemented via cost-benefit analysis.

Hutt et al. (2016) proposed retrofit techniques to increase the resilience of the 40-story MRF building mentioned which was found to be significantly vulnerable by Almufti et al. (2012). In order to reduce earthquake-induced transient and residual deformations, Hutt et al. (2016) constructed an elastic spine with steel bracing in the core. Alternatively, a base isolation system was implemented at the ground level. In addition to structural retrofit, non-structural enhancement was considered to reduce the earthquake-induced losses. As a consequence, up to a 92% reduction was obtained in loss estimation in comparison to the existing building.

2.7 Summary

This chapter presented the state-of-the-art in numerical modeling of three main damper types that are typically used in building applications to mitigate the effects of earthquake and wind-induced vibrations. Although several models exist the challenge of utilizing stable numerical integration schemes to compute the numerical solution of the equilibrium equations within nonlinear viscous and oil dampers without the use of small integration steps still remains. Currently available numerical models for buckling-restrained braces treat such devices as displacement-dependent. Therefore, the rate-dependence that is observed in low-yield stress steel materials tends to be ignored. Available methodologies for the design and evaluation of buildings designed with supplemental damping devices contain a number of limitations because they have not verified with comprehensive full-scale shake table experiments with buildings equipped with such devices. Prior studies associated with the dynamic response of high-rise steel-frame buildings designed between 1970s-1990s in seismically prone regions underscore their seismic deficiencies due to the lack of capacity-design principles as well as poor construction practices at the time of construction. Several researchers have attempted to retrofit such buildings with a variety of conventional and non-conventional techniques. The use of oil dampers that contain a valve relief

and therefore cap the forces transferred to framing members of the existing building seems to be promising; however, it has not been adequately explored.

Table 2.1: Structural applications of fluid viscous devices in Canada (from Taylor Devices).

Name and type of the structure	Location	Type and Number of Dampers	Date	Load	Additional Information
Quebec Iron and Titanium Smelter	Tracy, QC	Taylor Spring Dampers and Taylor Dampers Total: 22 450 kN ± 64mm stroke 225 kN ± 100mm stroke 130 kN ± 100mm stroke	1997	Seismic & Wind	Dual purpose spring dampers were used for seismic and wind protection of two smelter buildings. Dampers were used to prevent buildings from impacting during a seismic event.
New Westminster, BC Police Building	New Westminster, BC	Taylor Fluid Dampers Total: 12 890 kN ± 70mm stroke	2001	Seismic	Retrofit of a 4-story concrete frame/shear wall building built in 1939. Dampers were used in chevron braces inside new steel moment frames to balance irregularities in the building's stiffness.
BCBC Pandora Wing	Victoria, BC	Taylor Fluid Dampers Total: 76 220 kN ± 57mm stroke 130 kN ± 57mm stroke	2002	Seismic	Retrofit of a 7-story concrete frame/shear wall building built in 1974. Dampers were used in chevron braces.
Pearson Airport Control Tower	Toronto, ON	Taylor Fluid Dampers Total: 8 31 kN ± 89mm stroke	2003	Wind	New air traffic control tower uses dampers as part of a tuned mass damper to reduce motion caused by wind.
Whalley Reservoir	Surrey, BC	Taylor Fluid Dampers Total: 17 1000 kN ± 125mm stroke	2007	Seismic	Dampers surround this in-ground reservoir to control seismic drift of concrete lid.
Steel Mill Project	Tracy, QC	Taylor Lock-Up Devices Total: 8 200 kN ± 75mm stroke	2008	Seismic	Expansion of an existing steel structure. Lock up devices used to control seismic movement while allowing free thermal movement.
Red Hill Creek Pedestrian Bridge	Hamilton, ON	Taylor Viscous Dampers Total: 10 1 kN ± 50mm stroke	2010	Seismic	Tuned mass dampers were designed to control the effects of wind on the Pedestrian Bridge.
Mann Bridge	Coquitlam, BC	Taylor Viscous Dampers Total: 146 2200 kN ± 50mm stroke 2200 kN ± 75mm stroke 2600 kN ± 418mm stroke 2700 kN ± 50mm stroke 3200 kN ± 100mm stroke 3500 kN ± 160mm stroke	2010	Seismic	New cable-stayed bridge uses Fluid Viscous Dampers in approach spans between piers and deck to dissipate seismic energy. This replacement bridge (replaces aging, tied-arch bridge) boast a 470 meter main span, the 2nd longest in the Western Hemisphere, and a 50 meter wide deck - the widest of any cable stayed bridge in the world.
Alexandra Bridge	Ottawa, ON	Taylor Viscous Dampers Total: 8 1 kN ± 100mm stroke	2010	Pedestrian	This circa 1901 railway bridge was converted to a auto and pedestrian traffic in the 1970's. The tuned mass dampers were found to be required after a spike in pedestrian traffic caused excessive vibration during the July 1st "Canada Day" festivities.
RCMP Richmond Community Safety Building	Richmond, BC	Taylor Dampers Total: 20 600 kN ± 100mm stroke	2011	Seismic	This project is to upgrade to post-disaster standards and to renovate the existing building to accommodate the new RCMP Richmond Headquarters.
Newton Reservoir	Surrey, BC	Taylor Viscous Dampers Total: 16 1000 kN ± 50mm stroke	2011	Seismic	
DEH Cho Bridge	Northwest Territories	Taylor Lock up Devices Total: 40 739 kN ± 270mm stroke	2011	Seismic	This cable-stayed, new bridge will span the Mackenzie River near Fort Providence and is intended to replace the operations of the Merv Hardie Ferry & the Mackenzie Ice Crossing, available to link for all seasons.
BC Place Stadium	Vancouver, BC	Taylor Viscous Dampers Total: 96 2000 kN ± 60mm stroke 1500 kN ± 50mm stroke	2011	Seismic	Retrofit of football stadium for seismic protection and to act as an emergency shelter for Vancouver, BC.
LaSalle Bridge	Kingston, ON	Taylor Viscous Dampers Total: 2 378kN, 355 mm	2016	Bridge Movement	Hydraulic energy absorption for protection from overspeed impacts.

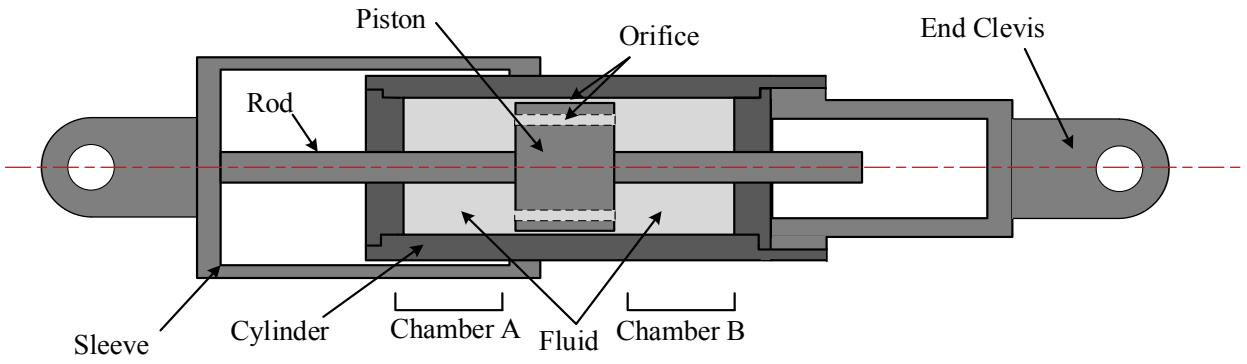

Figure 2.1: Typical cross-section of a double-ended fluid viscous damper

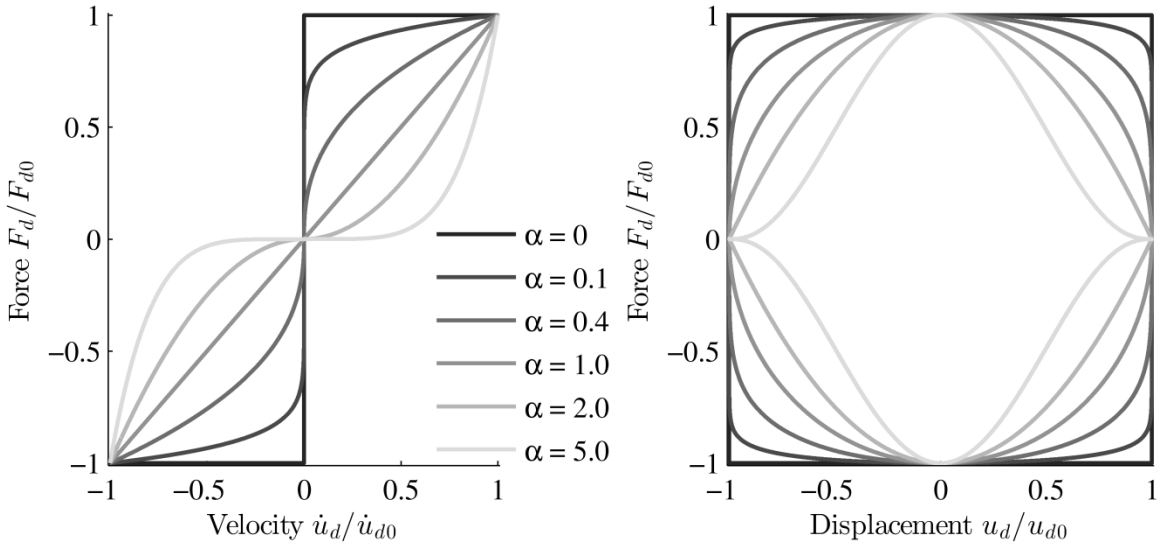

(a) (b)

Figure 2.2: (a) Force-velocity (b) Force displacement relationship of nonlinear viscous dampers possessing various velocity exponent subjected to sinusoidal motion

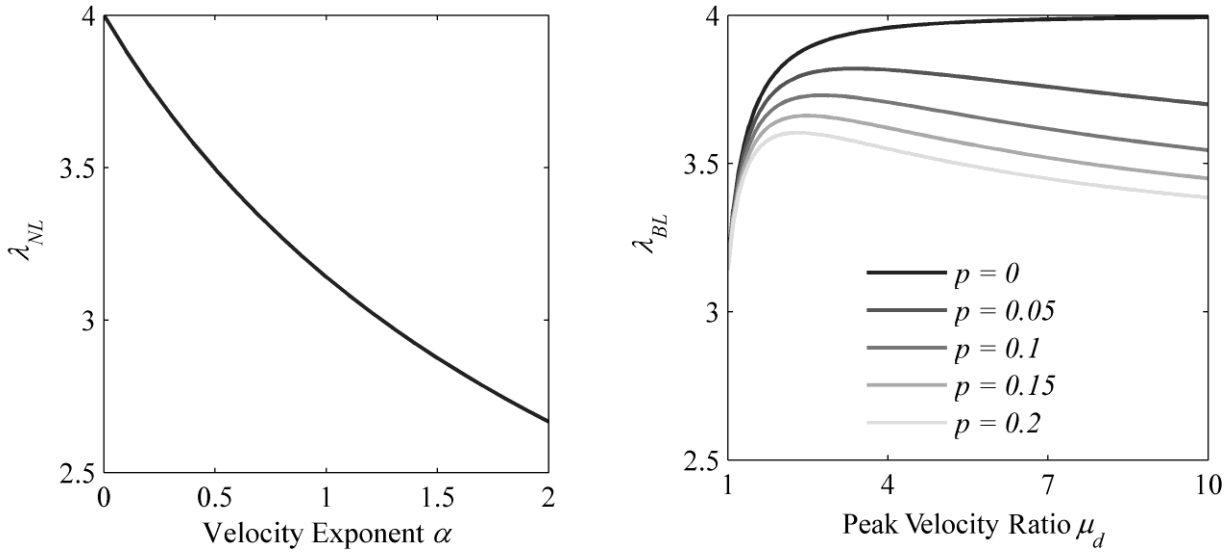

(a) (b)

Figure 2.3: The effect of parameters on the quality factor λ_{NL} *and* λ_{BL} for a) nonlinear b) bilinear viscous models, respectively

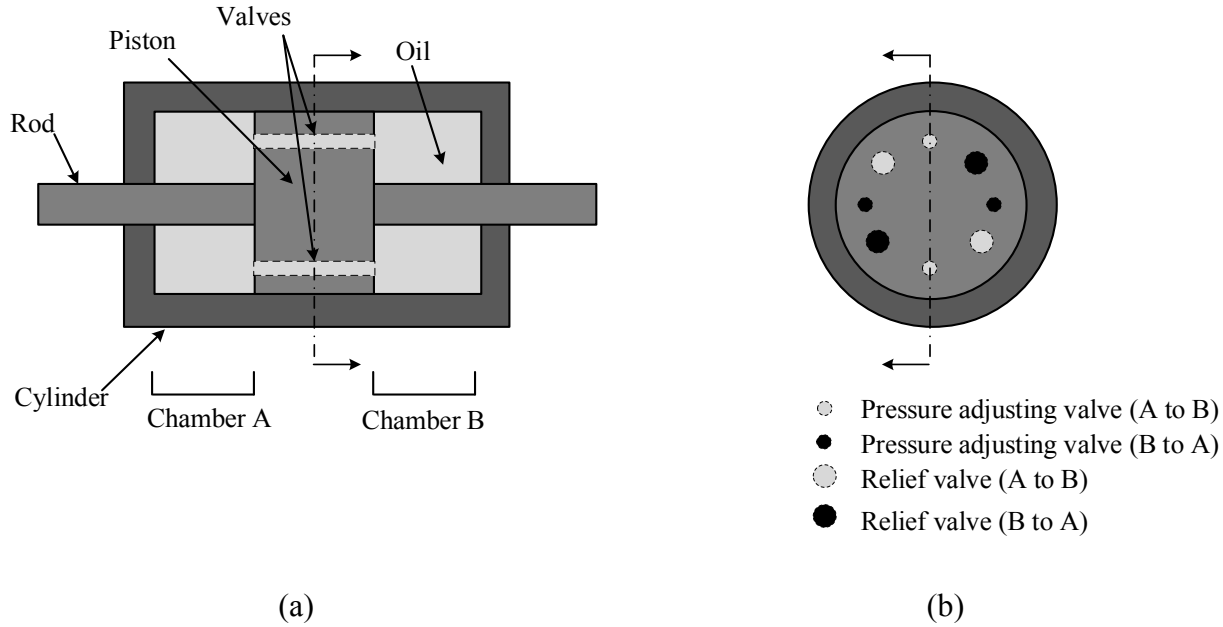

(a) (b)

Figure 2.4: Mechanism of a typical oil damper

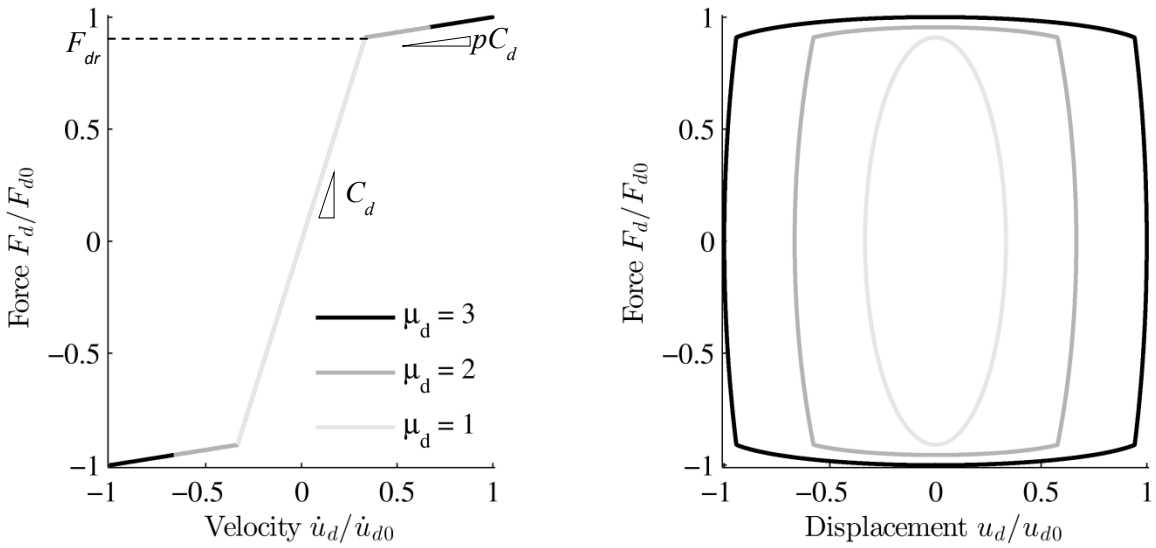

(a) (b)

Figure 2.5: (a) Force-velocity (b) Force displacement relationship of bilinear viscous dampers subjected to sinusoidal motion with incremental amplitudes

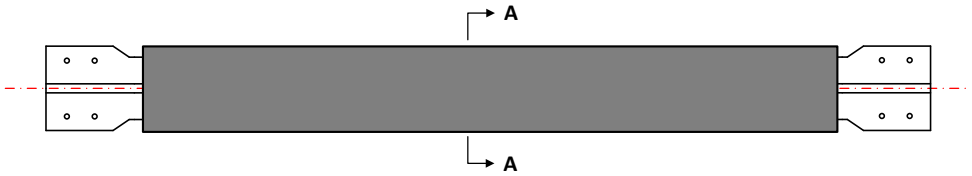

(a) Buckling-restrained brace: Steel brace and its buckling restrainer

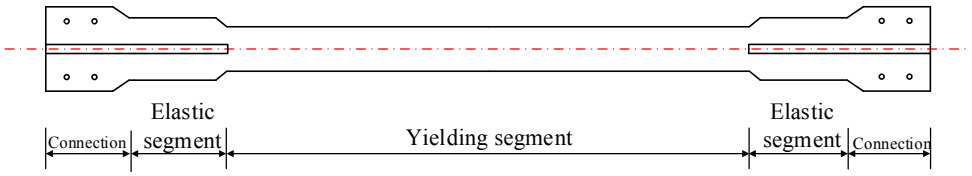

(b) Components of steel brace

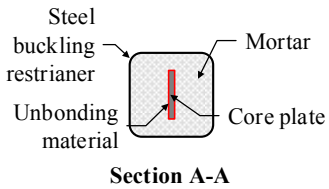

(c) BRB cross section at yielding segment

Figure 2.6: Typical design of a buckling-restrained brace

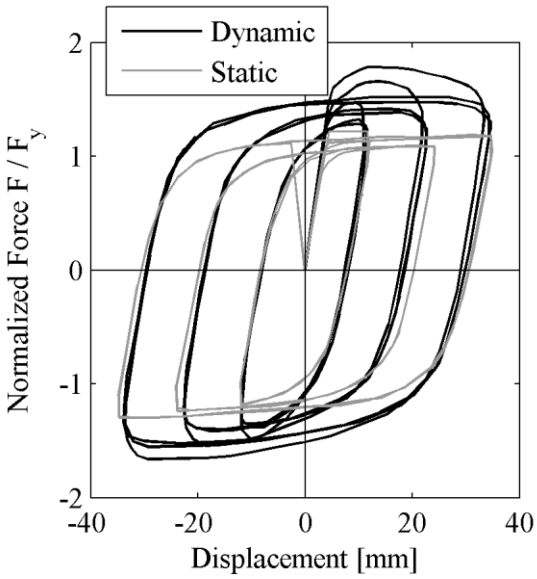

Figure 2.7: Static and dynamic test results of BRB specimens fabricated with LYP225 steel (E-Defense 2008)

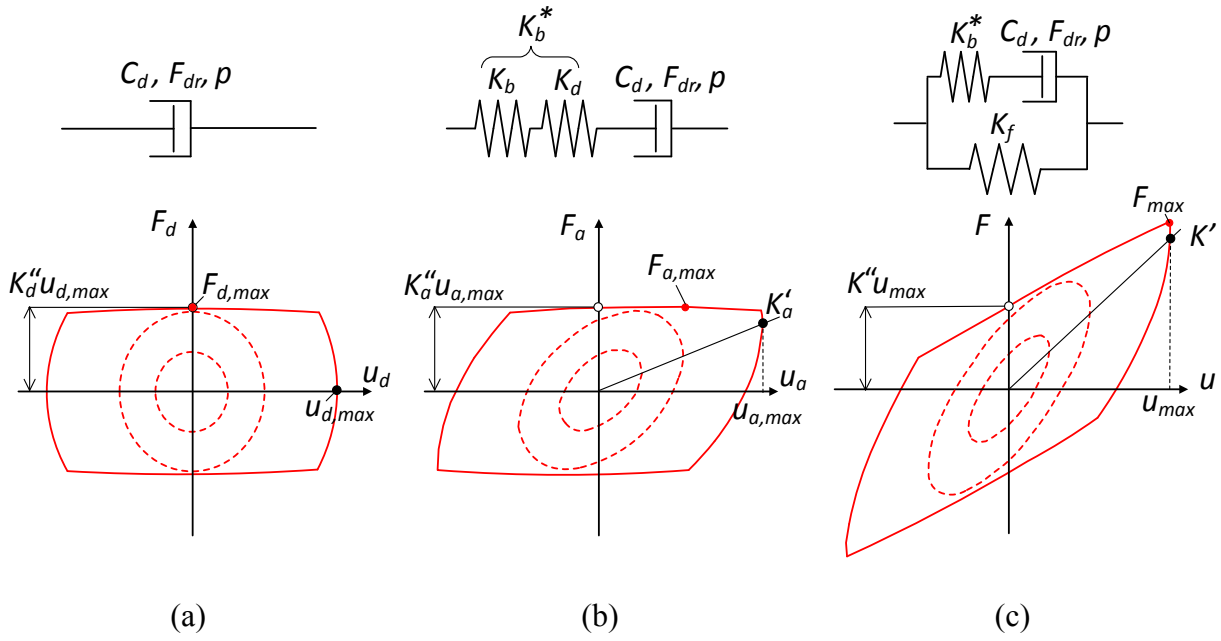

Figure 2.8: a) Bilinear dashpot only b) Maxwell c) Maxwell and frame combined

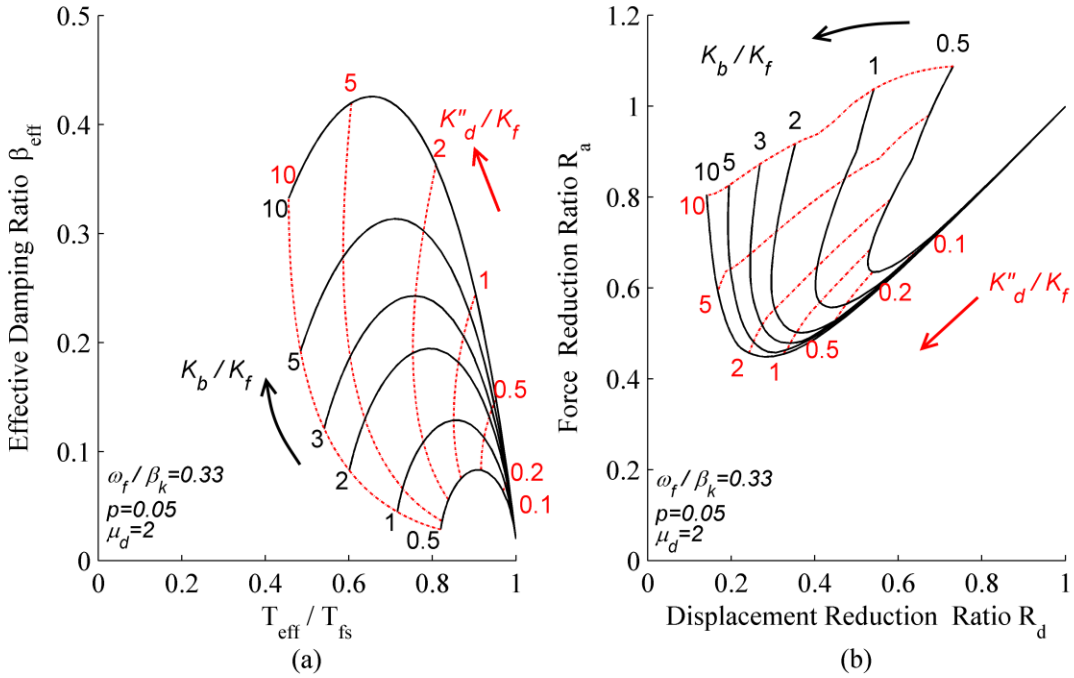

Figure 2.9: Performance curves for bilinear oil damper

CHAPTER 3 : Adaptive Numerical Method Algorithms for Nonlinear Viscous and Bilinear Oil Damper Models Subjected to Dynamic Loading

3.1 Introduction

In the past three decades various types of supplemental damping devices have been developed and utilized in frame buildings to control seismic and wind-induced vibrations (Constantinou and Symans 1993a; Soong and Dargush 1997; Christopoulos and Filiatrault 2006; Black and Makris 2007; Symans et al. 2008; Dong et al. 2015). To this end, viscous dampers are advantageous as the forces they develop are typically out-of-phase with displacement-induced forces within a frame building under earthquake loading (Constantinou et al. 1998). Recent earthquakes around the world have demonstrated the effectiveness of viscous dampers in response modification of conventional buildings to control structural and non-structural damage (Buchanan et al. 2011; Miranda et al. 2012; Kasai et al. 2013b).

For the successful implementation of viscous dampers into the earthquake engineering design practice the availability of mathematical models that represent accurately the hysteretic response of such devices is necessary. Furthermore, rigorous integration methods are essential for the numerical solution of these models when nonlinear response history analysis (NRHA) is

conducted. Unlike observed in solid viscoelastic dampers (Chang et al. 1995) the temperature dependency of fluid viscous dampers is relatively low (Kasai et al. 2004c; Symans et al. 2008). In contrast with the idealized assumption of purely viscous dashpot models, viscous dampers show stiffness dependency characteristics that generally undermine the effectiveness of a viscous damper (Makris and Constantinou 1991). A number of researchers, have studied the effect of axial stiffness of viscous dampers on the seismic performance of frame buildings (Constantinou et al. 2001; Singh et al. 2003; Chen and Chai 2011; Liang et al. 2011; Londoño et al. 2013), but they mainly focused on linear viscous dampers. In the case of nonlinear viscous dampers, a common practice has been to neglect the damper axial stiffness (Pekcan et al. 1999; Ramirez et al. 2001; Lin and Chopra 2002; Hwang et al. 2008; Diotallevi et al. 2012). This is a convenient assumption because a closed-form analytical solution of the damper force can be computed when NRHA is employed. Recent shake table experiments of a full-scale 5-story steel frame building equipped with viscous dampers that were conducted at the world's largest shake table around the world (Ooki et al. 2009; Kasai and Matsuda 2014) demonstrated that the consideration of the damper axial stiffness is critical in order to accurately predict both local and global seismic demands of the test structure (Kasai et al. 2007; Kasai and Matsuda 2014). Furthermore, a blind analysis contest that was conducted to challenge the existing modeling capabilities for steel frame buildings equipped with various types of dampers demonstrated that in the case of viscous dampers incorporating the brace and damper axial stiffness improves the overall prediction accuracy by more than 20% compared to the experimental data (Yu et al. 2013). Several researchers have proposed ways to account for the stiffening and frequency dependency of viscous dampers and to compute numerically their hysteretic response under harmonic and seismic excitations by employing the Maxwell model (Makris and Constantinou 1991;

Constantinou and Symans 1993a; Reinhorn et al. 1995; Takahashi and Sekiguchi 2001; Oohara and Kasai 2002; Singh et al. 2003). Typical fixed time-step integration algorithms that have been employed to obtain numerically the viscous damper hysteretic response may require considerably small integration steps to overcome convergence problems (Oohara and Kasai 2002). In particular, numerical convergence may still be a challenge for frame buildings equipped with nonlinear viscous dampers with high axial stiffness and small velocity exponents (Oohara and Kasai 2002). In such cases, smaller integration time step for the overall analysis is necessary. This reduces the computational efficiency of the analysis of building models with nonlinear viscous dampers. This may also be a fundamental constraint for the optimal seismic design and/or retrofit of frame buildings with nonlinear viscous dampers in which the locations as well as the damper sizes should be explicitly identified as part of the optimization problem (Lavan et al. 2008; Lavan and Avishur 2013). It is understood that improved integration algorithms should be utilized to reliably obtain the numerical solution of nonlinear viscous damper models. These algorithms should be computationally efficient when they are employed in NRHAs of large-scale structural systems equipped with viscous dampers.

This paper discusses the numerical implementation of an improved adaptive algorithm for the numerical solution of the constitutive equations of nonlinear viscous and bilinear oil damper material models under dynamic loading when the axial stiffness of the dampers is considered as part of the numerical solution. The efficiency of the proposed algorithm is compared with that of traditional integration schemes that are typically used for the numerical solution of initial value problems. The proposed numerical solution techniques are implemented in an open-source finite element simulation platform and are validated with full-scale component experiments on nonlinear viscous and bilinear oil dampers under sinusoidal excitations and various loading

frequencies. Furthermore, experimental data from a 5-story steel building with the same damper types that was tested at full-scale is utilized to demonstrate the efficiency of the proposed adaptive numerical method techniques in predicting global and local engineering demand parameters of frame buildings equipped with supplemental damping devices.

3.2 Hysteretic Behaviour of Viscous Dampers as Pure Viscous Models

Viscous dampers contain a polymer liquid and its flow through orifices leads to pressure differential across a piston head, which produces the damper force. The design of orifice dictates the relationship between the force and velocity. Thus, the general force-velocity relationship of nonlinear viscous models can mathematically be expressed as given in Equation (3.1) (Symans and Constantinou 1998),

$$F_d(t) = C_d \left|\dot{u}_d(t)\right|^{\alpha} \operatorname{sgn}\left(\dot{u}_d(t)\right) \tag{3.1}$$

in which, C_d is the damping coefficient and α is the velocity exponent that characterizes the viscous material; u_d is the displacement of the dashpot; and sgn represents the signum function. Thus, the peak force F_{d0} of a viscous damper under a harmonic displacement excitation that is described as $u_d(t) = u_{d0}\sin(\omega t)$, is as follows,

$$F_{d0} = C_d(\omega u_{d0})^{\alpha} \tag{3.2}$$

in which, u_{d0} and ω are the peak displacement amplitude and the circular frequency of the sinusoidal excitation, respectively. Figure 3.1 shows the normalized force-velocity and normalized force-displacement relations of nonlinear viscous models with different α values. A typical Bernoullian cylindrical shaped orifice produces forces, which are proportional to the square of the velocity (i.e., $\alpha = 2$). Such dampers are utilized for shock wave absorption. For $\alpha = 1$, a viscous damper becomes linear while for $\alpha = 0$ the force-displacement hysteretic relation

of a viscous damper becomes rectangular, which is typical for friction models (Pall and Marsh 1982). For seismic design applications of frame buildings the capability of limiting the damper force output under high velocity pulses is often desirable. Therefore for seismic applications, α should be selected such that $\alpha < 1$. Because linear viscous dampers produce forces that vary linearly with respect to the velocity demand, large damper forces may be generated under high velocity demands. This introduces uncertainties and conservatism in the capacity design of non-dissipative members. In order to overcome this undesirable response, bilinear oil dampers were developed that contain a relief mechanism, which suppresses the force after a certain limit (Ichihasi et al. 2000; Kasai and Nishimura 2004; Kasai et al. 2004c; Tsuyuki et al. 2004). This creates a bilinear relation between the damper force and velocity as shown in Figure 3.2a. Thus, the force produced by a bilinear viscous damper can be computed as follows,

$$F_d(t) = \begin{cases} C_d \acute{u}_d(t), & |F_d(t)| \le F_{dr} \\ \text{sgn}(\acute{u}_d(t)) F_{dr} + p(\acute{u}_d(t) - \acute{u}_{dr}), & |F_d(t)| > F_{dr} \end{cases} \tag{3.3}$$

in which, p is the post relief damping coefficient ratio; F_{dr} and $\acute{u}_{dr}$ are the relief force and velocity of the bilinear oil damper, respectively. The peak force F_{d0} of a bilinear viscous damper under sinusoidal displacement excitation $u_d(t) = u_{d0}\sin(\omega t)$ can be computed as follows,

$$F_{d0} = \left(p + \frac{1-p}{\mu_d} \right) C_d \omega u_{d0} \tag{3.4}$$

the peak damper velocity ratio, μ_d of a bilinear viscous damper, which is defined as the ratio of maximum velocity demand over the damper relief velocity can be computed as follows,

$$\mu_d = \frac{\acute{u}_{d0}}{\acute{u}_{dr}} = \frac{\omega u_{d0}}{\acute{u}_{dr}} \tag{3.5}$$

Figure 3.2b illustrates the hysteretic behaviour of a bilinear viscous damper under sinusoidal loading for different displacement amplitudes. In this figure, the x-axis has been normalized with

respect to the peak displacement amplitude. The damper was designed for a peak damper velocity, $\mu_d = 3$. The post-relief damping coefficient ratio was assumed to be $p = 0.1$. The displacement amplitudes were increased in three steps. During the first step the peak damper velocity was nearly equal to the damper relief velocity; therefore the hysteretic behaviour of the damper was identical to that of a linear viscous damper (Kasai et al. 2004c; Tsuyuki et al. 2004). Once the velocity demand exceeds the damper relief velocity, the relief mechanism is activated and the damping coefficient C_d suddenly drops as shown in Figure 3.2b.

3.3 Hysteretic Behaviour of Viscous Dampers as Maxwell Models

Based on prior experimental findings the hysteretic behaviour of a viscous damper is dependent on its axial stiffness due to viscoelasticity, K_d, as well as the frequency characteristics of the external applied force (Constantinou and Symans 1993a). Typically, K_d can be obtained empirically from experimental data as discussed in Makris and Constantinou (1991) and Kasai et al. (2004a; 2004b). Referring to Figure 3.3a, viscous dampers in frame buildings are typically installed with supporting braces that consist of several components such as steel braces, clevises, brackets and gusset plates. These components provide additional axial flexibility to the damper and affect its hysteretic behaviour under random vibrations. The axial flexibility of a viscous damper can be further decomposed into its various components as shown schematically in Figure 3b. In this figure, K_b, K_{cl}, K_{gus} are the stiffness contributions of the steel brace, clevis-brackets and gusset plates, respectively. The gap due to the fabrication tolerance of the damper clevis is noted as G_{cl} in the same figure. To this end, the Maxwell model (Maxwell 1867) has been found to be more appropriate to account for both the axial stiffness and frequency dependency of a viscous damper under dynamic loading (Makris and Constantinou 1991; Constantinou and Symans 1993a; Singh et al. 2003). In this case, a nonlinear dashpot and a linear spring are

connected in series as illustrated in Figure 3.3c. The axial stiffness of the damper portion, K_d, and that of the various supporting components (see Figure 3.3b) can be represented by an equivalent axial stiffness, K_s, as follows,

$$\frac{1}{K_s} = \frac{1}{K_d} + \frac{1}{K_b} + \frac{2}{K_{cl}} + \frac{2}{K_{gus}} \tag{3.6}$$

The force, F_d at the nonlinear dashpot and spring (F_s) are equal; therefore, the constitutive rules within a Maxwell model can be written as follows,

$$F_d(t) = F_s(t) = K_s u_s(t) \tag{3.7}$$

$$u_m(t) = u_s(t) + u_d(t) \tag{3.8}$$

$$\acute{u}_m(t) = \acute{u}_s(t) + \acute{u}_d(t) \tag{3.9}$$

in which, u_m ,u_d and u_s are the total, dashpot and spring displacements, respectively (see Figure 3.3c). The constitutive equation that describes the force and total velocity relation within a Maxwell model can be obtained if Equations (3.7) and (3.8) are substituted into Equation (3.9). For a nonlinear viscous damper this equation is as follows,

$$F_d'(t) = \left(\acute{u}_m(t) - \mathrm{sgn}(F_d(t)) \left(\frac{|F_d(t)|}{C_d} \right)^{1/\alpha} \right) K_s, \quad F_d(t_0) = F_{d0} \tag{3.10}$$

for a bilinear oil damper, the following equations hold true,

$$F_d'(t) = \begin{cases} \left(\acute{u}_m(t) - \dfrac{F_d(t)}{C_d} \right) K_s, & |F_d(t)| \le F_{dr} \\ \left(\acute{u}_m(t) - \dfrac{\mathrm{sgn}\left(F_d(t)\right)(p-1)F_r + F_d(t)}{pC_d} \right) K_s, & |F_d(t)| > F_{dr} \end{cases}, \quad F_d(t_0) = F_{d0} \tag{3.11}$$

Equations (3.10) and (3.11) are first order ordinary differential equations that can only be solved numerically in the case of a random vibration input loading.

3.4 Numerical Solution for Nonlinear Viscous and Bilinear Oil Dampers

This section discusses a numerical solution scheme for Equations (3.10) and (3.11). For this reason, both equations are treated as a general initial value problem that is described by Equation (3.12) as follows,

$$y' = f(t_n, y_n), \quad y(t_0) = y_0, \tag{3.12}$$

Oohara and Kasai (2002) implemented the classical 4th order Runge-Kutta (RK4) explicit iterative method (Kutta 1901; Butcher 1996) to solve Equation (3.12) for nonlinear viscous dampers. They stated that the classical RK4 method requires very small integration time steps, *h,* for large K_s values. For NRHA of frame buildings under earthquake excitations, the maximum value of *h* is limited by the overall analysis time step dt_a of the integration algorithm that is employed for the numerical solution of the equation of motion; while dt_a should be selected at most equal to the time step of the input ground motion *dt* depending on the selected integration algorithm to conduct the NRHA; the ratio of dt/dt_a should be an integer. Typical sampling time steps of recorded ground motions vary between 0.005-0.02 sec. However, for a large axial damper stiffness, K_s a much smaller step *h* should be considered for the utilization of the RK4 iterative method and subsequently the overall NRHA time step dt_a should be further decreased. This is computationally very expensive particularly in cases that a 3-dimensional model with several hundreds of degrees of freedom is utilized to describe the dynamic response of a frame building under earthquake excitations.

Alternatively, the use of adaptive solution algorithms is recommended. In this section, we utilize the Dormand-Prince (DP54) explicit iterative method (Dormand and Prince 1980) to solve numerically Equation (3.12). The solution of this equation is tested with the absolute error predicted between 4th and 5th order solutions. The 4th order solution and the associated absolute

error according to the DP54 iterative method for Equation (3.12) are computed based on Equations (3.13) and (3.14), respectively, as follows,

$$y_{n+1} = y_n + \frac{35}{384}k_1 + \frac{500}{1113}k_3 + \frac{125}{192}k_4 - \frac{2187}{6784}k_5 + \frac{11}{84}k_6 \tag{3.13}$$

$$\varepsilon_{n+1} = \left| \frac{71}{57600}k_1 - \frac{71}{16695}k_3 + \frac{71}{1920}k_4 - \frac{17253}{339200}k_5 + \frac{22}{525}k_6 - \frac{1}{40}k_7 \right| \tag{3.14}$$

in which y_{n+1} and y_n are the solutions for Equation (3.12) for the current and previous steps, respectively; ε_{n+1} is the absolute error of the numerical solution in the current step. From Equations (3.15) to (3.21), the DP54 explicit iterative method uses six function evaluations in order to calculate the 4th and 5th order accurate numerical solutions for Equation (3.14). These function evaluations are computed as follows,

$$k_1 = hf(t_n, y_n) \tag{3.15}$$

$$k_2 = hf(t_n + \frac{1}{5}h, y_n + \frac{1}{5}k_1) \tag{3.16}$$

$$k_3 = hf(t_n + \frac{3}{10}h, y_n + \frac{3}{40}k_1 + \frac{9}{40}k_2) \tag{3.17}$$

$$k_4 = hf(t_n + \frac{4}{5}h, y_n + \frac{44}{45}k_1 - \frac{56}{15}k_2 + \frac{32}{9}k_3) \tag{3.18}$$

$$k_5 = hf(t_n + \frac{8}{9}h, y_n + \frac{19372}{6561}k_1 - \frac{25360}{2187}k_2 + \frac{64448}{6561}k_3 - \frac{212}{729}k_4) \tag{3.19}$$

$$k_6 = hf(t_n + h, y_n + \frac{9017}{3168}k_1 - \frac{355}{33}k_2 + \frac{46732}{5247}k_3 + \frac{49}{176}k_4 - \frac{5103}{18656}k_5) \tag{3.20}$$

$$k_7 = hf(t_n + h, y_{n+1}) \tag{3.21}$$

Figure 3.4 shows a flowchart of a single solution step, $i+1$, within a response history analysis of a nonlinear viscous damper. In order to obtain the damper force for the current step, $F_{d,i+1}$, the required input parameters from the overall response history analysis are the integration time step

dt_a of the employed integrator for response history analysis (i.e., different than the one employed to obtain the damper force), the velocity of the current and previous steps, $\acute{u}_{i+1}$, $\acute{u}_i$, respectively, and the damper force, $F_{d,i}$ from the previous step, i of the response history analysis. The velocity $\acute{u}$ represents the velocity $\acute{u}_{\mathrm{m}}$ of the Maxwell model. During the initial iteration to compute the damper force, the numerical integration step, h of the DP54 method is set equal to dt_a. If the relative error ε_{rel} is larger than a pre-defined relative tolerance (noted as "RelTol") or if the absolute error is larger than the absolute tolerance (noted as "AbsTol"), the solution algorithm reduces its time step h by half (see Eq. (3.23)) using a half-step coefficient, s (see Eq. (3.24)) till Equation (3.22) is satisfied. In this case the velocity $\acute{u}_{n+1}$ at the current solution sub-step, which is required from the DP54 iterative method, should be interpolated linearly between $\acute{u}_i$ and $\acute{u}_{i+1}$ at the corresponding sub-step. Therefore, the computation of the acceleration $\ddot{u}_{\mathrm{i+1}}$ at the current solution step is needed. Similarly, velocity values within the function evaluations of DP54 iterative method should be linearly interpolated between $\acute{u}_n$ and $\acute{u}_{n+1}$ at the corresponding time increments. As the sum of half-step coefficients s_{tot} becomes equal to unity, we can obtain the damper force at the current solution step, $F_{d,i+1}$. In order to limit the number of iterations N_{it} within the material model, we can introduce a minimum step size h_{min}. This can simply be done by defining a maximum number of iterations, $N_{it,max}$, for the half step coefficient s as shown in Equation (3.24).

$$\varepsilon_{rel,n+1} \le \mathrm{RelTol} \;\text{ or }\; \varepsilon_{n+1} \le \mathrm{AbsTol} \tag{3.22}$$

$$h = s \cdot dt_a \tag{3.23}$$

$$s = 2^{-N_{it}}, \qquad N_{it} = \{0,1,2,...,N_{it,\max}\} \tag{3.24}$$

In order to investigate the effectiveness of the adaptive time step of the DP54 iterative method on the numerical solution of the force for nonlinear viscous dampers under a sinusoidal

displacement excitations, Figure 3.5 illustrates the force-displacement relation of nonlinear viscous dampers with varying velocity exponents, α (α varies from 0.01 to 2) and normalized damper axial stiffnesses, k_s (i.e., k_s varies from 0.1 to 1000). The sinusoidal displacement that represents the external loading is $u_{m0}\sin(\omega t)$ in which u_{m0} and ω are the peak displacement amplitude and the angular frequency ($\omega = 2\pi f$) of the external loading, respectively. In this case, $u_{mo} = 1$ and $f = 1$ Hz. The overall time step dt_a of the external loading was selected to be $dt_a = 0.01$ sec. The nonlinear viscous damper was designed such that if k_s is neglected then the peak damper force, F_{d0} becomes unity. Thus, F_{d0} can be computed from Equation (3.25) (i.e., pure viscous material) and therefore, $u_{d0} = u_{m0}$. In this case, the normalized damper stiffness k_s can be obtained from Equation (3.26). A relative tolerance RelTol = 10^{-6} and an absolute tolerance AbsTol = 10^{-10} are selected herein.

$$F_{d0} = C_d(\omega u_{m0})^{\alpha} \tag{3.25}$$

$$k_s = K_s \frac{u_{m0}}{F_{d0}} \tag{3.26}$$

The number of iterations, N_{it} required for the half step coefficient are reported for each case in Figure 3.5. From this figure, when k_s increases the required number of iterations in order to achieve convergence based on the pre-defined tolerances also increases. From the same figure, the damper exponent α variation has a relatively small influence on the required number of iterations for numerical convergence. The only exception is for $\alpha = 2$, in which a relatively large number of iterations is required to satisfy the pre-defined convergence tolerances (see Figure 3.5). This is due to the fact that for $\alpha = 2$ the absolute tolerance becomes the critical condition to minimize the error in the damper force prediction, while for all other α values the relative tolerance limits N_{it}. From Figure 3.5, it is evident that k_s strongly affects the peak damper

forces as well as the damper hysteretic shape. These issues are further investigated later on as part of this paper.

In order to illustrate the accuracy of the adaptive integration algorithm for obtaining the hysteretic response of nonlinear viscous dampers compared to traditional iterative numerical methods that have been previously employed, Figure 3.6 illustrates the force-displacement relations for the same nonlinear viscous dampers that were analyzed in Figure 3.5 when the classical 4th order RK4 iterative method is employed. From Figure 3.6, it is evident that when the RK4 iterative method is employed and for $dt_a = 0.01$sec it is not possible to obtain the numerical solution of Equation (3.10) if $k_s > 10$. Note that in this case, numerical convergence is achieved for only three α values (i.e., $\alpha = 0.5$, 1.0 and 2.0). In order to be able to obtain a stable numerical solution even in these cases an integration step $dt_a = 0.00005$ sec must be selected.

The adaptive DP54 iterative method can be implemented for the numerical solution of bilinear oil dampers. In this case, Equation (3.11) is solved numerically. Note that when $p = 0$ (i.e., constant damper force after relief), $F'_d(t)$ in Equation (3.11) becomes infinite; therefore the damper force, $F_{d,i+1}$ in this case should be directly equal to F_{dr}. Alternatively, we can compute the damper force $F_{d,i+1}$ through a finite difference approximation of Eq. (3.11) as follows,

$$F_d(t) = F_{d,i+1} \tag{3.27}$$

$$\acute{u}_m(t) = \acute{u}_{m,i+1} \tag{3.28}$$

$$F'_d(t) = \frac{F_{d,i+1} - F_{d,i}}{h} \tag{3.29}$$

After substituting Equations (3.27) to (3.29) into Equation (3.11), Equations (3.30) are obtained. First, $F_{d,i+1}$ shall be computed through Equation (3.30) assuming that the oil damper is linear

(i.e., $|F_{d,i+1}| \le F_{dr}$). If the computed damper force $|F_{d,i+1}| > F_{dr}$, then $F_{d,i+1}$ shall be recomputed using the sign value, sgn($F_{d,i+1}$) of the initially computed linear oil damper force prediction.

$$F_{d,i+1} = \begin{cases} \dfrac{F_{d,i} + \acute{u}_{m,i+1} K_s h}{1 + K_s h / C_d}, & \left|F_{d,i+1}\right| \le F_{dr} \\ \dfrac{F_{d,i} + \acute{u}_{m,i+1} K_s h + \left[\operatorname{sgn}\left(F_{d,i+1}\right)(p-1)F_{dr} K_s h\right] / \left(pC_d\right)}{1 + K_s h / C_d}, & \left|F_{d,i+1}\right| > F_{dr} \text{ and } p \ne 0 \\ \operatorname{sgn}\left(F_{d,i+1}\right), & \left|F_{d,i+1}\right| > F_{dr} \text{ and } p = 0 \end{cases} \tag{3.30}$$

Kasai et al. (2004c) recommended that in order to compute the bilinear oil damper force with a high precision, smaller integration steps should be employed. Therefore, in order to be compatible with the adaptive DP54 iterative method, the error of the numerical solution in this case is defined by subtracting the solution obtained in the current iteration from that of an additional step. For this reason, two numerical solutions are obtained per iteration, one computed with a time step h_1 and another one with h_2 as shown in Equation (3.31). Similar to the adaptive DP54 iterative method, for each iteration the integration time step is reduced by half, until the absolute error or the absolute relative error becomes smaller than the predefined tolerances, based on Equation (3.22).

$$h_1 = s \cdot dt_a, \quad h_2 = s/(s+1) \cdot dt_a \tag{3.31}$$

In order to compare the adaptive DP54 iterative method with the proposed adaptive numerical integration method discussed herein for the case of bilinear oil dampers, the force-displacement relations for oil dampers under a sinusoidal external loading with $u_{mo} = 1$ and f = 1 Hz are computed in Figures 3.7 and 3.8. The oil dampers are designed such that their peak force, F_{d0}, becomes unity when the damper axial flexibility is neglected. For oil dampers, F_{d0} can be computed based on Equation (3.32). Two cases are analyzed. In the first case, the peak damper

velocity ratios are fixed (i.e., $\mu_m = 2$) and p varies from 0 to 1.0 (see Figure 3.7). In the second case, the p value is fixed (i.e., $p = 0.05$) and μ_m varies from 1 to 20 (see Figure 3.8). For both cases, the normalized damper axial stiffness, k_s varies from 0.1 to 1000. The relative and absolute tolerances are set equal to RelTol=10^{-6} and AbsTol=10^{-10}, respectively.

$$F_{d0} = \left(p + \frac{1-p}{\mu_m} \right) C_d \omega u_{m0} \tag{3.32}$$

$$\mu_m = \frac{\omega u_{m0}}{\acute{u}_{dr}} \tag{3.33}$$

Figure 3.7 illustrates the computed hysteretic behaviour of oil dampers with varying p and k_s values based on the adaptive DP54 and finite difference approximation methods. In the same figure we have superimposed the number of iterations, N_{it} required for the half step coefficient based on both iterative methods. From Figure 3.7 it is concluded that for large k_s values (i.e., $k_s \geq 100$) a small integration time step is required when the adaptive DP54 method is employed; however, this is not the case when the alternative proposed integration scheme is employed. Therefore, for oil dampers that utilize $k_s \geq 100$ the alternative numerical integration method is able to provide the same accuracy in terms of solutions with the adaptive DP54 iterative method but with a much smaller number of iterations. For flexible bilinear oil dampers (i.e., $k_s < 100$) the adaptive DP54 iterative method typically satisfies the pre-defined tolerance criteria with a single iteration (see Figure 3.7). Similar conclusions hold true when p is fixed (i.e., $p = 0.05$) and the peak damper velocity ratio, μ_m varies (see Figure 3.8).

3.5 Sensitivity of Viscous Damper Behaviour to the Damper Axial Stiffness

This section investigates the effect of the axial stiffness, K_s due to viscoelasticity of a viscous damper on its hysteretic behaviour and dynamic stiffnesses based on the proposed adaptive

numerical method discussed above. In particular, a sensitivity study is conducted in order to quantify the effect of K_s on the reduction factor of the damper energy dissipation, e_K; the damper peak force, F_{do}; the damper storage stiffness, $K_{m,st}$; and the damper loss stiffness, $K_{m,l}$. A harmonic vibration is assumed for this purpose. A sinusoidal displacement that represents the external loading is applied with $u_{mo} = 1$ and $f = 1$ Hz. The evaluation is conducted in a normalized domain. In particular, similarly with the normalized stiffness k_s (see Equation (3.26)), the normalized storage and loss stiffnesses $k_{\mathrm{m,st}}$ and $k_{\mathrm{m,l}}$, respectively, can be obtained according to Equation (3.26). Figure 3.9 illustrates the graphical definition of these phenomena as well as the dynamic stiffnesses (see Figure 3.9c). The reduction factor of the damper energy dissipation, e_K is obtained by first computing the area under the corresponding damper hysteresis numerically and then dividing it into the energy produced by the pure viscous model under the same loading conditions. The energy dissipated by nonlinear and bilinear viscous models can be directly computed according to Constantinou and Symans (1993a) and Kasai and Nishimura (2004), respectively. The normalized peak damper force f_m is obtained by dividing the peak damper force into the peak force of a pure viscous model, which can be calculated, based on Equations (3.25) and (3.32) for nonlinear and bilinear viscous models, respectively. Nonlinear viscous dampers are employed with the utilization of the Maxwell model in order to facilitate the discussion in the next paragraph. The observations below are general and can be applied to bilinear oil dampers not discussed herein due to brevity.

Figure 3.10 illustrates the variation of e_K, f_m, $k_{\mathrm{m,st}}$ and $k_{\mathrm{m,l}}$ (values are normalized as discussed earlier and range between 0 to 1) with respect to the nonlinear viscous damper normalized stiffness k_s for a wide range of α values. From Figure 3.10, the following observations hold true,

- The change in e_K is relatively large for small α values (see Figure 3.10a). This is attributed to the fact that the smaller the exponent α it is, the more stable the damper force becomes with the increase of velocity (see Figure 3.1a). Therefore, a decrease in external total displacement (i.e. k_s) would mainly affect the dashpot displacement and not that of the spring because the spring force remains relatively constant and the spring displacement is proportional to its force. For instance, when $\alpha = 0$, for $k_s < 1$ the damper hysteretic energy diminishes. For $\alpha = 0$ (i.e., friction dampers) and $\alpha = 1$ (i.e., linear dampers) the reduction factor of the nonlinear viscous damper can be directly computed based on the following equation (Constantinou et al. 1998; Kasai et al. 2003),

$$e_{K,\alpha=0} = \frac{k_s - 1}{k_s}; \quad e_{K,\alpha=1} = \frac{k_s^2}{1 + k_s^2} \tag{3.34}$$

- From Figure 3.10b a decrease in k_s has a larger impact on the normalized peak forces (f_m) of a damper with large exponent α (e.g., $\alpha = 1$). Similarly, this is attributed to the fact that the damper force is relatively sensitive to the velocity variation once α becomes large. Therefore, a reduction in the dashpot displacement due to the axial flexibility causes relatively large force reductions when $\alpha = 1$. Note that specifically for friction and linear dampers the peak damper forces can be computed as follows,

$$f_{m,\alpha=0} = k_s; \quad f_{m,\alpha=1} = \frac{k_s}{\sqrt{1 + k_s^2}} \tag{3.35}$$

- The normalized storage stiffness $k_{m,st}$ is large for small α values; $k_{m,st}$ becomes maximum when $k_s = 1$ (see Figure 3.10c). This implies that even though the inclination angle of the damper hysteresis is small for $k_s < 1$ (see Figure 3.5), the $k_{m,st}$ is relatively small due to fact that the normalized peak forces, f_m significantly decrease for $k_s < 1$ as shown in Figure 3.10b. For $k_s > 1$ the $k_{m,st}$ reduces due to the changing shape of the damper

hysteresis. For large k_s values the damper hysteresis becomes similar to that of a pure viscous model, which has no storage stiffness. For friction and linear dampers the normalized storage stiffness can be computed as follows,

$$k_{m,st,\alpha=0} = k_s; \quad k_{m,st,\alpha=1} = \frac{k_s}{1+k_s^2} \tag{3.36}$$

- From Figure 3.10d the normalized loss stiffness, $k_{m,l}$ increases with the increase of k_s. Under the same loading conditions, a pure viscous model would have a normalized loss stiffness $k_{m,l} = 1$, because the maximum force occurs at zero displacement; thus the larger the k_s, the larger the $k_{m,l}$ becomes. Note that Equation (3.37) can be employed to compute the normalized loss stiffness for friction and linear dampers,

$$k_{m,l,\alpha=0} = k_s - 1; \quad k_{m,l,\alpha=1} = \frac{k_s^2}{1+k_s^2} \tag{3.37}$$

3.6 Experimental Validation

This section discusses the validation of the proposed adaptive integration techniques for the numerical models of nonlinear viscous and bilinear oil dampers. These models can be employed for nonlinear response history analysis of frame buildings with these two types of dampers. The validation is conducted with damper component experiments. System-level experimental data from a full-scale shake table test of a 5-story steel frame building with nonlinear viscous and bilinear oil dampers are also utilized.

3.6.1 Component Level Validation

Component level experiments for both nonlinear viscous and oil dampers are adopted from earlier experimental studies (Kasai et al. 2004c; Ooki et al. 2009; Hikino 2012). The nonlinear viscous damper that was tested as part of this experimental program had a viscous coefficient,

C_d = 196 KN/(mm/s)$^{0.38}$, axial stiffness, K_d = 438 KN/mm and a damper exponent, α = 0.38. The nonlinear viscous damper was subjected to sinusoidal loading with increasing displacement amplitudes and loading frequencies of 0.5Hz and 2Hz, respectively. Figure 3.11 illustrates the measured hysteretic response of the nonlinear viscous damper in terms of its force-displacement relation for the two loading frequencies of interest. In the same figure, we have superimposed the computed hysteretic response of the nonlinear viscous damper based on a Maxwell model. For the numerical solution of the constitutive equation of the Maxwell model with the proposed adaptive numerical technique an integration step of 0.01sec is employed. The adaptive DP54 method required 3 iterations (i.e. h = 0.00125 sec) to satisfy the pre-defined convergence criteria that were set to be equal to 10^{-6} and 10^{-10} for the relative and absolute tolerances, respectively. From Figure 3.11, the average absolute relative error of the predicted positive and negative peak damper forces per loading cycle versus the measured ones is 9% and 6% for 0.5 and 2.0Hz, respectively. This indicates that the proposed numerical model for nonlinear viscous dampers represents well the experimental data regardless of the employed loading frequency.

Similarly, for bilinear oil dampers the experimental data from Kasai et al. (2004c) is utilized. In this case, the oil damper that was tested dynamically at full-scale had an initial damper coefficient, C_d = 24.5 KN/(mm/s), an axial stiffness, K_d = 392.3 KN/mm, a relief velocity, V_r = 32 mm/s, and a post-relief coefficient ratio, p = 0.068 (Takahashi and Sekiguchi 2001). The oil damper was subjected to sinusoidal loading with increasing displacement amplitude of 1, 5 and 15 mm and loading frequencies of 0.25 Hz and 1 Hz. Figure 3.12 illustrates the measured hysteretic response of the bilinear oil damper for the two loading frequencies of interest. From Figure 3.12a, at 0.25 Hz the relief valve of the oil damper was not activated; therefore, the damper response was linear. However, at 1Hz and during the last loading cycle (i.e.,

displacement amplitude of 15 mm) the damper relief velocity was exceeded. Thus, a bilinear force-velocity relation was measured as shown in Figure 3.12b. In the same figure we have superimposed the computed hysteretic response of the same damper. The integration step of the proposed adaptive numerical technique that was employed was 0.01 sec. The adaptive DP54 method required 5 iterations (i.e. $h = 0.0003125$ sec) to satisfy the pre-defined convergence criteria that were set to be equal to 10^{-6} and 10^{-10} for the relative and absolute tolerances, respectively. Based on Figure 3.12, the computed hysteretic response of the oil damper is nearly identical with the one obtained from the experimental data regardless of the loading frequency. This is also indicated from the average absolute error of positive and negative peak damper forces per loading cycle that was 5% and 3% for 0.25 Hz and 1 Hz, respectively.

3.6.2 Validation with System-Level Experimental Data

This section discusses the efficiency of the proposed adaptive integration techniques for simulating the hysteretic response of nonlinear viscous and bilinear oil dampers based on the utilization of full-scale shake table experiments of a 5-story steel frame building that was tested at the world's largest shake table at E-Defense in Japan (Ohtani et al. 2004; Kasai et al. 2008c; Kasai et al. 2010; Hikino 2012; Kasai and Matsuda 2014). The test structure was tested with various types of dampers including nonlinear viscous and bilinear oil dampers (Ooki et al. 2009; Kasai et al. 2010; Hikino 2012). The employed numerical models including the adaptive integration techniques (noted as "ViscousDamper" and "BilinearOilDamper") discussed in this paper have been implemented in an open-source finite element simulation platform for nonlinear response history analysis of 2- and 3-Dimensional frame buildings under earthquake excitations [so called: Open System for Earthquake Engineering Simulation (*OpenSees*), (McKenna 1997)].

These models including their documentation are publically available to the earthquake engineering community (BilinearOilDamper 2015; ViscousDamper 2015).

Figure 3.13a shows the test structure after the installation on the E-Defense shake table. The test structure plan view was 10x12 m as (see Figure 3.13b). Its total height was 15.85 m and its overall weight was 4730 KN. Further information about the test structure, its geometry as well as the measured material properties of its various structural components have been reported extensively elsewhere and they not presented herein due to brevity (Ooki et al. 2009; Kasai et al. 2010; Kasai and Matsuda 2014).

Twelve dampers were installed in the test structure in total (four in the Y-loading direction; eight in the X-loading direction) as shown in Figures 3.13c and 3.13d. Table 3.1 provides the various properties of the nonlinear viscous and oil dampers based on damper component tests prior to the shake table experiments. In summary, Table 3.1 includes the damping coefficients, C_d, the stiffness properties (stiffness of damper portion, K_d and total stiffness K_s) of the corresponding dampers installed in the test structure. The velocity exponent, α, of the nonlinear viscous dampers was found to be, $\alpha = 0.38$. The relief velocity, V_r and post relief damping coefficient ratio, p of the bilinear oil dampers were found to be, $V_r = 64$ mm/sec and $p = 0.068$, respectively (Kasai et al. (2008c); Ooki et al. (2009); Hikino 2012).

The test structure was subjected to the three components of the JR Takatori record from the 1995 Kobe earthquake. These components were scaled incrementally at 50%, and 100% of the unscaled intensity of the same ground motion. These two seismic intensities represent a design basis and maximum considered earthquake in urban California (Akcelyan et al. 2016). Further details regarding the testing program can be found in Kasai and Matsuda (2014).

A 3-Dimensional (3D) model of the test structure was developed in the *OpenSees* simulation platform. The steel beams and columns were modeled with a single force-based distributed plasticity beam-column element with five integration points along their length. In order to trace flexural yielding within the cross sections a combined isotropic/kinematic material model (Menegotto and Pinto 1973) was assigned to the fiber-based cross sections that were assigned to the force-based nonlinear beam-column elements. The fiber discretization of each cross section consisted of 5x3 fiber elements along the width and thickness of flanges and webs, respectively. The measured material properties reported by (Kasai and Matsuda 2014) were explicitly assigned to the various steel beam and columns of the test structure. The reinforced concrete slab on top of the steel beams was modeled with a concrete material (Yassin 1994), which accounts for the effect of linear tension softening of the concrete. The effective width of the concrete slab was calculated based on Section I3.1a of ANSI/AISC 360-10 (AISC 2010c). Rigid diaphragms were assigned at each floor level. The P-Delta transformation was assigned to the steel members of the test structure to simulate the second order effects. The viscous damping forces of the test structure were simulated with the Rayleigh model. In particular, 2% damping ratio was assigned to the first and third modes of the 3-D model of the test structure. Two seismic intensities (50% and 100%) were taken into consideration for the evaluation presented herein. Nonlinear response history analysis with direct integration of the equations of motion was conducted. The Newmark's average acceleration method (Newmark 1959) was used for this purpose. The integration time step was taken equal to dt=0.01 sec. A detailed summary of the developed analytical model of the test structure can be found in Lignos (2012) and (Akcelyan et al. 2016).

Figure 3.14 shows a comparison of the measured and computed absolute peak values of story drift ratios, story shear forces and floor absolute accelerations along the height of the test

structure with nonlinear viscous dampers under 50% and 100% of the unscaled Takatori record in both loading directions (i.e., directions X and Y). In order to illustrate the efficiency of the proposed adaptive integration techniques for the numerical solution of viscous dampers including their axial flexibility, two types of nonlinear response history analyses are carried out. In the first one (noted as NRHA1) the axial flexibility of the dampers is neglected. In the second one (noted as NRHA2) the axial flexibility of the damper is considered. Note that the average absolute errors of global peak engineering demand parameters (EDPs) shown in Figure 3.14 increase from 7% to 27% when the axial flexibility of the damper is disregarded. In the Y-loading direction, the average absolute errors along the height of the test structure are much larger than those in the X-loading direction. In particular, the predicted peak EDPs are underestimated by more than 45% in average. Nearly identical findings hold true for the test structure with oil dampers. This can be seen in Figure 3.15 that shows a comparison of the predicted and measured global EDPs of interest along the height of the test structure with bilinear oil dampers in both loading directions of interest. These simple comparisons indicate the importance of rigorous mathematical models, such as the nonlinear Maxwell model, to accurately represent the hysteretic response of viscous dampers including their axial flexibility. In this case, the advantage of the proposed adaptive numerical method techniques to overcome typical convergence problems during nonlinear response history analyses of large-scale finite element models with fairly large integration steps is also pronounced.

Figure 3.16 illustrates the measured hysteretic response of the damper portion (K_d and C_d) of the nonlinear viscous and bilinear oil dampers installed in the first story of the test structure in X- and Y- loading directions, respectively, for the 100% seismic intensity of the JR Takatori record. In the same figure we have superimposed the simulated hysteretic response of the same

components based on NRHA of the 3D model representation of the test structure with nonlinear viscous dampers and bilinear oil dampers based on the proposed adaptive integration techniques discussed in this paper. From Figure 3.16 it is evident that in both cases the proposed numerical models are rational and are able to capture fairly well both the peak damper forces as well as the damper displacement amplitudes.

3.7 Summary and Conclusions

This paper discusses the implementation of advanced adaptive numerical integration algorithms for the numerical solution of the constitutive equations that describe the force-displacement relation of viscous dampers under random vibrations. In particular, the adaptive Dormand-Prince explicit integration method is implemented in an open source finite element analysis program that is widely used by the earthquake engineering community in order to calculate fourth- and fifth-order accurate numerical solutions of a damper force under random vibrations when the axial flexibility of the respective viscous damper is considered as part of its mathematical model representation within a finite element program (i.e., nonlinear Maxwell model). Through a sensitivity study, the efficiency of the adaptive integration algorithm over traditional integration schemes for the numerical solution of initial value problems is demonstrated. In particular, it is shown that even in cases that involve nonlinear viscous dampers with large axial stiffness and small velocity exponents a high-accuracy numerical solution of the force-displacement relations of the respective damper is achieved with relatively large integration steps and only few sub-step iterations. In the case of bilinear oil dampers with large axial stiffness an alternative adaptive numerical integration algorithm is also proposed. This integration scheme is able to provide same accuracy solutions with the adaptive Dormand-Prince iterative method but with much smaller number of sub-step iterations. The employed integration schemes allow for the investigation of

the sensitivity of the viscous damper behaviour to its axial stiffness. The adaptive integration schemes for the numerical solution of the nonlinear Maxwell model are validated through a series of comparisons with damper component tests as well as system-level experimental data from full-scale shake table tests of a 5-story steel frame building with nonlinear viscous and bilinear oil dampers. The validation studies indicate the efficiency of the proposed integration schemes in predicting the seismic response of global engineering demand parameters of interest such as story drift ratios, story shear forces and absolute floor accelerations along the height of frame buildings at a relatively low computational cost.

Table 3.1: Properties of nonlinear viscous dampers and oil dampers (Hikino, 2012).

		Nonlinear Viscous Damper ($\alpha = 0.38$)			Oil Damper ($V_r = 64$ mm/s, $p = 0.068$)		
Frame	Story	C_d [KN/(mm/s)$^{0.38}$]	K_d [KN/mm]	K_s [KN/mm]	C_d [KN/(mm/s)]	K_d [KN/mm]	K_s [KN/mm]
X direction (2 bays)	4	49	119[(a)]	60	3.13	88	57
	3	49	119[(a)]	60	6.25	137	85
	2	98	193	104	6.25	137	85
	1	98	193	101	12.5	274	146
Y direction (1 bay)	4	98	193	104	6.25	137	85
	3	98	193	104	12.5	274	154
	2	196	438	179	12.5	274	154
	1	196	438	171	18.75	441	242

(a) Estimated stiffness values (K_d) for damper portion due to lack of data of dampers at third and fourth story (Yu et al. 2013).

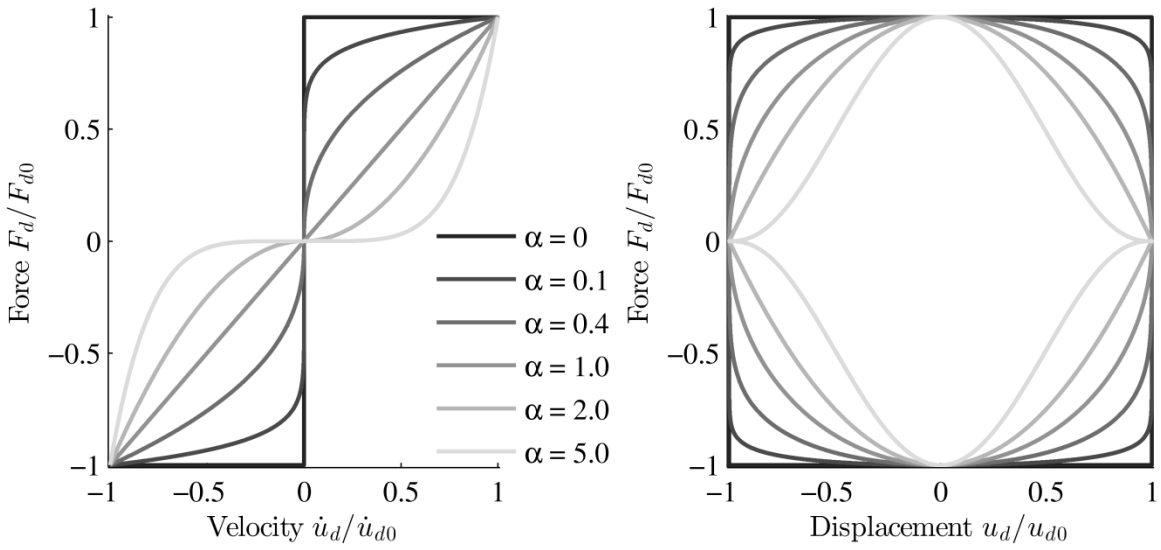

(a) Force versus velocity relation

(b) Force versus displacement relation

Figure 3.1: Hysteretic behaviour of nonlinear viscous dampers with various velocity exponents under sinusoidal motion

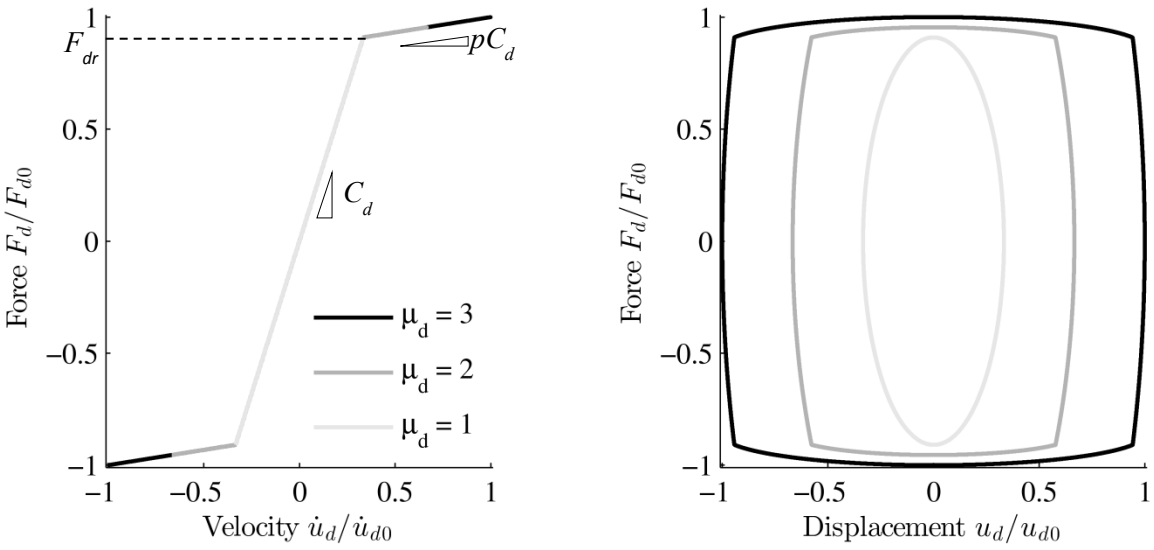

(a) Force versus velocity relation

(b) Force versus displacement relation

Figure 3.2: Hysteretic behaviour of bilinear oil dampers under sinusoidal motion with increasing loading amplitudes

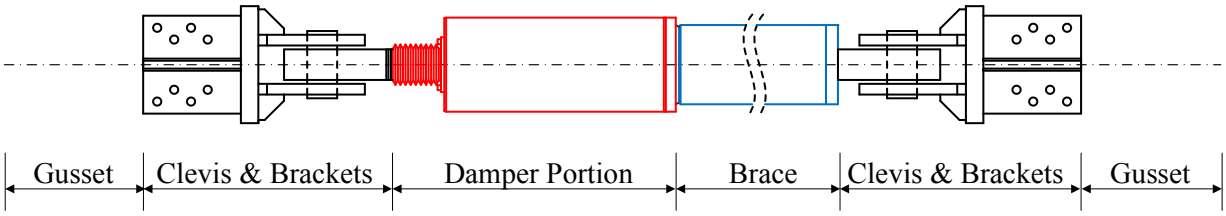

(a) Nonlinear viscous damper

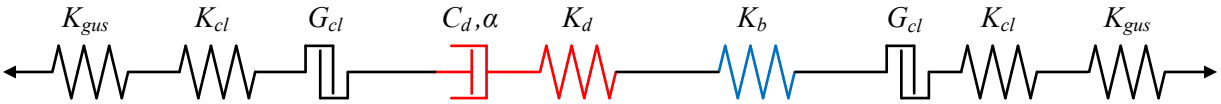

(b) Mechanical model for nonlinear viscous damper

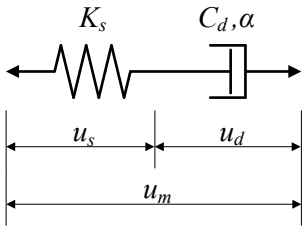

(c) Maxwell model

Figure 3.3: Schematic representation of nonlinear viscous damper including its mathematical model

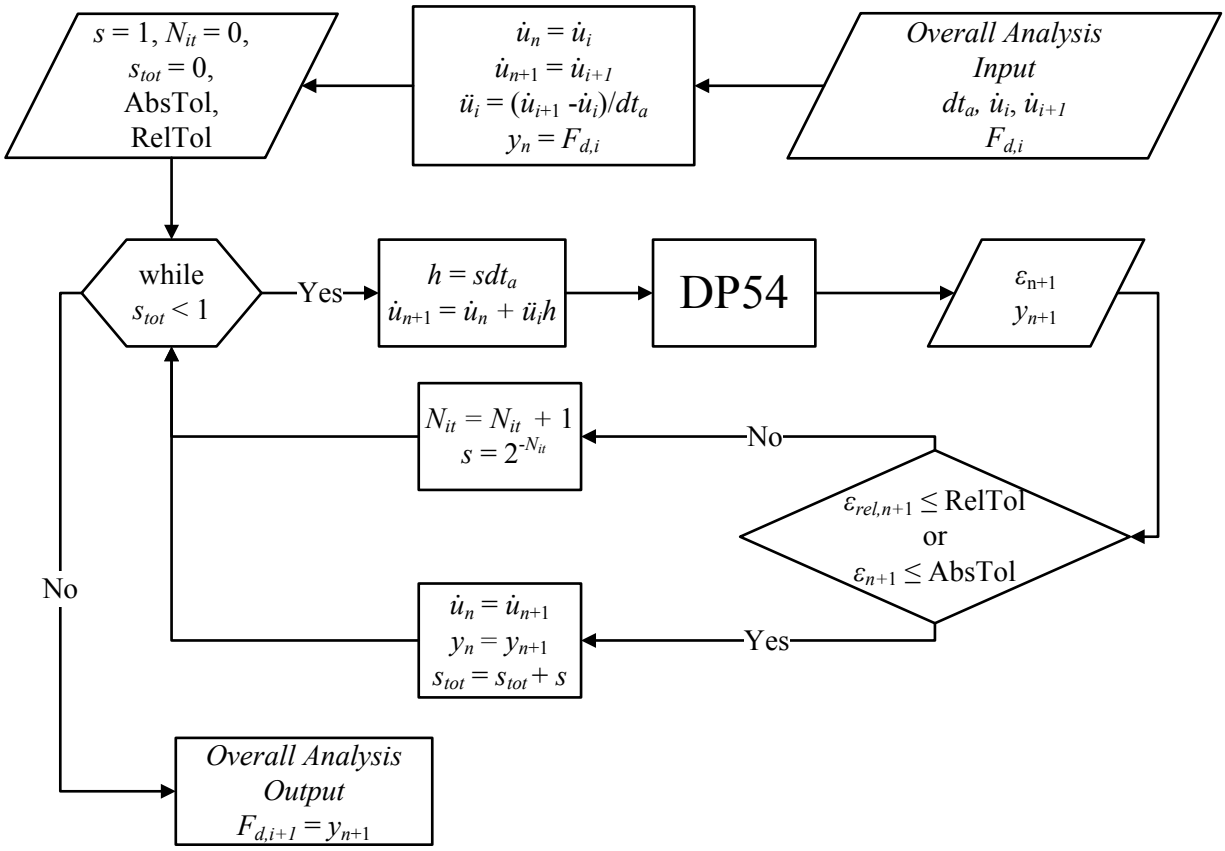

Figure 3.4: Flow chart of the numerical solution based on the adaptive DP54 explicit iterative method for nonlinear viscous dampers

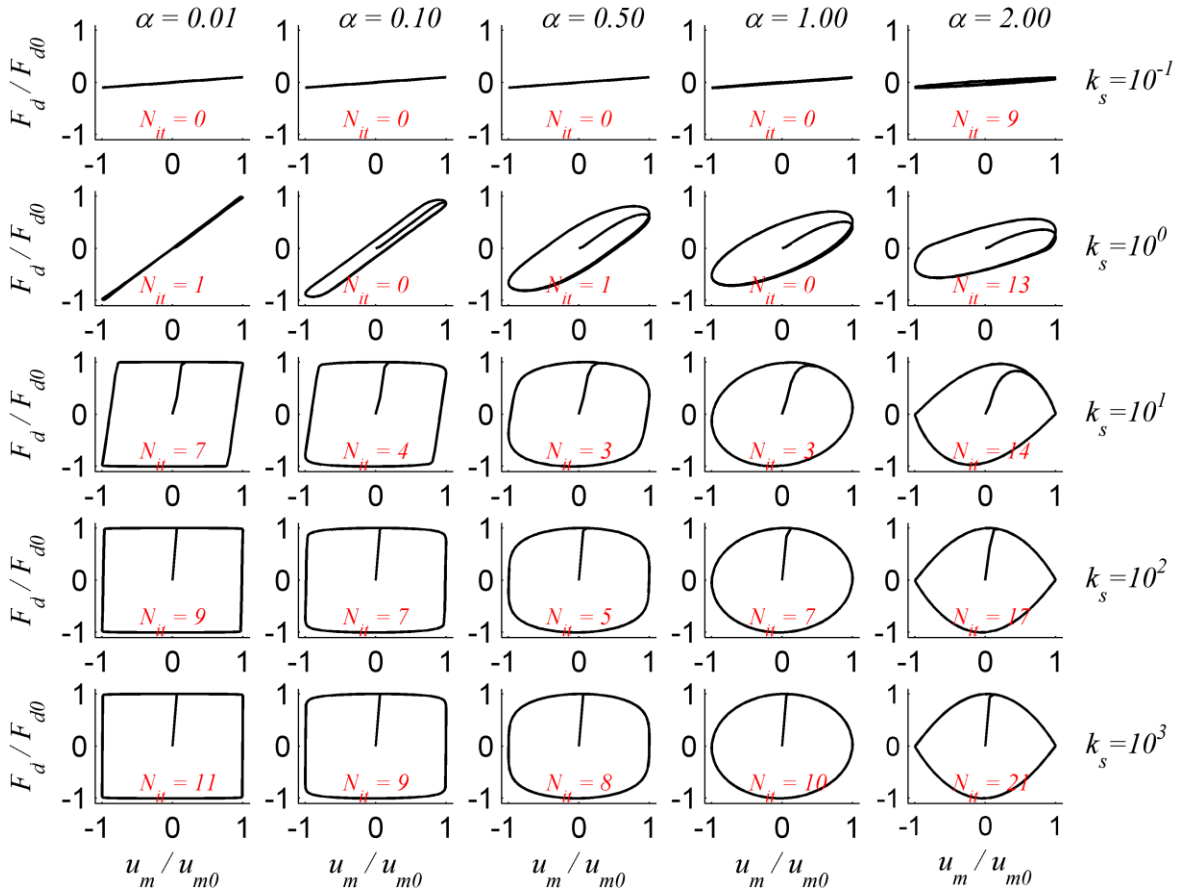

Figure 3.5: Force-displacement relations for nonlinear viscous dampers under sinusoidal displacement loading based on the adaptive DP54 iterative method

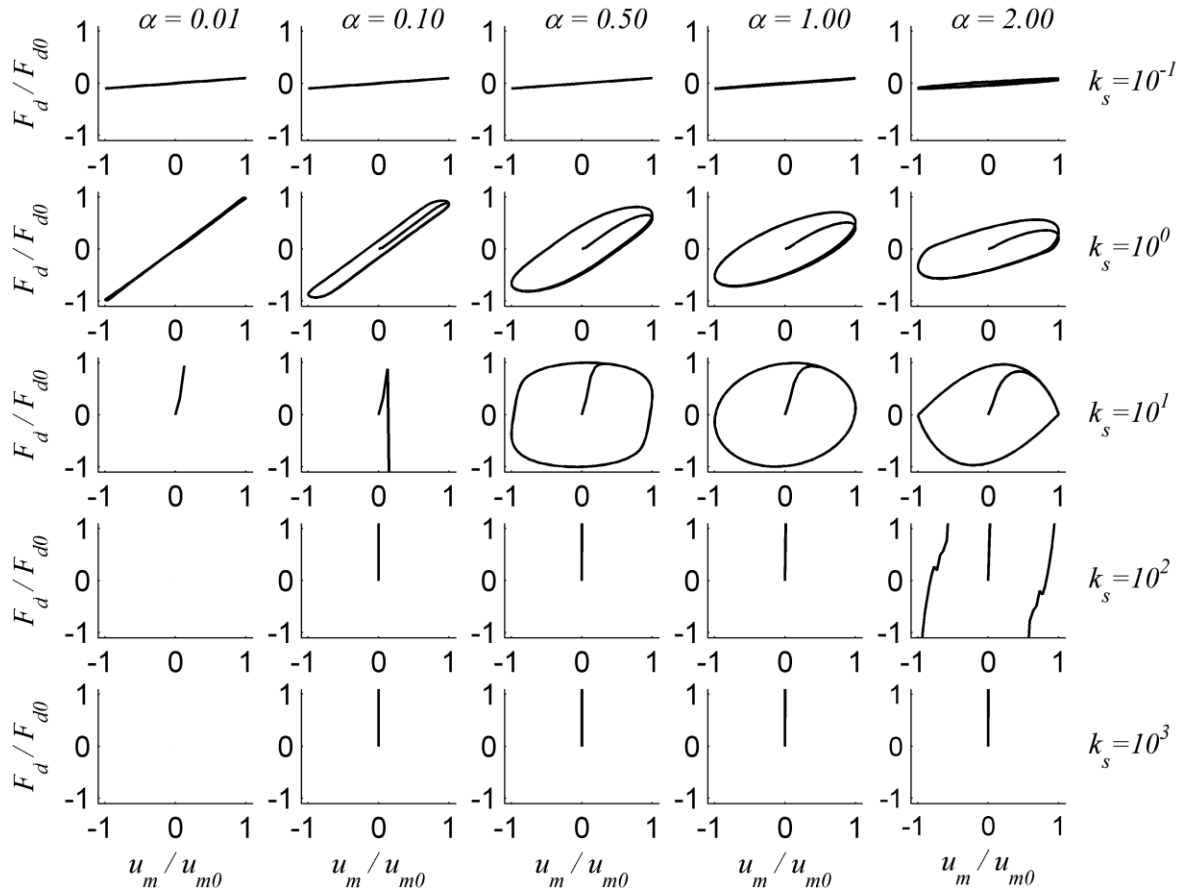

Figure 3.6: Force-displacement relations for nonlinear viscous dampers under sinusoidal displacement based on the classical 4th order Runge-Kutta method

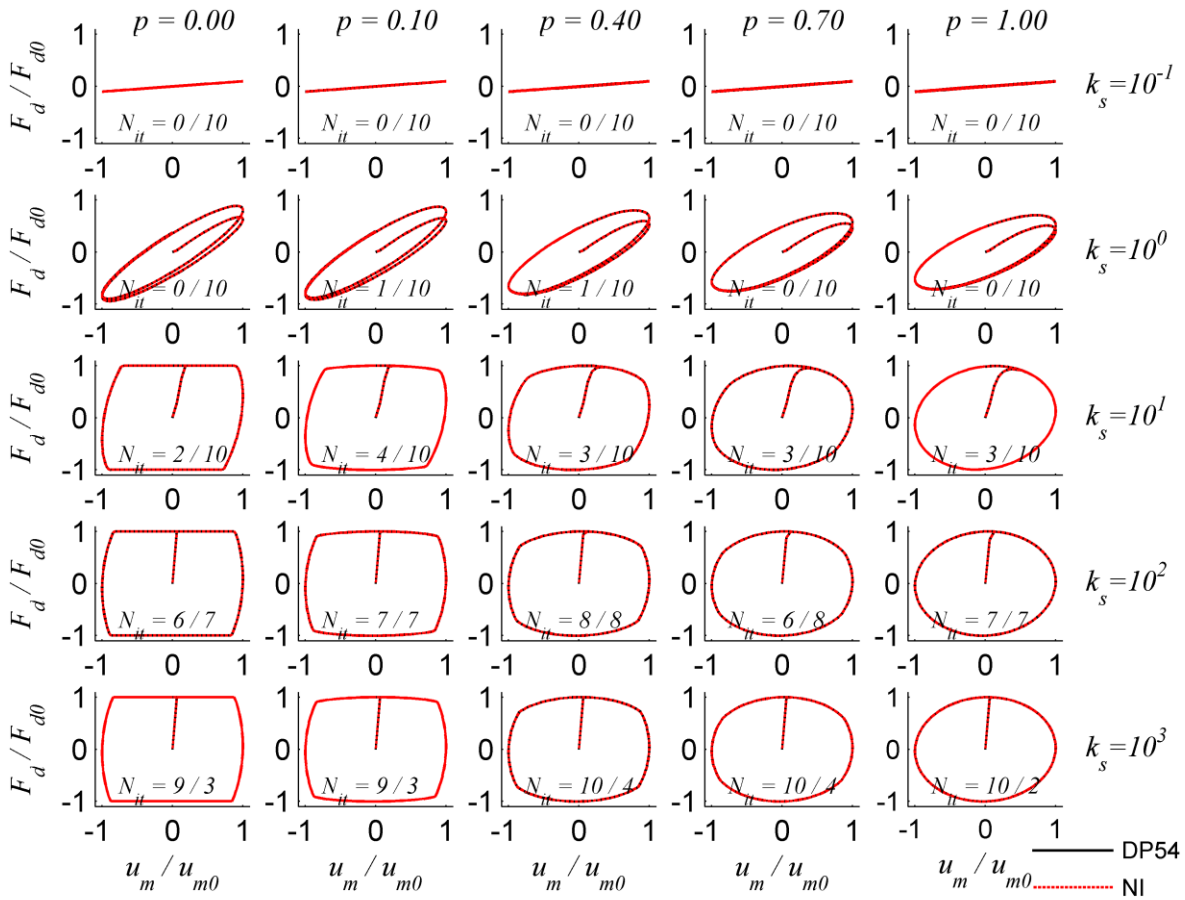

Figure 3.7: Comparison of the force-displacement relation predictions for bilinear oil dampers under sinusoidal displacement based on the adaptive DP54 iterative method and the alternative adaptive numerical integration algorithm (NI) for μ_m=2

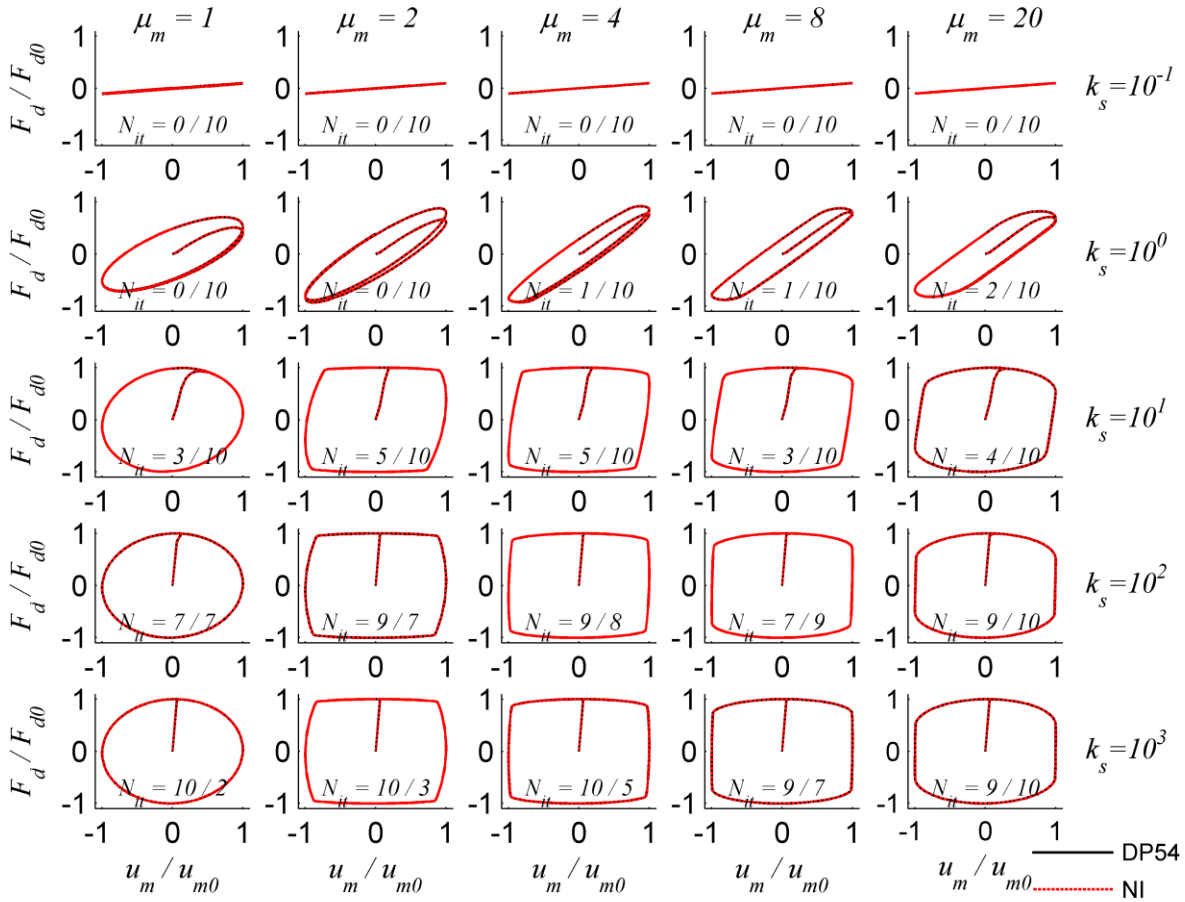

Figure 3.8: Force-displacement relations for bilinear oil dampers under sinusoidal displacement based on the adaptive DP54 iterative method and the alternative adaptive numerical integration algorithm (NI) for p=0.05

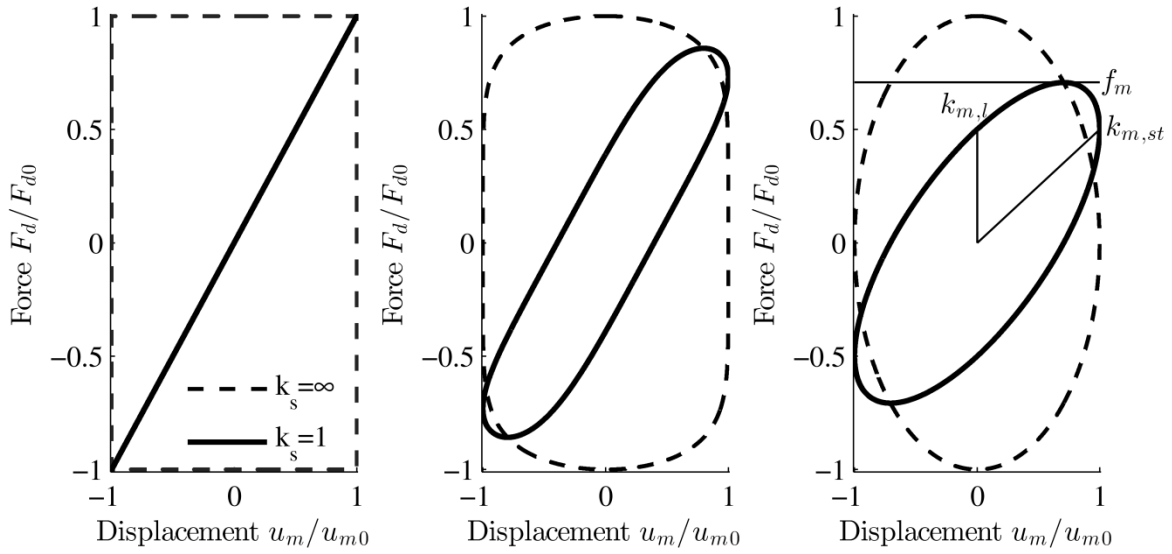

(a) α = 0 (b) α = 0.30 (c) α = 1.0

Figure 3.9: Variation of force displacement relationship of nonlinear viscous dampers with different parameters under sinusoidal displacement and graphical definition of dynamic stiffness.

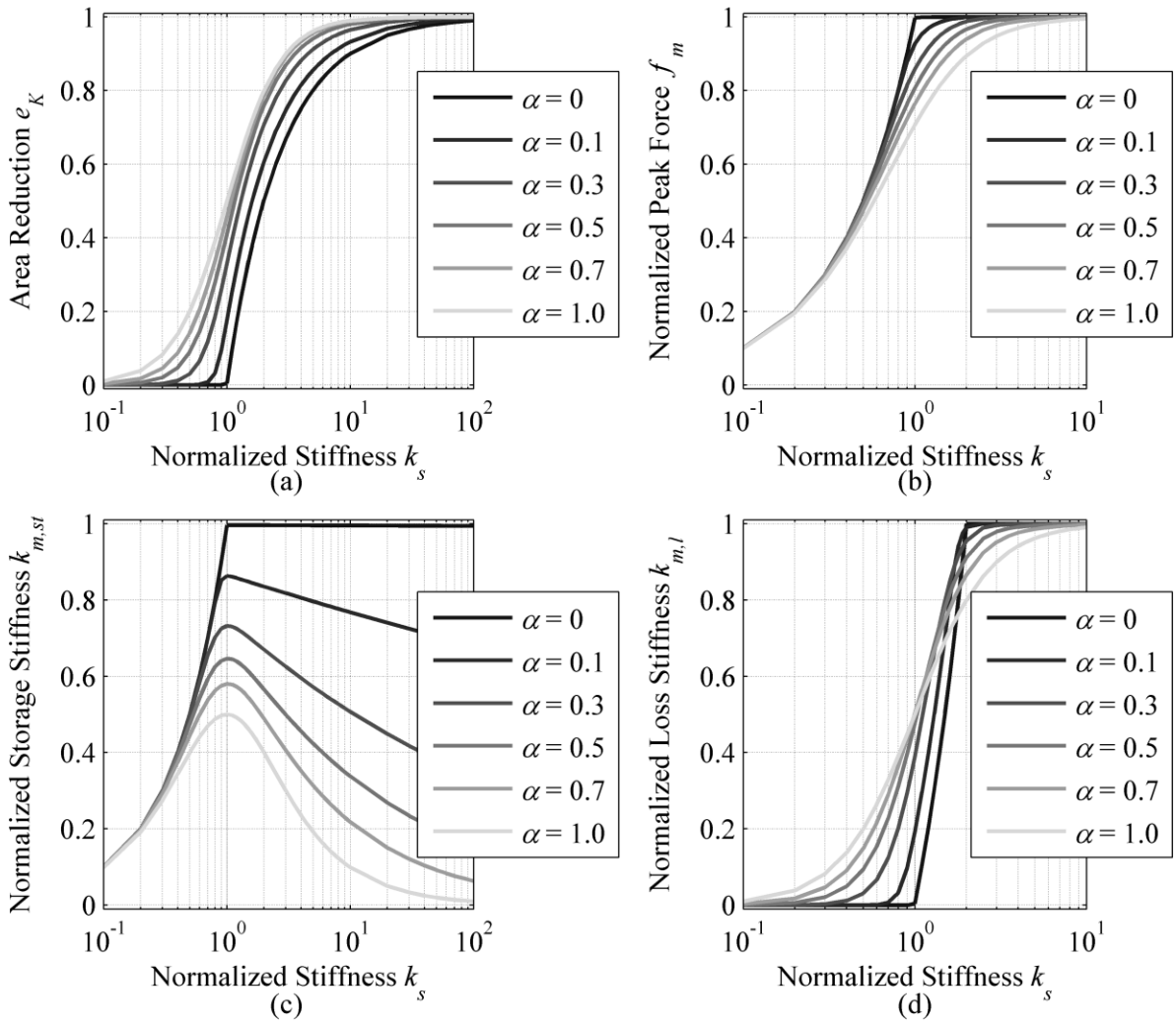

Figure 3.10: Effect of normalized stiffness on various properties of nonlinear viscous dampers with different velocity exponents

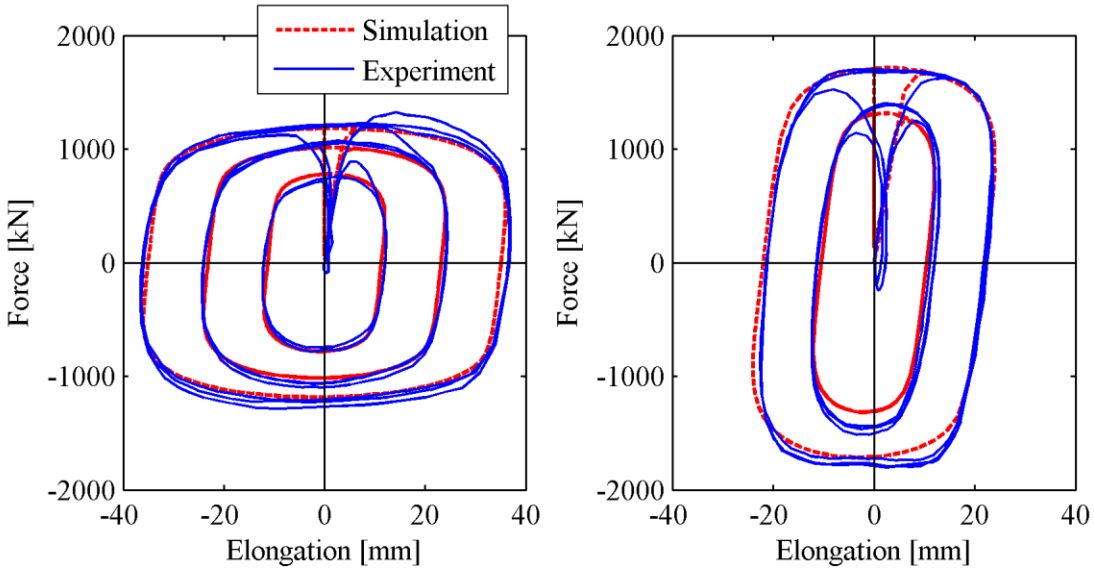

(a) 0.5 Hz (b) 2 Hz

Figure 3.11: Comparison of the simulated and experimental hysteretic response of nonlinear viscous dampers under dynamic sinusoidal loading (experimental data adopted from Kasai et al. 2004b)

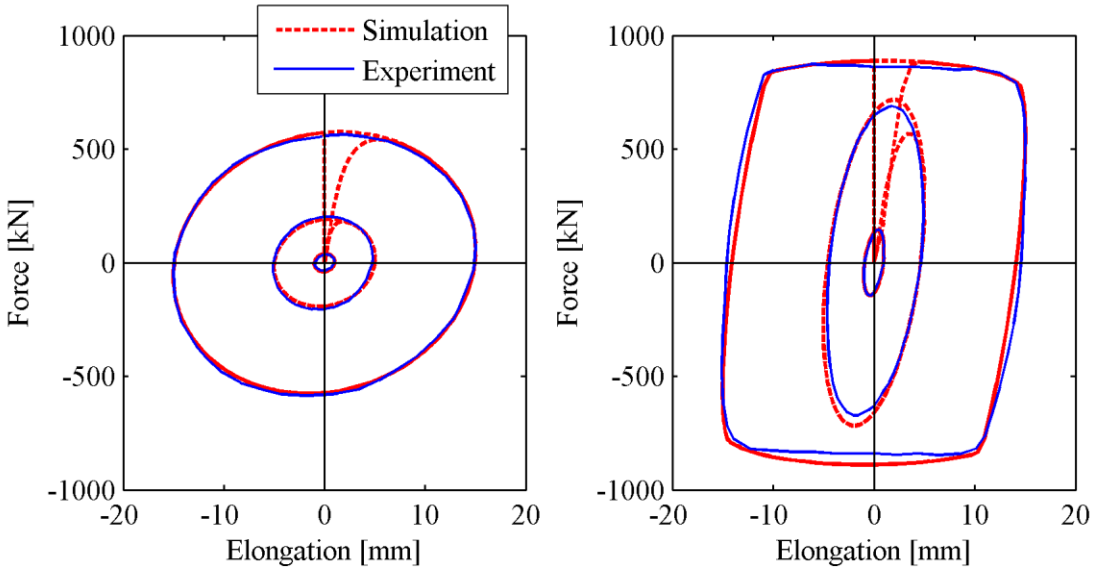

(a) 0.25 Hz (b) 1 Hz

Figure 3.12: Comparison of the simulated and experimental hysteretic response of bilinear oil dampers under dynamic sinusoidal loading (experimental data adopted from Kasai et al. (2004c)

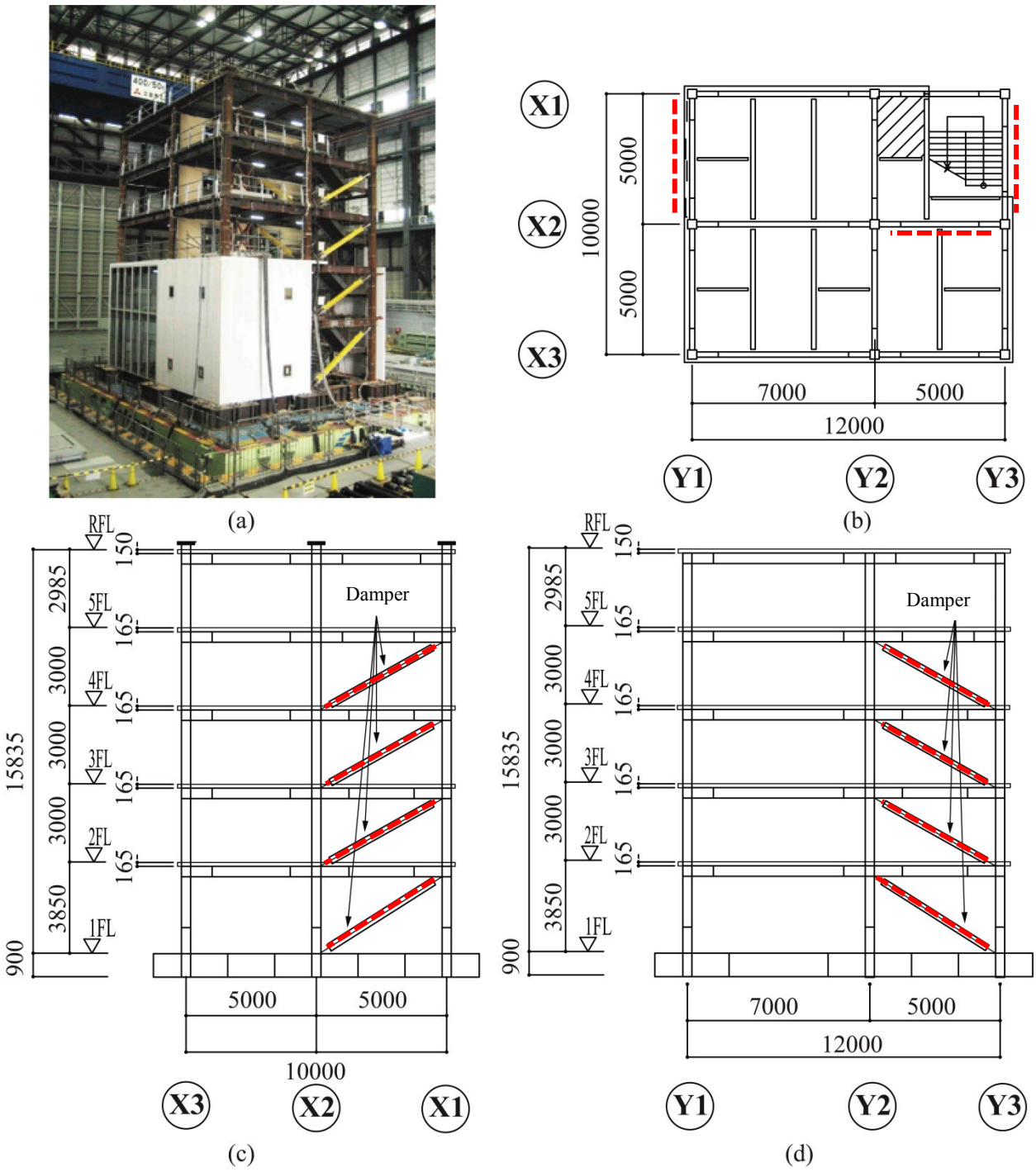

Figure 3.13: 5-story test-structure tested at E-Defense; (a) building after installation on the shake table; (b) plan view (c) elevation view in X- loading direction; (d) elevation view in Y-loading direction (images adopted from Akcelyan et al. (2016), dimensions in mm)

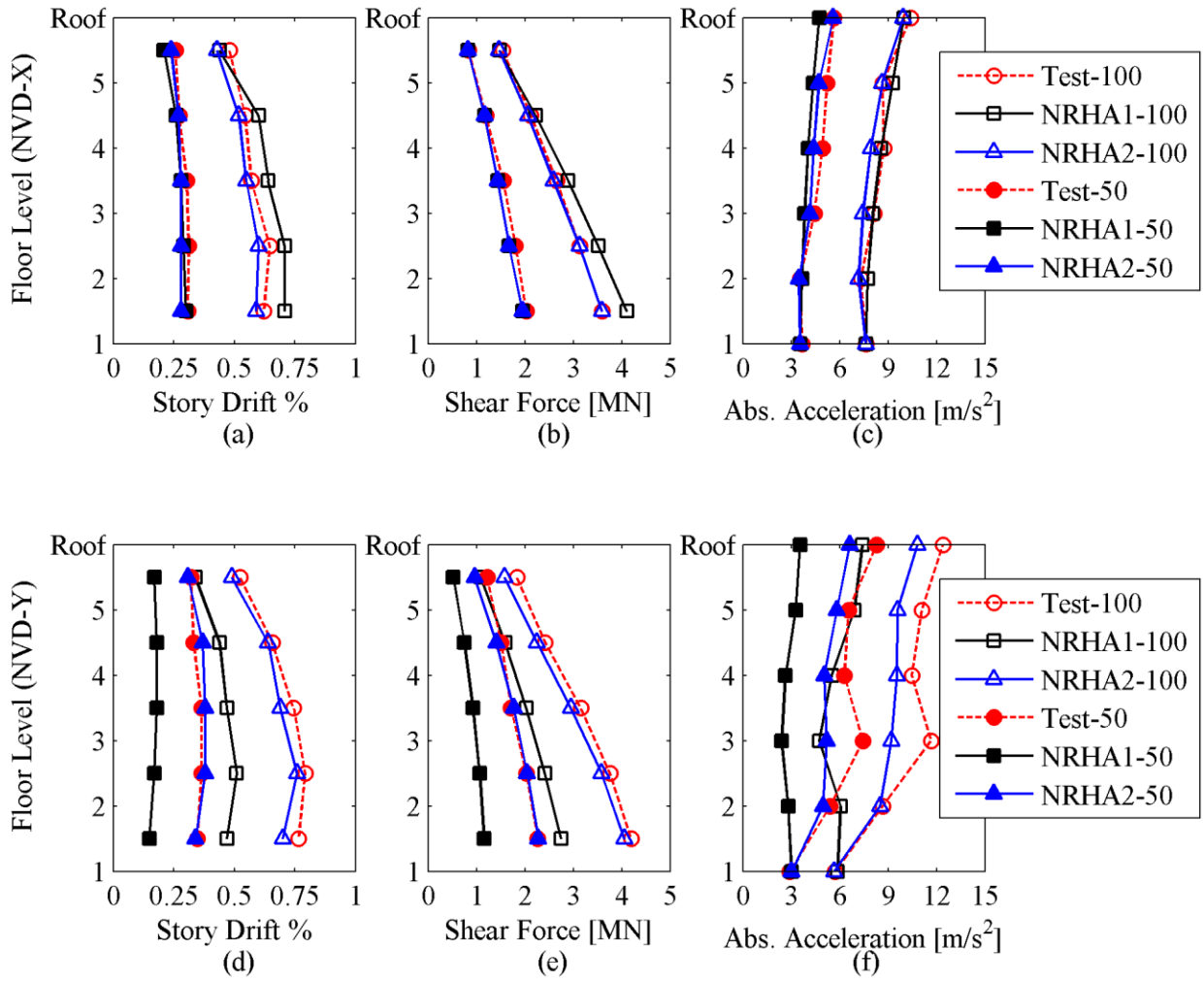

Figure 3.14: Comparison of computed and measured peak engineering demand parameters for the test structure with nonlinear viscous dampers

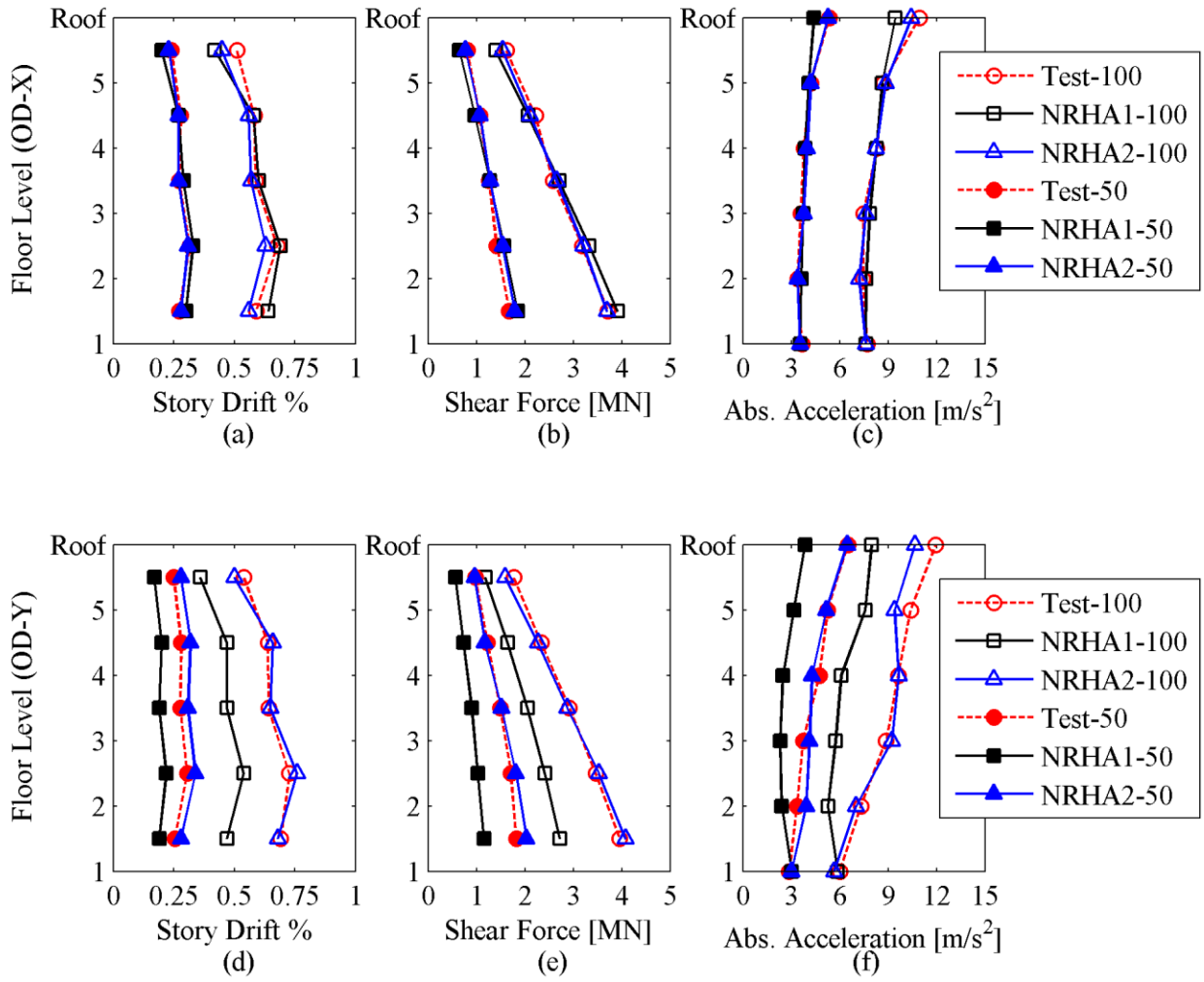

Figure 3.15: Comparison of computed and measured peak engineering demand parameters for the test structure with oil dampers

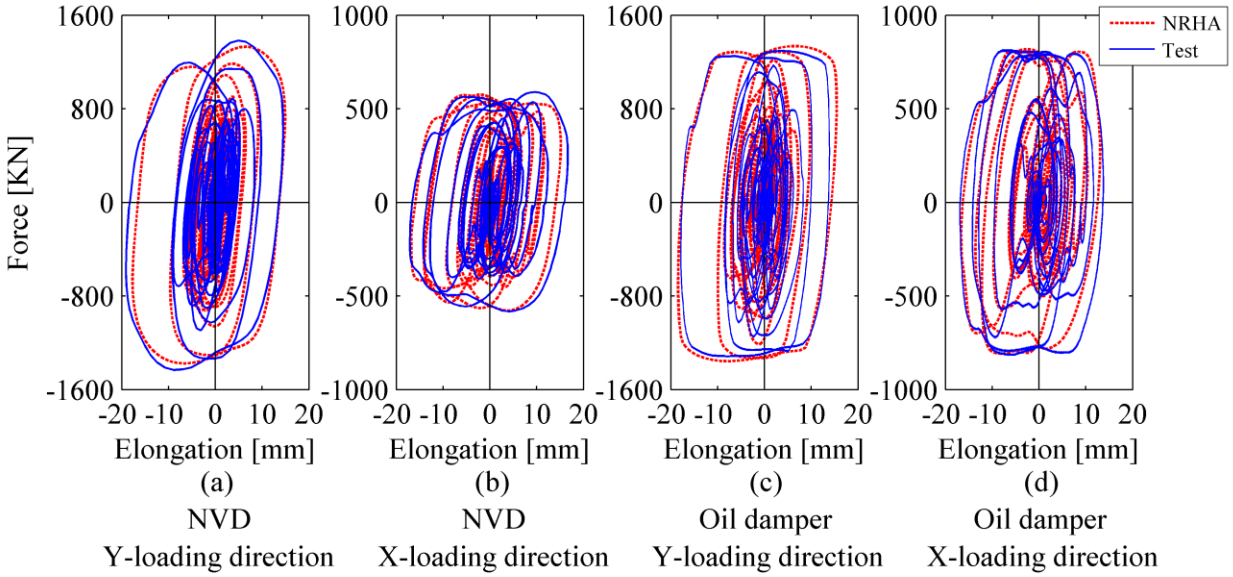

Figure 3.16: Comparison between the simulated and measured hysteretic response of nonlinear viscous and oil dampers installed in the first story of the test structure under the 100% seismic intensity of the JR Takatori record

CHAPTER 4 : Constitutive Model for Simulating the Loading-Rate Dependency of Buckling-Restrained Braces under Dynamic Excitations

4.1 Introduction

Since the earlier development of the first buckling-restrained braces (BRBs) (Wakabayashi et al. 1973; Kimura et al. 1976; Watanabe et al. 1988), extensive experimental research has been conducted for their further implementation into the seismic design practice (Merritt et al. 2003a; 2003b; Black et al. 2004; Tremblay et al. 2006; Fahnestock et al. 2007; Tsai et al. 2008; Kasai and Matsuda 2014). In North America, buckling-restrained braces are considered as an alternative solution to conventional braces (Tremblay et al. 2006; Symans et al. 2008). Lateral load resisting systems that utilize BRBs are categorized as buckling-restrained braced frames (BRBFs) in the North American seismic design specifications (CSA 2009; AISC 2010b). In Japan, BRBs are treated as yielding devices (i.e., steel dampers) that provide stiffness and supplemental hysteretic energy to control lateral drift demands (Kasai et al. 2008b). It is common to employ low-yield point steel, such LYP225 (σ_y = 225 MPa) and LYP100 (σ_y = 100 MPa) in BRBs (Saeki et al. 1998). In this case, BRBs can provide supplement damping to a building at relatively small story drift ratios (Chen et al. 2001). An equivalent yield load for BRBs can be

obtained by using reduced area for the steel core with higher strength steel. However, with the same length of yielding segment this design leads to lower effective stiffness of BRBs, which delays yielding of BRBs. Alternatively, shorter yielding segments can be utilized to initialize yielding at earlier displacements. However, in this case large plastic strain needs to be accommodated, which may lead to low-cycle fatigue fracture of the yielding segment (Tremblay et al. 2006). The hysteretic behavior of low-yield point steel shows significant dependency to the loading-rate compared to mild steel (Yamada et al. 2004; Ooki et al. 2009; Kasai et al. 2010). The amplification of BRB forces due to strain-rate effects leads to higher demands on non-dissipative structural elements, such as connections, beams and columns. These elements are expected to remain elastic during a low-probability of occurrence seismic event.

In the context of Performance-Based Earthquake Engineering we need reliable numerical models for simulating the nonlinear response of various structural components. Historically, BRBs have been modeled with bilinear elastoplastic models (Sabelli et al. 2003; Kiggins and Uang 2006). Others (Black et al. 2004; Yu et al. 2013) have utilized smooth hysteretic material models (Menegotto and Pinto 1973; Wen 1976) to simulate the Bauschinger effect as well as the combined kinematic/isotropic hardening that is typically evident in low yield stress point steel materials (Kanno 2016). Although the shear transfer of the steel core and mortar is minimized through the use of unbounding materials, recent experiments showed that the compressive strength of BRBs is higher than the corresponding tensile strength due to the contact between the steel core and the mortar caused by the Poisson effect (Chen et al. 2001; Black et al. 2004; Tremblay et al. 2006). For this reason, Zona and Dall'Asta (2012) proposed a nonlinear asymmetric smooth hysteresis model to simulate the behavior of BRBs. In a more recent study, Zsarnóczay (2013) modified the Menegotto-Pinto material model for the same purpose. The

aforementioned models share a limiting feature. In particular, they are not able to trace the steel material strain-rate dependency. Instead, they are only based on displacement-dependent constitutive relations. The dynamic force amplification due to strain-rate effects is typically captured through an adjustment of the steel core material yield strength such that the BRB hysteretic response of a certain loading frequency can be matched. This frequency is typically selected close to the fundamental frequency of the building under consideration (Yu et al. 2013). Although this approach is convenient, it requires the dynamic properties of the building *a priori*. In any case, such models are rate-independent; therefore, during the response history analysis the BRB force variation under different vibration frequencies is not captured. This could be a fundamental concern in tall buildings vibrating in higher modes. It is therefore understood that a reliable BRB model is needed that captures the strain-rate effects as part of its constitutive formulation. Yamada et al. (2004) found a nonlinear relation between the strain-rate and dynamic stress ratio based on a series of tests on BRBs fabricated with low yield point steel material (LYP100). They proposed a non-smooth hysteretic BRB model, which implicitly accounts for the strain-rate effects by amplifying the static stresses in the steel core with a dynamic stress ratio, which is a function of the strain rate. More recently, Kasai and Nishizawa (2010) attempted to capture the velocity-dependent characteristics of low-yield strength point BRBs by explicitly considering the viscoelastic shear behavior of the unbonding agent. An added complexity in this case is how to provide rational input model parameters that reliably trace this behavior.

This paper proposes a numerical model that captures both the displacement- and velocity-dependent forces of a BRB under dynamic excitations. The general calibration process of the input model parameters of the proposed model is demonstrated through an illustrative example.

The numerical model is implemented in an open source nonlinear simulation platform. Alternative BRB component modeling approaches are also proposed such that the proposed model can be utilized within a nonlinear building model with BRBs. The efficiency of the proposed model is further illustrated through nonlinear building simulations of a 5-story steel frame building equipped with BRBs. This building was tested at full-scale in the world's largest shake table at E-Defense in Japan.

4.2 Description of the Hysteretic Behavior of Low Yield Stress Buckling-Restrained Braces

This section intends to describe in brief the hysteretic behavior of a typical low yield stress BRB. Referring to Figure 4.1 the steel brace is composed of yielding (steel core plate) and non-yielding segments. A steel tube (typically HSS) filled with mortar surrounds the steel core and works as a steel buckling restrainer. In order to minimize the friction between the mortar and the steel core an unbonding material is utilized. Figure 7.3 shows the hysteretic behavior of two nominally identical BRBs subjected to quasi-static and dynamic sinusoidal loading with constant peak displacement amplitudes, respectively (E-Defense 2008; Ooki et al. 2009). The steel core plate is made of low yield strength steel (LYP225) and the average yield strength and the elastic modulus of steel core plates were measured to be 225 MPa and 205 GPa, respectively. With reference to Figure 4.1, Table 4.1 summarizes the basic BRB geometric properties.

Referring to Figure 7.3a, the quasi-static test indicates a typical steel hysteretic behavior with combined kinematic and isotropic material hardening. The absolute maximum compressive axial force was 1.1 times larger than the corresponding tensile axial force. For instance, the peak compressive force was 1.3 times of the yield force of steel core, F_y. Referring to Figure 7.3b, the

dynamic test shows a significant amplification of the axial yield strength. In particular, forces reached up to 1.78 and 1.66 times of the yield force in tension and compression, respectively. Unlike the quasi-static test, the peak forces did not occur at the peak displacements and the transition from loading to unloading (i.e., edges of hysteresis) was smooth. This is a clear evidence of the existence of viscoelastic forces. Kasai and Nishizawa (2010) demonstrated that these additional dynamic forces are generated by two distinct phenomena: (1) the strain-rate-dependent characteristics of low yield strength steel that is assigned to the steel core plate; (2) viscoelastic shear stresses on steel brace surface due to the interaction between the steel core, the unbounding material and the mortar. The latter is indicative of the abrupt increase of forces observed at the beginning of loading/unloading cycles. This results to the hardening behavior of viscoelastic materials at high strain rate and large strains (Kasai et al. 2004b).

4.3 Proposed Model for Simulating the Hysteretic Response of Buckling-Restrained Braces

This section discusses the specifics of a proposed model for simulating the hysteretic response of BRBs. The proposed model combines the steel material strain rate effects and the viscoelastic behavior of the unbonding material into one single velocity-dependent component. Referring to Figure 4.1, both the displacement- (static) and velocity-dependent (dynamic) components of the BRB forces are assumed to be generated within the plastic segment. Therefore, the axial stress of a given section of the steel core is composed of two parts. The first one is a displacement-dependent hysteretic model to simulate the yielding steel core stress-strain relation. This model is asymmetric to reflect the difference between the compressive and tensile strength of a typical BRB. The second one is a Maxwell material that consists of a bilinear dashpot model (oil

damper) to simulate the velocity-dependent forces of the steel core and the unbonding material. The resultant stress σ of the yielding segment is computed as follows,

$$\sigma = \sigma_{sta} + \sigma_{dyn} \tag{4.1}$$

Hence, the resultant BRB force is as follows,

$$F = \sigma A_{pl} \tag{4.2}$$

in which, σ_{sta} and σ_{dyn} are the static and dynamic stress components and A_{pl} is area of the BRB steel core. Referring to Eq. 4.3, the strain, ε of the yielding steel segment is equal to the strain of the static ε_{sta} and dynamic ε_{dyn} components,

$$\varepsilon = \varepsilon_{sta} = \varepsilon_{dyn} = \frac{u}{L_{pl}} \tag{4.3}$$

in which, u and L_{pl} are the total elongation and length of the yielding steel segment, respectively. In order to simulate the displacement-dependent nonsymmetrical smooth hysteresis of a BRB, the Menegotto-Pinto (MP) material model (Menegotto and Pinto 1973; Filippou et al. 1983) is refined as shown in Figure 4.3a. The refined material model is implemented in the Open System for Earthquake Engineering Simulation (*OpenSees*), (McKenna 1997) platform. Other nonsymmetrical smooth hysteretic models can be used for the same purpose (Zona and Dall'Asta 2012; Zsarnóczay 2013).

The stress σ_{sta} of the nonsymmetrical material model can be computed as follows,

$$\sigma_{sta} = \sigma^*_{sta}\left(\sigma_{sta,0} - \sigma_{sta,r}\right) + \sigma_{sta,r} \tag{4.4}$$

Referring to Equation 4.5, the normalized stress, σ_{sta}* for loading and unloading, respectively, can be computed as follows,

$$\sigma^*_{sta} = b_p\varepsilon^* + \frac{\left(1-b_p\right)\varepsilon^*}{\left[1+\left(\varepsilon^*\right)^{R_p}\right]^{1/R_p}} \text{ (loading)}; \qquad \sigma^*_{sta} = b_n\varepsilon^* + \frac{\left(1-b_n\right)\varepsilon^*}{\left[1+\left(\varepsilon^*\right)^{R_n}\right]^{1/R_n}} \text{ (unloading)} \tag{4.5}$$

in which ε^* is the normalized strain that is computed as follows,

$$\varepsilon^* = \frac{\varepsilon - \varepsilon_r}{\varepsilon_0 - \varepsilon_r} \tag{4.6}$$

in which, $\sigma_{sta,0}$ and ε_0 are the corresponding stress and strain at the intersection point of the initial and tangent lines. These values are influenced by the isotropic hardening component as discussed later on (see Equations (4.10) and (4.11)). Similarly, $\sigma_{sta,r}$ and ε_r are the stress and strain values, respectively, recorded at the location where the last strain reversal with stress of equal sign; b_p and b_n are the strain hardening ratios for tension and compression, respectively,

$$b_p = \frac{E_{shp}}{E}; \quad b_n = \frac{E_{shn}}{E} \tag{4.7}$$

in which, E_{shp} and E_{shn} are the post-yielding tangent modulus in tension and compression, respectively; R_p and R_n represent the Bauschinger effect in tension and compression, respectively, and are computed as follows,

$$R_p = R_{0p}\left(1 - \frac{C_{Rp1}\xi}{C_{Rp2} + \xi}\right); \quad R_n = R_{0n}\left(1 - \frac{C_{Rn1}\xi}{C_{Rn2} + \xi}\right) \tag{4.8}$$

in which, R_{0p}, C_{Rp1}, C_{Rp2} and R_{0n}, C_{Rn1}, C_{Rn2} are the parameters to be defined together for tension and compression, respectively; ξ is the plastic excursion updated following a strain reversal. The yield strains for positive (ε_{yp}) and negative (ε_{yn}) loading directions are determined as follows,

$$\varepsilon_{yp} = \frac{\sigma_{yp}}{E}; \quad \varepsilon_{yn} = \frac{\sigma_{yn}}{E} \tag{4.9}$$

in which, σ_{yp} and σ_{yn} is the tensile and compressive yield strength, respectively; and E is the elasticity modulus of steel core material. The ε_0 and $\sigma_{sta,0}$ values for loading and unloading can be computed as follows,

$$\varepsilon_0 = \frac{\sigma_{yp}\delta_p - E_{shp}\varepsilon_{yp}\delta_p - \sigma_{sta,r} + E_0\varepsilon_r}{E - E_{shp}} \text{ (loading)}; \ \varepsilon_0 = \frac{-\sigma_{yn}\delta_n + E_{shn}\varepsilon_{yn}\delta_n - \sigma_{sta,r} + E_0\varepsilon_r}{E - E_{shn}} \text{ (unloading)} \tag{4.10}$$

$$\sigma_{sta,0} = \sigma_{yp}\delta_p + E_{shp}\left(\varepsilon_0 - \varepsilon_{yp}\delta_p\right) \text{ (loading)}; \quad \sigma_{sta,0} = -\sigma_{yn}\delta_n + E_{shn}\left(\varepsilon_0 + \varepsilon_{yn}\delta_n\right) \text{ (unloading)} \quad (4.11)$$

in which, δ_p and δ_n is the shift of yield line due to isotropic hardening in the positive and negative direction, respectively. These are computed as follows,

$$\delta_p = 1 + a_{p1}\left(\frac{\varepsilon_{\max} - \varepsilon_{\min}}{2a_{p2}\varepsilon_{yp}}\right)^{0.8}; \quad \delta_n = 1 + a_{n1}\left(\frac{\varepsilon_{\max} - \varepsilon_{\min}}{2a_{n2}\varepsilon_{yn}}\right)^{0.8} \quad (4.12)$$

in which, ε_{max} , ε_{min} are the maximum and minimum strains at the instant of strain reversal. a_{p1}, a_{p2} and a_{n1}, a_{n2} define the yield line curve for the positive and negative strength, respectively.

It is known that the strain-rate and dynamic amplification relationship is nonlinear (Yamada et al. 2004); therefore, the viscoelasticity can be represented by a Maxwell model with a bilinear dashpot. This is typically used to simulate the hysteretic behavior of bilinear oil dampers (see Chapter 3). Because the dashpot and the uniaxial spring are connected in series (see Figure 4.3b and 4.3d), the dynamic stresses σ_{dyn} at the bilinear dashpot and at the elastic spring are equal; therefore, the constitutive rules within a Maxwell model can be written as follows,

$$\sigma_{dyn} = \begin{cases} \eta_d \dot{\varepsilon}_d = E_{sp}\varepsilon_{sp}, & \left|\sigma_{dyn}\right| \le \sigma_{rel} \\ \operatorname{sgn}\left(\dot{\varepsilon}_d\right)\sigma_{rel} + p\left(\dot{\varepsilon}_d - \dot{\varepsilon}_{rel}\right) = E_{sp}\varepsilon_{sp}, & \left|\sigma_{dyn}\right| > \sigma_{rel} \end{cases} \quad (4.13)$$

$$\dot{\varepsilon}_{rel} = \frac{\sigma_{rel}}{\eta_d} \quad (4.14)$$

in which, η_d is the damping coefficient of the dashpot, E_{sp} is the elastic stiffness of the spring, p is the post relief damping coefficient ratio, σ_{rel} and $\dot{\varepsilon}_{rel}$ are the relief force and relief strain-rate of the bilinear oil damper, respectively; ε_d and ε_{sp} are the strains at the dashpot and spring, respectively. Their summation is equal to the total strain of the yielding steel core as follows,

$$\varepsilon = \varepsilon_d + \varepsilon_{sp} \quad (4.15)$$

$$\dot{\varepsilon} = \dot{\varepsilon}_d + \dot{\varepsilon}_{sp} \tag{4.16}$$

Further details regarding the constitutive equations of a bilinear oil damper and its numerical solutions can be found in Chapter 3.

4.4 Calibration Process

The proposed model can be calibrated based on quasi-static and dynamic sinusoidal loading tests on BRBs with different loading frequencies and displacement amplitudes. This is shown schematically in Figure 7.3. The calibration of the proposed model is carried out in the stress-strain domain. Typically, the displacements at the BRB ends are measured with a reference point to be the restrainer ends. Therefore, the measured displacements may include the elastic segment elongation (see Figure 4.1). This elongation should be eliminated from the measured BRB displacement in order to obtain the yielding segment displacement, u. Eventually, the strain of the yielding steel segment (ε) is obtained as given in Equation (4.3).

First, the displacement-dependent MP model properties should be computed based on a conventional BRB quasi-static test. These include the yield strength, σ_{yp}, the post-yielding stiffness ratio, b_p and the parameters associated with the Bauschinger (R_{0p}, cR_{p1}, cR_{p2}) and isotropic hardening effects (a_{p1}, a_{p2}). If the quasi-static hysteresis is nonsymmetrical, the parameters that control the compressive behavior of the BRB (σ_{yn}, b_n, R_{0n}, cR_{n1}, cR_{n2}, a_{n1}, a_{n2}) should be calibrated accordingly.

Once, the displacement-dependent MP model parameters are determined, the parameters of the velocity-dependent bilinear oil damper model (E_{sp}, η_d, σ_{rel}, p) can be obtained based on a dynamic BRB test.

For a sinusoidal loading protocol, if only the force-displacement hysteresis of BRBs is available, assuming that the bilinear oil damper is within its linear stage for relatively low displacement amplitudes (see Figure 4.3b), the bilinear oil damper calibration can be carried out as follows: The stress corresponding to the peak displacement ($\sigma_{storage}$) and the stress corresponding to the zero displacement (σ_{loss}) of a bilinear damper model (see Figure 4.4) is found by subtracting the corresponding stresses from the quasi-static test. It is important to note that the calibration process ignores the abrupt hardening effect of the unbonding material, which typically occurs at the beginning of the cycle at large strain-rates (see Figure 4.2b). Therefore, the $\sigma_{storage}$ and σ_{loss} are calibrated based on the steady response of the hysteresis.

As shown in Figure 4.4a, from the Kelvin-Voigt model, the spring and dashpot are connected in parallel; therefore, the equivalent damping coefficient $\eta_{d,eq}$ and equivalent stiffness $E_{sp,eq}$ can be obtained as follows,

$$\eta_{d,eq} = \frac{\sigma_{loss}}{\omega \varepsilon_0} \tag{4.17}$$

$$E_{sp,eq} = \frac{\sigma_{storage}}{\varepsilon_0} \tag{4.18}$$

in which, ε_0 is the peak strain amplitude and ω is the circular frequency ($=2\pi f$) of the imposed sinusoidal excitation, respectively. Having determined the parameters of the Kelvin-Voigt model, one can compute the damping coefficient η_d and the stiffness E_{sp} of the Maxwell model (see Figure 4.4b) based on the equations summarized in Constantinou et al. (1998). In particular,

$$\eta_d = \eta_{d,eq}(1 + \tau^2 \omega^2) \tag{4.19}$$

$$E_{sp} = \frac{\eta_d}{\tau} \tag{4.20}$$

in which, τ is the relaxation time constant of the Maxwell model, which can be computed as follows,

$$\tau = \frac{E_{sp,eq}}{\eta_{d,eq}\omega^2} \tag{4.21}$$

Once E_{sp} and η_d are obtained, in order to account for the nonlinearity of the stress strain-rate relationship, the relief stress σ_{rel} and post-relief damping coefficient ratio p can be calibrated to match the hysteresis at larger strain demands; σ_{rel} can be set equal to maximum force $\sigma_{dyn,max}$ of the corresponding linear Maxwell model as follows,

$$\sigma_{dyn,\max} = \sqrt{\sigma_{loss}^2 + \sigma_{storage}^2} \tag{4.22}$$

4.5 Experimental Validation

4.5.1 Calibrations based on Buckling Restraint Brace Component Tests

This section provides an illustrative example of the proposed BRB model calibration based on full-scale component tests on BRBs conducted by (Ooki et al. 2009). The geometric and material properties of the BRB specimens are summarized in Table 4.1. The hysteretic response of the BRBs is shown in Figure 7.3 for both quasi-static and dynamic uniaxial cyclic loading. In brief, the asymmetric MP and bilinear oil damper material models are calibrated in two steps. Quasi-static BRB tests are utilized for the former and dynamic BRB tests are employed for the latter.

To calibrate the asymmetric MP material model, the force-displacement relation of the BRB based on a quasi-static test (see Figure 7.3a) is converted to an equivalent stress-strain curve. Referring to Figure 4.1, the elastic contribution of the elastic segments is subtracted. The yield stress under uniaxial tension, σ_{yp} refers to the 0.2% strain offset (Boresi et al. 1993; ASTM 2016) of the equivalent stress-strain curve shown in Figure 4.5. The compressive yield stress set

to $\sigma_{yn} = 1.1\sigma_{yp}$ to account for the increased stresses in compression(Tremblay et al. 2004). The strain hardening ratios b_p, and b_n are then calibrated such that the post-yield hardening ratio between the measured and simulated data match. The R_0, C_R, a_1 and a_2 parameters are then calibrated such that the total relative error between the simulated and measured stress throughout the imposed strain history becomes minimal. Referring to Table 4.2, different parameters were utilized in uniaxial tension and compression to achieve the best match. This is due to the contact between the steel core and the mortar that is caused by the Poisson effect. Figure 4.5 suggests an excellent match between the simulated and measured equivalent stress-strain response of the yielding segment of the BRB under quasi-static cyclic loading.

In a second step, the bilinear oil damper material model is calibrated based on dynamic sinusoidal uniaxial cyclic BRB component tests shown in Figure 4.2b. In this case, the excitation frequency is $f = 2$ Hz. Referring to Figure 4.2b, the measured uniaxial force-displacement relation of the BRB is converted to an equivalent uniaxial stress-strain relation after subtracting the elastic deformation from the elastic segments. Figure 4.6 illustrates the calibration steps of the proposed BRB model. In particular, each figure shows a comparison between the deduced stress-strain relation and the simulated one. In this figure, we have also superimposed the displacement-dependent (blue) and velocity-dependent (green) components of the BRB response. Referring to Figures 4.6a and 4.6b, we assumed that during the first loading cycle (i.e., $\varepsilon_0 = 0.0041$) the stress-strain rate relation at the dashpot is linear. The loss and storage stresses can then be obtained after subtracting the equivalent stresses from the static simulation from those obtained from the dynamic tests. In this case, the loss and storage stresses were equal to $0.18\sigma_{yp}$. The damping coefficient η_d and the elastic stiffness of the spring E_{sp} can be computed based on Equations 18-23. Table 4.3 summarizes the calibrated η_d and E_{sp} values. Referring to

Figure 4.6a, if a large E_{sp} value was assumed, the proposed model would overestimate the BRB forces near zero displacement.

Referring to Figure 4.6c, the relief stress σ_{rel} is calibrated based on the peak equivalent stress of the first loading cycle (i.e., $\sigma_{rel} = 0.255\sigma_{yp}$). The post relief damping coefficient ratio, p is p=0.15 after matching the simulated response of the proposed model with the experimental data at the loading cycles with 0.8 and 1.2% strain amplitudes. Referring to Figure 4.6d, the strain hardening ratio, b_n in the compressive range is refined. Table 4.3 summarizes the calibrated parameters for the rate dependent portion of the proposed BRB model.

4.5.2 Component Models for Buckling Restrained Braces

This section discusses two component modeling approaches for BRBs that utilize the proposed material model discussed earlier. Both approaches can be implemented into nonlinear building models for system level studies. The first approach employs typical beam-column elements as shown in Figure 4.7a. Referring to Figure 4.7b, a simplified approach can be employed in which the BRB can be idealized with a single link (or truss) element. This is similar with the approach discussed in Yu et al. (2013). Due to its simplicity, the second approach is convenient and can be easily implemented in three dimensional building models. Both modeling approaches are compared with component models that are built within the *OpenSees* (McKenna 1997) simulation platform.

Referring to Figure 4.7a, the BRB is idealized with five beam-column elements. The yielding segment of the BRB is modeled with forced-based distributed plasticity beam-column element. The rectangular steel core is discretized into 3x4 fibers along its width and length, respectively. The displacement-dependent material model is assigned to the fiber cross-section. The non-

yielding BRB segments are idealized with elastic beam-column elements. Referring to Figure 4.7a, the velocity-dependent component of the BRB is idealized with a link element assigned between the end points of the yielding steel segment in parallel to the displacement-dependent component. The *BilinearOilDamper* material model is utilized for this purpose. The constitutive relation within the damper is solved numerically with the adaptive integration methods implemented in Chapter 3. The damping coefficient C_d, stiffness of the spring K_{sp} and relief load F_{rel} assigned to the link element can be computed as follows,

$$C_d = \eta_d \frac{A_{pl}}{L_{pl}} \tag{4.23}$$

$$K_{sp} = E_{sp} \frac{A_{pl}}{L_{pl}} \tag{4.24}$$

$$F_{rel} = \sigma_{rel} A_{pl} \tag{4.25}$$

in which the bilinear oil damper model parameters (E_{sp}, η_d, σ_{rel}, p) are utilized from Table 4.3.

Referring to Figure 4.7b, if a BRB is idealized with a single link (or truss) element, the effective stiffness of the displacement-dependent component K_{eff} should be computed as follows,

$$\frac{1}{K_{eff}} = \frac{1}{K_{pl}} + \frac{2}{K_{el}} + \frac{2}{K_{con}} \tag{4.26}$$

in which, K_{pl}, K_{el} and K_{con} are the axial stiffnesses of the yielding steel segment and the elastic steel segments, and connections, respectively. The inferred kinematic and isotropic hardening parameters of the yielding segment should be adjusted in order to be assigned to the link element. This can be done based on the stiffness ratio of the yielding steel core, K_{pl} to the effective stiffness K_{eff}. In particular, the strain hardening ratio of the link element in tension and compression can be computed as follows,

$$b_{p,eff} = b_p \frac{K_{pl}}{K_{eff}}; \quad b_{n,eff} = b_n \frac{K_{pl}}{K_{eff}} \tag{4.27}$$

Similarly, referring to Equation (4.12), the coefficients of ε_{yp} and ε_{yn} should be adjusted as follows,

$$a_{p2,eff} = a_{p2} \frac{K_{eff}}{K_{pl}}; \quad a_{n2,eff} = a_{n2} \frac{K_{eff}}{K_{pl}} \tag{4.28}$$

For BRBs with typical dimensions it was found that the all practical purposes differences associated with the Bauschinger effect between the two approaches are negligible.

Regarding the velocity-dependent portion of the BRB, the inferred stiffness of the bilinear oil damper model can be assumed equal to K_{sp} assigned to the nonlinear beam-column model. This is due to the fact that contribution of elastic segments to the total strain is much lower compared to yielding segment.

Figure 4.8 shows a comparison of the force-displacement relation obtained based on the beam-column and the single link element modeling approaches. The K_{pl}/K_{eff} = 1.49 in this case. The properties of this BRB model are those of the BRB, which is placed in the second story of the 5-story test structure in Y-loading direction that are summarized Tables 4.4 and 4.5, Further details of this test structure and its numerical validation are discussed in next section. The hysteretic behavior of the displacement and velocity-dependent components of the BRB models are illustrated in Figures 4.9a and 4.9b, respectively, while Figure 4.9c shows their combined action. The displacement-dependent component of the model with link element with corrected effective parameters, slightly underestimated the BRB forces at the point that the Bauschinger effect is evident, while it slightly overestimated the velocity-dependent force contribution as expected. These contradicting errors of the link model cancel each other within the combined model as

shown in Figure 4.9c. There is practically no difference between the two modeling approaches. Note that $K_{pl}/K_{eff} = 1.49$ is the maximum value in Table 4.5, therefore less error is expected in the numerical simulation of other BRBs.

4.5.3 Nonlinear Building Simulations and Comparison with Full-Scale Shake Table Experiments

In this section, the efficiency of the proposed BRB model is demonstrated through system level validation studies. For this purpose, we utilize the test results from the full-scale shake table experiment of the 5-story steel frame building equipped with BRBs (Hikino 2012; Kasai and Matsuda 2014). This test was conducted at the world's largest shake table at E-Defense in Japan (Ohtani et al. 2004).

Figure 4.9a shows the 5-story test structure on the shake table. Referring to Figures 4.9b to 4.9d, the test structure had a plan view of 10x12m and consisted of two-bay moment resisting frames per loading direction. The test structure was equipped with twelve dampers (four in the Y-loading direction; eight in the X-loading direction). The BRBs were fabricated with low yield strength steel (LYP225). Their geometric and material properties are summarized in Table 4.4 as reported in Kasai et al. (2012). The total height of the test structure was 15.8 m and its overall weight was 4734 KN. Due to brevity, further details regarding the geometric properties and member sizes of the test structure can be found in prior studies (E-Defense 2008; Ooki et al. 2009; Kasai et al. 2010; Kasai and Matsuda 2014).

The test structure was subjected to the 3-component earthquake motion of the JR Takatori record from the 1995 Kobe earthquake. The dynamic properties of the test structure were obtained with a white noise motion as discussed in Ji et al. (2013) and Kasai and Matsuda (2014).

A 3-Dimensional (3D) numerical model representation of the test structure is developed in the *OpenSees* simulation platform. Its frame components are modelled with nonlinear beam-column elements as discussed in prior studies by the authors (Lignos 2012; Akcelyan et al. 2016). Viscous damping is modelled with the Rayleigh damping model by assuming 1% damping ratio to the first and third modes of the building model. This value is consistent with prior damping identification studies (Ji et al. 2013).

The BRBs are modeled with the link element discussed in the previous section. Table 4.5 summarizes the computed input model properties assigned to each link element. Referring to Eqn. (4.26), for the effective stiffness, K_{eff} computation it was assumed that the section area between connections and working points is equal to the area of the connections. The BRBs were fabricated with LYP225 steel and the same unbonding material with the ones tested by Ooki et al. (2009). Therefore, the parameters of the displacement-dependent material model of the yielding segment were assumed to be the same with the ones summarized in Table 4.2. These parameters were just transformed to be properly assigned to the link element based on Equations (4.27) and (4.28). The fundamental natural frequencies of the test structure equipped with BRBs in both directions were close to 2 Hz (Kasai and Matsuda 2014). Therefore, the input model parameters for the velocity dependent component of the proposed BRB model (i.e., the damping coefficient, C_d, the axial stiffness K_{sp} and the relief load, F_{rel}) were computed based on the values summarized in Table 4.3.

The evaluation was carried out for two seismic intensities, namely the 40% and 100% of the unscaled JR Takatori record. Nonlinear response history analysis (NRHA) was conducted by means of direct integration of the equations of motion using the Newmark's average acceleration method (Newmark 1959). The analysis was conducted with an integration time step

$dt = 0.01$ sec. In order to explore the effect of the velocity-dependent component of the BRB model on the global building response, two cases were analyzed. In the first one (noted as NRHA1) only the displacement-dependent component of the proposed model was considered. In the second case (noted as NRHA2) the velocity dependent component was also considered.

Figure 4.10 compares the absolute peak values of the engineering demand parameters (EDPs) [story drift ratios, story shear forces and floor absolute accelerations] obtained from the nonlinear building simulation and the experimental results from the 40% and 100% of the unscaled Takatori record in both loading directions. Figure 4.11 shows a comparison between the simulated and measured force-displacement relation of various BRBs within the 5-story test structure for the 100% of the unscaled Takatori record. From these comparisons, the following observations hold true:

- Referring to Figures 4.10a to 4.10c, the average error between the predicted story-based peak EDPs and the test data is fairly consistent in the X-loading direction regardless of the employed BRB model.
- Referring to Figure 4.10d, the peak story drift ratios along the height of the test structure in the Y-loading direction tend to be over predicted when the velocity-dependent component of the BRB is neglected. These differences become larger while the ground motion seismic intensity increases. Consider that in this case, the strong component of the JR Takatori record was imposed in the Y-loading direction. This is attributed to the fact that in NRHA1 the BRBs dissipate less energy and the test structure displaces more. Same observations hold true for the peak absolute floor accelerations shown in Figure 4.10f.

- Referring to Figure 4.11, if the local BRB response is of interest then the displacement history obtained from test results is utilized to simulate the BRB hysteretic behavior. To this end, similar to calibration procedure, the recorded force-displacement relation of the BRBs is converted to an equivalent axial stress-strain as discussed earlier. the peak BRB forces are significantly underestimated if the velocity dependent component of the BRB is neglected. This may be critical in cases that BRBs are employed for seismic retrofit of existing steel frame buildings. The forces transferred to the framing members could be considerably underestimated in this case.

It should be noted that the proposed BRB model neglects the abrupt strain hardening of the viscoelastic unbonding material under large shear strain amplitudes at high frequencies. This is the main reason that the peak tensile and compressive BRB forces are underpredicted by about 10%, on average, compared to the test data.

4.6 Summary and Conclusions

This paper proposes a new numerical model to simulate the hysteretic behavior of buckling restrained braces (BRBs) under dynamic loading. The proposed model incorporates the strain rate effects in its constitutive formulation. This is achieved by combining a nonsymmetric smooth hysteretic material and a bilinear oil damper material model. The former simulates the displacement-dependent component and the latter captures the velocity-dependent component of a BRB. A two-step calibration process of the proposed model is also proposed. This process requires two BRB component tests with a quasi-static and a dynamic sinusoidal uniaxial cyclic loading protocol. The calibration process is presented based on an illustrative example that employed test data from a prior experiment program.

The proposed model is implemented in a nonlinear finite element simulation platform. Two BRB component modeling approaches are proposed. The first approach utilizes beam-column elements while the second one is simpler and requires a single link element. The required relationships to map the proposed BRB model input parameters from one approach to the other are provided. It is shown that both approaches provide nearly identical results.

The efficiency of the proposed BRB model is illustrated through a system level study that utilized the experimental data from a full-scale shake table test of a 5-story steel frame building equipped with BRBs. A comparison of the simulated and experimental results suggests that when the velocity-dependency in the BRB model is neglected the BRB local forces are significantly under estimated. This may be fairly critical if BRBs are utilized as a seismic retrofit strategy in existing steel frame buildings. Depending on the frequency characteristics of the seismic excitation, similar differences may be observed in the predicted story-based engineering demand parameters, such as story-drift ratios and peak absolute floor accelerations.

Suggestions to further refine the capabilities of the proposed BRB model are proposed such that the nonlinear velocity-dependent characteristics of the unbending material can be considered.

Table 4.1: Properties of the BRB specimen (E-Defense 2008; Ooki et al. 2009)

L_{pl} [mm]	A_{pl} [mm^2]	L_{el} [mm]	A_{el} [mm^2]	σ_y [MPa]	E [GPa]
2861	4400	384.4	12276	225	205

Table 4.2: Calibrated parameters for asymmetric Menegotto-Pinto model (LYP225, E=205 GPa)

σ_{yp} [MPa]	σ_{yn} [σ_{yp}]	b_p	b_n	R_{0p}	C_{Rp1}	C_{Rp2}	R_{0n}	C_{Rn1}	C_{Rn2}	a_{p1}	a_{p2}	a_{n1}	a_{n2}
225	1.1	0.005	0.005 (0.015)	30	0.925	0.15	26	0.925	0.15	0.020	1.0	0.025	1.0

Table 4.3: Calibrated parameters for bilinear oil damper model (LYP225, E=205 GPa, f=2 Hz)

σ_{loss} [MPa]	$\sigma_{storage}$ [MPa]	η_{eq} [GPa·s]	E_{eq} [GPa]	τ [s]	η_d [GPa·s]	E_{sp} [GPa]	σ_{rel} [MPa]	p
168.3 ($0.18\sigma_{yp}$)	168.3 ($0.18\sigma_{yp}$)	0.79	9.95	0.080	1.58	19.89	57.38 ($0.255\ \sigma_{yp}$)	0.15

Table 4.4: Characteristic lengths and cross sectional areas of buckling-restrained braces of the 5-story test structure (E-Defense 2008)

Frame	Story	L_{pl} [mm]	A_{pl} [mm^2]	L_{el} [mm]	A_{el} [mm^2]	L_{con} [mm]	A_{con} [mm^2]	σ_y (1) [MPa]
X direction (2 bays)	4	2900	1408	277.3	3840	285	7264	217
	3	2900	1408	277.3	3840	285	7264	217
	2	2750	2204	303.3	5909	295	8569	227
	1	3600	2204	258.1	5909	295	8569	227
Y direction (1 bay)	4	2600	2794	393.3	7568	280	9856	220
	3	2600	2794	393.3	7568	280	9856	220
	2	2450	4400	469.5	12276	230	12276	220
	1	3300	4400	434.4	12276	230	12276	220

(1) The actual yield stress values reported by Kasai et al. (2012)

Table 4.5: Properties of developed BRB models assigned to a single link element

Frame	Story	F_{yp} [KN]	K_{eff} [KN/mm]	K_{pl}/K_{eff}	C_d [KN/(mm/s)]	K_{sp} [KN/mm]	F_{rel} [KN] (=0.255F_{yp})	p
X direction (2 bays)	4	306	81	1.23	0.77	9.66	77.8	0.15
	3	306	81	1.23	0.77	9.66	77.8	0.15
	2	500	126	1.31	1.27	15.94	127.4	0.15
	1	500	105	1.20	0.97	12.18	127.4	0.15
Y direction (1 bay)	4	615	161	1.38	1.70	21.38	156.5	0.15
	3	615	161	1.38	1.70	21.38	156.5	0.15
	2	968	248	1.49	2.84	35.72	246.4	0.15
	1	968	209	1.32	2.11	26.52	246.4	0.15

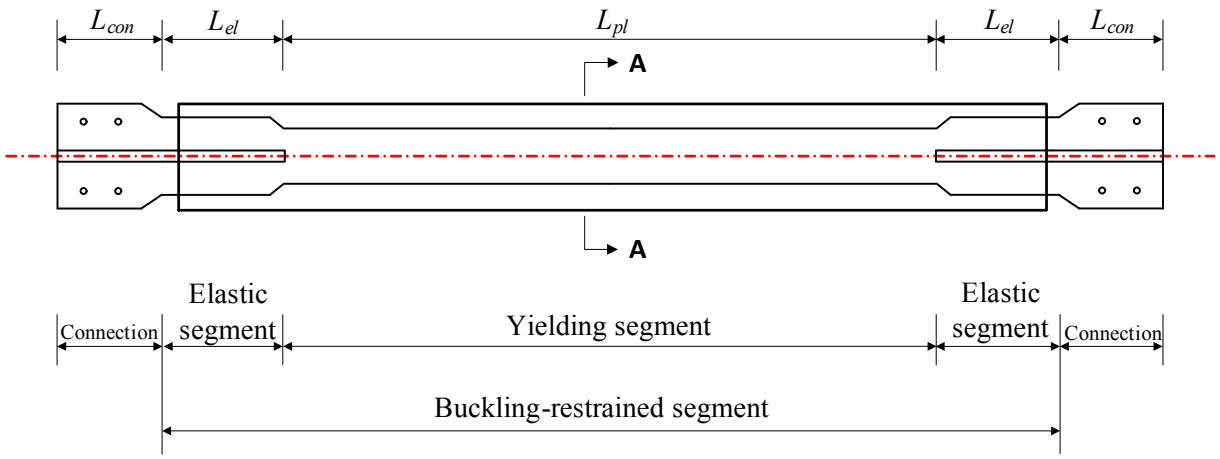

(a) Buckling-restrained brace: Steel brace and restrainer

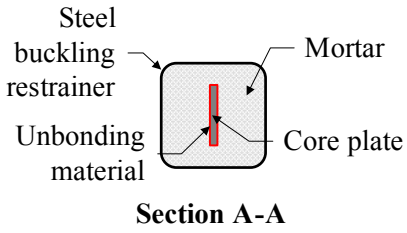

(b) BRB cross section at yielding segment

Figure 4.1: Typical buckling-restrained brace

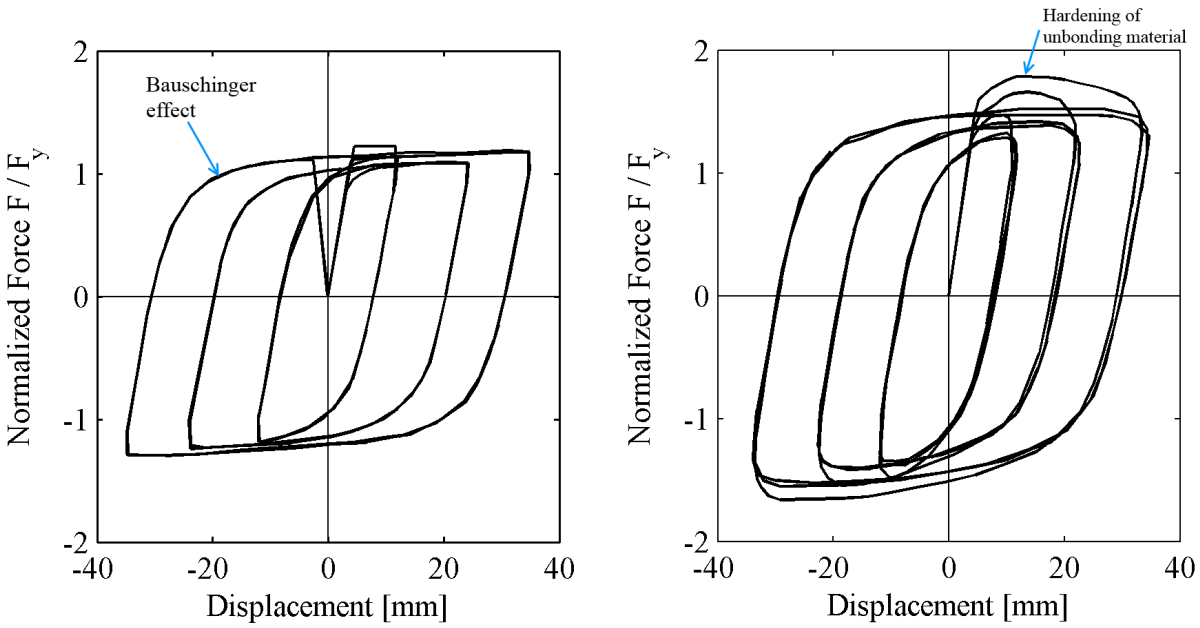

(a) Quasi-static test, f=0.05%/s (b) Dynamic test, f=2Hz

Figure 4.2: Static and dynamic hysteretic response of BRBs fabricated with LYP225 steel (experimental data from Ooki, 2009)

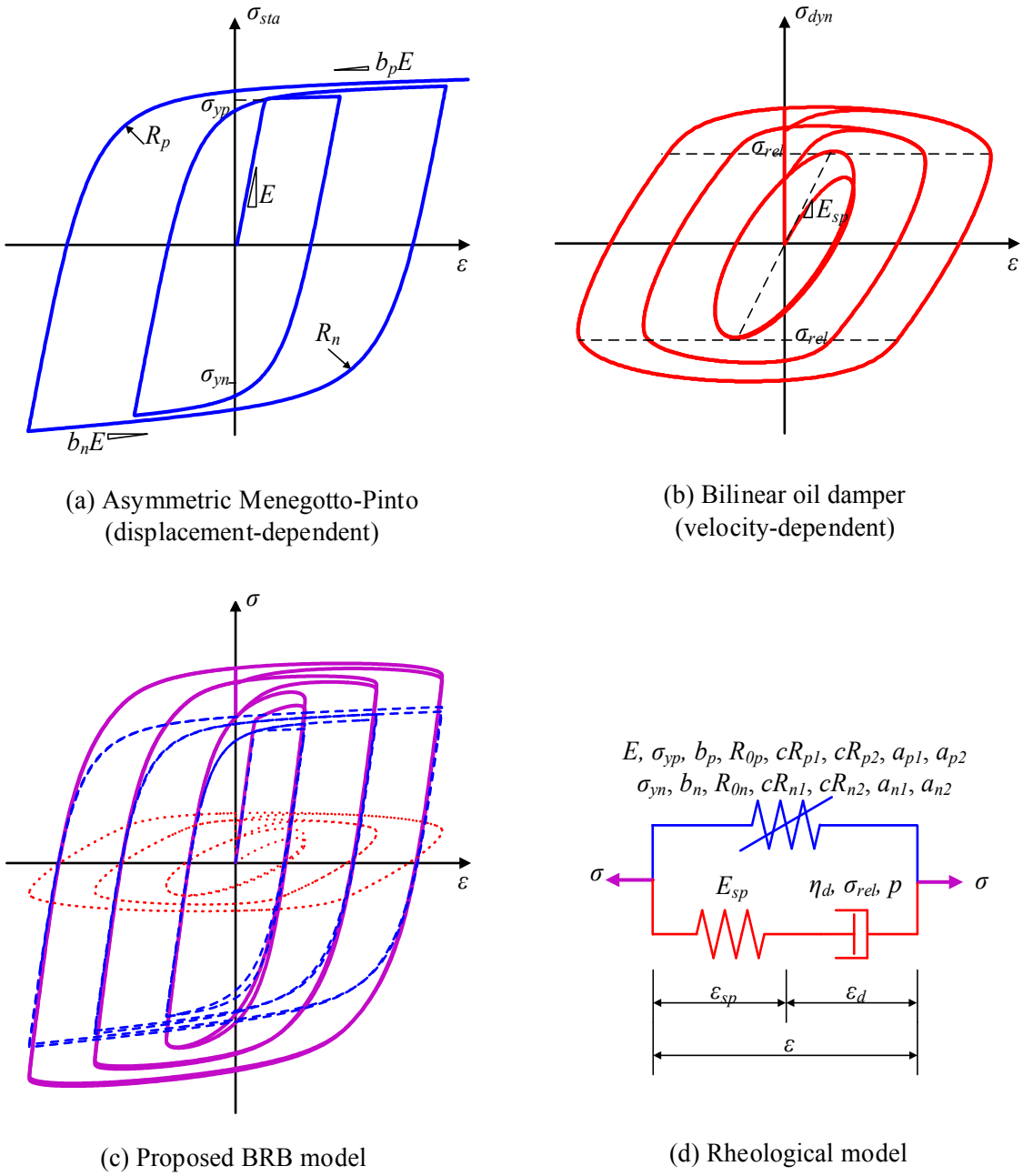

(a) Asymmetric Menegotto-Pinto (displacement-dependent)

(b) Bilinear oil damper (velocity-dependent)

(c) Proposed BRB model

(d) Rheological model

Figure 4.3: Proposed BRB model; displacement and velocity dependent components and rheological model presentation

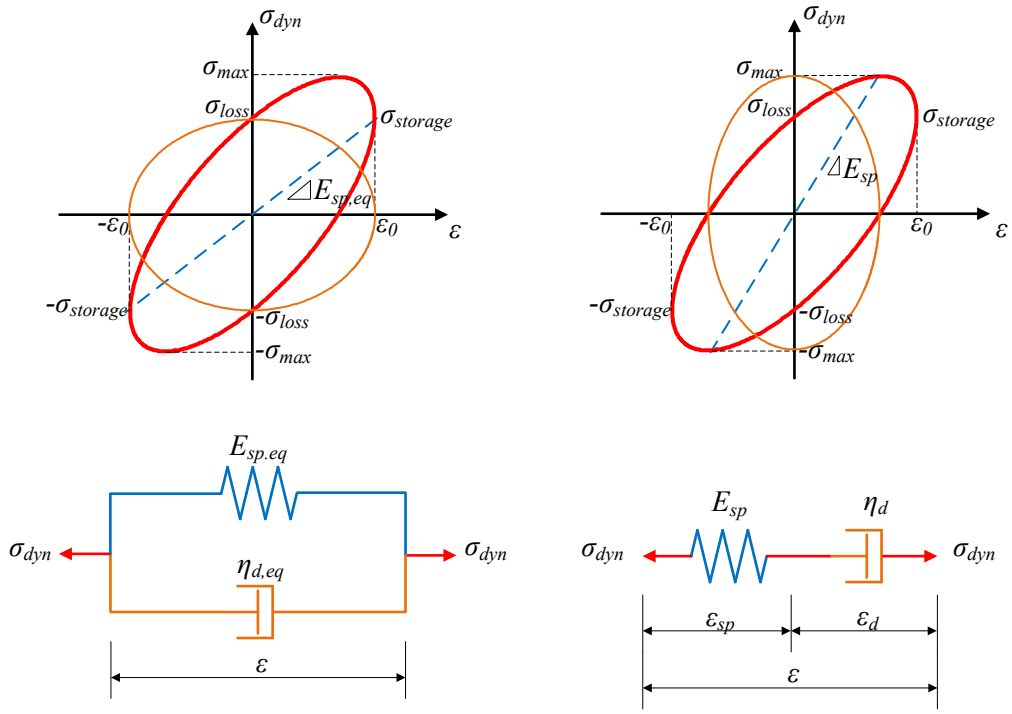

a) Kelvin-Voigt Model b) Maxwell Model

Figure 4.4: Equivalent viscoelasticity models and their response under sinusoidal loading

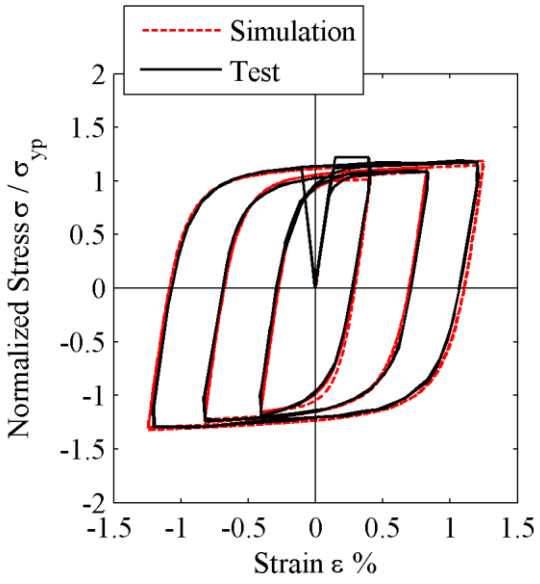

Figure 4.5: Simulation of quasi-static BRB test under cyclic loading

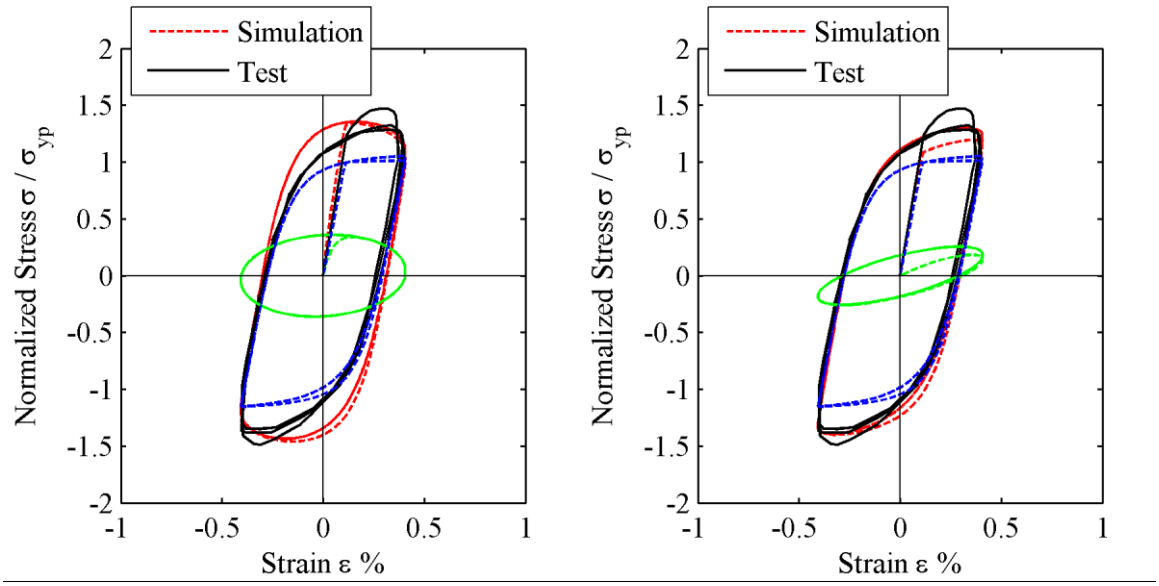

(a) Large E_{sp} value (E_{sp}=205GPa)

(b) Calibrated E_{sp} value (E_{sp}=19.89GPa)

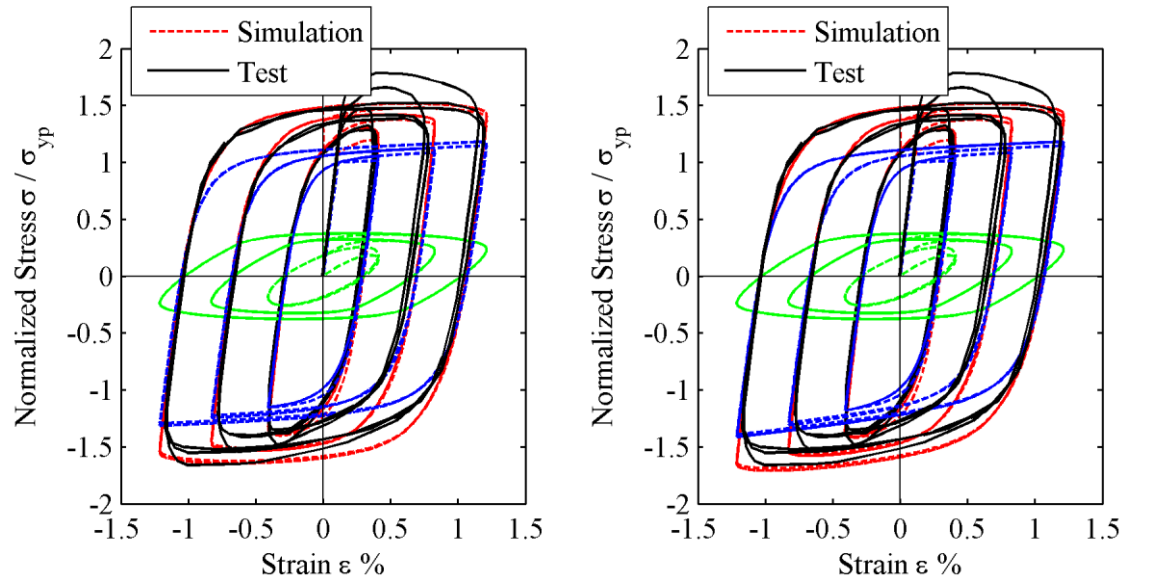

(c) Calibration of σ_{rel} = 0.255σ_{yp} and p =0.15

(d) Refined compressive strain hardening ratio, b_n=0.015

Figure 4.6: Calibration process of the proposed BRB model

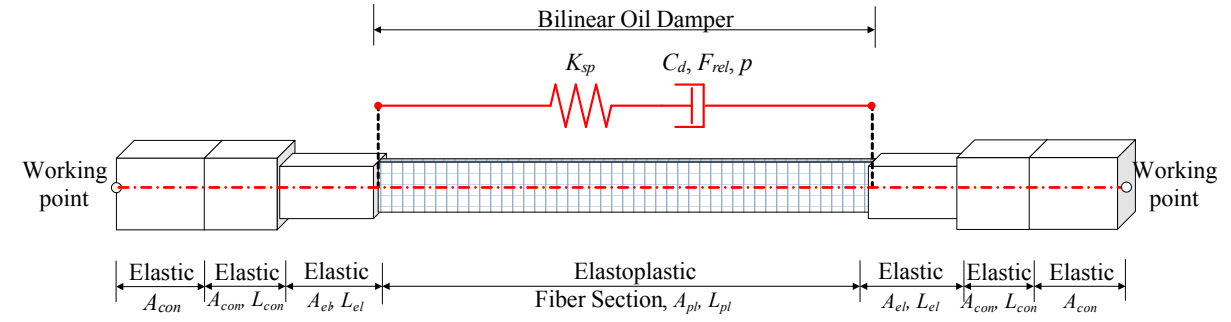

(a) BRB model with beam -column elements

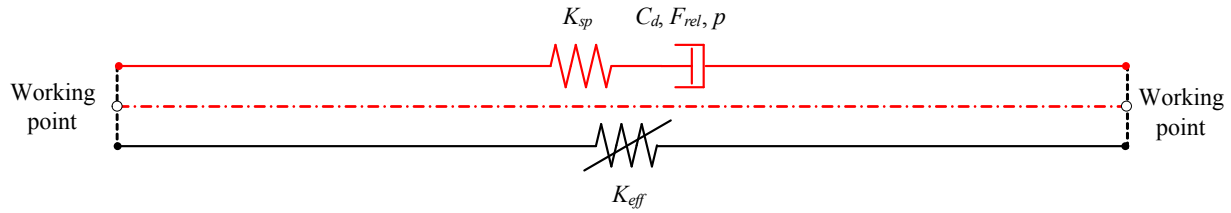

(b) Simplified BRB model with link (or truss) element

Figure 4.7: BRB modeling approaches: beam-column versus simplified link (or truss) element

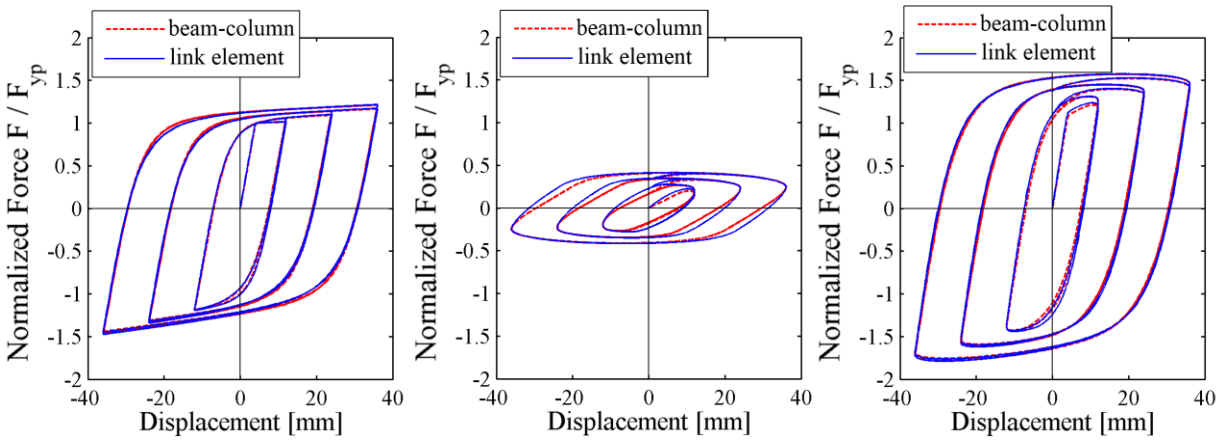

(a) Displacement-dependent component

(b) Velocity-dependent component

(c) Combined hysteretic response

Figure 4.8: Comparison of BRB modeling approaches with beam-column and link elements (K_{pl}/K_{eff}=1.49)

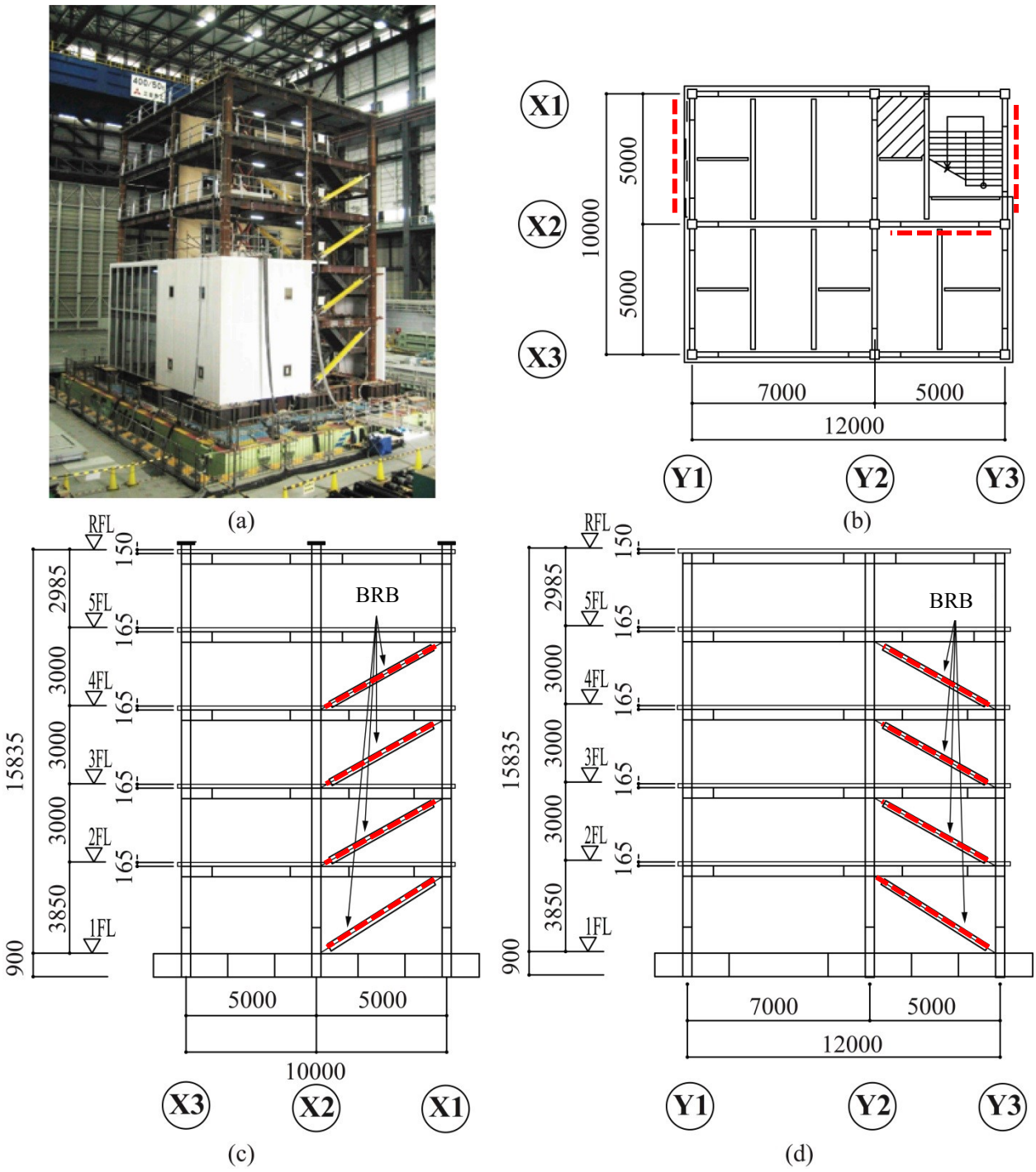

Figure 4.9: 5-story test-structure tested at E-Defense; (a) building after installation on the shake table; (b) plan view (c) elevation view in X- loading direction; (d) elevation view in Y-loading direction (images adopted from Akcelyan et al. (2016), dimensions in mm)

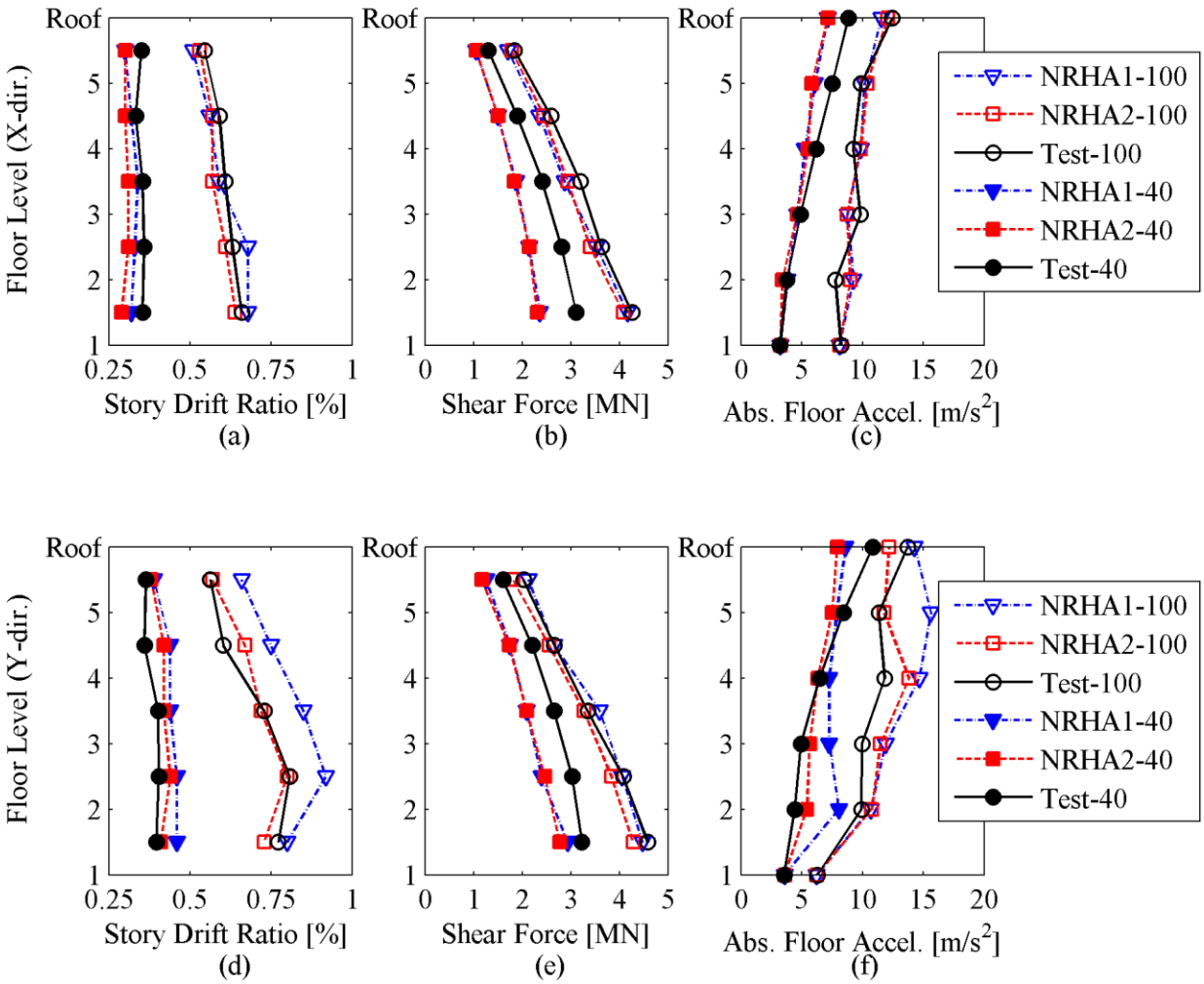

Figure 4.10: Comparison of simulated and measured peak story-based engineering demand parameters

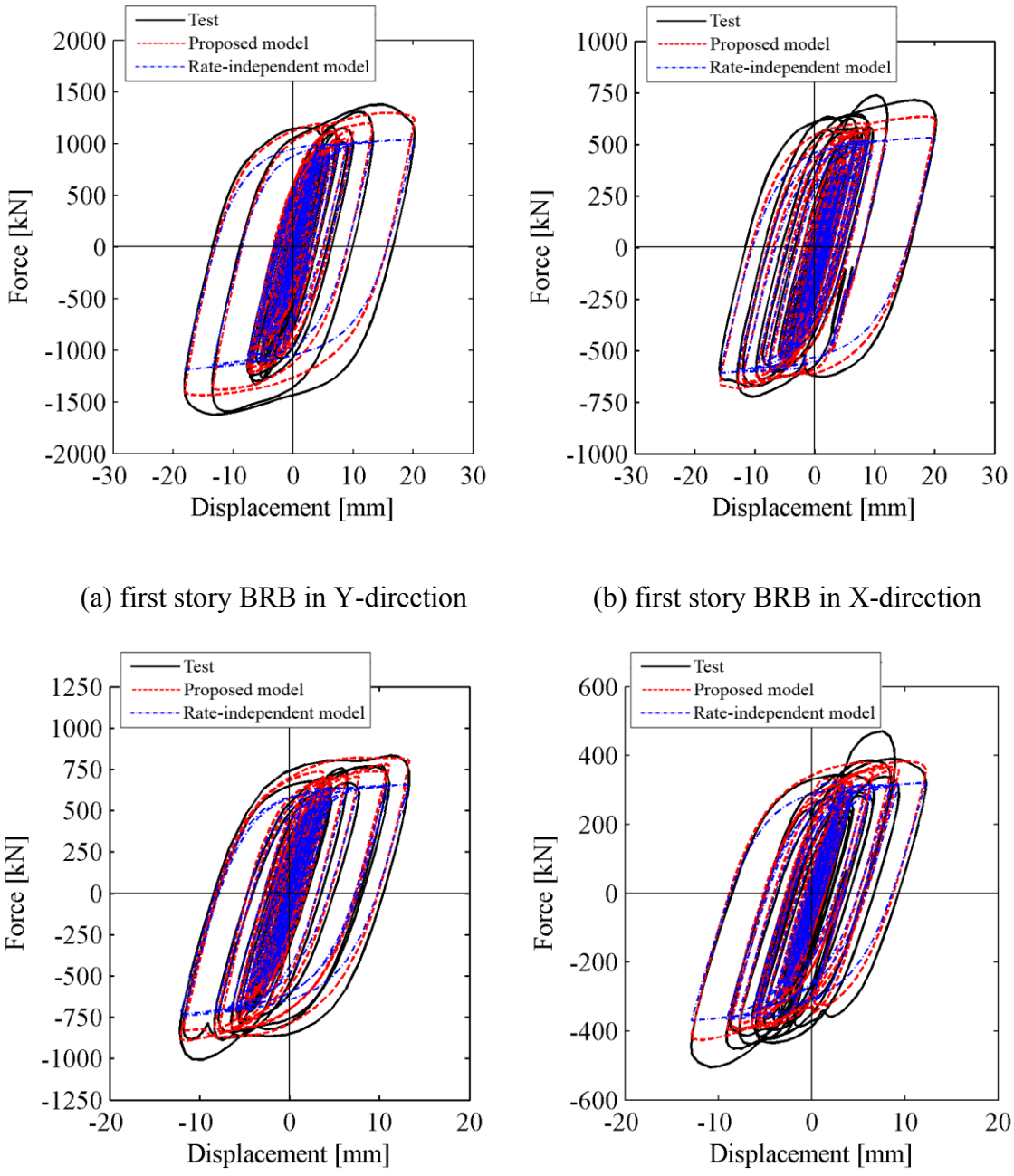

(a) first story BRB in Y-direction

(b) first story BRB in X-direction

(c) forth story BRB in Y-direction

(d) forth story BRB in X-direction

Figure 4.11: Comparison of the simulated and experimental hysteretic response of BRBs under the 100% seismic intensity of the JR Takatori record

CHAPTER 5 : Evaluation of Simplified and State-of-the-Art Analysis Procedures for Steel Frame Buildings Equipped with Supplemental Damping Devices Based on E-Defense Full-Scale Shake Table Tests

5.1 Introduction

The concept of resilient cities is becoming essential (Cimellaro et al. 2010). Recent earthquakes (e.g., Chile in 2010; Christchurch in 2011) in developed countries demonstrate that although conventional buildings designed according to regional seismic provisions had minimal structural damage afterwards they were still nonoperational because of extensive nonstructural damage. (Dhakal et al. 2011; Miranda et al. 2012). To this end, response modification (e.g., base isolation, supplemental damping devices, weakening) is widely advocated. Damage-free lateral load-resisting systems (e.g., self-centering and rocking systems) have also been developed that minimize structural damage in the aftermath of an earthquake (Christopoulos and Filiatrault 2006). The use of such systems is widely used in the current seismic design practice (Buchanan et al. 2011; Kasai et al. 2013b).

Because of the increasing use of supplemental damping devices for the design and/or the seismic retrofit of existing frame buildings, it is important to validate and refine various assessment procedures that are currently used for the evaluation of these buildings. Rigorous nonlinear response history analysis (NRHA) may be employed for this purpose. However, this may not be practical for a structural engineer because several iterations may be required to achieve the desired design objectives with an optimal use of damping devices. Therefore, the computational cost of NRHA may be significant. The difficulty of selecting and scaling representative ground motions that describe the regional seismicity may be another important consideration. To this end, several simplified assessment procedures have been developed for the seismic design and the performance evaluation of frame buildings equipped with supplemental damping devices. These methods include linear and nonlinear static procedures in accordance with ASCE 41-13 (ASCE/SEI 2014) and FEMA 274, 356, and 440 (FEMA 1997; 2000a; 2005) as well as performance curves (Kasai et al. 1998; Kasai and Ito 2005; Kasai et al. 2007), which are primarily based on linearization and transformation of frame buildings with dampers into equivalent linear single-degree-of-freedom (SDF) systems. More recently, a performance spectra (so-called P-Spectra) method (Guo and Christopoulos 2013a; 2013b) was proposed for the simplified design and retrofit of frame buildings with hysteretic and linear viscous/viscoelastic dampers. The P-Spectra method also provides an estimate of the expected residual deformations of a frame building with dampers (Kasai et al. 2008c). The aforementioned methods have not been evaluated with full-scale experimental data from frame buildings equipped with supplemental damping devices.

Several experimental studies have been conducted with frame buildings equipped with supplemental damping devices (Constantinou and Symans 1993b; Lai et al. 1995; Fahnestock et

al. 2007). These tests were either conducted in small scale and/or were unidirectional. Therefore, issues related to (1) three dimensional effects, (2) the composite action due to the presence of the floor slab, (3) the effectiveness of supplemental damping devices on limiting non-structural component damage were not addressed. During March 2009, a series of full-scale shake table tests of a "value-added" 5-story steel building equipped with four types of dampers was conducted at the world's largest shake table facility at E-Defense in Japan (Hikino 2012). This building was designed according to the Japanese design practice for buildings with supplemental damping devices [Japan Society of Seismic Isolation (JSSI) 2005]. The available experimental data provided insight for (1) the validation and refinement of current design methodologies; and (2) the refinement of modeling capabilities for conducting NRHA (Yamashita et al. 2010; Yu et al. 2013) for steel frame buildings equipped with supplemental damping devices. Similarly, other full-scale experiments conducted at the E-Defense shake table served for the aforementioned purposes (Maison et al. 2009; Dao et al. 2013; Lignos et al. 2013). However, to the best of authors' knowledge, there has never been an attempt to evaluate the effectiveness of various simplified methods in predicting the seismic response of frame buildings equipped with supplemental damping devices that are currently used in the engineering practice.

The present paper focuses on the evaluation of simplified assessment methods for steel frame buildings equipped with buckling-restrained braces (BRBs) and nonlinear viscous dampers (NVDs). This evaluation is based on full-scale experimental data that became available from recent shake table tests that were conducted at the E-Defense facility in Japan. Guidance is provided on limitations of various simplified methods depending on the supplemental damping device type. Several modeling approaches are also explored in different analysis platforms that

are currently used by researchers and engineering practitioners. Guidance on the minimum level of sophistication for NRHA of steel frame buildings with BRBs and NVDs is also provided.

5.2 Outline of Full-Scale Test

Figure 5.1a shows the "value-added" 5-story building that was tested at full-scale at the E-Defense shaking table facility in March 2009. The test structure plan view dimensions were 10x12 m as shown in Figure 5.1b. The total height and overall weight of the test structure were 15.8 m and 4730 KN, respectively. The test structure consisted of three two-bay steel moment-resisting frames in each loading direction as shown in Figures 5.1(c and d), respectively. The columns were designed as standard BCR295 (i.e., f_y = 295 MPa) cold-formed hollow square sections (HSS) with a 350 mm depth; the steel beams were fabricated from 400 mm deep rolled or built-up wide-flange sections with standard SN490 (i.e, f_y = 325 MPa) steel. The beam-to-column connections of the test structure were fully restrained and strengthened with haunches at the end of the beams. At bays where dampers were installed gusset plates were welded. On top of the steel beams 165 mm thick slabs were casted in place at floors 1 to 4. The slab at the roof of the building had a thickness of 155 mm. The slabs consisted of 80 mm thick concrete (f_c'=24 MPa) poured above a 75 mm thick corrugated metal deck. Precast lightweight concrete and glass curtain walls were provided around the first and second story of the test structure (see Figure 5.1a). Partition walls with doors, ceilings with sprinkler systems, and mechanical equipment were also installed in the test structure. Further details regarding the test structure can be found in Kasai et al. (2010) and (Hikino 2012).

Four different types of supplemental damping devices were evaluated as part of the testing program. Because the test structure itself was expected to remain elastic only the dampers were replaced throughout the entire testing program. The first test was conducted with BRBs (i.e.,

noted as steel dampers in Japan). The test series continued with viscous, oil and viscoelastic dampers, respectively. The test structure itself (i.e., without dampers) was also tested after the completion of the main testing program.

In total, 12 dampers were installed (4 in the Y-loading direction and 8 in the X-loading direction) as shown in Figures 5.1(c and d). Prior to the shaking table tests, a series of component experiments was conducted under quasi-static and dynamic loading to obtain the properties of the various dampers (Hikino 2012). The BRBs were fabricated with low yield strength steel (LY225) with an elastic modulus $E = 205$ MPa and an average engineering yield stress of 225 MPa obtained from quasi-static cyclic tests. The characteristic lengths and cross sectional areas of the plastic (i.e., L_{pl}, A_{pl}), the elastic (i.e., L_{el}, A_{el}), and the connection (i.e., L_{con}, A_{con}) portions of the BRBs that were used as part of the testing program are shown in Figure 5.2. Their corresponding values are summarized in Table 5.1. The properties of the employed NVDs in terms of the velocity coefficient C_{di} as well as the axial internal stiffnesses of the damper portion (K_{ci}) and axial equivalent stiffnesses of the entire NVD (K_{di}), which includes the axial stiffness of the internal damper, the steel brace (K_{bi}), the clevis, brackets (K_{cli}) and gusset plates are shown in Figure 5.3 and summarized in Table 5.2. The same figure illustrates the mechanical model for a NVD (see Figures 5.3b and c). According to dynamic sinusoidal displacement tests with varying amplitudes, the velocity exponent, α, of all the NVDs was found to be equal to 0.38 (Kasai et al. 2008).

The predominant periods of the test structure in the X- and Y- loading directions were $T_{1x} = 0.650$ sec and $T_{1y} = 0.705$ sec, respectively. The same periods of the test structure with BRBs were $T_{1x} = 0.469$ sec and $T_{1y} = 0.487$ sec and those of the test structure with NVDs were $T_{1x} = 0.536$ sec and $T_{1y} = 0.575$ sec. Note that the effect of non-structural components on the

lateral stiffness of the test structure with various types of dampers was considered. The corresponding damping ratios for the test structure (i.e., bare frame) were 1.0%; while for the test structure with BRBs and NVDs was 1.4% and 4.3%, respectively. Further information regarding the dynamic characteristics of the test structure with various damping configurations can be found in Kasai et al. (2011) and Ji et al. (2013). Notably, the nonstructural components of the building contributed to about 30% of its total lateral stiffness (Kasai et al. 2010). The experimental periods and damping ratios of the respective test structure were determined with the linear identification method based on low-amplitude white noise tests as well as low-amplitude ground motion shaking with the JR Takatori record from the 1995 Kobe earthquake as discussed in the next section (Kasai et al. 2010). During these tests the BRBs remained elastic.

5.3 Testing Protocol

The test structure with various damper types in place was subjected to the three components of the JR Takatori record from the 1995 Kobe earthquake. This record was scaled incrementally at 15, 40, 70 and 100% of its unscaled intensity. Figure 5.4(a and b) illustrate the 5% damped pseudo-acceleration and pseudo-velocity spectra of the 40% and 100% JR Takatori record, respectively, in the X- and Y-loading directions of the test structure. From this figure, at the highlighted range of periods under consideration (0.47-0.71 sec) the pseudo-velocity of the 100% JR Takatori record in the Y-loading direction is about 1.4 times higher than that in the X-loading direction (see Figure 5.4b). Superimposed in Figure 5.4 is the pseudo-acceleration and pseudo-velocity spectra based on a Level-2 earthquake in Japan (BCJ 2008). To put things in perspective, the pseudo-velocity of the unscaled ground motion in the Y-loading direction is about 1.1 times larger than that of a Level-2 earthquake in Japan (see Figure 5.4b). In the same figure the authors have superimposed the pseudo-acceleration and velocity spectra that

correspond to a maximum considered earthquake (i.e., 2% probability of exceedance in 50 years) in urban California (location: 37.779°N, 122.419°W) for soil class D per (ASCE 2010), whereas the 40% intensity of the JR Takatori record is closer to a design level earthquake (i.e., 10% probability of exceedance in 50 years) in the same location.

Finally, Figures 5.4(c and d) show the relative displacement response spectra of the unscaled JR Takatori record in X and Y-loading directions for damping ratios ranging from β=2% to 30%. From Figure 5.4c, the expected relative displacement demands in the X-loading direction are not affected by much with respect to the damping ratio for the range of periods of interest (i.e., 0.47-0.65 sec). This is not the case in the Y-loading direction (see Figure 5.4d). A damping ratio increase from 2 to 30% results to a decrease of the relative displacement demands by about one third for the same range of periods.

5.4 Seismic Performance of the Test Structure with Buckling-Restrained Braces and Nonlinear Viscous Dampers

The test structure with BRBs and NVDs behaved nearly elastically for the 15% of the JR Takatori record. Therefore, this section summarizes in brief the seismic performance of the test structure with BRBs and NVDs only for the 40% and 100% scaled intensities of the JR Takatori record. Figures 5.5 and 5.6 illustrate the peak story drift ratios, peak story shear forces and peak absolute floor accelerations along the height of the test structure with BRBs and NVDs, respectively, under the 40% and 100% of the JR Takatori record. In these figures the experimental data is noted as "Exp". The seismic intensity of interest (i.e., 40% and 100%) is noted after. Superimposed in the same figure are the same engineering demand parameters of interest as predicted from rigorous NRHA with various nonlinear model representations

discussed in detail in the following section. From Figures 5.5(a and d) and 6(a and d), the retrofitted test structure did not exceed 1% story drift ratio along its height regardless of the loading direction and the damper type. This was the expected yield story drift ratio of the test structure without dampers (Kasai et al. 2008c). From Figure 5.5b peak story shear forces were relatively large at 40% of the JR Takatori record when BRBs were employed compared to the test structure with NVDs (see Figure 5.6b). This is attributed to the additional lateral stiffness that BRBs provided to the test structure compared to that of the NVDs. Similar observations hold true for the peak absolute floor accelerations as shown in Figures 5.5(c and f) and 5.6(c and f) for the test structure with BRBs and NVDs, respectively.

5.5 Nonlinear Response History Analysis of the Test Structure with Buckling-Restrained Braces and Nonlinear Viscous Dampers

The test structure is modeled in two different simulation platforms. The first one is *SAP2000* (CSI v14.2.4), which is a commercial software widely used by structural engineering offices in North America. The second one is the Open System for Earthquake Engineering Simulation (*OpenSees*) platform (McKenna 1997). A 3-Dimensional (3D) model of the test structure is developed in both platforms. For comparison purposes a 2-Dimensional (2D) model is also developed in *OpenSees*. For the 2D model representation, all three moment resisting frames per loading direction (see Figures 5.1c and d) are modeled in series and linked at each floor level with axially rigid truss elements in order to simulate the rigid diaphragm action. The 2D models consider the panel zone shear deformation based on the Krawinkler (1978) model. For both the 2D and 3D *OpenSees* models the steel beams and columns of the test structure are modeled with single force-based distributed plasticity beam-column elements. Five integration points are considered in order to trace the onset of yielding and cyclic hardening of steel beams and

columns. The steel cross sections of the wide flange beams and HSS columns are discretized with a 5x3 fiber element grid along the width and thickness of the flange and web, respectively. The Giuffré-Menegotto-Pinto (Menegotto and Pinto 1973) steel material model is assigned at each fiber element. The measured material properties of the steel cross sections as reported by Kasai et al. (2010) were explicitly assigned to the respective beam and column elements of the various numerical models of the test structure. In the *SAP2000* model, steel beams and columns are modeled as elastic elements. The composite action due to the presence of the slab is explicitly considered in all model representations. In particular, in the *OpenSees* numerical models of the test structure, this is done with a fiber cross section on top of the bare steel wide-flange section. The reinforced concrete slab is modeled with a concrete (Concrete02) material (Yassin 1994), which accounts for the concrete linear tension softening. The effective width of the concrete slab is calculated based on Section I3.1a of ANSI/AISC 360-10 (AISC 2010c). The contribution of non-structural components to the lateral resistance of the test structure is not considered. In a prior study (Lignos 2012), the Autoclaved Lightweight Concrete (ALC) panels that represent part of the non-structural components of the test structure were simulated with the SAW hysteretic model (Folz and Filiatrault 2001) through diagonal struts that were installed around the perimeter of the test structure. Based on Lignos (2012), the effects of non-structural components on the lateral resistance of the test structure with dampers did not seem to be important. Geometric nonlinearities are considered with the P-Delta transformation.

In order to model numerically a BRB in *OpenSees*, such element is divided into three parts. A force-based distributed plasticity beam-column element is employed to model the core (center) portion of the BRB in which extensive axial yielding is expected; the rectangular section is discretized into 5 x 10 fibers along its width and the length, respectively. The portions that are

expected to remain elastic, as well as the end connections of the BRBs are modeled with elastic beam-column elements. The core portion of the BRB is modeled with the Giuffré-Menegotto-Pinto (Menegotto and Pinto 1973) material model. The input parameters to define an engineering stress-strain curve for the BRB core are obtained from calibrations with experimental data available from the E-Defense Blind Analysis Contest (E-Defense 2008) as shown in Figure 5.7a. In this figure, the hysteretic response of the BRB includes the deformations from both the elastic and plastic steel brace segments (see Figure 5.2). The BRB models were also calibrated with component test results obtained from dynamic loading with a 2 Hz frequency by adjusting the cyclic hardening parameters of the Giuffré-Menegotto-Pinto material model to inherently capture the strain-rate effects on the axial strength of the BRBs. The 2 Hz frequency approximately corresponds to the natural fundamental frequency of the building with BRBs (Hikino 2012). The required amplification factor to obtain the dynamic axial yield stress from the static one was found to be equal to 1.32. This study employed different isotropic hardening parameters for axial tension and compression in order to take into account the higher axial yield strength in compression than that in tension due to the restrainer-core interaction within a BRB. Similarly, in the *SAP2000* 3D model representation of the test structure with BRBs, these were modeled as diagonal link elements by utilizing the plastic Wen model (Wen 1976) with 1% post-yield stiffness ratio and a yield exponent equal to unit. The equivalent BRB axial stiffness was computed as discussed in Yu et al. (2013) and summarized in Table 1.

In order to simulate the hysteretic behavior of NVDs the Maxwell model (Makris and Constantinou 1991) was employed, which consists of a nonlinear dashpot and an elastic spring element in series. The input parameters for the NVDs (see Table 5.2) are the velocity coefficient C_{di}, velocity exponent, α, and the equivalent damper stiffness K_{di}, which represents the

equivalent axial stiffness of the damper including its brace portion. In order to solve the ordinary differential equation (ODE) that expresses the force equilibrium within a NVD a new material model was implemented into *OpenSees* platform (i.e., "ViscousDamper") that utilizes the Dormand-Prince method (Dormand and Prince 1980) with an adaptive step size. The details of this implementation are summarized in Chapter 3. The absolute relative error between 5^{th} and 4^{th} order solutions of the first order ODE is employed to control the sub-stepping within the material model. This implementation does not require small integration steps during the NRHA when NVDs with small values of α or large values of K_{di} are employed. In *SAP2000* the NVDs in the 3D model of the test structure are modeled with the Maxwell model assigned to a "damper" link element available in *SAP2000*. Figure 5.7b shows the hysteretic behavior of a NVD similar to the one used as part of the shaking table test series (i.e., velocity exponent $\alpha = 0.38$). In this figure, the measured displacement of the NVD corresponds to the deformation of the damper portion only (see Figure 5.3). The NVD is subjected to sinusoidal dynamic loading with 2 Hz frequency. In the same figure we have superimposed the simulated behavior of the NVD as predicted by the numerical model discussed earlier. From this figure, it is evident that the proposed model represents reasonably well the hysteretic behavior of a NVD.

In all cases, the Rayleigh damping model is considered with 2% damping ratio assigned to the first and third translational modes of vibration of the respective numerical model of the test structure with dampers. The Newmark average acceleration method (Newmark 1959) is employed for time integration of the equations of motion. The integration step for the NRHA is assumed to be 0.01 sec. This was found to be adequate to guarantee both the numerical stability and accuracy of the simulated results with respect to the experimental data.

In Figures 5.5 and 5.6 we have superimposed the numerical results from the 2D and 3D numerical model representations of the test structure with BRBs and NVDs, respectively, in terms of peak story drift ratios, peak story shear forces and peak absolute floor accelerations for the two seismic intensities of interest of the JR Takatori record (i.e., 40 and 100%). In these figures, the numerical simulation results based on the *OpenSees* models are simply referred as "OS-2D" and "OS-3D". Results from the *SAP2000* 3D model are noted as "SAP-3D". The responses of the 3D model were recorded at the geometric centers of each floor. Minor torsion was observed during the simulation. However, even at largest seismic intensities (e.g., 100% of the un-scaled JR Takatori record), the maximum story drift ratios computed at perimeter frame corner nodes of the test structures with BRBs and NVDs were found to be 10 and 5% larger than those computed at the geometric centers of each floor, respectively. Figures 5.5 and 5.6 indicate that for regular plan view low-rise steel frame buildings, there is no clear advantage between 3D and 2D analyses, regardless of the type of the passive control device (i.e., BRB or NVD). From the same figures, there is practically no difference between the simulated results from the 3D *OpenSees* and *SAP2000* numerical models. This indicates that steel frame buildings equipped with BRBs or NVDs with virtually no structural damage of the bare frame do not require the utilization of sophisticated nonlinear modeling approaches for computing various engineering demand parameters (*EDP*s) of interest for structural and nonstructural damage control (i.e., story drift ratios, story shear forces and absolute floor accelerations). Emphasis should only be placed on the numerical model that represents the selected damper type.

Figure 5.8 illustrates the measured base shear histories of the test structure with NVDs in both loading directions when subjected to the 100% JR Takatori record. In the same figure the predicted response of the same quantities based on the 2D model representation of the same

building is superimposed. The predicted response is nearly identical with the measured one regardless of the loading direction only when the axial flexibility of the NVDs is considered in the nonlinear response history analysis (noted as "NRHA2"). In this case, the average absolute relative error of the peak base shear forces is 7%. In the same figure, the predicted response in terms of base shear response histories is superimposed when the axial flexibility of the NVD is neglected (noted as "NRHA1"). In this case, the average absolute relative error over the peak base shear forces is 33%.

Figure 5.9 illustrates the measured hysteretic response of the BRBs (see Figures 5.9a and b) and NVDs (see Figures 5.9c and d) installed in the 1st and 4th story of the test structure in the Y-loading direction. In the same figure, the authors have superimposed the simulated response of the same supplemental damping devices based on the proposed modeling approach discussed earlier for the 2-D *OpenSees* model of the 5-story test structure. From this figure, the numerical results correlate well with the experimental data.

Because the 2D model representations of the test structure provided reliable *EDP* estimates for both the 40% and 100% intensities of the JR Takatori record, because of brevity the discussion below is based on results from these models. Figure 5.10 illustrates the relative error in terms of predicting the absolute peak roof displacement δ_t based on NRHA with respect to the experimental data from the test structure with BRBs and NVDs, respectively, under the 40% and 100% intensities of the JR Takatori record. The same figure compares the relative error for the same *EDP* of interest as predicted by a number of simplified assessment methods discussed in detail in the subsequent sections. When BRBs are employed (see Figures 5.10a and b), the relative error in terms of predicting δ_t with NRHA is less than 15% regardless of the loading direction. Note that the relative error in predicting δ_t for the 40% JR Takatori record is larger than

that for the unscaled record. Based on a number of parametric studies that were conducted to assess these differences, this is attributed to the modeling assumptions associated with (1) the composite action and (2) the damping model.

For the test structure with NVDs (see Figures 5.10c and d) the relative errors in predicting δ_t are in average 30 to 35% when the axial flexibility of the NVDs is ignored as part of the analytical model representation (noted as "NRHA1"). The same errors become substantially smaller when the axial flexibility of the NVDs is considered as part of the nonlinear response history analysis (noted as "NRHA2"). Similar findings hold true for the predicted peak base shear response of the test structure regardless of the type of damper employed (see Figure 5.11). In this figure, the relative error in peak base shear forces is also predicted with simplified linear and nonlinear assessment methods that are currently used in engineering practice. These are discussed in the next section.

5.6 Evaluation of Simplified Assessment Methods for Steel Buildings with Buckling-Restrained Braces and Nonlinear Viscous Dampers

With reference to Figures 5.10 and 5.11, in this section the efficiency of several simplified assessment methods for steel frame buildings with BRBs or NVDs is discussed. These methods include the (1) linear static procedure (LSP); (2) the nonlinear static procedure (NSP); and (3) the performance spectra (i.e., P-Spectra) methods. The evaluation is based on how such methods predict the peak roof displacements as well as the peak base shear with reference to the experimental data from the full-scale tests conducted at E-Defense. The efficiency of each method is justified based on the relative error of the predicted values with respect to the experimental data at 40% and 100% seismic intensities of the JR Takatori record per loading

direction. In the linearization methods discussed in this paper the authors utilized the spectral displacement directly from the damped displacement spectra, $S_d(T_{eff},\beta_{eff})$ of the respective ground motion record rather than the spectral damping modification factors (i.e., *B*-factors in ASCE 41-13). This was done with the intent of conducting a fair comparison between the effective damping recommendations suggested by different linearization methods. For instance, from Figures 5.4(c and d), if spectral damping modification factors were to be utilized for a single ground motion record this would result in significant errors in the predicted damped spectral displacement values. However, in the design practice, we typically employ the linearization methods by utilizing an idealized design spectrum. In this case, damping modification factors are valid.

5.6.1 Linear Static Procedure

A linear static procedure (LSP) involves a transformation and linearization of a nonlinear multi-degree-of-freedom (MDF) system to an equivalent linear single-degree-of-freedom (SDF) system. Two LSP methods have been utilized herein. The first one (noted as "LSP1") is based on ASCE 41-13 (ASCE/SEI 2014) and FEMA 274, 356 (FEMA 1997; FEMA 2000a). The second one (noted as "LSP2") is based on the current Japanese practice for the design of frame buildings with supplemental damping devices (Kasai and Ito (2005); Kasai et al. (2007). This method is also known as performance-curve. The fundamental difference between LSP1 and LSP2 arises in the calculation of the effective damping ratio, β_{eff} of the equivalent SDF system. In particular, based on LSP1 if it is assumed that that the excitation frequency of a harmonic motion is the same as the cyclic frequency of the equivalent linear SDF system, its β_{eff} can be computed as follows,

$$\beta_{eff} = \beta_0 + \frac{2(\mu_d - 1)(1-p)}{\pi \mu_d (1 - p + p\mu_d)}, \quad p = \frac{1}{1 + K_d / K_f}, \quad \mu_d = \frac{\sum_{i=1}^{N} (\mu_{di} F_{dyi} \cos\theta_i \phi_{ri})}{\sum_{i=1}^{N} (F_{dyi} \cos\theta_i \phi_{ri})} \tag{5.1}$$

in which, β_0 is the inherent viscous damping ratio of the frame building without dampers; μ_d is the SDF displacement-ductility ratio defined as the BRB peak-to-yield displacement ratio; K_d and K_f are the lateral stiffnesses of the BRBs and bare frame within the equivalent SDF system, respectively; μ_{di} is the displacement-ductility ratio of BRBs at level i in the horizontal direction. This is computed based on the displacement of a relative mode shape, ϕ_{ri}, by assuming a uniform drift profile. F_{dyi} and θ_i are the tensile yield force and inclination angle of BRBs at level i, respectively. In particular, from Eq. 5.1, it is understood that LSP1 is an iterative procedure because the effective damping and period formulations employed from ASCE 41-13 (ASCE/SEI 2014) are displacement-dependent. The iterative procedure to obtain μ_d and β_{eff} was repeated until the initially assumed displacement demand matched the computed one. It should be pointed out that the absolute acceleration response spectrum of the JR Takatori record was employed to conduct such iterations.

However, according to LSP2 (Kasai and Ito 2005), the effective damping ratio formulation, β_{eff} can be computed as follows,

$$\beta_{eff} = \beta_0 + \frac{2}{\mu_d \pi p} \ln\left(\frac{1 - p + p\mu_d}{\mu_d^p}\right) \tag{5.2}$$

The damping formulation in Eq. (5.2) is the average damping ratio during an earthquake that accounts for the variation of ductility instead of computing it directly at a peak displacement of the equivalent SDF system (see Eq. 5.1). For both methods the effective period of the equivalent linear SDF system, T_{eff} can be obtained as follows,

$$T_{eff} = T_f \sqrt{\frac{p\mu_d}{1-p+p\mu_d}} \tag{5.3}$$

where T_f is the predominant period of the bare frame. For frame buildings with NVDs, unlike LSP1, the LSP2 method incorporates the axial flexibility of NVDs; therefore, the NVDs are explicitly represented as a Maxwell model. For frame buildings with NVDs that concentrate their inelastic behavior into NVDs, the effective damping ratio and period formulations of the equivalent linear SDF system can be obtained as follows based on the LSP2 method,

$$\beta_{eff} = \beta_0 + \frac{\psi K_d'' u_c^2}{2\pi\left(K_a' + K_f\right)u^2}, \quad T_{eff} = \frac{T_f}{\sqrt{1+K_a'/K_f}}, \quad K_d'' = \frac{C_d \omega_{eff}^{\alpha}}{u_c^{1-\alpha}} \tag{5.4}$$

in which, ψ is a function of the velocity exponent, α, of the NVD, which can be approximately computed as $4e^{-0.24\alpha}$; K_d'' and C_d are the loss stiffness and damping coefficient of the nonlinear dashpot, respectively; K_a' is the storage stiffness of the Maxwell model; K_f is the lateral stiffness of the bare frame; and u is the maximum displacement of the frame building with dampers. Further details regarding the computation of the β_{eff} based on the LSP2 method can be found in Kasai et al. (2007). If the axial flexibility of NVDs is neglected, then the maximum displacement of the nonlinear dashpot, u_c, becomes equal to the maximum displacement u of the equivalent linear SDF system of a frame building with NVDs. Thus, K_a' becomes zero and the effective angular frequency of the frame building with NVDs (ω_{eff}) becomes equal to that of the bare frame (ω_f). Consequently, β_{eff} becomes the same with the one proposed by Ramirez et al. (2001) for frame buildings with fluid viscous devices,

$$\beta_{eff} = \beta_0 + \frac{\psi K_d''}{2\pi K_f} \tag{5.5}$$

Equation 5.5, which refers to LSP1, is identical to Eq. (14.33) from ASCE 41-13 (see Section 14.3.4.1.2, ASCE/SEI 2014) for frame structures with fluid viscous devices.

Figures 5.10 and 5.11 show the relative error of LSP1 and LSP2 methods in predicting the peak roof displacements and base shear, respectively, of the test structure with BRBs and NVDs for the 40% and 100% intensities of the JR Takatori record. From these figures and for the test structure with BRBs, LSP1 underestimates the two EDPs of interest compared to the experimental data by about 20-30% regardless of the loading direction and ground motion intensity (see Figures 5.10a and b; and Figures 5.11a and b).

When the LSP2 method is employed the relative error of the predicted EDPs is in the order of 10% or less (see Figures 5.10 and 5.11). This notable difference is primarily attributed to the effective damping ratio formulation (see Eqs. 1,2) and to a lesser extent to higher mode effects that are not captured by either one of the linearization methods discussed in this paper. In order to illustrate this issue more clearly, Figure 5.12a shows the effective damping ratio, β_{eff} and period T_{eff} variation with respect to displacement-based ductility, μ_d, as computed by LSP1 and LSP2 methods. From this figure, for the corresponding displacement-based ductility levels for the test structure with BRBs in the Y-loading direction at 40% (i.e., μ_d = 1.9) and 100% (i.e., μ_d = 3.6) intensities of the JR Takatori record when the LSP1 method is employed β_{eff} is over-predicted by at least a factor of two compared to that from the LSP2 method. This indicates that the ASCE 41-13 (ASCE/SEI 2014) and FEMA 356 (FEMA 2000a) effective damping ratio formulation (i.e., Eq. 5.1) may not be representative and should account for the displacement-based ductility variation of BRBs as reflected by Eq. 5.2.

For the test structure with NVDs, for moderate earthquake events (i.e., 40% of the JR Takatori record), the LSP1 method underestimates both EDPs of interest by more than 60% in the Y-loading direction (see Figures 5.10c and 5.11c). However, in the X-loading direction the relative

error of the predicted peak roof displacements and base shear of the test structure with NVDs is in the range of 10% or less. This is attributed to the fact that the reduction of the displacement spectrum of the JR Takatori record in the X-loading direction in the range of effective periods under consideration is less sensitive to supplemental damping compared to that in the Y-loading direction. This is shown in Figures 5.4(c and d).

For higher ground motion intensities (i.e., 100% of the JR Takatori record), the relative error of the computed EDPs of interest based on the LSP1 method is in the range of 20 to 40% (see Figures 5.10d and 5.11d). However, the same error drops to about 10% or less when the LSP2 method is employed. This is attributed to the consideration of the axial flexibility of NVDs as part of the LSP2 method. This issue can be further explained based on Figures 5.12b that shows the effective damping ratio and period of the equivalent linear SDF oscillator based on the LSP1 and LSP2 methods with respect to $K_d^{"}/K_f$ ratio in the Y-loading direction. The curves representing LSP2 method are constructed for the case of $p = 0.54$, where p is computed as defined in Eq. (5.1). However, in this case K_d is the lateral stiffness of NVDs within the equivalent SDF system. Based on the results of LSP2 method in Y-loading direction, note that $K_d^{"}/K_f$ = 0.84 and 0.41 at 40% and 100% intensities of the JR Takatori record, respectively. The larger the roof displacements of the test structure the smaller the expected $K_d^{"}/K_f$ ratio. This is attributed to the fact that $K_d^{"}/K_f$ is inversely proportional to the damper axial displacement in case that the velocity exponent α of the NVD becomes smaller than unit. From Figures 5.12b, it is clear that based on the LSP1 method β_{eff} is overestimated by more than two times compared to that based on the LSP2 method. According to ASCE 41-13 (see Section 14.3.4) the LSP1 method should not be used if the computed $\beta_{eff} > 30\%$. This is the case for both loading directions of the test structure with NVDs. Furthermore, from Figure 5.12b, the LSP2 method is able to capture

the softening of the T_{eff} of the equivalent linear SDF system with respect to the bare frame only while the ground motion intensity increases. The LSP1 method neglects this issue.

5.6.2 Nonlinear Static Procedure

This section discusses the efficiency of the nonlinear static procedure (NSP) for evaluating the seismic performance of steel frame buildings equipped with BRBs or NVDs. The NSP is implemented as discussed in Section 14.3.5.1 in ASCE 41-13 (ASCE/SEI 2014) and FEMA 356 (FEMA 2000a). In summary, the base shear–roof displacement relation of the bare frame is first computed based on its first mode lateral-load pattern. This is illustrated in Figure 5.13(a and b) for the test structure for X and Y-loading directions, respectively. A bilinear idealization of this curve is then constructed based on the equal area rule (Chopra and Goel (2001). Based on the idealized bilinear curves (see Figure 5.13) it is evident that the test structure yields globally at around 140 mm roof displacement (i.e., 0.9% roof drift). Because the peak roof displacement of the test structure with dampers installed at various excitations was always less than 140mm for all practical purposes the test structure did not yield during the entire testing program (Kasai et al. 2008). Therefore, a NSP is conducted for the test structure with BRBs only. In Figure 5.13 we have superimposed the base shear-roof displacement relation of the test structure with BRBs based on its first mode lateral load pattern per loading direction. From this figure, the BRBs yield well before the test structure does (i.e., around 40mm roof displacement); thus, unlike with what ASCE 41-13 suggests (i.e., bilinear approximation), the pushover curve of a steel frame building with BRBs should have been idealized as a trilinear curve. This agrees with recommendations by Ramirez et al. (2001). In this paper this assumption is considered as an alternative evaluation procedure (see Approach 3). In order to compute the target roof displacement to conduct a NSP three different approaches are evaluated. These approaches are summarized as follows:

Approach 1-ASCE 41 Method 1: This approach refers to the coefficient method for calculating the target displacement of a frame building in accordance with Section C3.3.3.3 of FEMA 274 (FEMA 1997) and FEMA 356 (FEMA 2000a) based on a bilinear idealization of the test structure with BRBs. It is assumed that BRBs are treated as displacement-dependent devices. Because the use of BRBs results in substantially small displacement demands along the height of a frame building, the effect of hysteretic energy dissipated by a BRB is not considered on the calculation of the target displacement (i.e., analogy of a shear link in eccentrically braced frames per FEMA 274). This indicates that the corresponding target displacement of the test structure with BRBs should be computed based on a 2% viscous damping ratio.

Approach 2-ASCE 41 Method 2: This method refers to the base-shear-roof displacement relation (i.e., capacity curve) of a rehabilitated frame building in accordance with Section C3.3.3.3 of FEMA 274 (FEMA 1997) and Section 6.2 of FEMA 440 (FEMA 2005). The capacity curve of the test structure with BRBs is developed based on its base shear-roof displacement relation (see Figure 5.13). In this case, for ductility values less than 4.0, the damping ratio and effective predominant period to be employed for a target displacement estimate is as follows,

$$\beta_{eff} = \beta_0 + A(\mu - 1)^2 + B(\mu - 1)^3, \quad T_{eff} = T_e\left[G(\mu - 1)^2 + H(\mu - 1)^3 + 1\right] \tag{5.6}$$

in which, T_e is the elastic period of the idealized bilinear SDF oscillator; μ is the displacement-based ductility demand computed as the ratio of the maximum-to-yield displacement of the idealized bilinear capacity curve; *A, B, G, H* are constants that depend on the hysteretic type. Because the post-yield stiffness ratio of the idealized bilinear curve of the equivalent SDF system is 0.20, based on FEMA 440 (see Tables 6.1 and 6.2), A=4.6, B=-0.99, G=0.10 and H=-0.015.

Approach 3-Equiv.SDF: The third option for computing a target roof displacement of a frame building with BRBs is a trilinear equivalent SDF system that is subjected to the ground motion of interest. Nonlinear response history analysis is conducted in this case. To facilitate these computations a versatile nonlinear SDF analysis tool called IIIDAP (Lignos 2010), which is available online is employed. For the case of the test structure with BRBs such trilinear idealization is shown in Figure 5.13.

Figures 5.10(a and b) and 5.11(a and b) illustrate the relative error in predicting the peak roof displacement and peak base shear, respectively, of the test structure with BRBs per loading direction and ground motion intensity based on the three approaches discussed above. The main observations from these figures are summarized as follows:

- Regardless of the ground motion intensity, the relative error in peak roof displacement predictions compared to the experimental data is more than 30% when Approach 1 is employed (see Figures 5.10a and b). This is due to the fact that this approach does not take into account the effect of hysteretic energy due to BRB yielding on the β_{eff} of the idealized bilinear SDF oscillator that is used to compute the target roof displacement of the test structure with BRBs.
- From Figures 5.10a and b there is practically no difference between Approaches 1 and 2 for computing the target roof displacement of the test structure with BRBs. This is attributed to the bilinear idealization of the base shear-roof displacement relation of the test structure with BRBs. From Figure 5.13, BRBs yield at about 40mm in the two loading directions. This would contribute to an adjustment of β_{eff} of the bilinear SDF oscillator to be used to compute the target displacement of the test structure with BRBs. However, due to the bilinear idealization of the base shear–roof displacement relation of the test structure with BRBs,

there is practically no adjustment in β_{eff} of the idealized bilinear SDF oscillator as suggested by Eq. 5.6.

- When a trilinear Equiv.SDF is employed (i.e., Approach 3: NSP-Equiv.SDF) the relative error of the computed peak roof displacement of the test structure with BRBs is in the order of 10% or less. This is due to fact that such SDF oscillator is able to trace the onset of yielding of the BRBs prior to the test structure yielding; therefore, Approach 3 is much more efficacious than the ASCE 41-13 Methods 1 and 2 (i.e., noted as Approaches 1 and 2 herein) regardless of the ground motion intensity (see Figures 5.11a and b). This agrees with earlier findings on reinforced concrete shear wall structures that a trilinear shear force-roof displacement relation characterizes their demand/capacity (NIST 2010a; Lignos et al. 2011; Lignos et al. 2015).
- Unlike the rest of the simplified procedures discussed in this paper, NSP Methods 1 and 2 overestimate the peak base shear of the test structure with BRBs by about 12% or less (see Figures 5.11a and b) due to the fact that the respective target roof displacements are consistently overestimated based on the same methods. Approach 3 generally under predicts the peak base shear of the test structure with BRBs by about 15% or less in average for the 40 and 100% seismic intensities of the JR Takatori record (see Figures 5.11a and b). This is attributed to the dynamic amplification of story shear forces due to higher mode effects, which tends to amplify story shear forces compared to those obtained from a pre-determined lateral load pattern that is typically employed in NSP predictions (NIST 2010a; Lignos et al. 2015).

5.6.3 Performance Spectra (P-Spectra)

Another alternative for the seismic performance evaluation of steel frame buildings equipped with supplemental damping devices is the use of Performance Spectra (so called P-Spectra) as proposed in (Guo and Christopoulos 2013a; 2013b). This approach provides to a structural engineer a spectra of the absolute peak roof displacements, base shear as well as estimates of potential residual deformations for frame buildings equipped with displacement-based and linear viscous/viscoelastic dampers. The values of the three aforementioned EDPs of interest are computed based on the properties of the respective damper. Therefore, a structural engineer is able to select the optimal properties of a specific type of damper through a P-Spectra without having to conduct a large number of design iterations. Normally, the P-Spectra is developed for designing retrofit solutions or new buildings that utilize supplemental damping devices. In this case, P-Spectra is typically presented as plots of normalized EDP responses of the equivalent damped SDF system arranged in a specific manner (Guo and Christopoulos 2013a, b). However, in the case discussed herein, the test structure with BRBs and NVDs has already been designed. Therefore, P-Spectra is used for the prediction of peak responses of the test structure with known damper properties. Thus, it is preferred in this case to construct P-Spectra without normalizing the EDPs of interest. In particular, dual plots that illustrate as separate curves the roof displacement and base shear in the vertical axis are developed. The horizontal axis is utilized such that it can illustrate the variation in the damper properties and subsequently the consequences on the overall building response.

In order to construct P-Spectra for the test structure with BRBs (i.e., hysteretic damper), an equivalent SDF system is constructed based on two parallel elastoplastic springs as shown in Figure 5.14a. The first spring represents the test structure (i.e., bare frame) and the second one

the BRBs. The yield and lateral stiffness properties of the test structure (stiffness K_f; yield force F_y; post-yielding stiffness ratio r_f) may be obtained from a NSP based on its first mode lateral load pattern. Assuming that the BRBs are installed as brace elements, the damper stiffness K_d and damper yield force F_{dy} of the equivalent SDF system with seismic modal mass M^* is derived as follows:

$$K_d = \Gamma_1^2 \sum_{i=1}^{N} K_{di} \left(\phi_{ri} \cos\theta_i\right)^2, \quad F_{dy} = \sum_{j=1}^{m} F_{dy1,j} \cos\theta_1, \quad M^* = \Gamma_1 L_1^h = \frac{\left(\sum_{i=1}^{N} m_i \phi_{1i}\right)^2}{\sum_{i=1}^{N} m_i \phi_{1i}^2} \tag{5.7}$$

where Γ_1 is the modal participation factor of the assumed mode shape of the frame building with dampers; ϕ_{ri} and θ_i are the relative mode shape and BRB inclination angle at level i, respectively; K_{di} is the axial stiffness of the BRBs installed in the i^{th} story; $F_{dy1,j}$ is the yield tensile force of the j^{th} BRB out of m installed within story 1, assuming that for conventional frame buildings with BRBs the ones installed in the first story would typically yield first due to the highest story shear demands compared to other stories; L_1^h is $\sum_{i=1}^{N} m_i \phi_{1i}$; m_i is the floor mass at level i; and φ_{1i} is the first mode shape at floor level i. It is understood that K_d represents the stiffness contribution of the BRBs in the equivalent SDF system. This system is assumed to have the same base shear force with the one shown in the pushover relation. However, the roof displacement of the equivalent SDF system is divided by Γ_1. For the computation of K_d and F_{dy} values, a triangular mode shape is assumed instead of a shear mode of the bare frame as suggested by Guo and Christopoulos (2013a). In order to construct a P-Spectra, μ_d is computed as the peak-to-yield displacement ratio obtained from NRHA of the equivalent SDF with BRBs. The yield displacement, u_{dy} of the equivalent SDF system is equal to F_{dy}/K_d depending on the loading direction of interest. For the test structure with BRBs the following parameters can be identified

per loading directions: $K_{d,x} = 38.1$, $K_{d,yv} = 37.8$ KN/mm and $F_{dy,x} = 1062$, $F_{dy,y} = 1059$ KN, respectively.

The P-Spectra can be constructed for both loading directions of the test structure with BRBs for the 100% JR Takatori record as shown in Figures 5.15(a and b), respectively. The damper stiffness, K_d was kept constant while the BRB yield force, F_{dy} was varied in order to check how the test structure's performance changes for various BRB displacement-ductility ranges. The P-Spectra for the 40% JR Takatori record is not shown herein due to brevity. From Figure 5.15a the displacement-based damper ductility, μ_d equal to unity corresponds to a retrofit design with elastic BRBs. However, this is not desirable because the base shear of the frame building under consideration becomes much larger than alternative retrofit designs that BRBs yield (see Figure 5.15a). While μ_d increases the P-Spectra develops a valley that its minimum indicates what should the BRB displacement-based ductility be in order to minimize both the base shear as well as the roof displacement of the test structure. In order to predict the peak roof displacement and corresponding base shear of the test structure with BRBs one should select a displacement-based ductility level in the range of $\mu_d = 3$ to 4 in both loading directions (see Figures 5.15a and b). For instance, referring to Figures 5.15a and b, $\mu_d = 2.9$ refers to the displacement-based ductility obtained for the test structure with BRBs in the Y-loading direction. For comparison purposes with other simplified assessment methods, the relative error of the predicted peak displacement and base shear compared to the experimental data is also shown in Figures 5.10(a and b) and 11(a and b) for the 40% and 100% intensities of the JR Takatori record, respectively. From these figures it is evident that a P-Spectra approach generally yields to smaller relative errors in terms of relevant EDPs of interest compared to most of the other simplified assessment approaches regardless of the ground motion intensity and loading direction of interest. Note that with the use

of P-Spectra a structural engineer is able to obtain potential residual deformations in any loading direction of the test structure. As expected these are nearly zero as shown in Figures 5.15(a and b). For $\mu_d > 15$, the expected residual roof displacements of the test structure with BRBs would become significant. This indicates that a P-Spectra can be used as a tool for estimating such EDPs along the height of a steel frame building with BRBs. This is particularly important because residual deformations were recently employed as part of loss estimation methodologies to evaluate earthquake-induced losses due potential building demolition because of large residual deformations (FEMA 2012; Ramirez and Miranda 2012).

The proposed approach by Guo and Christopoulos (2013a 2013b) to construct a P-Spectra for frame buildings with supplemental damping devices is extended herein for the case of nonlinear viscous dampers. In summary, in order to construct a P-Spectra for a frame building rehabilitated with NVDs an equivalent SDF oscillator should be constructed as shown in Figure 5.14b. This oscillator consists of (1) an elastoplastic spring that represents the bare frame without dampers (i.e., K_f, F_y, r_f); and (2) a nonlinear Maxwell model that represents the NVDs in parallel with the elastoplastic spring. From Figure 5.14b, the damper coefficient C_d of the equivalent SDF system can be derived as follows:

$$C_d = \Gamma_1^{1+\alpha} \sum_{i=1}^{N} C_{di} \left(\phi_{ri} \cos\theta_i \right)^{1+\alpha} \tag{5.8}$$

where C_{di} are the damper coefficients of the NVD installed in story i. The equivalent stiffness K_d of the Maxwell model can be similarly found based on Eq. 5.7. Note that C_d in Eq. 5.8 represents the damping coefficient of the equivalent SDF system. Therefore, the roof displacement in the P-Spectra plots are computed by multiplying the peak displacement of the equivalent SDF system obtained from NRHA with Γ_1. For frame buildings with NVDs the fundamental mode shape of

the bare frame is considered as suggested by (Guo and Christopoulos 2013a). For the test structure with NVDs, C_d is found to be 79.6 KN/(mm/s)$^{0.38}$ regardless of the loading direction. Similarly, $K_{d,x} = 35.6$ KN/mm and $K_{d,y} = 30.5$ KN/mm per loading direction. There is a perception that the axial flexibility of NVDs may be ignored when the predicted response of frame buildings equipped with NVDs is computed with simplified assessment techniques. In order to evaluate this assumption, two SDF oscillators are developed. One considers the axial flexibility of NVDs and the other does not.

Figures 5.15c and d show the P-Spectra for the test structure with NVDs in the X- and Y-loading directions, respectively, under the 100% JR Takatori record. In order to construct the P-Spectra in this case the equivalent SDF oscillator with the inclusion of the axial flexibility of the NVD is considered. The C_d value of the NVD is varied unlike the axial stiffness of the NVD, K_d that is considered to be constant (i.e., $K_{d,x} = 35.6$, $K_{d,y} = 30.5$ KN/mm). From Figures 5.15(c and d), the response of the test structure with NVDs under the 100% JR Takatori record in the Y-loading direction is more sensitive to the increase of the corresponding NVD damping coefficient than that in the X-loading direction. From Figures 5.15(c and d), if a $C_d = 79.6$ KN/(mm/s)$^{0.38}$ is selected the expected minimum peak base shear and peak roof displacement of the test structure with NVDs can be computed for both loading directions. The relative error of such predictions compared to the experimental data for the 40 and 100% of the JR Takatori record is shown in Figures 5.10(c and d) and 5.11(c and d) for the peak roof displacement and base shear, respectively (noted as "P-Spectra2"). From Figures 5.10(c and d), for the selected C_d value, the relative error of the predicted peak roof displacement compared to the experimental data is comparable with that of the LSP2 and in average smaller than that of the other simplified assessment techniques. Both the LSP2 and P-Spectra2 consider the axial flexibility of NVDs.

The same observation holds true for the peak base shear predictions based on the P-Spectra2 approach for the 40% JR Takatori record (see Figure 5.11c). For the unscaled intensity of the JR Takatori record (see Figure 5.11d) for the selected C_d value, the P-Spectra2 method predicts the peak base shear of the test structure with a relative error less than 5% in the X-loading direction. In the Y-loading direction, LSP2 is still the method that predicts the same EDP with less than 10% relative error. Therefore, given the simplicity of LSP2 approach it is advisable that a combination of LSP2 and P-Spectra2 approaches should be employed for the seismic assessment of steel frame buildings equipped with NVDs.

A fundamental issue to be addressed in the case of frame buildings with NVDs is to quantify the relative error of their peak roof displacement and base shear under a seismic event when the axial flexibility of the NVD is ignored as part of the equivalent SDF oscillator for the construction of P-Spectra. Figures 5.10(c and d) and 5.11(c and d) illustrate the predicted response of these two EDPs of the test structure with NVDs for the 40% and 100% JR Takatori record in both loading directions (noted as "P-Spectra1"). In all cases, the effect of axial flexibility of the NVDs on the predicted EDP of interest can be critical if the response of the building under consideration is sensitive to the increase of the corresponding NVD damping coefficient. For example, in the Y-loading direction, for low ground motion intensities (e.g., 40%) the relative error in the prediction of both the peak roof displacement and base shear drops from about 65-70% to about 9-17% (see Figures 5.10c and 5.11c). For higher ground motion intensities (e.g., 100%) the relative errors in the prediction of the same EDPs become smaller but they are still in the range of 50% different (see Figures 5.10d and 5.11d). According to ASCE 41-13 (ASCE/SEI 2014) Section C1. 14.3.3.2.3, linear fluid viscous dampers exhibiting stiffness in the frequency range $0.5f_1$ to $2.0f_1$ (f_1: fundamental frequency of the rehabilitated building) shall be modeled as fluid

viscoelastic devices. This may be valid for linear viscous dampers. However, if nonlinear fluid viscous dampers with K_d/K_f ratios smaller than 10 are modeled as fluid viscous devices (i.e., $K_d/K_f = \infty$) the displacement demands may be significantly underestimated (Kasai et al. 2007).

The numerical models that have been developed for the test structure (i.e., bare frame structure without dampers) as part of the present work have been validated with shake table experiments of the test structure (i.e., no dampers installed) as well as other steel frame structures tested at the E-Defense facility in previous years (Lignos 2012; Lignos et al. 2013). Therefore, the authors have confidence on the performance of the developed numerical models discussed in this paper once the test structure becomes nonlinear. In the same manner, in case that the main frame behaves in its nonlinear range then the effective damping and period formulations in linearization methods should be adjusted accordingly. Prior studies (e.g., Ramirez et al. 2001, Guo and Christopoulos 2013a, b) provide guidance related to this scenario for buildings with BRBs and NVDs. However, it should be pointed out that in the aforementioned studies the flexibility of NVDs was neglected. In cases that inelastic deformations concentrate in a single story of the frame building then simplified methods are not able to capture the expected building performance when traditional mode shape assumptions are employed.

5.7 Conclusions

This paper summarizes a comprehensive evaluation of simplified and state-of-the-art methods for the performance evaluation of steel frame buildings equipped with buckling-restrained braces (BRBs) and nonlinear viscous dampers (NVDs). The assessment is based on unique experimental data from a full-scale shake table test of a 5-story steel building equipped with BRBs and NVDs among other damper types. Guidance is also provided on the minimum level of modeling sophistication of regular plan view low-rise steel frame buildings with BRBs or NVDs

with various software simulation platforms to conduct rigorous nonlinear response history analysis. The main findings of this paper are summarized as follows:

- There is no clear advantage between 3D and 2D nonlinear response history analyses, regardless of the type of the employed passive control device (BRB or NVD). Furthermore, there is practically no difference between the 3D simulated results from commercially available (e.g., *SAP2000*) and research-oriented (e.g., *OpenSees*) software platforms that are widely used within the earthquake engineering community.
- Steel frame buildings with virtually no structural damage that concentrate their inelastic behavior into the BRBs or NVDs do not require the utilization of sophisticated nonlinear modeling approaches for computing various *EDP*s of interest for structural and nonstructural damage control. Emphasis should be placed on the nonlinear modeling of the employed supplemental damping device.
- The current effective damping ratio formulation that is recommended by FEMA 356 (FEMA 2000a) and ASCE 41-13 (ASCE/SEI 2014) to be used in linear static procedures (LSPs) for evaluating EDPs in frame buildings with BRBs and NVDs may be unconcervative. It is advisable that such formulation should consider the displacement-based ductility demand variation of BRBs in the case of frame buildings with BRBs. The equivalent formulation for frame buildings with NVDs should consider the axial flexibility of the dampers. This is consistent with linear static procedures that are currently being used in the Japanese design practice (Kasai and Ito (2005); Kasai et al. (2007).
- Currently employed nonlinear static procedures (NSP) as discussed in ASCE 41-13 (ASCE/SEI 2014) and FEMA 356/FEMA 440 (FEMA 2000a) may overestimate the predicted roof displacement demands in frame buildings with BRBs for moderate and

extreme ground motion intensities associated with design level and maximum considered earthquakes in North America. This is in part attributed (1) to the idealized bilinear approximation of the base shear-roof displacement relation of frame buildings with BRBs and (2) the effective damping formulations proposed in FEMA 273/356/440 (FEMA 1997; 2000a; 2005). A simple trilinear equivalent SDF oscillator with a versatile nonlinear SDF analysis tool retains the simplicity of NSP procedures for evaluating frame buildings with BRBs; in this case, based on the available full-scale experimental data the relative errors in the respective EDPs of interest are in the range of 10% or less regardless of the ground motion intensity and loading direction of interest.

- When a performance spectra (i.e., P-Spectra) approach is employed to validate the efficiency of various damper solutions on the dynamic response of the test structure, the relative errors in predicting both the peak roof displacement and base shear of the test structure with BRBs are in general smaller than those from currently employed nonlinear static approaches. The same conclusion holds true for the test structure with NVDs when the axial flexibility of such dampers is considered for the construction of P-Spectra. This is also confirmed with rigorous nonlinear response history analysis with a 3-dimensional representation of the test structure with NVDs.
- A P-Spectra approach is able to provide a more realistic representation of the structural system performance including estimates of residual deformations. Traditional static approaches are not able to predict such EDP, which is essential for structural and nonstructural damage control.

Table 5.1: Characteristic lengths and cross sectional areas of buckling-restrained braces used as part of the testing program (data from Hikino 2012)

Frame	Story	L_{pl} [mm]	A_{pl} [mm^2]	L_{el} [mm]	A_{el} [mm^2]	L_{con} [mm]	A_{con} [mm^2]	Core Plate [mm]	K_{di}[(a)] [KN/mm]	F_{dyi}[(b)] [KN]
X direction (2 bays)	4	2900	1408	277.3	3840	285	7264	16X88	81	317
	3	2900	1408	277.3	3840	285	7264	16X88	81	317
	2	2750	2204	303.3	5909	295	8569	19X116	126	496
	1	3600	2204	258.1	5909	295	8569	19X116	105	496
Y direction (1 bay)	4	2600	2794	393.3	7568	280	9856	22X127	161	629
	3	2600	2794	393.3	7568	280	9856	22X127	161	629
	2	2450	4400	469.5	12276	230	12276	22X200	249	990
	1	3300	4400	434.4	12276	230	12276	22X200	209	990

(a) Equivalent stiffness of BRBs used in *SAP2000* model and simplified methods. The area between connections and working points is assumed equal to A_{con}.

(b) Average yield strength of BRBs under quasi-static loading. The values are multiplied by 1.32 in simulation and simplified methods to account for the dynamic amplification of strength due to rate effects.

Table 5.2: Properties of nonlinear viscous dampers (Hikino 2012)

Frame	Story	L [mm]	L_d [mm]	A_d [mm^2]	L_b [mm]	A_b [mm^2]	C_{di} [KN/(mm/s)$^{0.38}$]	K_{ci}[(a)] [KN/mm]	K_{di}[(b)] [KN/mm]
X direction (2 bays)	4	4024.5	535	8034	2429	9121	49	119[(c)]	60
	3	4024.5	535	8034	2429	9121	49	119[(c)]	60
	2	3946.6	606	12880	2104	8380	98	193	104
	1	4706.1	606	12880	2864	8380	98	193	101
Y direction (1 bay)	4	3946.6	606	12880	2104	8380	98	193	104
	3	3946.6	606	12880	2104	8380	98	193	104
	2	3848.9	689	28124	1542	15323	196	438	179
	1	4628.7	689	28124	2322	15323	196	438	171

(a) The internal stiffness values of damper portions were obtained based on the calibration of experimental data (E-Defense 2008).

(b) The equivalent axial stiffness of NVDs used in all evaluations methods. It includes the stiffness of damper portion, brace, clevis, brackets and gussets (Hikino 2012).

(c) Estimated stiffness values (K_{ci}) for damper portion due to lack of data of dampers at third and fourth story (Yu et al. 2013).

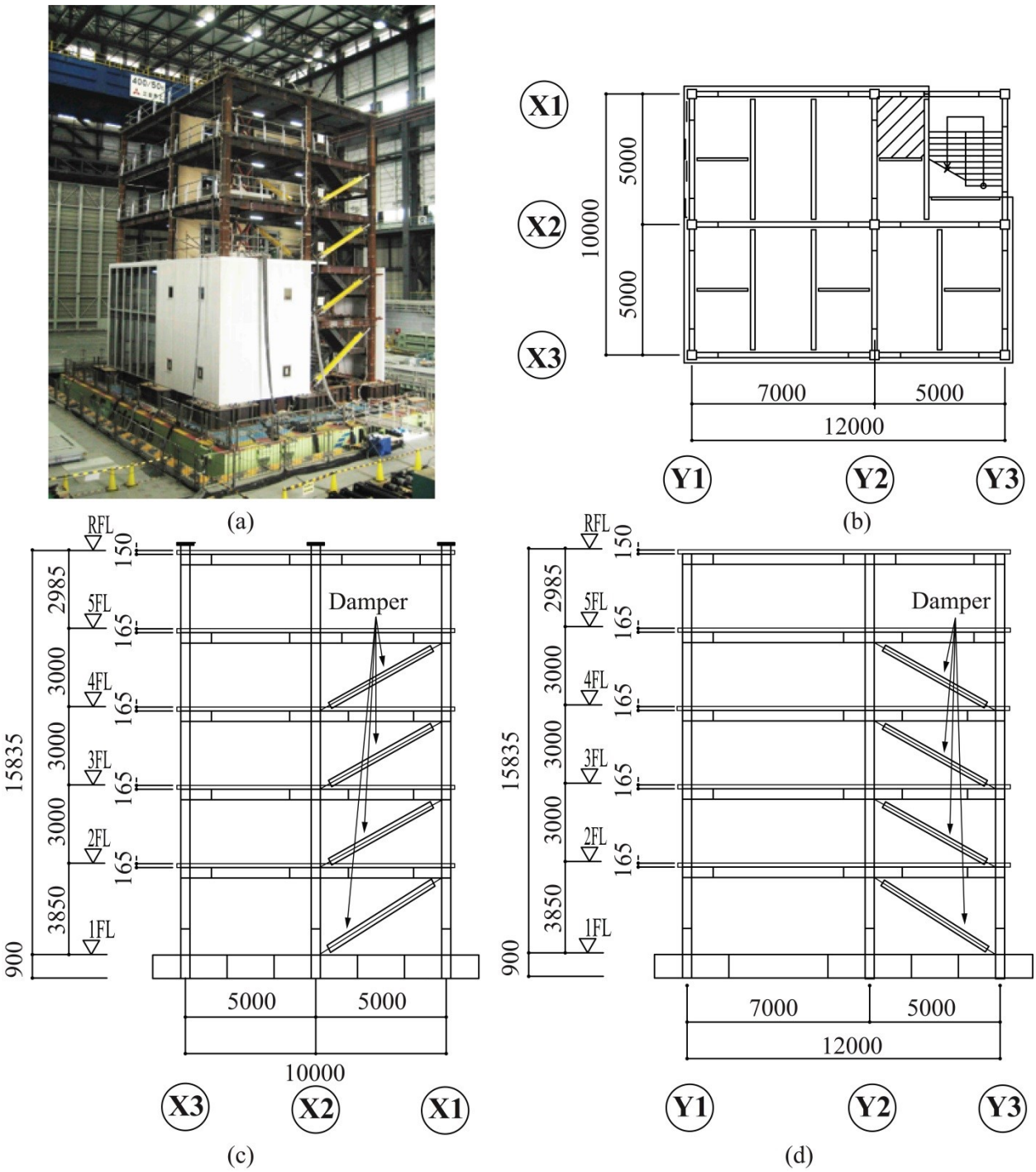

Figure 5.1: Five-story steel building tested at E-Defense; (a) building after installation on the shake table; (b) plan view (c) elevation view in X-loading direction; (d) elevation view in Y-loading direction (dimensions in mm)

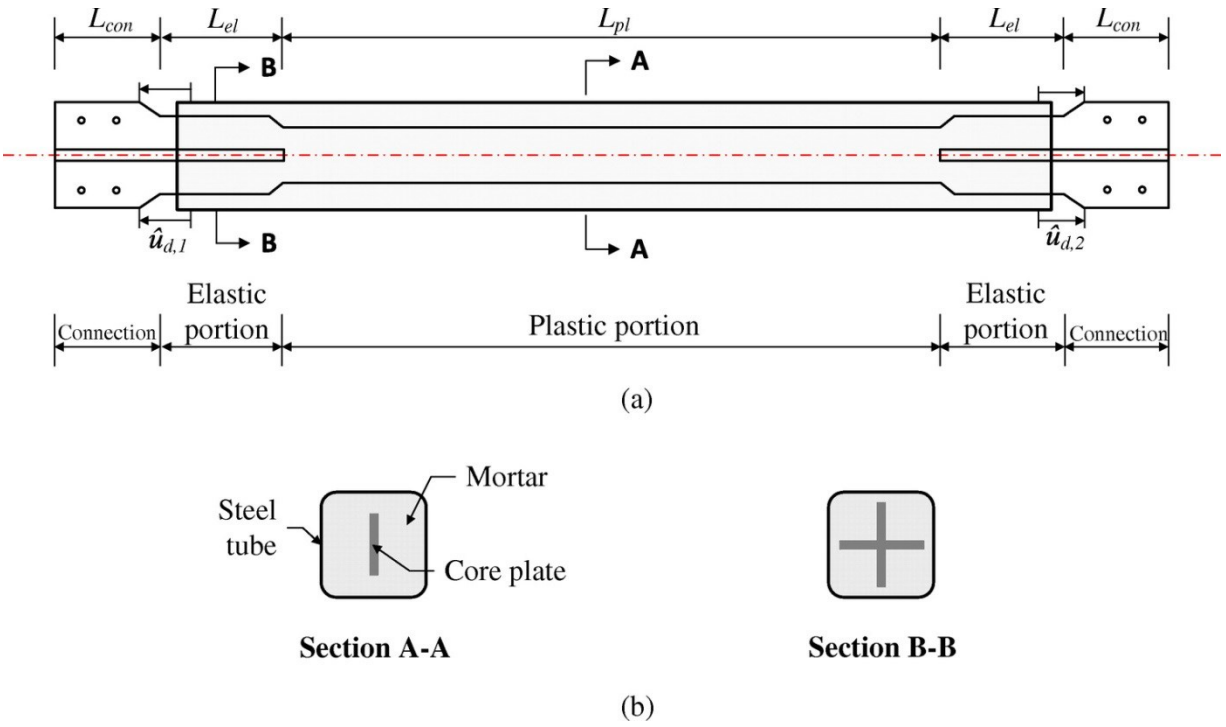

Figure 5.2: Schematic representation of a typical buckling restrained brace (BRB) including its main parts

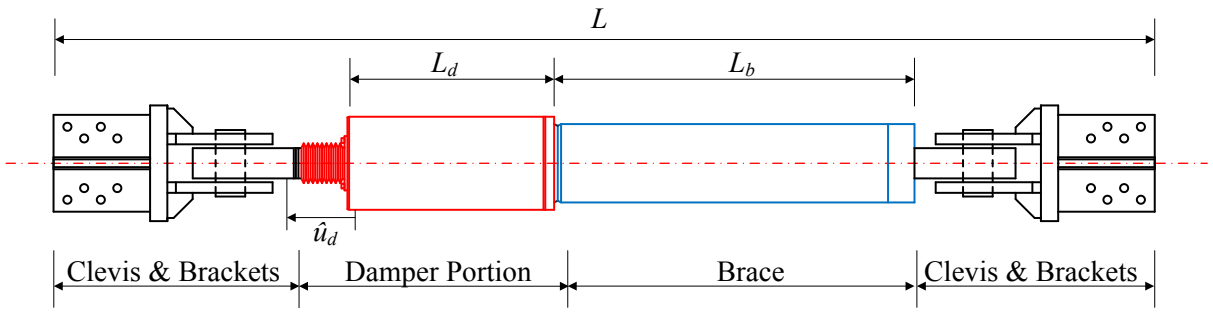

(a) Nonlinear viscous damper: Damper portion and bracing components

(b) Mechanical model for nonlinear viscous damper

(c) Maxwell model for nonlinear viscous damper

Figure 5.3. Schematic representation of a typical nonlinear viscous damper including its main parts and mathematical model representation

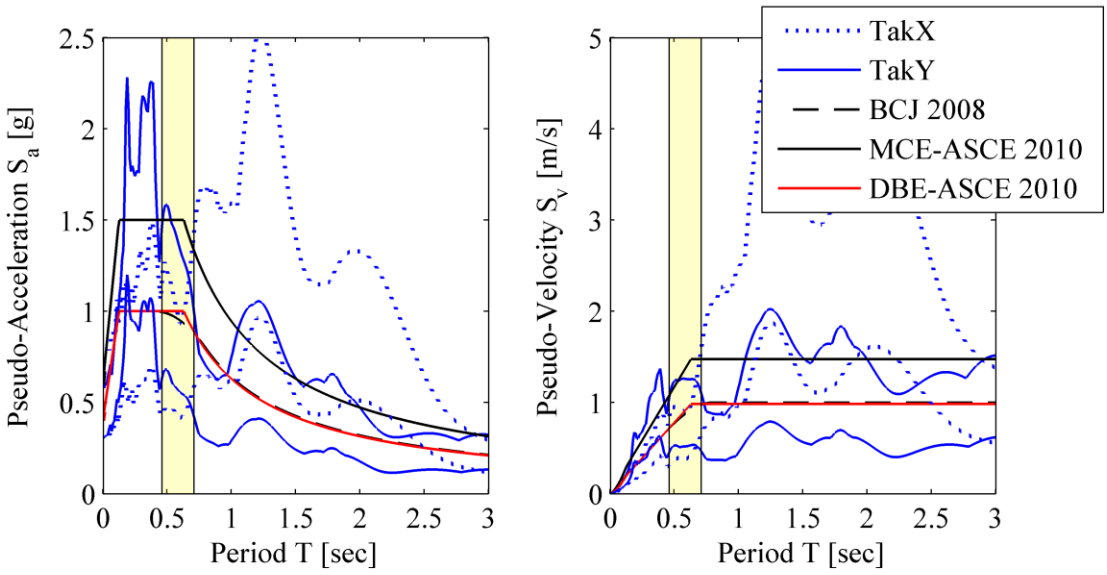

(a) pseudo-acceleration response spectrum (b) pseudo-velocity response spectrum

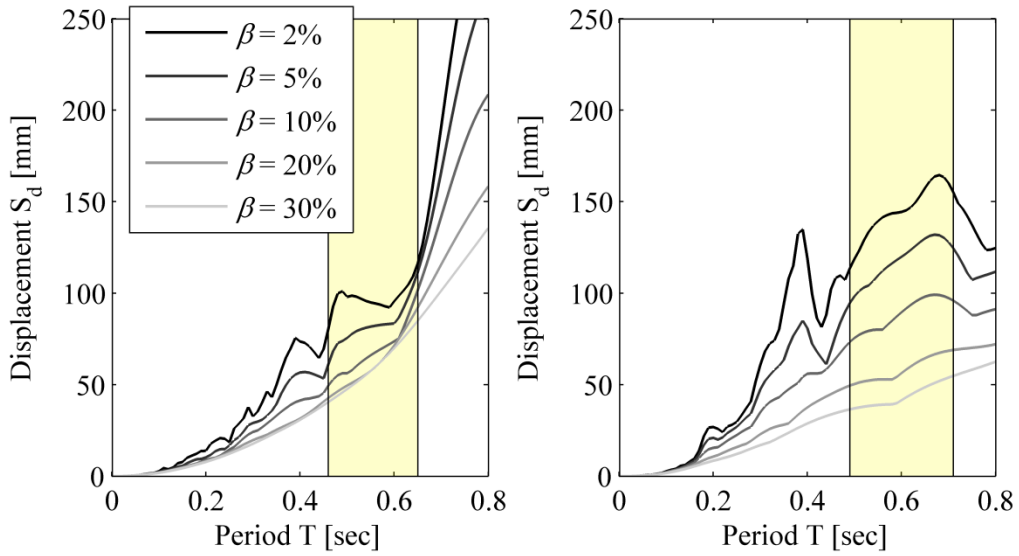

(c) displacement response spectrum (d) displacement response spectrum

X-loading direction Y-loading direction

Figure 5.4: Response spectra of the 40% and 100% scaled intensities of the JR Takatori record

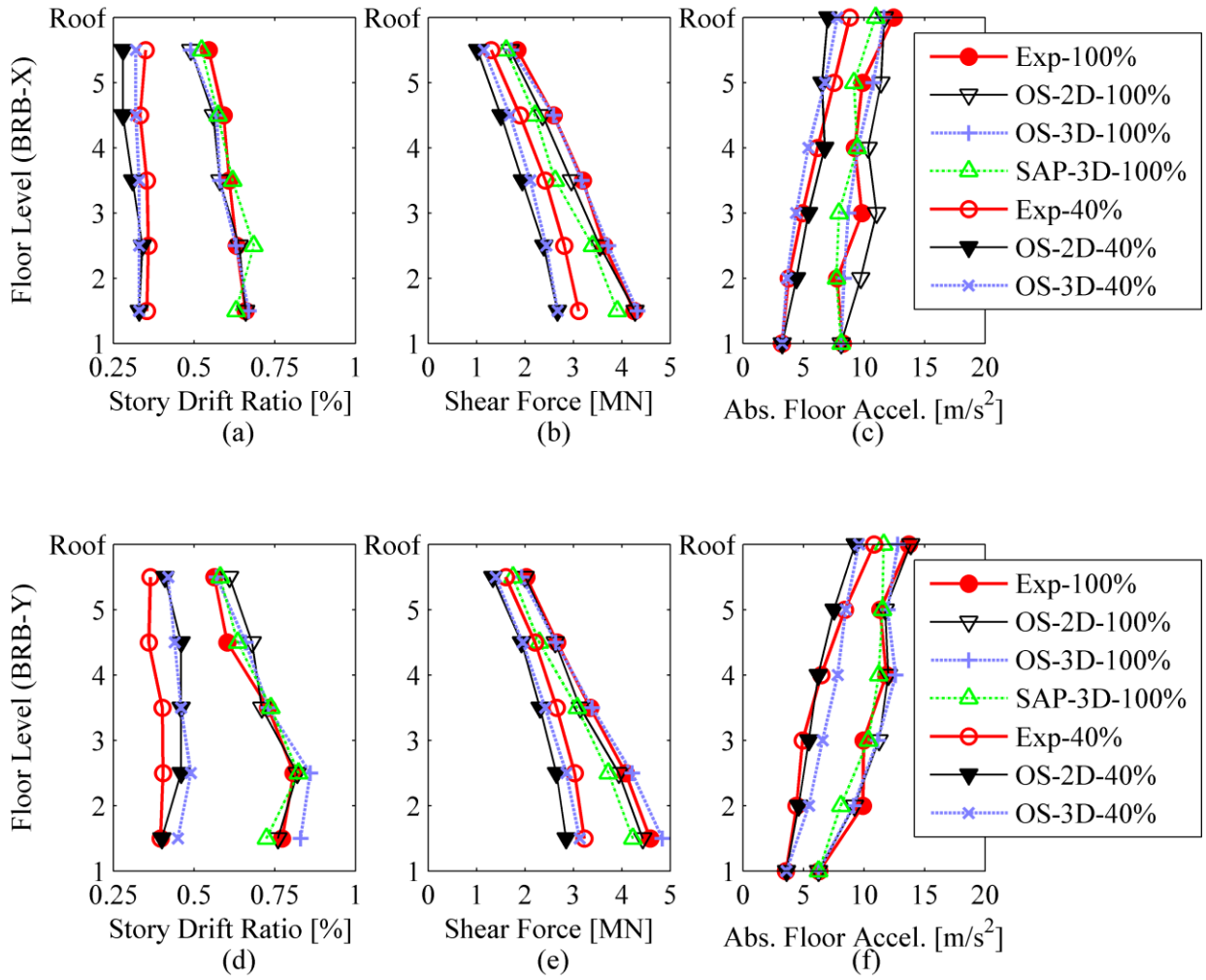

Figure 5.5: Peak response of test structure with BRBs for 40 and 100% of the JR Takatori record

(a to c: X-loading direction; d to f: Y-loading direction)

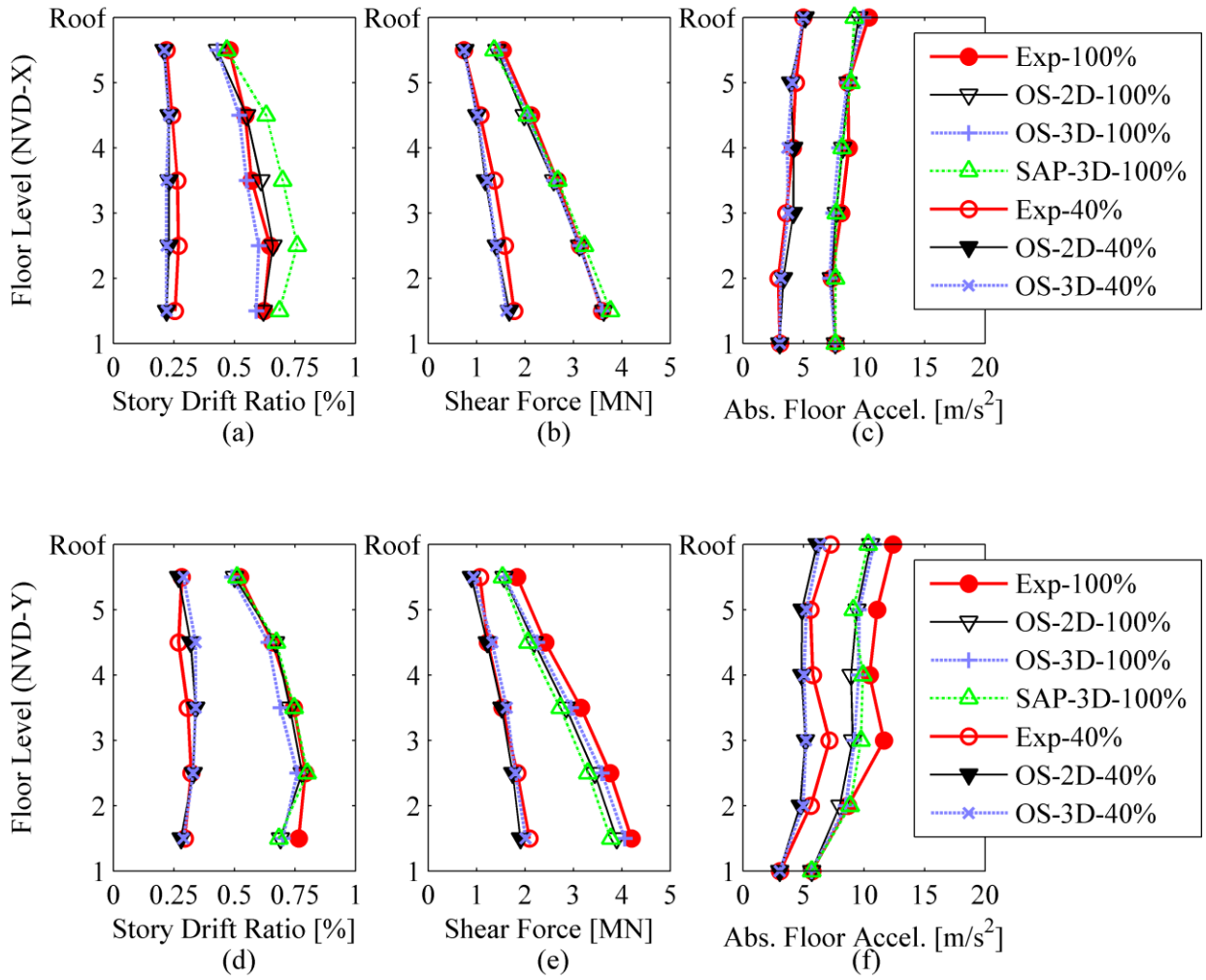

Figure 5.6: Peak response of test structure with NVDs for 40 and 100% of the JR Takatori record (a to c: X-loading direction; d to f: Y-loading direction)

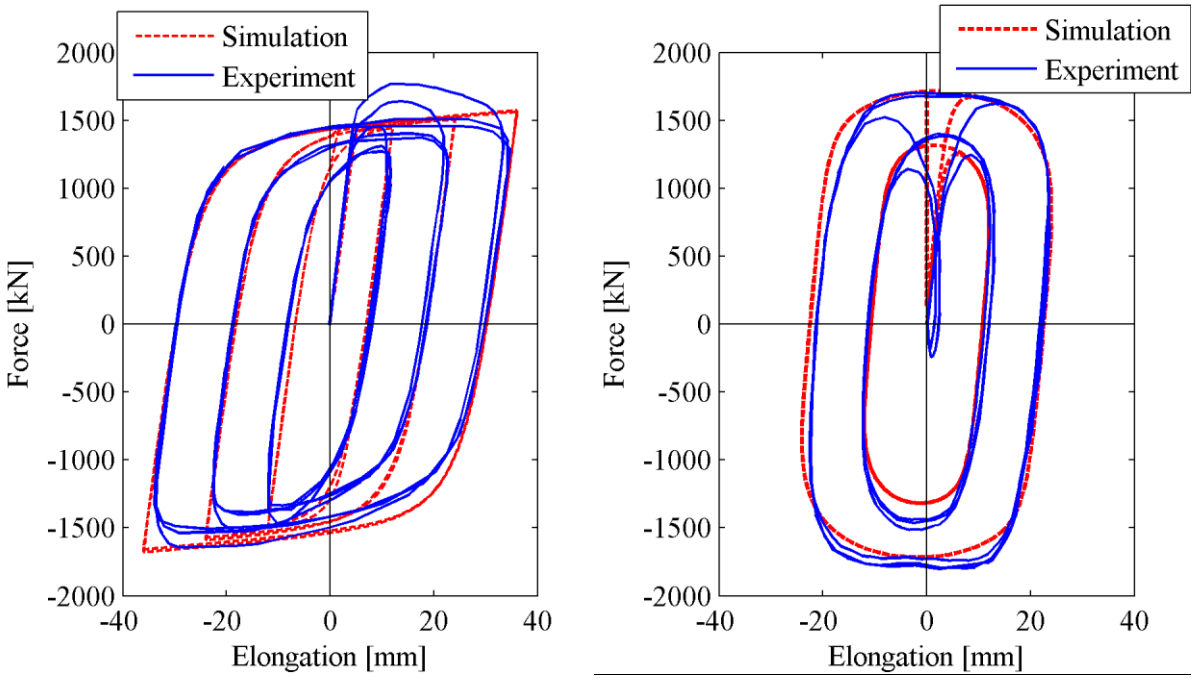

(a) Buckling-restrained brace (b) Nonlinear viscous damper

Figure 5.7: Comparison between experimental data and analytical predictions (data from (E-Defense 2008))

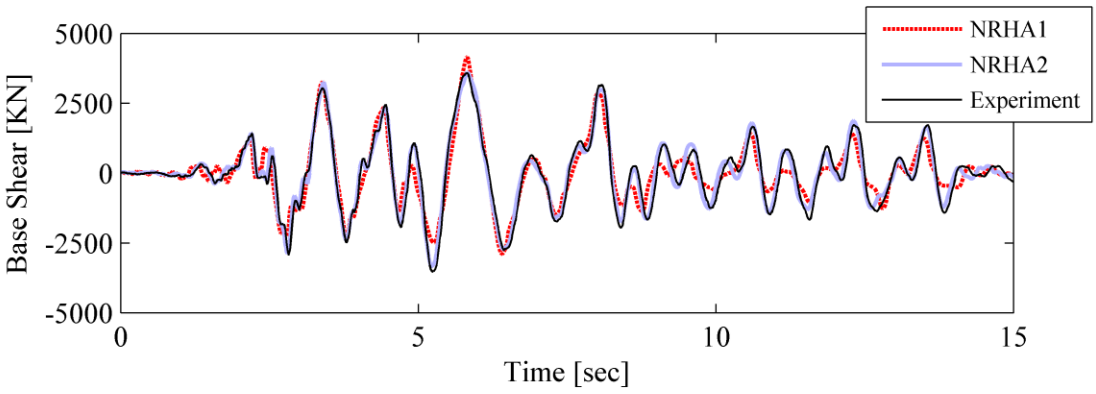

(a) X-loading direction

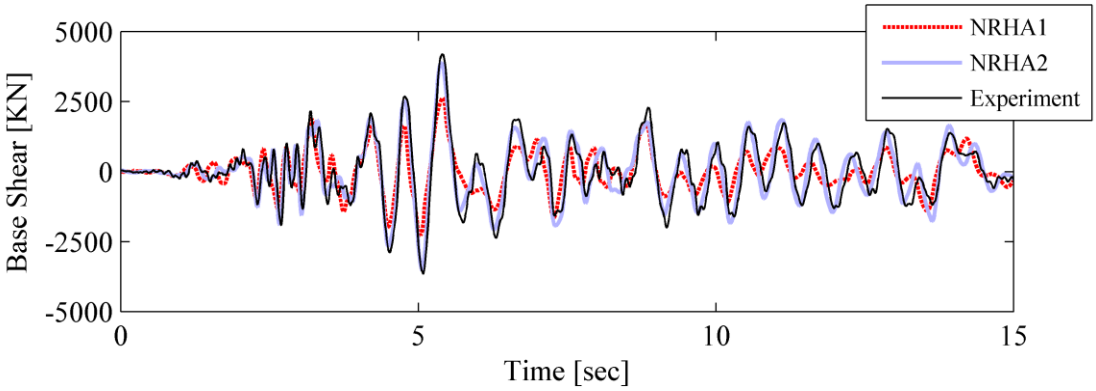

(b) Y-loading direction

Figure 5.8: Base shear response histories of the test structure with NVDs for 100% JR Takatori record

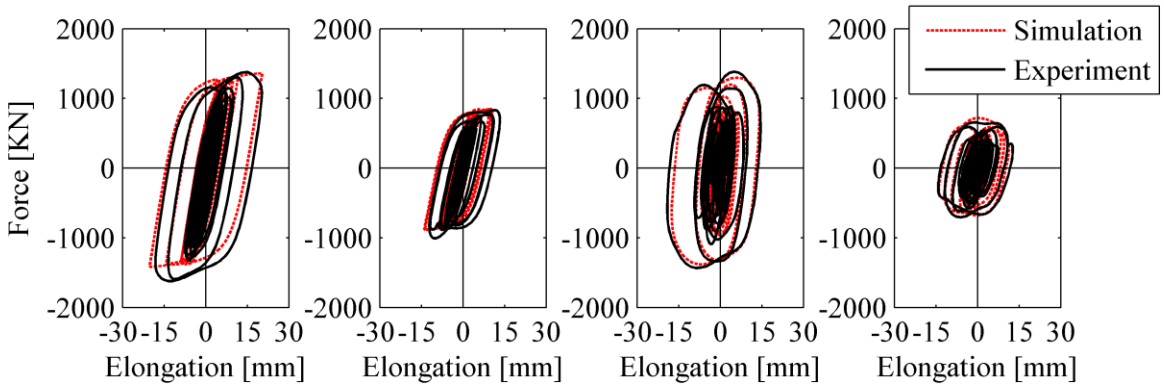

(a) 1st story BRB (b) 4th story BRB (c) 1st story NVD (d) 4th story NVD

Figure 5.9: Damper hysteretic response in Y-loading direction at 100% JR Takatori record; comparison of experimental data with analytical predictions from the 2-D *OpenSees* model of the five-story test structure

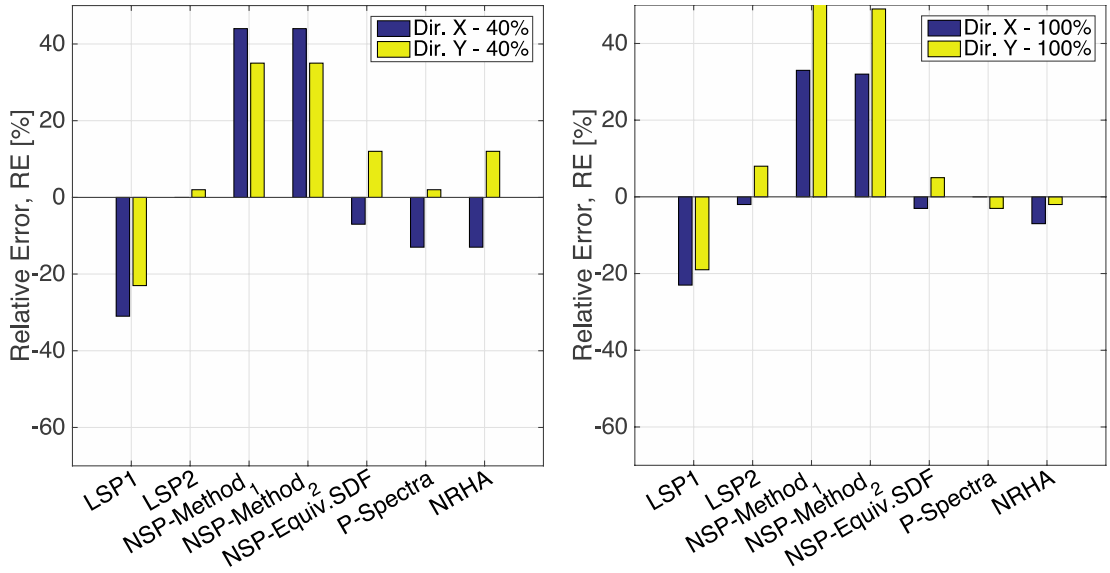

(a) test structure with BRBs – 40% JR Takatori

(b) test structure with BRBs – 100% JR Takatori

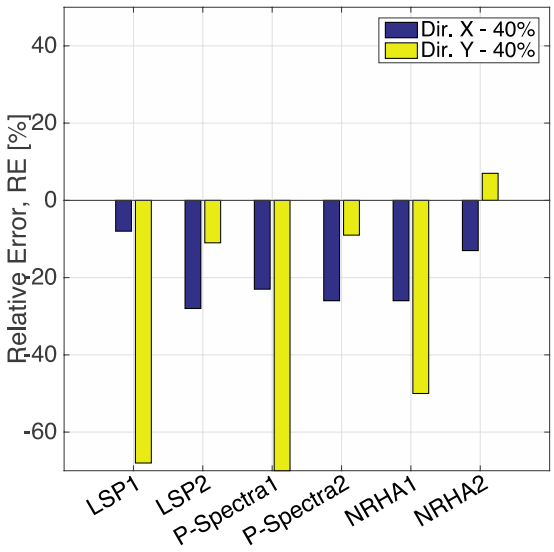

(c) test structure with NVDs – 40% JR Takatori

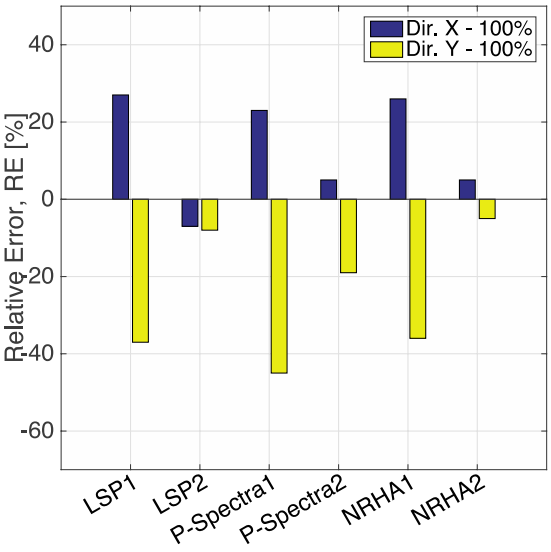

(d) test structure with NVDs – 100% JR Takatori

Figure 5.10: Relative error in prediction of peak roof displacement for the five-story test structure equipped with BRBs and NVDs

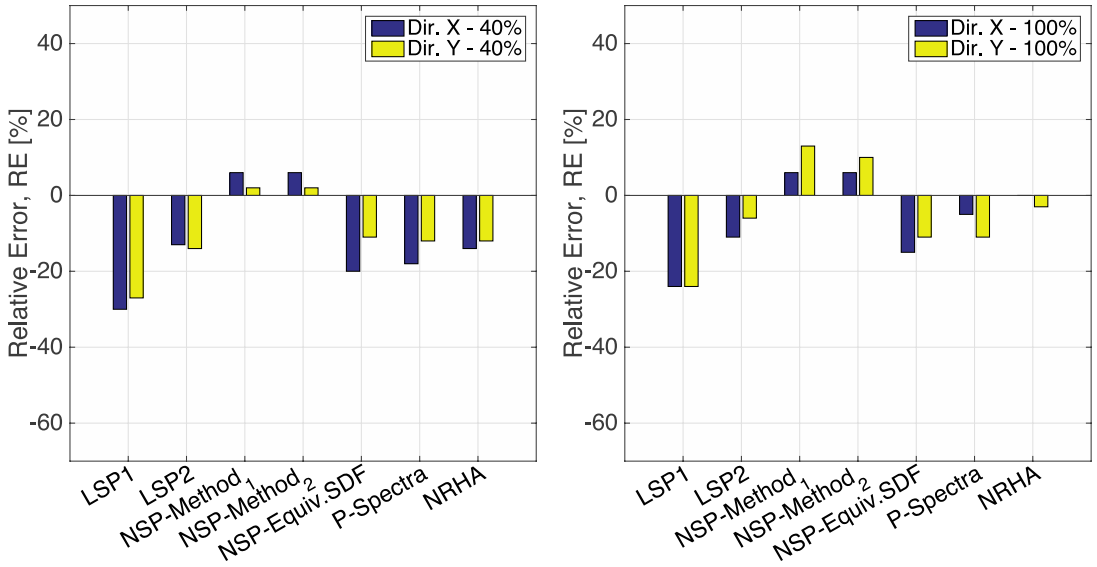

(a) test structure with BRBs – 40% JR Takatori (b) test structure with BRBs – 100% JR Takatori

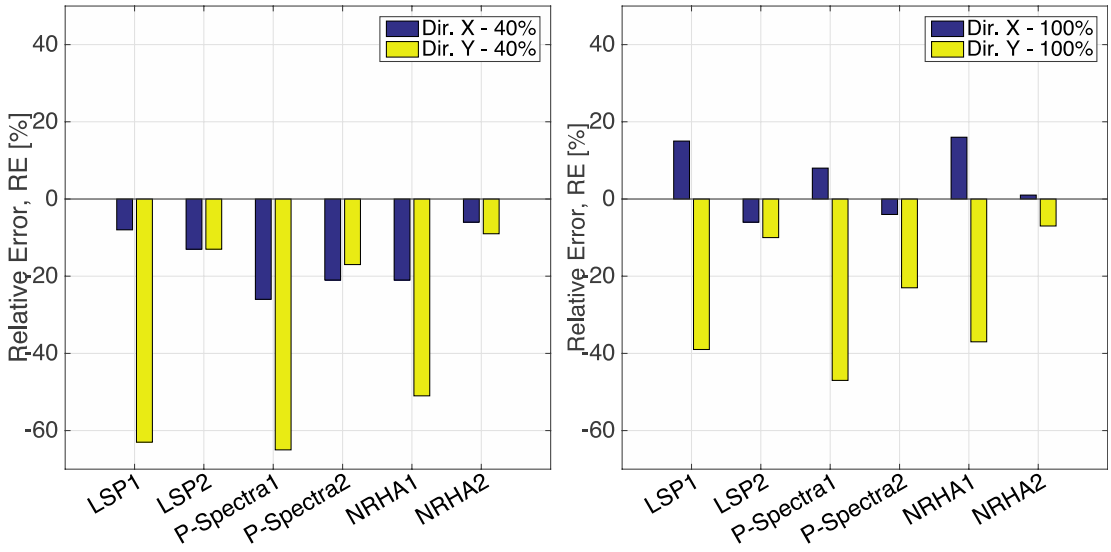

(c) test structure with NVDs – 40% JR Takatori (d) test structure with NVDs – 100% JR Takatori

Figure 5.11: Relative error in prediction of peak base shear for the five-story test structure equipped with BRBs and NVDs

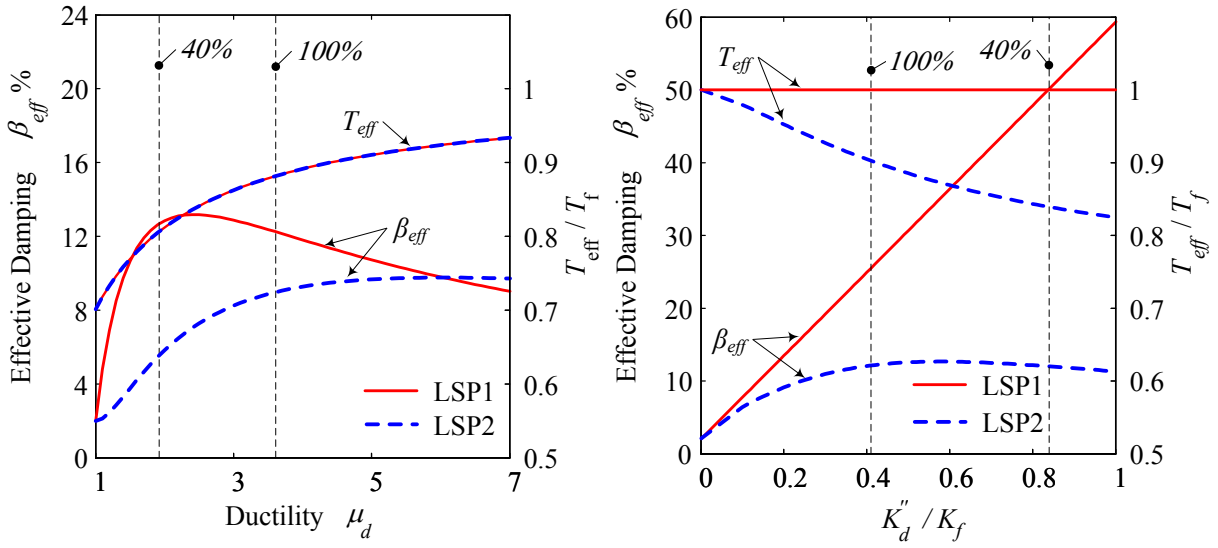

(a) test structure with BRB (p=0.49) (b) test structure with NVD (p=0.54)

Figure 5.12: Effective damping ratio and period variation of equivalent linear SDF system based on LSP1 and LSP2 methods in Y-loading direction

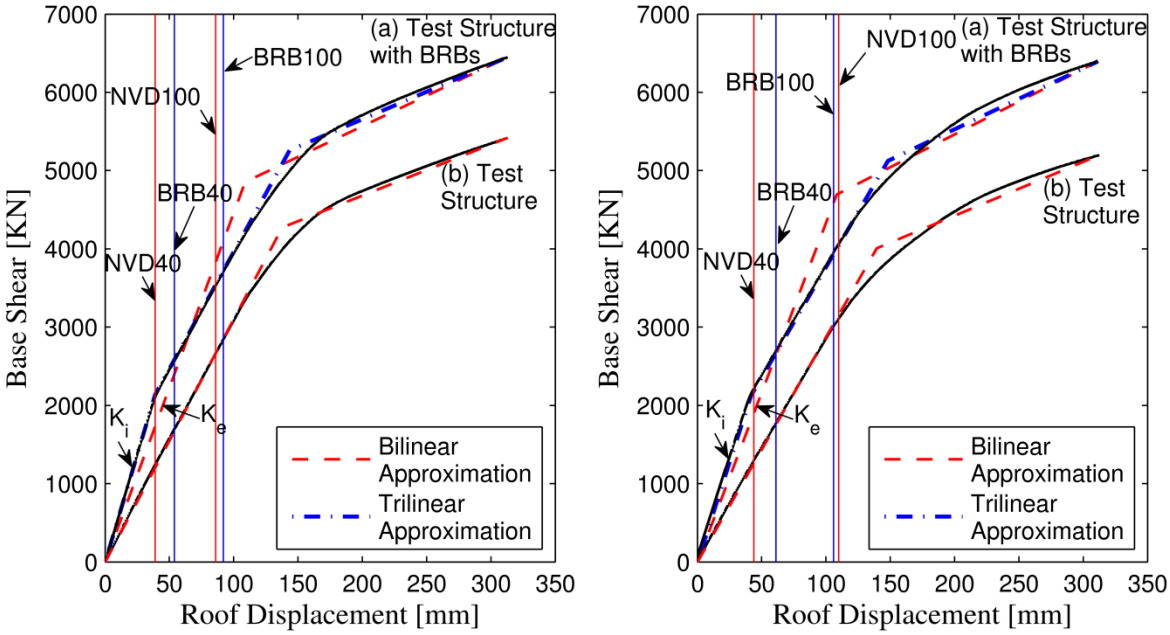

(a) X-loading direction (b) Y-loading direction

Figure 5.13: Base shear-roof displacement relation of the test structure with/without BRBs based on its first mode lateral load pattern per loading direction

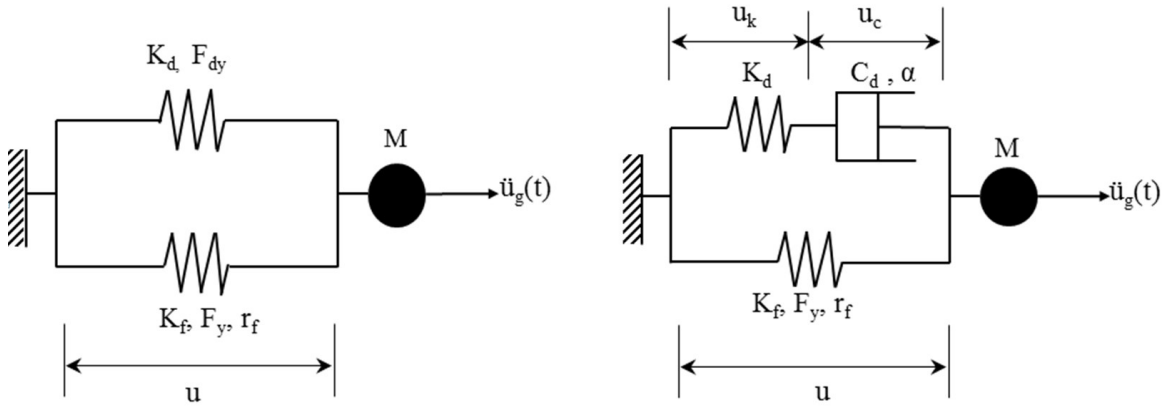

(a) SDF idealization for test structure with BRBs

(b) SDF idealization for test structure with NVDs

Figure 5.14: Equivalent SDF system for frame buildings with supplemental damping devices

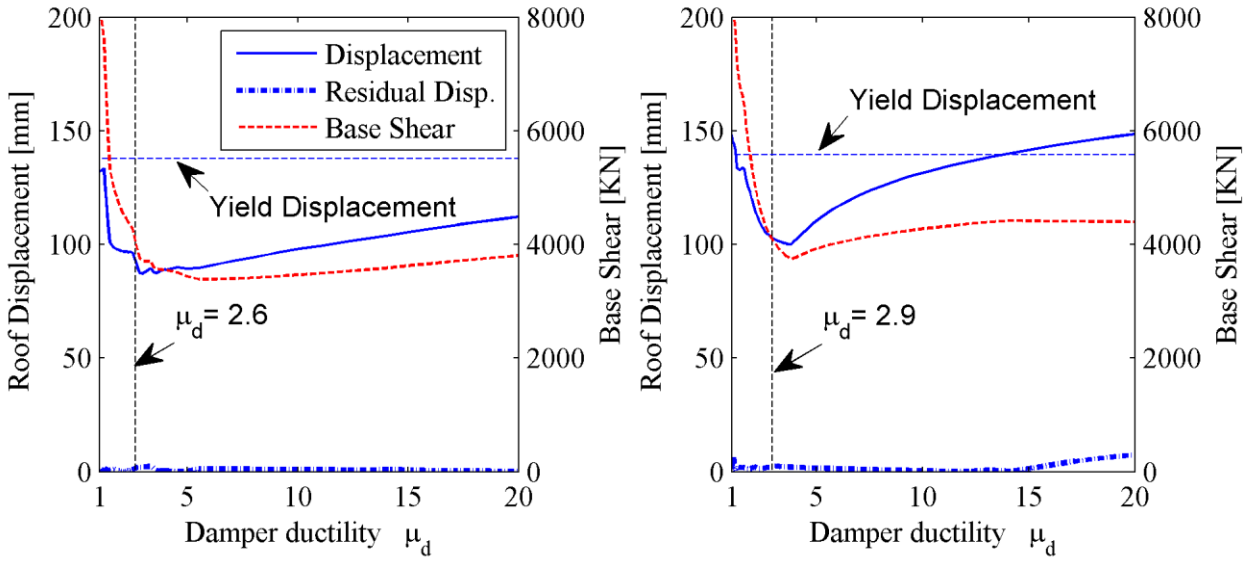

(a) test structure with BRB X-loading direction

(b) test structure with BRB Y-loading direction

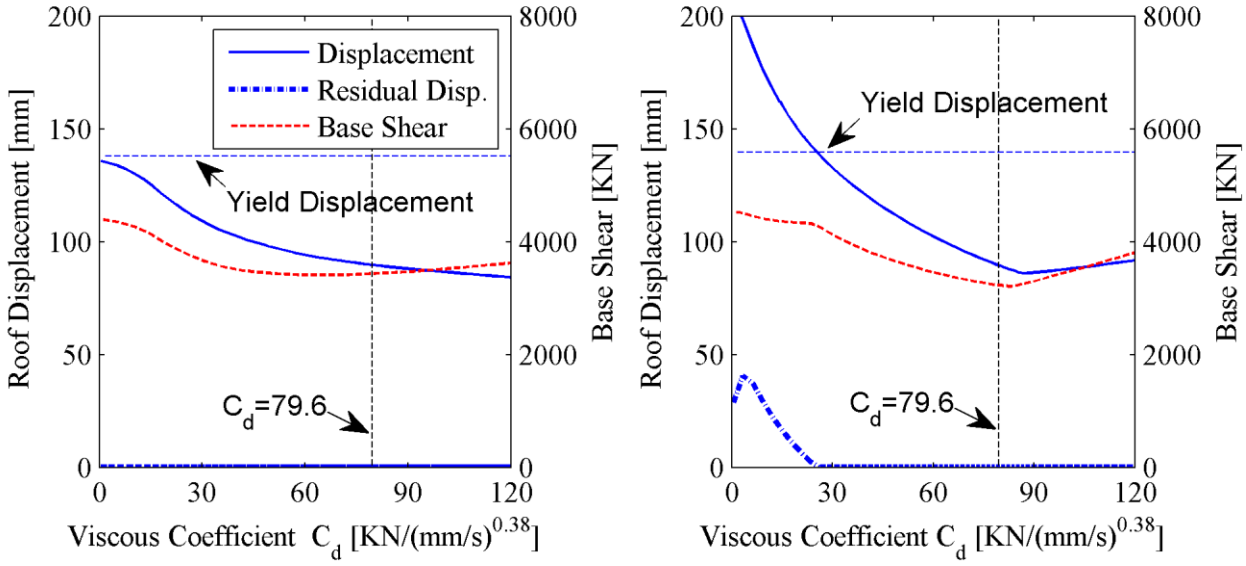

(c) test structure with NVD X-loading direction

(d) test structure with NVD Y-loading direction

Figure 5.15: Performance spectra for test structure with BRBs and NVDs for the 100% JR Takatori record

CHAPTER 6 : A Practical Design Method for Tall Buildings with Supplemental Damping Devices

6.1 Introduction

The use of supplemental damping devices have gained momentum to mitigate the seismic effects in existing buildings designed without any capacity design principles (Christopoulos and Filiatrault 2006). To this end, in the late 1990s, seismic guidelines were developed for the simplified evaluation of buildings equipped supplemental damping devices (FEMA 1997). Among these methods, linear analysis procedures (LAPs) have been widely adopted and implemented in the design of buildings with supplemental damping, due their practicality and computational efficiency. Linear analysis procedures do not require any prior selection of site specific ground motions, which was not a very straightforward task in 1990s. Recent studies suggest that the implementation of LAPs may result in significant errors in predicting story-based engineering demand parameters (EDPs) for buildings with supplemental damping (Akcelyan et al. 2016). The main source of error stems from the linearization method type, which assumes linear effective properties for the dynamic properties (i.e., damping and period) of a structure. The effective damping and period formulations used in LAPs should be derived for each damper type due to their unique force-displacement response. Several novel damping technologies, such as oil dampers with relief valve are not currently addressed in any of the

design and evaluation guidelines, such as ASCE 41-13 (ASCE/SEI 2014). In particular, bilinear oil dampers have been widely used in Japan to mitigate seismic-induced vibration in buildings. For instance, tall buildings equipped with oil dampers with relief valve showed promising performance during 2011 Tohoku-Oki Earthquake (Kasai et al. 2013b). The technology developed based on a number of coordinated experimental and numerical studies (Ichihasi et al. 2000; Takahashi and Sekiguchi 2001; Kasai and Nishimura 2004; Kasai and Matsuda 2014).

Linear analysis procedures are based on a classical damping approximation. However, supplemental damping systems introduce non-classical damping. This could lead to erroneous prediction of story-based EDPs, particularly if the damping distribution is irregular along the height of the building. The ASCE 41-13 (ASCE/SEI 2014) provisions limit the use of LAPs, if energy dissipation devices are not present in all stories (see Section 14.3.4). Often times dampers are only placed in few stories (Kasai et al. 2013a; Kasai et al. 2013b). Notably, the computation of LAPs is mostly conducted under the assumption of a shear-type of deformation; therefore the flexural (bending) deformations are neglected. This may have a significant impact on the damper efficiency (Kasai and Iwasaki 2006; Hwang et al. 2008; Ishii and Kasai 2010; Kasai et al. 2013a). In tall steel moment-resisting frame (MRF) buildings that global flexural deformations are relatively large due to the column axial deformations this assumption contributes to large errors in LAPs. Higher mode effects are also significant in tall buildings. Therefore, instead of a linear static procedure (LSP) the ASCE 41-13 (ASCE/SEI 2014) provisions recommend using a linear dynamic procedure (LDP), which requires inclusion of higher modes in the linearization methods.

Nonlinear response history analysis (NRHA) is the most rigorous and reliable method to evaluate the building performance with dampers of any kind. Although today we can utilize high-

performance computing to conduct NRHA of tall buildings, there is still a need to refine simplified design methodologies for tall buildings with dampers to avoid excessive iterations for the damper design and verification of the local demands in framing members. Recent studies utilizing NRHA of equivalent single-degree-of-freedom (SDF) systems have been developed, such as performance spectra (P-Spectra) (Guo and Christopoulos 2013a) for buildings that behave in the nonlinear regime. However, errors were observed in the story-based EDP demand predictions, particularly for absolute floor acceleration and residual story drift, which are strongly related to the multi-degree-of-freedom (MDF) response of the nonlinear frame.

In this chapter, we propose a simplified MDF tool for the design of supplemental damping devices in tall buildings. To this end, the damper design concept and various vertical damping distributions are first presented. The damper design method is based on the performance curves methodology developed by Kasai et al. (2008a). Guidelines are provided on how to develop appropriate simplified models for tall buildings equipped with dampers. In order to illustrate the proposed methodology, a 40-story steel frame building is utilized as a case study. Several issues related to the damping distributions, higher modes and global bending deformation are addressed through parametric studies that utilize NRHAs of simplified MDF models. Finally, the MDF performance curves are constructed. Although the proposed method can be implemented for any damper type, this chapter focuses on bilinear oil dampers.

6.2 Damper Design via the Performance Curves Method

A commonly used simplified design method for designing passive control devices is the so called "performance curves" (Kasai et al. 2008b). Performance curves have been initially developed for yielding and viscous/viscoelastic devices (Fu and Kasai 1998; Kasai et al. 1998). More recently, they were extended to nonlinear viscous (fluid) dampers and oil dampers with relief valve (Kasai

et al. 2007; Kasai et al. 2008a). Performance curves are constructed by examining the dynamic response of single-degree-of-freedom (SDF) shear systems with dampers and utilizing linearization methods. This chapter discusses the case of oil dampers with relief valve (i.e., bilinear oil dampers); however, the methodology can simply be implemented for various types of dampers as mentioned earlier. For instance, Figure 6.1a shows the SDF response of a bilinear dashpot under sinusoidal dynamic excitation with a damping coefficient C_d, relief load F_{dr}, and post-relief damping coefficient ratio p. Figure 6.1b illustrates a bilinear oil damper as a Maxwell model by accounting for the combined damper axial stiffness, K_b^*, which includes the stiffness of the damper portion, K_d and that of the supporting brace, K_b. Finally, as a representative of a SDF building equipped with bilinear oil damper, Figure 6.1c illustrates a building equipped with oil dampers that is represented as a shear frame with elastic shear stiffness, K_{fs} connected in parallel with a bilinear oil damper. The graphical definition of dynamic stiffnesses, such as loss (K_d'', K_a'', K'') and storage stiffnesses (K_d', K_a', K') of each case are illustrated. Not that the storage stiffness $K_d' = 0$ in the first case. Kasai et al. (2008a) compared the three systems above and computed the effect of K_d''/K_{fs} and K_b/K_{fs} ratios on the SDF system response. Based on this assessment they developed performance curves for bilinear oil dampers in terms of displacement-force reduction (R_d and R_a) with respect to undamped bare frame as shown in Figure 6.2b. The performance curves for bilinear oil dampers are constructed as a function of the damper properties to be utilized. Therefore, engineering judgment is initially required to adequately estimate the damper properties to be used, which are mainly related to the fundamental period of the structure under consideration. These properties are the shear frame frequency, ω_{fs}, the stiffness-to-damping coefficient ratio of the internal damper, β_k, the post-relief damping coefficient ratio, p and the peak damper velocity ratio μ_d.

Referring to Figure 6.2, the performance curves are constructed for ω_{fs}/β_k=0.33, p=0.05, μ_d = 2. It is assumed that the parameter a for a damping modification factor is 75 (see Eq. 6.22) and the fundamental period of the structure lies within the constant pseudo-velocity spectrum region. Figure 6.2a illustrates the variation of the effective damping and effective period with respect to K_d''/K_{fs} and K_b/K_{fs} ratios. The higher the supporting brace stiffness of the damper (K_b) the higher the effective damping ratio. This reduces the relative displacement and floor absolute acceleration demands. Referring to Figure 6.2a, if oil dampers are treated as fluid viscous devices (i.e., K_b and $\beta_k = \infty$) this assumption may significantly overestimate the supplemental damping. In reality the K_b/K_{fs} ratio has a finite value and it can be computed based on available damper sizes. Furthermore, increasing K_d''/K_{fs} may not be always beneficial. In an overly damped system story shear forces/floor absolute accelerations as well as displacements may increase. Consequently, the key point in the damper design is the appropriate selection of K_d''/K_{fs} and K_b/K_{fs} ratios for the given building to achieve the desired performance objectives.

In this thesis, we refer to shear frame properties, such as shear frame stiffness K_{fs}, rather than that of the frame (K_f). Typically, simplified methods assume that a structure has shear-type of deformation only. In reality the lateral displacement of a MRF is composed of shear and flexural deformations. The flexural deformation is mainly caused by column axial elongation and/or shortening; therefore the contribution of flexural deformations to the lateral displacement is relatively small in low-rise steel buildings; thus its effect is typically ignored. In tall buildings flexural deformations may become very significant, particularly in the upper stories. In this thesis, we suggest that design should be based on K_{fs} due to a number of reasons. Under the shear building assumption a design based on K_f, which is smaller than K_{fs}, may result in underestimation of the reduction factors due to the over-prediction of the effective damping.

Secondly, the shear stiffness of a story in a MRF is stable regardless of its displaced shape, while bending stiffness varies. The minimum bending stiffness is obtained when the structure displaces in its first mode. Because the design is based on a first mode shape, the effect of bending stiffness is highly over-predicted when it is considered. Furthermore, the effect of flexural deformations depends on the horizontal placement of the dampers. Typically, exterior bays exhibit larger flexural deformations than interior bays. Consequently, accounting for the flexural deformation and its effect on the initial damper design would result into inaccurate estimations. Structural damage is directly related to the shear deformations. In this thesis, the effects of bending deformation on the story-based EDPs are not computed as part of the design procedure. The prediction of EDPs is obtained directly from simplified MDF model representations of the respective building.

6.3 Vertical Distribution Methods for Supplemental Damping

Having determined the SDF design parameters for the dampers via performance curves, the supplemental damping should be distributed along the height of the building in the most efficient way. There are various ways to distribute damping vertically. Several studies have been conducted to identify the optimal damper placement (Whittle et al. 2012; Hwang et al. 2013). Advanced optimization methods, such as gradient based or utilizing genetic algorithms (Singh and Moreschi 2002; Lavan and Levy 2006; Lavan and Dargush 2009; Takewaki 2009) exist, but they mostly require extensive computations and they are out of the scope of the present research. In this thesis we focus on conventional damping distribution methods that can simply be utilized by practicing engineers. The vertical damping distribution can be assumed to be uniform, proportional to stiffness; proportional to story shear force and proportional to story shear strain energy as discussed in Hwang et al. (2013). In these distribution methods, many researchers treat

viscous dampers as fluid viscous devices by ignoring their axial flexibility; however, because the internal damper portion as well as the supporting members are not rigid, the existence of damper storage stiffness might have an impact on the story drift distribution. In addition, higher mode effects is an important concern for the seismic response of a tall building. These effects should be accounted for the vertical distribution of the dampers.

Kasai et al. (2008a) proposed a damping distribution method by considering the axial stiffness of the dampers. This method desirably results in a uniform drift profile under the expected story shear distribution to avoid damage concentration and story mechanisms at a particular level. Referring to Figure 6.3, in a building with supplementing damping systems the effective storage stiffness K_i' within story *i* is considered as the sum of the story shear stiffness of the bare frame, K_{fsi} and the total storage stiffness of the damper assembly, K_{ai}'. Thus, targeting that damped building will exhibit a uniform drift distribution under the code-based story shear force distribution one can obtain the required storage stiffness of the damper K_{ai}' at each story *i* as given in Equation 6.1. In other words, the effective storage stiffness, K_i' of a story is designed proportional to the story shear demand. This implies that if the story shear stiffness, K_{fsi} is proportionally designed to the shear demand (noted as standard S-Type), the damper distribution will also be proportional to the story shear distributions as seen in Figure 6.3a. If the story shear stiffness K_{fsi} is not designed in proportion to the story shear demand, such as at stories where the total stiffness is already provided by the frame itself, dampers may not be required at all levels. Referring to Figure 6.3b, the deformation demands are mostly concentrated in the upper stories of the building (i.e., U-Type). Therefore, the required damping at lower stories should be relatively low, in comparison to a S-Type building (see Figure 6.3a). In an L-Type building, the deformation demands are mainly concentrated in the lower stories of the building. In order to

mitigate this issue the dampers are mainly placed in the lower stories as shown in Figure 6.3c. From Figure 6.1, The required storage stiffness K'_{ai} of dampers at story *i* can be found as follows,

$$K'_{ai} = K'_i - K_{fsi} \tag{6.1}$$

The lateral story shear stiffness of the existing frame (K_{fsi}) can be simply computed by utilizing the lateral mode shape obtained from the computer model (Guo and Christopoulos 2013a). Alternatively, one can perform linear static analysis under a lateral force load pattern (see Equation 6.3) to obtain the lateral frame shear stiffness at each level (Kasai et al. 2013a). Note that unless if any special measure is taken, the story stiffness will include the contribution of the flexural deformations of the building model,

$$K_{fsi} = \frac{\omega_{fs}^2 \sum_{i=i}^{N} m_i \phi_{fs1i}}{\Delta\phi_{fs1i}}; \quad K_{fsi} = \frac{V_i}{\left(u_{i+1} - u_i\right)} \tag{6.2}$$

in which, ω_{fs} is the fundamental circular frequency of the shear frame without dampers; and ϕ_{fs1i} is the fundamental shear frame mode shape; $\Delta\phi_{fs1}$ is the relative mode shape; u_i is the floor displacement at level *i*. According to ASCE 7-10 (ASCE 2010) the seismic design story shear at any story V_x can be computed as follows,

$$F_x = \frac{w_x H_x^k}{\sum_{i=1}^{N}\left(w_i H_i^k\right)} V_b, \quad V_x = \sum_{i=x}^{N}\left(F_i\right) \tag{6.3}$$

in which, F_x is the lateral seismic force at level *x*; V_b is total design based shear. At this stage, V_b can be taken as an arbitrary value, such as 1; w_i and w_x are the portions of the total effective seismic weight located or assigned to level *i* or *x,* respectively; H_i and H_x are the heights from the base to level *i* or *x*, respectively; *k* is an exponent related to the predominant period of the building. For buildings having a period of 2.5 s or more (e.g., tall buildings), *k*=2 in order to account for higher mode effects. For a more rigorous computation of the shear force distribution

mode superposition can be employed through the use of response spectrum analysis. Thus, by targeting a uniform drift profile the lateral storage stiffness K'_{ai} at each story can be found as follows,

$$K'_{ai} = \left(1 + \frac{K'_a}{K_{fs}}\right)\frac{V_i}{h_i}\frac{\sum_{i=1}^{N}\left(K_{fsi}h_i^2\right)}{\sum_{i=1}^{N}\left(V_i h_i\right)} - K_{fsi} \tag{6.4}$$

in which, h_i is the height of story i; in case that $K'_{ai} < 0$ no dampers are required at that particular level. By using the equivalence between linear and bilinear oil dampers, the loss stiffness of the bilinear dashpot, K''_d can be computed approximately as follows (Kasai et al. 2008a),

$$K''_d = \left(\lambda + \frac{1}{\lambda\left\{f\left(p,\mu_d\right)\right\}^2}\right)K'_a \tag{6.5}$$

in which, λ is the loss stiffness K''_d-to-combined axial stiffness K^*_b ratio of the dampers. This ratio can be computed by Equation 6.6,

$$\lambda = \frac{K''_d}{K^*_b} = \frac{K''_d}{K_b} + \frac{\omega_{eff}}{\beta_k} \tag{6.6}$$

$f(p,\mu_d)$ is the function of equivalency between linear and bilinear damping coefficients, which can be obtained as given in Equation 6.7,

$$f\left(p,\mu_d\right) = p + \frac{2\left(1-p\right)}{\mu_d} - \frac{1-p}{\mu_d^2} \tag{6.7}$$

By combining Equations 6.4 and 6.5 the damper loss stiffness of each story K''_{di} can be directly obtained from Equation 6.8, as recommended by Kasai et al. (2008a),

$$K''_{di} = \left(\lambda + \frac{1}{\lambda\left\{f\left(p,\mu_d\right)\right\}^2} + \frac{K''_d}{K_{fs}}\right)\frac{V_i}{h_i}\frac{\sum_{i=1}^{N}\left(K_{fsi}h_i^2\right)}{\sum_{i=1}^{N}\left(V_i h_i\right)} - \left(\lambda + \frac{1}{\lambda\left\{f\left(p,\mu_d\right)\right\}^2}\right)K_{fsi} \tag{6.8}$$

Alternatively, combining Equations 6.2, 6.3 and 6.5, Equation 6.7 can be rewritten as follows,

$$K''_{di} = \left(\lambda + \frac{1}{\lambda \left\{ f\left(p, \mu_d\right) \right\}^2} \right) \left(\frac{\omega_{eff}^2 \sum_{i=i}^{N} m_i \phi_{1i}^k}{\Delta \phi_{1i}} - K_{fsi} \right) \tag{6.9}$$

in which, ω_{eff} is the effective circular frequency of the shear frame with dampers and ϕ_{1i} and $\Delta\phi_{1i}$ are the design and relative design mode shapes, respectively. The above equation is more convenient in case that the lateral load distribution is a function of the mode shape as per ASCE 7-10 (ASCE 2010). Because this method targets to distribute the effective storage force of the respective story proportionally to the story shear force distribution, it is named as effective shear force proportional damping distribution (SFPDD).

If the design mode shape ϕ_{1i} is assumed to be equal to the fundamental shear frame mode shape ϕ_{fs1i} and k is taken as unity, then the loss stiffness K''_{di} is distributed proportionally to the frame shear stiffness, as recommended by Guo and Christopoulos (2013a). In this case, Equation 6.9 becomes,

$$K''_{di} = \frac{K''_d}{K_{fs}} K_{fsi} \tag{6.10}$$

Another special case of Equation 6.9 can be derived if the damper force distribution is proportional to the design story shear force (i.e. direct SFPDD). This can be simply obtained from Equation 6.10; however, assuming that the frame stiffness is proportional to the story shear distribution then,

$$K''_{di} = \frac{K''_d}{K_{fs}} \frac{\omega_{fs}^2 \sum_{i=i}^{N} m_i \phi_{1i}^k}{\Delta \phi_{1i}} \tag{6.11}$$

In case that the design mode shape ϕ_{1i} is assumed to be different than the fundamental shear frame mode shape (e.g., triangular mode shape), and/or the higher mode effects on the vertical load distribution are considered by assuming $k > 1$, the outcome of the vertical damping distribution in Equations 6.8, 6.9 and 6.11 may alter the SDF design damping parameter, K_d''/K_{fs}. This can be checked by post-evaluating the K_d''/K_{fs} value using Equation 6.12,

$$\frac{K_d''}{K_{fs}} = \frac{\sum_{i=1}^{N} K_{di}'' \Delta\phi_{1i}^2}{\sum_{i=1}^{N} K_{fsi} \Delta\phi_{1i}^2} \tag{6.12}$$

Regardless of the employed vertical damping distribution method, the K_d''/K_{fs} ratio computed from Equation 6.12 should be equal to the initially selected K_d''/K_{fs} ratio. To this end, the distribution can be simply iterated by changing the K_d''/K_{fs} or ω_{eff} values only in Equations 6.8, 6.9 and 6.11, till Equation 6.12 matches the initial design assumption.

Having conducted the distribution of the damper loss stiffness of each story, the initial damping coefficients C_{di} and the combined axial stiffness K_{bi}^* and relief load of the oil dampers F_{dri} can be obtained for the simplified models as follows,

$$C_{di} = \frac{K_{di}''}{\omega_{eff}} \tag{6.13}$$

$$K_{bi}^* = \frac{K_{di}''}{\lambda} \tag{6.14}$$

$$F_{dri} = C_{di} v_{dri} \tag{6.15}$$

in which, the relief velocity v_{dri} can be computed as follows,

$$v_{dri} = \frac{u_{di,\max}}{\mu_d} \omega_{eff} \tag{6.16}$$

In which $u_{di,max}$ is the maximum displacement expected in the dashpot at level i. Further information regarding the design of oil dampers can be found in Kasai et al. (2008a).

Note that the design of dampers herein is based on linear static procedure. The impact of higher modes and the flexural deformations on the estimated response reduction are not considered. These effects can be obtained directly from the analysis of simplified models as discussed below.

6.4 Simplified Models for MDF Systems

Once the lateral damper properties are computed simplified MDF model representations of the building of interest can be developed as seen in Figure 6.4. In this case, bilinear oil dampers are used as the main base case. However, the approach is general and other damper types can be employed. The subsequent discussion presents the three main MDF model types.

6.4.1 Shear Beam Models (SBMs)

Shear beam models assume that the total deformation in a building is due to shear deformations. Two types of SBM models are constructed as shown in Figure 6.4. Referring to Figure 6.4a, the first model (SBM-1E) is composed of an elastic frame with story shear stiffness K_{fsi}. This forms the basis for the performance curve and vertical distribution methods. Referring to Figure 6.4b, the second model (SBM-2E) incorporates the influence of story bending stiffness K_{fbi} on dampers. The story stiffness K_{fi} to be used in the shear beam models can be computed based on Equation 6.2 based on a two-dimensional (2D) model and the ASCE 7-10 shear force distribution within the elastic range. Typically, this stiffness includes both the shear and bending stiffness of the structure under consideration. In order to obtain the story shear stiffness K_{fsi} for the SBM-1E model one can simply limit the axial deformations of elastic columns in the 2D model by considering a relatively large axial area in these columns. Thus, the elastic story

stiffness is the story shear stiffness, K_{fsi} in this case. In SBM-2E models, to compute the global bending stiffness K_{fbi} due to column axial deformations it is assumed that the story bending stiffness and shear stiffness are in series (Kasai et al. 1998); thus the bending stiffness K_{fbi} can be computed as follows,

$$K_{fbi} = \frac{K_{fsi} K_{fi}}{K_{fsi} - K_{fi}} \tag{6.17}$$

If the analysis with the respective 2D model considers P-delta effects, then the elastic frame stiffness as well as the idealized curves include P-Delta effects. If SBM is constructed in the *OpenSees* platform (McKenna 1997), *zeroLength* elements can be utilized for each story by assigning the *Elastic* and *BilinearOilDamper* material models as discussed in Chapter 3. The former is employed for the MRF and the latter for the bilinear oil dampers.

6.4.2 Flexural-Shear Beam Models (FSBMs)

Shear beam models are appropriate for MDF systems with low bending deformations. If bending deformations are large then more advanced models are required. In particular, flexural-shear beam models (FSBM-E) (Wada and Huang 1995) should be considered. Such a model is shown in Figure 6.4c. The FSBM-E and SBM-2E models yield to identical responses when subjected to a static lateral load pattern as per ASCE 7-10 (see Figure 6.5). Such equivalency can be utilized to obtain the story rotational stiffness, K_{ri} of a FSBM-E model. Similarly to SBM-2E, the relative displacement at each floor is composed of shear and flexural deformations as follows,

$$\Delta u_i = \Delta u_{fsi} + \Delta u_{fbi} \tag{6.18}$$

The story shear stiffnesses are identical in both models as shown in Figure 6.5. In the *OpenSees* platform, a *twoNodeLink* element can be utilized to implement a flexural-shear beam model. In the *twoNodeLink* element, the story drift ratio due to flexural deformations is the average of the

lower and upper floor node rotations, θ_{fbj} and θ_{fbj+1}. Thus the relative displacement at each floor due to flexural deformation Δu_{fbi} can be computed as follows,

$$\Delta u_{fbi} = \left(\theta_{fbj} + \theta_{fbj+1}\right)\frac{h_i}{2} \tag{6.19}$$

$$\theta_{fbj} = \sum_{i=1}^{i=j-1}\left(\frac{\bar{M}_i}{K_{ri}}\right); \quad \theta_{fbj+1} = \sum_{i=1}^{i=j}\left(\frac{\bar{M}_i}{K_{ri}}\right); \quad \bar{M}_i = \frac{M_j + M_{j+1}}{2} \tag{6.20}$$

in which, $\overline{M}_i$ is the average overturning moment at story i. It is computed by taking the average of overturning moments at lower and upper floor levels M_j, M_{j+1}; K_{ri} is the rotational stiffness of the *twoNodeLink* element at each story. The overturning moments M_j can be computed based on the assumed story shear distribution V_i as per ASCE 7-10 (ASCE 2010). Thus, combining Equations 6.19 and 6.20, K_{ri} can be computed as follows,

$$K_{ri} = \frac{\bar{M}_i}{2\left(\frac{\Delta u_{fbi}}{h_i} - \theta_{fbj}\right)}; \quad \Delta u_{fbi} = \frac{V_i}{K_{fbi}} \tag{6.21}$$

In this equation, Δu_{fbi} can be obtained by dividing the story shear force V_i into the lateral bending stiffness K_{fbi} obtained previously from Equation 6.17.

6.5 Case Study 40-Story Steel Frame Building

The proposed methodology for the damper design is illustrated in an existing tall building that should be retrofitted. The building is representative of the steel design and construction practice in early 1970s in the West Cost of the US. The lateral force resisting system of the building consists of steel moment-resisting space frames. Specific details regarding the building design as well as its seismic performance can be found in Chapter 7 of this thesis. In order to obtain the story stiffness properties of the simplified models, 2D model representations of the building are developed in the *OpenSees* simulation platform (McKenna 1997). Figure 6.6 and 6.7 show the

first six natural modes of vibration of the building in the X- and Y-loading directions, respectively. In the same figure we have superimposed the respective modes of the building after eliminating the axial flexibility of the respective MRF columns in the 2D models (noted as 2DShear). Based on the 2D models, the tall building has a fundamental period of 5.29 sec and 5.25 sec in the X- and Y-loading directions, respectively. When the 2DShear models are employed, the fundamental periods of the building become 4.05 sec and 4.81 sec in X- and Y-loading directions, respectively. The period reduction was more remarkable in the X-loading direction where the ratio of period of shear frame to that of the actual frame, T_{fs}/T_f was 0.77; In the Y-loading direction the same ratio becomes, T_{fs}/T_f =0.92. This indicates that the bending deformations are relatively large in the X-loading direction. Note that the difference of frame and shear frame mode shapes and periods becomes negligible for higher modes of vibration. This is attributed to the fact that the flexural deformations are cumulative and the influence of flexural deformations at each level reduces in higher modes, as the number of nodes in the mode shape increases.

Table 6.1 summarizes the elastic frame story stiffness K_{fi}, elastic frame story shear and bending stiffnesses, K_{fsi} and K_{fbi}, as computed based on the ASCE 7-10 (ASCE 2010) lateral force distribution based on the steps outlined in Section 6.4. In the same table the K_{fi} / K_{fsi} ratios are reported per story for both loading directions. Note that the K_{fi} / K_{fsi} ratio becomes lower in the upper stories. This is because the influence of bending deformations increases cumulatively with the building height. Referring to Table 6.1, the bending effects are more dominant in the X-loading direction than those observed in the Y-loading direction. Similarly, in order to construct the FSBM-E model the rotational story stiffness K_{ri} is computed for each story based on Equation 6.21.

6.5.1 Comparison SBMs and FSBMs without Dampers

Both the SBM and FSBM-E models are developed in the *OpenSees* platform, using *zeroLength* and *twoNodeLink* elements, respectively. Figure 6.8 shows the comparison of the dynamic properties of the two simplified models (i.e., SBM-2E and FSBM-E) in comparison with the 2D model in the X-loading direction. The first mode properties were identical in all cases; however, SBM-2E was more flexible in higher modes in comparison to the 2D model. In the SBM-2E model the K_{fbi} was obtained from the first mode shape; therefore, the flexibility due to flexure (bending) became constant at each level, regardless of the mode shape. Referring to Figure 6.9, the errors in estimating the mode shapes and periods of vibration based on the SBM-2E are relatively small in the Y-loading direction. This is due to the relatively low bending deformations in this loading direction.

Figure 6.10 and 6.11 show the median peak EDPs obtained from NRHA based on 40 ground motions scaled to the Basic Safety Earthquake Level 2 for existing buildings (BSE-2E) per ASCE 41-13 (ASCE/SEI 2014) in the X- and Y-loading directions, respectively. The seismic response is computed based on the 2D elastic model of the tall building. Details regarding the ground motion selection and analysis can be found in Chapter 7. In the same figures we have superimposed the median of NRHA results obtained from SBM-1E, SBM-2E and FSBM-E models. In all cases the results obtained from the FSMB-E model correlate well with those of the building 2D model. Although the SBM-2E model predicts reasonably well the peak floor displacements along the height of the building, it over predicts the peak story drift ratios at the upper stories of the building in the X-loading direction (see Figure 6.10a). While the average absolute relative errors in peak SDRs were 13.8% and 2.6% based on the SBM-2E and FSBM-E

models, respectively, the corresponding maximum absolute relative errors were 122% and 6.2%, respectively.

Referring to Figure 6.10c, the absolute relative error in the predicted peak absolute floor accelerations in the X-loading direction was, on average, 15% based on the FSBM-E model. This is attributed to the assignment of a low damping ratio (i.e., 1.5%) in the Rayleigh damping model. This model can magnify even the smallest difference in mode shapes and periods of higher vibration modes if peak absolute floor accelerations are of concern. Referring to Figure 6.11, the corresponding average absolute relative errors in peak SDRs were 7.7% and 2.1% based on SBM-2E and FSBM-E models, respectively, in the Y-loading direction. However, the maximum absolute relative errors are still large when the SBM-2E model is employed (77%), while it was 6.4% for FSBM-E, respectively. Thus, considering large error in the prediction in both directions shear beam models should be avoided for the simplified evaluation of tall buildings.

6.5.2 Performance Curves for the Case Study Tall Building

The case specific performance curves are constructed and utilized for the proper selection of the SDF damping parameters. In order to construct the performance curves for bilinear oil dampers the parameters p, μ_d, ω_{fs}/β_k should be initially estimated. In this case, ω_{fs}=1.55 and 1.31 rad/sec in the X- and Y-loading directions, respectively. The rest of the parameters are related to the oil damper to be used. Typically, the damper load capacities vary between 250 KN to 2000 KN (see Tables A1 and A2 in Appendix A). The relief velocities of the bilinear oil dampers are between 1.8 and 12.8 cm/sec with a maximum allowable speed of 30 cm/sec. Based on the available products, if linear oil dampers are utilized, the ratio of internal damper stiffness $\widehat{K}_d$ to damper coefficient $\hat{C}_d$, β_k is around 50. For long period structures the story velocity demands are lower

than short period structures, therefore it is more practical to select bilinear oil dampers with low damper relief velocity, such as $\hat{v}_{dri}$ = 1.8 cm/sec, to achieve $\mu_d > 1$ for the equivalent SDF systems. In this case p=0.02 and β_k = 4.5 (Kasai et al. 2008a). Thus, for oil dampers with low damper relief velocity ω_{fs} /β_k =0.34.

An important part of the design procedure in a supplemental damping system is to estimate the damped spectral demand accurately. According to the performance curve method by Kasai et al. (2008a), the damping modification factor D_h can be computed as follows,

$$D_h = \sqrt{\frac{1 + a\beta_0}{1 + a\beta_{eff}}} \tag{6.22}$$

in which, a is a value range from 25-75; β_0 is the inherent damping ratio of the frame without dampers, which is assumed to be 1.5% in this case; β_{eff} is the total effective damping ratio of the frame with supplement damping. In order to obtain a for our case, we compare the pseudo-velocity spectra with various damping ratios as shown in Figure 6.12. In this figure, the median pseudo velocity spectra of the selected and scaled ground motions are plotted for damping ratios 1.5%, 5%, 10% 15% and 20%. The mean values of each median damped pseudo velocity spectra have been computed between 0.2T and 1.5T and plotted with red dashed lines. For comparison purposes, the 5% code-based damped spectra at the BSE-2E seismic intensity is superimposed in the same figure. It can be seen that, the mean 5% damped pseudo spectral velocity is about 1.08 larger than the 5% code-based damped spectra at the BSE-2E level. In order to computer the parameter a, the 5% code-based damped spectrum has been selected as a reference spectrum and normalized to the mean of 5% pseudo velocity spectrum (to red dashed line) and other damped spectra have been derived using Equation 6.22 as shown in Figure 6.12. The parameter a is found to be 33 in this case based on the least squared error. Figure 6.12 shows that the damped

spectra match relatively well with the mean damped pseudo velocity spectra by using a=33. From Figure 6.12 it is clear that the fundamental period of the structure lies within the constant pseudo-velocity region of the spectrum.

Figures 6.13a, b and 6.13c, d illustrate the case-specific performance curves for bilinear oil dampers with $\mu_d \leq 1$ and $\mu_d = 2$, respectively, after determining all the required model parameters needed. Referring to Figures 6.13a and b, although $\mu_d \leq 1$, the performance curves still use the properties of bilinear oil dampers and not that of linear oil dampers. This represents the case in multistory structures in which the relief velocity of dampers can be exceeded due to high story velocity demands, even though they are designed to satisfy $\mu_d \leq 1$. From Figures 6.13 and 6.14 when $\mu_d = 2$, it results in lower R_a, nevertheless, the difference is not large.

6.6 Parametric Study: Three Damping Levels

6.6.1 Design of Dampers

In order to examine the influence of supplemental damping provided by the dampers, the vertical damping distribution, higher mode effects and flexural deformation on the EDPs a parametric study is conducted based on the simplified model representations of the 40-story case study building. Three levels of supplemental damping are considered. This is illustrated in Figure 6.13d and it is also summarized in Table 6.2. The design was based on case-specific performance curves (see Figure 6.13d) as discussed in the previous section. For the tall building under consideration, we assume that p=0.02, β_k=4.5 and $\mu_d = 2$. These values were found to be reasonable. Typically, the higher the supplemental damping is the stiffer the supporting brace needs to be. Therefore, it was assumed that $K_b/K_d'' = 2.0$ (Kasai et al. 2008a). Referring to Figure 6.13d, in the 'low damping' case, the expected effective damping was about 6%. For a

'medium damping' level, the damping ratio increased to 11%. Finally, 18% effective damping was achieved for the 'high' damping case.

Three vertical distribution methods, namely, the stiffness, shear force and effective shear force proportional methods were implemented herein. The design was based on the BSE-2E spectrum of the ASCE 41-13 (ASCE/SEI 2014) with a $S_{pv}(T_f,\beta_0)$=1852 mm/sec in both directions. For the stiffness proportional damping distribution, the design mode shape ϕ_{1i} is assumed to be equal to that of the bare frame's fundamental mode. For the shear force proportional damping distribution cases, a uniform drift profile is assumed and the k=2 as per ASCE 7-10 (ASCE 2010). The damper properties are designed based on the exact values obtained from the design procedure. Table 6.3 summarizes the damper properties to be used in the simplified models per story for each distribution method, based on the 'high' damping level in the X-loading direction. The selection of available damper sizes for the building and its effect on SDF parameters is further discussed in Chapter 8.

Figures 6.14 to 6.16 show the vertical distribution of the frame and damper stiffnesses as computed based on 'low' and 'high' damping in the X-loading direction for the various vertical damper distribution methods. Figures 6.14a and 6.14c show the amount of frame shear stiffness K_{fsi}, damper loss stiffness K''_{di}, damper storage stiffness K'_{ai} and total stiffness K_i of each story computed based on the stiffness proportional damping distribution at low and high damping levels. Figures 6.14b and 6.14d illustrate the same figures by normalizing the results with respect to the frame shear stiffness K_{fsi}. Because the employed damping distribution is stiffness proportional, the normalized curves are uniform along the building height with the same ratio assumed in the SDF system, such as K''_d/K_{fs} =0.25 and 1.0, respectively.

Figures 6.15a and 6.15c show the vertical distribution of the frame and damper properties computed based on a story shear force proportionality, for low and high damping cases, respectively. From these figures, K''_{di} followed the shape of the ASCE 7-10 story shear force along the building height. Unlike the stiffness proportional damping distribution, the normalized curves in Figures 6.15b and 6.15d indicate that there was a shift of K''_{di}/K_{fsi} ratios along the height. Figure 6.16 show the same plots based on effective shear force proportional damping distribution. In this case, the effective storage stiffness K'_i followed the shape of the ASCE 7-10 story shear distribution. Not that unlike other cases, dampers were not provided in all stories, K''_{di} was concentrated in the upper half of the building in order to compensate the missing storage stiffness K'_{ai}. No damper is required in the lower half of the building in the 'low' damping case (see Figure 6.16a). The larger the damping level the larger the damper's storage stiffness K'_{ai} should be. Therefore, the number of stories that required dampers increased in the 'high damping' case. This is indicted in Figure 6.16c. Table 6.3 summarizes the damper parameters computed for the three vertical damping distribution cases for simplified models at high damping level ($K''_d/K_f = 1.0, K_b/K_f = 2$). Same findings hold true for the Y-loading direction of the same building but not reported herein due to brevity.

6.6.2 Evaluation of Damper Designs via Simplified Models

The evaluation of the damper design is carried out by utilizing two simplified models. In particular, the SBM-1E and FSBM-E models are selected. The shear building is evaluated at the SBM-1E intensity, which is the basis of the design procedure, while the FSBM-E is a better representation of the actual building. The comparison of both systems is useful to identify the effect of bending deformations on the building response reduction after the damper placement.

Figure 6.17 shows the median of the NRHA results based on the SBM-1E model and from 9 different damper designs in the X-loading direction. The initials L, M, H stand for low, medium and high damping; K, E and V represent the stiffness proportional, effective shear force proportional, and direct shear force proportional vertical damping distributions. It is clear that the effective SFPDD method provides a better control of story drift demands than other cases. Referring to Figure 6.17a, for the H-E case (i.e., high damping and effective SFPDD) the story drift ratio profile is relatively uniform in comparison to the H-K and H-V cases. The higher the supplemental damping the more uniform the story drift ratio profile becomes given that an effective shear SFPDD is employed. This is attributed to the fact that the damper design in high damping case dramatically altered the shape of the total story storage stiffness K_i' along the height of the building. This is shown in Figure 6.16c. The rest of the damping distribution methods are not able to alter the frame's displaced shape. Referring to Figure 6.17c, the effective SFPDD results into relatively low absolute floor acceleration demands compared to the rest of the methods. Nevertheless, the roof absolute acceleration remains relatively large, because when an effective SFPDD is employed no damper is placed at this location (see Figure 6.16). Referring to Figure 6.18, similar trends are observed in the Y-loading direction. In this case the difference between the vertical damping distribution methods becomes less obvious (see Figure 6.18d). This is attributed to the fact that the shear frame without dampers shows a relatively linear displacement profile in this loading direction as shown in Figure 6.11d.

Figures 6.19 and 6.20 illustrate the median EDPs obtained from NRHAs based on the FSBM-E model in the X- and Y-loading direction, respectively. Referring to Figure 6.19a, the peak SDRs increase with the building height. Same observations hold true for the displacement profiles (see

Figure 6.19d). This is attributed to the inclusion of flexural deformations, which also reduces the observed differences between different vertical damping distribution methods.

In order to clarify the influence of different design and modelling assumptions on the EDP response reduction, Figures 6.21 and 6.22 show the reductions in peak EDPs with respect to results obtained from the case without dampers in both loading directions based on a SBM-1E and FSBM-E model, respectively. Note that herein the average refers to the average of median peak EDPs between all stories/floor levels. The difference between different distribution methods becomes generally minimal when flexural deformations are considered in the simplified MDF model. The damping level (i.e., low, medium, high) plays an important role in the building EDP reduction after the damper design and placement. Referring to Figure 6.21a, when the effective shear force proportional distribution method is considered, the average peak SDRs reduce by 59%, 51% and 42% for low, medium and high damping levels in the X-loading direction, respectively. The dampers are not so effective in terms of controlling the average peak absolute floor accelerations. In this case, the corresponding reduction factors are 0.67, 0.62, 0.56 for low, medium and high damping levels, respectively. Similar results hold true for the Y-loading directions (see Figure 6.21b).

When comparing the above reduction factors with those of the performance-curves method (see Table 6.2) the errors were generally below 10%. This is to be expected because the comparison was conducted based on results obtained from shear beam models (SBM-1E)

In order to compare the effect of flexural deformation on the reduction factors, Figure 6.22 indicates the average response reductions obtained from NRHAs based on the FSBM-E model with respect to NRHAs based on the FSBM-E model of the frame without dampers. The

influence of flexural deformations on the X-loading direction can be seen in Figure 6.22a. For instance, the reduction factors in peak roof drift ratio increased by 17% to 36% in all design cases compared to those obtained based on the SBM-1E model (Figure 6.21a). Note that the largest increase is observed in high damping levels. On the other hand, the difference in the average peak absolute floor accelerations and the peak base shear is general below 10%. This suggests that the relative floor displacement and story drift demand reductions are more sensitive to flexural deformations in comparison to absolute floor accelerations and the base shear. The least increase is observed in absolute floor accelerations, which is, on average, 5% in all design cases. Referring to Figure 6.22b, the differences in the Y-loading direction are relatively low as expected in peak roof drift, average peak story drift and average peak base shear. There is practically no difference in the absolute floor accelerations compared to those obtained from the SBM-1E model. The reason is that in this loading direction the effect of bending deformations on the building response is relatively low.

6.7 Development of MDF-Performance Curves

Similar to the procedure conducted with three levels of damping, a wider range of damping levels can be taken into account for the design to find the optimum damping level considering MDF aspects, such as story drifts, absolute floor accelerations and story shear forces. The same procedure is carried out by using 23 different K_d''/K_{fs} values ranging from 0.05 to 5.0 and assuming $\mu_d = 2.0$, $p = 0.02$, $\beta_k = 4.5$ and $K_b/K_d'' = 2.0$. Two vertical distribution methods are considered herein, namely, the effective shear force proportional and the stiffness proportional damping distribution. Figure 6.23 shows the EDPs obtained from the median values of NRHAs based on the FSBM-E model that was designed by using the effective shear force distribution. Twenty three different damping levels are considered. The case without dampers is also

illustrated in the same figure. Referring to Figures 6.23a and b, the larger the K_d''/K_{fs} the smaller the SDR and floor displacements. The absolute floor accelerations and base shear tend to revert after a certain value of K_d''/K_{fs}. In order to observe these trends more clearly, MDF performance curves are constructed as shown in Figure 6.25 by tracking the peak EDP demand variations. For instance, Figure 6.25a shows the spectra of roof drift, average story drift and maximum story drift ratios. Similarly, Figure 6.25c illustrates the variation of normalized base shear (V_1/W), average and maximum absolute floor acceleration. By utilizing the MDF performance curves a designer can directly obtain the values of maximum and average story demands of the corresponding damper design without any error related to linearization, transformation and flexural deformations. The first point in the spectra represents the case without dampers (i.e., $K_d''/K_f = 0$). Referring to Figure 6.25a, the peak SDR ratio of the bare frame was 3.8%. The maximum peak SDR reduced to 2.9%, 2.3%, 2.1%, 1.75% and 1.23% for $K_d''/K_f = 0.1$, 0.25, 0.5, 1.0 and 5, respectively. Thus, the designer can choose the desired K_d''/K_f to satisfy the maximum peak SDR limit under consideration. Another design limitation could be the base shear force such that the foundation is not damaged. Referring to Figure 6.25b, the base shear coefficient V_1/W = 0.306, 0.230, 0.204, 0.189, 0.176 0.174 at K_d''/K_f =0, 0.1, 0.25, 0.5, 1.0 and 5, respectively. Controlling the absolute floor accelerations is important to minimize the non-structural component damage. From Figure 6.25b, the maximum absolute floor accelerations become 1.52, 1.13, 1.00, 0.98 0.86 and 0.77g at $K_d''/K_f = 0.1$, 0.25, 0.5, 1 and 5, respectively. Similarly, the MDF performance curves are constructed for a stiffness proportional distribution (see Figure 6.26). Notably, the peak absolute floor acceleration in the top story is significantly larger when the effective shear force proportional distribution is considered. This is attributed to the fact that the effective shear force proportional distribution provides no damping at the top

story while the stiffness proportional distribution is more redundant and provides supplemental damping at each story. It can be concluded that the base shear and maximum absolute floor accelerations can be reduced up to about 50% in comparison to the elastic bare frame. There is also no reduction for a $K_d''/K_{fs} > 1$.

In order to observe the drift reduction by providing supplemental damping more clearly, the drift reduction spectra (R_d) is constructed as shown in Figure 6.25b. In this figure, the drift spectra are normalized with respect to that of the bare frame. Similarly, Figure 6.25d shows the reduction for base shear and acceleration (R_v and R_a).. Similar plots are presented for Y-loading direction (see Figures 6.27 to 6.30). From Figures 6.29 and 6.30, the difference between roof drift ratio, maximum SDR, average SDR was less in comparison to the X-loading direction (Figure 6.25a). This is associated with the uniform drift profile in the Y-loading direction.

6.8 Summary and Conclusions

This chapter presented a practical design methodology for dampers installed in tall buildings. The proposed method consists of three main steps including: (1) the design and determination of SDF damper parameters via the performance curves method; (2) the vertical damper distribution by utilizing various methods, such as the stiffness, shear force and the effective shear force proportional distributions; (3) the story-based EDP predictions by using simplified MDF models of the respective building with dampers. To this end, guidance on the development of simplified models, such as the shear beam and flexural shear beam models was provided. In order to illustrate the proposed methodology, a 40-story steel MRF building designed in 1970s was utilized as a case study. The simplified models were validated by comparing the dynamic properties and NRHA results of the 2D models of the building in both loading directions. Case-specific performance curves were developed. A parametric study was carried out with 3 different

damping levels (e.g. low, medium and high) and vertical damping distribution methods. The evaluation of the design in the parametric study was conducted with a shear beam as well as flexural shear beam models to quantify the effect of flexural deformations on the building response reduction. Finally, MDF performance curves were constructed by executing the three main steps of the methodology for various damping levels.

The proposed MDF performance curves method herein provides a practical design tool for dampers by combining a preliminary design method with the linear static procedure of performance curves and an intermediate evaluation method with MDF flexural shear beam models. By utilizing the MDF performance curves, a designer can directly obtain the peak EDPs of the corresponding damper design. Therefore, the proposed method eliminates the errors due to conventional linear analysis procedures, such as linearization of period and damping, transformation from an MDF to an SDF system, flexural deformations, higher mode effects and irregular damper placement along the building height. Emphasis was placed on bilinear oil dampers. However, the proposed methodology is general and it can be simply implemented to other types of supplemental damping devices, such as hysteretic, nonlinear viscous and viscoelastic dampers. The main findings with respect to the case study building are summarized as follows:

- The effect of flexural deformation was large in the X-loading direction of the building, in which the ratio of the period of the shear frame to that of the frame, T_{fs}/T_f was 0.77; while in the Y-loading direction, $T_{fs}/T_f = 0.92$.
- Although the floor displacements were predicted well by utilizing shear beam models (SBM-2E) the error in predicting peak SDRs was significant, particularly, in the upper stories of the building in the X-loading direction. When a flexural shear beam model

(FSBM-E) was utilized, the predicted building response was nearly identical with the one computed from a 2D model of the building. Despite of the low flexural deformation in the Y-loading direction, the error was still large (6.4% and 77% average and maximum relative error, respectively) when a shear beam model (SBM-2E) was employed. Therefore, SBM-2E models should not be considered for the seismic evaluation of new and existing tall buildings.

- The dampers were provided only in few stories based on the effective shear force proportional damping distribution method for a low damping level (i.e. $K_d''/K_{fs} = 0.25$). The number of stories equipped with dampers increased with the increase of the damping level. On the other hand, the dampers were distributed at all levels when the shear force and stiffness proportional damping distribution methods were employed regardless of the damping level.
- When a SBM-1E model was employed, the effective SFPDD method altered the peak SDR distribution and resulted in a relatively uniform drift profile, particularly at high damping levels (i.e. $K_d''/K_{fs} = 1.0$). On the other hand, the direct SFPDD and stiffness proportional damping distribution methods did not practically change the drift concentrations observed in the bare frame.
- When a FSMB-E model was employed, the observed differences in predicted SDRs were less influenced by the employed vertical damping distribution method. More importantly, the corresponding reduction factors were significantly higher than those obtained based on the shear beam models. For the building with $T_{fs}/T_f = 0.77$, the peak roof drift was under predicted by up to 36% when a high damping level was considered, if the computation of the reduction factor was based on a shear frame model (SBM-1E) of the building with and

without dampers. On the hand, the corresponding maximum error in the base shear and the average absolute floor acceleration was 13% and 7%. This shows that the response reduction in absolute floor accelerations and the base shear was less sensitive to flexural deformations than that observed in floor displacements and SDRs.

- At a BSE-2E level, when the MDF performance curves are employed the base shear and maximum absolute floor accelerations were reduced by up to about 50% in comparison to the bare frame, but there was no reduction for $K_d''/K_{fs} > 1$.

Table 6.1: Properties of simplified models derived from 2D model of the 40-story building.

	X-loading direction				Y-loading direction			
#	K_{fi} (KN/mm)	K_{fsi} (KN/mm)	K_{fbi} (KN/mm)	K_{fi}/K_{fsi}	K_{fi} (KN/mm)	K_{fsi} (KN/mm)	K_{fbi} (KN/mm)	K_{fi}/K_{fsi}
40	59	215	81	0.27	140	303	259	0.46
39	118	322	185	0.37	254	442	598	0.57
38	139	320	245	0.43	278	430	791	0.65
37	158	331	302	0.48	296	425	973	0.70
36	182	369	358	0.49	309	423	1144	0.73
35	210	426	415	0.49	319	423	1307	0.76
34	229	452	466	0.51	329	425	1464	0.77
33	252	492	516	0.51	342	435	1605	0.79
32	276	539	564	0.51	356	447	1742	0.80
31	293	561	613	0.52	370	462	1863	0.80
30	314	596	663	0.53	393	490	1967	0.80
29	339	647	712	0.52	420	528	2055	0.80
28	358	676	759	0.53	434	543	2167	0.80
27	388	745	807	0.52	445	553	2287	0.81
26	424	839	856	0.51	455	561	2409	0.81
25	442	864	904	0.51	466	571	2524	0.82
24	455	870	955	0.52	485	595	2629	0.82
23	469	876	1008	0.54	511	629	2725	0.81
22	487	896	1065	0.54	532	654	2838	0.81
21	526	985	1127	0.53	569	705	2939	0.81
20	585	1134	1207	0.52	620	777	3070	0.80
19	609	1166	1273	0.52	640	799	3198	0.80
18	627	1173	1345	0.53	650	806	3355	0.81
17	644	1174	1425	0.55	659	810	3525	0.81
16	663	1179	1514	0.56	673	822	3714	0.82
15	688	1197	1614	0.57	705	860	3913	0.82
14	711	1212	1717	0.59	739	901	4112	0.82
13	737	1233	1830	0.60	757	916	4346	0.83
12	782	1300	1963	0.60	767	920	4621	0.83
11	849	1417	2121	0.60	777	921	4946	0.84
10	890	1451	2302	0.61	788	925	5338	0.85
9	935	1486	2520	0.63	807	937	5811	0.86
8	973	1503	2759	0.65	822	945	6333	0.87
7	1010	1512	3041	0.67	836	951	6955	0.88
6	1048	1515	3401	0.69	851	956	7754	0.89
5	1092	1520	3875	0.72	874	970	8846	0.90
4	1151	1543	4534	0.75	928	1018	10478	0.91
3	1267	1645	5506	0.77	1015	1101	13021	0.92
2	1393	1744	6939	0.80	1060	1132	16636	0.94
1	959	1087	8162	0.88	829	864	20286	0.96

Table 6.2: Damping levels and its SDF parameters obtained from performance curve (p=0.02, β_k=4.5, $\mu_{d=}$2, X-loading direction).

Case	K_d''/K_{fs}	K_b/K_{fs}	T_{eff} [sec]	β_{eff} [%]	R_d	R_a
Bare Frame	-	-	4.05	1.5	1.0	1.0
Low Damping	0.25	0.5	3.89	6.4	0.66	0.72
Medium Damping	0.5	1.0	3.74	10.7	0.53	0.63
High Damping	1.0	2.0	3.50	17.5	0.41	0.57

Table 6.3: Damper properties for simplified models based on various damping distribution, high damping level, X-loading direction

	Effective SFPDD			Stiffness Proportional			Direct SFPDD		
#	C_{di} (KNs/mm)	K^*_{bi} (KN/mm)	F_{dri} (KN)	C_{di} (KNs/mm)	K^*_{bi} (KN/mm)	F_{dri} (KN)	C_{di} (KNs/mm)	K^*_{bi} (KN/mm)	F_{dri} (KN)
40	0	0	0	120	239	587	58	115	778
39	1	3	18	179	358	1369	133	266	1798
38	172	345	2332	178	355	1835	176	353	2386
37	314	627	4242	184	368	2290	218	435	2944
36	402	803	5432	206	411	2732	257	513	3469
35	455	909	6150	237	474	3167	294	587	3971
34	549	1097	7425	251	502	3593	329	657	4444
33	611	1222	8265	273	547	4000	361	722	4885
32	656	1310	8867	300	600	4395	393	784	5308
31	734	1466	9921	312	624	4769	422	843	5704
30	783	1566	10595	332	663	5129	449	897	6073
29	802	1603	10846	360	719	5494	475	949	6421
28	849	1697	11480	376	751	5844	499	997	6746
27	825	1648	11152	415	829	6184	521	1042	7048
26	759	1517	10262	467	932	6519	543	1084	7337
25	795	1589	10749	481	960	6835	562	1124	7604
24	855	1709	11561	484	968	7137	581	1160	7851
23	911	1822	12325	487	973	7422	597	1194	8079
22	938	1875	12687	499	996	7694	613	1225	8288
21	851	1701	11511	548	1095	7964	627	1253	8478
20	698	1394	9435	631	1260	8347	648	1295	8765
19	692	1383	9355	649	1297	8600	660	1319	8927
18	723	1444	9773	653	1304	8831	671	1341	9072
17	757	1513	10241	653	1306	9048	681	1360	9203
16	783	1566	10594	656	1311	9250	689	1377	9319
15	783	1565	10590	666	1331	9439	697	1392	9421
14	786	1571	10629	674	1348	9616	704	1406	9513
13	776	1551	10493	686	1371	9778	709	1418	9593
12	689	1378	9321	723	1445	9927	714	1428	9661
11	519	1038	7025	788	1576	10067	719	1436	9719
10	480	959	6490	807	1613	10193	722	1443	9767
9	436	871	5894	827	1652	10308	725	1449	9807
8	418	835	5647	836	1671	10408	728	1454	9839
7	410	819	5545	841	1681	10497	729	1458	9864
6	412	823	5570	843	1684	10574	731	1461	9883
5	408	815	5518	845	1689	10640	732	1463	9897
4	374	747	5054	858	1715	10692	733	1464	9906
3	213	426	2884	915	1829	10734	733	1465	9912
2	58	116	786	970	1938	10765	733	1465	9915
1	40	81	873	605	1209	10785	458	916	9917

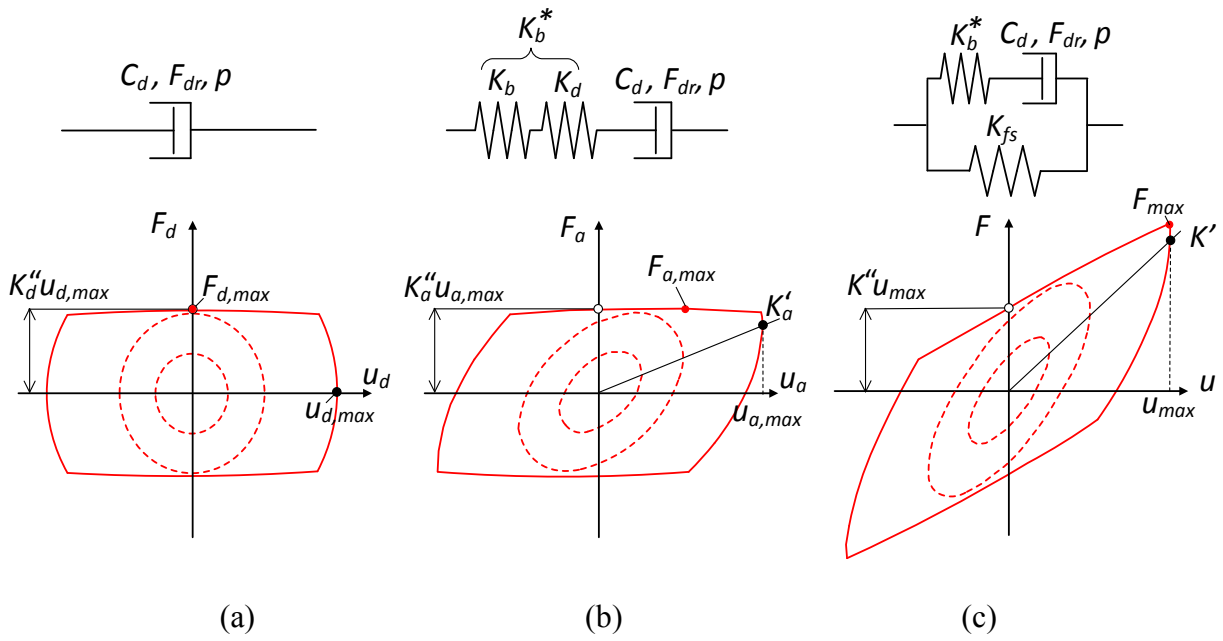

Figure 6.1: Mathematical model representations; a) Bilinear dashpot only b) Maxwell model c) Maxwell model and shear frame combined

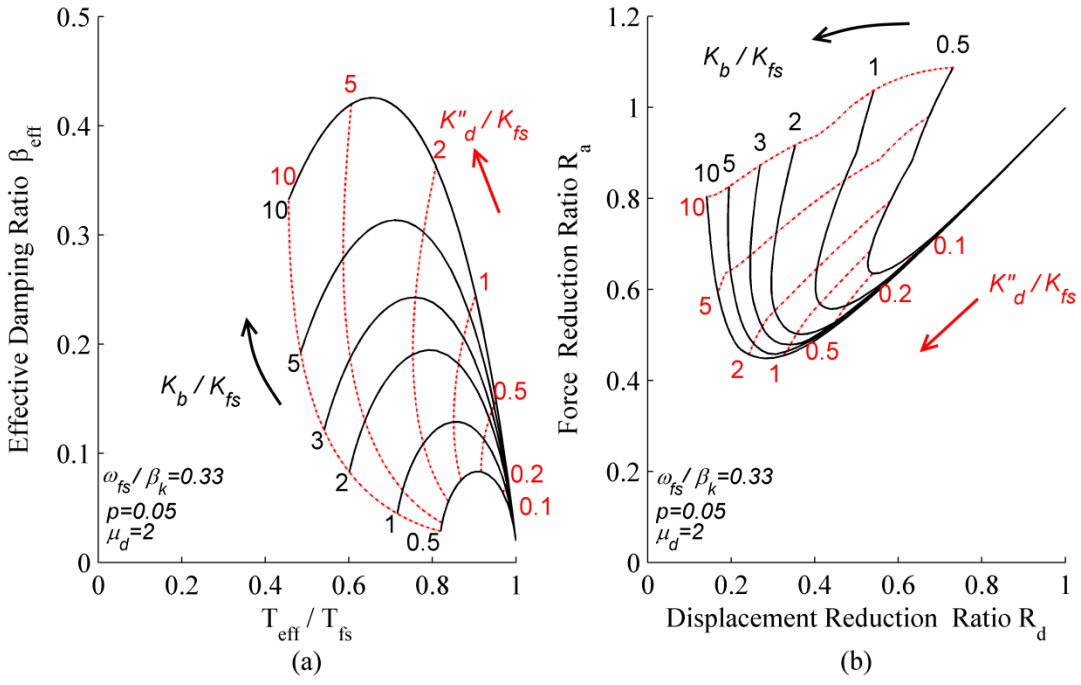

Figure 6.2: Performance curves for bilinear oil damper

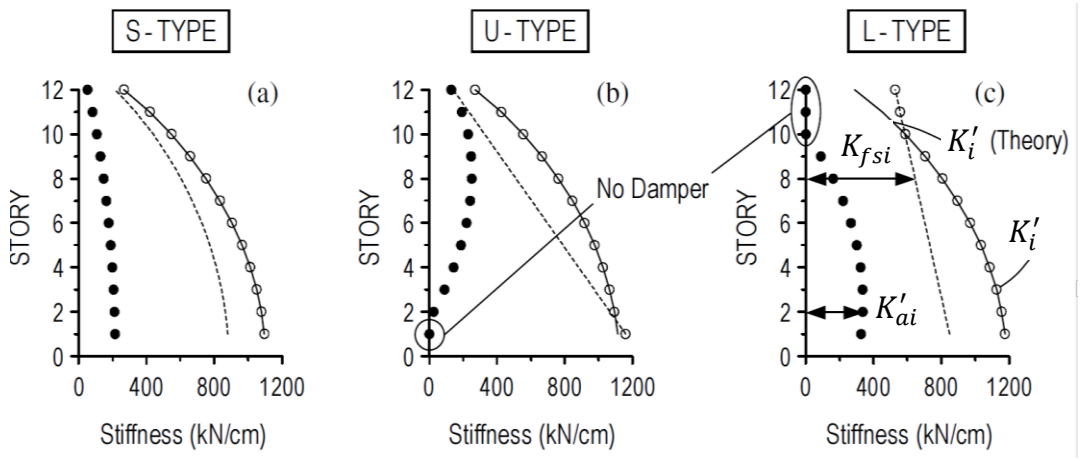

Figure 6.3: Vertical stiffness distribution of dampers (adopted from Kasai and Ito (2004))

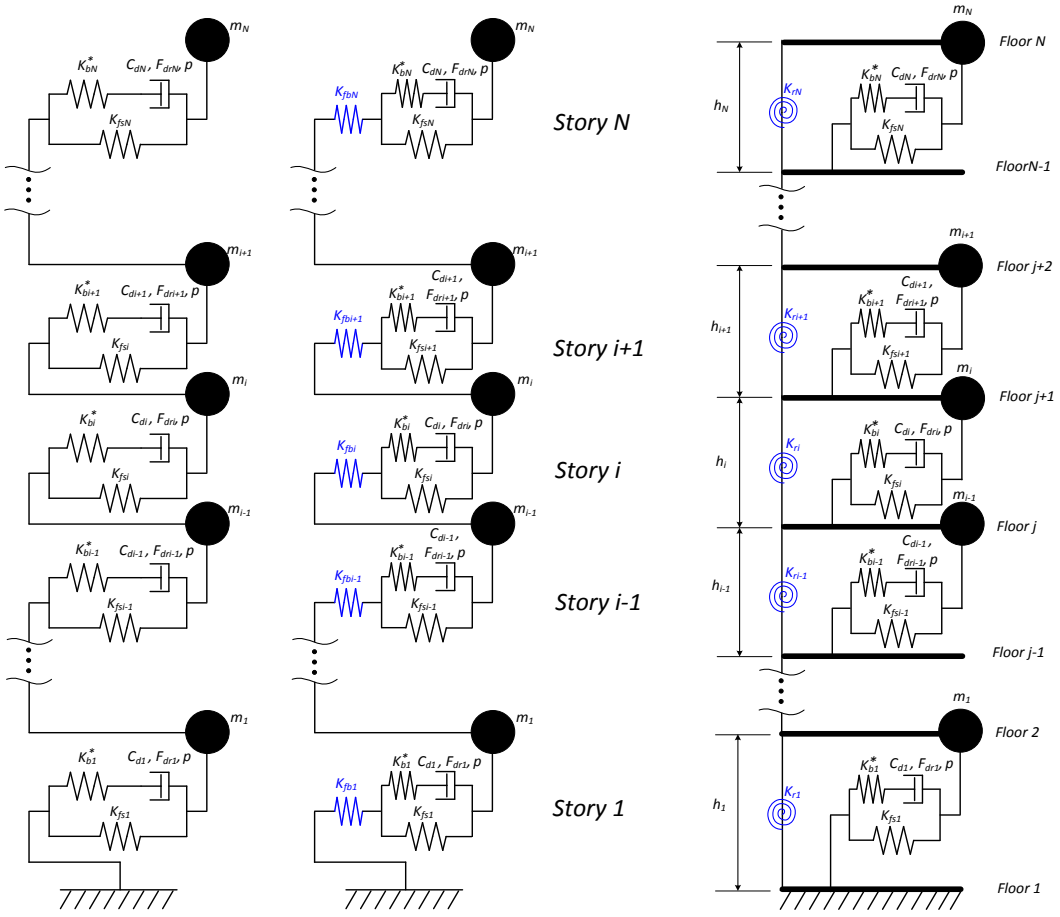

(a) SBM-1E: (b) SBM-2E (c) FSBM-E

Figure 6.4: Simplified MDF models for a building equipped with bilinear oil dampers

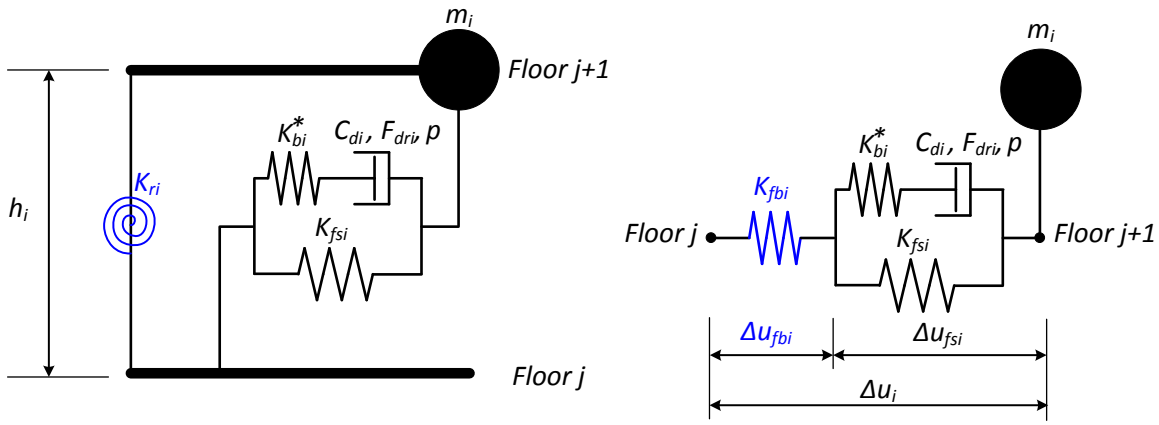

(a) FSBM-E: (b) SBM-2E:

Figure 6.5. Comparison between FSBM-E and SBM-2E models

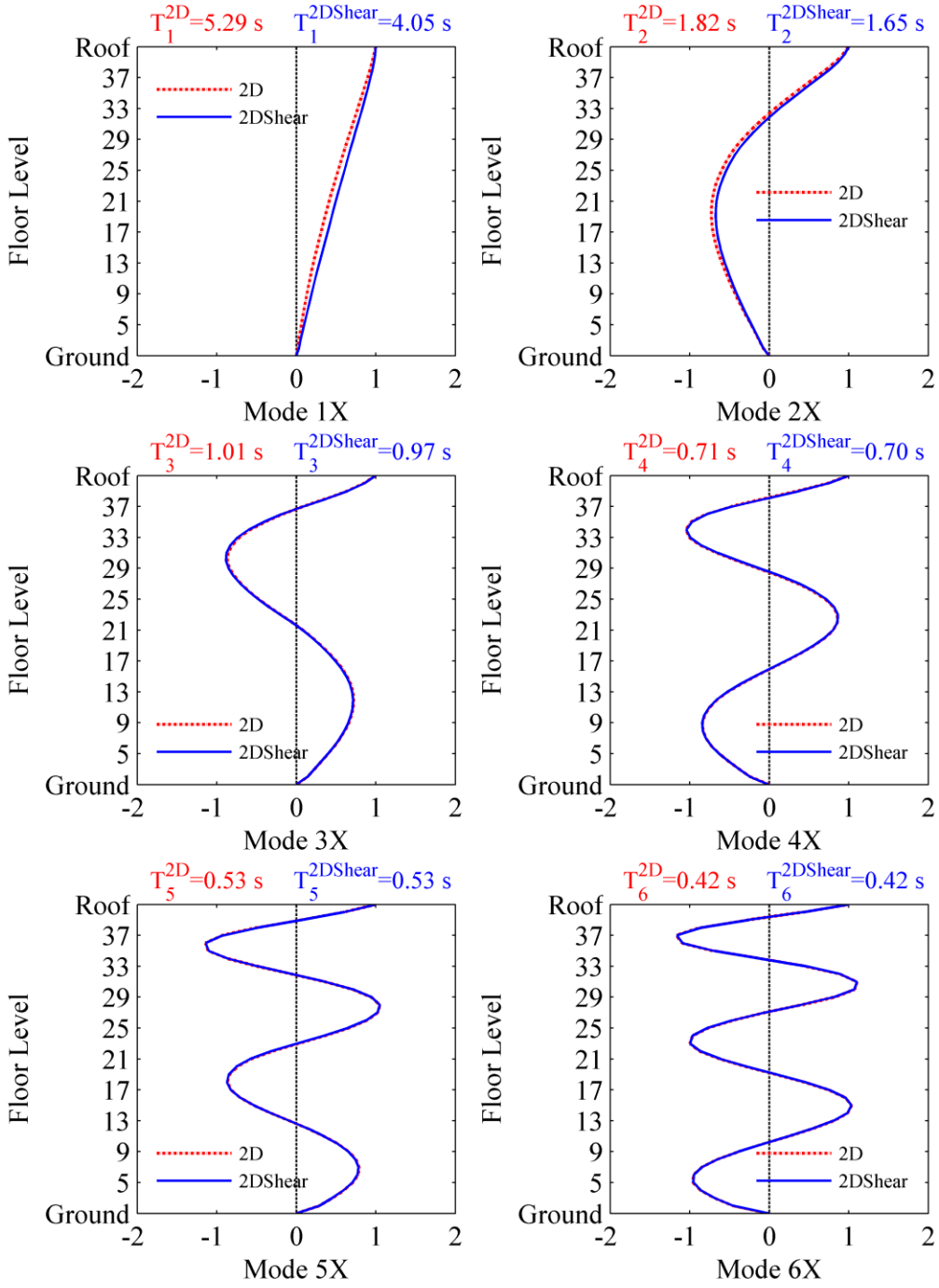

Figure 6.6: Comparison of dynamic properties between 2D modal and 2D-shear modal, X-loading direction

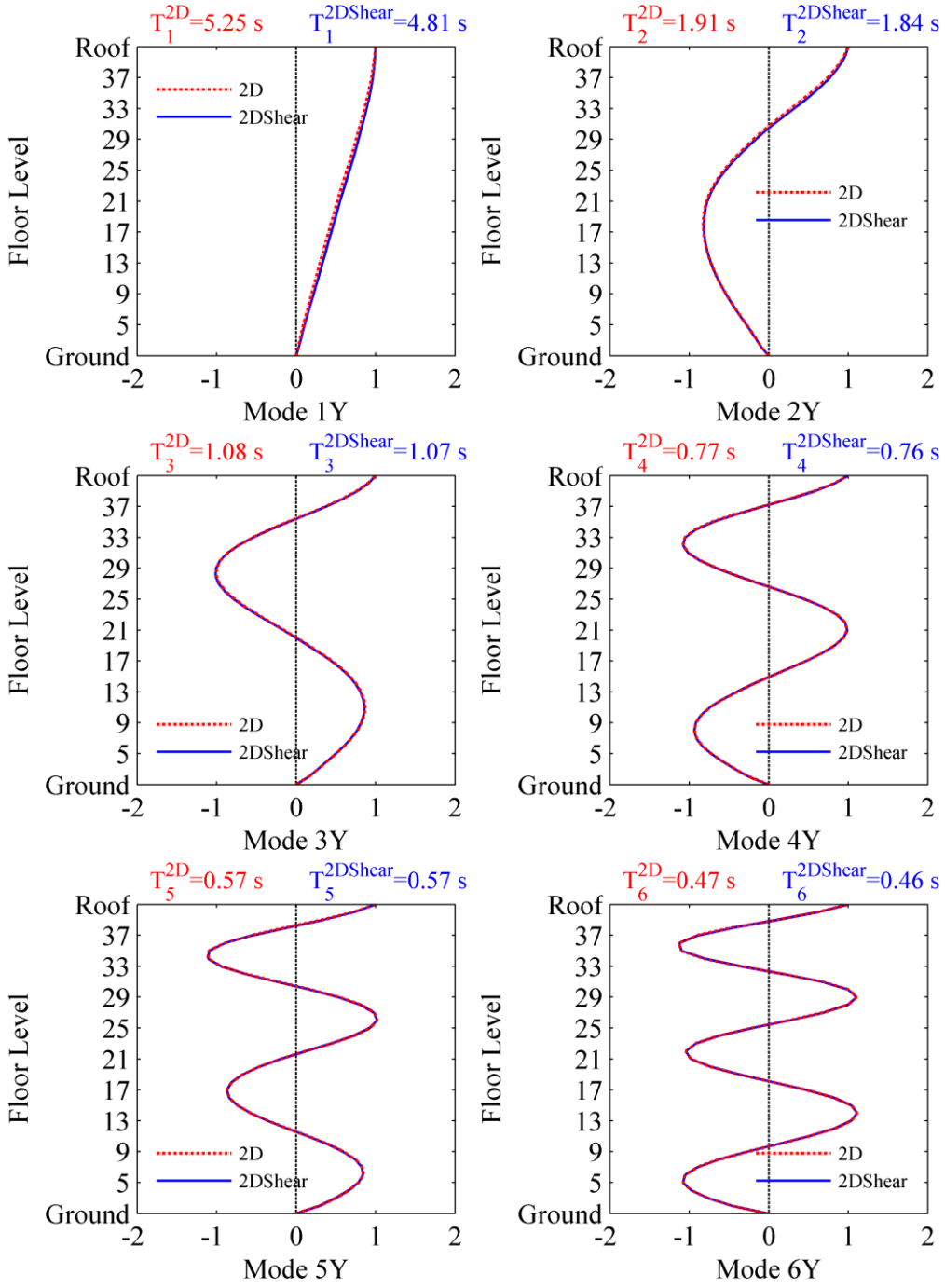

Figure 6.7: Comparison of dynamic properties between 2D and 2D shear model, Y-loading direction

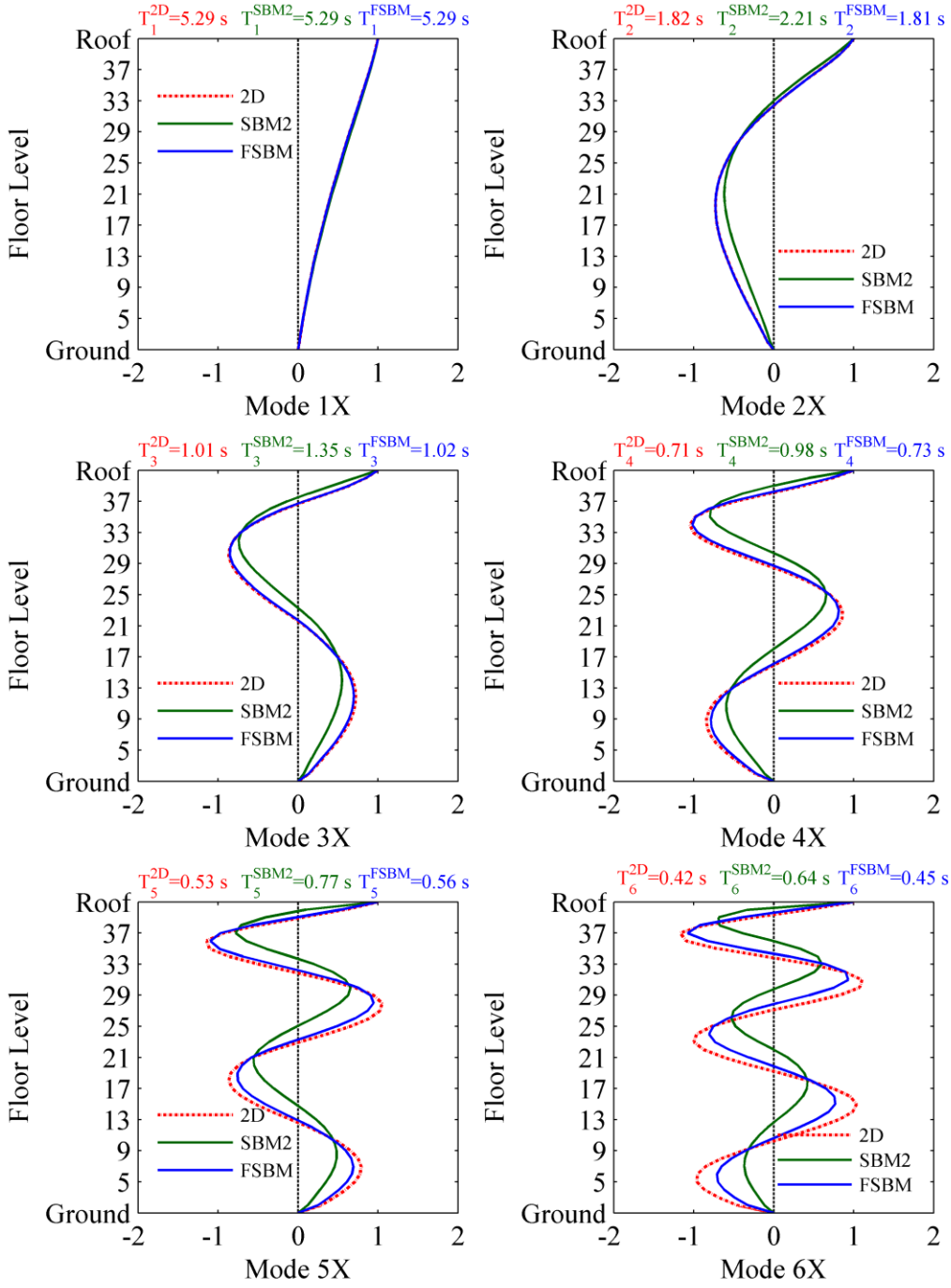

Figure 6.8: Comparison of dynamic properties between 2D modal and SBM, X-loading direction

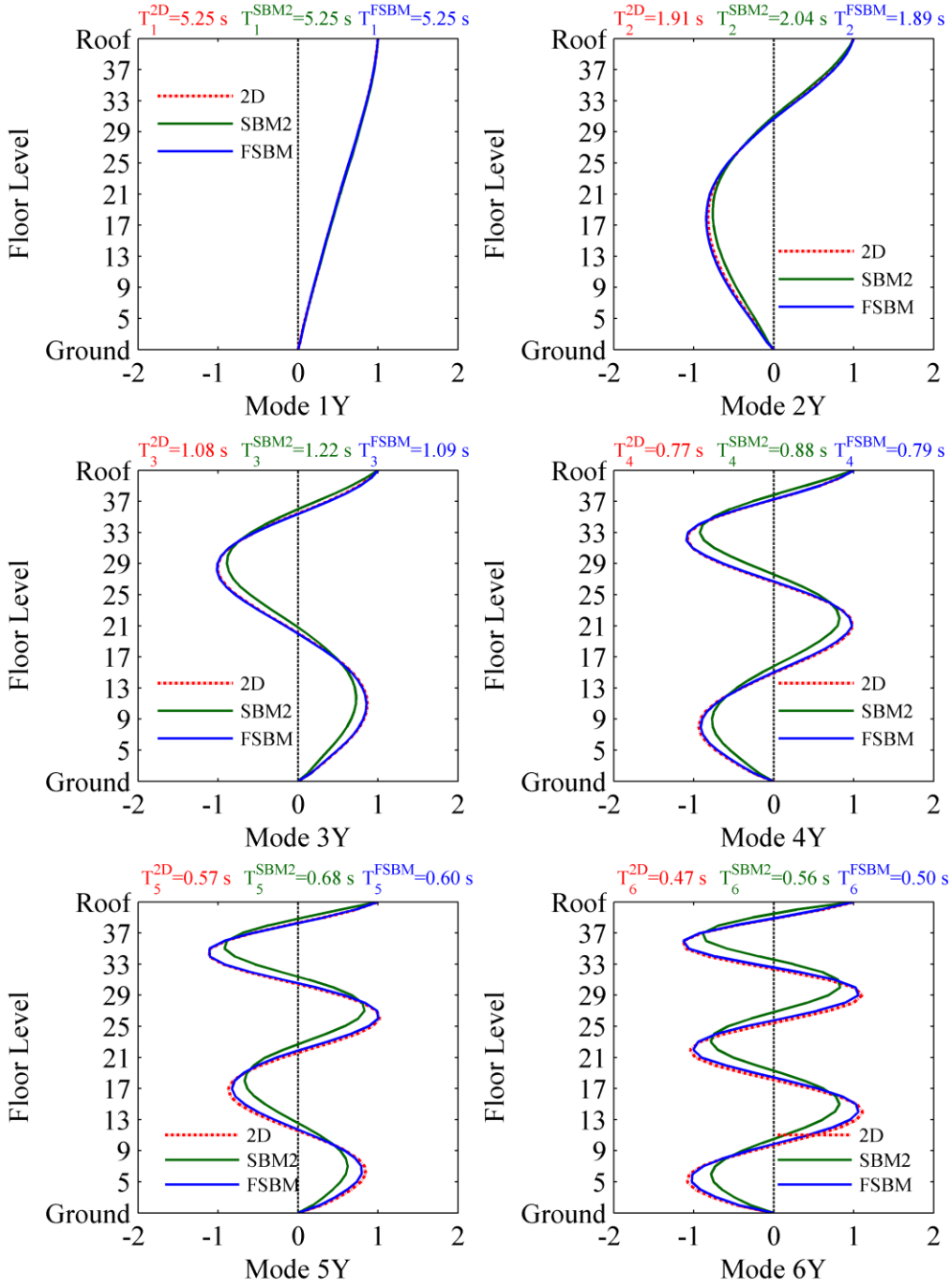

Figure 6.9: Comparison of dynamic properties between 2D modal and simplified models, Y-loading direction

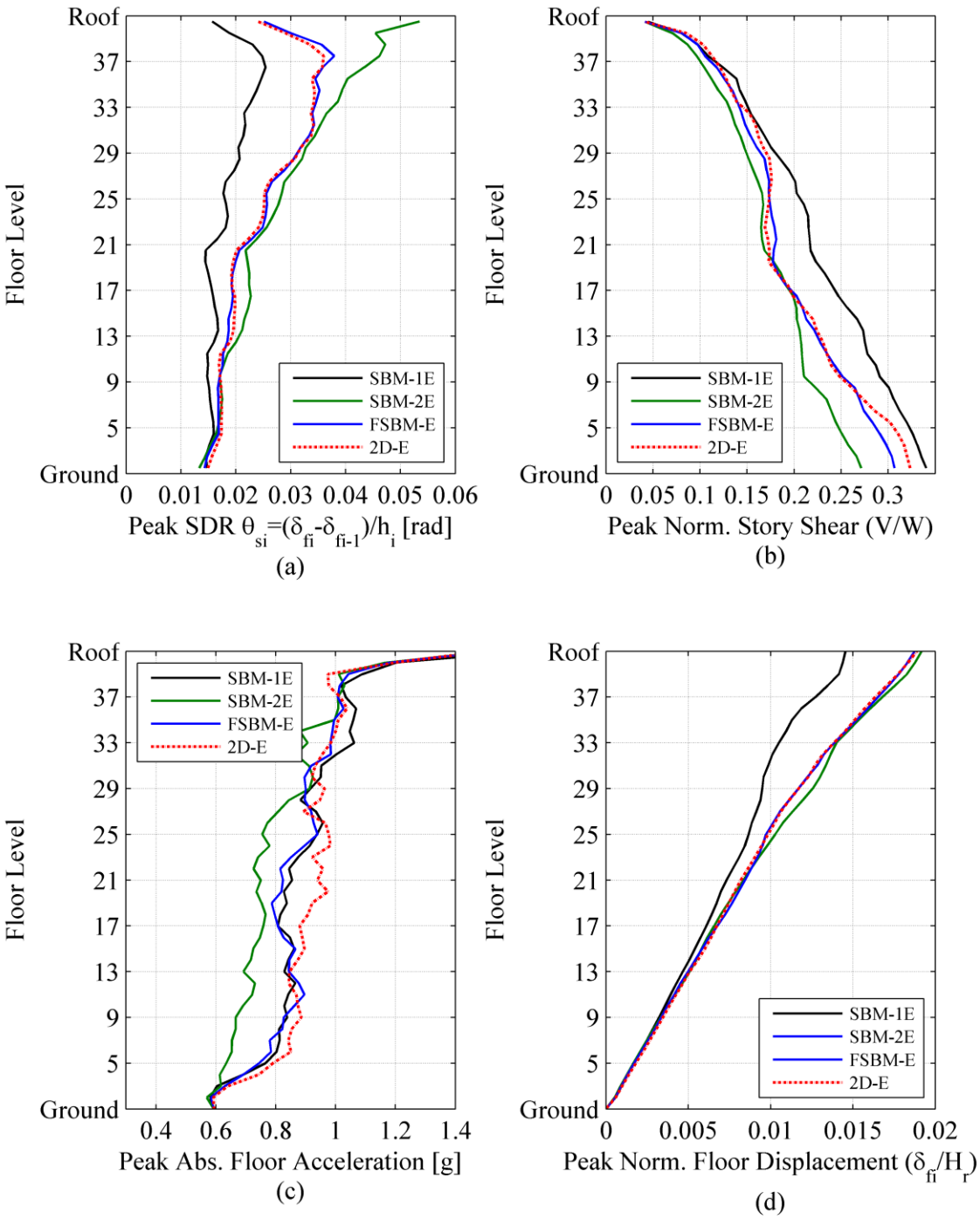

Figure 6.10: NRHA results (median) of simplified models in comparison with 2D bare frame model, X-loading direction

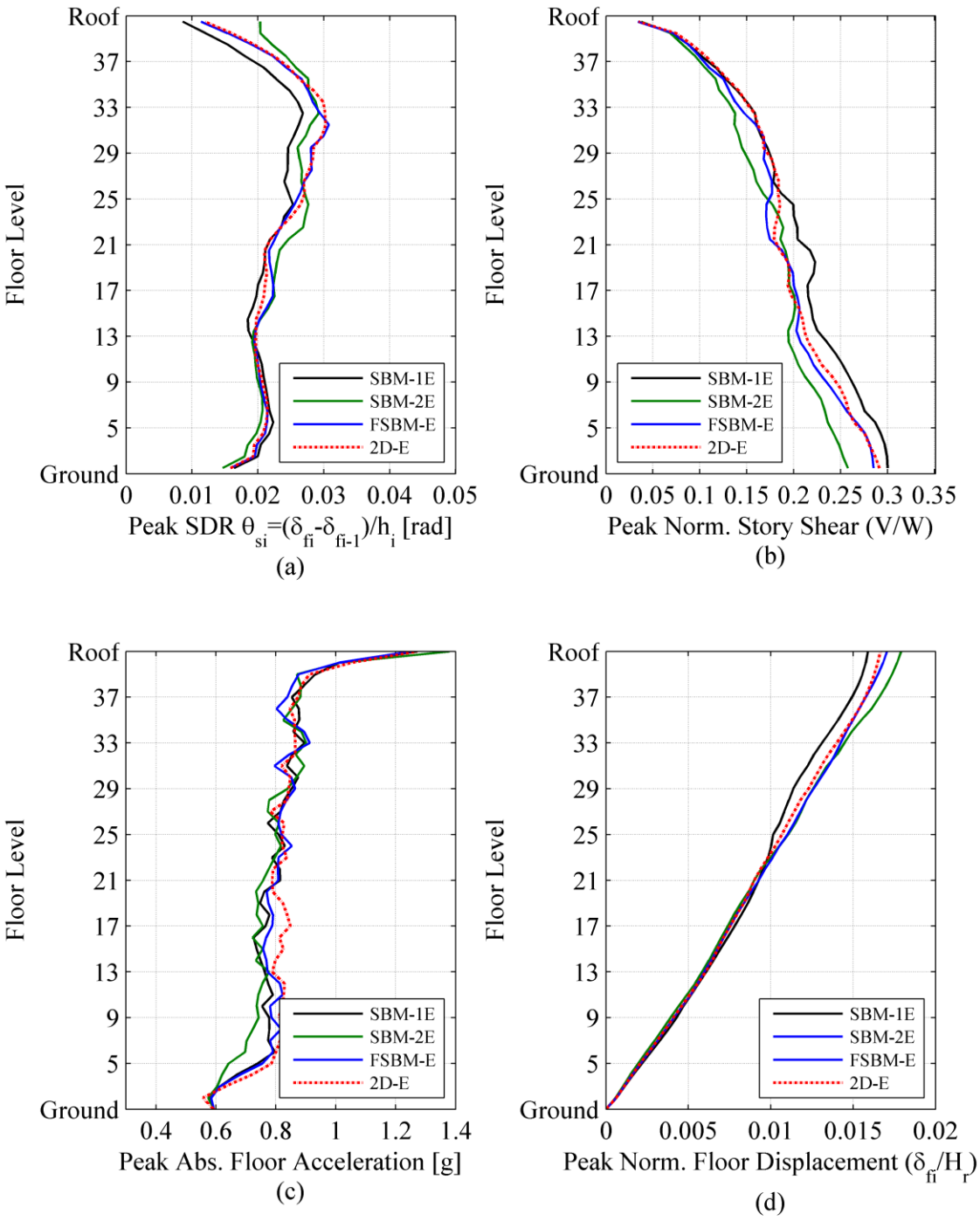

Figure 6.11: NRHA results (median) of simplified models in comparison with the 2D bare frame model, Y-loading direction

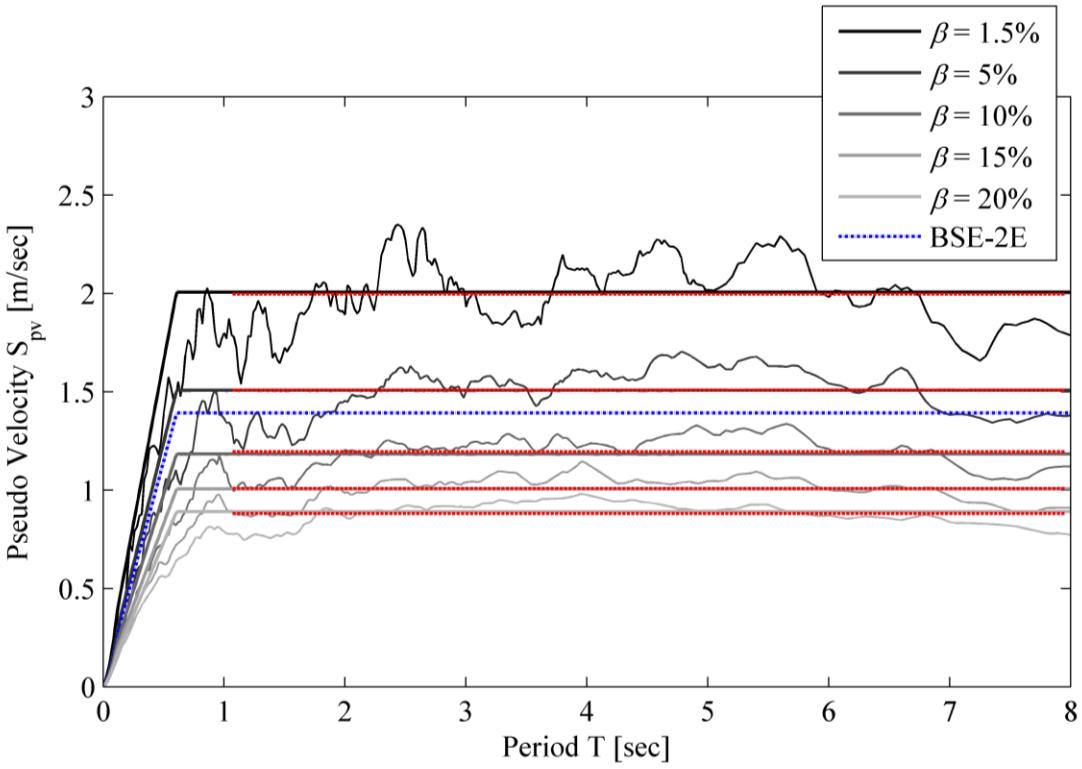

Figure 6.12: Calibration of damping modification factor via median pseudo velocity spectra (*a*=33)

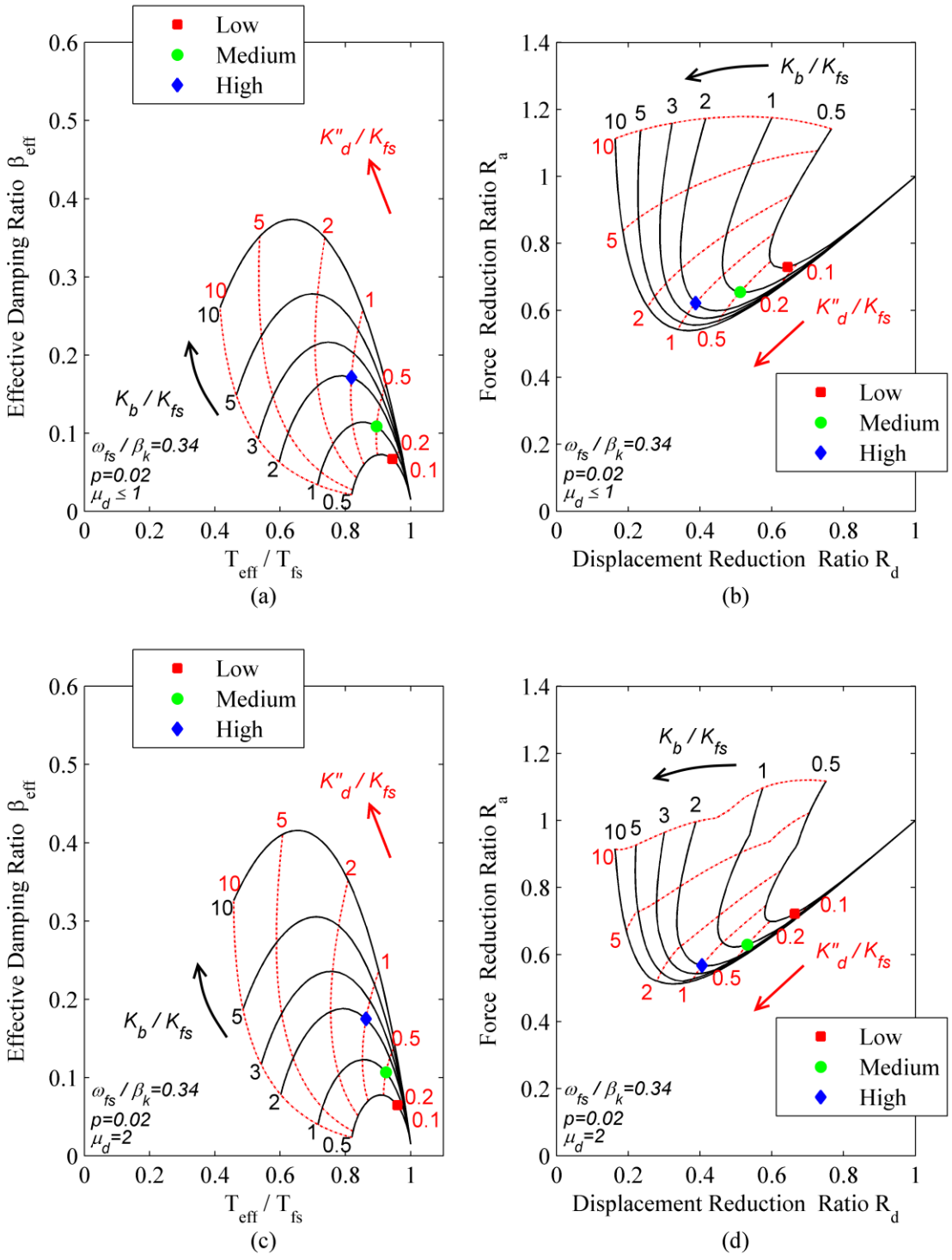

Figure 6.13: Case-specific performance curves for bilinear oil damper with $\mu_d \leq 1$ and $\mu_d = 2$

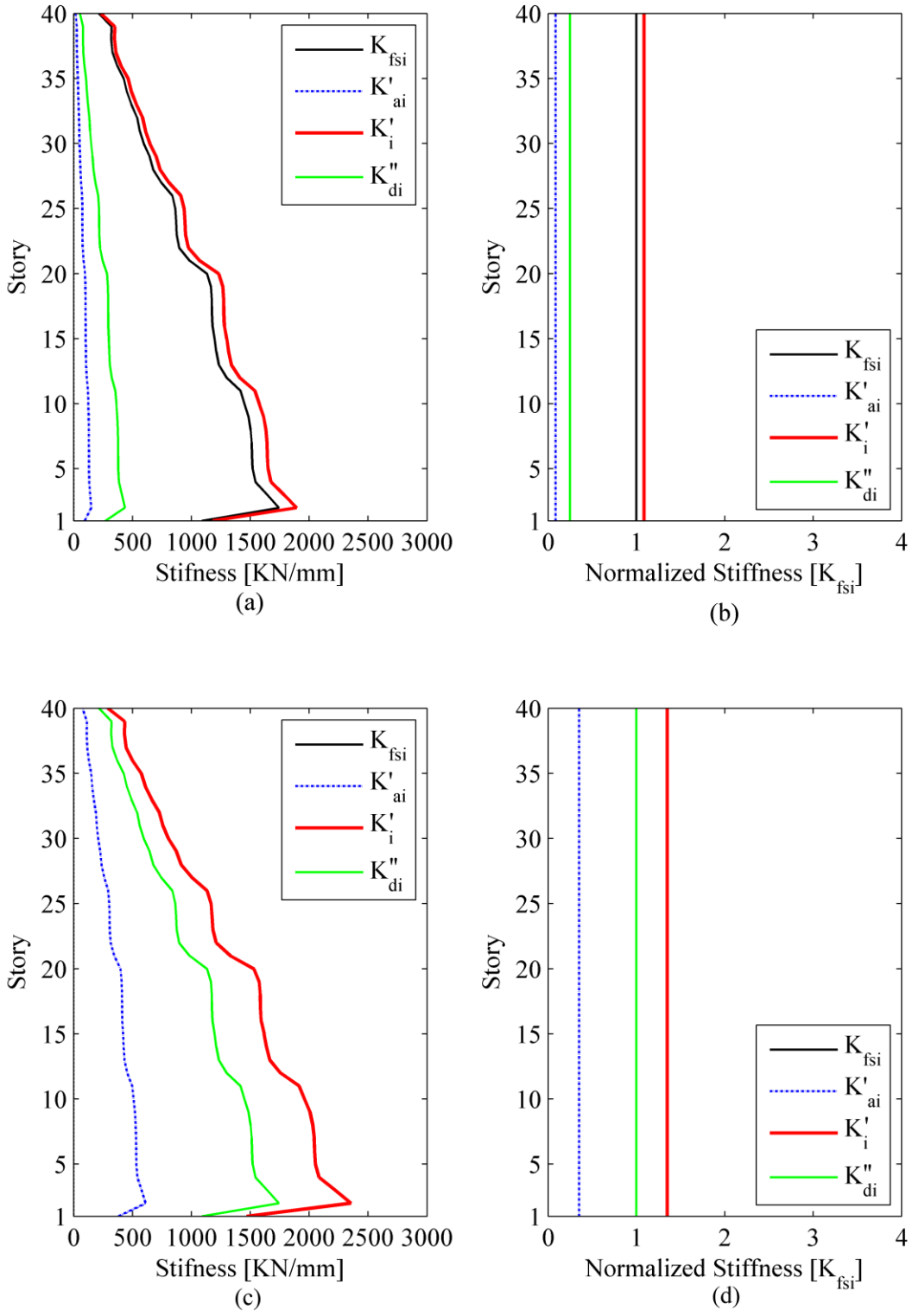

Figure 6.14: Stiffness proportional damping design (low and high damping), X-loading direction

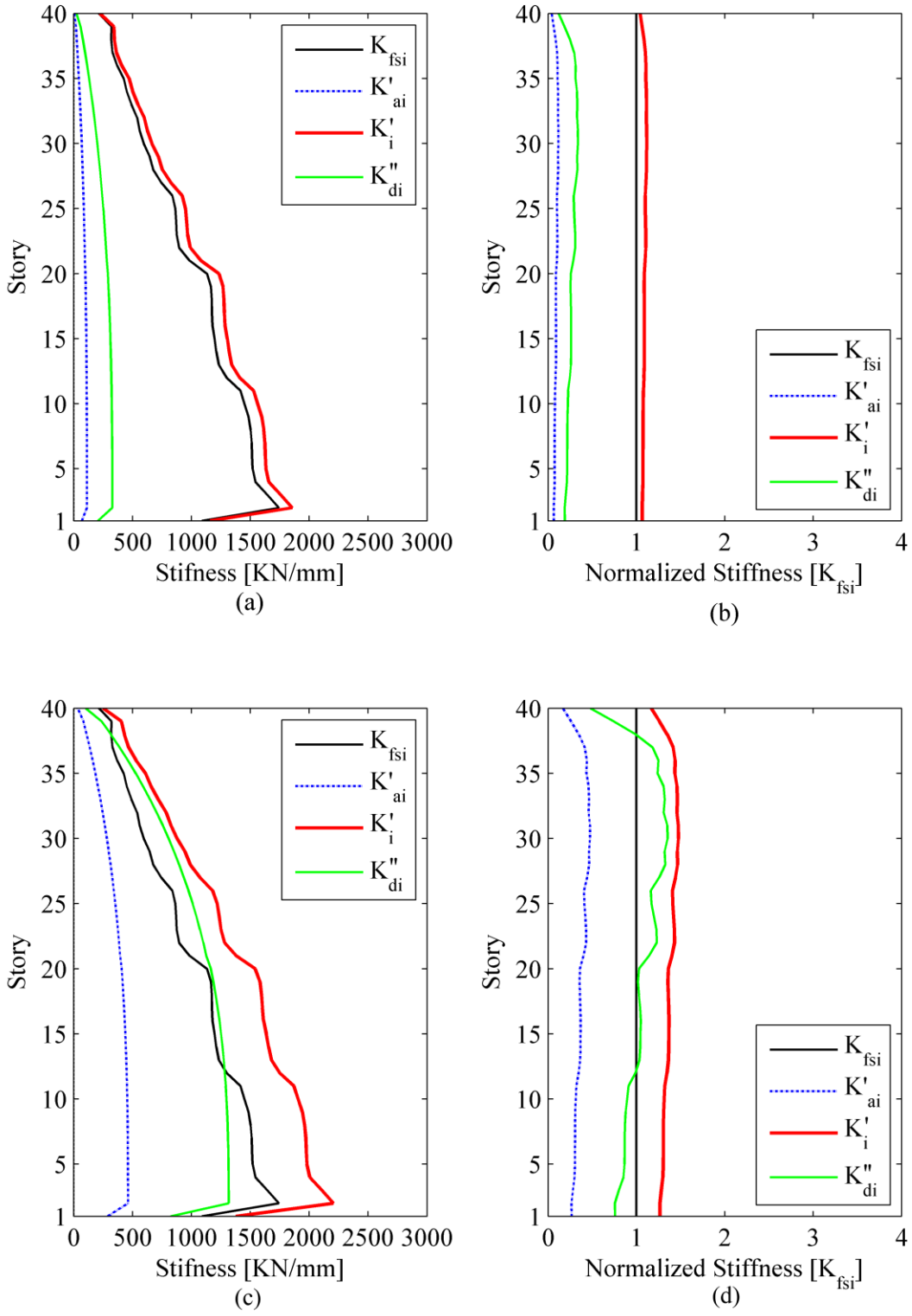

Figure 6.15: Shear force proportional design (low and high damping), X-loading direction

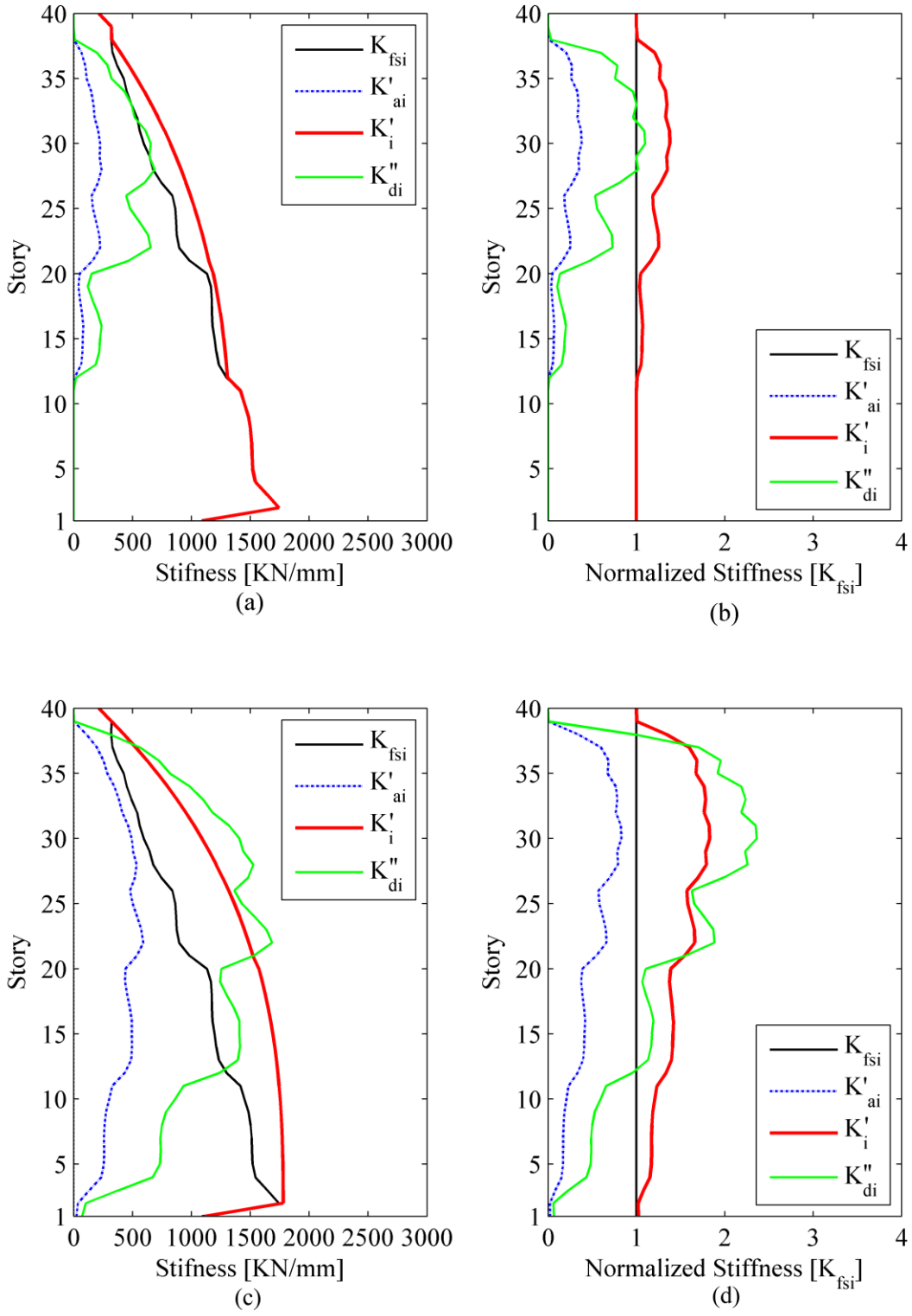

Figure 6.16: Effective shear force proportion design (high damping), X-loading direction

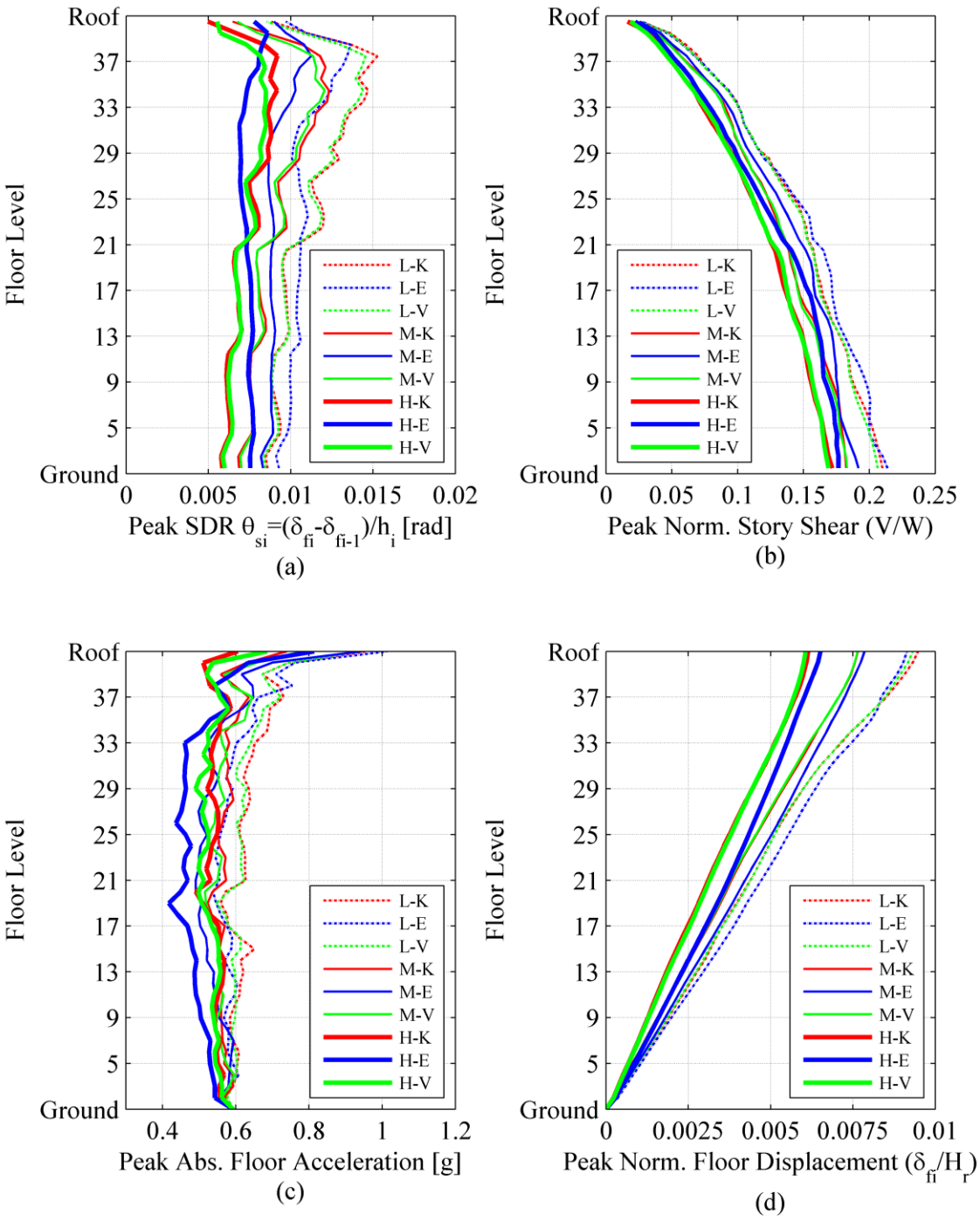

Figure 6.17: EDP comparison of vertical damping distribution; SBM-1E model in X-loading direction

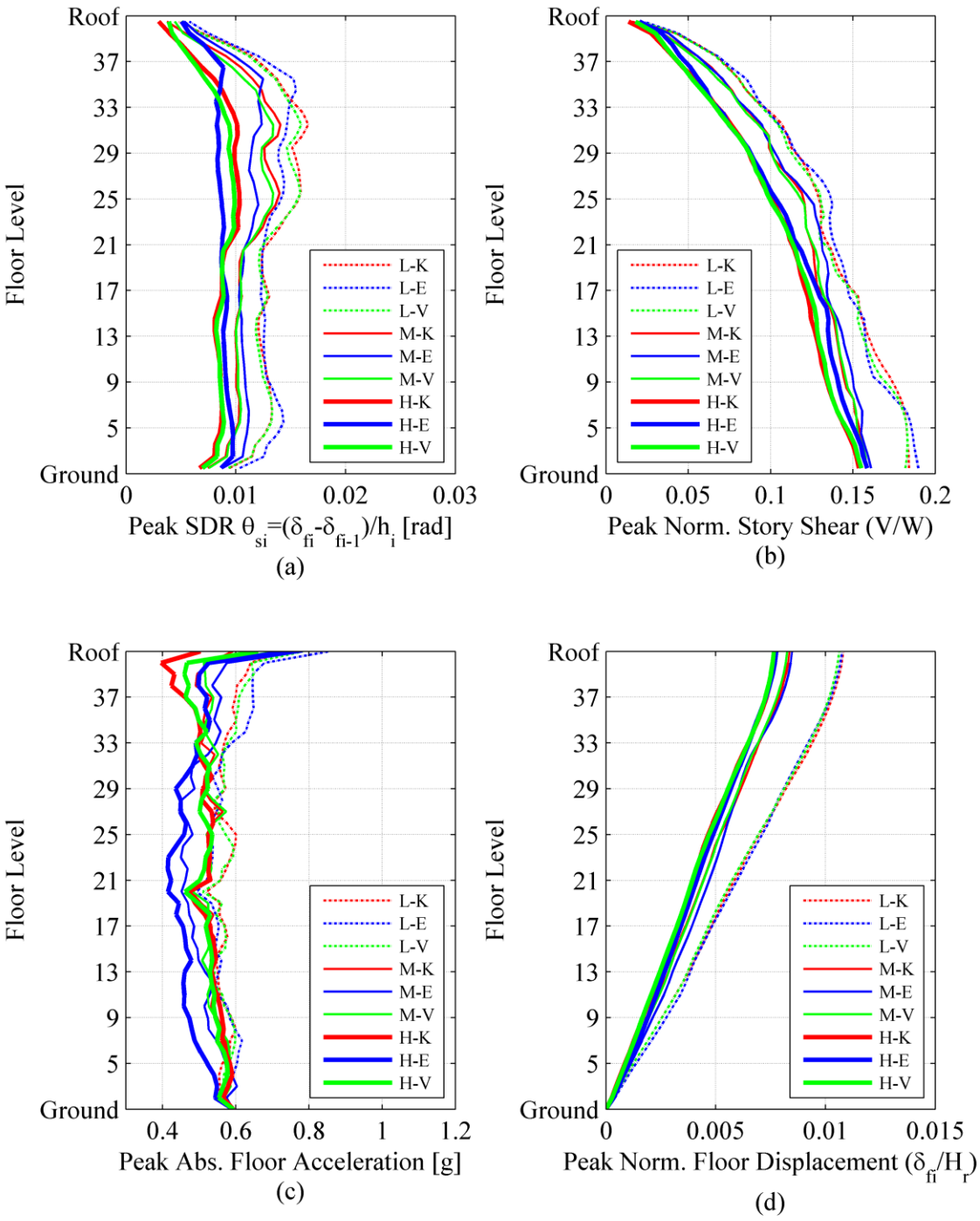

Figure 6.18: EDP comparison of vertical damping distribution; SBM-1E model in Y-loading direction

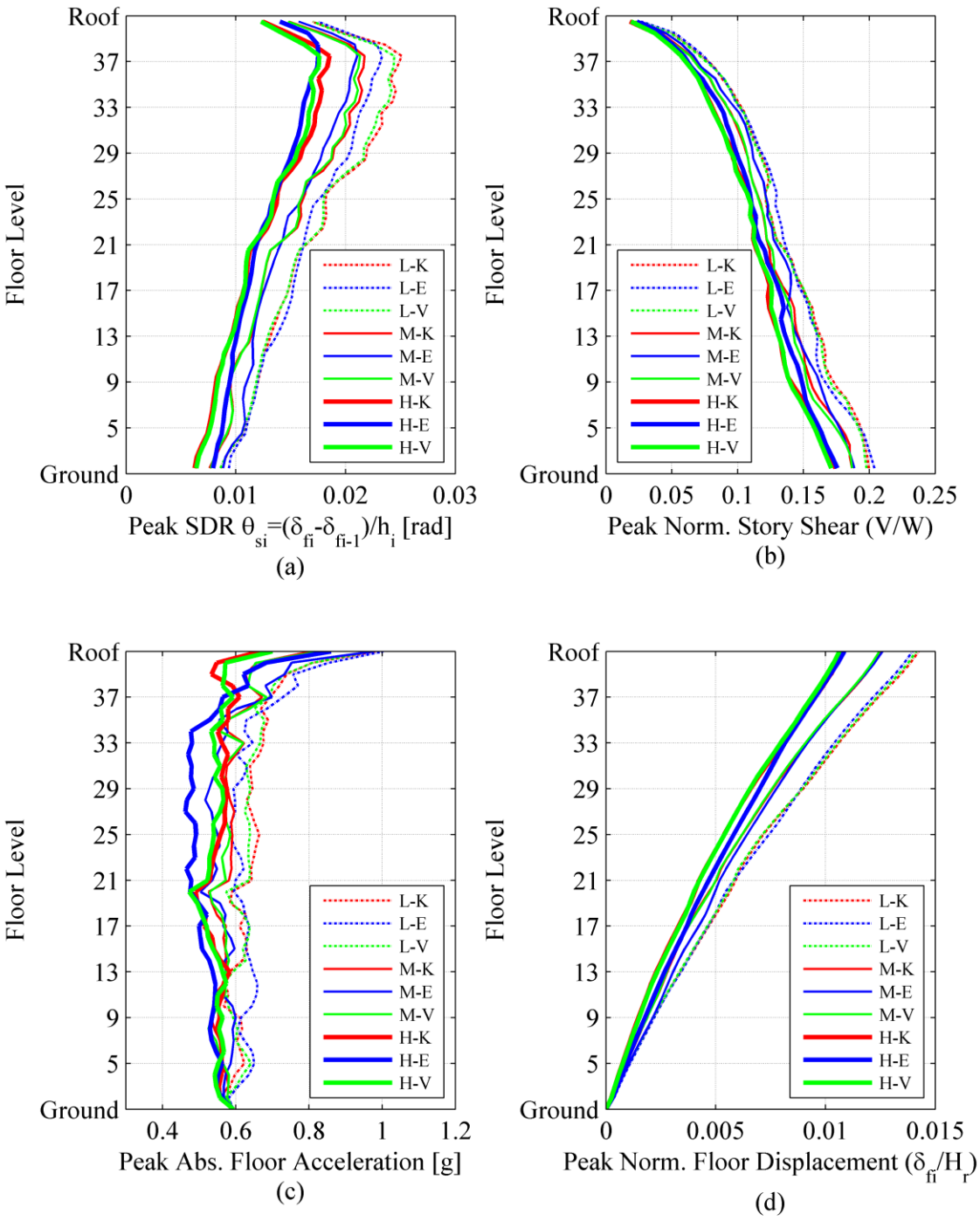

Figure 6.19: EDP comparison of vertical damping distribution; FSBM-E model in X-loading direction

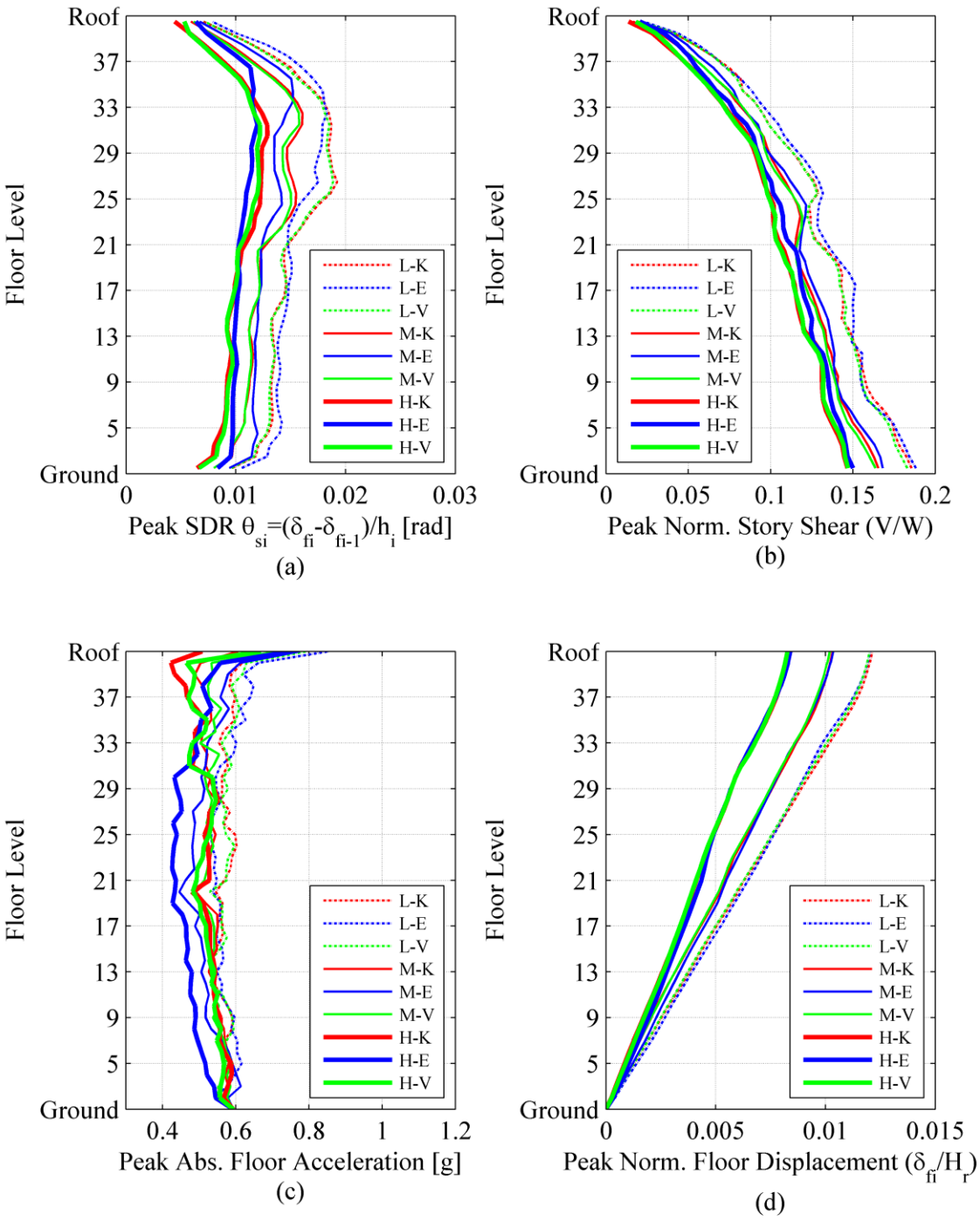

Figure 6.20: EDP comparison of vertical damping distribution; FSBM-E model in Y-loading direction

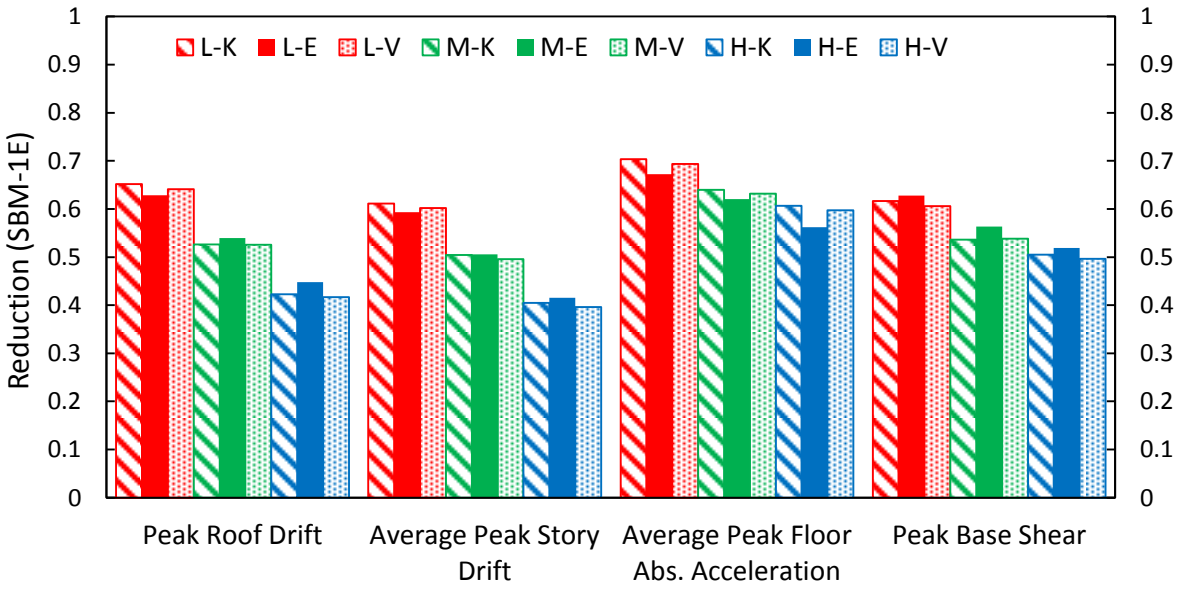

(a) X-loading direction

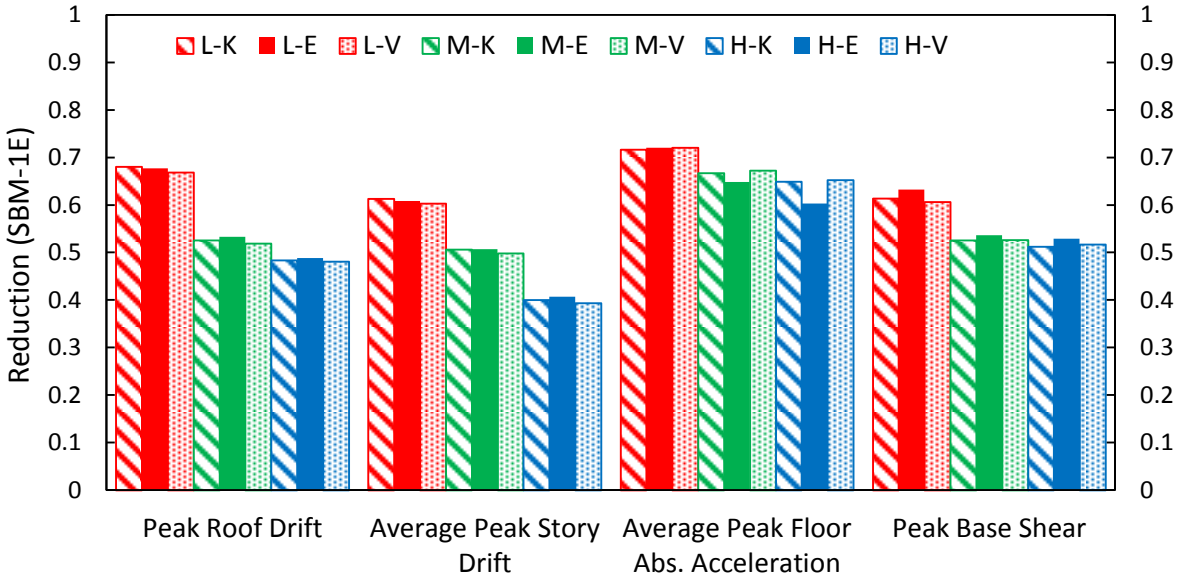

(b) Y-loading direction

Figure 6.21: EDP reduction with respect to SBM-1E model

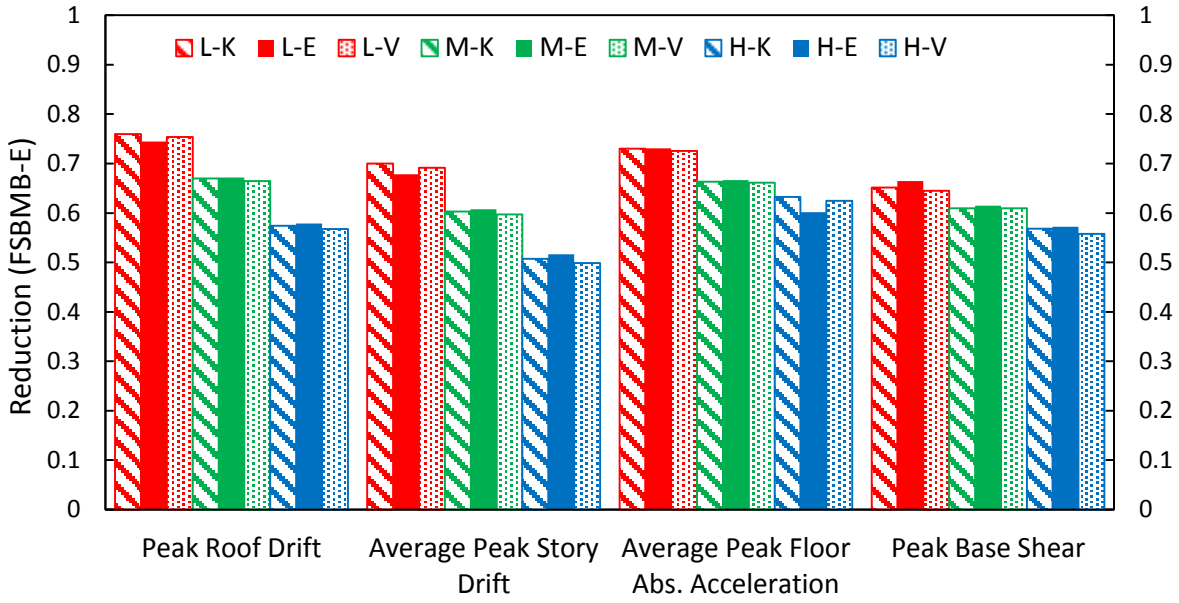

(a) X-loading direction

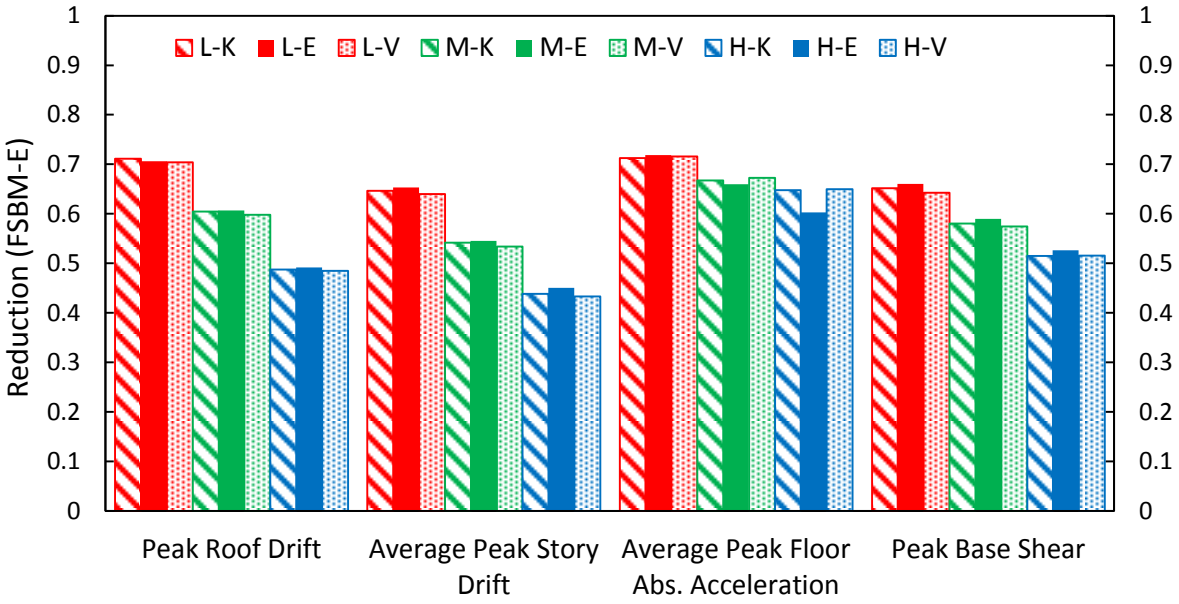

(b) Y-loading direction

Figure 6.22: EDP reduction with respect to FSBM-E model

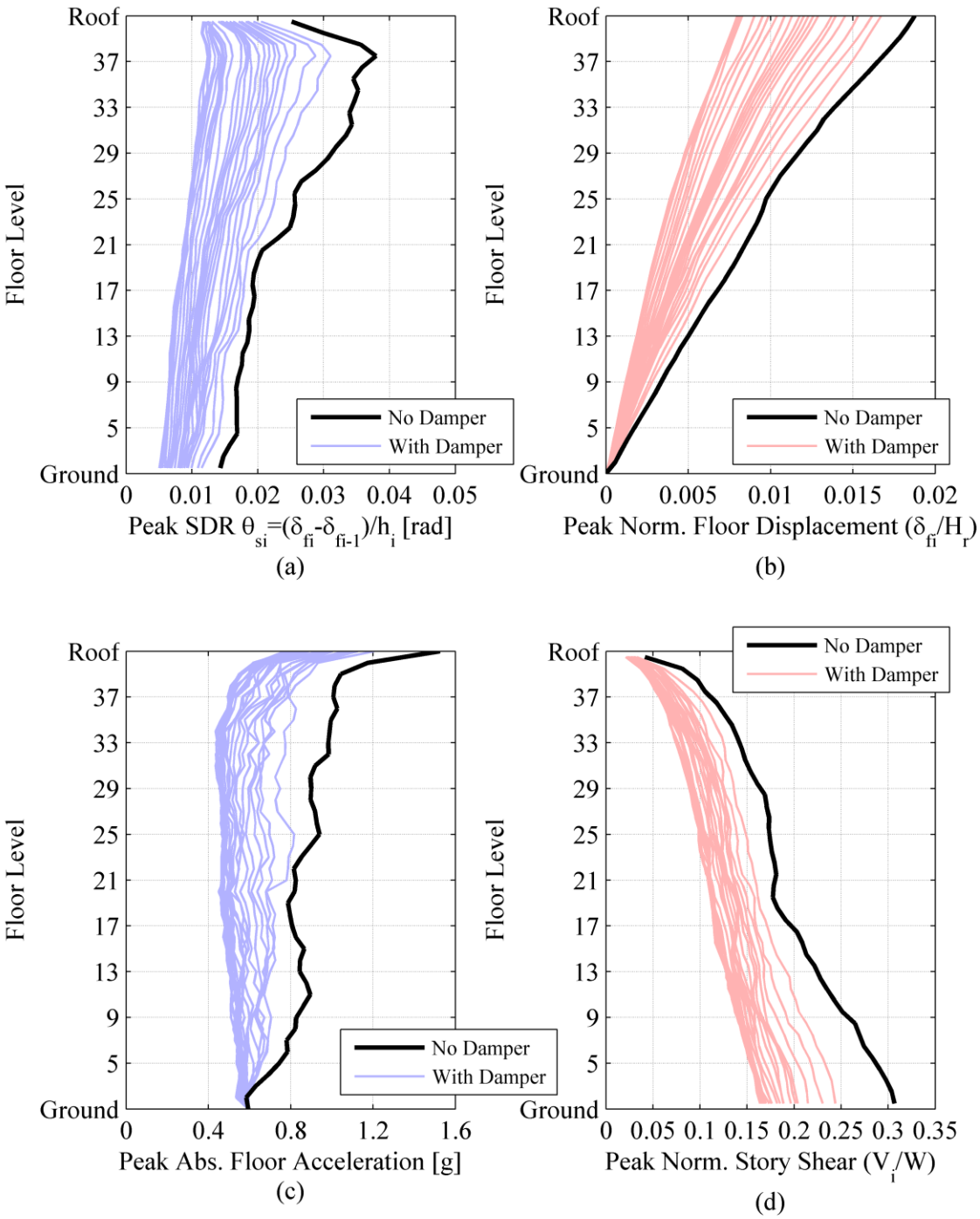

Figure 6.23: EDP demands with/without dampers ($K_d''/K_f = 0.05 - 5$) - X-loading direction - effective shear force proportional damping distribution

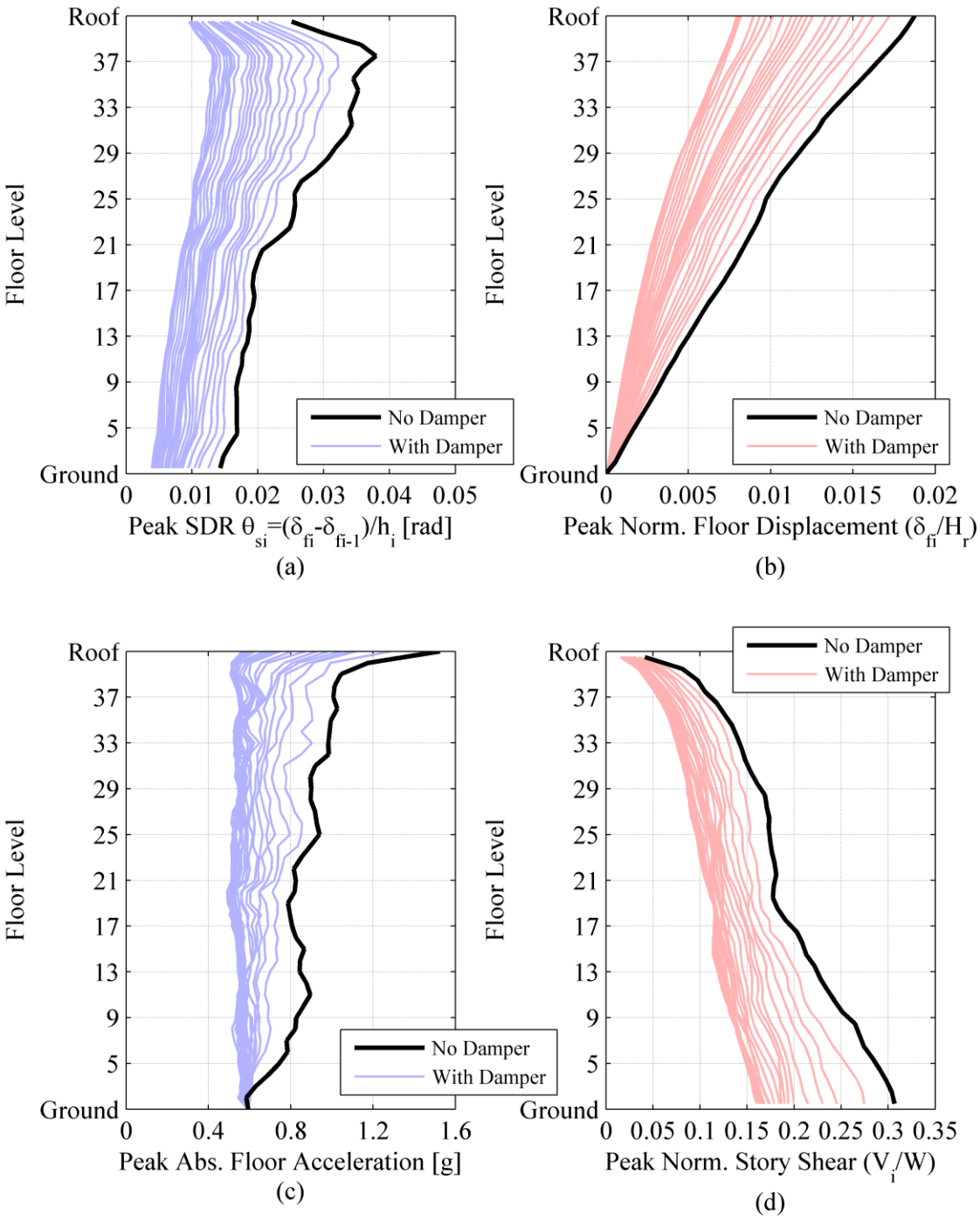

Figure 6.24: EDPs without and with dampers ($K_d''/K_f = 0.05 - 5$)-X-loading direction, stiffness proportional damping distribution

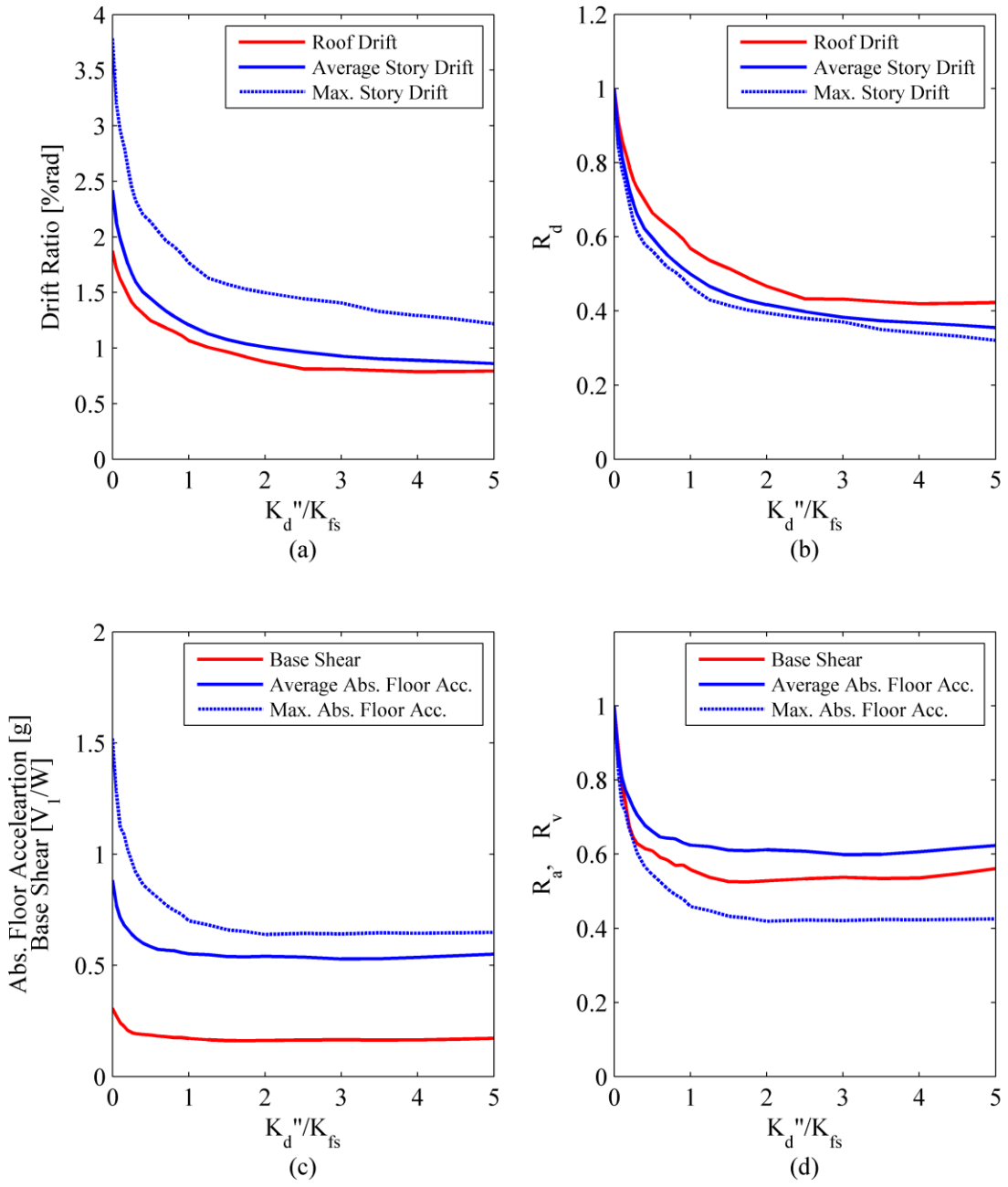

Figure 6.25: MDF performance curves of drift, absolute floor acceleration and base shear, X-loading direction, effective shear force proportional distribution

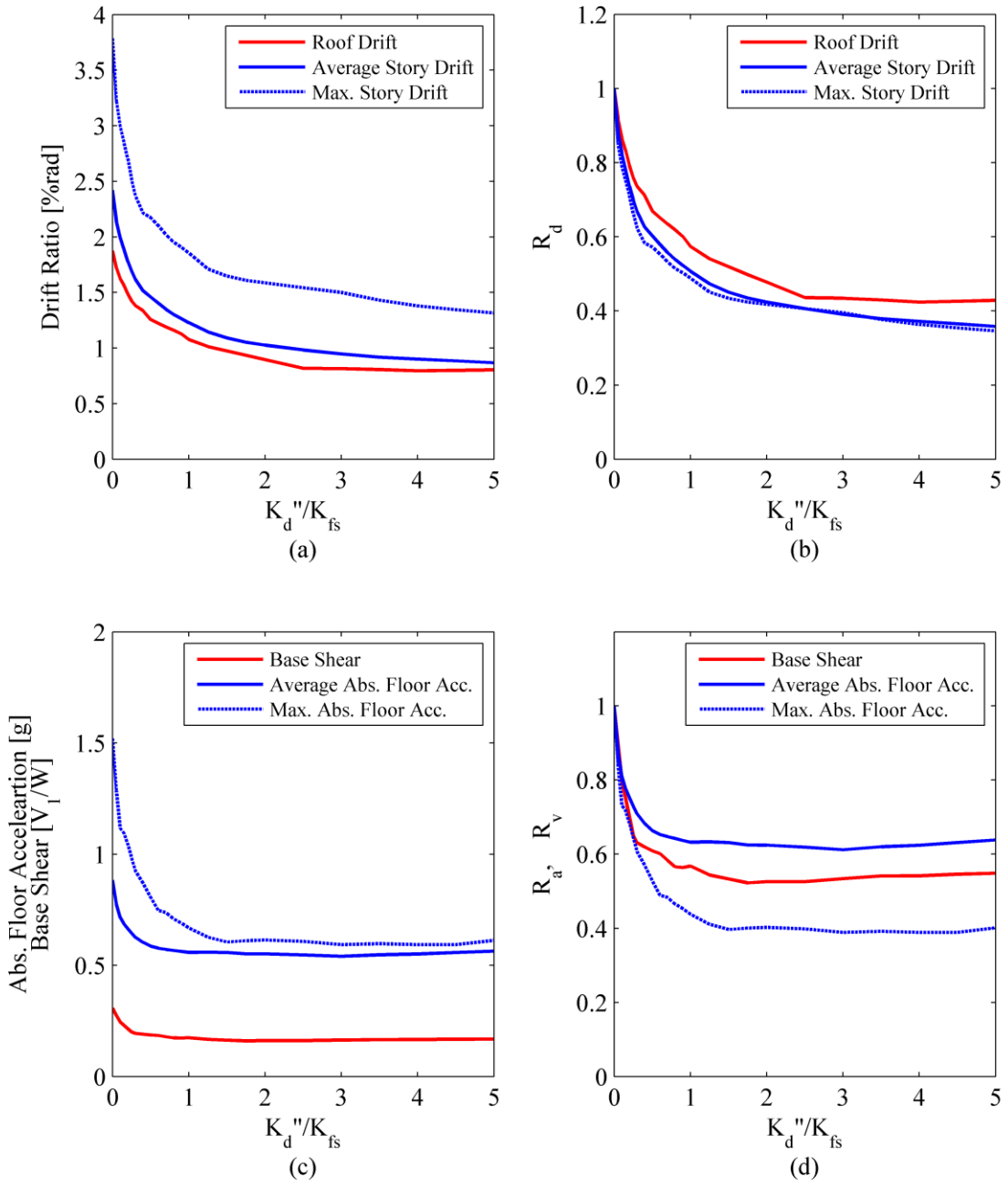

Figure 6.26: MDF performance curves of drift, absolute floor acceleration and base shear spectra, X-loading direction, stiffness proportional distribution

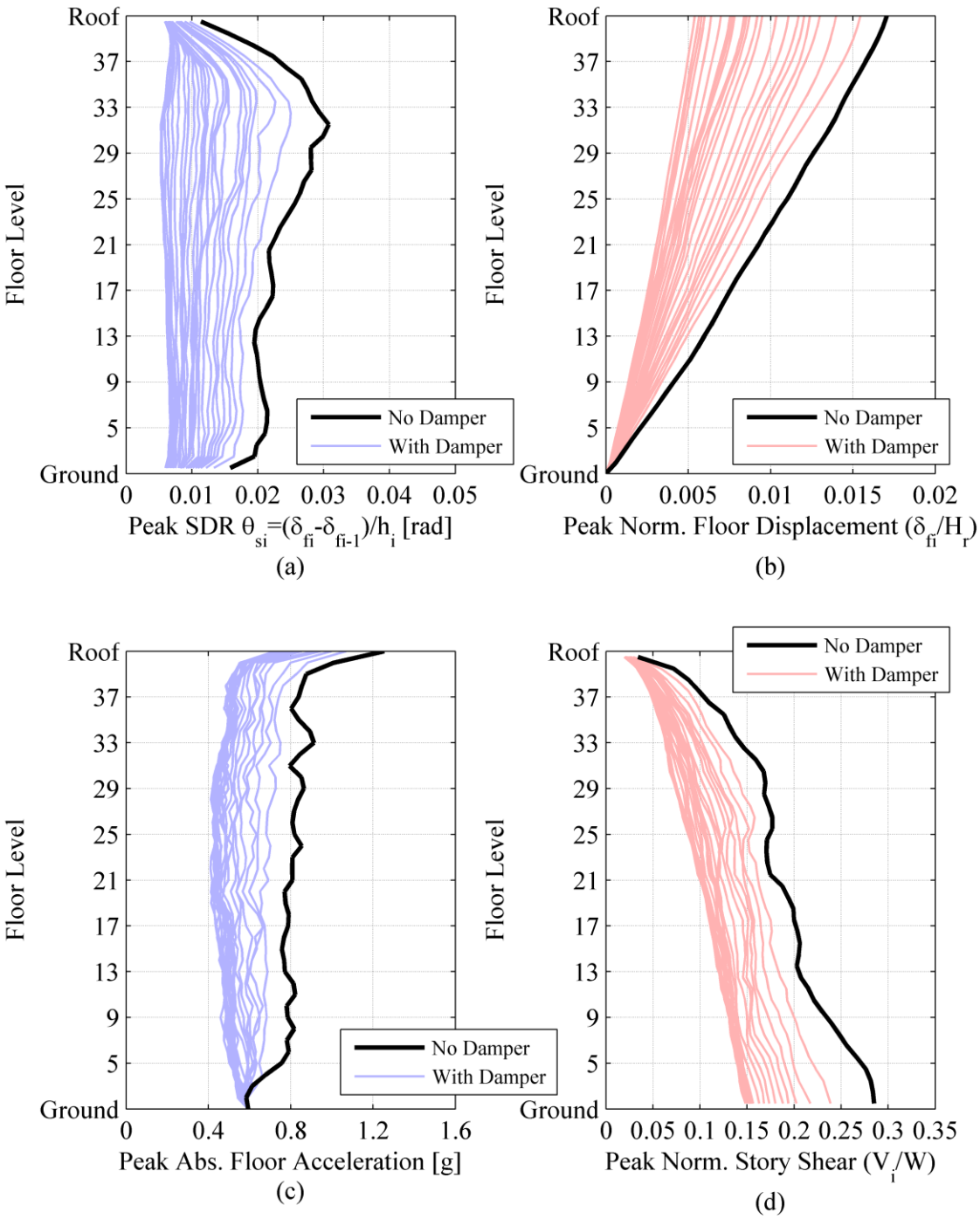

Figure 6.27: EDPs without and with dampers ($K_d''/K_f = 0.05 - 5$) - Y-loading direction - effective shear force proportional damping distribution

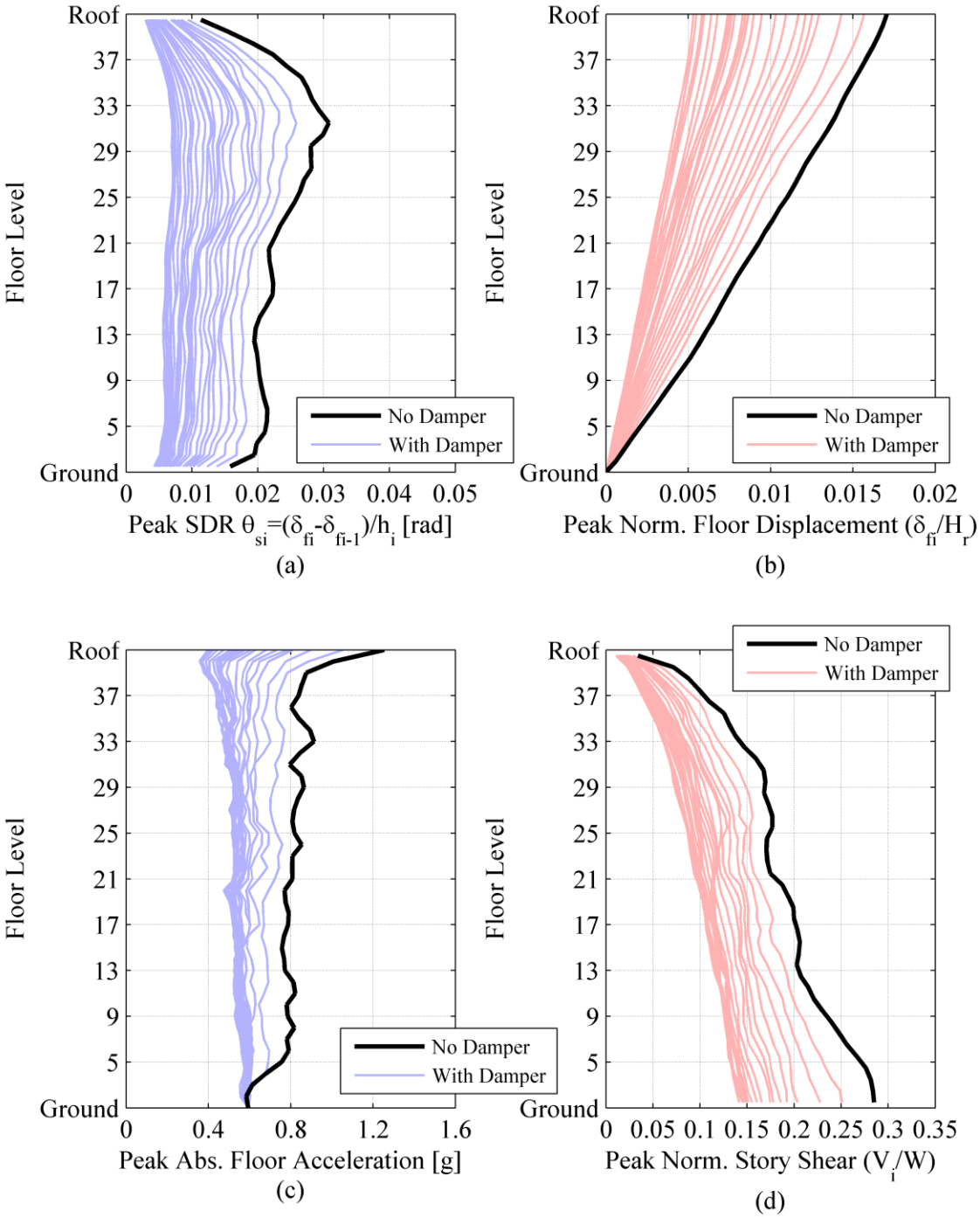

Figure 6.28: EDPs without and with dampers ($K_d''/K_f = 0.05 - 5$) - Y-loading direction - stiffness proportional damping distribution

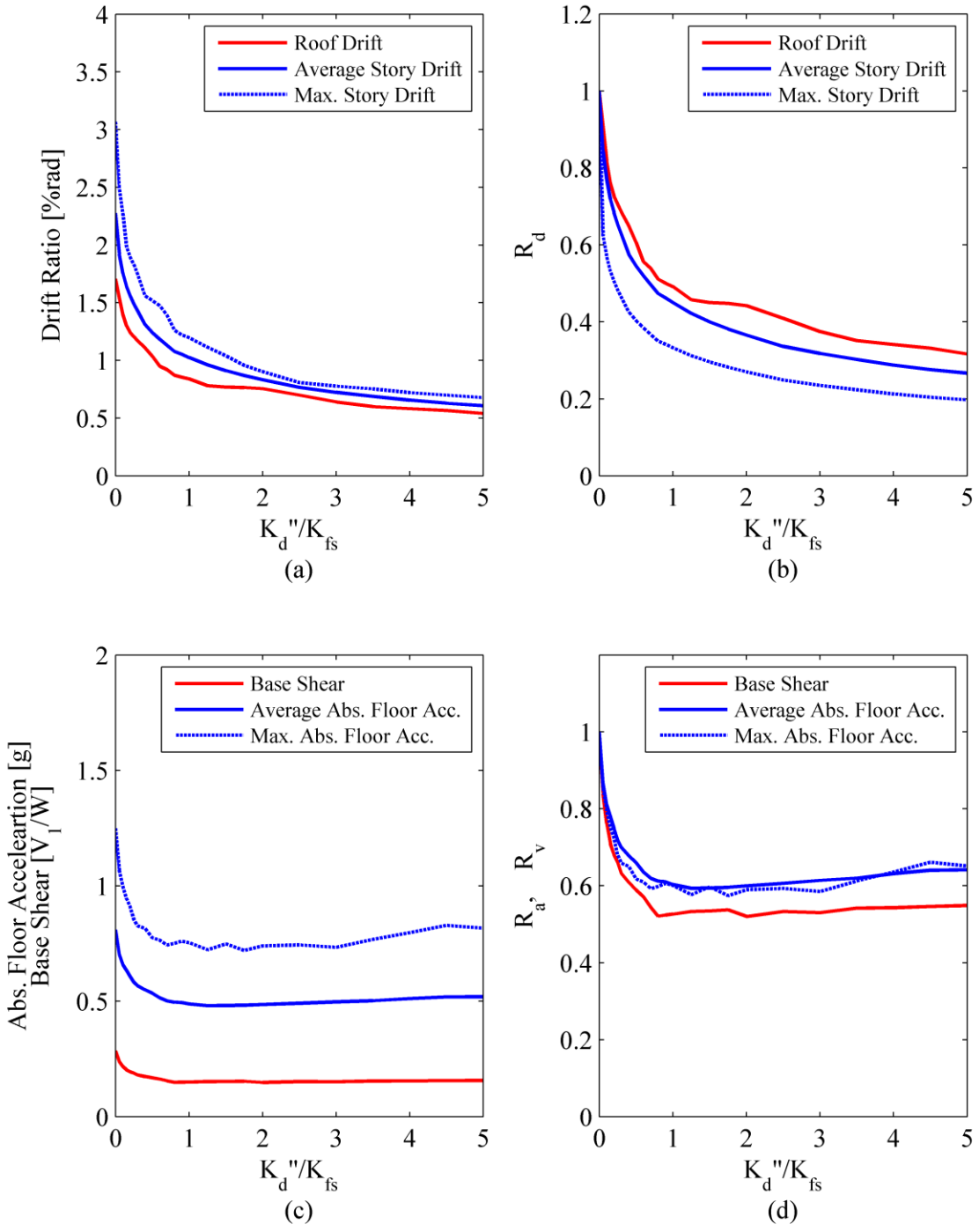

Figure 6.29: MDF performance curves of drift, absolute floor acceleration and base shear spectra - Y-loading direction - effective shear force proportional distribution

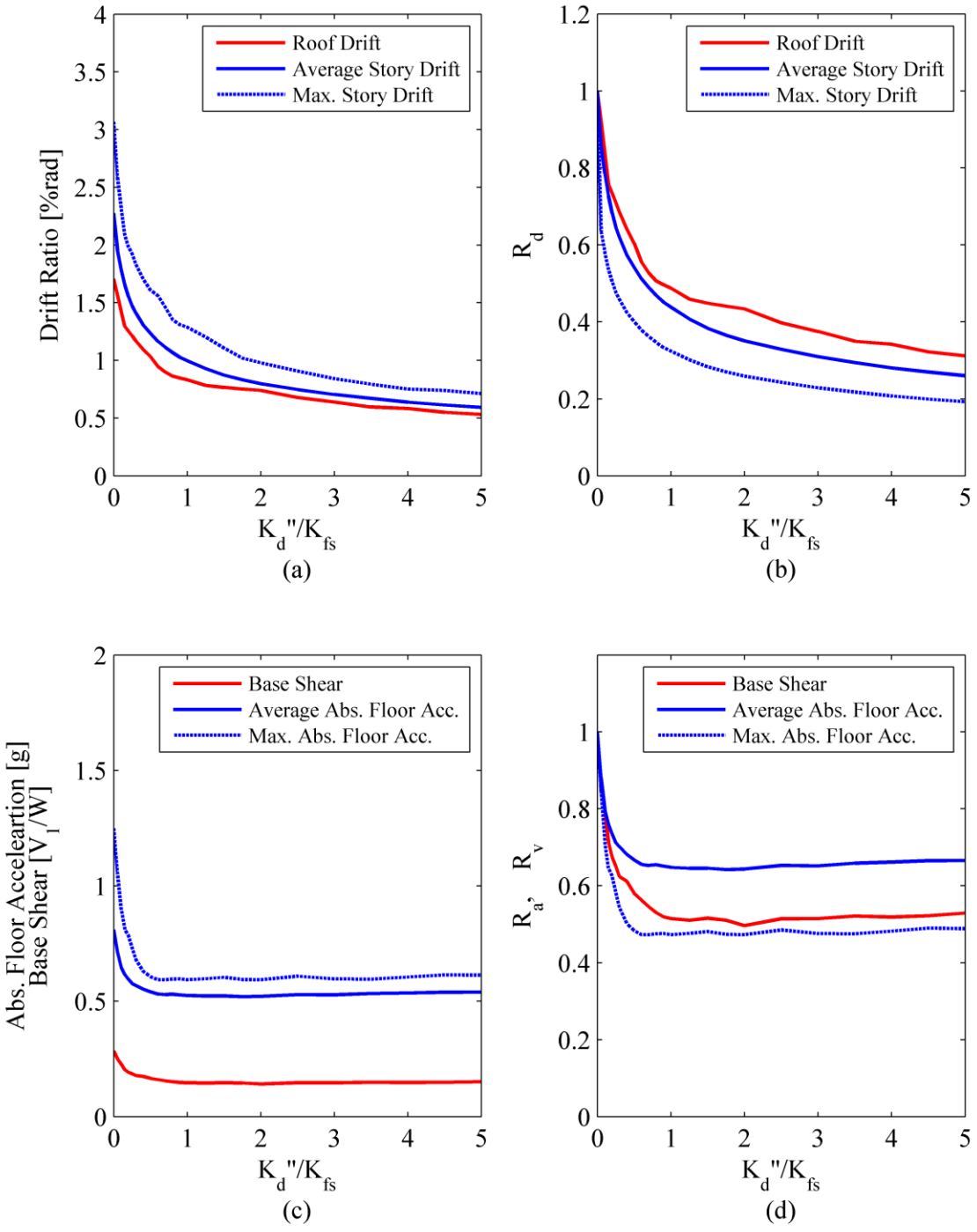

Figure 6.30: MDF performance curves of drift, absolute floor acceleration and base shear spectra - Y-loading direction – stiffness proportional distribution

CHAPTER 7 : Performance-Based Evaluation of a 1970s High-Rise Steel Frame Building

7.1 Introduction

Well-engineered tall buildings typically perform better than low- to -midrise buildings during earthquakes (Naeim and Graves 2005). Tall buildings are relatively flexible. Earthquakes generally release less energy at longer periods. On the other hand, the seismic design of tall building requires more advanced design and analysis procedures. The majority of the construction worldwide consists of low and midrise buildings. Most of the design guidelines fail to address specific issues that may arise in the design and assessment of high-rise buildings (Naeim 2010). To this end, several guidelines have been recently published (CTBUH 2008; PEER 2010; LATBSDC 2014) in order to provide rational recommendations for the performance-based seismic design and evaluation of new tall buildings.

Several existing steel tall buildings still remain in the West Coast of the US. These buildings were designed prior to 1990s (CTBUH 2016). Steel moment-resisting frames (MRFs) are the most commonly used lateral load resisting system in high-rise buildings constructed between 1960 and 1990 in seismic areas, particularly those with above 35 stories (Almufti et al. 2012), which do not meet today's basic capacity design principles. These include the strong

column/weak beam ratio, panel zone strength requirements, prequalified beam-to-column connection detailing, as well as, column splicing detailing and weld deficiencies. The 1994 Northridge and 1995 Kobe earthquakes highlighted several deficiencies associated with the beam-to-column connection performance (Bonowitz and Youssef 1995; Mahin 1998; FEMA 2000b; Nakashima et al. 2000). Past experimental studies indicated that column splices with partial joint penetration (PJP) groove welds compromise their behaviour under cyclic loading (Bruneau and Mahin 1990). Moreover, panel zone design requirements have also been revised over the past few decades (Krawinkler et al. 1975; FEMA 2000b).

Recent experimental and numerical studies (Nakashima et al. 2007; Lignos et al. 2013; Elkady and Lignos 2014) suggests that current strong column/weak beam design requirements are not sufficient to prevent soft story mechanisms at low probability of occurrence earthquakes. This is due to the additional flexural demands from the composite action and the steel material cyclic hardening.

Unlike what ASCE 41-13 (ASCE/SEI 2014) suggests, recent experimental studies (Elkady and Lignos 2016; Lignos et al. 2016; Suzuki and Lignos 2016) showed that seismically compact columns in steel frame buildings can accommodate appreciable plastic deformations without experiencing sudden loss of their axial load carrying capacity stability even under high axial loads. This is directly related to steel columns in bottom stories of tall buildings.

Several researchers studied multi-story pre-Northridge steel MRF buildings (Hall et al. 1995; Maison and Bonowitz 1999; Gupta and Krawinkler 2000; Luco and Cornell 2000; Lee and Foutch 2002; Muto and Krishnan 2011) with less than 20 stories. More recently, research studies on existing tall buildings located in the West Coast of US were conducted in order to

assess their seismic performance and explore potential seismic retrofit strategies (Bech et al. 2015; Lai et al. 2015; Hutt et al. 2016).

This chapter provides assesses the seismic performance of a prototype 40-story steel MRF building representative of the 1970s-tall building construction practice. To assess the seismic performance of the prototype building advanced nonlinear modeling techniques are utilized. The outcome of the nonlinear building assessment aims to identify the seismic deficiencies of the prototype building such that guidance for potential retrofit solutions can be provided.

7.2 Design of a 40-Story Tall Building based on UBC 1973

Tall steel buildings designed in 1970s had a redundant load-resisting system by utilizing space frames (Anderson and Bertero 1989; Bech et al. 2015; Lai et al. 2015). For instance, according to UBC 1973 (ICBO 1973) buildings in seismic regions, which were taller than 49 m (160 feet), had ductile moment-resisting space frames as part of their lateral load-resisting system.

7.2.1 Prototype Building

Figures 7.1 and 7.2 show the floor plan and elevation view of the prototype building to be used as the main case study of this thesis. The geometry of this building is fairly similar with the one studied by others (Almufti et al. 2012; Hutt et al. 2016). Referring to Figure 7.1, the lateral load-resisting system of the building consists of steel MRFs in both loading directions. The prototype building consists of 43 stories including 3 stories below the ground floor. The total height of the building is 154.7 m (507.5 ft) above the ground level as illustrated in Figure 7.2. The typical story height is 3 m (10 ft), while the story heights at the ground and basement levels are 6.1 m (20 ft) and 3.8 m (12.5 ft), respectively. The building mainly serves as office space. Two mechanical floors are located at 21st and 40th floors. The ground level is utilized as a lobby and

three basement levels are used as a parking space. A 76 mm (3 in.) thick concrete slab on 63.5 mm (2.5 in) metal deck supported by steel beams forms the floor system at each level. The superimposed dead loads and unreduced live loads for typical office floors are assumed to be 1.9 KPa (40psf) and 2.7 KPa (56 psf), respectively. For design purposes, a three dimensional model of the prototype building was constructed in the *ETABS* software (CSI v. 9.7.4). According to the Tall Building Initiative (TBI) (PEER 2010) the total effective seismic weight, W, was computed as the summation of the dead and expected live load,

$$W = D + L_{\text{exp}} \tag{7.1}$$

in which, L_{exp} is the 25% of the unreduced live load. The total seismic effective weight of the building above the ground level was found to be 288 MN (64700 kips). The computation of the lateral design forces (wind and earthquake) and the steel design are summarized below.

7.2.2 Computation of Lateral Loads and Drift Limitation per UBC 1973

Wind Load

UBC 1973 provides wind pressures based on the geographical region and the height zone. Figure 4 of UBC 1973 indicates the wind pressure map of the US, which is categorized into 7 areas ranging from 0.96-2.39 KPa (20-50 psf) at 9.1 m (30 ft) height above the ground; Table 23 F of the same design code provides wind pressure values for various height zones corresponding to the 7 wind-pressure areas. According to this map, the reference wind pressure in the West Coast is 0.96 and 1.20 KPa (20-25 psf) for the southern and northern regions of the Bay Area, respectively. The dominant wind pressure reference level was 0.96 KPa (20 psf) across California (SEAOSC 2010). Therefore, the wind design loads were considered to satisfy 0.96 KPa (20 psf) wind pressure level. According to UBC 1973 the horizontal wind pressure shall be applied to the area of the vertical projection of that of the building. Using 0.96 KPa

(20 psf) as a reference wind pressure level at 9.1 m (30 ft) height, the wind pressure varies between 0.72 to 1.68 KPa (15 to 35 psf) along the height of the building. Thus, the wind base shear was found as $V/W = 0.027$ and 0.018 in the X- and Y- loading directions, respectively.

Earthquake Load

According to UBC 1973 the seismic design is based on the equivalent static force procedure. The seismic base shear V is computed as follows,

$$V = ZKCW \tag{7.2}$$

in which, Z is a numerical coefficient dependent upon the zone number taken from the seismic map. The prototype building was designed in Zone 3. In this case, $Z = 1.0$; For steel MRFs, $K = 0.67$; C is a coefficient, which is computed as follows,

$$C = \frac{0.05}{\sqrt[3]{T}} <= 0.1 \tag{7.3}$$

In which, T is the fundamental period of the building in the direction under consideration. For MRFs T=0.1N; N is the number of stories above the ground. Thus, the fundamental period of the building in both directions is 4.0 sec based on the empirical period formulation; the total seismic force coefficient, $V/W = 0.021$. The seismic lateral force shall be distributed to the floors proportional to the floor height and associated mass; a portion of the V shall be applied at the top of the building, which shall not exceed 0.15V.

Figures 7.3a and 7.3b compare the design shear force due to wind and earthquake along the height of the building for the X and Y-loading directions. In the X-direction, the wind base shear is about 1.6 times larger than the base shear induced by seismic loading, while in the Y-direction they are almost equal. Notably, in the X-loading direction the seismic load governs in upper stories. However, the wind shear governs the design of the lower stories.

In today's standards (ASCE 2010), the dynamic analysis becomes mandatory for buildings taller than 49 m (160 ft). The earthquake loads are based on rigorous probabilistic seismic hazard assessment and response spectra are provided for each location by considering soil properties of the building location. In addition to the design base shear that is obtained from the design spectrum, a minimum design base shear requirement is set to address uncertainties in spectral demands at longer periods, which generally controls the seismic design base shear for long period structures in seismic regions. Moreover, story drift limits are provided for different type of structures which depends on the risk category of the building to be designed.

Drift Limits

According to Section 2314 (f) of the UBC 1973 "*lateral deflections or drift of a story relative to its adjacent stories shall be considered in accordance with accepted engineering practice*". In order to clarify the accepted design practice, the Los Angeles Building Department had issued a memorandum in consultation of several practicing engineers. According to this document, the allowable story drift ratio under wind and earthquake loads was limited to 0.25% to 0.5%, respectively (Johnston 1972). Figures 4c and 4d illustrate the drift profiles based on design wind and earthquake loading.

7.2.3 Steel Design per UBC 1973

The use of welded box section with width sizes ranging from 508 to 660 mm (20 to 26 inches) and thickness up to 102 mm (4 inches) was common for steel columns in existing pre-Northridge high-rise buildings (Anderson and Bertero 1989; Bech et al. 2015; Lai et al. 2015). Beams were typically made of wide flange sections (W-sections) made of ASTM A36 [i.e., nominal yield stress, F_y=248 MPa (36 ksi)] steel; box columns were typically made of ASTM A36 and/or ASTM A572 Gr. 42 [i.e., nominal yield stress, F_y=290 MPa (42 ksi)] steel. Table 1 summarizes

the section sizes of beams and columns of the prototype building. Beams and columns were made of ASTM A36 and ASTM A572 Gr. 42 steel, respectively. Columns were spliced every three stories. The column splice was placed at 1.2 m (4 ft) above the respective floor. Partial joint penetration groove welds were considered for the column splices to reflect the design practice of the time of construction (Bruneau and Mahin 1990).

In early 1970s the steel design was based on allowable stress design (ASD) (AISC 1969). Unfactored load combinations were typically used. The allowable stresses were permitted to be increased by one-third when considering the wind or earthquake loading either acting alone or when combined with vertical loads. According to UBC 1973, members subjected to both axial compression and bending stress (i.e., beam-columns) with axial stress ratio $f_a / F_a > 0.15$, shall meet the following requirement,

$$\frac{f_a}{F_a} + \frac{C_{mx} f_{bx}}{\left(1 - \frac{f_a}{F'_{ex}}\right) F_{bx}} + \frac{C_{my} f_{by}}{\left(1 - \frac{f_a}{F'_{ey}}\right) F_{by}} \leq 1.0 \tag{7.4}$$

in which, f_a is the computed stress due to axial load only; f_{bx} and f_{by} is the computed bending stresses at the extreme fibers with respect to the major and minor bending axis of the respective cross-section, respectively; F_a is the allowable axial stress permitted in the absence of bending stress. In case of axial tensile stress, $F_a = 0.60F_y$, where F_y is the specified minimum yield strength of the type of steel being used. For Gr.42 steel, $F_y = 290$ MPa (42 ksi). For compressive stress the allowable stress depends on the global slenderness of the member; F_{bx} and F_{by} are the allowable bending stresses in the absence of axial stress, which are taken as $0.66F_y$ for compact cross-sections; C_{mx} and C_{my} are coefficients applied to the bending term dependent upon the column curvature caused by the applied moments. For compression members in sidesway frames, $C_m = 0.85$; F'_{ex} and F'_{ey} are the Euler stresses with respect to the major and minor

bending axis divided by a factor of safety. As part of beam and column member design, live loads can be reduced; however, this reduction shall not exceed 40% and 60% of the unreduced live load for beams and columns, respectively.

It is important to note that the prototype building design was mainly governed by the drift limitation due to the wind load, particularly in the X-loading direction (see Figure 7.3). This was more critical for the bottom stories of the building; while in upper stories beams were sized according to their flexural strength to satisfy the seismic loading requirements. This led to appreciable over-strength in the lower stories, where stress ratios in this case were generally below 70%.

7.2.4 Strong Column/Weak Beam Check

Capacity design was not fully adopted in UBC 1973. Therefore, it is useful to identify potential seismic deficiencies of the building by checking today's capacity design requirements. To this end, the SCWB check is carried out using LRFD approach in accordance with AISC 341-10 (AISC 2010b),

$$\frac{\sum M^*_{pc}}{\sum M^*_{pb}} > 1 \tag{7.5}$$

in which, M^*_{pb} is the moment at the intersection of the beam and column centerlines determined by projecting the beam maximum developed moments from the column face (Eq. 7.6), while M^*_{pc} is the moment at the beam and column centerline determined by projecting the sum of the nominal column plastic moment strength, reduced by the axial load P_{uc} from the top and bottom of the beam-to-column moment connection as given in Equation 7.7,

$$M^*_{pb} = 1.1 R_y F_{yb} Z_b + M_{uv} \tag{7.6}$$

$$M_{pc}^{*} = \left(1 - \frac{P_{uc}}{P_{yc}}\right) Z_c F_{yc} \tag{7.7}$$

in which, $R_y F_{yb}$ and F_{yc} are the expected material yield strength of beams and nominal material yield strength of columns, respectively. According to Tables 9-1 and 9-3 of the ASCE 41-13 (ASCE/SEI 2014) modeling recommendations, the expected material yield stress for A36 steel material between 1961-1990 Group 1 is assumed to be $R_y F_{yb} = 334$ MPa (48.4 ksi), while columns are fabricated from Grade 42 steel; therefore, the nominal yield strength of this material is, $F_{yc} = 290$ MPa (42 ksi); P_{yc} is the nominal axial yield strength of the column member; Z_b and Z_c are the plastic section modulus of the beam and column, respectively; M_{uv} is the additional moment due to the shear amplification from the location of the plastic hinge to the column centerline.

For simplicity, the column axial load due to vertical loads $P_{uc}^{G+E_v}$ and lateral earthquake load $P_{uc}^{E_h}$ is computed separately. Thus, the maximum $P_{uc}^{G+E_v}/P_{yc} = 0.48$. Because beam cross-sections are uniform at each level; the resultant axial force on interior columns due to the formation of a beam mechanism is expected to be minimal. On the other hand, very high axial load demands (i.e. $P_{uc}^{E_h} / P_{yc} > 1$) can be generated in exterior columns, such as in C1 and C3 (see Figure 7.1) columns due to the formation of a beam mechanism in the X-loading direction. However, it is unlikely that all beams simultaneously develop a mechanism at each level during a seismic excitation. Therefore, this assumption is very conservative, especially for the bottom story columns of the prototype building. Moreover, in MRFs with pre-Northridge beam-to-column connections, deep beams (i.e., W36) may experience premature fracture at relative low rotational demands prior to reaching their plastic moment capacity. This should further reduce the axial force demands on the exterior columns. Therefore, a 50% reduction is applied on the computed

$P_{uc}^{E_h} / P_{yc}$ ratio when calculating the SCWB ratio in exterior beam-to-column joints. Despite of the 50% reduction of axial load demands on exterior columns, the frames in the X-direction (C1 and C3 columns) are found to have very low SCWB ratios. This suggests that exterior column moment capacities may be inevitably exceeded under low probability of occurrence earthquakes due to high axial load demands.

7.3 Nonlinear Building Model of the Prototype Tall Building

The prototype tall building discussed previously is in a high risk category (i.e., Category III). It also contains several seismic deficiencies in its members and connections. Because of the number of stories, basic evaluation procedures are limited. Therefore, Tier 3 systemic evaluation of the building is required as per ASCE 41-13 (ASCE/SEI 2014). Therefore, the seismic performance evaluation of the prototype building is conducted through rigorous nonlinear response history analysis (NRHA). Nevertheless, a nonlinear static procedure is also conducted to (a) identify basic yielding mechanisms; and (b) assess the influence of different modeling assumptions on the building performance in the nonlinear regime.

In order to evaluate the building performance via nonlinear static and dynamic analyses, two-dimensional (2D) nonlinear building models in the X- and Y-loading direction are developed in the *OpenSees* simulation platform (McKenna 1997). Due to the symmetry and the odd number of the lateral load resisting frame systems in the X-loading direction (see Figure 7.1) two frames (1-1 and 3-3) with a leaning column are assumed to be representative of the building in X-loading direction, while in Y-loading direction all 5 frames are explicitly modeled. Soil-structure interaction is not considered, hence the floors at and below the ground level are assumed to be restrained in the horizontal loading direction. A rigid diaphragm action is considered at each

floor. Geometric nonlinearities are considered with the P-Delta transformation. Figure 7.4 illustrates the modeling assumptions for a typical frame bay and story. The details regarding the beam, column and panel zone modeling are described in detail below.

7.3.1 Nonlinear Modeling of Steel Beams

Beams are modeled using an elastic beam-column element with concentrated plasticity spring elements at their ends as shown in Figure 7.4. The elastic flexural stiffness of the concentrated plasticity spring elements $K_{el,bsp}$ is computed as follows,

$$K_{el,bsp} = n\frac{6EI_{b,\mathrm{mod}}}{L_b}, \quad I_{b,\mathrm{mod}} = \frac{n+1}{n} I_b \tag{7.8}$$

in which, n is a factor used to adjust the initial stiffness of the backbone curve, which in theory should be infinite, but taken as $n = 10$ in order to avoid convergence problems during the analysis (Ibarra and Krawinkler 2005; Zareian and Krawinkler 2006). The modulus of elasticity of the steel material E is assumed to be 200GPa (29000ksi). To compensate the additional elastic flexibility of the rotational spring elements, the strong axis moment of inertia of the beams, I_b, is modified as shown in Equation (7.8); $I_{b,mod}$ is the modified moment of inertia of the elastic beam-column element (Zareian and Krawinkler 2006); L_b is taken as the clear beam length in accordance with Section 8.7 of AISC-358-10 (AISC 2010a).

Steel MRF building inspections and experimental studies on steel beams as part of welded unreinforced flange (WUF) beam-to-column connections after the 1994 Northridge earthquake revealed that the expected hysteretic behaviour of such connections is brittle. Past numerical studies (Maison and Bonowitz 1999; Luco and Cornell 2000; Lee and Foutch 2002) that focused on steel MRF buildings with low redundancy (e.g. perimeter MRFs) assumed that the behaviour of all their beam-to-column connections was brittle. Therefore, the phenomenological beam

spring models were considered to undergo through sudden loss of flexural strength. Such a modeling assumption is fairly conservative considering that several steel beams exhibited a ductile behaviour and gradual strength deterioration due to local buckling (Popov and Stephen 1970; Youssef et al. 1995). The FEMA-355D (FEMA 2000b) states that a better performance was observed in buildings built in 1970s than those in the late 1980s and early 1990s. Steel buildings from 1970s were highly redundant and almost all frames were designed to be part of the lateral load resisting system. As a consequence, beam depths were relatively smaller than those in typical perimeter steel MRFs. Beam tests (Popov and Stephen 1970) with smaller depths showed a relatively ductile performance. According to the design practice in mid 1980s, the inelastic shear deformation in beam-to-column web panel-zones was permitted. This resulted in increased local stress and strain demands near the flange welds.

In brief, three modeling cases are considered and analysed regarding the moment-rotation relation of steel beams on the global building response. The first case, is called 'brittle'. The properties of all the beams are based on typical pre-Northridge beam-to-column connections. In the second case (so called 'ductile'), we utilized the moment-rotation relation of typical non-RBS beams as part of fully-restrained beam-to-column connections as discussed in Lignos and Krawinkler (2011). Finally, the third case, which is considered as the base-case model in this thesis, assumes that only 25% of the beam-to-column connections is ductile and the rest is brittle. This agrees with prior studies regarding the seismic behaviour of existing tall buildings (Muto and Krishnan (2011). The ductile beam-to-column connection locations are randomly distributed for the X- and Y-loading directions, respectively. To simulate a typical beam as part of a pre-Northridge beam-to-column connection, the nonlinear backbone curve parameters of the respective springs are obtained from Hartloper (2016) and ASCE 41-13 (ASCE/SEI 2014). In

particular, the effective yield moment $M^*_{y,b}$, the capping moment strength $M_{cap,b}$ and the residual moment strength $M_{r,b}$ of the respective steel beam are computed as follows,

$$M^*_{y,b} = S_b F_{ye,b}, \quad M_{cap,b} = 1.1 Z_b F_{ye,b}, \quad M_{r,b} = 0.2 M^*_{y,b} \tag{7.9}$$

in which, S_b is the elastic section modulus of the steel beam with respect to its strong axis. According to Tables 9-1 and 9-3 in ASCE 41-13 (ASCE/SEI 2014) the expected material yield stress of the steel beams (A36 between 1961-1990 Group 1) is, $F_{ye,b}$ = 334 MPa (48.4 ksi). The pre-capping plastic rotation, $\theta_{cap,pl}$, post-capping rotation, θ_{pc} and ultimate rotation, θ_u are computed as discussed in Hartloper (2016),

$$\theta_{cap,pl} = \begin{cases} 0.046 - 0.0013 d_b, & \text{if } d_b < 24\text{" and } F_{y,b}/F_{t,b} < 0.6 \\ 0.008, & \text{if } d_b \geq 24\text{" or } F_{y,b}/F_{t,b} \geq 0.6 \end{cases} \tag{7.10}$$

$$\theta_{pc} = \begin{cases} -0.003 - 0.0007 d_b, & \text{if } d_b < 24\text{" and } F_{y,b}/F_{t,b} < 0.6 \\ 0.035 - 0.0006 d_b, & \text{if } d_b \geq 24\text{" or } F_{y,b}/F_{t,b} \geq 0.6 \end{cases} \tag{7.11}$$

$$\theta_u = \begin{cases} 0.05, & \text{if } d_b < 24\text{" and } F_{y,b}/F_{t,b} < 0.6 \\ 0.035, & \text{if } d_b \geq 24\text{" or } F_{y,b}/F_{t,b} \geq 0.6 \end{cases} \tag{7.12}$$

in which, $F_{y,b}$ and $F_{y,t}$ are the nominal yield and tensile stresses of the steel material. Based on Table 9-1 of the ASCE 41-13 (ASCE/SEI 2014), $F_{y,b}$ = 303 MPa (44 ksi) and $F_{y,t}$ = 427 MPa (62 ksi), thus $F_{y,b}$ / $F_{y,t}$ > 0.6. Note that θ_{pc} is very low in comparison to the expected value of a typical post-Northridge beam-to-column connection (Lignos and Krawinkler 2011; 2013).

The modeling parameters for beams as part of ductile beam-to-column connections are based on the modeling recommendations proposed by Lignos and Krawinkler (2011). The effective yield moment, the capping moment strength $M_{cap,b}$ and residual moment strength of $M_{r,b}$ in this case are computed as follows,

$$M^*_{y,b} = 1.1 Z_b F_{ye,b}, \quad M_{cap,b} = 1.1 M^*_{y,b}, \quad M_{r,b} = 0.4 M^*_{y,b} \tag{7.13}$$

The associated plastic deformation capacities of non-RBS connections can be found in Lignos and Krawinkler (2011).

Figure 7.5 shows the moment-rotation relations for a ductile and a brittle case. The former is modelled with the *Bilin* material model in *OpenSees* (see Figure 7.5a). The latter is modelled with the *Hysteretic* material model combined with the *MinMax* material to simulate the loss of strength once the ultimate rotation capacity is attained (see Figure 7.5b).

7.3.2 Steel Column Modelling

Box columns are modeled with single force-based distributed plasticity beam-column elements as shown in Figure 7.4. If a column splice connection exists, the columns are modeled with two elements connected at 1.2 m (4 ft) above the lower floor level. For each element five integration points are considered. The steel cross sections are discretized with 50 fibers (5 fibers for the flange and 20 fibers for the web) in parallel to the axis of bending. The Giuffré-Menegotto-Pinto (Menegotto and Pinto 1973) steel material model is assigned at each fiber element to capture material yielding and cyclic hardening. According to Tables 9-1 and 9-3 of the ASCE 41-13 (ASCE/SEI 2014), the expected material yield stress of the columns is assumed to be 1.1 times the nominal yield stress, $F_{ye,c}$ = 319 MPa (46.2 ksi). The strain hardening ratio is taken as 2% (Lignos and Krawinkler 2011). Column splices are not explicitly modeled. Nevertheless, similarly with the methodology proposed by Galasso et al. (2015) we recorded the stress-strain history of the extreme fibers of the cross-section above the column splice (i.e., smaller cross-section) to assess possible splice failures due to premature fracture.

7.3.3 Modeling of Panel Zones

The beam-to-column web panel zone shear deformation is explicitly modeled in the 2D model representations of the prototype building. A trilinear shear force-shear distortion model is

considered in this case as proposed by Krawinkler (1978). This is shown in Figure 7.4. Thus, the yield shear strength $V_{y,pz}$, elastic stiffness $K_{el,pz}$ and plastic stiffness $K_{pl,pz}$ of a panel zone is computed as follows,

$$V_{y,pz} = 0.55F_{ye,c}d_c t_p, \quad K_{el,pz} = 0.95Gd_c t_p, \quad K_{pl,pz} = 0.95Gb_{fc}t_{fc}^2 / d_b \tag{7.14}$$

in which, d_c, b_{fc} and t_{fc} are the depth, the flange width and flange thickness of the steel column, respectively; t_p is the panel zone thickness, which in case of a hollow square box section with equal flange and web thickness, $t_p = 2t_{fc}$; G is the shear modulus of steel material. The shear distortion at yielding γ_y, at plastic γ_{pl} and ultimate γ_r are computed as follows,

$$\gamma_y = V_{y,pz} / K_{el,pz}, \quad \gamma_{pl} = 4\gamma_y, \quad \gamma_r = 100\gamma_y \tag{7.15}$$

Using the above equations we can obtain the effective yield moment $M^*_{y,pz}$, plastic moment $M_{pl,pz}$, and ultimate moment $M_{r,pz}$ to simulate the panel zone inelastic behaviour, if any,

$$\begin{aligned} M^*_{y,pz} &= V_{y,pz}d_b, \\ M_{pl,pz} &= M^*_{y,pz} + K_{pl,pz}d_b\left(\gamma_{pl} - \gamma_y\right), \\ M_{r,pz} &= M_{pl,pz} + \alpha_s K_{el,pz}d_b\left(\gamma_r - \gamma_{pl}\right) \end{aligned} \tag{7.16}$$

in which, α_s is the post-capping strain hardening ratio (Elkady and Lignos 2014; 2015).

7.4 Seismic Performance Assessment of the Prototype Tall Building

7.4.1 Gravity and Eigenvalue Analysis

Gravity analysis is carried out under the load combination of dead loads and 25% of the unreduced live loads (i.e., D+0.25L). The analysis results obtained from 3D *ETABS* model are utilized to compute the distributed and point gravity loads on beams and columns. These loads are assigned to the 2D nonlinear building models in *OpenSees*. The peak gravity load ratio with respect to the expected yield strength of the columns ($P_{c,G} / P_{ye,c}$) for the 2D steel MRFs in the X

and Y-loading directions, respectively, are 31% and 34% at the same column in 9th story. The $P_{c,G} / P_{ye,c}$ ratio of the same column was 32% based on the 3D *ETABS* model. For all practical purposes, the peak $P_{c,G} / P_{ye,c}$ ratios are the same for the 2D and 3D models. The peak $P_{c,G} / P_{ye,c}$ ratio is comparable with a recent study by Bech et al. (2015) on an existing 38-story steel frame building designed in early 1970s, in which the peak $P_{c,G} / P_{y,ec} = 37\%$ (i.e. $P_{c,G} / P_{y,c} = 0.41$).

The eigenvalue analysis is conducted after the gravity load application. Based on the *OpenSees* model, the fundamental translational period in the X- and Y-loading directions are found to be 5.29 and 5.25 sec, respectively. The corresponding fundamental period based on the 3D *ETABS* model is 5.8 sec. The difference in the computed periods between the 2D and 3D models is attributed to the consideration of the panel zone in the 2D model and to the shear deformations that are neglected in the 2D model. According to the 2D model, the first five vibration periods of higher modes are 1.82, 1.01, 0.71, 0.53, 0.42 sec and 1.91, 1.08, 0.77, 0.57, 0.47 sec in the X- and Y-loading directions, respectively. The first modal mass participating ratio are found to be 69% and 74% of the total mass of the floors above the ground level. The second mode attracted 17% and 14% of the total modal mass in the X and Y-loading directions, respectively.

7.4.2 Nonlinear Static (Pushover) Analysis

A conventional nonlinear static procedure (so-called pushover analysis) alone cannot be considered as a reliable evaluation method in cases that higher modes effect are significant (Krawinkler and Seneviratna 1998). Nevertheless, pushover analysis is carried out in both loading directions based on the first mode lateral load pattern per loading direction to provide insight on the building behaviour under lateral loading. Figures 7.6 and 7.7 show the pushover curves and the peak story drift ratios (SDR) obtained from “ductile”, “25% ductile” and “brittle” modeling cases for the steel MRFs in the X- and Y-loading directions, respectively.

Characteristic points, such as initial yielding, capping and collapse (i.e., green, red and black dots, respectively) are superimposed in the same figures. Notably, for the "brittle" and the "25% ductile" cases, yielding of the first beam initiates at a base shear force of $0.06W$ at about 0.5-0.6% roof drift in both loading directions. The peak base shear is around $0.09W$ for the two aforementioned cases. Up to this point, the peak SDRs along the building height are less than 2%. The steel MRFs become unstable at around 1.3% and 1.1% roof drift ratios in the X- and Y-loading directions, respectively. In the X-loading direction the structural damage is evident between stories 9 to 20, whereas in the Y-loading direction a story collapse mechanism forms in between stories 5 to 13. Referring to Figures 7.6 and 7.7, once the beam end rotation exceeds the capping rotation, steel MRFs in both loading directions experience a sudden strength loss. This is likely to cause numerical convergence issues for both the "brittle" and "25% ductile" cases. To illustrate the post-capping behaviour of the steel MRFs and overcome the convergence issues for the two aforementioned cases, the beam post-capping and ultimate rotation capacities were slightly increased; thus, the obtained pushover curves after the post-capping strength are shown with a dashed line. On the other hand, for the "ductile" case, the pushover analysis converges till lateral instability is attained. In this case, the assumption of ductile beams results to an increase in the global strength capacity and the associated roof drift that capping occurs. Referring to Figures 7.6b and 7.7b, both 2D models are able to accommodate peak SDRs up to 2.5% prior to the initiation of strength deterioration.

7.4.3 Nonlinear Response History Analysis

According to Tier 3 procedure as per ASCE 41-13 (ASCE/SEI 2014), the evaluation of existing buildings should be carried out for the BSE-1E and BSE-2E hazard levels, which have a probability of exceedance of 20% and 5% in 50 years (i.e. 225 and 975 years mean return

periods), respectively. The prototype building is assumed to be located at 37.7897°N, 122.4003°E; the corresponding soil type at the design location of interest based on the NEHRP soil classification is D. This can be obtained from the interactive database map available from the United States Geological Survey (USGS). Figures 7.8a and 7.8b show the 5% damped response spectra for BSE-1E and BSE-2E hazard levels, respectively.

Ground motion selection

The ground motion selection is carried out based on NIST (2010b). The ASCE 7-10 (ASCE 2010) provisions recommend using minimum 7 accelerogram sets to reliably estimate the mean engineering demand parameters of a building. Similarly, the TBI suggests a larger set of ground motions (20 to 30) if the intent of the analysis is to characterize the associated response dispersion. To fulfill both objectives we select 40 ground motions as part of this thesis (see in Appendix A, Table A3). The NGA-West2 ground motion database (Ancheta et al. 2014) is utilized for this purpose. The ground motions are selected to be representative of the data obtained from site specific hazard disaggregation. According to disaggregation data at a period of 5 secs, the main controlling hazard source is the San Andreas Fault. This is a strike-slip fault, which is located 15 km West from the building location. The selected ground motions are from 15 different seismic events. At most 6 records are selected from the same seismic event. The selected ground motions are generated by earthquakes having moment magnitudes between 6.2 and 7.62. The fault mechanisms of the selected earthquakes are mainly strike-slip, with the exception of Chi-Chi earthquake with M_w=7.62. The Jan Boyner and rupture distances of the selected ground motions vary from 10 km to 49 km, with a median value of 19 km. Because the site is not located within 5 km of an active fault, no specific measure is taken to consider near fault and directivity effects. The average shear wave velocity of top 30 meters V_{s30} of the site,

where ground motion are recorded, is between 180-450 m/s. A median shear wave velocity of 245 m/s, approximately represents the shear valve velocity interval of D-type soil. In the context of this thesis we utilize magnitude scaling only. The ground motions are selected such that, the maximum scale factor to be applied for the BSE-2E level should be less than 5.0 for the 2D nonlinear response history analysis. This is done because the larger the scale factor is the less realistic the ground motion becomes (Luco et al. 2012). The mean value of scale factors to be used at BSE-2E and BSE-1E levels are 3.1 and 2.0, respectively. Ground motion records are scaled such that the mean spectral ordinate of the 5%-damped response spectrum is not less than that of the 5%-damped target spectrum over a period range from $0.2T_n$ to $1.5T_n$; in which T_n is the fundamental period of in the respective loading direction in accordance with ASCE (2010). Figures 7.8a and 7.8b show the response spectra of the selected and scaled ground motion records including their mean spectra. In the same figures the target spectra at BSE-2E and BSE-1E levels is superimposed for comparison purposes.

Numerical Simulation Assumptions

Nonlinear response history analysis (NRHA) is carried out with the 2D building models in both loading directions by utilizing the selected and scaled ground motion records. In order to consider the inherent damping of the tall building, the Rayleigh damping model is implemented based on the first and sixth translational modes of the 2D models in the loading direction of interest. The critical damping ratio is assumed to be 1.5% for both modes as suggested in PEER/ATC (2010) recommendations (i.e., Equation 2-10, $\alpha/N=60/40$). The time integration of the equations of motion is conducted with the Newmark average acceleration method (Newmark 1959). Adaptive time-step as well as different solution algorithms are employed to overcome numerical convergence issues. In brief, the analysis is carried out initially with the Newton-

Raphson algorithm. If convergence is not achieved, an accelerated Newton algorithm based on Krylov subspaces is applied, which has superior numerical performance than Newton-Raphson (Scott and Fenves 2010). Story drift ratios are tracked during NRHA and the analysis is terminated if one or more stories exceeds a story drift ratio of more than 15%. This has been successfully employed in prior studies associated with the earthquake-induced collapse assessment of steel frame buildings (Lignos and Karamanci 2013; Elkady and Lignos 2014; Elkady and Lignos 2015).

Building Seismic Response

Figures 7.9 to 7.12 show the peak SDRs, peak normalized story shear forces, the maximum absolute floor accelerations and the peak normalized floor displacements obtained from each NRHA under the BSE-1E and BSE-2E levels. Superimposed in the same figure are the median and 16th and 84th percentiles of the story-based EDPs. Referring to Figure 7.10a, upper story collapse mechanisms form in the building. These collapse mechanisms are not captured based on a first-model pushover analysis. In 6 other cases, the bottom story collapse mechanisms form as shown in Figure 7.10a and 7.10d. The upper story collapse mechanisms are attributed to two factors: the first one is associated with the high axial deformation of columns and shorter frame dimensions; the flexural frame deformation is significantly larger in the X-loading direction than that in the Y-loading direction. This causes relatively high story drift ratios in the upper stories, which can amplify the P-Delta effects. Referring to Figure 7.3a, the second factor has to do with the wind design shear force that becomes the governing loading case in the lower stories. The steel MRF is overdesigned for the seismic action in comparison to the upper stories in which the seismic design force is indeed the controlling loading case. Referring to Figures 7.10b and 7.11b, the median base shear is around $0.11W$ in both loading directions at the BSE-2E level. The

median maximum absolute floor accelerations along the height of the building is nearly uniform and around 0.4 and 0.6g at BSE-1E and BSE-2E levels, respectively.

Figures 7.13a and 7.14b illustrate the histograms of the peak SDRs; those of residual SDRs are shown in Figures 7.13b and 7.14b for the X- and Y-loading directions, respectively. From these figures, at the BSE-2E level, the building collapses in 29 and 13 ground motions out of 40 in the X- and Y-loading directions, respectively. At the BSE-1E seismic intensity, the number of collapses is reduced to 5 in the X-loading direction. No collapses are observed in the Y-loading direction. Referring to Figure 7.13a, the prototype building in X-loading direction does not accommodate a SDR larger than 5% at the BSE-2E level; at the BSE-1E level, the building reaches SDRs up to 5%-6.6% SDR without experiencing collapse only in 5 cases. At these SDR range, the restoring forces cannot not prevent structural collapse due to P-Delta effects. The same building performs better in the Y-loading direction. In particular, it is able to accommodate peak SDRs up to 8% without experiencing dynamic instability. Figures 7.15 and 7.16 show the residual SDRs for the non-collapsed cases in both X- and Y-loading directions, respectively. From Figure 7.15, if the building does not collapse it does not develop large residual deformations in its bottom stories in the X-loading direction. However, due to beam premature fractures the same building experiences large residual deformations in its upper stories.

7.4.4 Local Engineering Demand Parameters

A more detailed post-processing of the NRHA results is conducted herein via *MATLAB* (v. R2013b). The emphasis is on the distribution of the plastic hinge formation, the beam plastic rotations, the column axial force demands and the attained column splice stresses. Due to brevity, only the median (or 84% percentile) response is shown.

Plastic Hinge Location based on Onset of Yielding

The location of beam, column and/or panel zone yielding is shown in Figure 7.17 for the X-loading direction at the BSE-2E level based on the 84% percentile of the corresponding responses. The dots represent the case that the beam and panel zone moment demands exceed the effective yield moment $M^*_{y,b}$ (i.e., red dot) and $M^*_{y,pz}$ (i.e., green dot) respectively; for columns the reduced plastic moment capacities, $M^*_{pe,c}$ (i.e., black dot) are taken into account by considering the interaction of t the axial load and bending for compression,

$$\begin{aligned} &\frac{P_c}{2P_{ye,c}} + \frac{M_c}{M_{pe,c}} < 1.0, \qquad P_c < 0.2P_{ye,c} \\ &\frac{P_c}{P_{ye,c}} + \frac{8}{9}\frac{M_c}{M_{pe,c}} < 1.0, \qquad 0.2P_{ye,c} \le P_c \le 0.5P_{ye,c} \\ &\frac{P_c}{P_{ye,c}} + \frac{M_c}{M_{pe,c}} < 1.0, \qquad P_c > 0.5P_{ye,c} \end{aligned} \tag{7.17}$$

and tension,

$$\frac{T_c}{T_{ye,c}} + \frac{M_c}{M_{pe,c}} < 1.0 \tag{7.18}$$

in the above equations, $M_{pe,c} = Z_c F_{ye,c}$, $P_{ye,c} = A_c F_{ye,c}$ and $T_{ye,c} = A_c F_{ye,c}$; in which P_{ye} and T_{ye} are the expected compressive and tensile yield force of the columns, respectively; M_c, P_c and T_c are the bending moment, compressive and tensile force demands at the column ends; Z_c and A_c are the plastic section modulus and the gross section area of a column, respectively.

Referring to Figure 7.17, in almost all the cases, the beam end moment demands exceed their effective yield moment capacity. According to the P-M interaction relation, significant column yielding is observed in both the upper and lower stories. This is attributed to the observed collapse mechanisms forming in these stories in the X-loading direction. Exterior columns experience high axial load demands (see 3-3 frame in the X-loading direction). No yielding is

observed in the panel zones. This may be associated with the fact that the panel zone of a box section consists of two webs; therefore the panel zone shear strength may be larger than that of the W-shape columns. More detailed observations regarding the behaviour of steel beams and columns are summarized below.

Steel Beam Behaviour

Figure 7.18 shows the maximum value (in 0.1% rad) and corresponding location of the beam plastic rotation based on the 84th percentile obtained from 40 NRHAs in the X-loading direction. Beam at located at floors above levels 28, exceed their ultimate rotation capacity. Similarly, beams between floors 5th and 10th exceed their ultimate rotation capacities. The former is associated with the collapses in the upper stories the latter is associated with the collapses in the lower stories. Beams located between floors 11 and 27 exhibit yielding; however, their plastic deformation demands mostly remained below the associated capping rotation (0.8% rad).

Steel Column Behaviour

Figures 7.19 and 7.20 show the normalized peak column compressive and tensile forces along the building height obtained from 40 NRHAs at the BSE-2E level in the X- and Y-loading directions, respectively. Figures 7.19a and 7.19b illustrate the normalized peak compressive forces ($P_{c,E}/P_{ye,c}$ ratios) and tensile forces ($T_{c,E}/T_{ye,c}$ ratios) due to seismic loading only; while Figure 7.19c and 7.19d show the normalized peak compressive forces ($P_{c,G+E}/P_{ye,c}$ ratios) and peak tensile forces ($T_{c,G+E}/T_{ye,c}$ ratios) including the gravity load for the X-loading direction. These are the maximum values of the normalized peak column compressive/tensile forces within a story. From these figures, the column normalized forces are significantly higher in the X-loading direction. Typically, higher forces are seen in the lower stories. The highest values are observed in the third story exterior columns (see 3-3 Frame). In particular, the peak compressive

axial load ratio becomes close to unity; the corresponding tensile forces exceed $0.5T_{ye,c}$. Same observations hold true for the BSE-1E level; in few cases the column compressive axial forces became higher at the BSE-1E level. This may be attributed to the associated collapses that occurred in the upper stories and lead to lower column force demands at the BSE-2E level. Figures 7.21 and 7.22 show the median peak normalized column compressive and tensile forces in the X-loading direction, respectively. From these figures, the third story exterior columns (see 3-3 frame) are subjected to varying axial load ranging from $0.8P_{ye,c}$ in compression to $0.3T_{ye,c}$ in tension, while the compressive force in the interior columns is less than $0.5P_{ye,c}$; notably, no tension is observed in such cases. Experimental studies (Elkady and Lignos 2016; Lignos et al. 2016; Suzuki and Lignos 2016) conducted on steel columns with seismically compact sections showed that these members can accommodate appreciable plastic deformation demands when they are subjected to high axial compressive load demands (e.g. 0.5 and $0.75P_{ye,c}$). Therefore, they should not be treated as force-controlled elements as suggested in ASCE 41-13 (ASCE/SEI 2014). Suzuki and Lignos (2015) concluded that exterior columns subjected to collapse-consistent lateral loading histories with high axial load variation experience relatively slow flexural strength deterioration compared to interior columns. On the other hand, high tensile forces may lead to column splice fracture if PJP welds are employed (Bruneau and Mahin 1990). This requires a more detailed assessment of the column splice stress demands.

Column Splice Stress Demands

Figure 7.23 indicates the locations of column splices and their peak tensile stresses in MPa, σ_D, recorded at the fiber extremity of the smallest of the two column sections forming a column splice in the X-loading direction. The σ_D values shown in this figure are the median peak tensile stresses obtained from 40 NRHAs at the BSE-2E level. The blue dots represent sections that no

tensile stresses are observed. Sections with tensile stresses are highlighted with orange dots and the peak tensile stresses are reported. The peak stresses that exceed the estimated stress capacity, σ_C, (Galasso et al. 2015; Lai et al. 2015; Stillmaker et al. 2016) given below are highlighted in red,

$$\sigma_D \geq \sigma_C = \frac{K_{IC}}{\left[9.91\left(\frac{a}{t_{c,fl}^{up}}\right)^2 - 1.22\left(\frac{a}{t_{c,fl}^{up}}\right)^2 + 1\right]\sqrt{\pi a}} = \frac{474.8}{\sqrt{t_{c,fl}^{up}}} \tag{7.19}$$

in which, fracture toughness of weld K_{IC} = 1736 MPa$\sqrt{\text{mm}}$ (50 ksi$\sqrt{\text{in}}$), $t_{c,fl}^{up}$ is thickness of the upper column flange, a = 0.5$t_{c,fl}^{up}$ (Lai et al. 2015). Referring to Figure 7.23, almost all exterior column splices at lower half of the building and splices in the upper stories exhibit tensile stresses. The latter is attributed to fact that majority of collapses occurred in the upper stories. In 34% of the column splices the corresponding stress demands exceeded the estimated stress capacity σ_C; therefore these splices are highly vulnerable to weld fracture during a BSE-2E level seismic event.

7.5 Summary and Conclusions

This chapter provides a comprehensive evaluation of an existing 40-story tall building with space steel moment-resisting frames (MRFs) designed in early 1970s. The prototype building design was carried out based on UBC 1973 (ICBO 1973). Advanced 2D nonlinear building model representations in both translational directions are developed. Pushover analysis is conducted based on the first model lateral load pattern. In order to carry out nonlinear response history analyses, 40 ground motions were selected and scaled to be compatible with the BSE-1E and BSE-2E hazard levels as per ASCE 41-13 (ASCE/SEI 2014). Nonlinear response history analysis was carried out for the two seismic hazard levels and story-based engineering demand

parameters (EDPs) from NRHA results were summarized. A comprehensive discussion related to the local EDP parameters associated with beams, columns, column splices and panel zones was also provided. The main findings are summarized as follows:

- According to UBC 1973, the seismic design base shear was $0.021W$, while the design wind base shear forces were $0.027W$ and $0.018W$ in the X- and Y-loading directions, respectively. The steel design was mainly governed by the wind load drift limitation, particularly in the lower stories. It was found as expected that the design heavily violated the SCWB requirement of AISC (2010b) in exterior columns due to high axial load demands.
- The peak column axial load due to the effective gravity load $P_{c,G}$ was $0.32P_{y,ec}$. The fundamental periods of vibration were around 5.30 sec in both loading directions based on the corresponding 2D nonlinear building models.
- The building performance was evaluated through nonlinear static (pushover) analysis. Three scenarios were considered to model the beam end moment-rotation relation, namely 'brittle', '25% ductile' and 'ductile' cases. Interestingly, the 'brittle' and '25% ductile' cases did not demonstrate remarkable difference in both strength and associated collapse mechanisms. The onset of yielding and the peak base shear force were observed at $0.06W$ and $0.09W$ in both loading directions, respectively. Pushover analysis shows that at around 1% roof drift ratio the building performance was significantly compromised due to a sudden strength loss. At this point , the corresponding peak SDRs were below 2%. In all cases, multiple-story collapse mechanisms occurred in the lower half of the building.
- Out of 40 records 29 lead to collapse at the BSE-2E level. In the X-loading direction collapse occurred in the upper stories of the building. In the rest of the cases, the peak residuals SDRs were mainly concentrated at the upper stories.

- Almost all the beams exhibited flexural yielding. However, no yielding was observed in the panel zones. This is attributed to the box column sections.
- Exterior columns in the lower stories of the building in the X-loading direction experienced high compressive and tensile forces. In certain cases, the compressive force reached up to the expected column yield strength. The same columns experienced, on average, axial load demands ranging from $0.8P_{ye,c}$ in compression to $0.3T_{ye,c}$ in tension. the interior columns within the same stories experience compressive axial forces up to $0.5P_{ye,c}$. No significant difference in column axial loads was obtained between BSE-1E and BSE-2E levels. This implies that unless if the reduction in SDRs is considerable, the column axial load demands are expected to remain high at the BSE-2E level even if the building is retrofitted with nonconventional techniques, such as supplemental damping.
- About 34% of the column splices were found to be vulnerable in the building's X-loading direction at the BSE-2E level. On the other hand, a considerable number of interior column splices exhibited no and low tensile stresses. This indicated that the column splice retrofit may not be necessary for the entire building.

The findings summarized above based on rigorous nonlinear analysis procedures are used as recommendations for effective retrofit strategies with supplemental damping devices discussed in the following chapter.

Table 7.1: Lateral force resisting system section sizes as per UBC 1973 design

Story/ Floor	Wide Flange Beams				Square Box Columns*	
	Exterior X 1-7	Interior X 3-5	Exterior Y A-E	Interior Y B-C-D	Exterior Y A-E	Interior Y B-C-D
40/41	W21X50	W24X76	W21X50	W33X118	B20X0.75	B26X1
39/40	W21X50	W24X76	W21X50	W33X118	B20X0.75, B 20X0.75	B26X1, B26X1
38/39	W21X50	W24X76	W21X50	W33X118	B20X0.75	B26X1
37/38	W21X50	W24X76	W21X50	W33X118	B20X0.75	B26X1
36/37	W21X50	W24X76	W21X50	W33X118	B20X0.75, B20X0.75	B26X1, B26X1
35/36	W24X76	W24X94	W21X50	W33X118	B20X0.75	B26X1
34/35	W24X76	W24X94	W21X50	W33X118	B20X0.75	B26X1
33/34	W24X76	W24X94	W21X50	W33X118	B20X1, B20X0.75	B26X1.25, B26X1
32/33	W24X84	W27X102	W21X55	W33X118	B20X1	B26X1.25
31/32	W24X84	W27X102	W21X55	W33X118	B20X1	B26X1.25
30/31	W24X84	W27X102	W21X55	W33X118	B20X1, B20X1	B26X1.25, B26X1.25
29/30	W27X94	W27X114	W24X76	W33X118	B20X1	B26X1.25
28/29	W27X94	W27X114	W24X76	W33X118	B20X1	B26X1.25
27/28	W27X94	W27X114	W24X76	W33X118	B20X1.25, B20X1	B26X1.5, B26X1.25
26/27	W27X114	W30X132	W24X76	W33X118	B20X1.25	B26X1.5
25/26	W27X114	W30X132	W24X76	W33X118	B20X1.25	B26X1.5
24/25	W27X114	W30X132	W24X76	W33X118	B20X1.25, B20X1.25	B26X1.5, B26X1.5
23/24	W27X114	W30X132	W27X84	W33X118	B20X1.25	B26X1.5
22/23	W27X114	W30X132	W27X84	W33X118	B20X1.25	B26X1.5
21/22	W27X114	W30X132	W27X84	W33X118	B20X1.5, B20X1.25	B26X1.75, B26X1.5
20/21	W30X124	W33X152	W30X108	W33X118	B20X1.5	B26X1.75
19/20	W30X124	W33X152	W30X108	W33X118	B20X1.5	B26X1.75
18/19	W30X124	W33X152	W30X108	W33X118	B20X1.5, B20X1.5	B26X1.75, B26X1.75
17/18	W30X124	W33X152	W30X108	W33X118	B20X1.5	B26X1.75
16/17	W30X124	W33X152	W30X108	W33X118	B20X1.5	B26X1.75
15/16	W30X124	W33X152	W30X108	W33X118	B20X2, B20X1.5	B26X2, B26X1.75
14/15	W30X124	W33X152	W30X124	W33X118	B20X2	B26X2
13/14	W30X124	W33X152	W30X124	W33X118	B20X2	B26X2
12/13	W30X124	W33X152	W30X124	W33X118	B20X2, B20X2	B26X2, B26X2
11/12	W33X130	W36X160	W30X124	W33X118	B20X2	B26X2
10/11	W33X130	W36X160	W30X124	W33X118	B20X2	B26X2
9/10	W33X130	W36X160	W30X124	W33X118	B20X2.5, B20X2	B26X2.5, B26X2
8/9	W33X130	W36X160	W30X124	W33X118	B20X2.5	B26X2.5
7/8	W33X130	W36X160	W30X124	W33X118	B20X2.5	B26X2.5
6/7	W33X130	W36X160	W30X124	W33X118	B20X2.5, B20X2.5	B26X2.5, B26X2.5
5/6	W33X130	W36X160	W30X124	W33X118	B20X2.5	B26X2.5
4/5	W33X130	W36X160	W30X124	W33X118	B20X2.5	B26X2.5
3/4	W33X130	W36X160	W30X124	W36X150	B20X3.5, B20X2.5	B26X3, B26X2.5
2/3	W36X150	W36X182	W30X124	W36X150	B20X3.5	B26X3
1/2	W36X150	W36X182	W30X124	W36X150	B20X3.5, B20X3.5	B26X3, B26X3
-1/1	W36X150	W36X182	W30X124	W36X150	B20X3.5	B26X3
-2/-1	W36X150	W36X182	W30X124	W36X150	B20X3.5	B26X3
-3/-2	W36X150	W36X182	W30X124	W36X150	B20X3.5	B26X3

*Splice at 1.2 m (4 ft) above the floor level

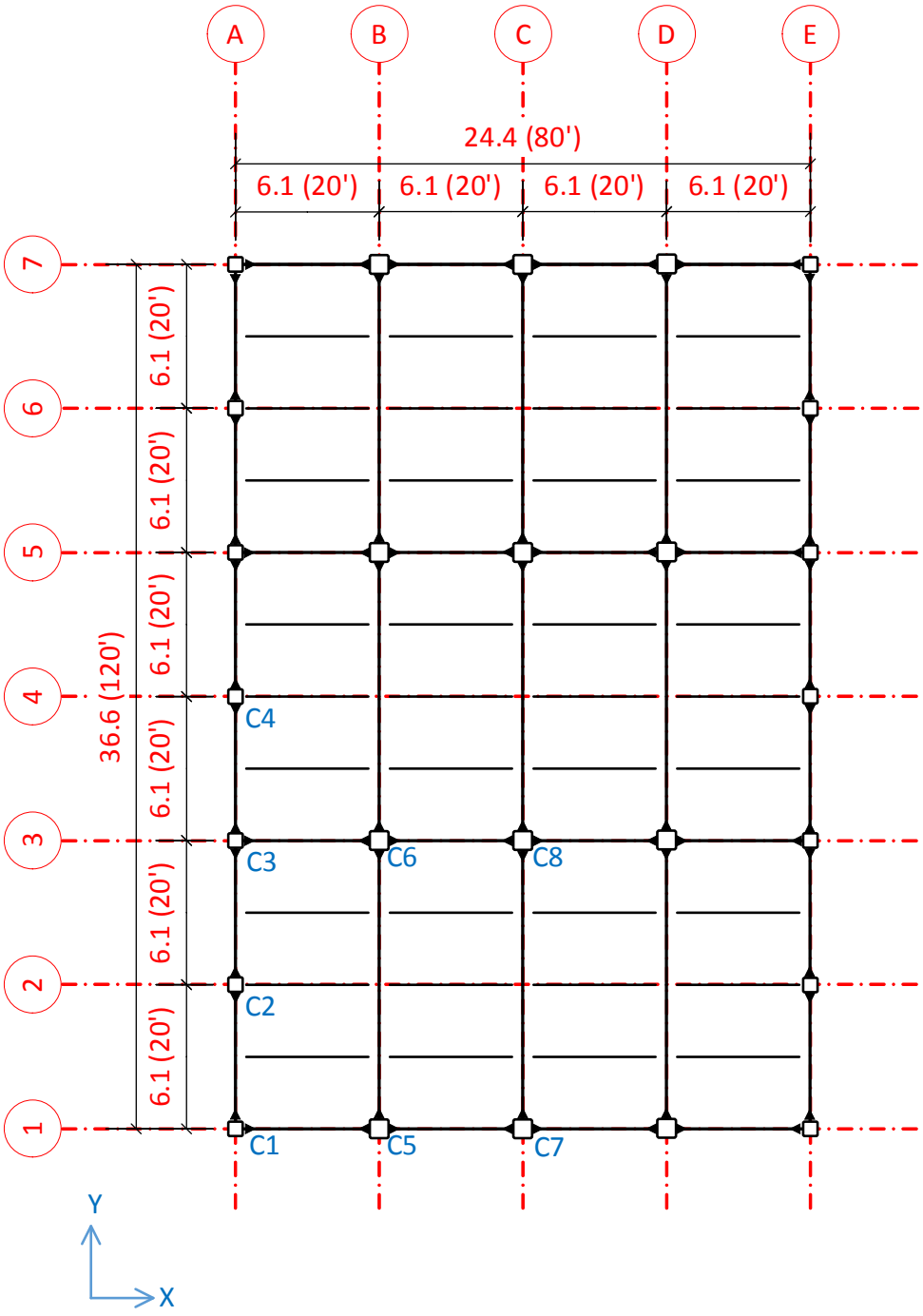

Figure 7.1: Floor plan of the building, dimensions in m (ft)

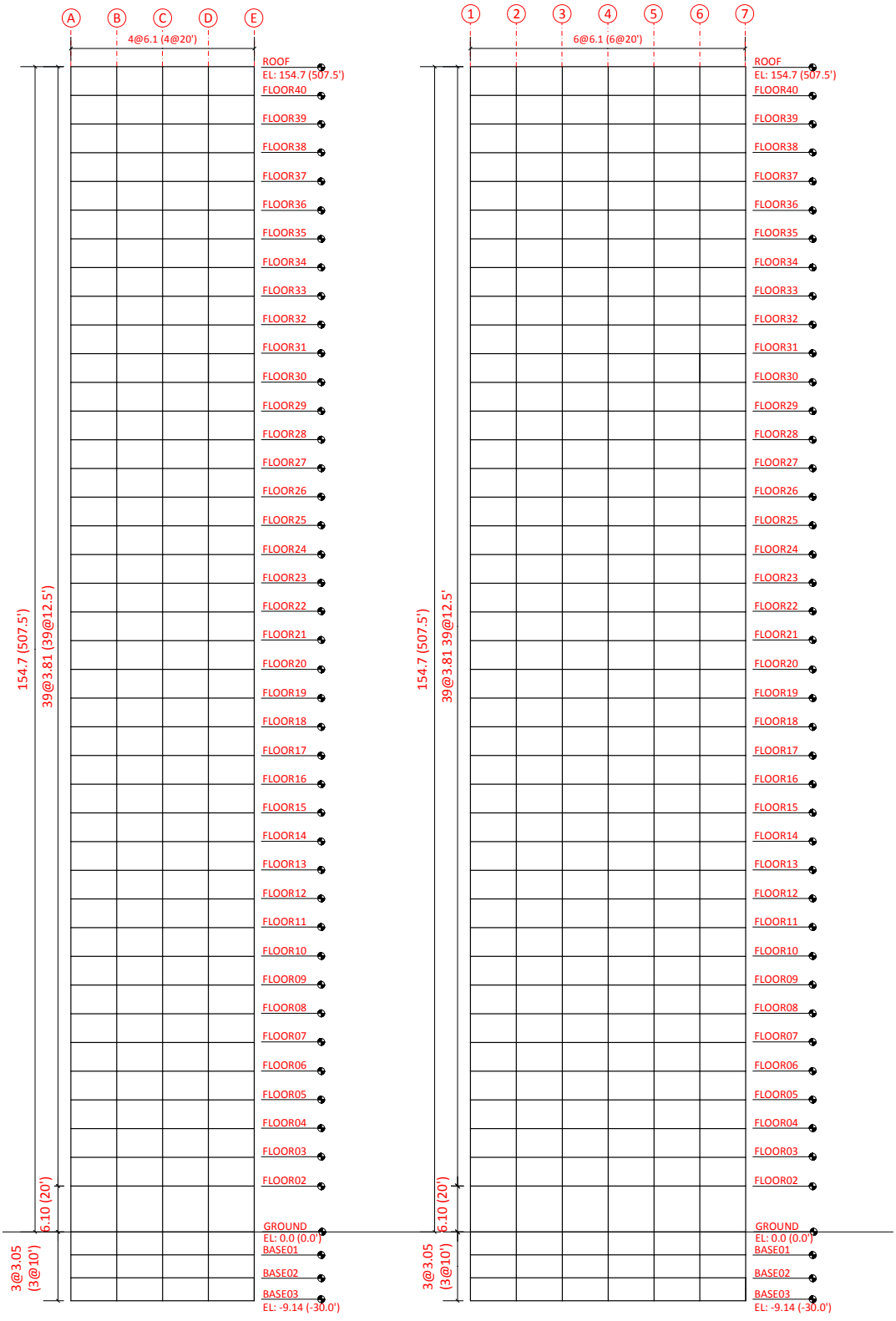

a) X-direction (all frames) b) Y-direction (A-A frame)

Figure 7.2: Elevation view of the building, dimensions in m (ft)

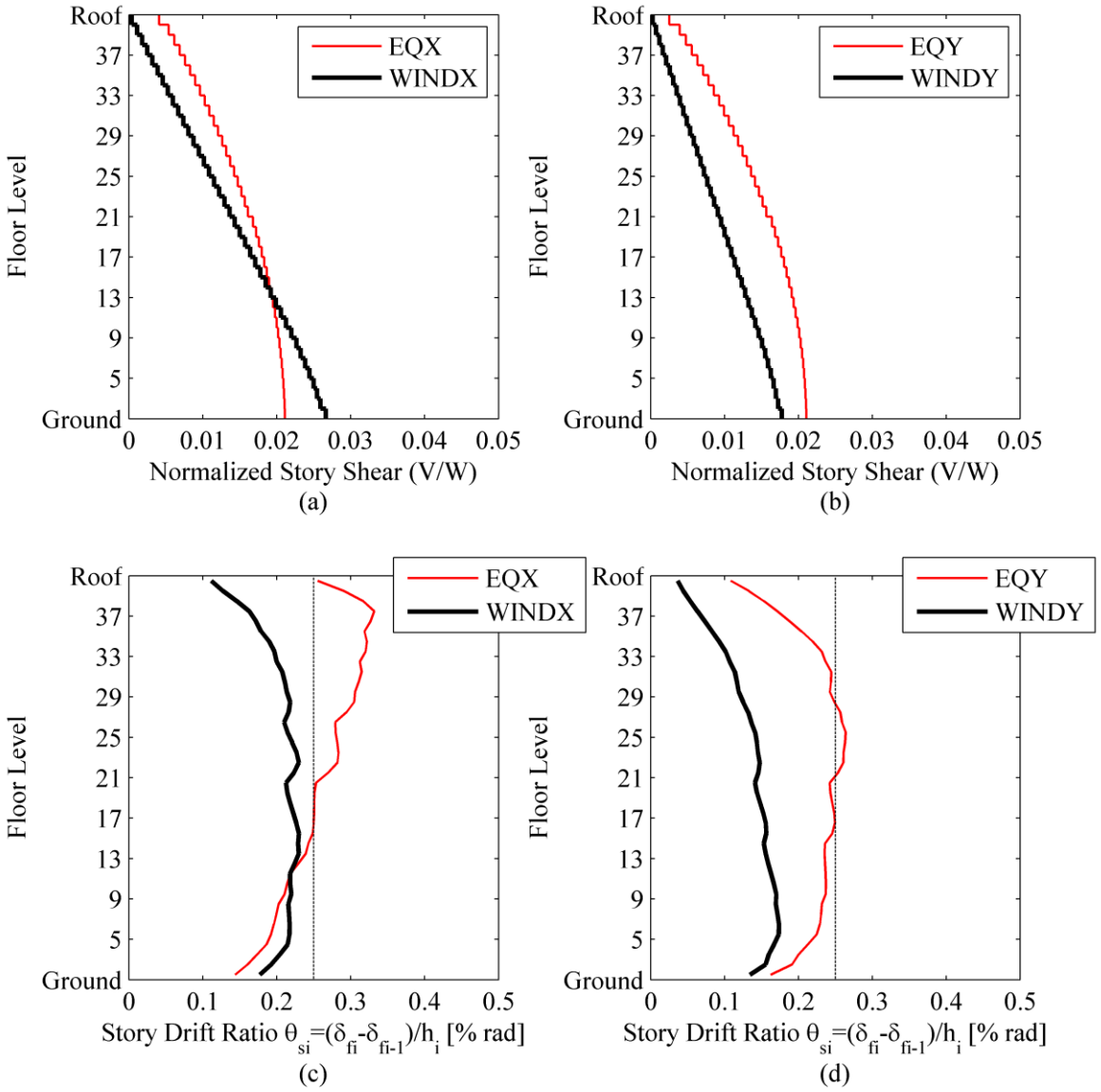

Figure 7.3: Design story shear and the resultant story drift ratio for earthquake and wind loads per UBC 1973 in the X and Y-loading directions

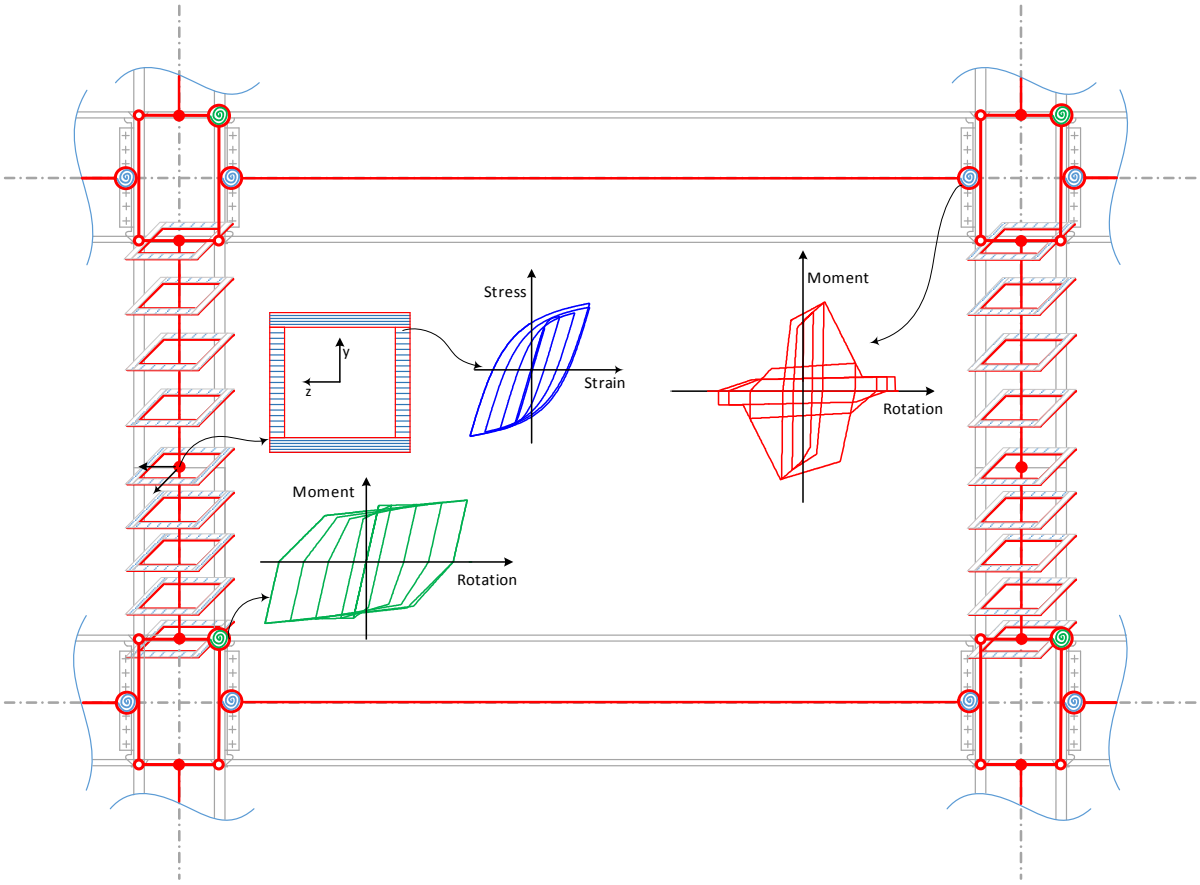

Figure 7.4: Representation of beam, columns and panel zone models in *OpenSees* platform.

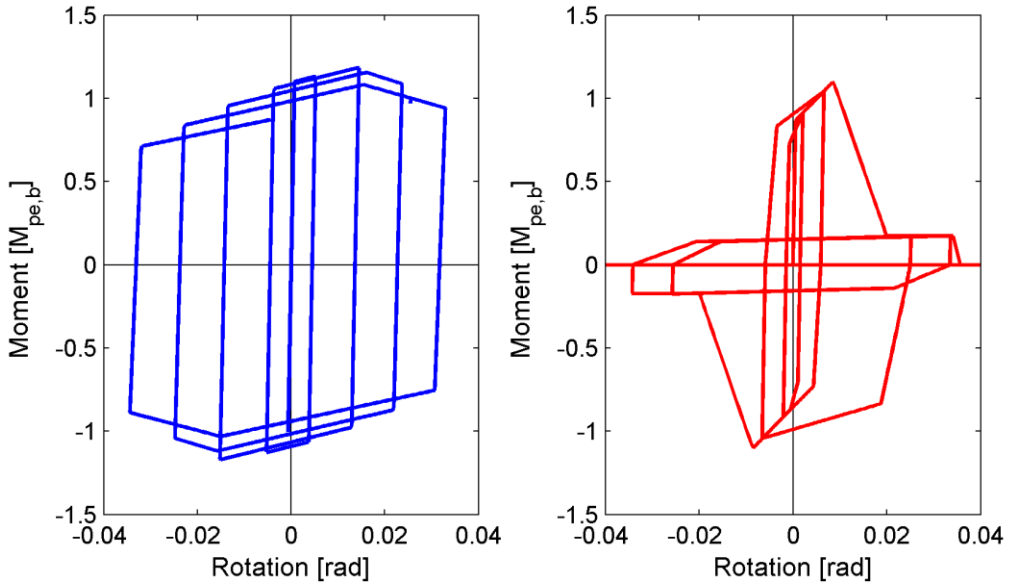

a) Ductile Case b) Brittle Case

Figure 7.5. Moment-rotation relation of steel beams: ductile versus brittle case

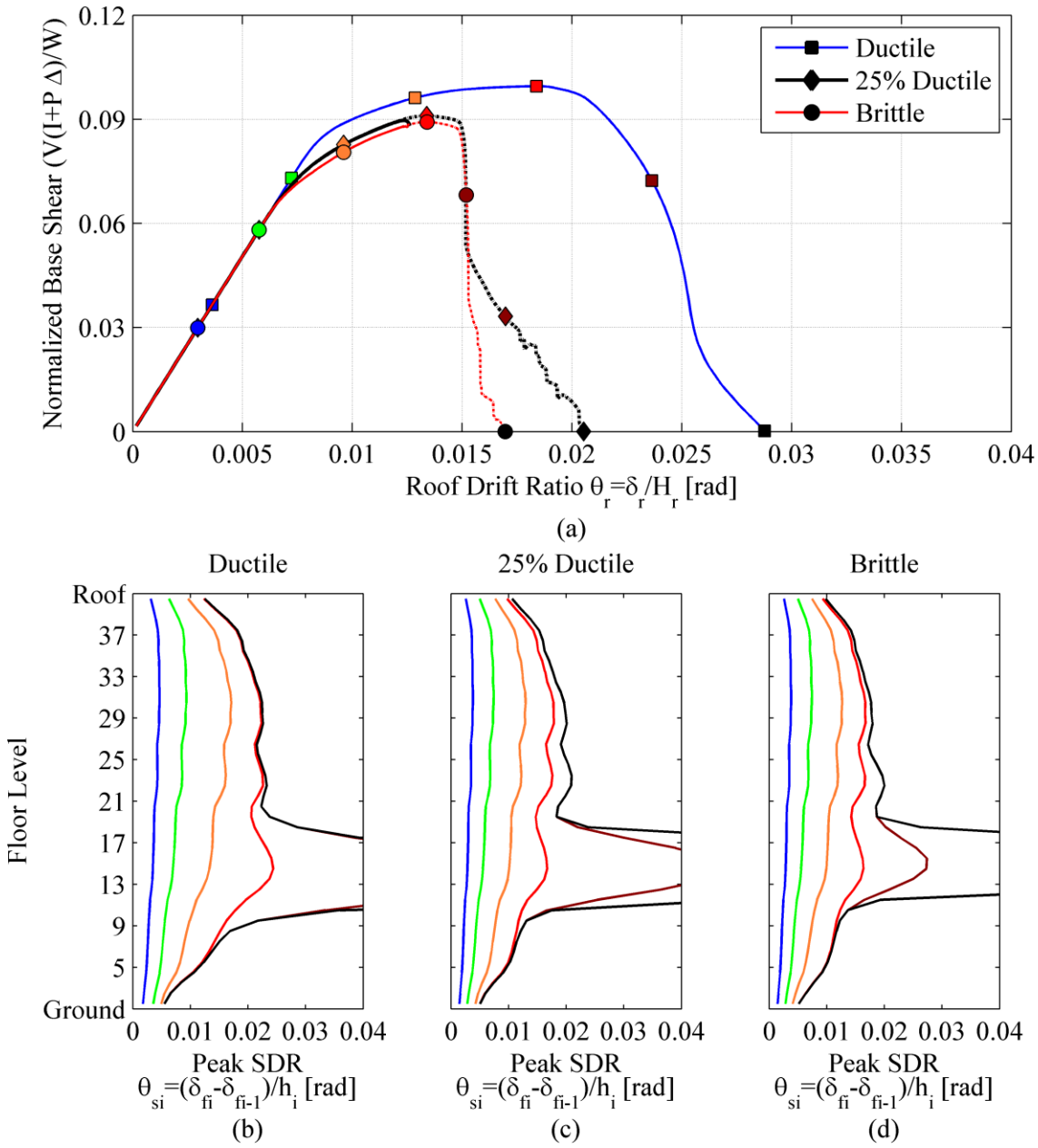

Figure 7.6: Comparison of pushover curves and story drift ratios in X-loading direction

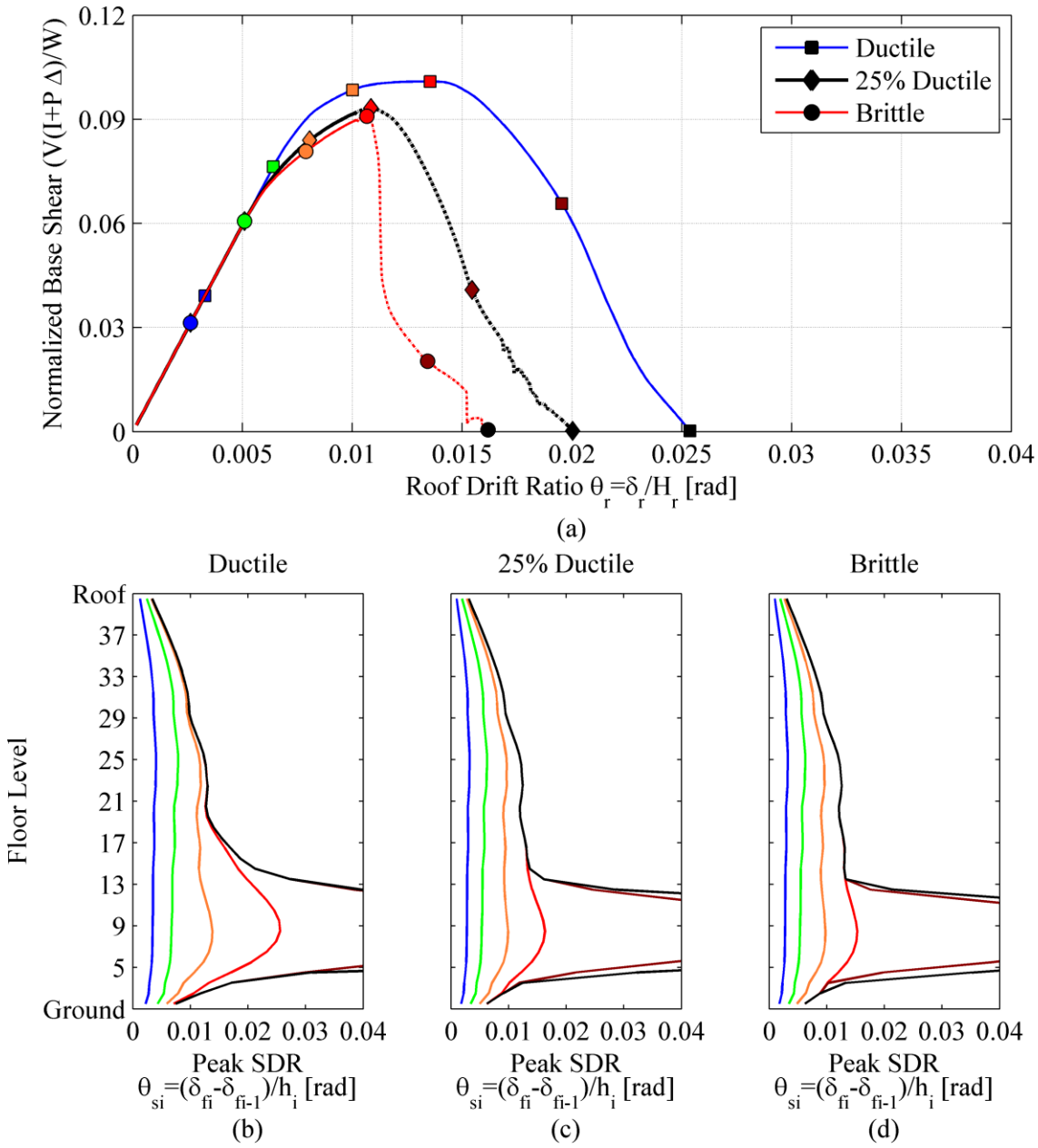

Figure 7.7: Comparison of pushover curves and story drift ratios in Y-loading direction

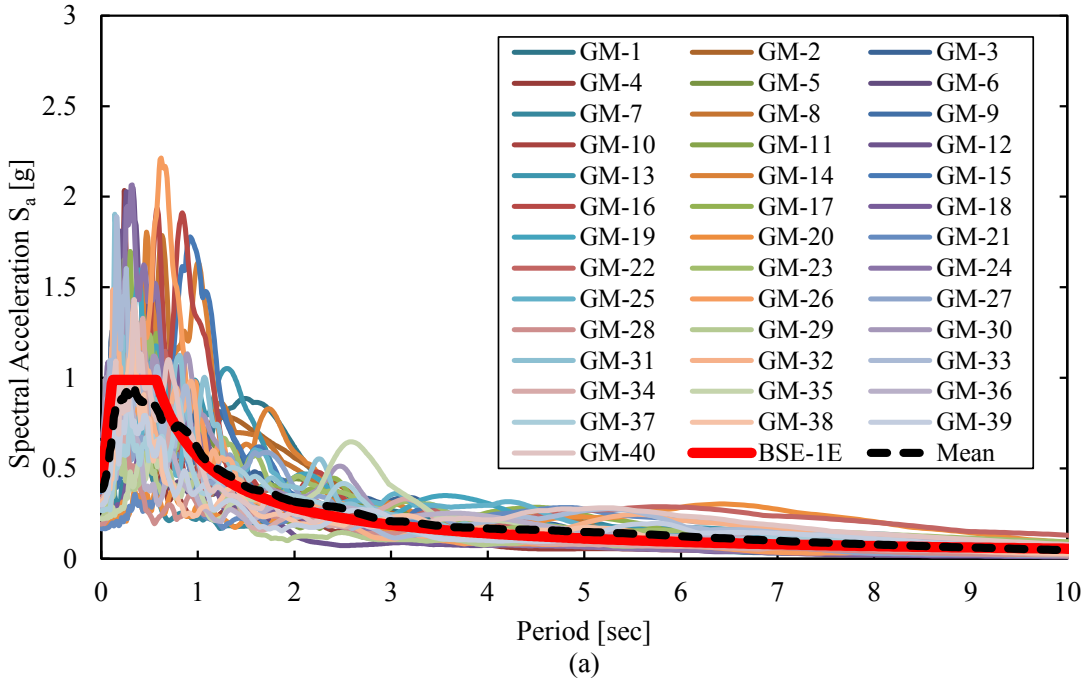

(a)

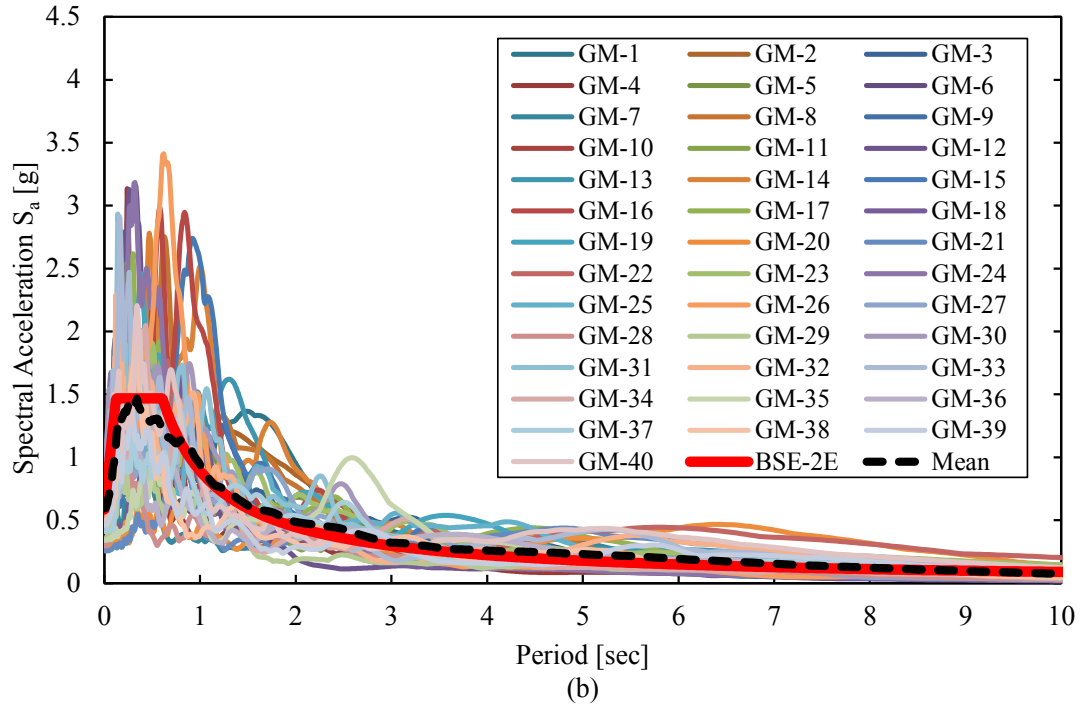

(b)

Figure 7.8: 5% damped response spectra of selected and scaled ground motions in comparison with ASCE-41-13 target spectrum for two-dimensional analyses; (a) BSE-1E and (b) BSE-2E level

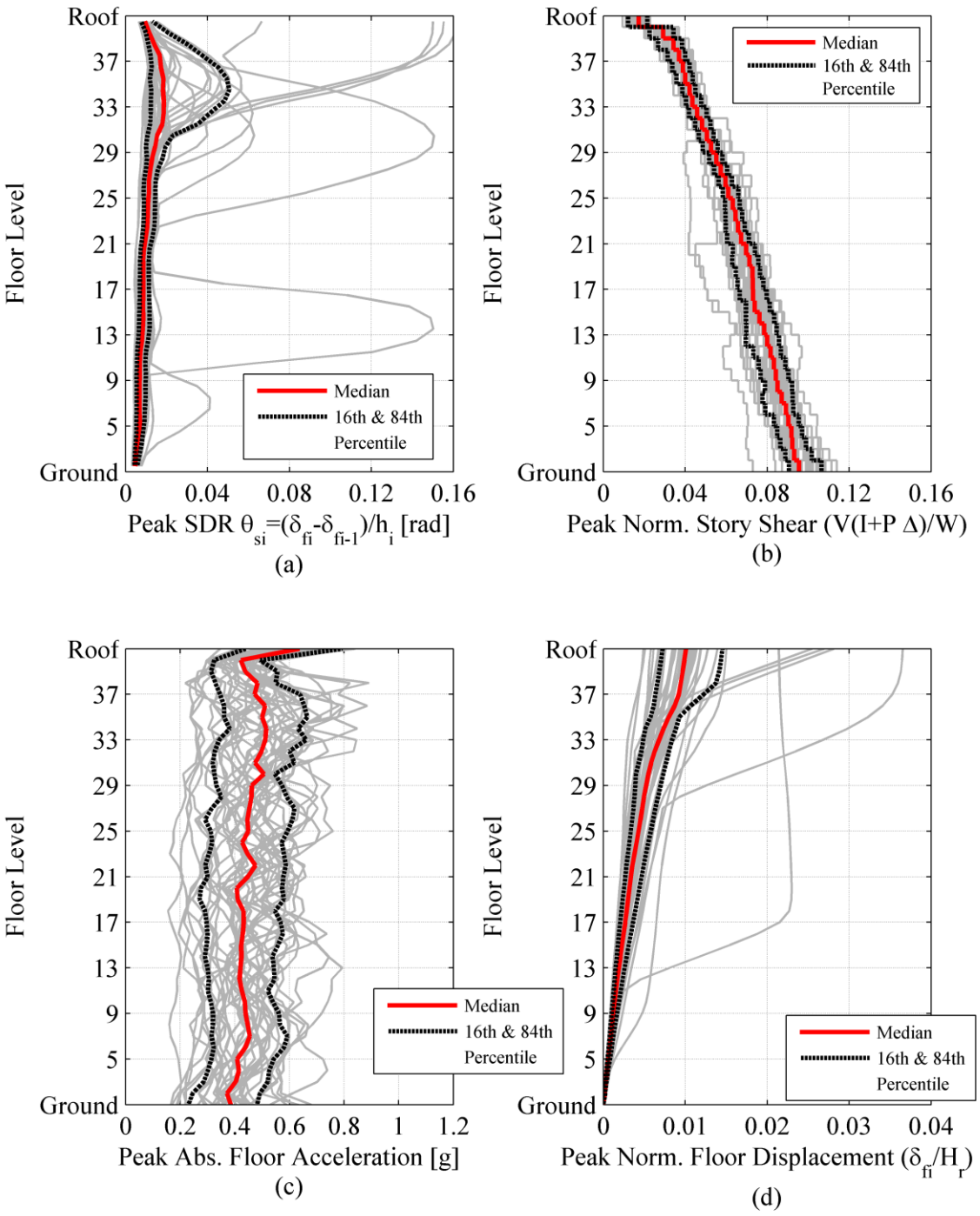

Figure 7.9: Engineering demand parameters in X-loading direction (BSE-1E)

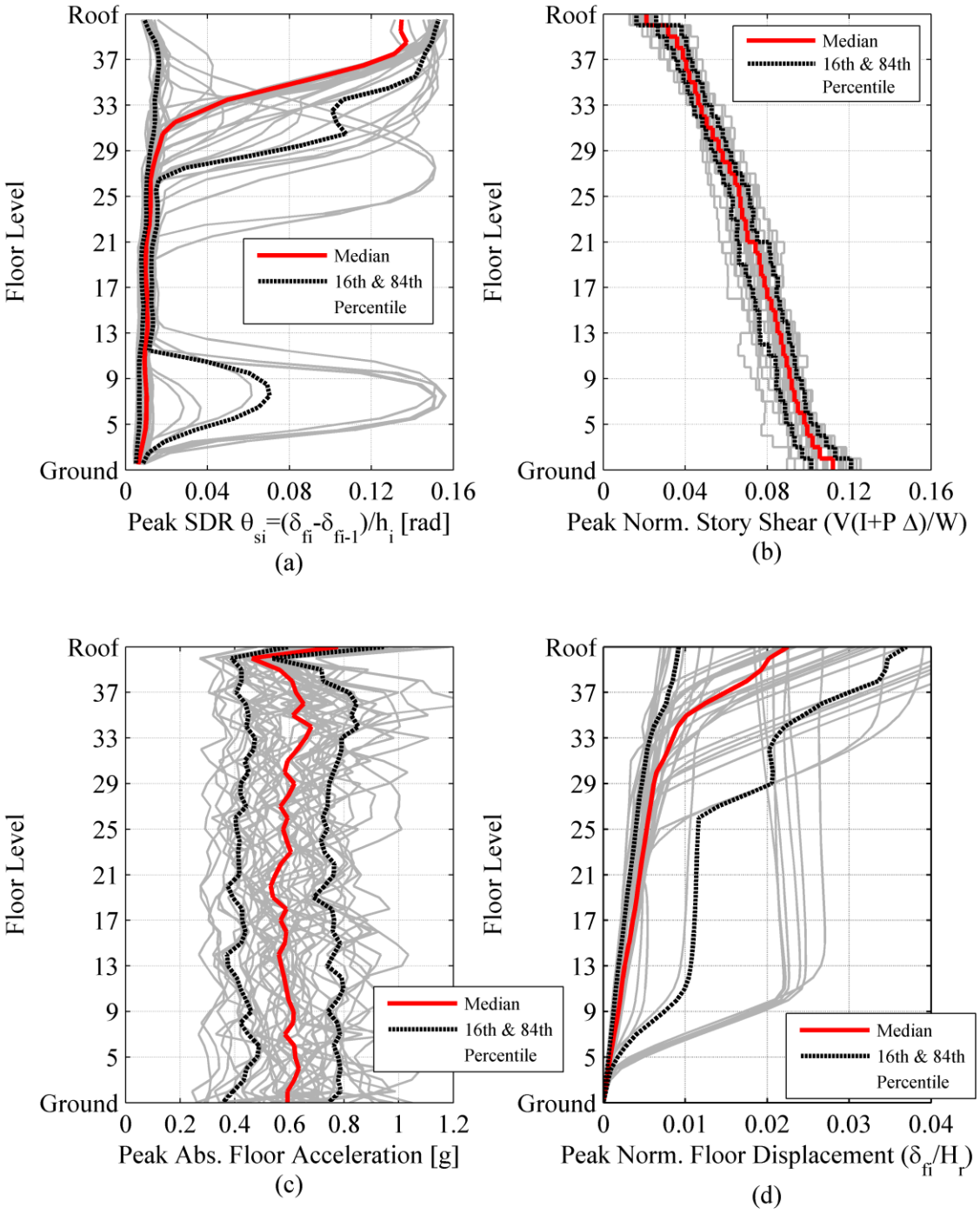

Figure 7.10: Engineering demand parameters in X-loading direction (BSE-2E)

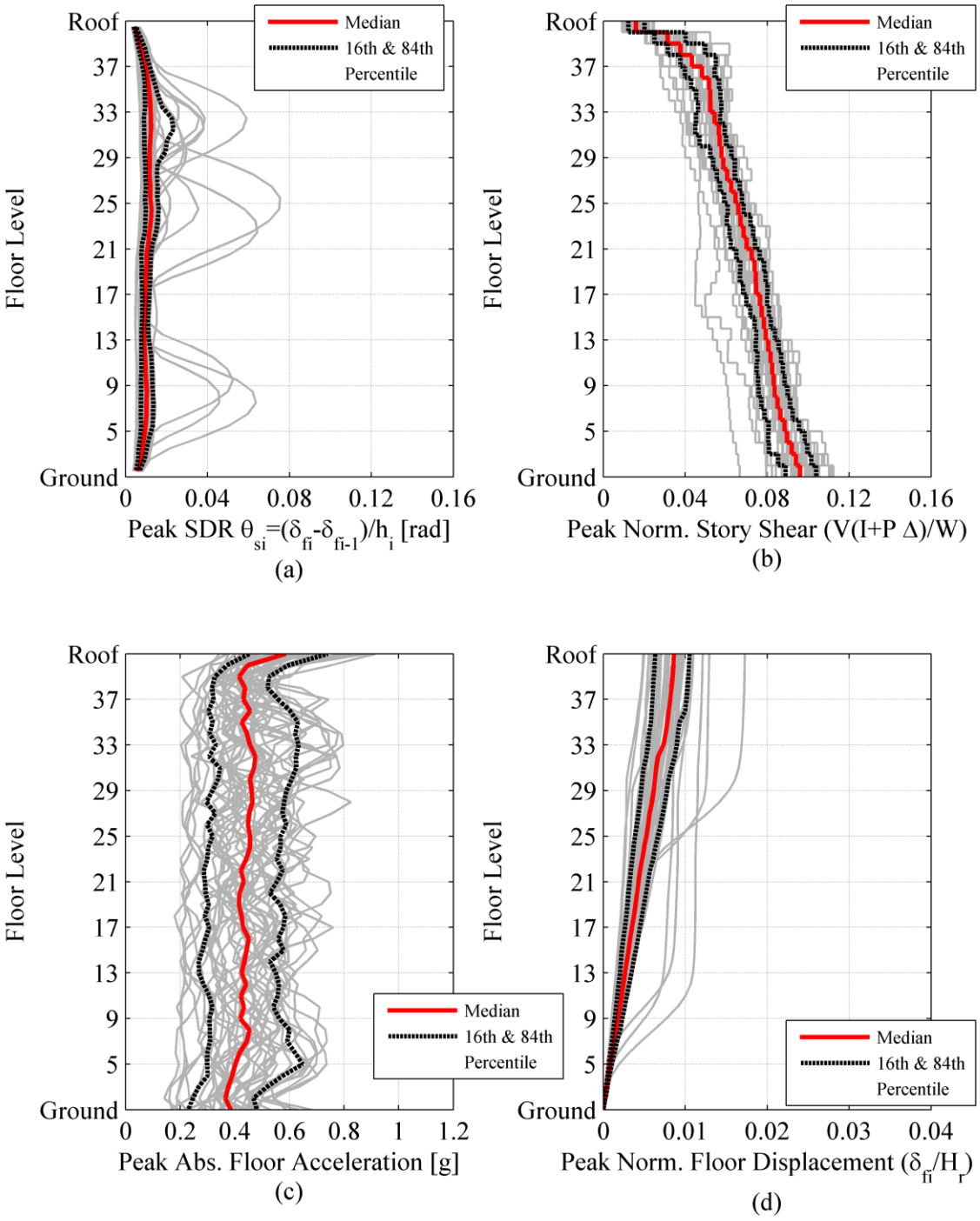

Figure 7.11: Engineering demand parameters in Y-loading direction (BSE-1E)

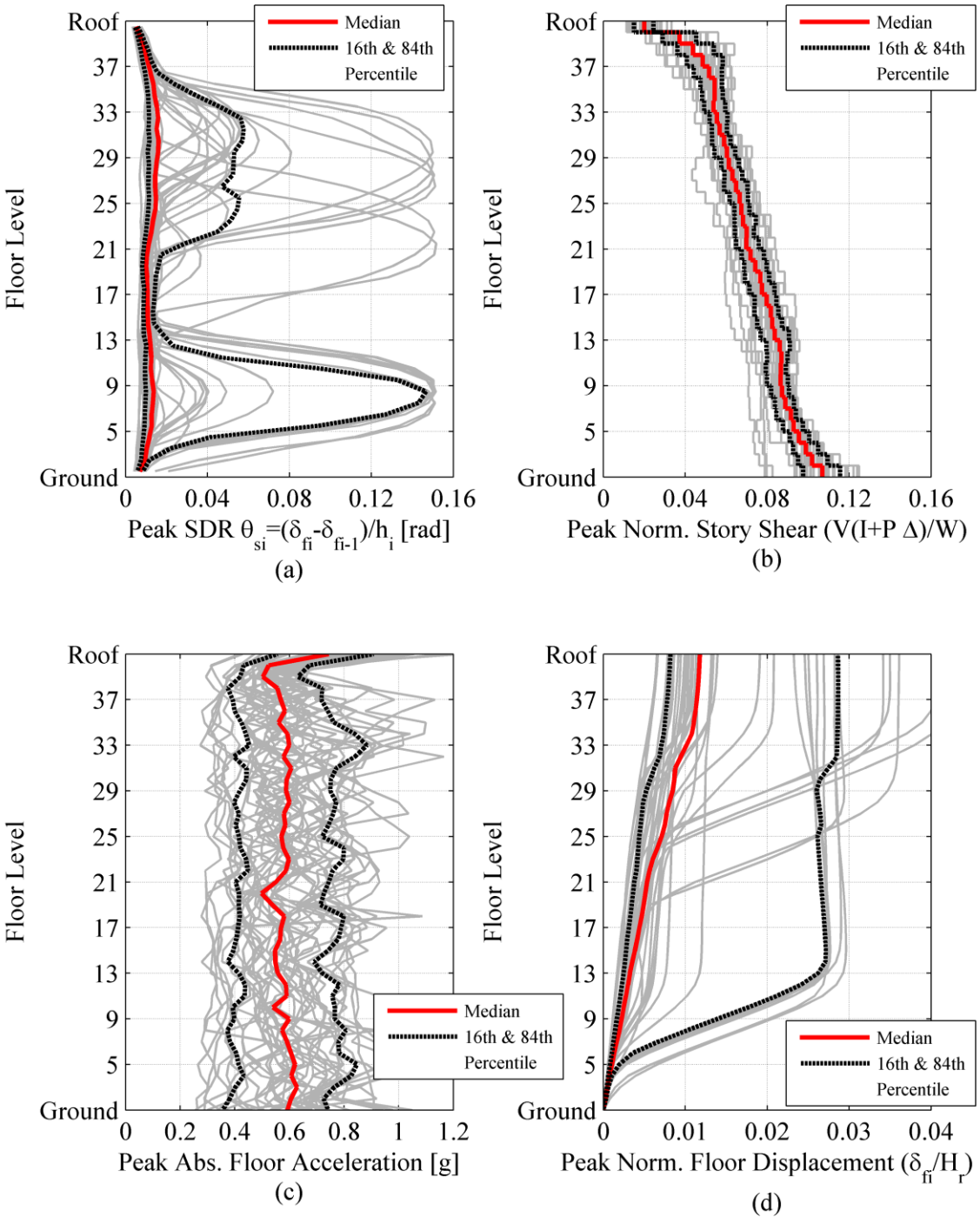

Figure 7.12: Engineering demand parameters in Y-loading direction (BSE-2E)

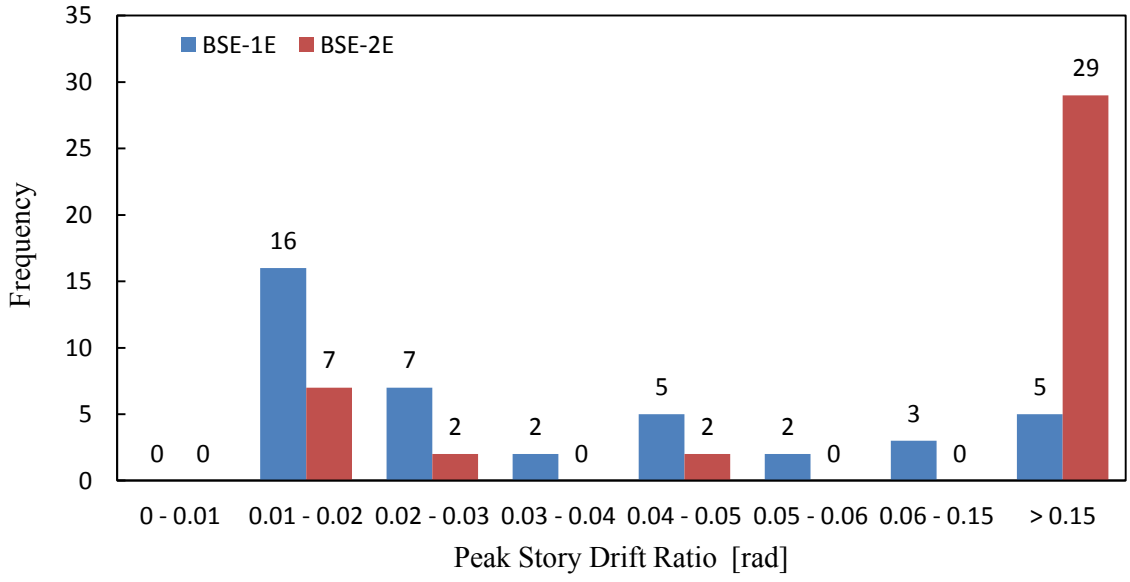

(a)

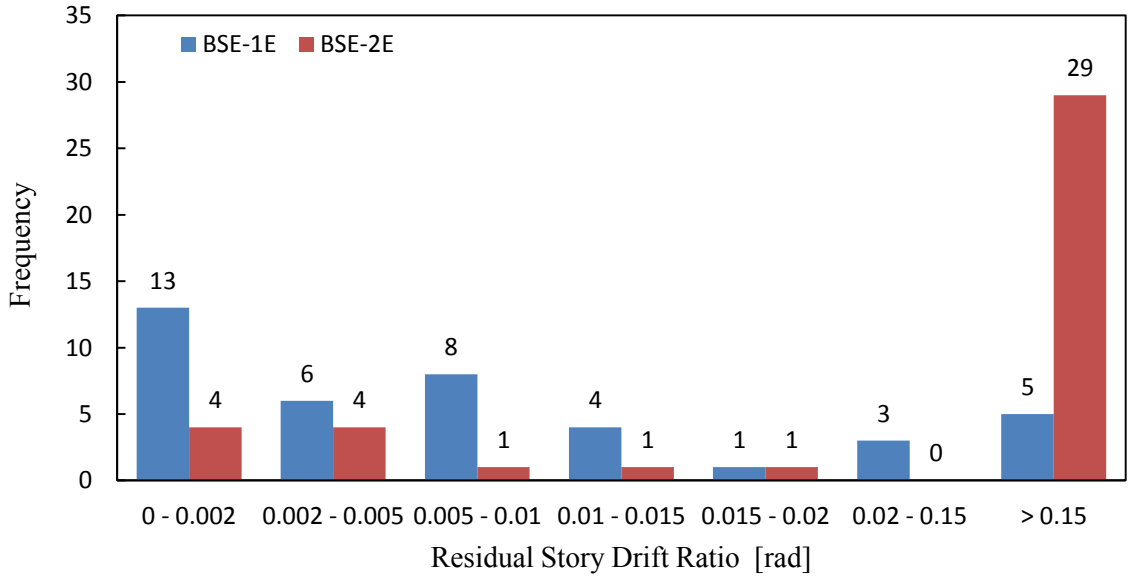

(b)

Figure 7.13: Maximum transient and residual story drift ratios obtained from 40 NRHAs in X-loading direction

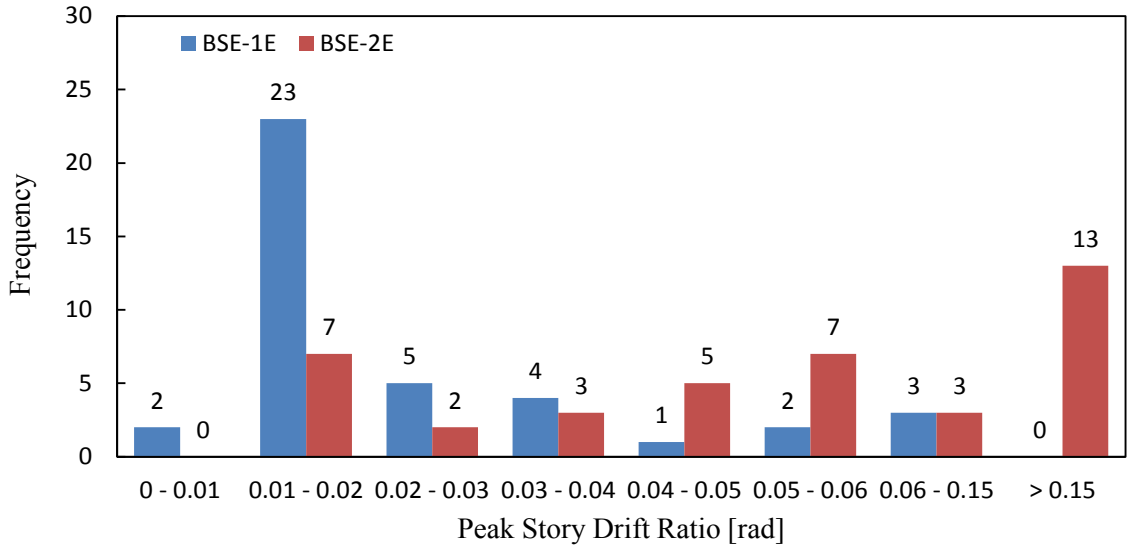

(a)

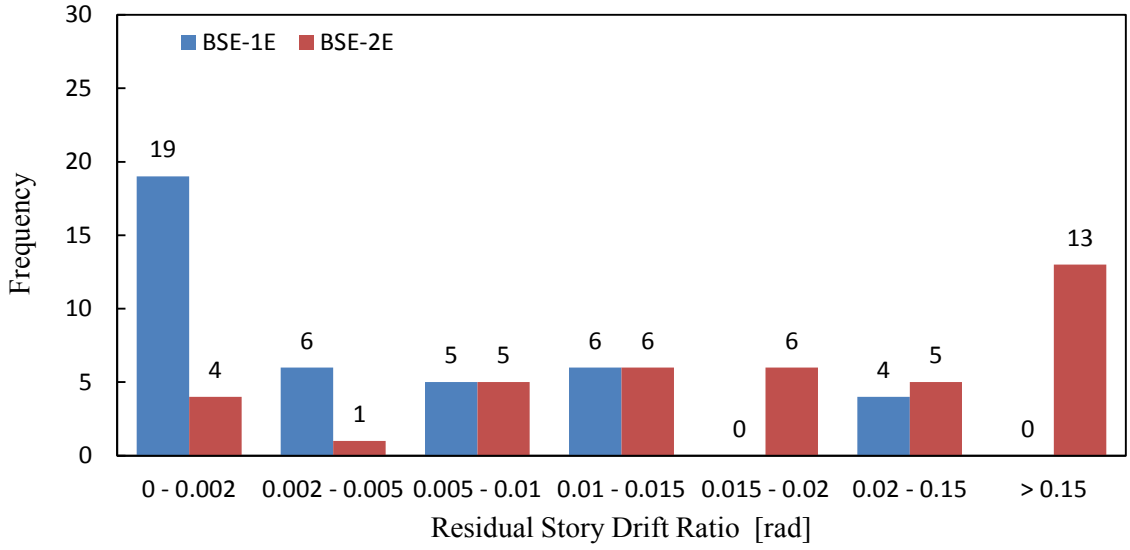

(b)

Figure 7.14: Maximum transient and residual story drift ratios obtained from 40 NRHAs in Y-loading direction

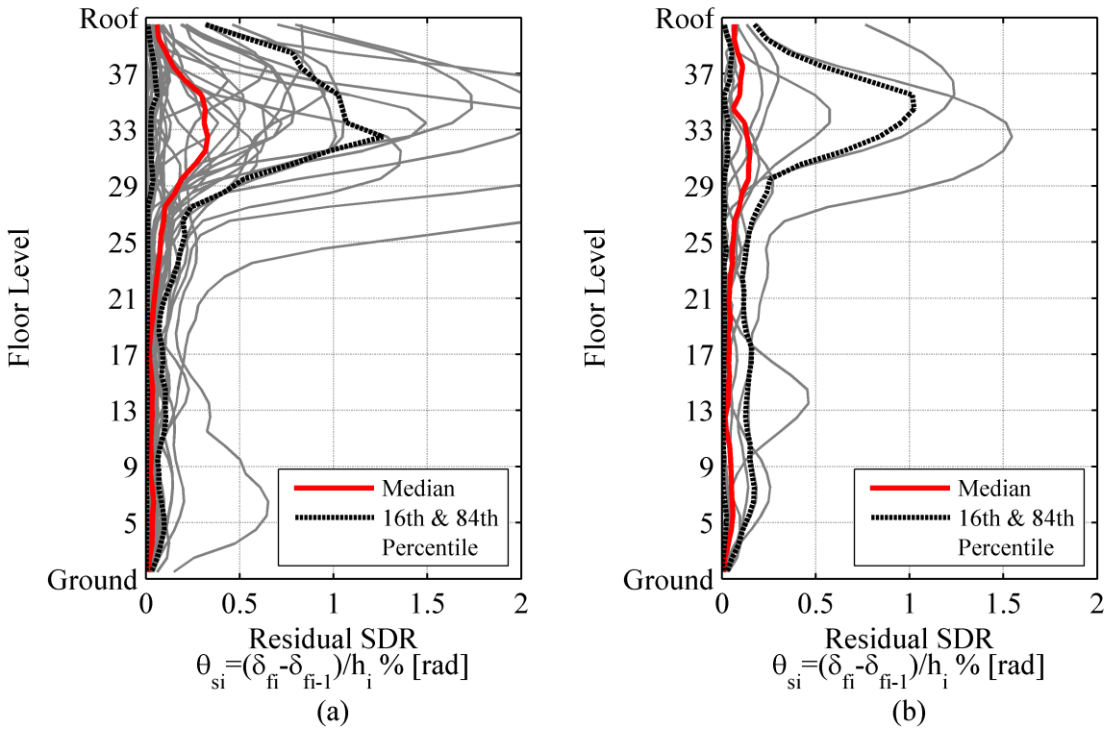

Figure 7.15: Residual story drift ratios in X-loading direction (BSE-1E and BSE-2E).

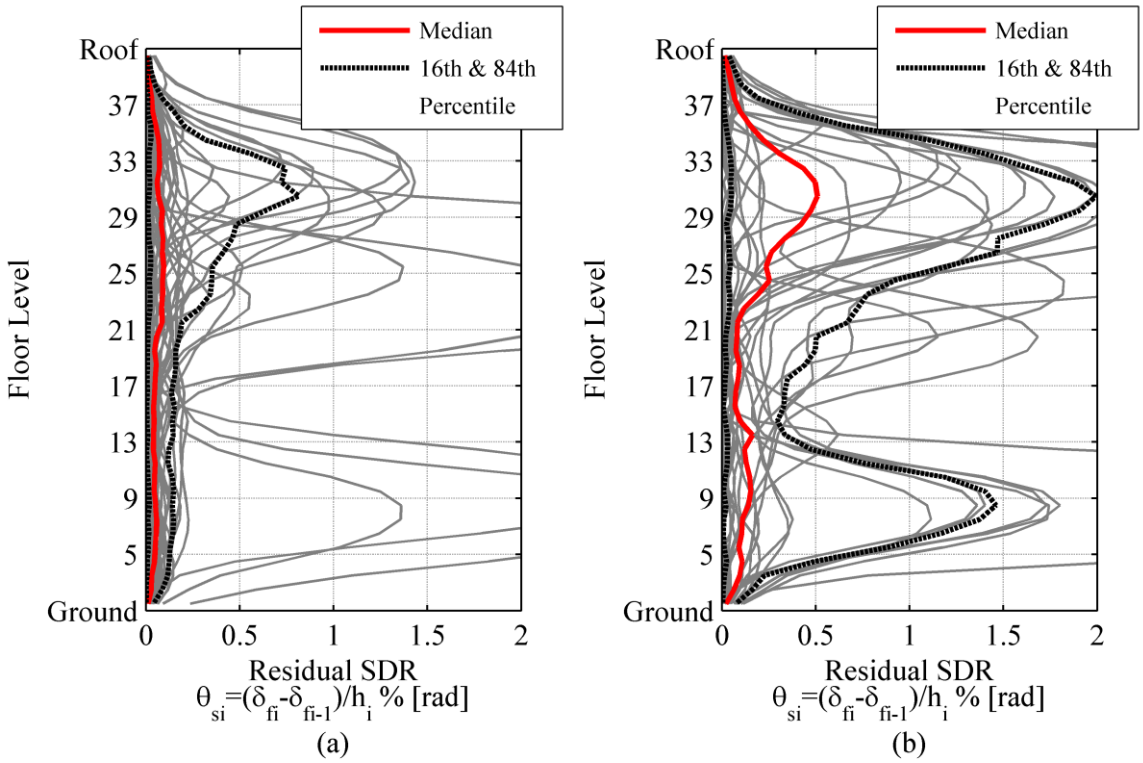

Figure 7.16: Residual story drift ratios in Y-loading direction (BSE-1E and BSE-2E)

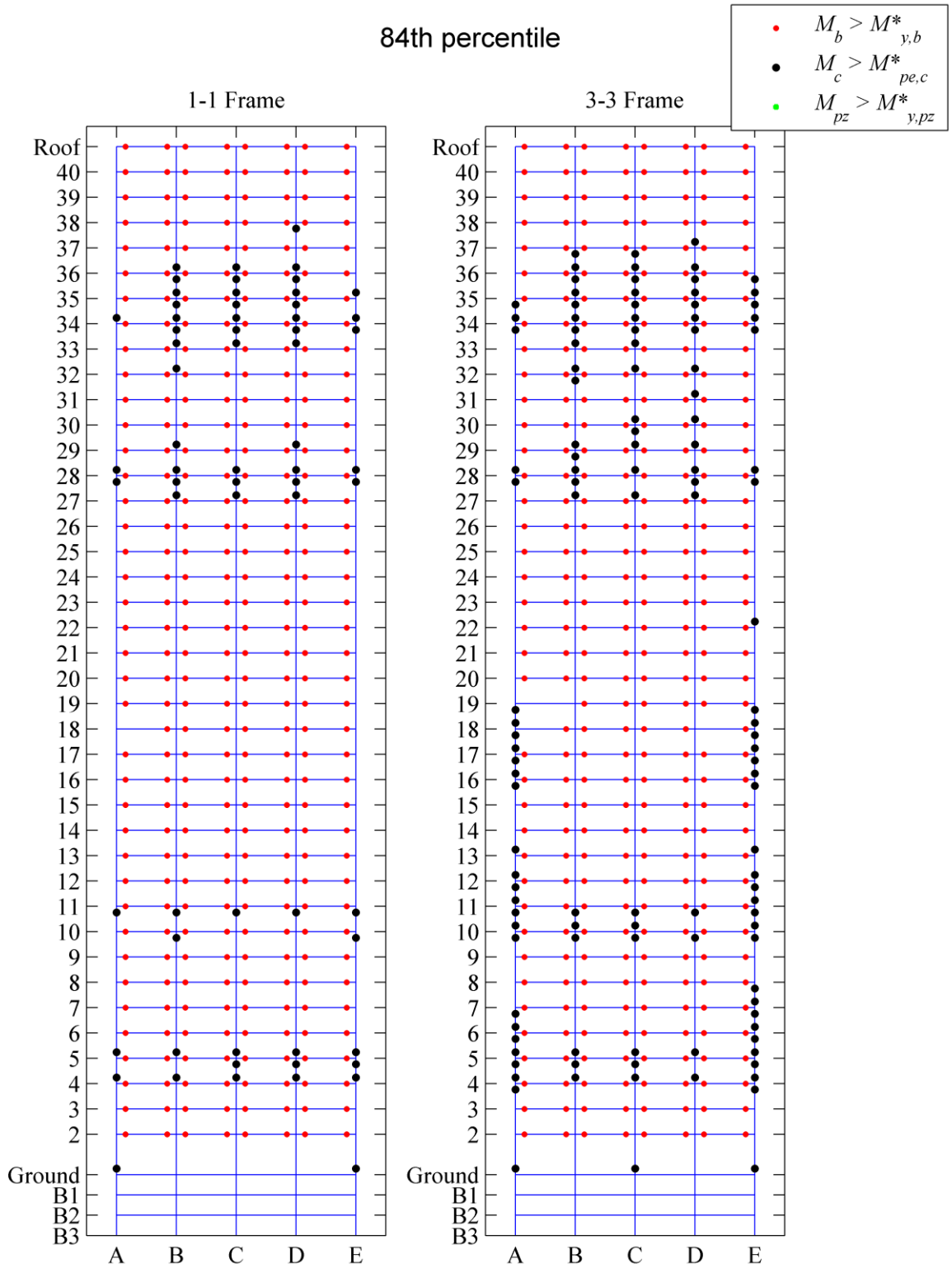

Figure 7.17: Distribution of plastic hinge formation based on the onset of yielding according to the 84th percentile NRHA response in X-loading direction (BSE-2E)

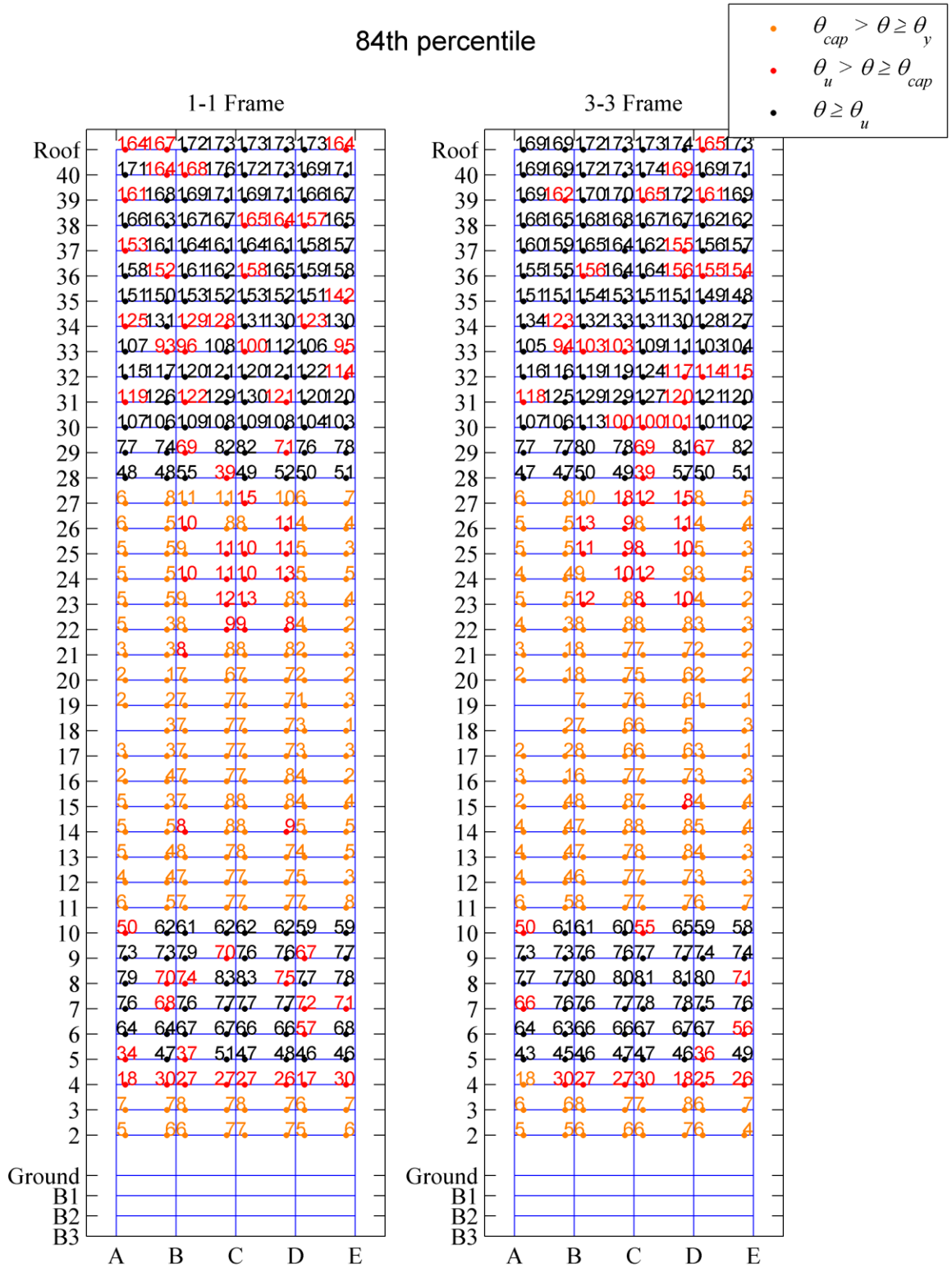

Figure 7.18: 84th percentile of peak beam plastic rotation from NRHA results in X-loading direction (BSE-2E)

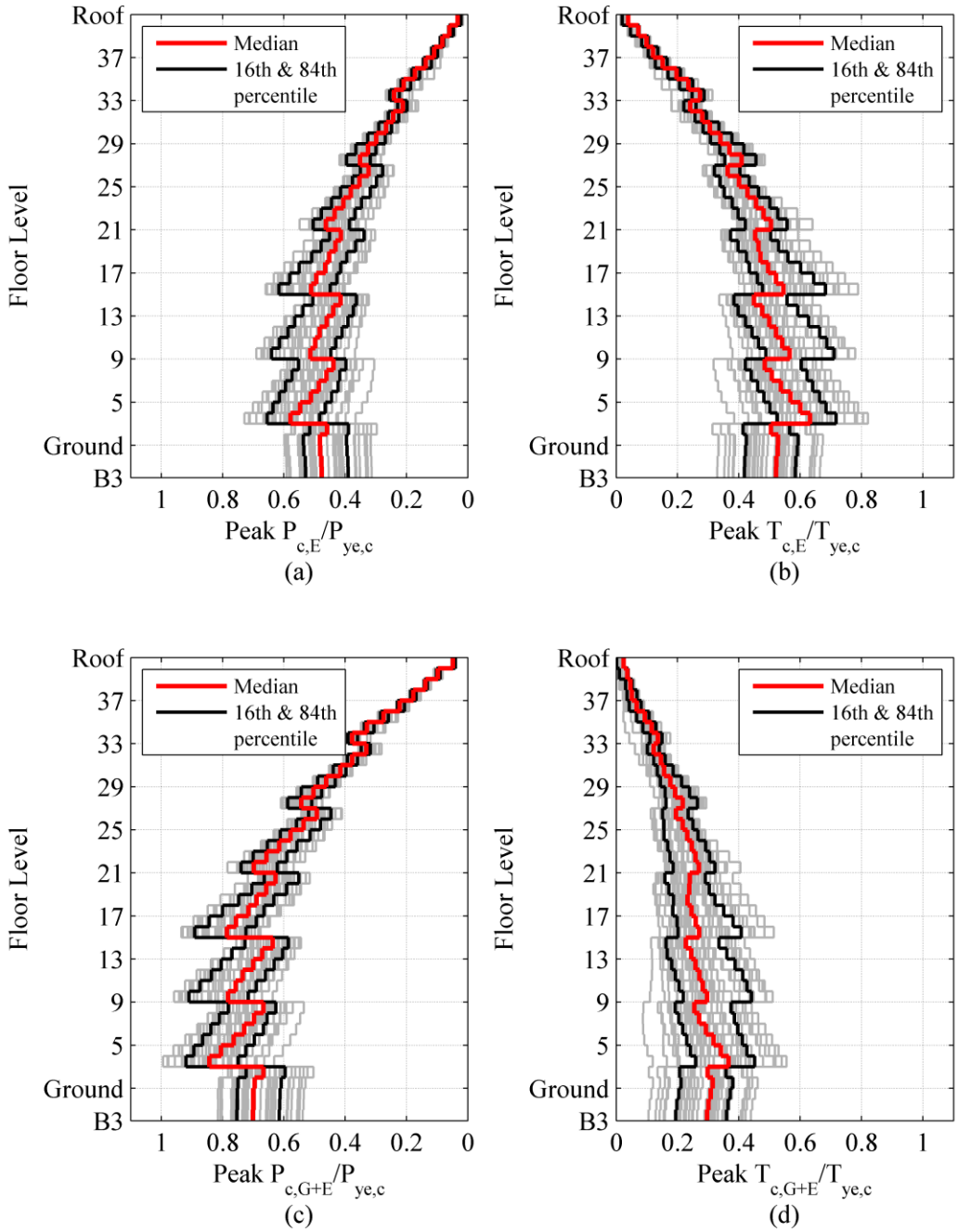

Figure 7.19: Column normalized peak tensile and compressive force due to seismic loading (E) and combined gravity and seismic loading (G+E); NRHA results in X-loading direction (BSE-2E)

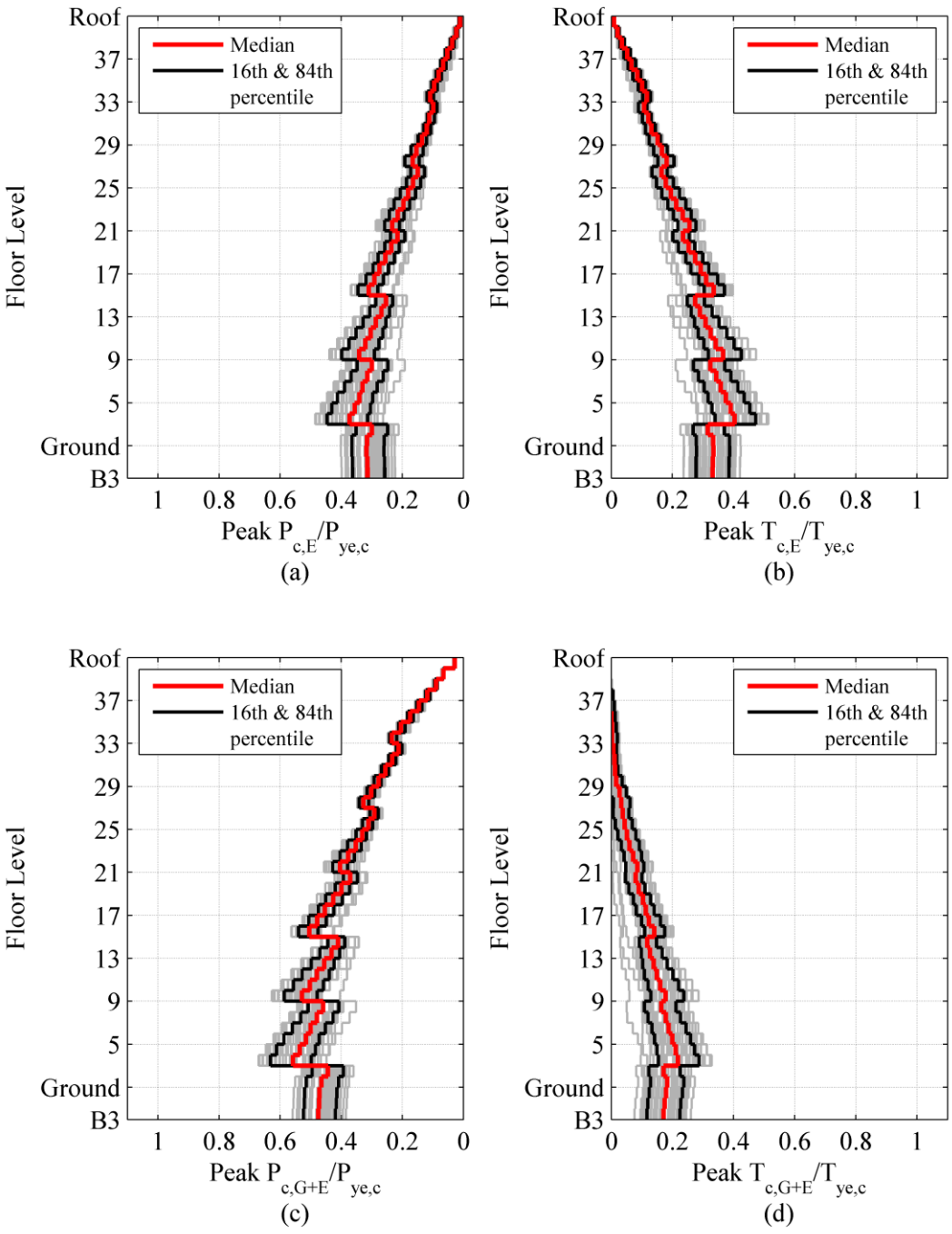

Figure 7.20: Column normalized peak tensile and compressive force due to seismic loading (E) and combined gravity and seismic loading (G+E), NRHA results in Y-loading direction (BSE-2E)

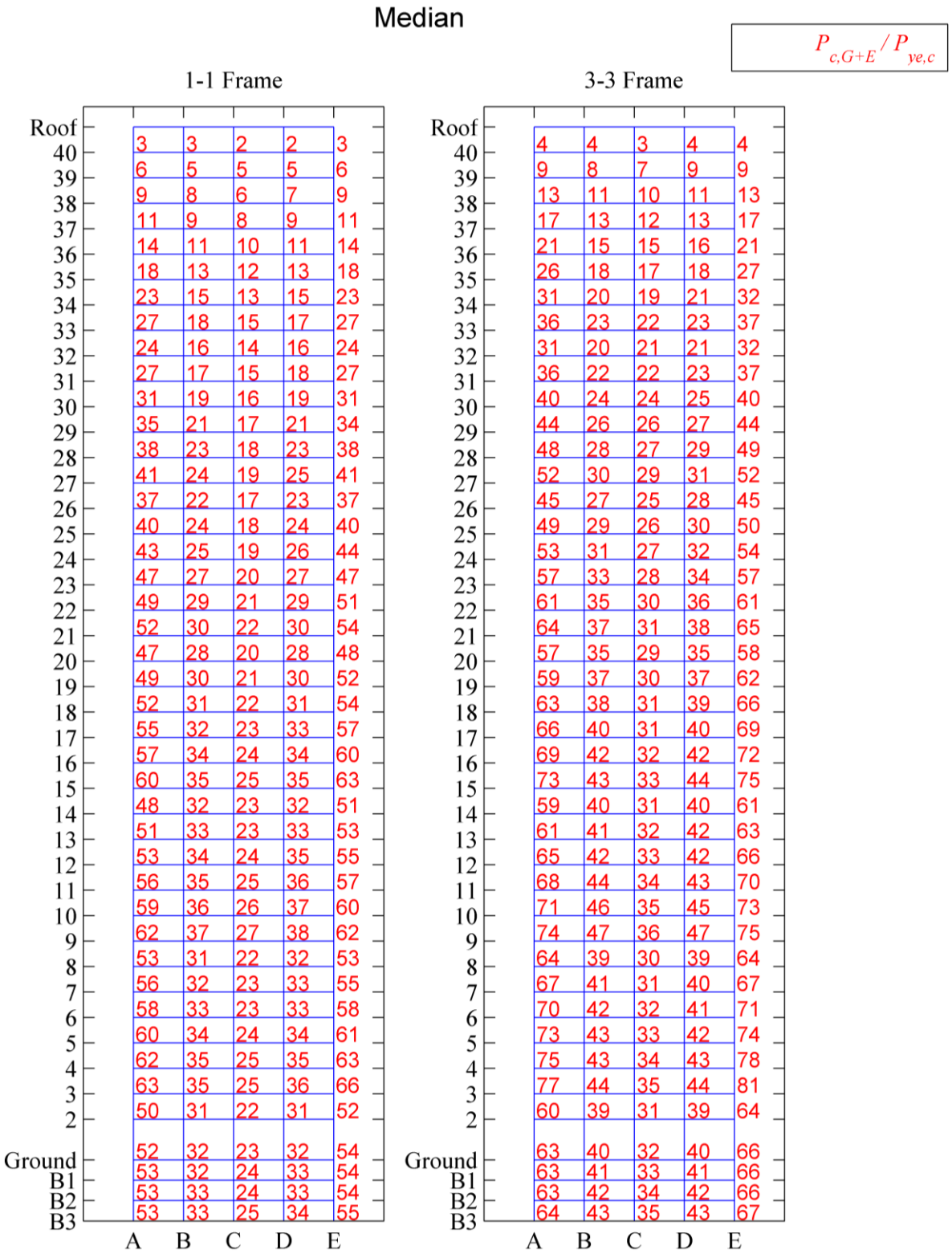

Figure 7.21: Median column normalized peak compressive force (in %) due to seismic and gravity loads (G+E), NRHA results in X-loading direction (BSE-2E)

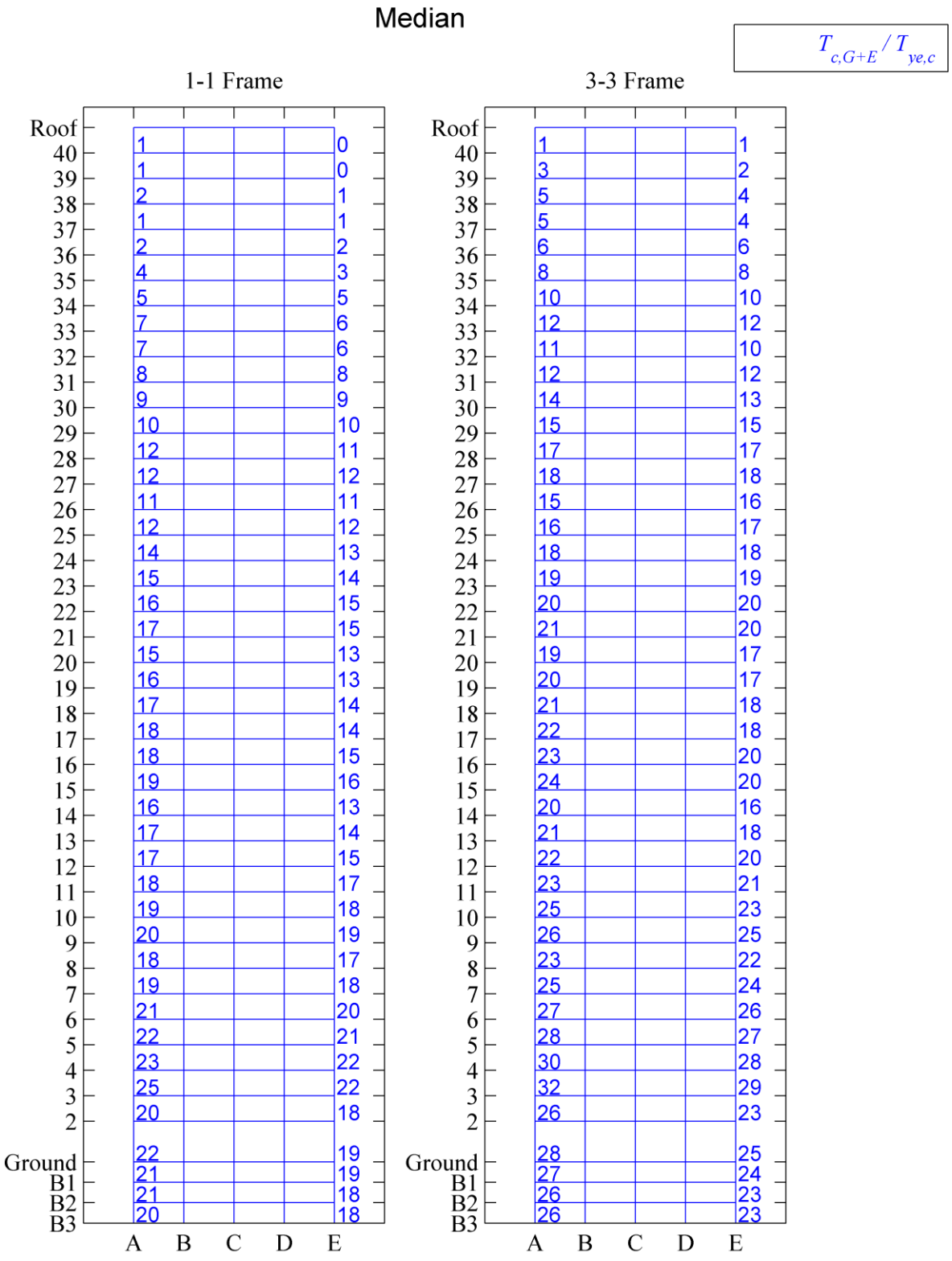

Figure 7.22: Median column normalized peak tensile force (in %) due to seismic and gravity loads (G+E), NRHA results in X-loading direction (BSE-2E)

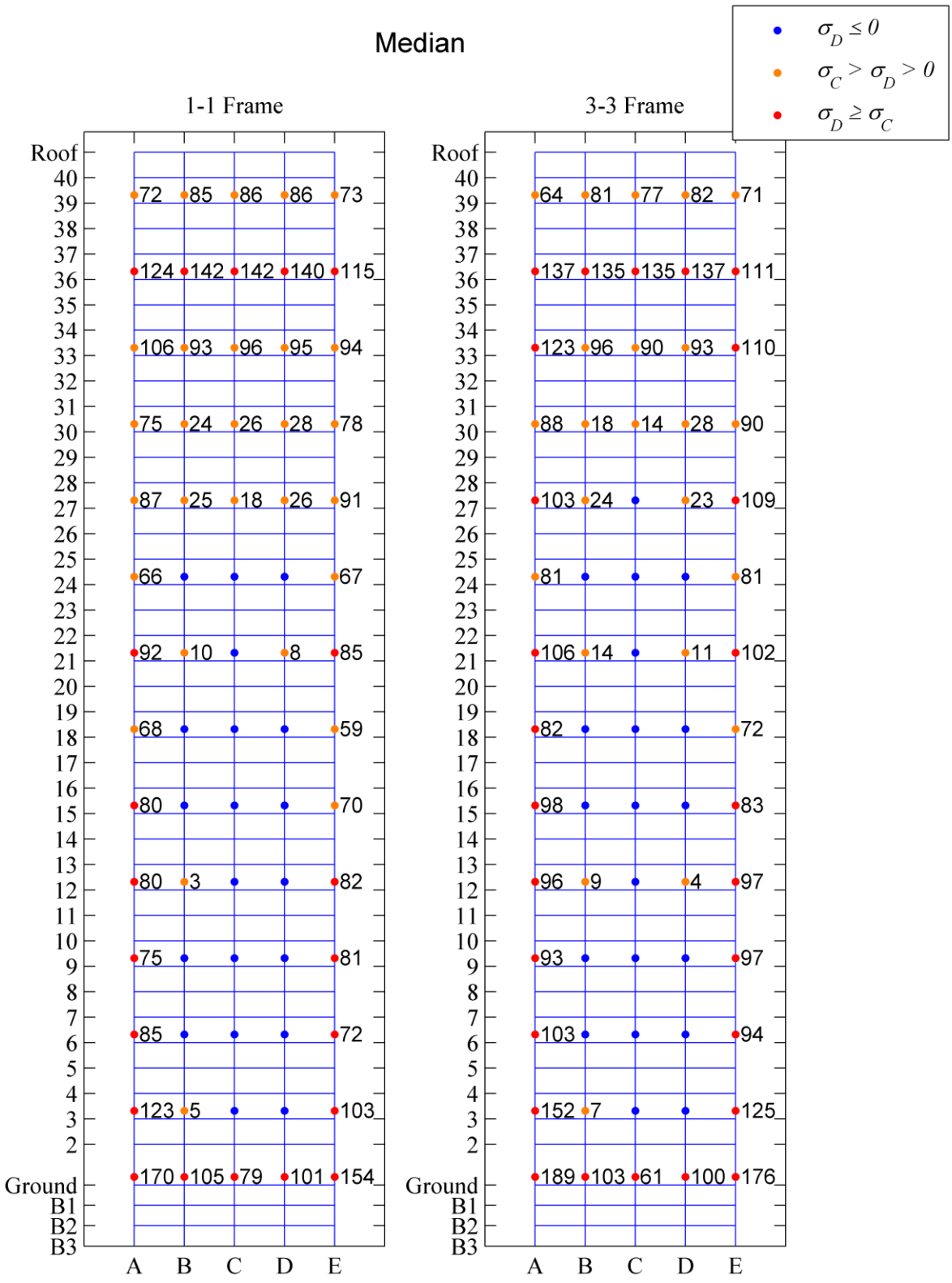

Figure 7.23: Median peak tensile stress at column splices [MPa], NRHA in X-loading direction (BSE-2E)

CHAPTER 8 : Seismic Retrofit of a 1970s High-Rise Steel Frame Building with Supplemental Damping Devices

8.1 Introduction

A number of tall buildings were constructed between 1960 and 1990 in seismic regions of the West Coast of North America. Particularly those with above 35 stories consist of steel space moment-resisting frames (MRFs) (Almufti et al. 2012). Many of these buildings have been designed according to codes (ICBO 1973), in which seismic design loads were not based on a detailed seismic hazard assessment. Notably, dynamic analysis methods were not mandatory for the seismic assessment of tall buildings. These buildings were not designed to satisfy modern capacity design principles. The seismic vulnerability of pre-Northridge steel MRF buildings was demonstrated by numerous past studies (Hall et al. 1995; Maison and Bonowitz 1999; Gupta and Krawinkler 2000; Luco and Cornell 2000; Lee and Foutch 2002; Muto and Krishnan 2011) as well as the nonlinear seismic assessment of the prototype 1970s high-rise steel-frame building shown in Chapter 7. Several other existing steel-frame buildings have not been retrofitted due to financial challenges and reluctance of their owners (Bjornsson 2014). Recent studies with 1970s

tall buildings showed clearly the necessity of their seismic rehabilitation (Bech et al. 2015; Lai et al. 2015; Hutt et al. 2016).

Conventional upgrade techniques for tall buildings, such as stiffening (e.g., by adding steel braces), generally leads to an increase of the seismically-induced forces; often times the strengthening of framing members as well as the foundation is inevitable (Bjornsson 2014). Energy dissipation devices, such as velocity-dependent dampers may be effectively utilized in this case. For instance, fluid viscous dampers have been implemented in various buildings in North America (Constantinou et al. 1993; Symans and Constantinou 1998; Uriz and Whittaker 2001; Symans et al. 2008; Malley et al. 2011). Alternatively, oil dampers with relief valve have been widely used in several buildings in Japan. Recent shake-table tests underscore the effectiveness of such devices (Kasai and Matsuda 2014). Notably, tall buildings equipped with oil dampers demonstrated high performance during the 2011 Tohoku earthquake in Japan (Kasai et al. 2013b).

Guidance for the design and assessment of energy dissipation devices for buildings can be found in ASCE 7-10 (ASCE 2010) and ASCE 41-13 (ASCE/SEI 2014). Nonetheless, the focus of these guidelines is mainly on low- to mid-rise buildings. More recently, guidelines have been developed for the performance-based design and assessment of tall buildings (CTBUH 2008; PEER 2010; LATBSDC 2014), however, the challenge on how to effectively retrofit existing tall buildings still remains. The use of novel damper technologies, such as oil dampers with relief valves is also not covered.

A commonly used simplified design methodology for designing oil dampers is the performance curves Kasai et al. (2008a) that is based on linearization methods. Due to the linearization

method errors (see Chapter 6), an improved methodology has been proposed in Chapter 7, which uses simplified models to overcome several of the linearization method shortcomings. Past research considered cases that although the existing steel-frame building was retrofitted it still behaved in the nonlinear regime (Ramirez et al. 2001; Guo and Christopoulos 2013a). These studies are limited to low- and mid-rise buildings. More recent studies illustrated the implementation of several retrofit solutions for existing tall buildings in seismically prone areas. These solutions include conventional and buckling-restrained braces (Bjornsson 2014), nonlinear fluid viscous dampers (Lai et al. 2015), as well as base isolation and elastic rocking wall spine (Hutt et al. 2016). In this context, the use of oil dampers with relief valves is interesting because the axial force that is transmitted to the steel columns of the tall building can be capped if deemed to be necessary.

This chapter presents a seismic retrofit strategy for 1970s tall buildings by means of utilizing oil dampers with relief valve. The 40-story prototype building that was presented in Chapter 7 is used as the base case. Its main seismic deficiencies were identified and summarized in the same chapter. Several retrofit schemes are proposed and discussed based on the MDF performance curve methodology that was proposed in Chapter 6. The effect of various damping levels and vertical distributions methods on the building's performance is assessed by a comparative study that considers the potential nonlinearity of the building itself. A vertical damping distribution method is also proposed that could be useful in cases that frame yielding is inevitable.

8.2 Design Objectives for Retrofit

According to ASCE 41-13 (ASCE/SEI 2014) in case the building is selected to be at Risk Category II per ASCE 7-10 (ASCE 2010), the performance objective for the existing building at BSE-1E and BSE-2E hazard levels are life safety and collapse prevention, respectively. If the

Risk Category III is selected, performance objectives are increased to damage control and limited safety, respectively. The aim of this study is not to satisfy a certain objective, but to explore multiple retrofit options and demonstrate the effect of different damping levels and damping distribution methods on the response of the building. In Chapter 7, results from nonlinear static analysis showed that the tall building under consideration (see Figure 8.1 and 8.2) exhibited first yielding and collapse at roof drifts greater than 0.5% and 1%, respectively. One of our main retrofit design objectives is to minimize the inelastic deformations within the steel MRFs. To achieve this a 0.5% roof yield drift ratio can be targeted from the nonlinear static analysis conducted in Chapter 7 (see Section 7.4.2). This corresponds to a required reduction factor of about R_d = 0.3. From Chapter 6 (see Figure 6.25), a damper loss stiffness to frame stiffness ratio K_d''/K_f=5, corresponds to a highly-damped building that it may not be economically feasible or practical. On the other hand, low supplemental damping (i.e., $K_d''/K_f = 0.1$) may not improve the significantly the building performance. The base shear force (or floor absolute acceleration) reduction is another important objective of an efficient seismic retrofit design. The MDF performance curves (see Figure 6.25c) suggest that K_d''/K_f ratio shall not exceed 1.0 for optimal force control. Oversized dampers may result into a high seismic base shear, which may require an additional retrofit of the foundation system. Stresses in framing members, such as columns and splices may also increase in this case.

Three levels of supplemental damping are considered (i.e., K_d''/K_f =0.25, 0.5, 1.0) as summarized in Table 8.1. According to the initial design assumptions (see Table 6.2), in the 'low damping' case (K_d''/K_f =0.25) the expected effective damping ratio is about 6%. At this damping level, excessive plastic deformation is expected in the existing frame. For 'medium damping' (K_d''/K_f =0.5) the effective damping ratio increased to 11%. Finally, for the 'high damping' case,

(K_d''/K_f =1.0) 18% effective damping is provided. At this level, limited inelastic behavior is expected in the frame. The initial design assumptions should be verified due to limited number of available damper sizes as discussed in the subsequent section.

8.3 Design of Oil Dampers and its Effect on Initial Design Assumptions

In Chapter 6 the lateral damper properties at each story were determined for the prototype building through performance-curves method. These properties should be transformed to design the properties of each damper within a story. Figure 8.3 shows the typical damper components of a bilinear oil damper. If the dampers are installed in a diagonal brace configuration, the required initial damping coefficient $\hat{C}_{di,j}$, the internal damper stiffness $\hat{K}_{di,j}$, the supporting brace stiffness $\hat{K}_{bi,j}$, the relief load $\hat{F}_{dri,j}$ and the relief velocity $\hat{v}_{dri,j}$ of the damper j at story i can be determined as follows,

$$\sum_{j=1}^{n_{di}} \hat{C}_{di,j} \cos^2 \theta_{i,j} \geq C_{di} \tag{8.1}$$

$$\sum_{j=1}^{n_{di}} \hat{K}_{di,j} \cos^2 \theta_{i,j} \geq K_{di}, \quad \sum_{j=1}^{n_{di}} \hat{K}_{bi,j} \cos^2 \theta_{i,j} \geq K_{bi} \tag{8.2}$$

$$\sum_{j=1}^{n_{di}} \hat{F}_{dri,j} \cos^2 \theta_{i,j} \geq F_{dri} \tag{8.3}$$

$$\hat{v}_{dri,j} = \frac{\hat{F}_{dri,j}}{\hat{C}_{di,j}} \tag{8.4}$$

in which, n_{di} is the number of dampers at story i; $\theta_{i,j}$ the inclination angle of the dampers; C_{di}, K_{bi} and F_{dri} are the total lateral damping coefficient, brace stiffness and damper force at each story computed in design, respectively. In order to maximize the peak damper velocity ratio, μ_d, the dampers sizes with the lowest relief velocity (1.8 cm/s) are selected. In this case, the post relief

damping coefficient ratio of $p = 0.0168$. The brace stiffness $\widehat{K}_{bi,j}$ and internal damper stiffness $\widehat{K}_{di,j}$ are computed based on the largest available stroke of the corresponding damper size. The internal damper stiffness can be directly obtained from Table A1 (see Appendix A), while the stiffness of the supporting brace $\widehat{K}_{bi,j}$ can be computed as follows,

$$\hat{K}_{bi,j} = \frac{E_b A_{bi,j}}{L_{bi,j}} \tag{8.5}$$

$$L_{bi,j} = L_{toti,j} - L_{di,j} - L_{rigidi,j} \tag{8.6}$$

in which, E_b is the modulus of elasticity of the supporting steel brace (205 GPa); $A_{bi,j}$ and $L_{bi,j}$ are the cross-sectional area and the length of the supporting brace; $L_{toti,j}$ is the total diagonal length between working points; $L_{di,j}$ is length of the damper portion which can be obtained from Table A1; $L_{rigidi,j}$ is the rigid zone length, which is 1000 mm in this case. The supporting brace's length, $L_{bi,j}$ refers to the damper assembly length excluding the damper portion and the rigid zone length. It is also assumed that $A_{bi,j}$ is valid for the entire $L_{bi,j}$. Thus, the mechanical model that represents the bilinear oil dampers in Figure 8.3b reduces to that shown in Figure 8.3c.

Table 8.1 summarizes the final design SDF parameters according to the performance curve methodology for the X-loading direction for three damping levels. At the initial design stage, a designer should identify the K_b/K_{fs} (or K_b/K_d'') ratio, the internal damper stiffness ratio β_k or the peak damper velocity ratio, μ_d to be used to satisfy the retrofit design objectives. The initial SDF design parameters may require adjustment to assure compatibility between the design and the selected damper properties. To this end, the resultant K_b/K_{fs} and K_b^*/K_{fs} ratios are computed and compared with K_d''/K_{fs} of the initial design assumption. Nine different design scenarios (3 damping level x 3 distribution methods) are considered for the X-loading direction. Among all the design cases, the available damper sizes led to a K_b/K_d'' ratio between 4.4 to 6.3

and a K_b^*/K_d'' ratio between 1.6 and 2.4. A $K_b/K_d'' = 4.0$ is considered for SDF design. Referring to Table A1 and Table A2 (see Appendix A), dampers with a relief velocity $\hat{v}_{dri,j} =$ 1.8 cm/s have an internal damper stiffness coefficient β_k that varies between 4.6 to 8.2 depending on the maximum damper force and stroke. The most commonly used dampers achieve a maximum force of 2000 KN. Therefore, based on their largest stroke it is assumed that $\beta_k = 4.6$ for the SDF design. The initial design aims for $\mu_d = 2$ for all three damping levels. However, the required damper relief velocities $\hat{v}_{dri,j}$ from Eq. 8.4 is found lower than 1.8 cm/s in medium and high damping cases. Therefore, μ_d is reduced to 1.2 and 1.5 for the medium and high damping levels, respectively, in order to assure compatibility between the design and the selected damper properties. The damper design is based on the required relief force. Care is given not to oversize the dampers in order to provide a fair comparison between different design cases. The mean over strength ratio of dampers in all design cases is between 1.07-1.11. Details regarding the damper design and placement for the examined scenarios are presented in the next sections.

8.4 Horizontal and Vertical Damper Distribution

The damper configuration and placement has significant impact on the efficiency of the retrofit solution (Constantinou et al. 2001; Liang et al. 2011; Hwang et al. 2013). This is particularly evident in tall buildings. The dampers are placed as diagonal braces mainly in exterior frames, which are considered to be more effective for controlling torsional vibrations. Furthermore, installing dampers at the same locations is more practical because it reduces the number of work locations (Malley et al. 2011). Due to the limited number of available bays in exterior frames of the X-loading direction (e.g. 1-1 frame) some of the dampers are placed in the interior frames as well (e.g. 3-3 frame). Figure 8.1 shows the typical damper locations for the selected design

scenarios (i.e., low, medium and high damping levels). The larger the damping level the more bays are required for the damper placement.

A preliminary comparative study with different damping levels and distribution methods was carried out in the X-loading direction only. Ten ground motions (GMs) were only employed in this case for the nonlinear building assessment. The dampers are modelled diagonally by utilizing truss elements (i.e., *twoNodeLink*). The *BilinearOilDamper* material model that was developed and presented in Chapter 3 is assigned to the truss elements.

8.4.1 Effect of Horizontal Damper Placement on Engineering Demand Parameters

The effect of flexural deformation of the frame on the dampers may vary depending on the horizontal damper placement. In order to examine the efficiency of the damped bays, the displacement transmission factors $\alpha_{N,i,j}$ can be computed. These are the horizontal damper end displacement to the relative story displacement ratios (Kasai and Iwasaki 2006; Kasai et al. 2013a). To this end, the 2D model of the tall building is displaced under the code-based lateral load pattern (ASCE 2010). By using dummy braces at each bay the brace displacement $\hat{u}_{aN,i,j}$ is recorded. Therefore, the displacement transmission factors $\alpha_{N,i,j}$ can be computed as follows,

$$\alpha_{N,i,j} = \frac{\hat{u}_{aN,i,j} / \cos\theta_{i,j}}{u_{N,i+1} - u_{N,\mathrm{i}}} \tag{8.7}$$

in which, $u_{N,i+1}$ and $u_{N,i}$ are the floor displacement at floor *i* and *i +1*. The subscript *N* denotes here no axial stiffness is provided by the dummy braces when the displacements are recorded.

Figure 8.4 shows the displacement transmission factors $\alpha_{N,i,j}$ for the inverted-V type damper placement in the 1-1 and 3-3 frames of the X-loading direction. Note that the $\alpha_{N,i,j}$ values correlate with the frame stiffness to the frame shear stiffness ratios K_{fi}/K_{fsi} (see Chapter 6

Table 6.3). It is clear that the contribution of the shear deformation to the total displacement is minimal in the upper stories when the building remains elastic. The $\alpha_{N,i,j}$ values are larger in interior bays and smaller in exterior bays due to the higher column axial deformations of exterior columns. The K_{fi}/K_{fsi} ratio at each level can be considered as the mean value of the $\alpha_{N,i,j}$ values of the corresponding story, conditioned that the only source of loss of displacement transmission is the axial deformation of the columns. To verify this assumption, the column axial deformations were limited. Thus, the $\alpha_{N,i,j}$ ratios became closer to unity as shown in Figure 8.5. Nevertheless, there was still 0-10% loss of displacement transmission. This is attributed to the panel-zone flexibility considered in the 2D model. In this case, the dampers are placed between panel-zone joints, as implemented in practice. In centerline models, the $\alpha_{N,i,j}$ ratios become exactly equal to 1.0. Similar trends are observed in the A-A frame of the Y-loading direction (see Figure 8.6). The results suggest that placing dampers in interior bays maximizes the damper efficiency. This is also beneficial for exterior columns that exhibit high axial stresses particularly in the X-loading direction.

In order to observe the effect of horizontal damper placement on the story-based engineering demand parameters (EDPs), a comparative study is conducted by considering different damper placement for low damping level, because the difference in EDPs could be more evident in this case. Two damper configurations are considered. In particular, the dampers are placed at the interior bays and the exterior bays as shown in Figures 8.7 and 8.8, respectively. Response history analysis was carried out with 10 GMs to compare the results with simplified flexural-shear beam model (FSBM) as discussed in Chapter 6. In this case, the 2D frame model is kept elastic. Referring to Figure 8.9, the FSBM predicts well the response of the retrofitted building. If the dampers are placed in interior bays, the story drift ratios are lower than anticipated based

on the FSBM. If the dampers are placed in the exterior bay, the story drift ratios become larger. This is attributed to the difference of $\alpha_{N,i,j}$values from K_{fi}/K_{fsi} ratios for the corresponding damper placement. The reason why EDPs predicted by FSBM were slightly closer to the 2D interior bay case, is attributed to the fact that the non-flexural 0-10% loss of displacement transmission led to small increase in EDPs that were obtained from the 2D models. In our case non-flexural $\alpha_{N,i,j}$ values are minimal and may be ignored.

8.4.2 Effect of Vertical Damping Distribution

In Chapter 6 it was shown that the effective shear force proportional damping distribution (SFPDD) was the most effective method in terms of achieving a uniform story drift ratios among the methods that were considered. This comparison was conducted based on an elastic frame.

In this case, the efficiency of the damping distribution method is examined on the basis of potentially nonlinear frames. The dampers are designed based on two distribution methods, the effective and the direct SFPDD. Figures 8.7, 8.10-8.14 show that maximum damper design forces and their locations based on the considered distribution methods for low, medium and high damping levels, respectively. In the X-loading direction the dampers are placed mainly at the upper half of the building based on the effective SFPDD method. According to the direct SFPDD method damping is provided at each level it decreases gradually with the increasing height similarly to the story shear forces.

After the damper designs are completed, NRHAs are conducted with nonlinear 2D models of the building in the X-loading direction by utilizing 10 GMs scaled at the BSE-2E level. Figures 8.15 - 8.17 show the median EDPs for different design cases for low, medium and high damping levels. In these figures, L-E, M-E and H-E stand for effective SFPDD for low, medium and high

damping levels; L-V, M-V, H-V represent the direct SFPDD cases. Referring to Figure 8.15, the design at low damping level according to the effective SFPDD method led to bottom story collapses. This is not in agreement with the elastic frame analysis based on the effective SFPDD method in which a more-or-less uniform peak SDR distribution was achieved. The peak SDRs are observed in the upper stories of the building based on the direct SFPDD method. In this case, the number of collapses was less. The higher the damping level becomes the less concentration of peak SDRs is observed in all design cases (see Figure 8.17). This is due to the limited inelastic behavior of the retrofitted frame.

8.4.3 Balanced Vertical Damping Distribution

The effective SFPDD method determines the required loss stiffness K''_{di} of the damper based on its storage stiffness K'_{ai}; while the required storage stiffness K'_{ai} of the damper is obtained from subtracting the total storage stiffness K'_i from the elastic frame shear stiffness K_{fsi}. This implies that the effective SFPDD method assumes that the building will maintain its elastic stiffness during an earthquake. This assumption may not be valid for low-probability of occurrence earthquakes. If the direct SFPDD is employed, the required loss stiffness K''_{di} of the damper is computed in proportion to the shear force distribution without considering the frame's stiffness distribution. Referring to Figure 8.19a and Figure 8.19c, a comparison of the required loss stiffness K''_{di} according to the effective and direct SFPDDs is shown for the low damping level in X-loading direction, respectively.

The effective SFPDD is an adequate solution if the building remains elastic, whereas the direct SFPDD is appropriate if the retrofitted building experiences excessive yielding. An appropriate distribution method should be efficient for seismic intensities associated with both serviceability and collapse prevention. A balanced distribution method should be employed (noted as balanced

SFPDD). To compute the loss stiffness based on the balanced SFPDD ($K''_{di,B}$) the weighted average of the loss stiffness obtained from the effective ($K''_{di,E}$) and direct SFPDDs ($K''_{di,V}$) can be considered,

$$K''_{di,B} = \gamma K''_{di,\mathrm{E}} + (1-\gamma) K''_{di,V} \tag{8.8}$$

in which, γ is a weight factor, ranging between 0 and 1. This parameter is dependent on the expected level of displacement ductility exhibited by the building. When the frame ductility increases, γ approaches zero and the damping distribution is essentially identical with the direct SFPDD. The parameter γ approaches unity otherwise. In the considered design scenarios, frame yielding is expected; therefore it is assumed that $\gamma = 0.5$. However, further study is required to assess the effect of frame inelasticity on the effective damping and response reduction in order determine the optimal γ factor.

Figure 8.20 indicates the required loss stiffness of the dampers ($K''_{di,B}$) according to the balanced SFPDD method. Unlike the effective SFPDD method, supplemental damping is provided at every story that makes the proposed retrofit solution more redundant. Moreover, the elastic distribution and possible vertical irregularity of the frame stiffness is considered by partially accounting for the effective SFPDD method. Figures 8.21 to 8.23 show the damper design for the seismic retrofit of the tall building based on the balanced SFPDD method for low, medium and high damping levels, respectively. The comparative study was conducted with 10 GMs. Comparisons of the median values are shown in Figures 8.15 to 8.17. It can be seen that the balanced SFPDD provides the most uniform distribution, specifically for low and medium damping levels (L-B, M-B, H-B) compared to the effective and SFPDD methods. Figure 8.18 shows a comparison of the maximum peak story drift ratios obtained from 10 GMs, with three damping levels and distribution methods. In all cases, the peak SDRs were reduced by

considering the highest damping level. The balanced SFPDD method reduces the peak SDRs below 1.5% in 5 cases at medium damping level, compared to 3 and 2 cases observed in effective and direct SFPDD methods, respectively. The number of collapses is 4, 2 and 1, in the case of the effective, balanced and direct SFPDD methods at the lowest damping level, respectively. This could be attributed to the fact that the peak SDR distribution is dependent on the flexural deformations in addition to those from shear; thus a uniform peak SDR distribution along the building height does not guarantee a uniform damage distribution. This would require shear deformation demands at the lower stories in order to balance the additional SDRs due to flexural deformation seen in the upper stories. In theory, the target for the optimal balanced SFPDD is to provide a uniform story shear deformation distribution, as the loss stiffness of the dampers is distributed by accounting for the shear frame properties (see Chapter 6). However, in order to achieve this objective a more rigorous estimation of the γ factor is required, which is outside the scope of this thesis. The comparative evaluation was carried with the GMs scaled at the BSE-2E level, which led the non-retrofitted building to collapse. In this case, the effective SFPDD method is typically not expected to provide an efficient retrofit solution, particularly at a low damping level. If a high damping level were to be considered none of the distribution methods suggest that building collapse occurs. In fact, the peak SDRs range between 0.01-0.03.

8.5 Final Retrofit Solution and Seismic Assessment of the Retrofitted Building

A final retrofit solution is selected based on the balanced distribution method and the medium damping level. Thus, NRHAs are carried out with the numerical model representation of the retrofitted building. Forty GMs are employed in this case that are scaled at the BSE-1E and BSE-2E seismic intensities in both loading directions as discussed in Chapter 7.

8.5.1 Seismic Assessment of the Retrofitted Building

Figures 8.24 and 8.25 illustrate the peak story-based EDPs (i.e. peak normalized story shear forces, the maximum absolute floor accelerations and the peak normalized floor displacements) for a medium damping level obtained from NRHAs in the X-loading direction at the BSE-1E and BSE-2E levels, respectively. The median, 16th and 84th percentile responses are superimposed in the same figures. Referring to the two figures, the observed difference in the roof drift ratio is more remarkable than that in peak SDRs between the two seismic intensities. This is attributed to a number of reasons: (a) the fact that the story drifts in the upper stories is mostly controlled by flexural deformations; (b) at higher seismic intensities, the story drift demands migrate in lower stories. This is consistent with prior studies (Gupta and Krawinkler 1999; NIST 2010a; Elkady and Lignos 2014; Elkady and Lignos 2015); (c) the balanced SFPDD method is effective in controlling peak SDRs. Referring to Figures 8.24a and 8.25a, the 84^{th} peak SDR percentiles amplify in the lower stories. This is more evident at the BSE-2E level (see Figure 8.25a).

Referring to Figures 8.24b and 8.25b, the median peak normalized base shear is $0.107W$ and $0.124W$ at the BSE-1E and BSE-2E seismic intensities, respectively. The peak response of the median absolute floor accelerations (0.57g and 0.69g at BSE-1E and BSE-2E levels, respectively) along the building height is observed at the roof. Same observations hold true for the seismic performance of the retrofitted building in the Y-loading direction (see Figures 8.26 and 8.27).

The histogram of the peak and residual SDRs in the X-loading direction of the building is shown in Figure 8.28 for low, medium and high damping levels at the BSE-2E seismic intensity. For comparison purposes, the non-retrofitted building response is superimposed in the same figure. From the same figure, it is evident that for medium and high damping levels the retrofitted building achieves the collapse prevention objective.

Referring to Figure 8.28b in 12, 14 and 23 cases the peak residual SDRs are below 0.2% at low, medium and high damping levels, respectively. Residual deformations are mainly observed in the bottom stories of the retrofitted building unlike the non-retrofitted one. Figure 8.29 shows the peak SDRs and residual peak SDRs for the medium damping level in the X-loading direction at the BSE-1E and BSE-2E seismic intensities. Note that the retrofitted building did not experience any collapse at the BSE-1E level. In 32 of the GMs, the peak residual SDRs is below 0.2%, implying that the building remains elastic or almost elastic for most of the GMs scaled at the BSE-1E intensity. Same observations hold true for the Y-loading direction (see Figure 8.30). The number of collapses is reduced from 13 to 3 at the BSE-2E seismic intensity. Notably, in 37/40 GMs the maximum of the residual SDRs is less than 0.2% at the BSE-1E seismic intensity.

8.5.2 Local Engineering Demand Parameters (EDPs)

A more comprehensive discussion for the retrofitted building seismic assessment is carried out. In this case the focus is on local member EDPs (i.e., plastic hinge location, beam plastic rotations, column axial force demands, column splice stresses, peak damper stroke, damper forces and post relief velocities). This is achieved through a post-processing script that is written in *MATLAB* (v. R2013b).

Plastic Hinge Location based on Onset of Yielding

Figure 8.31 shows the location of beam, column and panel zone yielding in the X-loading direction of the retrofitted building configuration. The values represent the 84% percentile of the 40 NRHAs at the BSE-2E hazard level. The effective yield moment of the beams ($M^*_{y,b}$) and that of the panel zones ($M^*_{y,pz}$) as well as the column reduced plastic moment capacities, $M^*_{pe,c}$ are computed as discussed in Chapter 7 (see Section 7.4.4). Referring to Figure 8.31, the effective yield moment of all the beams is exceeded in the X-loading direction at the BSE-2E hazard level.

The column moment demands are less than their reduced plastic moment capacity in the upper half of the retrofitted building indicating a significantly improved seismic performance compared to the non-retrofitted building. This is associated with the fact that collapses in the upper stories are prevented. However, no improvement is observed in the exterior column demands in the lower half of building. This is attributed to the column axial force demand increase at the BSE-2E level, which is discussed later on. The panel zones remained elastic regardless of the seismic intensity of interest.

Beam Rotational Demands

The plastic rotation of each beam is recorded and compared with its characteristic rotation levels, such as yielding, capping and ultimate rotation, which are computed as discussed in Hartloper (2016) and Lignos and Krawinkler (2011) for beams in pre-Northridge (so-called brittle) and post-Northridge (so-called ductile) fully restrained beam-to-column connections, respectively. Referring to Figure 7.18, the peak beam plastic rotation is generally below their corresponding capping rotation in the upper stories, which is a significant improvement compared to what was observed in the non-retrofitted building; however, the lower story beams exhibit high plastic rotation demands. Many of them exceed their ultimate rotation capacity. Due to the non-uniform distribution of the flexural deformations along the building height, the lower stories experience higher shear deformation demands. This explains that dynamic instability occurred in four cases that are associated with bottom story mechanisms at the BSE-2E level.

Column Axial Load Demands

Figure 8.33 shows the column peak normalized compressive and tensile forces at each story of the retrofitted building in the X-loading direction at the BSE-2E level. Figures 8.33c and 8.33d show the column normalized peak compressive forces ($P_{c,G+E}/P_{ye,c}$) and peak tensile forces

($T_{c,G+E}/T_{ye,c}$ ratios). By subtracting the compressive forces due to gravity loading, Figures 8.33a and 8.33b indicate the normalized peak compressive forces ($P_{c,E}/P_{ye,c}$ ratios) and tensile forces ($T_{c,E}/T_{ye,c}$ ratios) due to earthquake loading only.

The column normalized compressive forces are higher than those observed in the non-retrofitted building in the same loading direction (see Figure 7.19 in Chapter 7). Due to the lesser number of collapses in the retrofitted configuration, the forces induced by the mechanisms developed at beams are successfully transmitted through the columns to the bottom stories. The peak values are more scattered compared to the non-retrofitted building. In many cases, the peak compressive forces exceed the axial yield capacity $P_{ye,c}$ of the columns. The column compressive forces are about $0.1P_{ye,c}$ less than those observed in the non-retrofitted building at the BSE-1E seismic intensity. Referring to Figure 8.33d, higher tensile forces are observed, in few ground motions. In particular, the tensile forces exceed $0.6T_{ye,c}$.

Figures 8.34 and 8.35 show the effect of damper placement on the column forces. In this case, the median column normalized peak compressive forces between exterior and interior B-axis columns is larger than the non-retrofitted building. This is more evident in 1-1 Frame, where dampers are densely installed. This increase is due to the additional forces that the framing members experience due to the damper placement.

Referring to Figure 8.35, although the tensile forces at B-axis columns in 1-1 Frame slightly increase in comparison to the non-retrofitted building (see Figure 7.22) the damper placement in internal bays is a wise strategy because the interior columns should not be upgraded. There is practically no difference in the force demands in the majority of middle-interior C-axis columns. This is achieved with the inverted-V diagonal placement of the dampers, thus, if the damper

sizes are equal then the compressive and tensile damper forces cancel each other. For instance, in the upper stories of the 1-1 frame (i.e., from 36th to 40th stories as shown in Figure 8.22) the dampers are single or do not have the same size; therefore, the interior column compressive forces at story 36 increase from $0.10P_{ye,c}$ to $0.16P_{ye,c}$ in the retrofitted configuration.

Column Splice Demands

The partial joint penetration weld fractures in column splices is closely related to the peak flange tensile stress demand and the estimated flange fracture stress capacity σ_C of splices is dependent to the material toughness, the crack length, the flange thickness of the upper and lower columns (Galasso et al. 2015; Stillmaker et al. 2016). The peak tensile stress, σ_D, at the smallest column cross-section joining a splice is extracted in the same manner as discussed in Section 7.4.4 of Chapter 7. Figure 7.23 shows the median peak tensile stresses at the column splices at the BSE-2E seismic intensity. The orange dots indicate that the splice is subjected to tensile stresses; if the stress exceeds the corresponding capacity then it is marked with a red dot. The dots are blue if no tensile stress is observed.

The exterior column splices of the retrofitted building experience tensile stresses. Compared to the non-retrofitted building there is a significant reduction of the tensile stresses in the upper story column splices; while the stresses increase in the lower stories. This is attributed to the prevention of collapse mechanisms in the upper stories of the building due to the damper placement. From the same figure, despite of the drastic reduction in the peak SDRs of the retrofitted building configuration, the reduction in the tensile stresses at the column splices is fairly minimal. However, if the retrofit strategy is based on the median response then it is not necessary to retrofit the upper story column splices at the BSE-2E hazard level. The ones at the lower half exterior columns as well as the first story column splices need only to be updated.

Damper Stroke and Post-Relief Velocity Ratios and Forces

Comparing the computed peak damper response demands (i.e., damper stroke, velocity and force) with the allowable values is an important step towards the proper damper properties selection. Figure 8.37 indicates the median values of the peak damper strokes obtained from 40 NRHAs at the BSE-2E level in the X-loading direction. In order to compare with the damper stroke limits, peak damper displacements $\hat{u}_{di,j}^{\max}$ are computed after subtracting the supporting brace displacement, $\hat{u}_{bi,j}$ from the total displacement of the damper assembly $\hat{u}_{ai,j}$ as follows,

$$\hat{u}_{di,j}^{\max} = \max\left|\hat{u}_{ai,j}(t) - \frac{\hat{F}_{di,j}(t)}{\hat{K}_{bi,j}}\right| \tag{8.9}$$

The standard dampers have a stroke capacity of 60-120 mm (see Table A2 in Appendix A). If dampers are placed diagonally, at these stroke levels the corresponding shear deformation-induced SDRs are around 2-4% for 60-120 mm strokes, respectively. If the flexural deformations are assumed to be negligible in the lower stories, SDRs larger than 2-4% in the lower stories result into the exceedance of the stroke limits depending on the selected damper stroke. Referring to Figure 8.37, the median peak damper displacements are less than 30 mm. This is well below the smallest damper stroke limit (60 mm). Figure 8.38 shows the 84th percentile peak damper displacement response. In this case, the damper displacements reach up to 142 mm in the bottom stories; therefore, they exceed the maximum stroke limit. The corresponding SDR is larger than 4% in this case (see Figure 8.25).

Another important parameter to check is the damper peak velocities and the corresponding peak damper post relief velocity ratio $\hat{\mu}_{di,j}^{\max}$, which is computed as follows,

$$\hat{\mu}_{di,j}^{\max} = \max\left|\frac{\hat{v}_{ci,j}(t)}{\hat{v}_{dri,j}}\right| \tag{8.10}$$

in which, $\hat{v}_{ci,j}$ is the dashpot velocity , which can be derived from the dashpot displacement, $\hat{u}_{ci,j}$. The dashpot displacement at each step can be computed as follows,

$$\hat{u}_{ci,j}(t) = \hat{u}_{ai,j}(t) - \frac{\hat{F}_{di,j}(t)}{\hat{K}^{*}_{bi,j}} \tag{8.11}$$

The allowable post relief velocity ratio of the dampers is 30 mm/sec (see Table A2 in Appendix A), which corresponds to a $\hat{\mu}^{\max}_{di,j} = 17$. Figure 8.39 indicates that the median values of the peak post relief velocity ratio vary from 2.3 to 9.8. The ratio is around 3.0 in most of the mid-stories. The largest values are observed in the lower and upper stories. Note that according to the SDF design via performance curves, the expected post relief velocity ratio is 1.5 at the medium damping level (see Table 8.1). This implies that velocities at each level are amplified due to higher mode effects. Hence, even though oil dampers are designed to remain linear in the equivalent SDF system, the relief velocity is likely to be exceeded due to higher demands. This phenomenon emphasizes the advantage of using bilinear oil dampers over linear viscous dampers. Figure 8.40 shows the median peak damper forces in the X-loading direction of the building at the BSE-2E level. Although the relief velocity is exceeded in all the dampers, unlike linear viscous dampers the increase in damper forces is very limited. The peak damper forces are below the allowable damper forces. Figure 8.41 shows the force-displacement ($\hat{u}_{ai,j}$) relation of oil dampers in stories 10, 20, 30 and 40 in the X-loading direction of the building subjected to GM#32 at the BSE-2E seismic intensity. It is clearly shown that the dampers exceed their relief forces, particularly at story 40.

8.6 Conclusions

This chapter provided guidance for the seismic retrofit design of a 1970s tall building. Oil dampers with relief valve were employed for this purpose. The damper design was carried out

according to the performance curves method. Multiple retrofit solutions were exploited through a comparative study. The comparative study was carried out with 2D nonlinear building models by utilizing a set of ground motions scaled at the BSE-2E hazard level. The main conclusions are summarized as follows,

- The oil damper design according to the performance curves method utilizing different damping levels resulted in a K_b/K_d'' ratio between 4.4 to 6.3, and a K_b^*/K_d'' ratio between 1.6 and 2.4. Although the peak damper velocity ratio target was 2.0 in the initial design, it was reduced to 1.5 and 1.2 for medium and high damping levels, respectively, due to the available damper sizes for low relief velocity and the damper demand reduction.
- It was found that the damper placement at internal bays of the exterior frame was very effective in reducing the story-based engineering demand parameters. This was attributed to the relatively high displacement transmission factors observed in the internal bays of the building.
- The effect of vertical damping distribution on the building performance was significant. If the retrofitted frame still exhibits inelastic behaviour, the effective SFPDD is the most inefficient retrofit solution that causes damage concentration at stories where dampers are not provided, particularly at low and medium damping levels. On the other hand, the direct SFPDD method provides the most efficient solution especially when collapse prevention is the main objective.
- The peak SDRs were large in the bottom stories when the effective SFPDD method was employed, whereas in direct SFPDD the peak SDRs increased with the building height. Therefore, a balanced SFPDD method was proposed and implemented to balance the peak SDR distribution.

A detailed seismic performance assessment of the building retrofitted with the proposed retrofit solution (based on the balanced SFPDD method at medium damping level) was conducted based on rigorous nonlinear response history analysis (NRHA). For this reason, 40 ground motions were selected and scaled to be compatible with the BSE-1E and BSE-2E hazard levels as per ASCE 41-13 (ASCE 2014). Both global and local EDPs were examined. In conclusion, the main findings are summarized as follows,

- At the BSE-2E hazard level, the number of collapses was reduced from 29 to 4 and 13 to 3, in the X- and Y-loading directions, respectively. The collapse mechanisms involved bottom stories in both cases. Residual SDRs were mostly concentrated in the bottom stories.
- High demands in the upper story columns of the non-retrofitted building were minimized after the implementation of the seismic retrofit solution. No reduction was observed in the bottom story exterior column compressive and tensile forces in the X-loading direction, at the BSE-2E hazard level. Furthermore, the damper installation led to an increase in the interior column forces. However, the difference in forces at mid-interior columns was minimal due to the inverted-V damper configuration. Consequently, the lower story exterior column upgrading is inevitable.
- Tensile stresses at upper story column splices were reduced. The opposite was observed in the bottom story exterior columns. On average, about 27% of column splices were found vulnerable at the BSE-2E hazard level. It is recommended to strengthen the exterior column splices at the lower half of the building as well as its first story columns.
- The median peak damper displacements were less than the damper stroke limit (60mm). If the 84th percentile damper response is considered, then few dampers in the bottom stories of the retrofitted building may exceed their stroke limit. Although according to SDF design the

post relief velocity ratio was 1.5, the median values of the post relief velocity ratio were between 2.3 to 9.8. This is due to the higher mode effects. However, the corresponding damper forces were not large. This underscores the main advantage of utilizing bilinear oil dampers for seismic retrofit applications.

Table 8.1: Three damping levels and SDF parameters obtained from performance curve compared to existing building in X-loading direction

Case	K_d''/K_{fs}	K_b/K_{fs}	μ_d	T_{eff} [sec]	β_{eff} [%]	R_d
Bare Frame	-	-		4.05	1.5	1.0
Low Damping	0.25	1.0	2.0	3.92	7.4	0.64
Medium Damping	0.5	2.0	1.5	3.72	13.3	0.48
High Damping	1.0	4.0	1.2	3.40	22.2	0.36

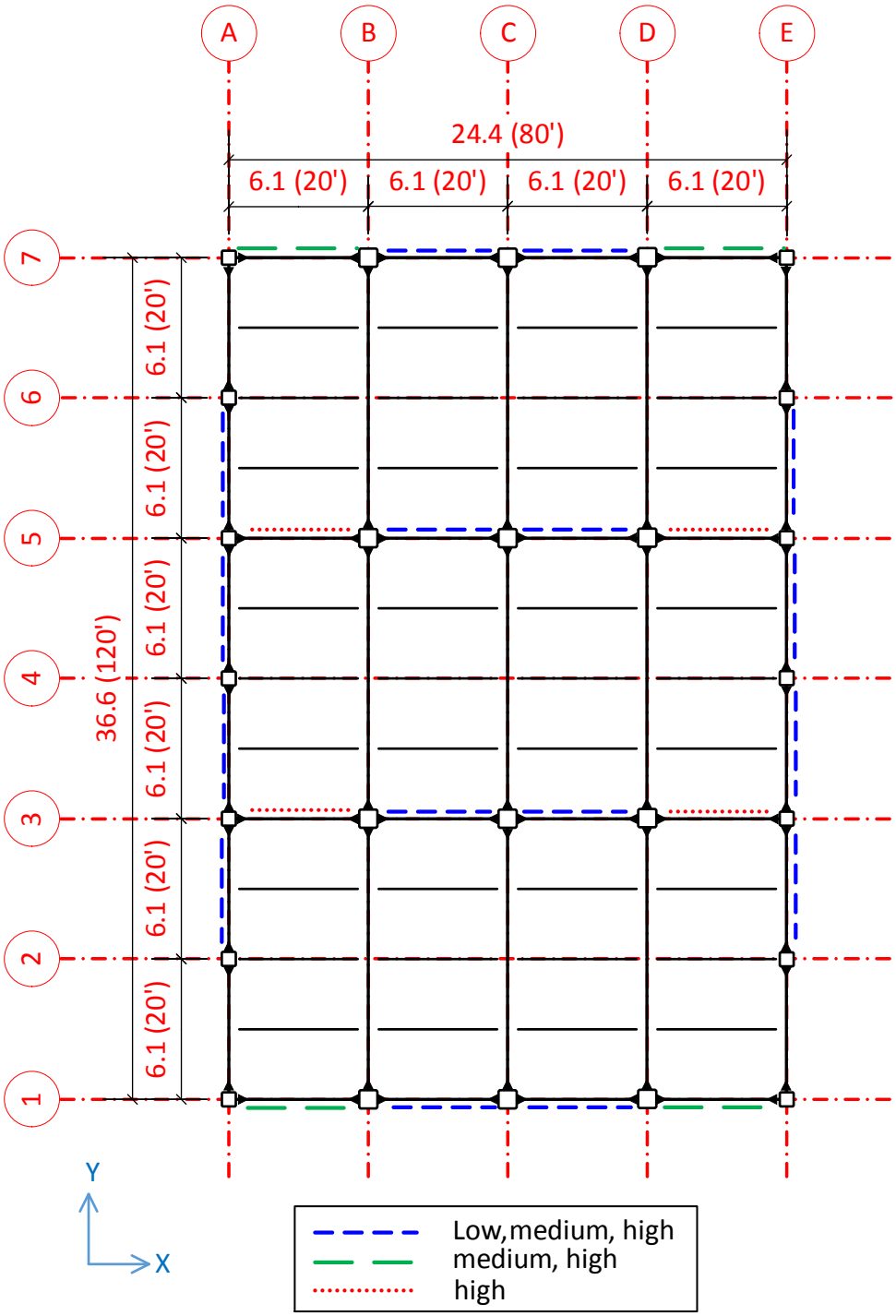

Figure 8.1: Floor plan of the building and typical damper locations, dimensions in m (ft)

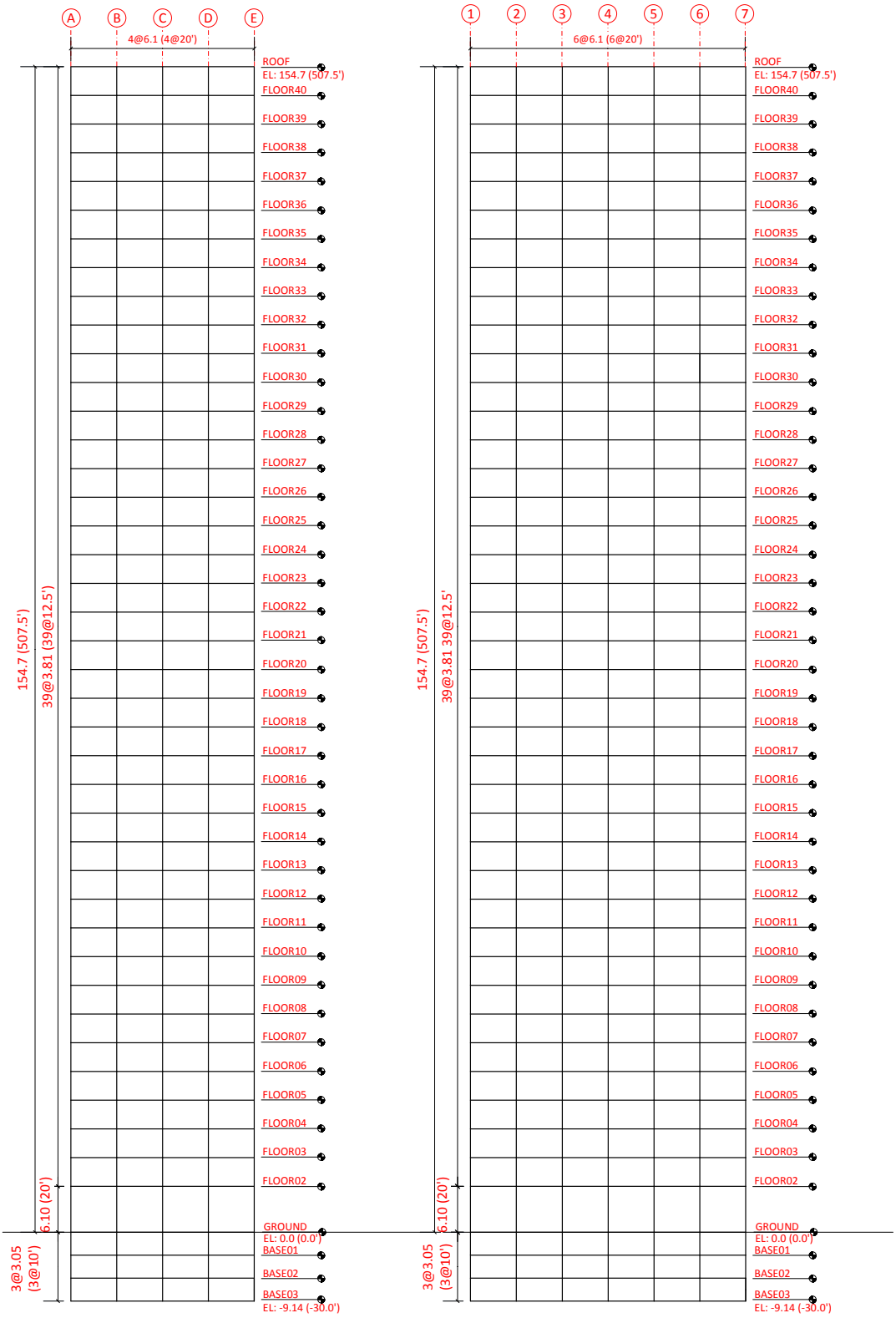

c) X-direction (all frames) d) Y-direction (A-A frame)

Figure 8.2: Elevation view of the building, dimensions in m (ft)

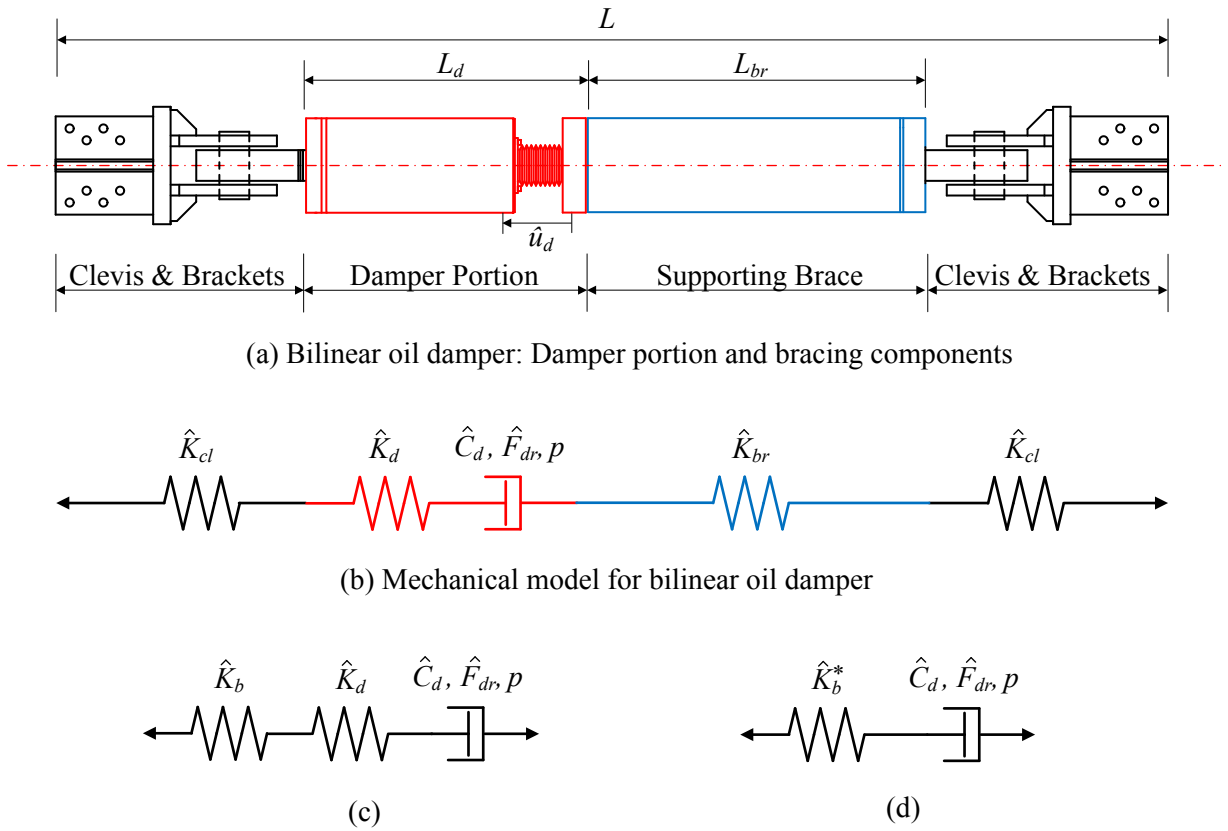

Figure 8.3. Representation of typical bilinear oil dampers and its mathematical models

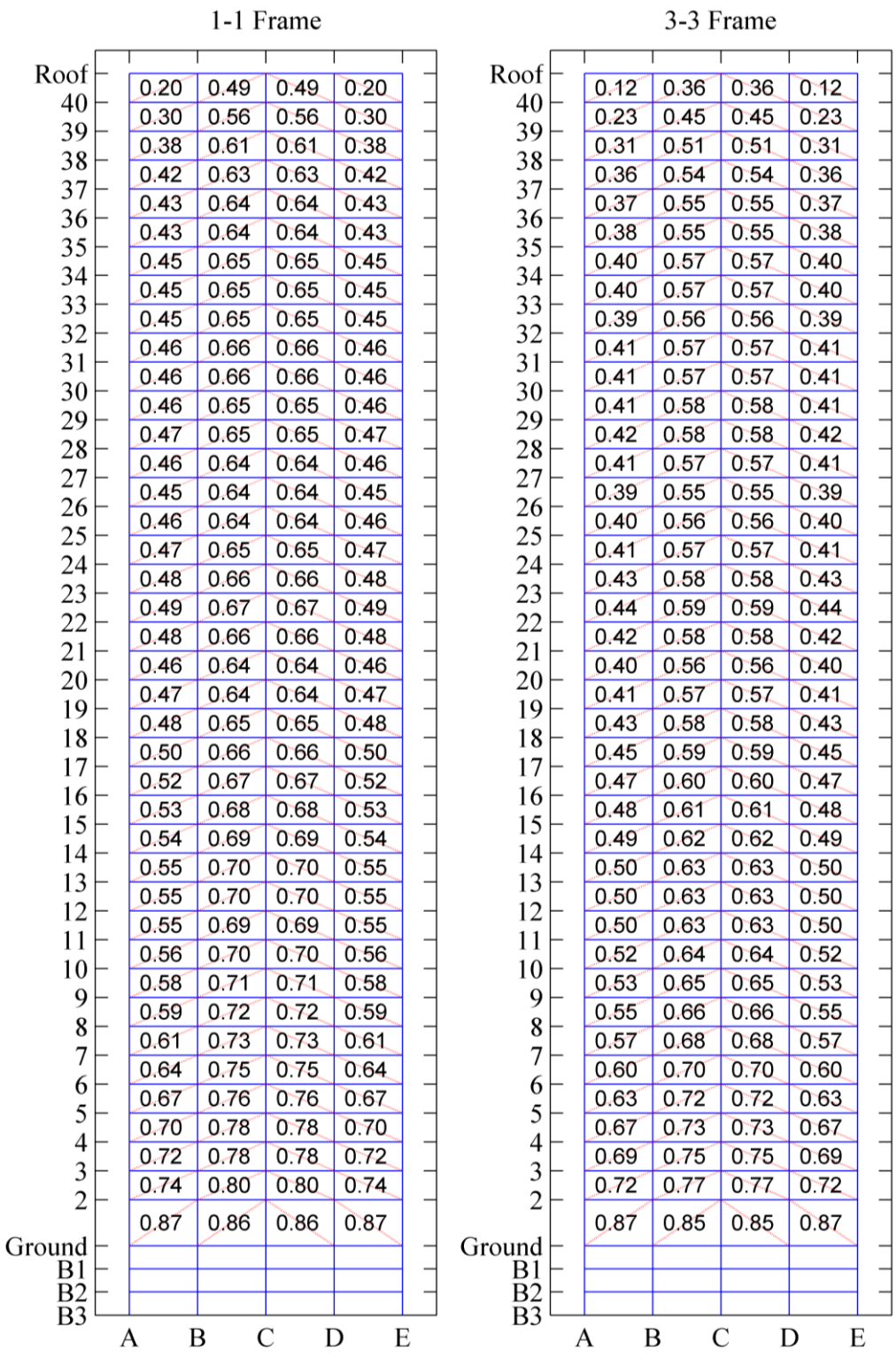

Figure 8.4: Total damper end displacement reduction factors $\alpha_{N,i,j}$, inverted-V type diagonals

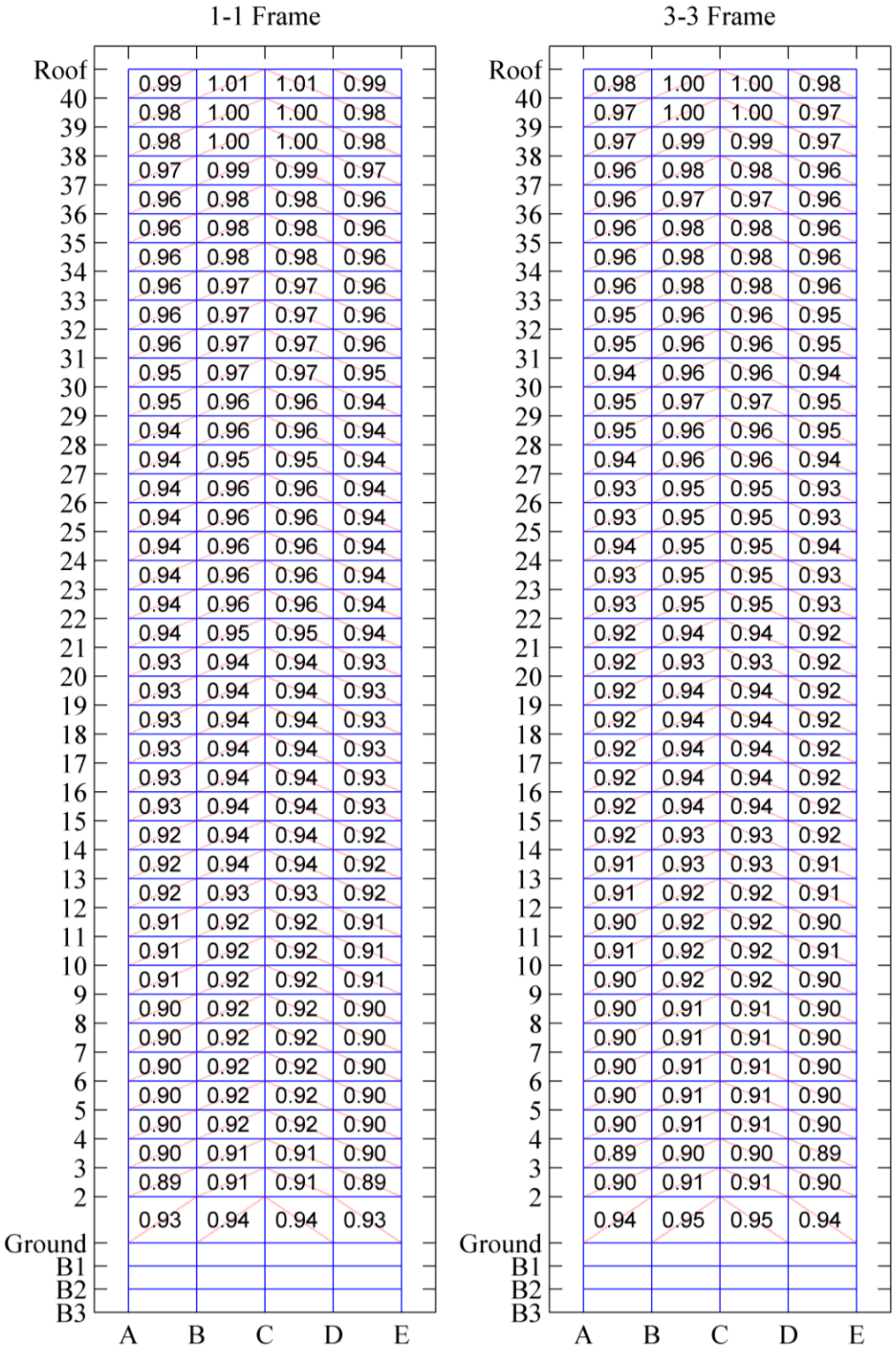

Figure 8.5: Total damper end displacement reduction factors $\alpha_{N,i,j}$, inverted-V type diagonals, axially rigid columns

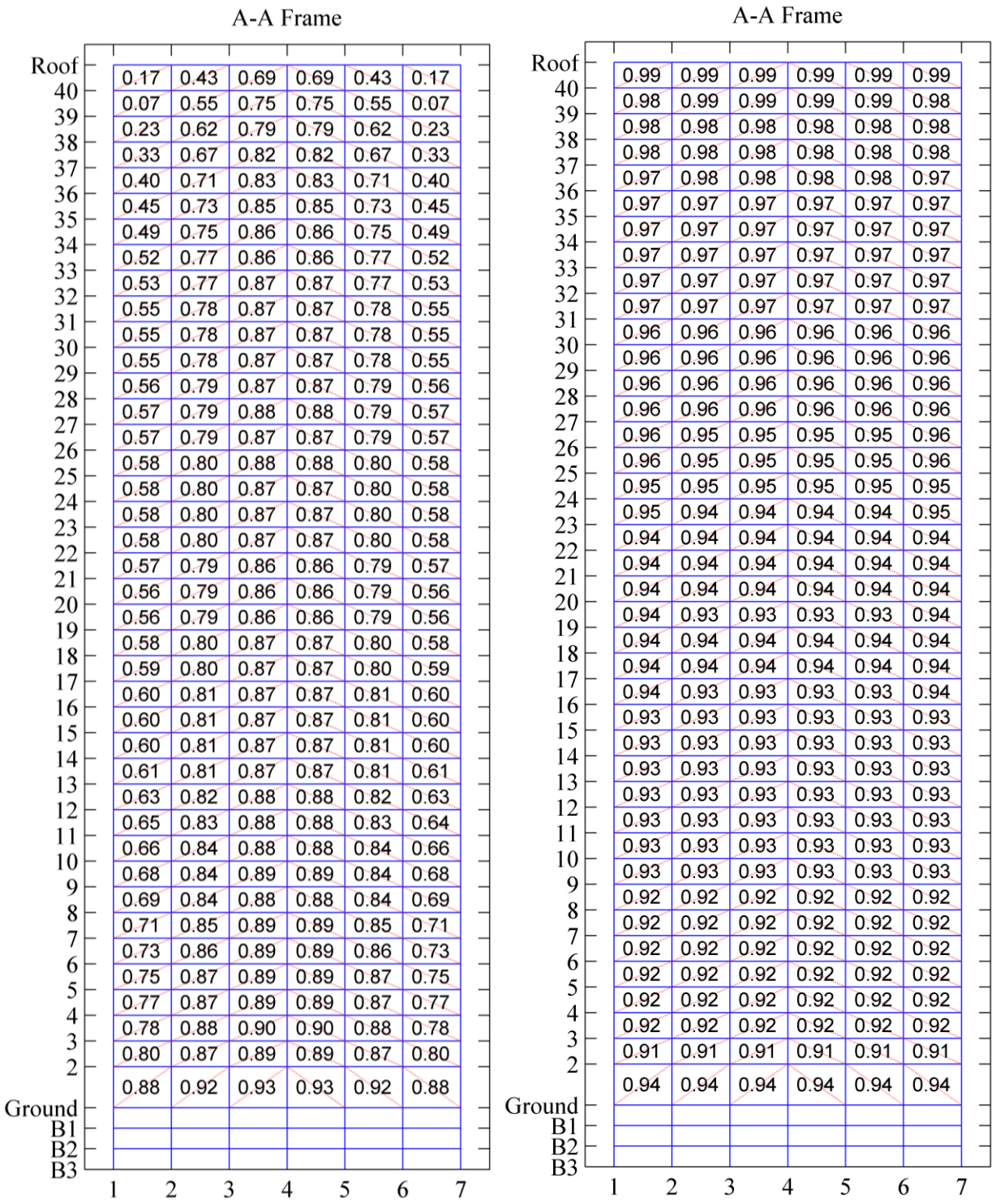

a) b)

Figure 8.6: Total damper end displacement transmission factors $\alpha_N^{i,j}$, inverted-V type diagonals, Y-loading direction b) axially rigid columns

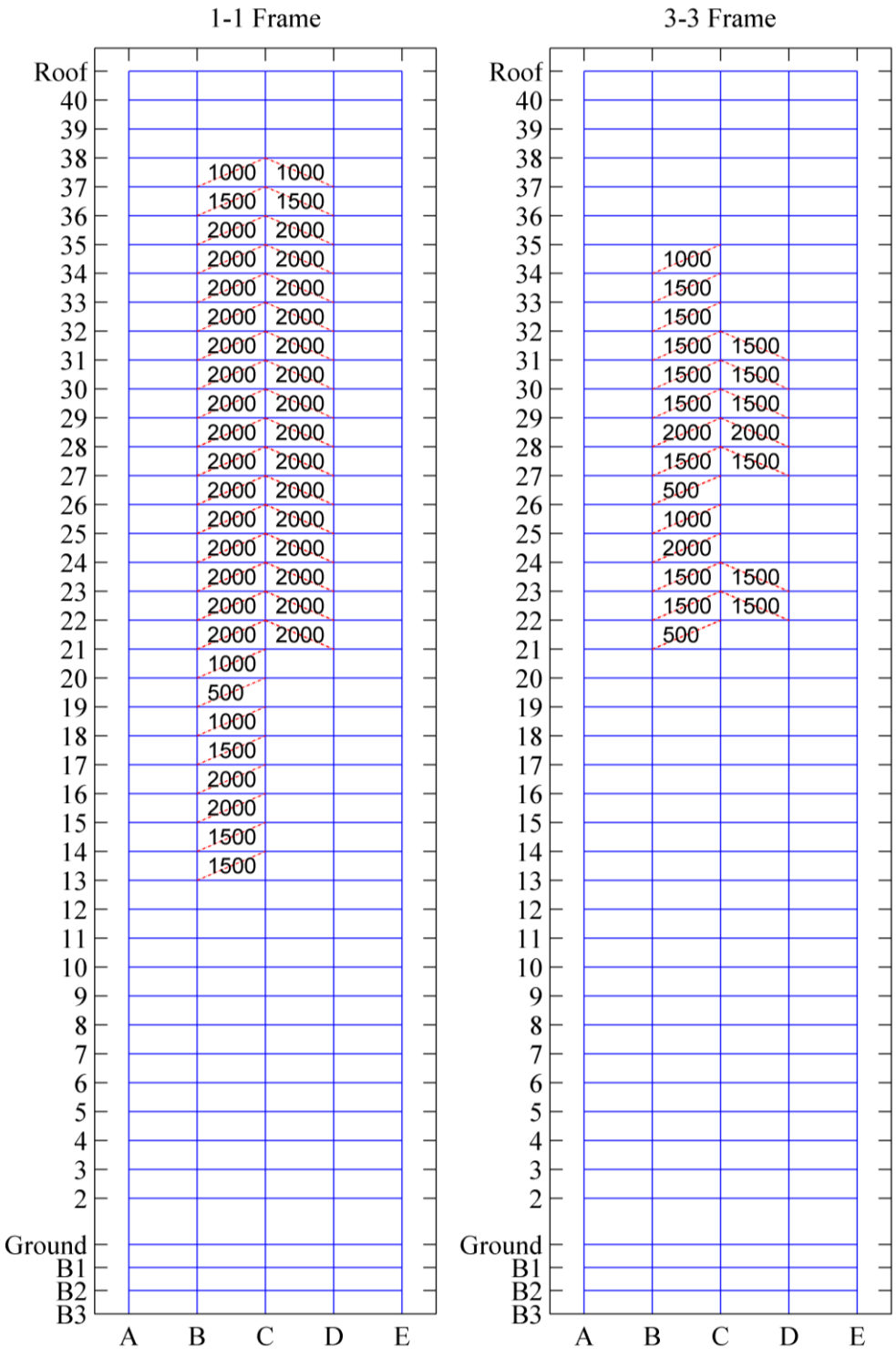

Figure 8.7: Damper design (maximum allowable forces in KN), low damping level, X-loading direction, internal bays (effective distribution)

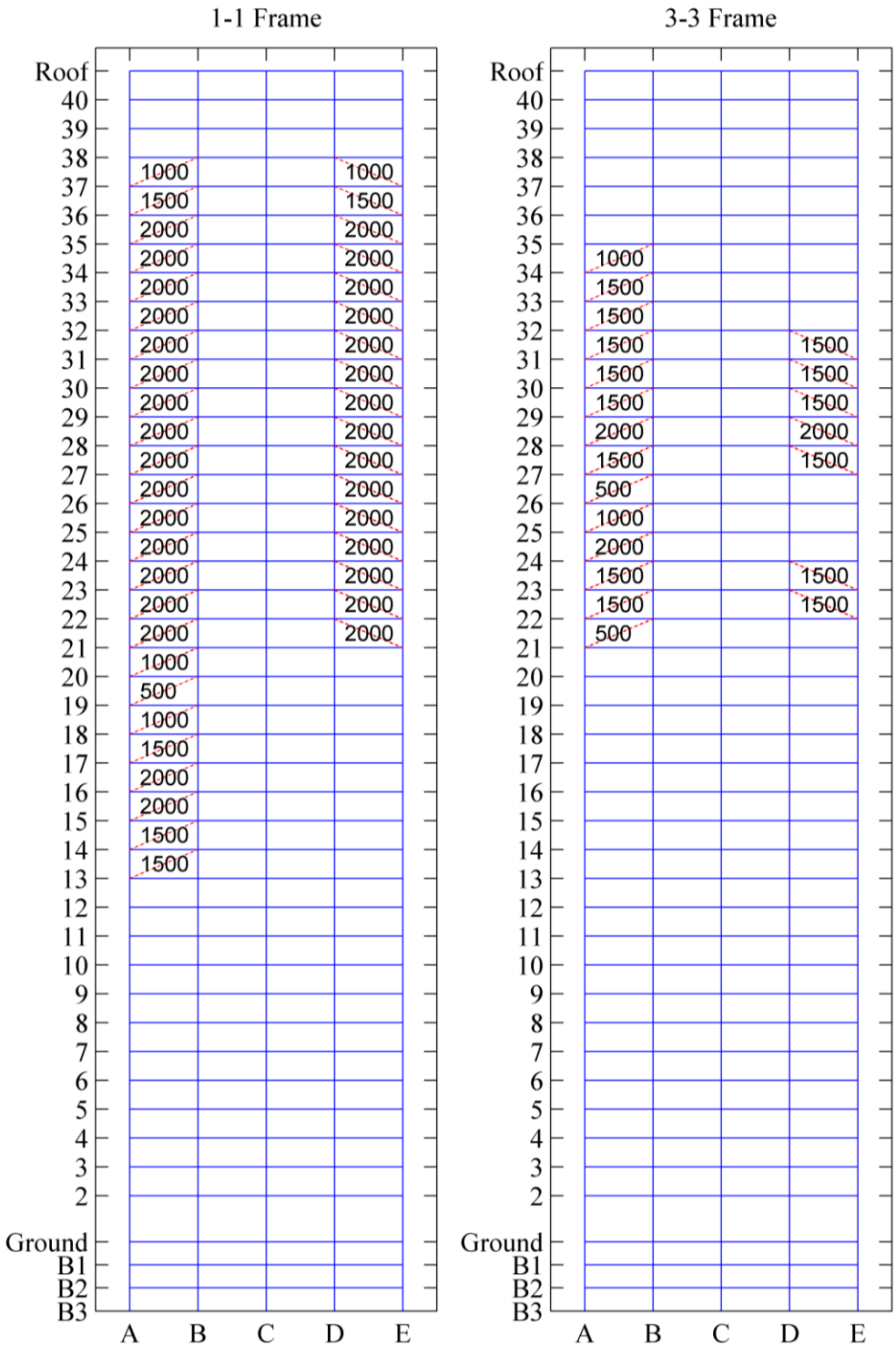

Figure 8.8: Damper design (maximum allowable forces in KN) low damping level, X-loading direction, external bays (effective SFPDD)

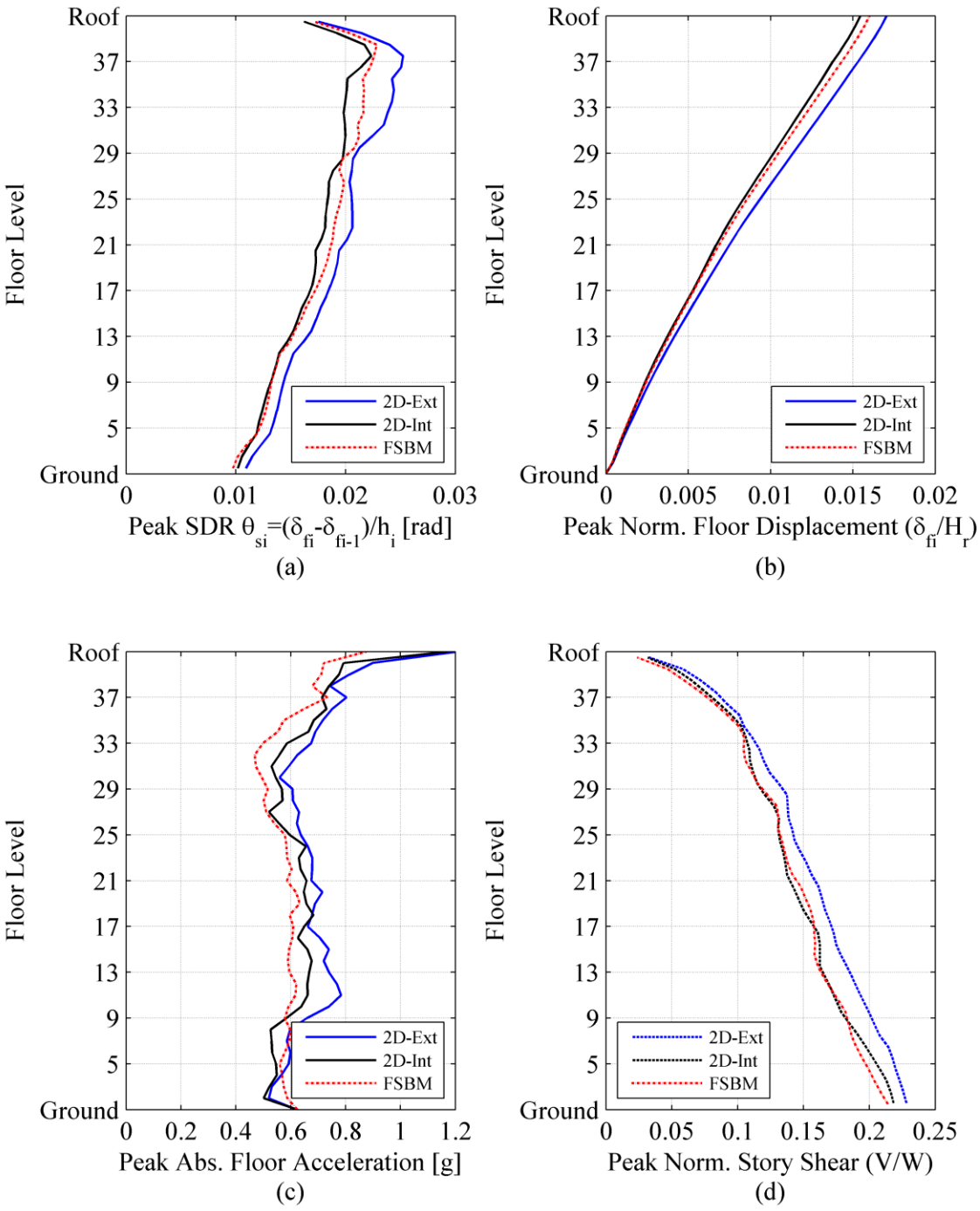

Figure 8.9: Comparison of FSBM with 2D model equipped with dampers at exterior and interior bays

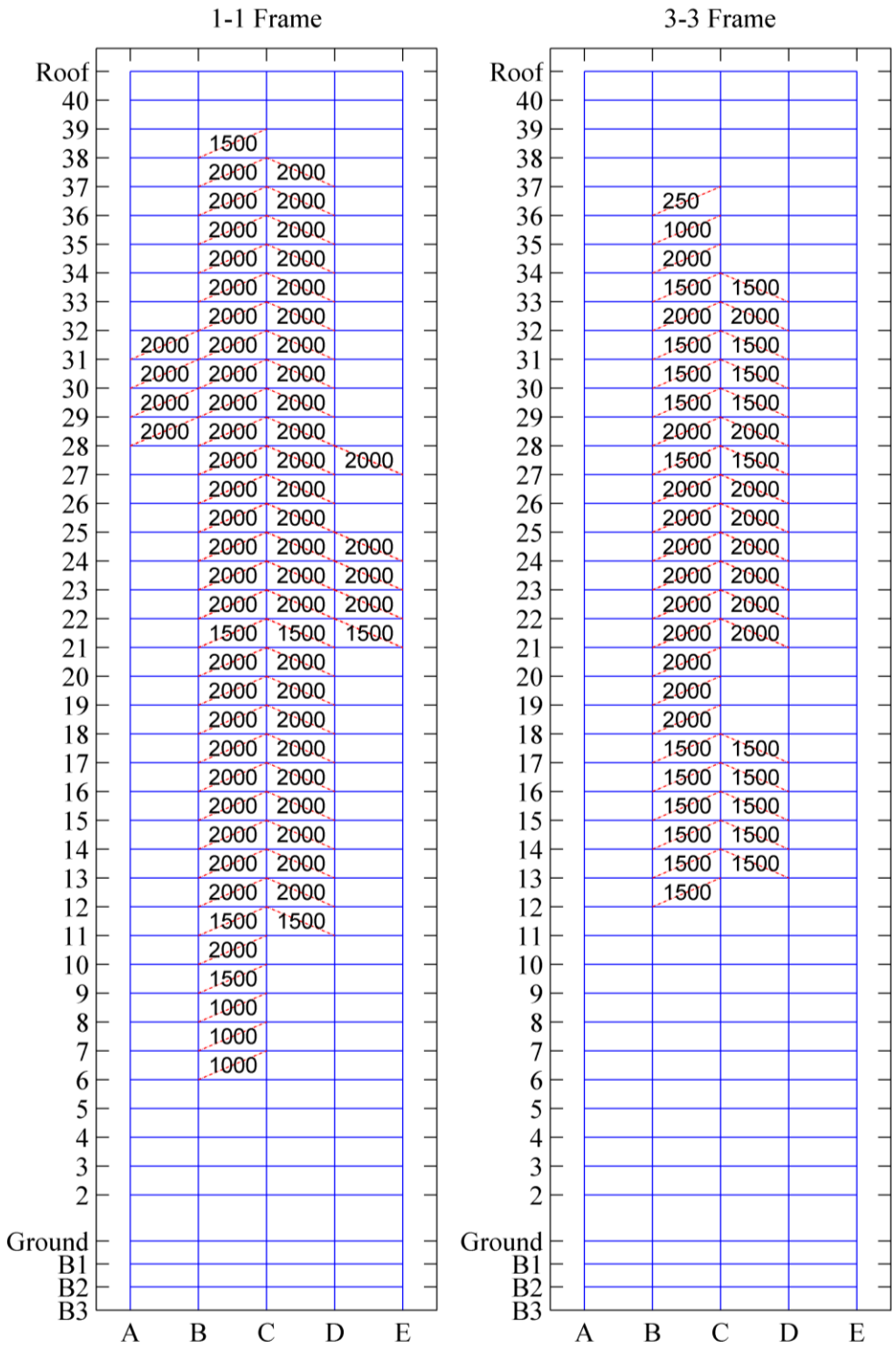

Figure 8.10: Damper design (maximum allowable forces in KN) medium damping level, X-loading direction (effective SFPDD)

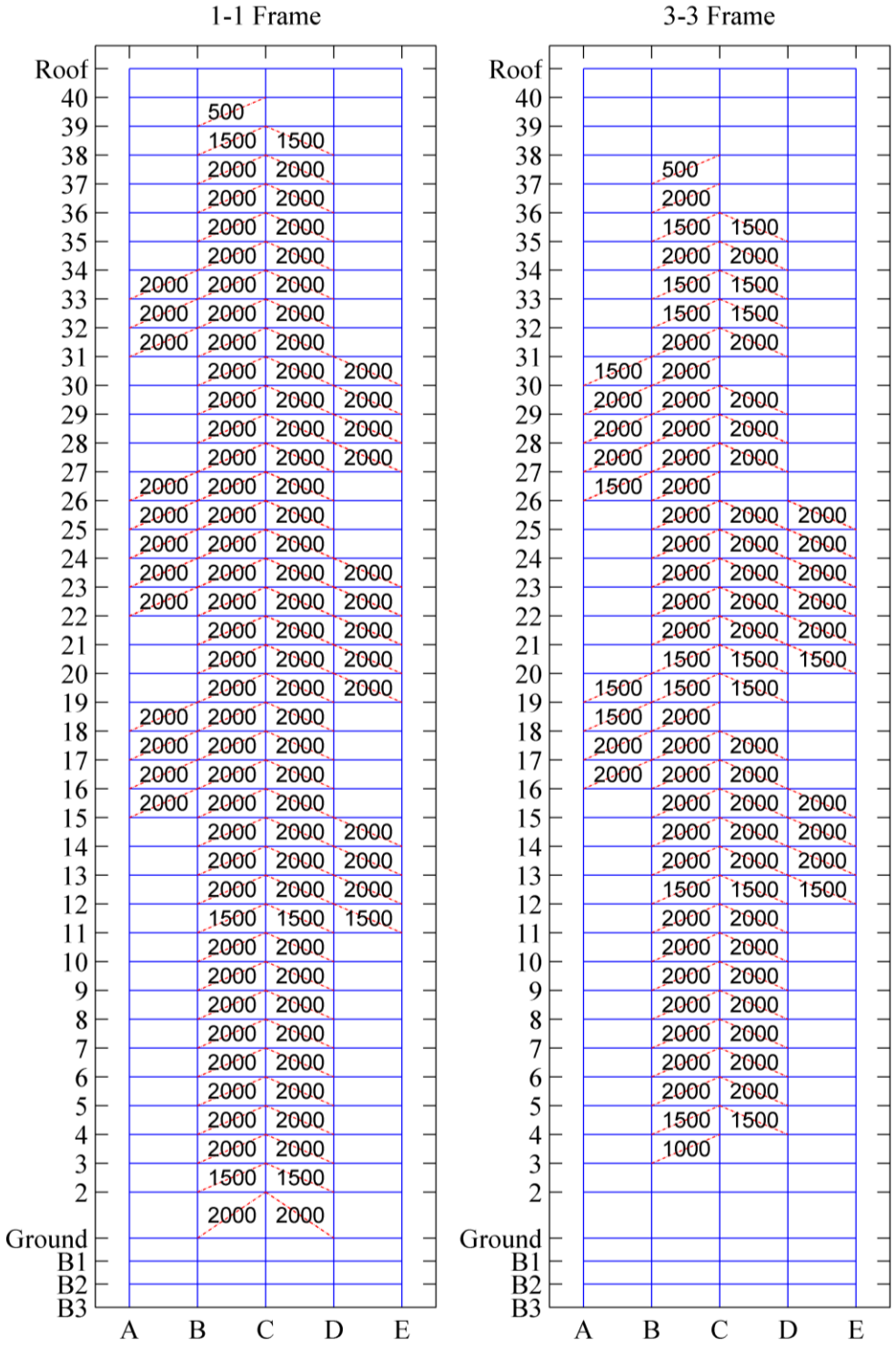

Figure 8.11: Damper design (maximum allowable forces in KN) high damping level, X-loading direction (effective SFPDD)

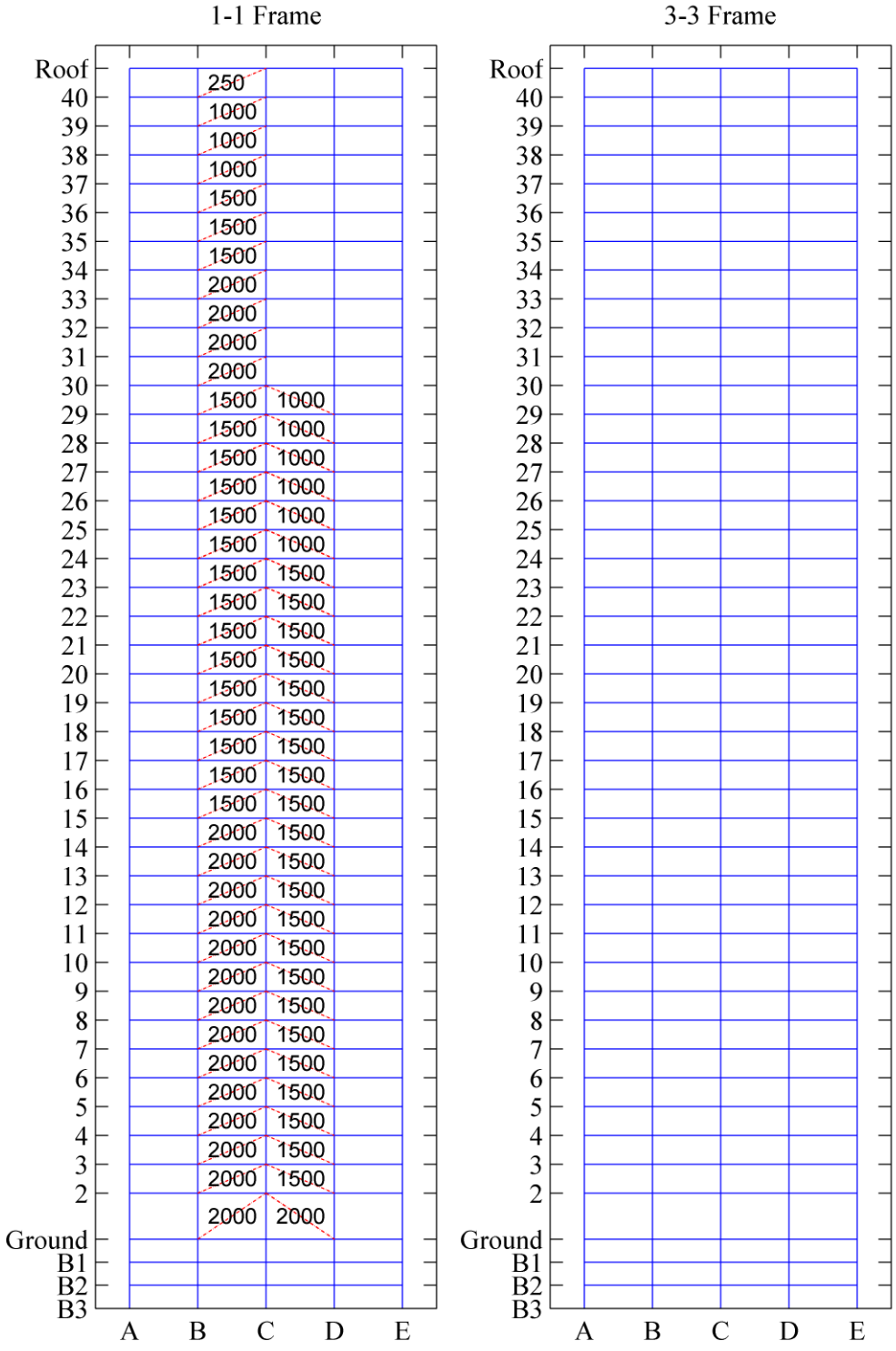

Figure 8.12: Damper design (maximum allowable forces in KN) low damping level, X-loading direction (direct SFPDD)

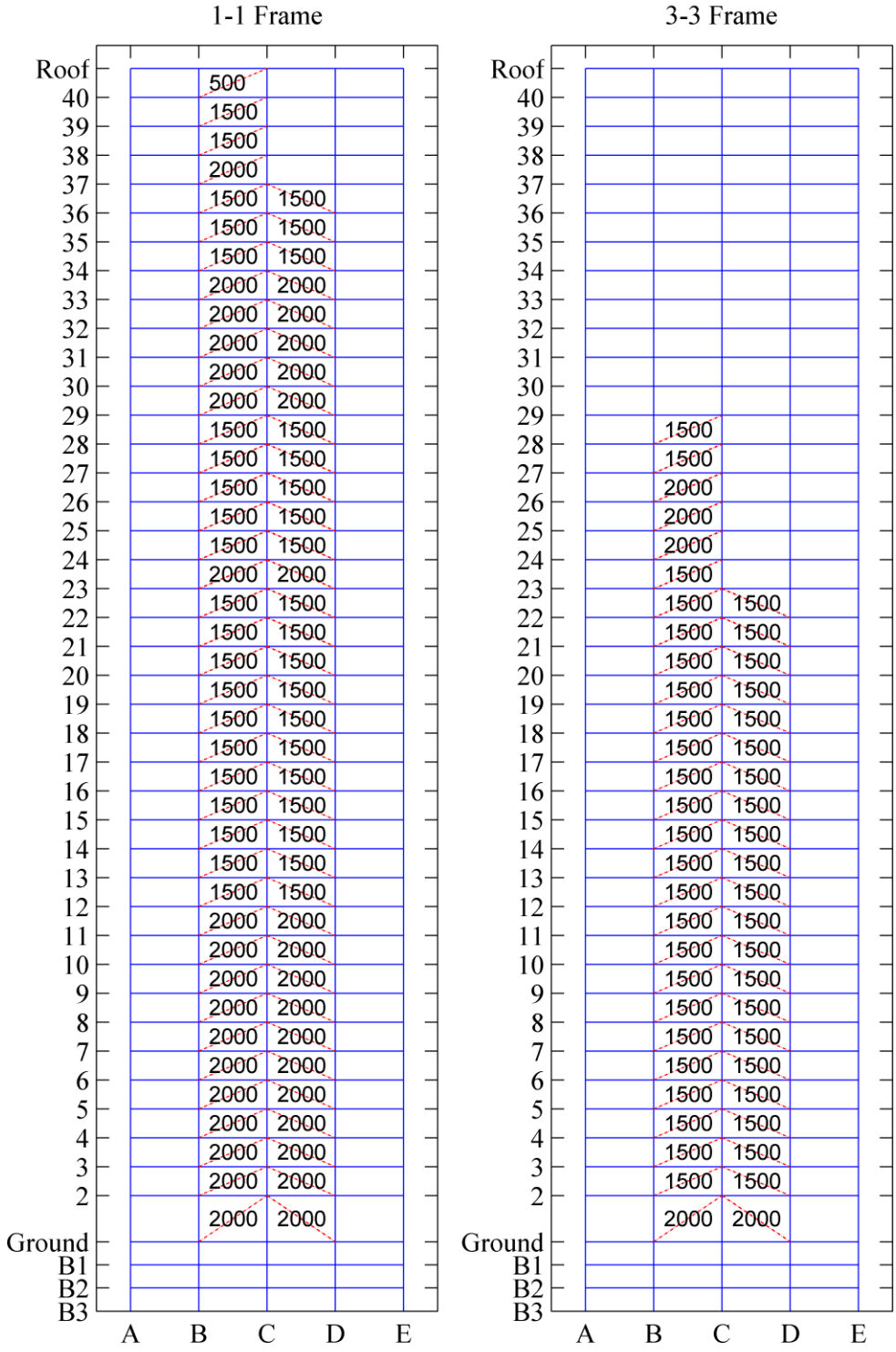

Figure 8.13: Damper design (maximum allowable forces in KN) medium damping level, X-loading direction (direct SFPDD)

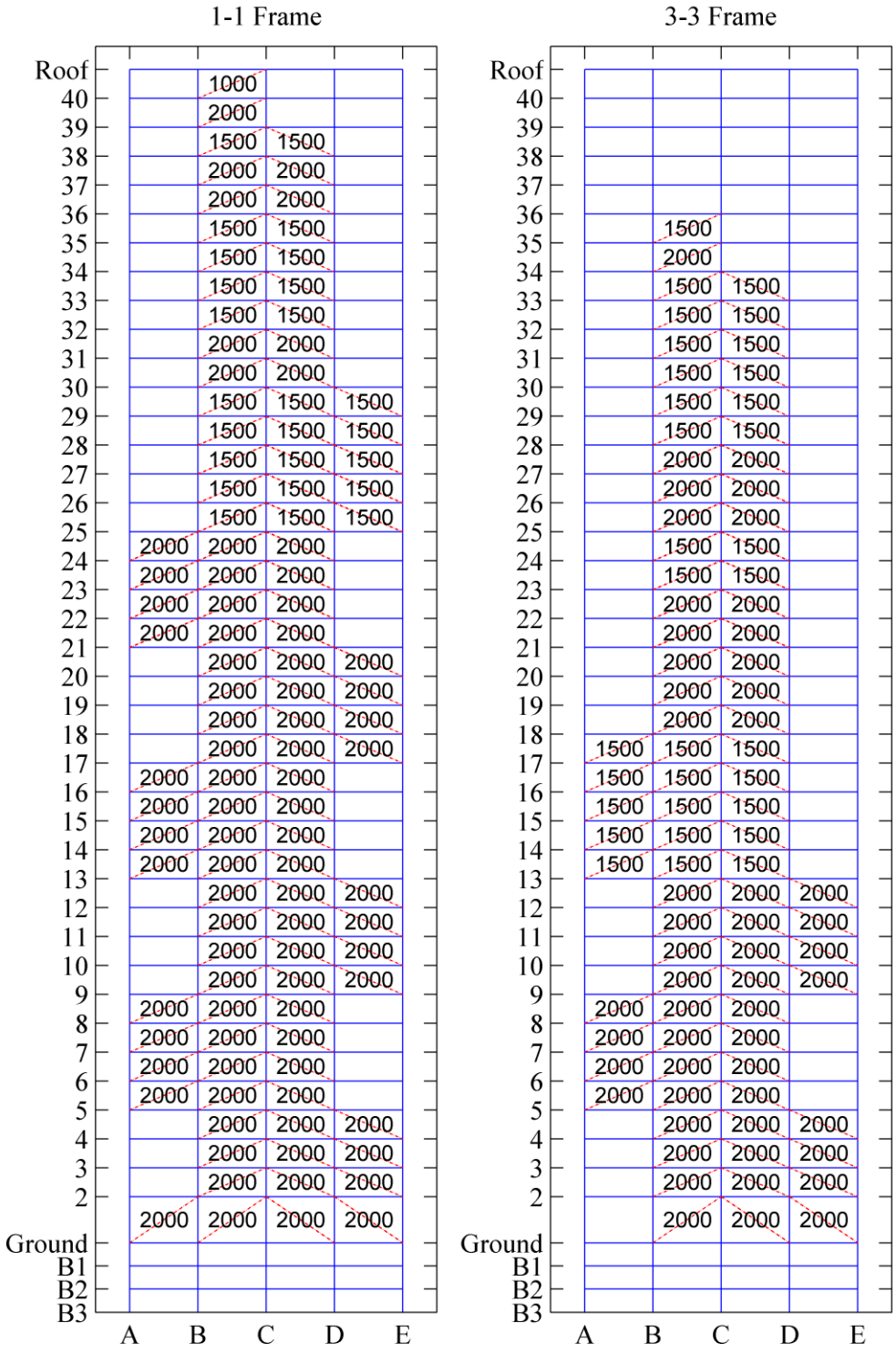

Figure 8.14: Damper design (maximum allowable forces in KN) high damping level, X-loading direction (direct SFPDD)

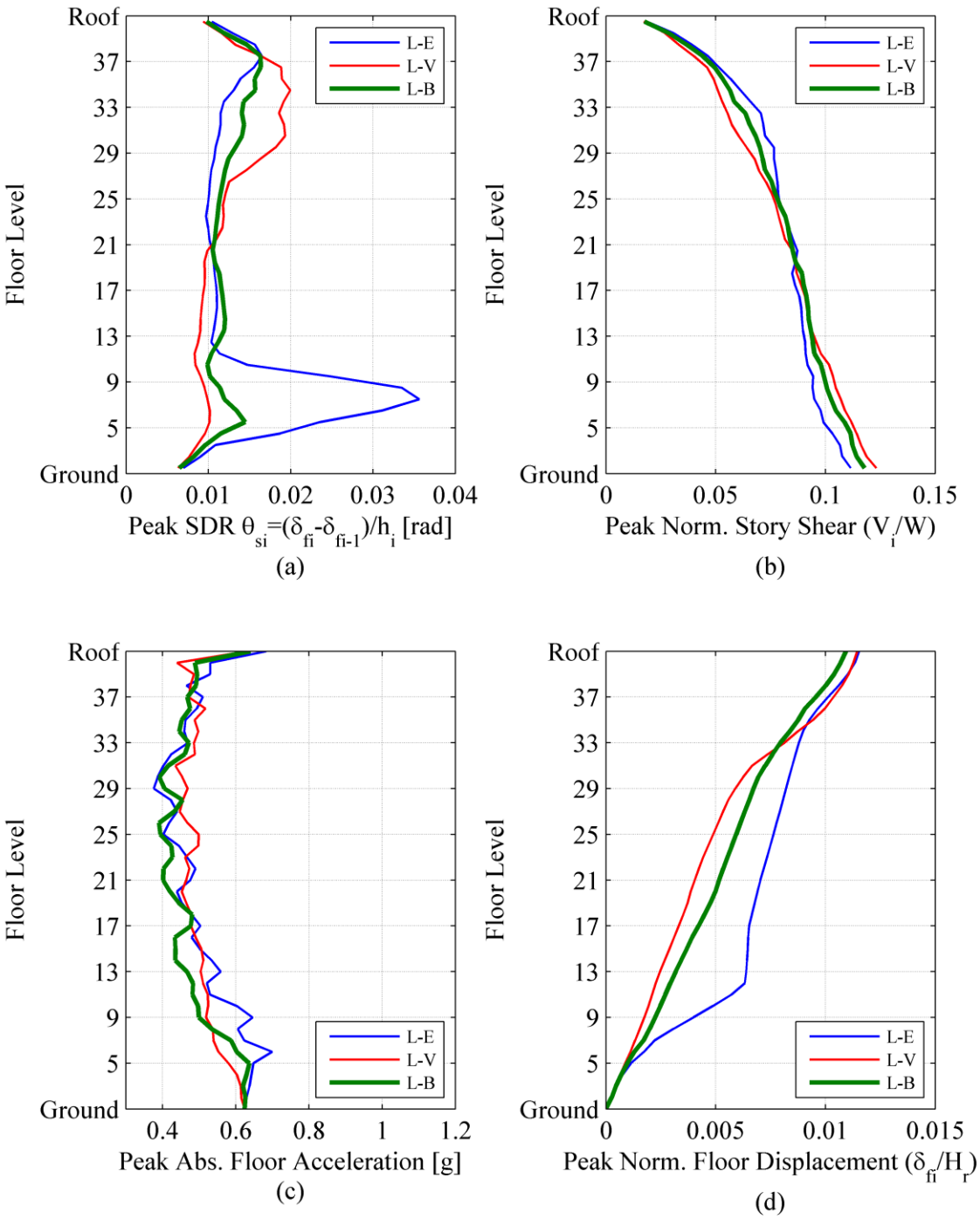

Figure 8.15: Comparison of median EDPs with 10GMs, with various damping distributions (low damping, X-loading direction)

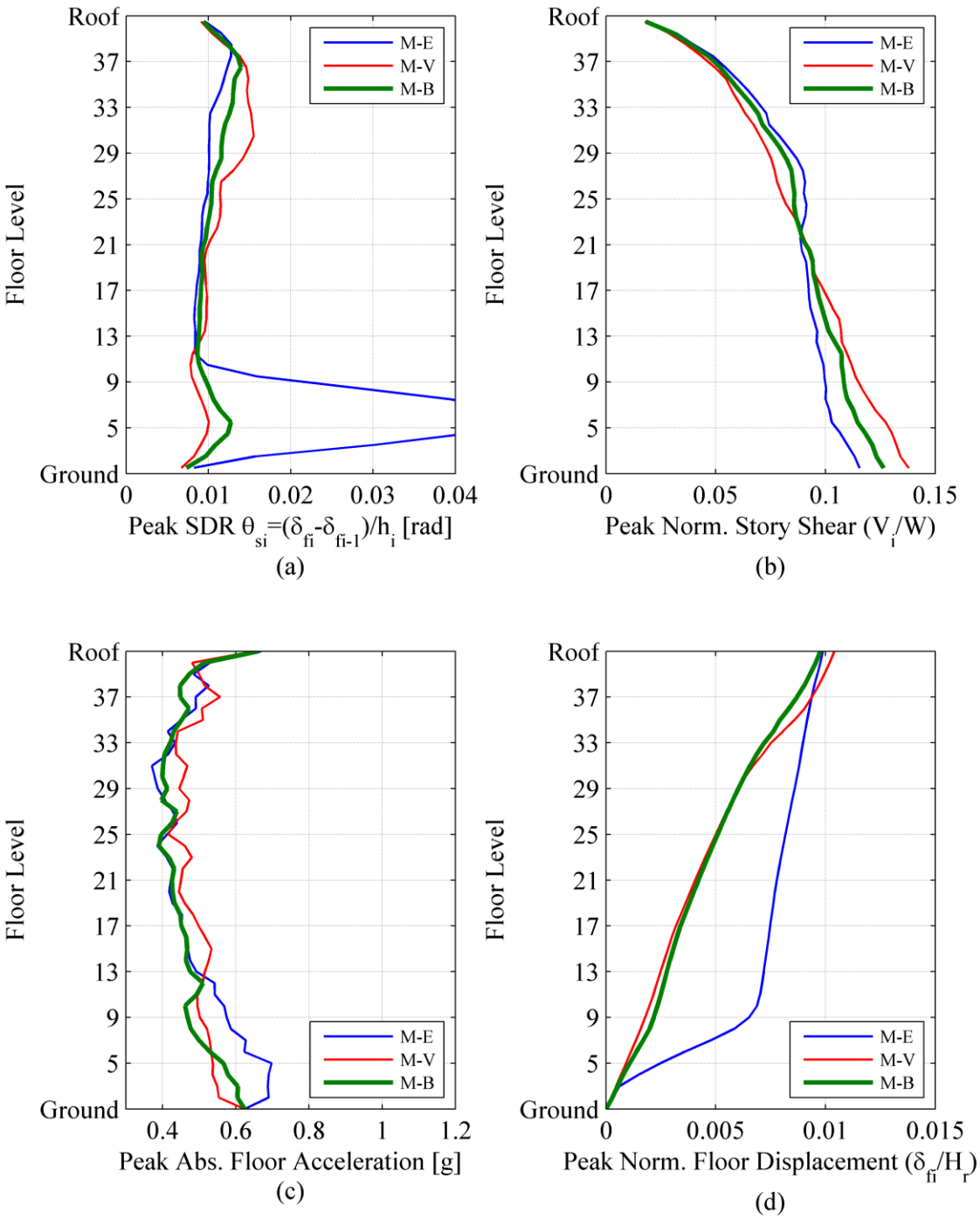

Figure 8.16: Comparison of median EDPs with 10GMs, with various damping distributions (medium damping, X-loading direction)

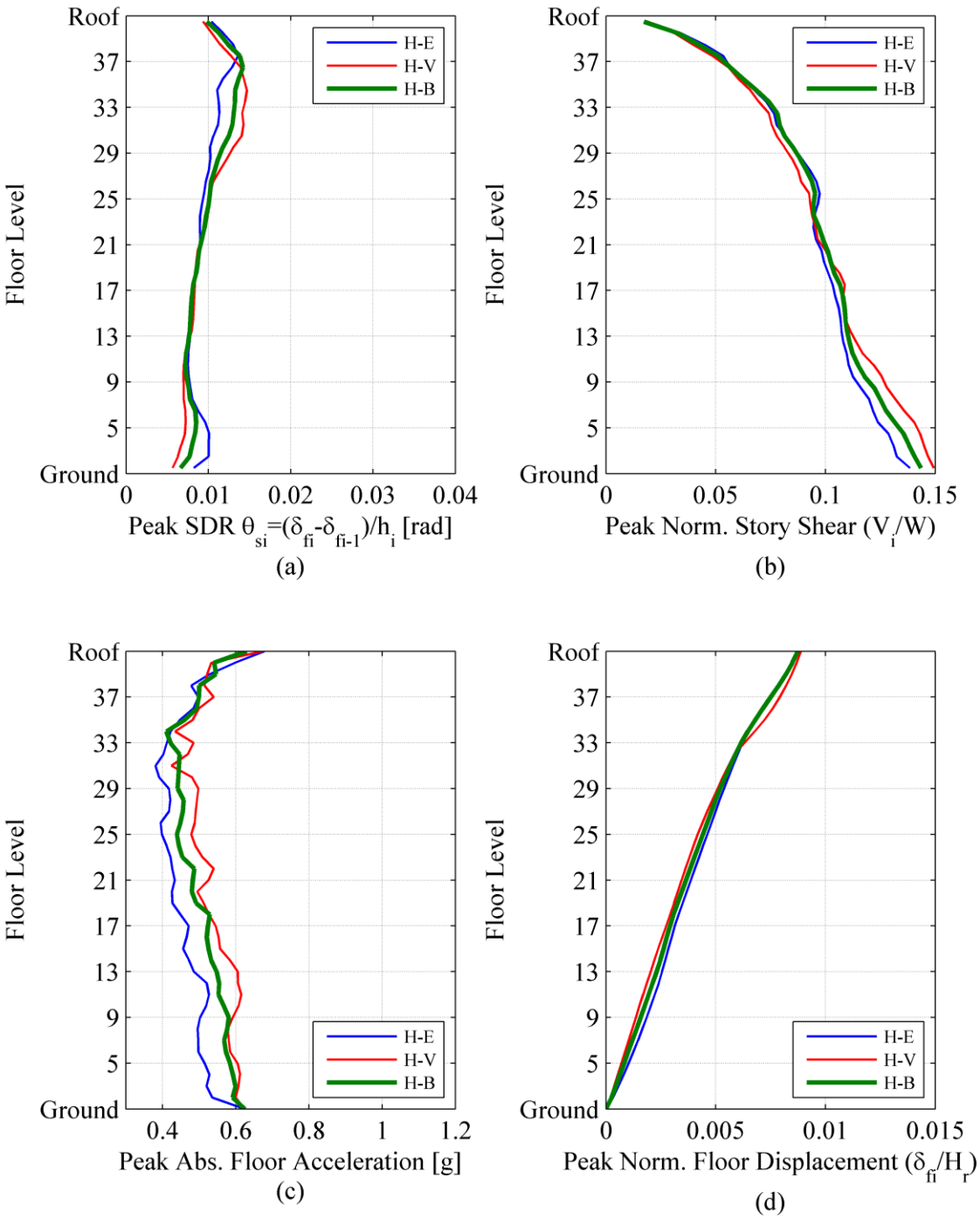

Figure 8.17: Comparison of median EDPs with 10GMs, with various damping distributions (high damping, X-loading direction)

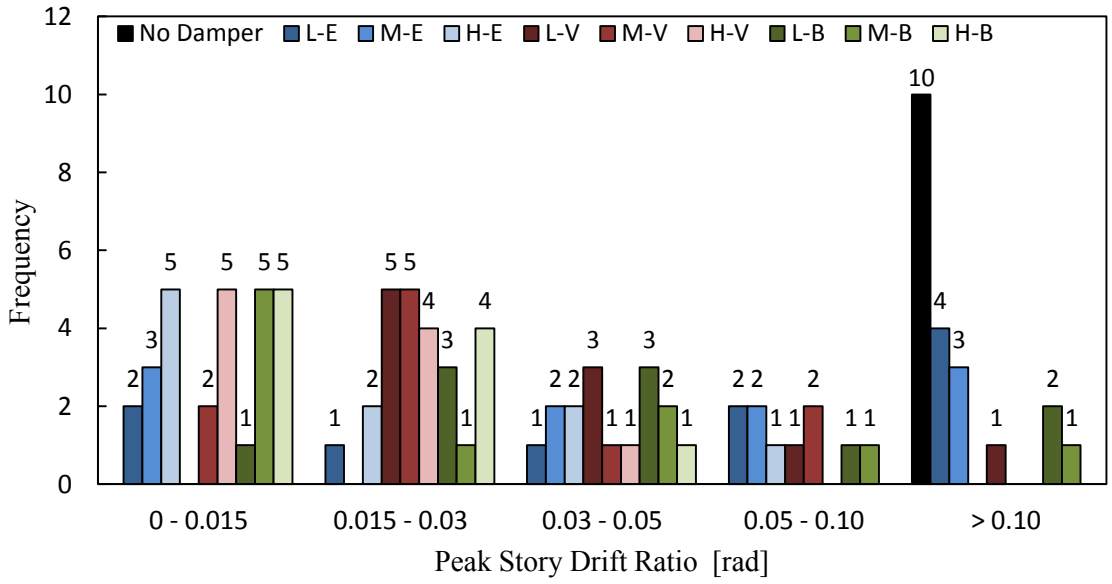

Figure 8.18: Maximum peak story drift ratios obtained from 10GMs, with various damping levels and distributions

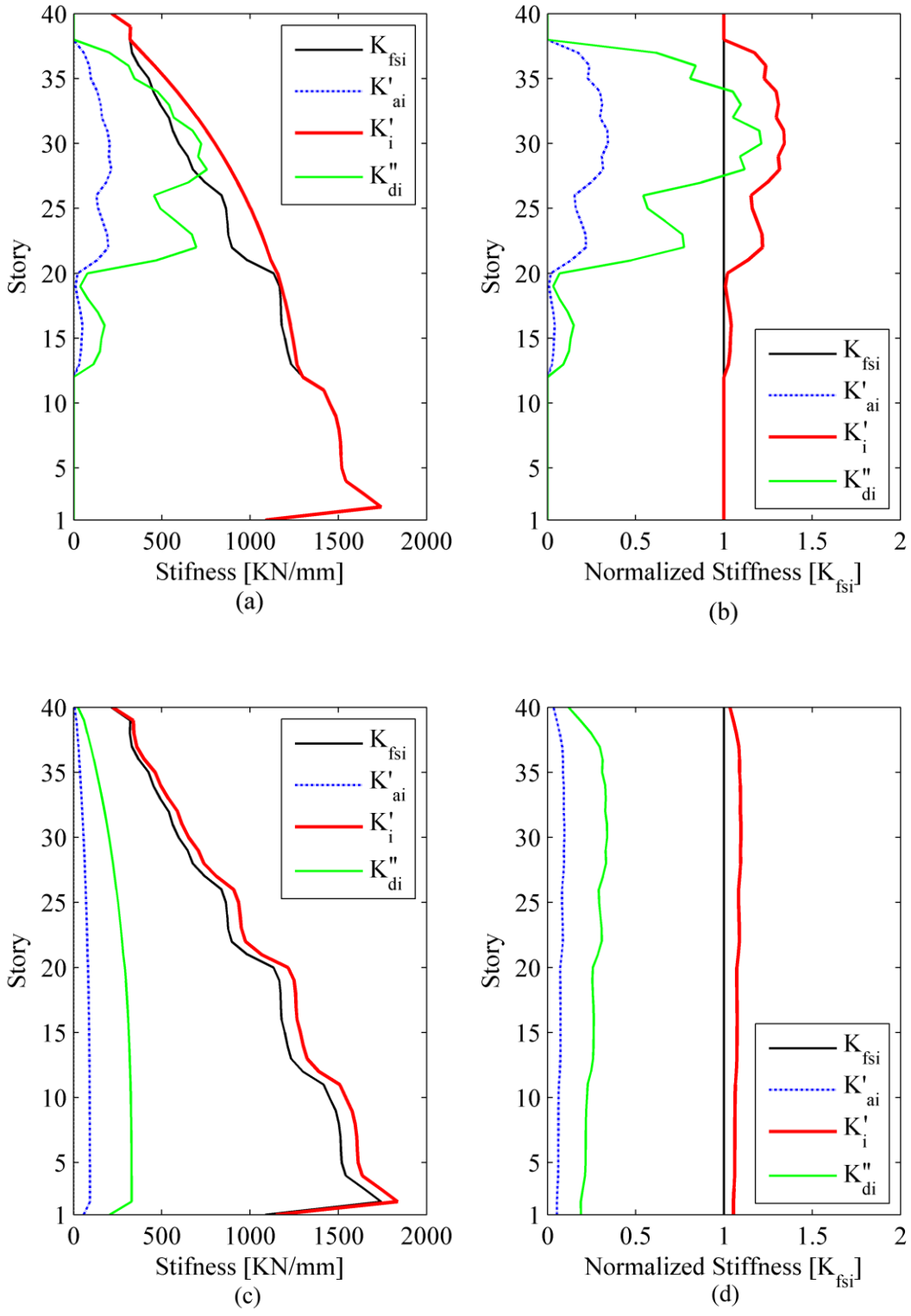

Figure 8.19: Effective and direct SFPDD design (low damping), X-loading direction

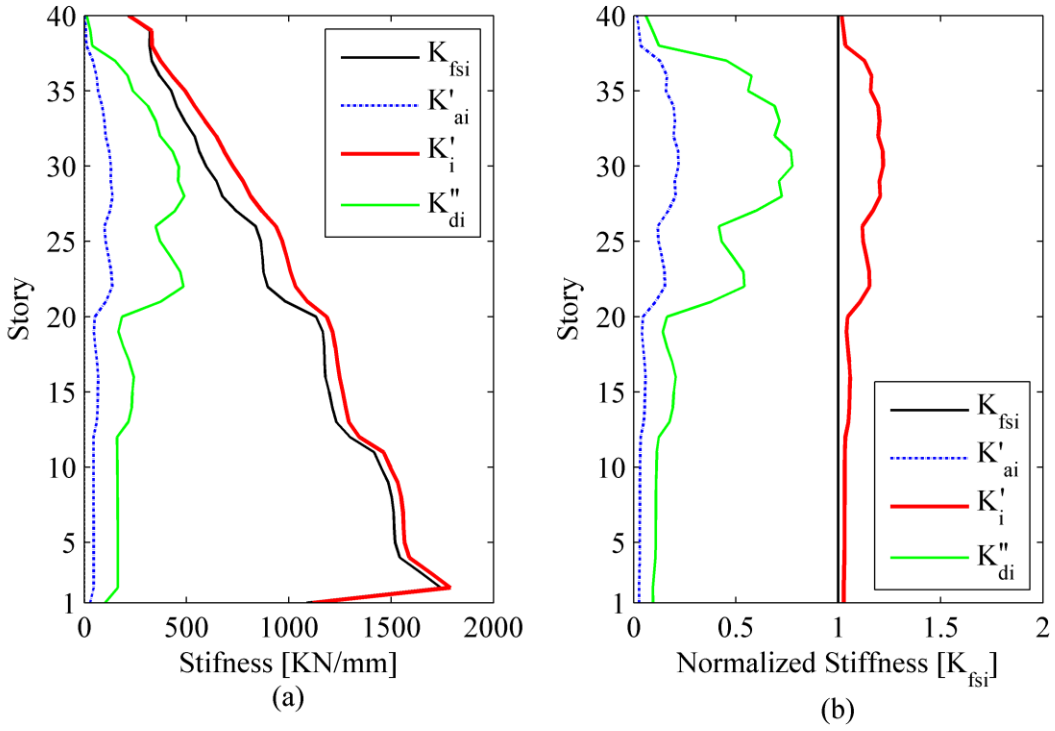

Figure 8.20: Balanced SFPDD (low damping), X-loading direction

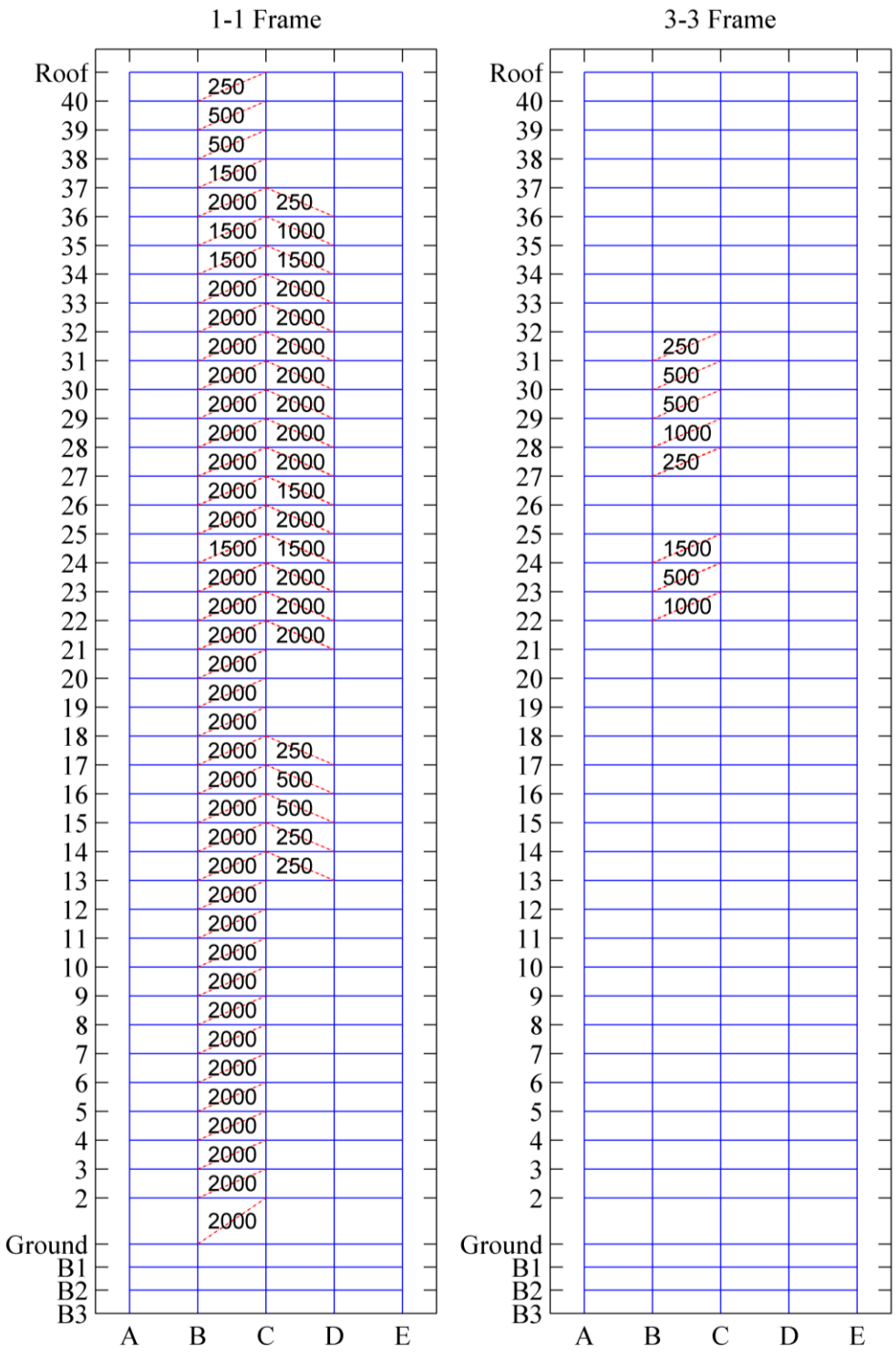

Figure 8.21: Damper design (maximum allowable forces in KN), low damping level, X-loading direction (balanced SFPDD)

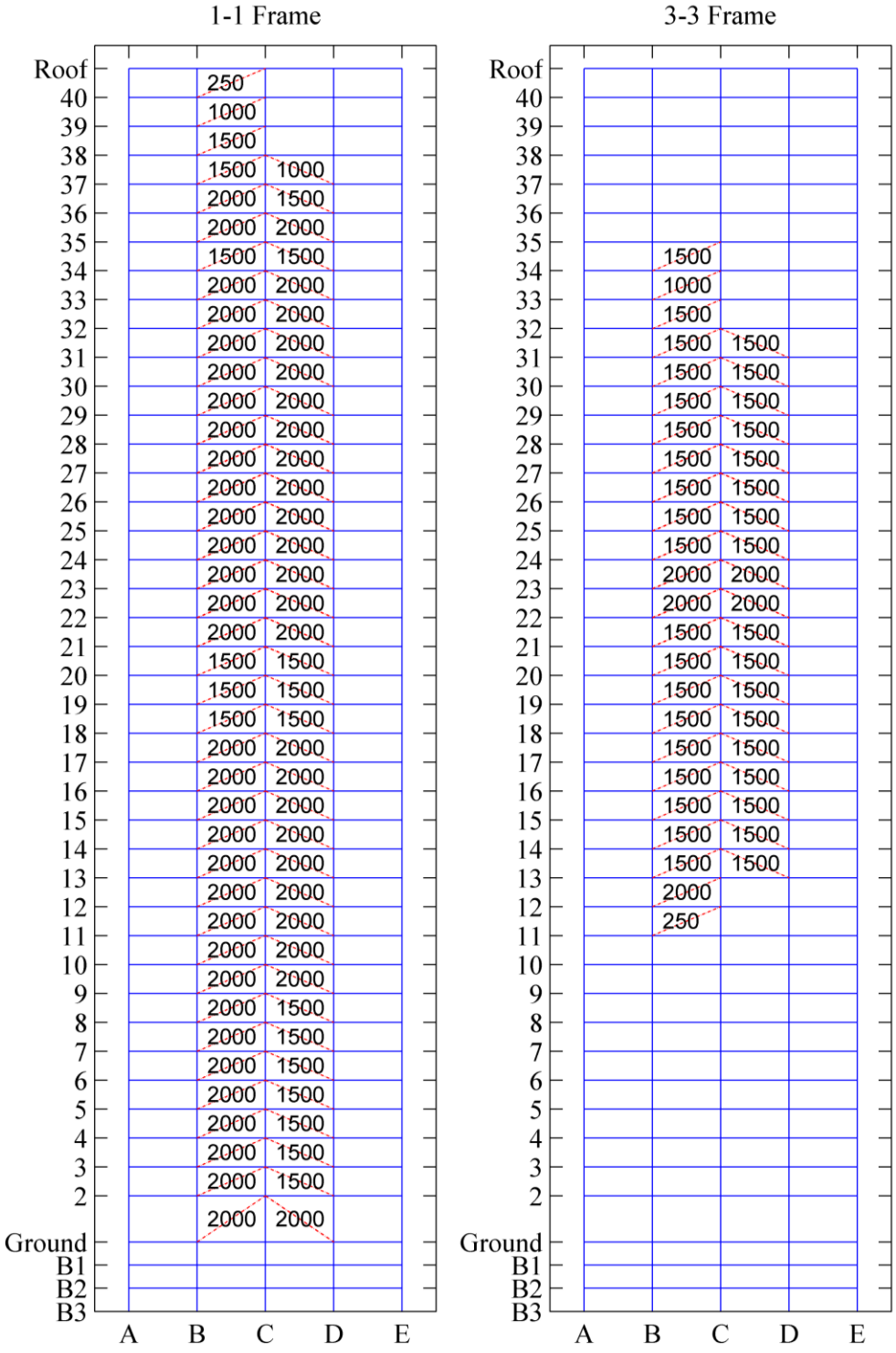

Figure 8.22: Damper design (maximum allowable forces in KN), medium damping level, X-loading direction (balanced SFPDD)

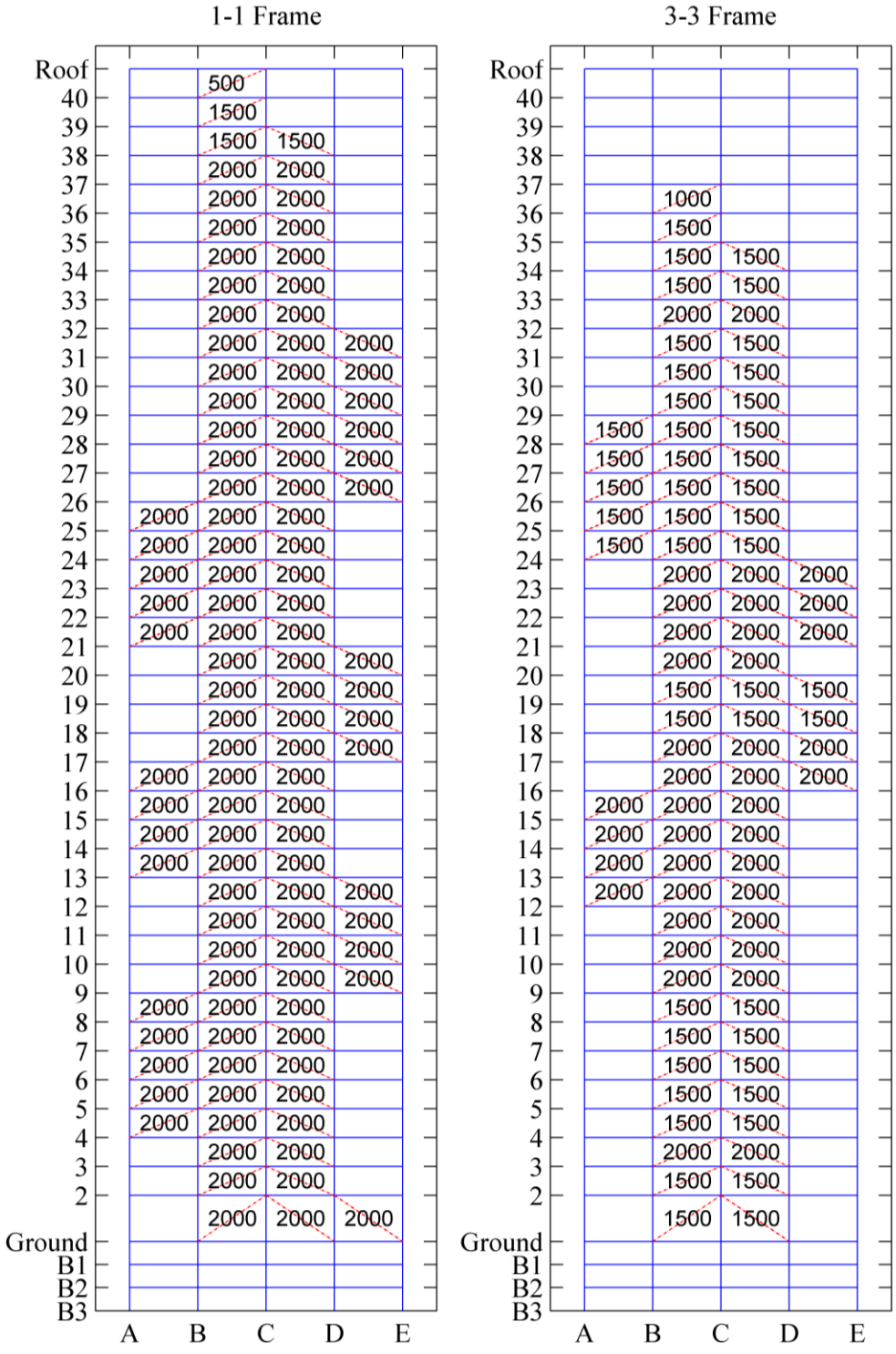

Figure 8.23: Damper design (maximum allowable forces in KN), high damping level, X-loading direction (balanced SFPDD)

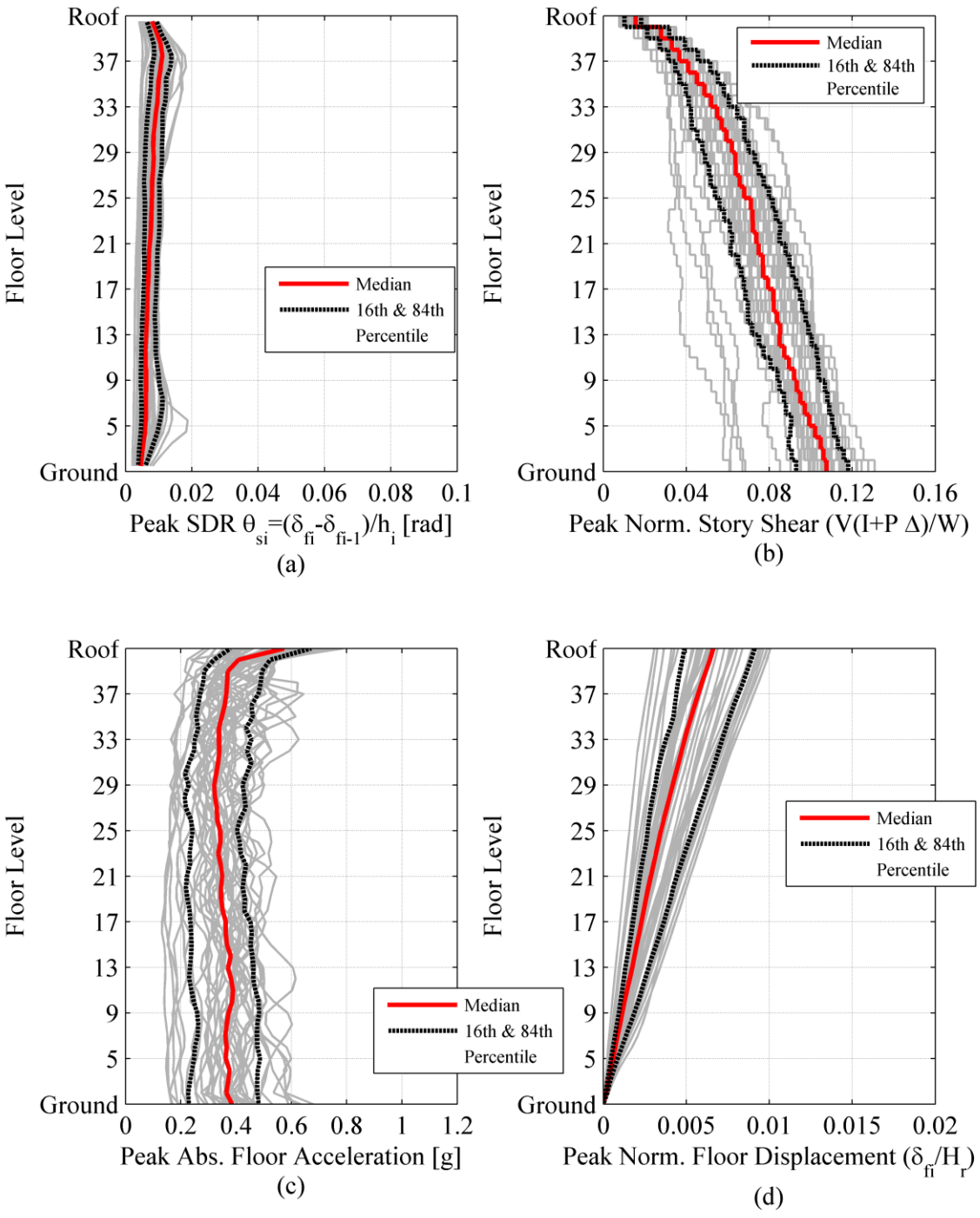

Figure 8.24: Engineering demand parameters, medium damping level, X-loading direction, BSE-1E (balanced SFPDD)

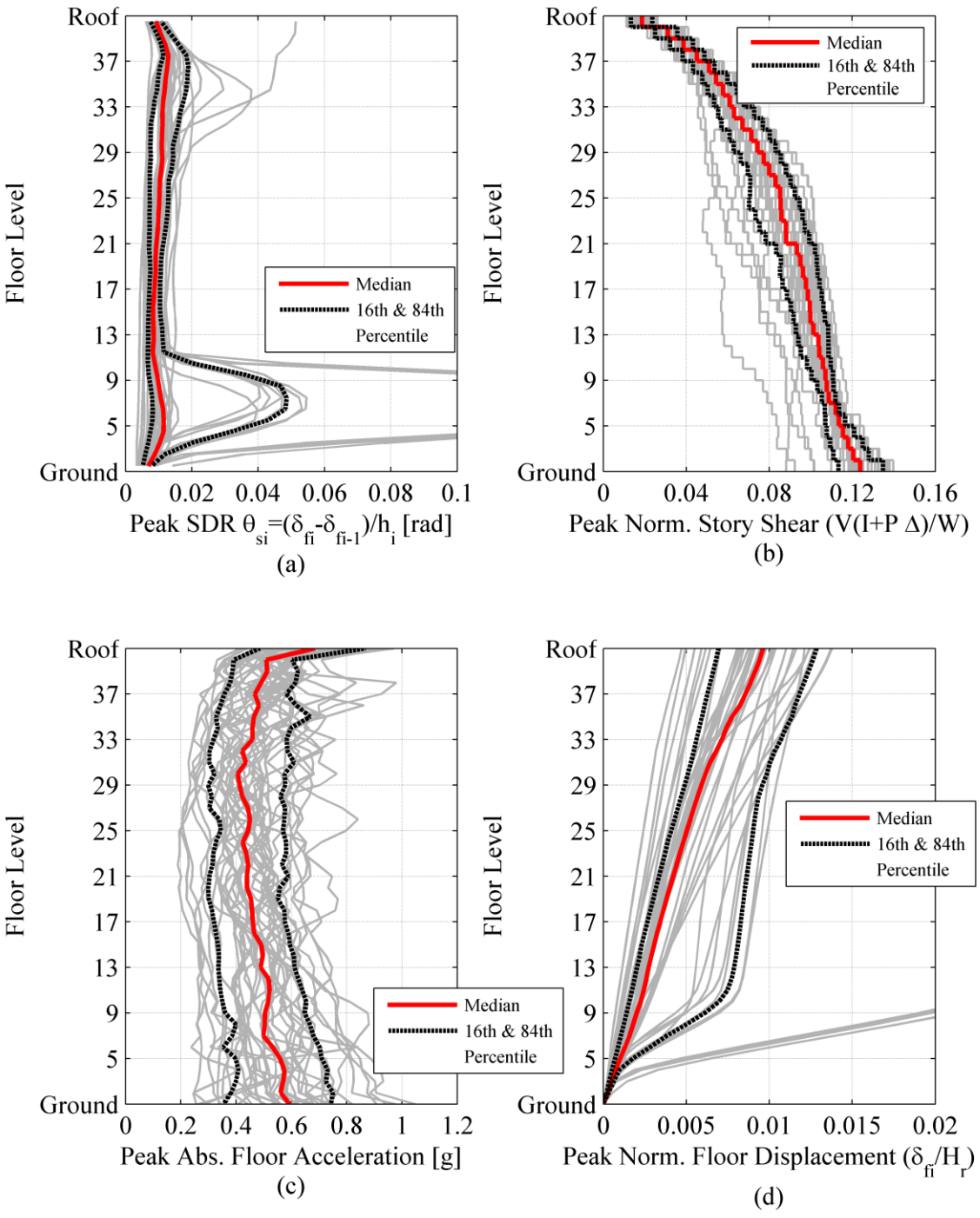

Figure 8.25: Engineering demand parameters, medium damping level, X-loading direction, BSE-2E (balanced SFPDD)

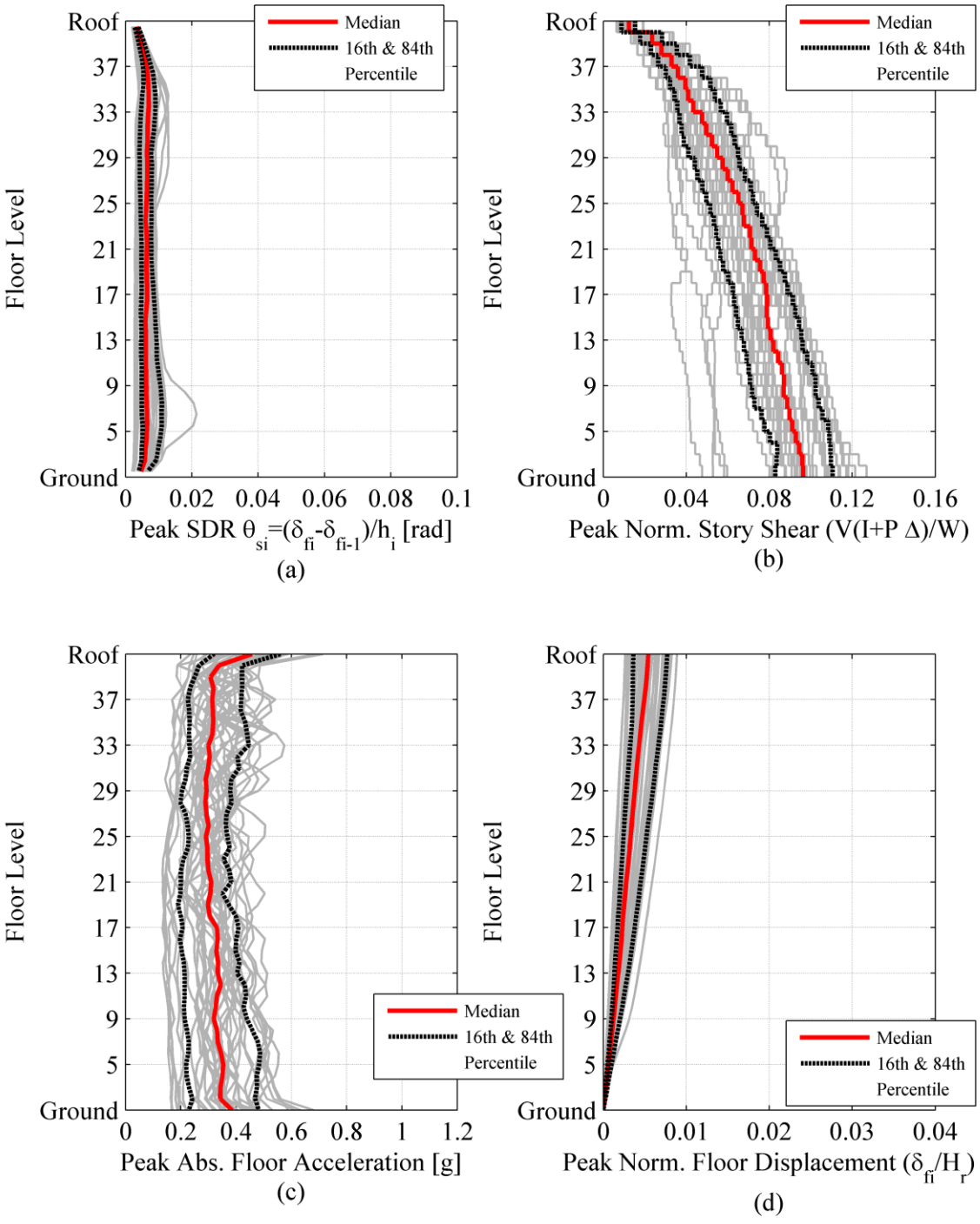

Figure 8.26: Engineering demand parameters, medium damping level, Y-loading direction, BSE-1E (balanced SFPDD)

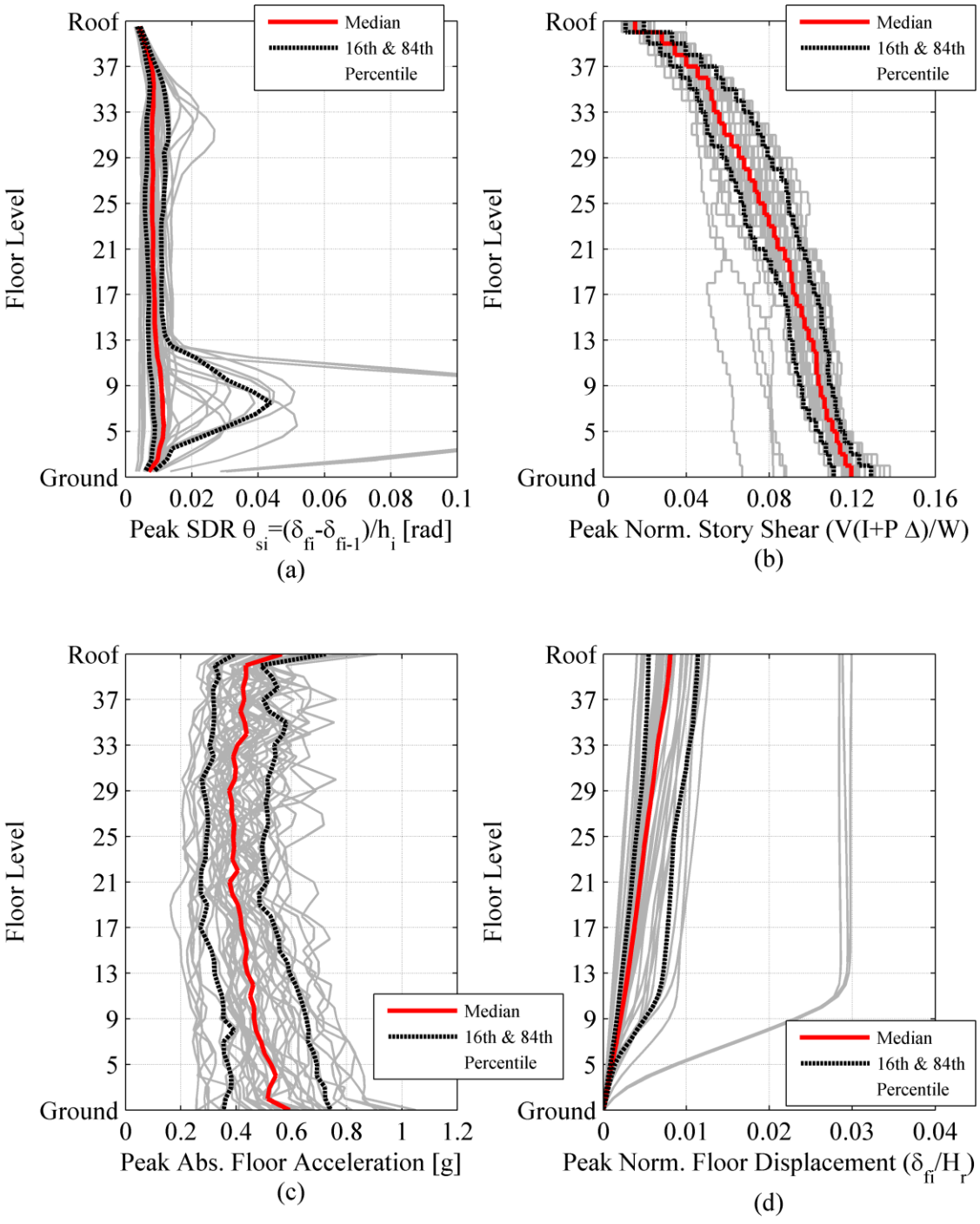

Figure 8.27: Engineering demand parameters, medium damping level, Y-loading direction, BSE-2E (balanced SFPDD)

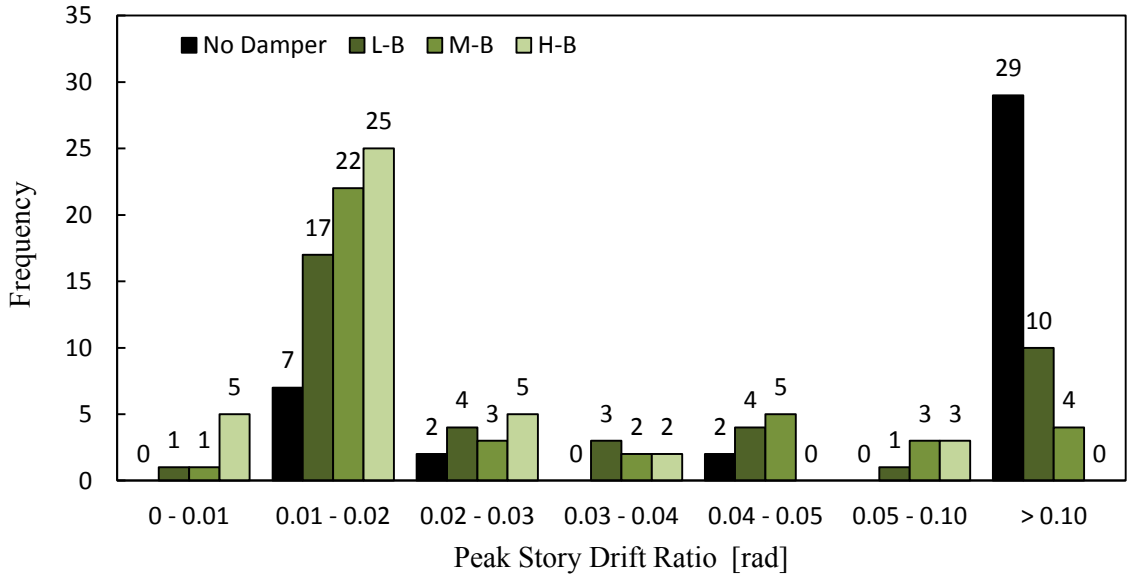

(a)

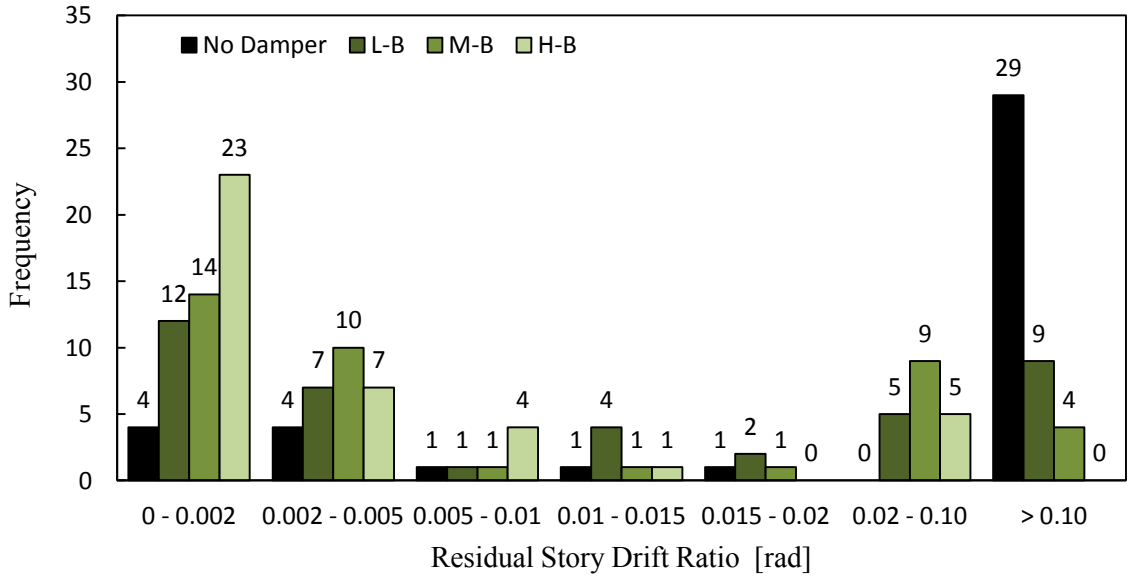

(b)

Figure 8.28: Peak SDRs and residual SDRs in the X-loading direction (BSE-2E level)

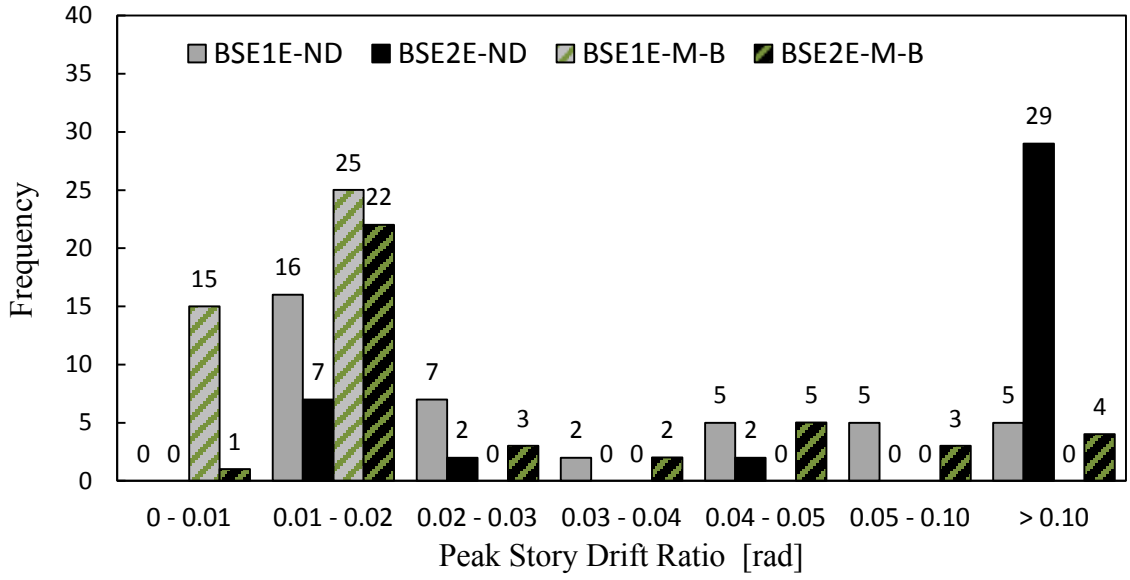

(a)

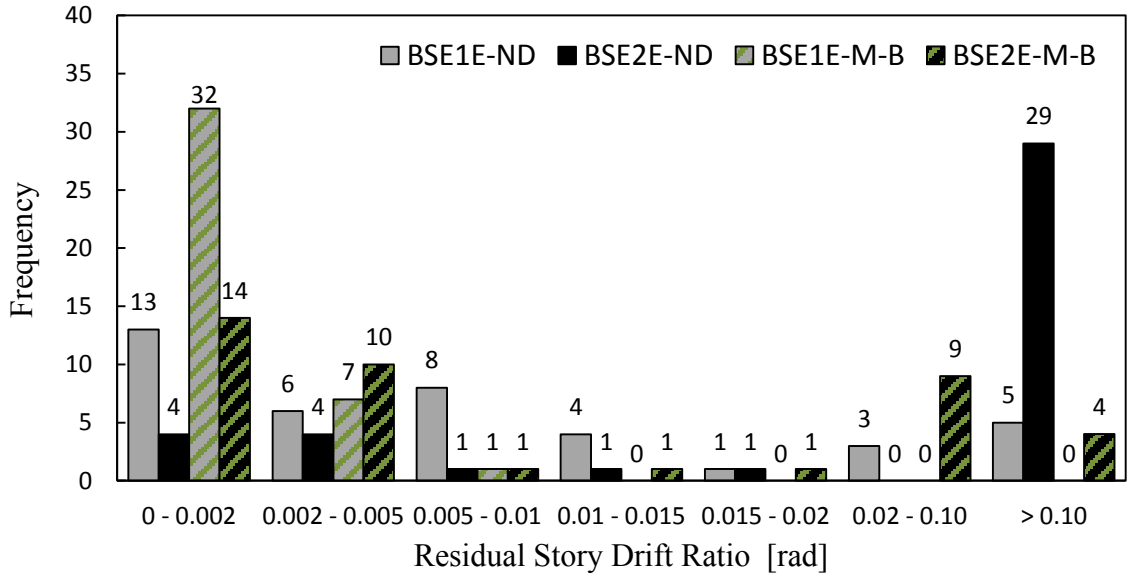

(b)

Figure 8.29: Peak SDRs and residual SDRs in the X-loading direction (BSE-1E and BSE-2 level)

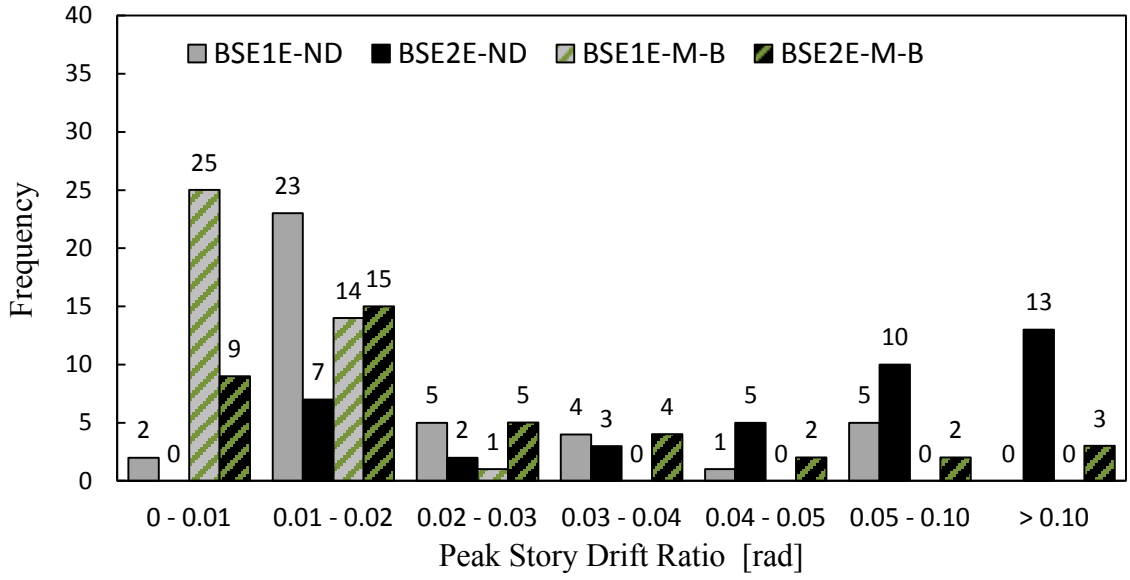

(a)

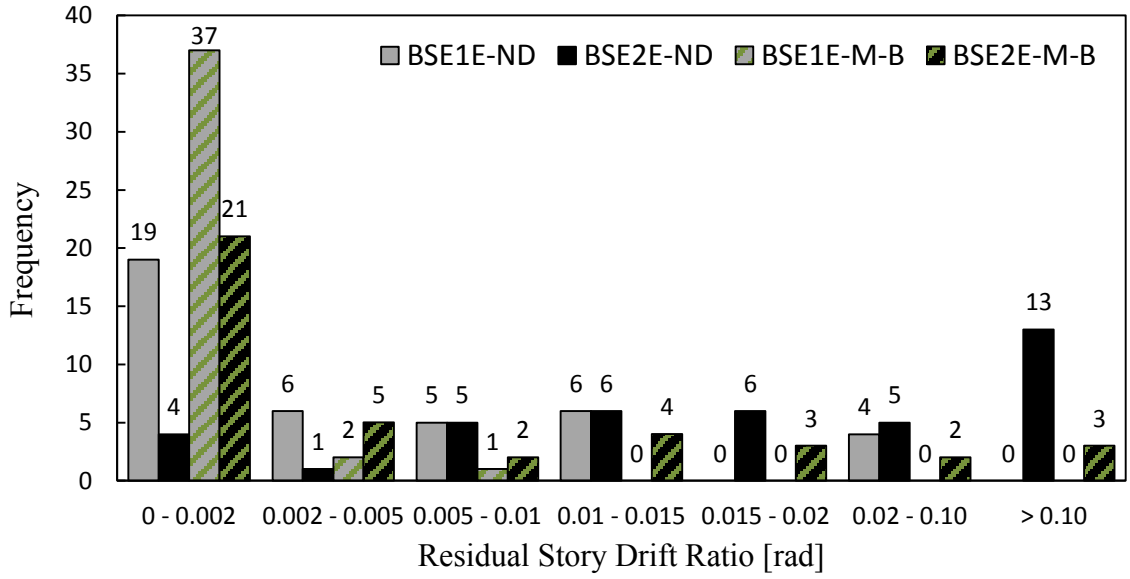

(b)

Figure 8.30: Peak SDRs and residual SDRs in the Y-loading direction (BSE-1E and BSE-2 level)

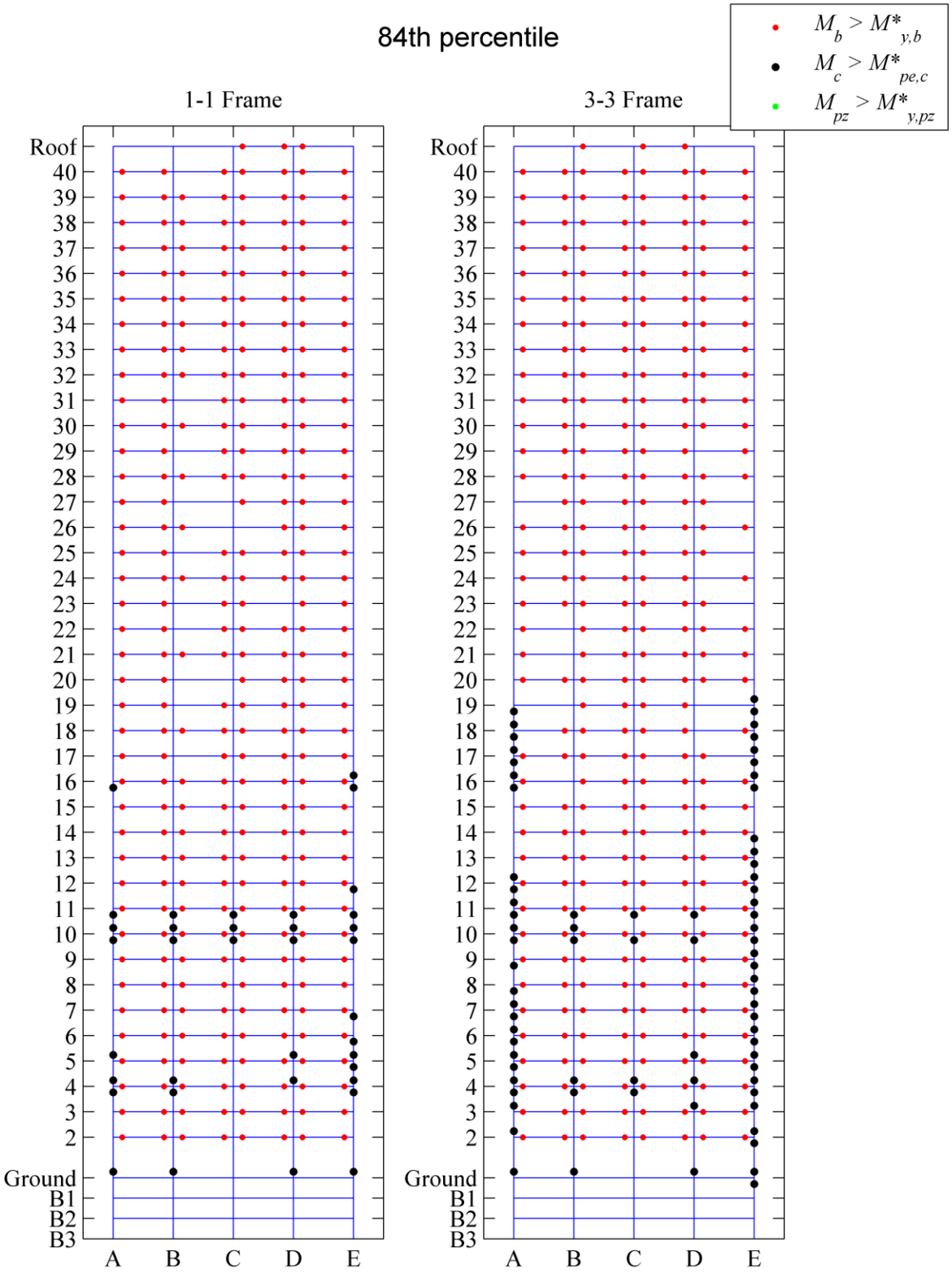

Figure 8.31: Plastic hinge location based on onset of yielding according to the 84th percentile response in X-loading direction (BSE-2E)

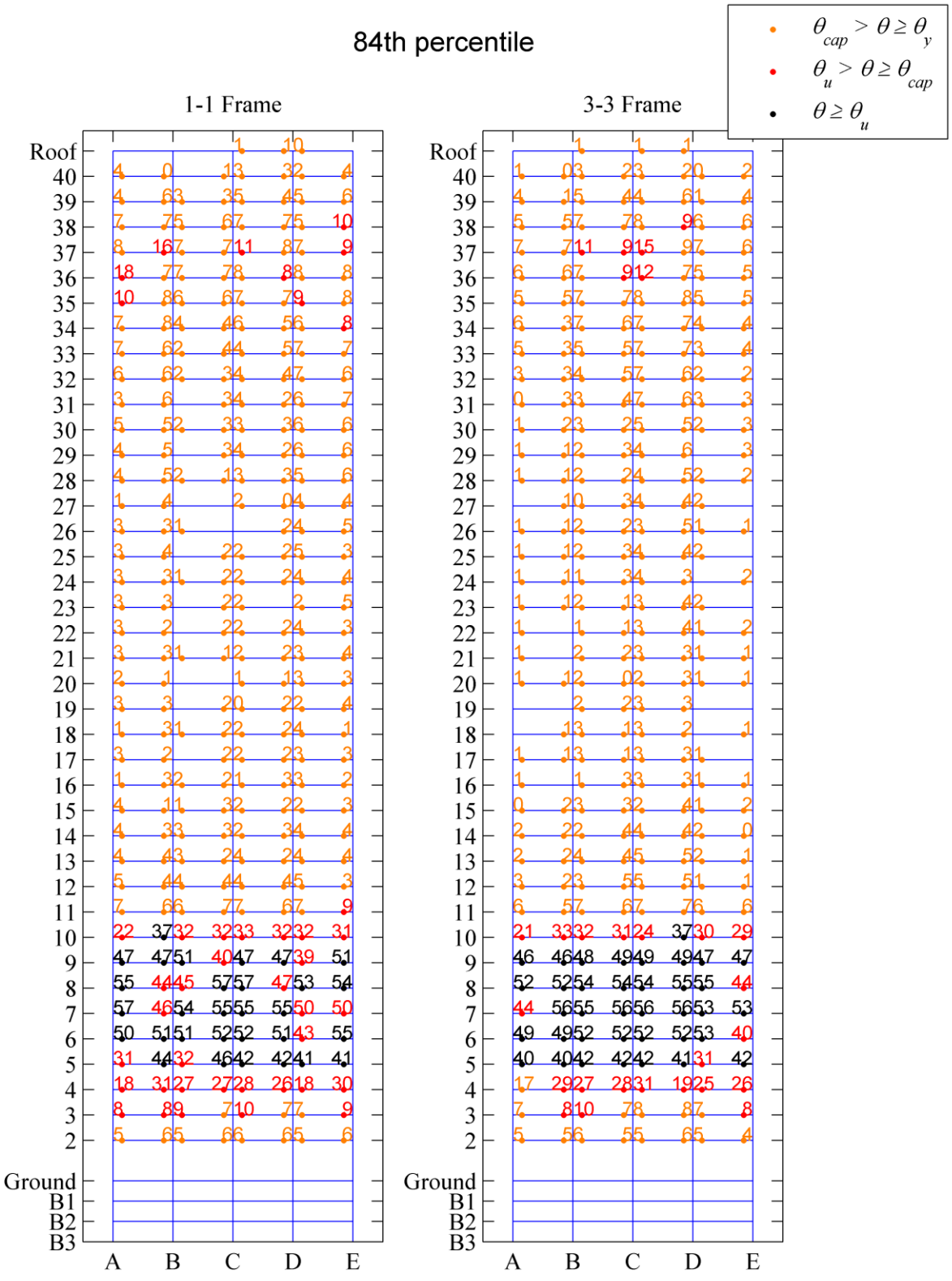

Figure 8.32: 84th percentile of beam peak plastic rotation in X-loading direction (BSE-2E)

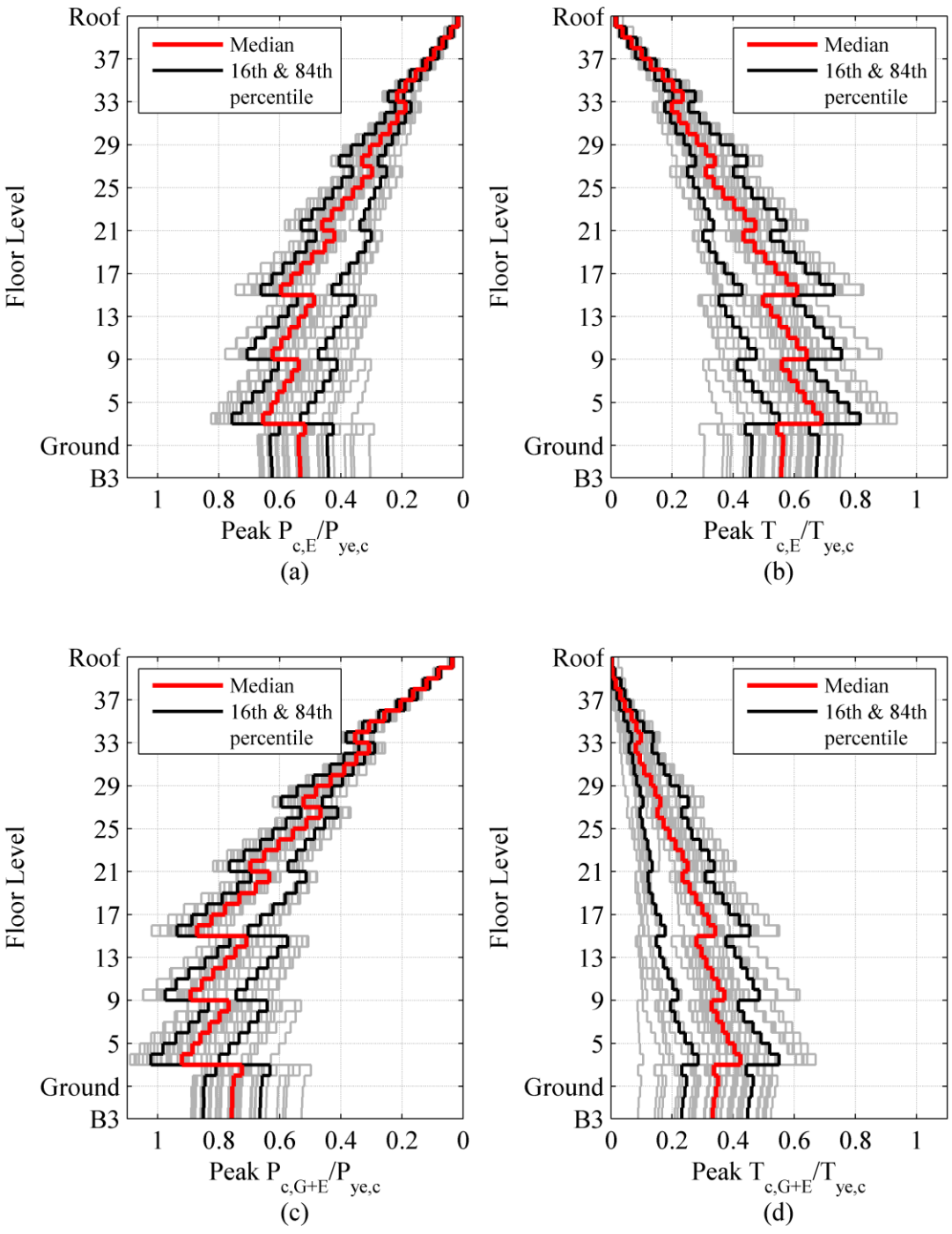

Figure 8.33: Column normalized peak tensile and compressive forces due to seismic loading (E) and combined gravity and lateral loading (G+E), - X-loading direction (BSE-2E)

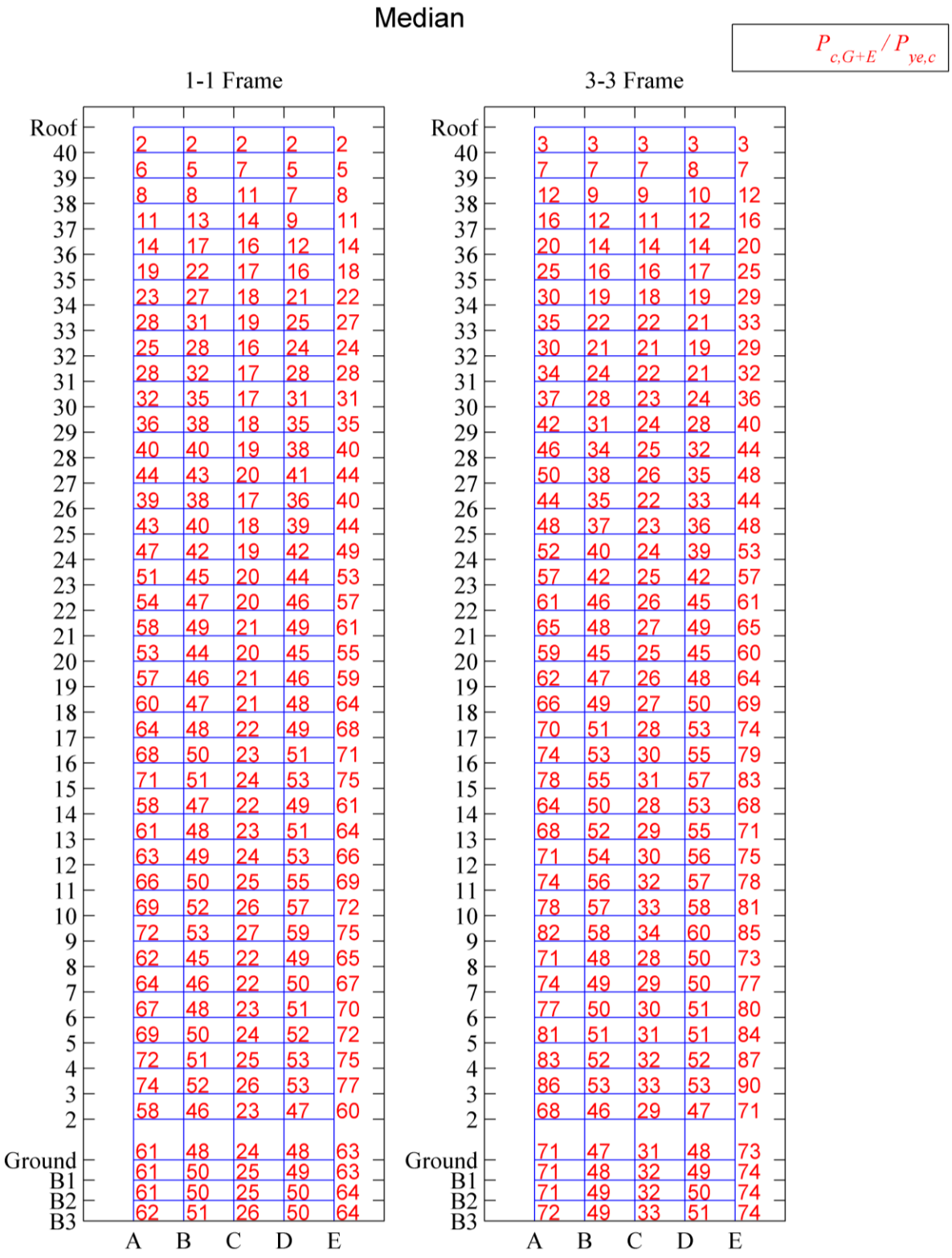

Figure 8.34: Median column normalized peak compressive forces (in %) due to seismic and gravity loading (G+E) - X-loading direction (BSE-2E)

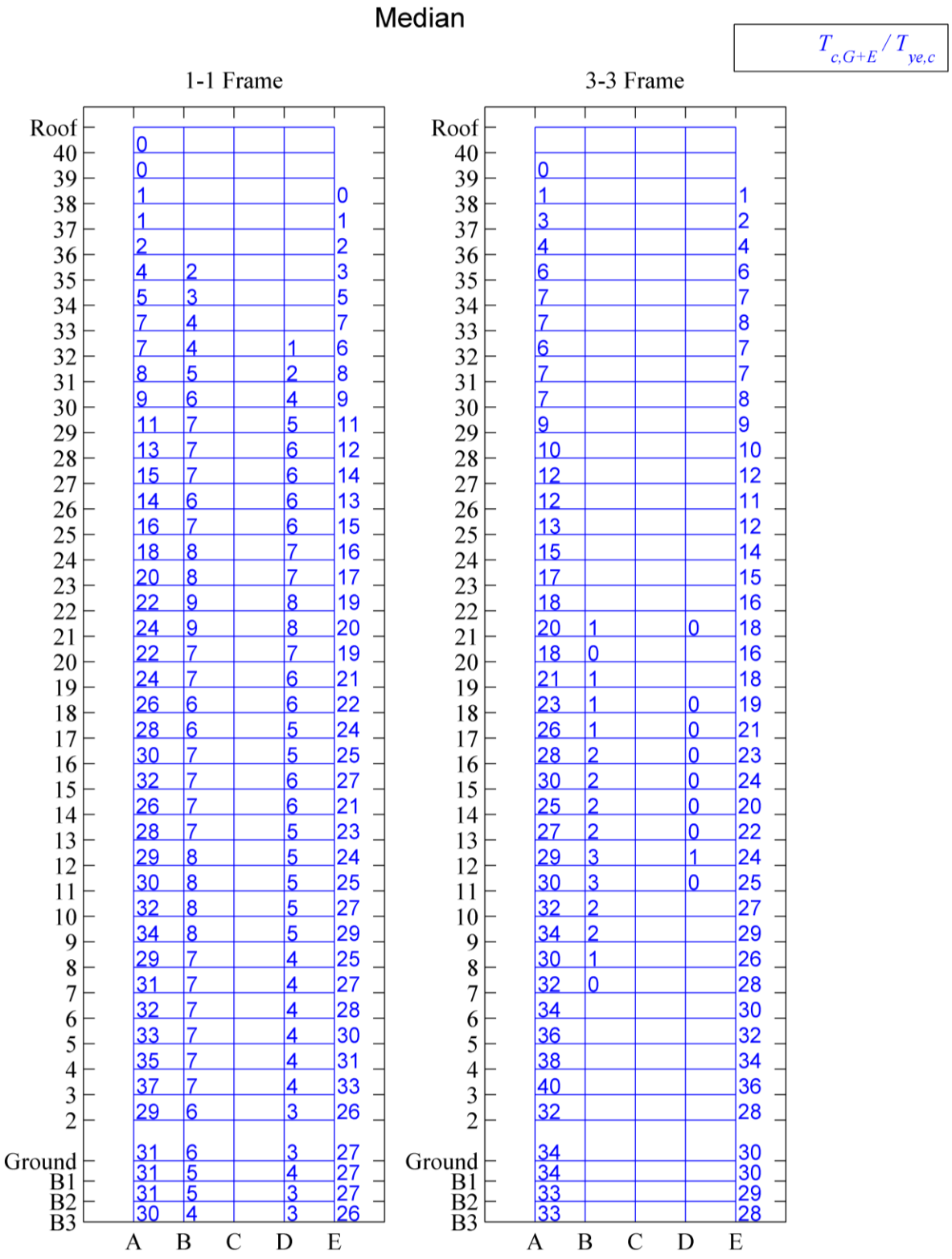

Figure 8.35: Median column normalized peak tensile forces (in %) due to seismic and gravity loading (G+E) - X-loading direction (BSE-2E)

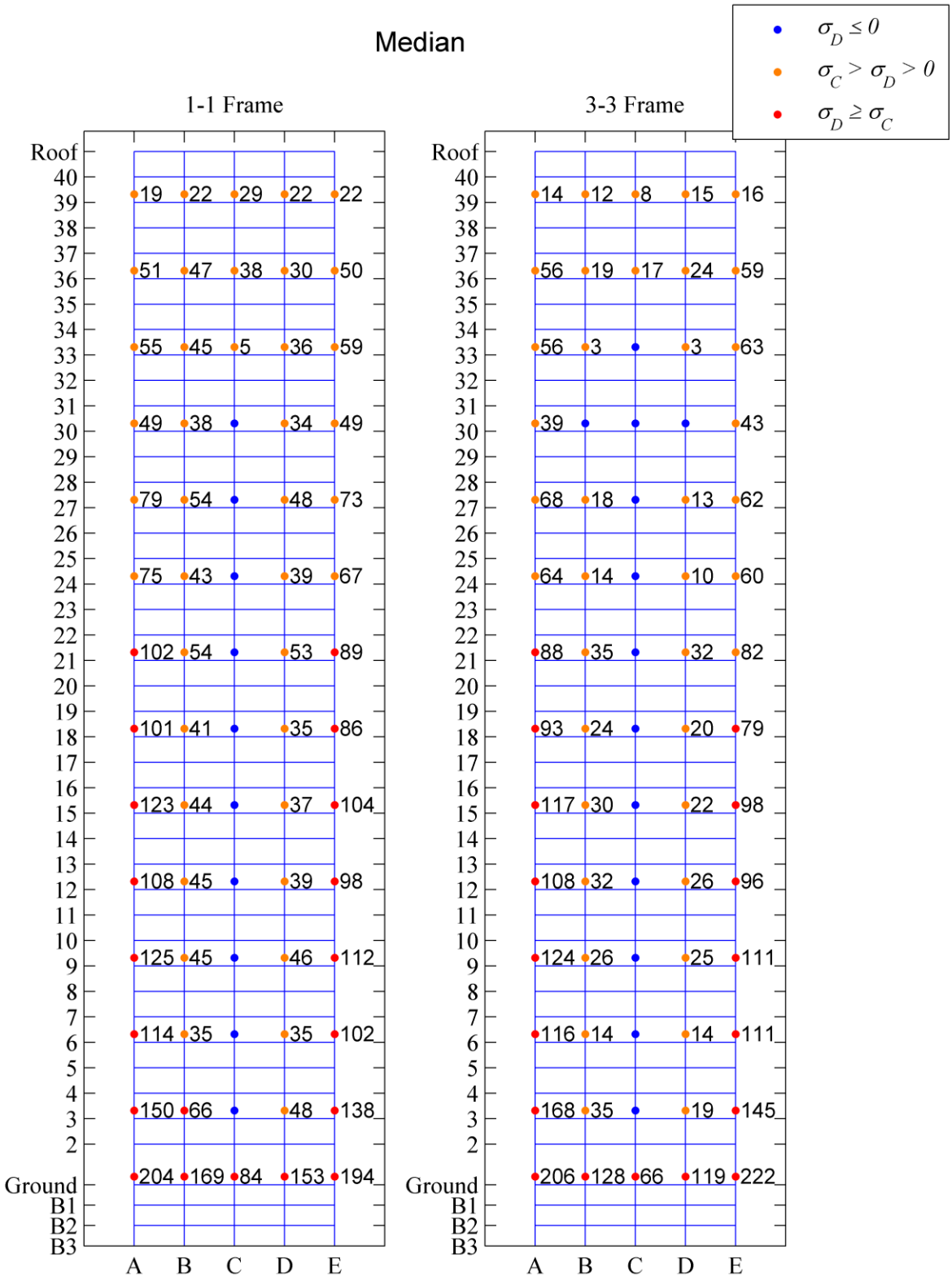

Figure 8.36: Median peak tensile stresses at column splices [MPa] - X-loading direction (BSE-2E)

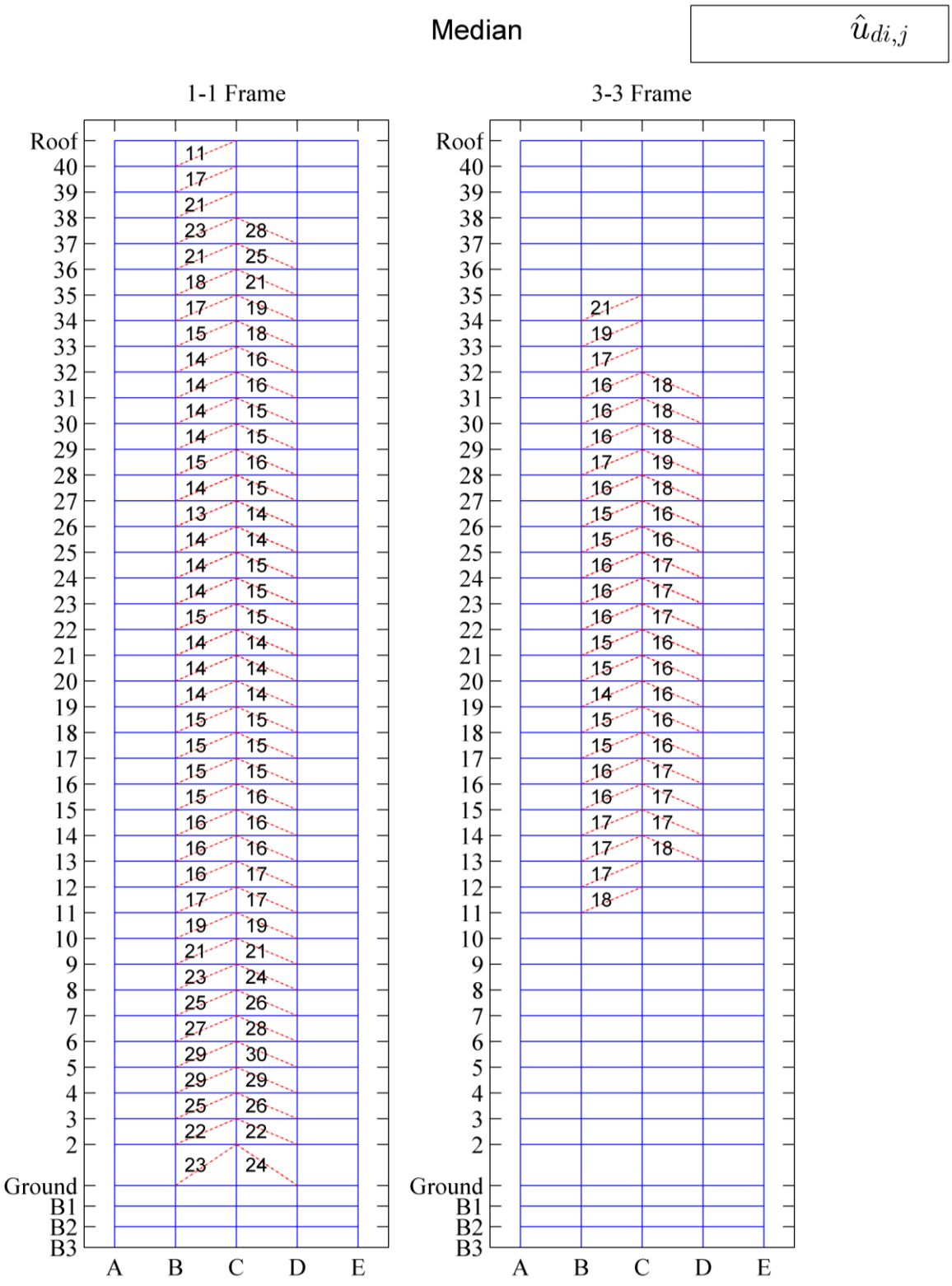

Figure 8.37: Median peak damper displacements [mm] - X-loading direction (BSE-2E)

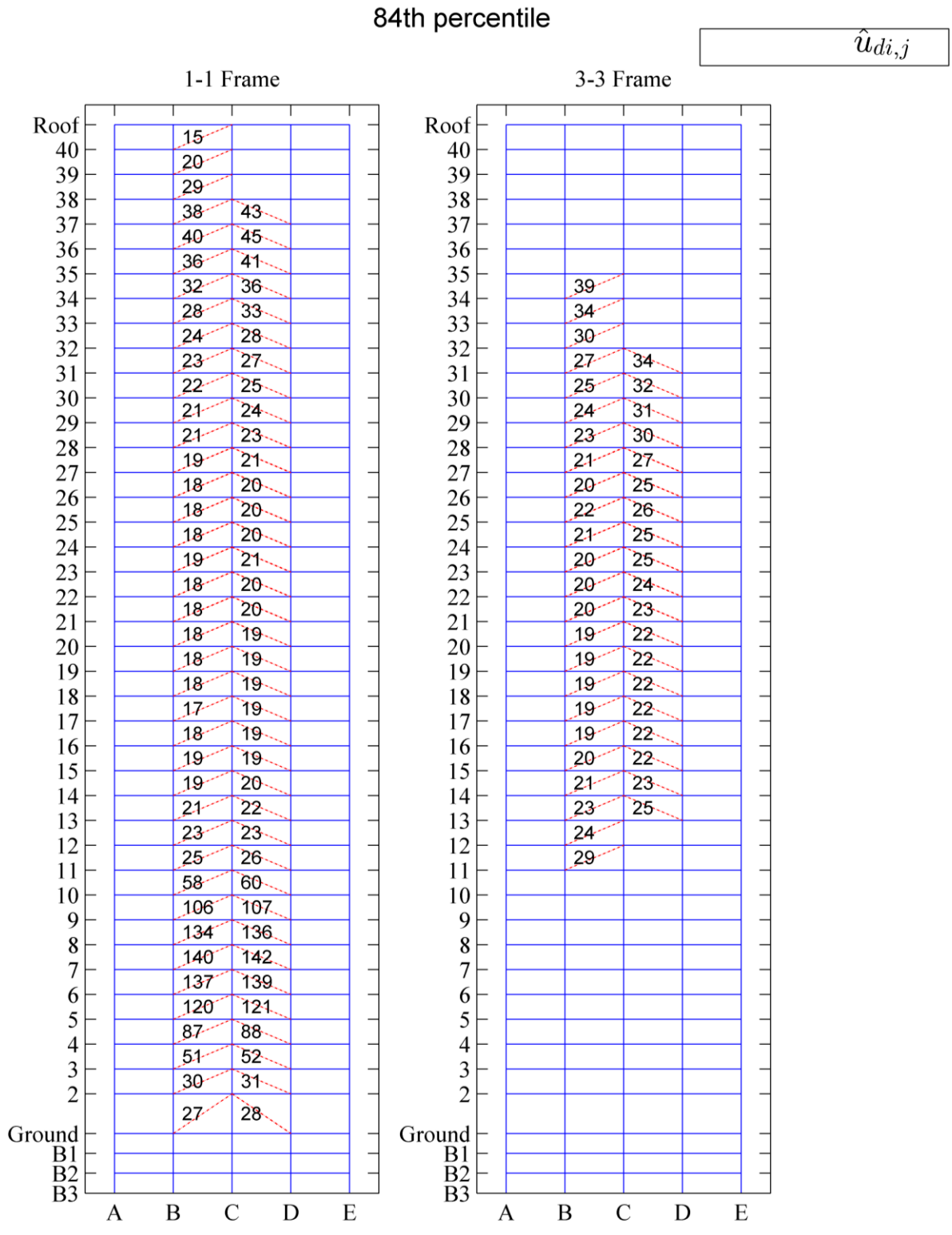

Figure 8.38: 84th percentile of peak damper displacements [mm] - X-loading direction (BSE-2E)

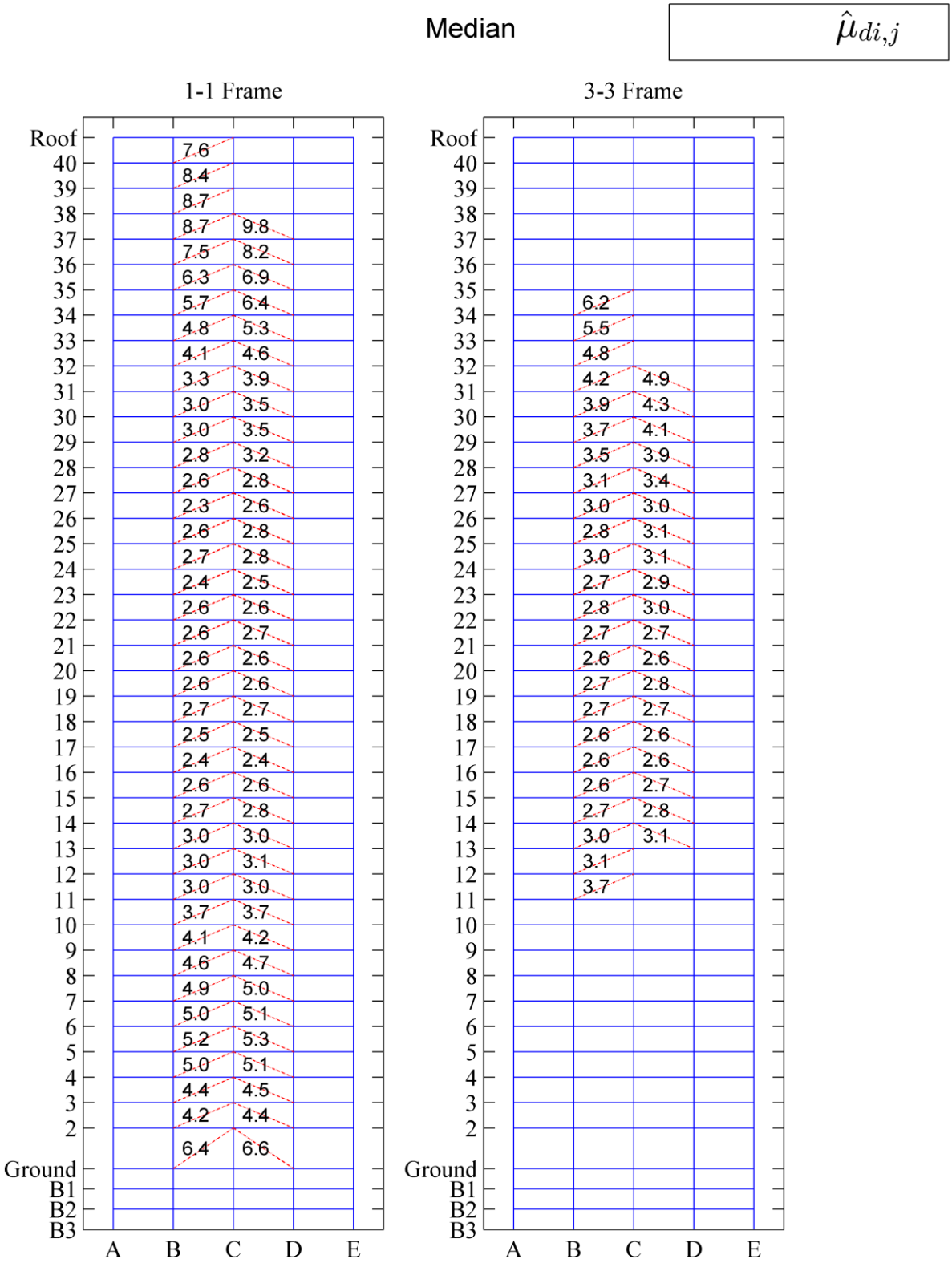

Figure 8.39: Median damper post-relief velocity ratio - X-loading direction (BSE-2E)

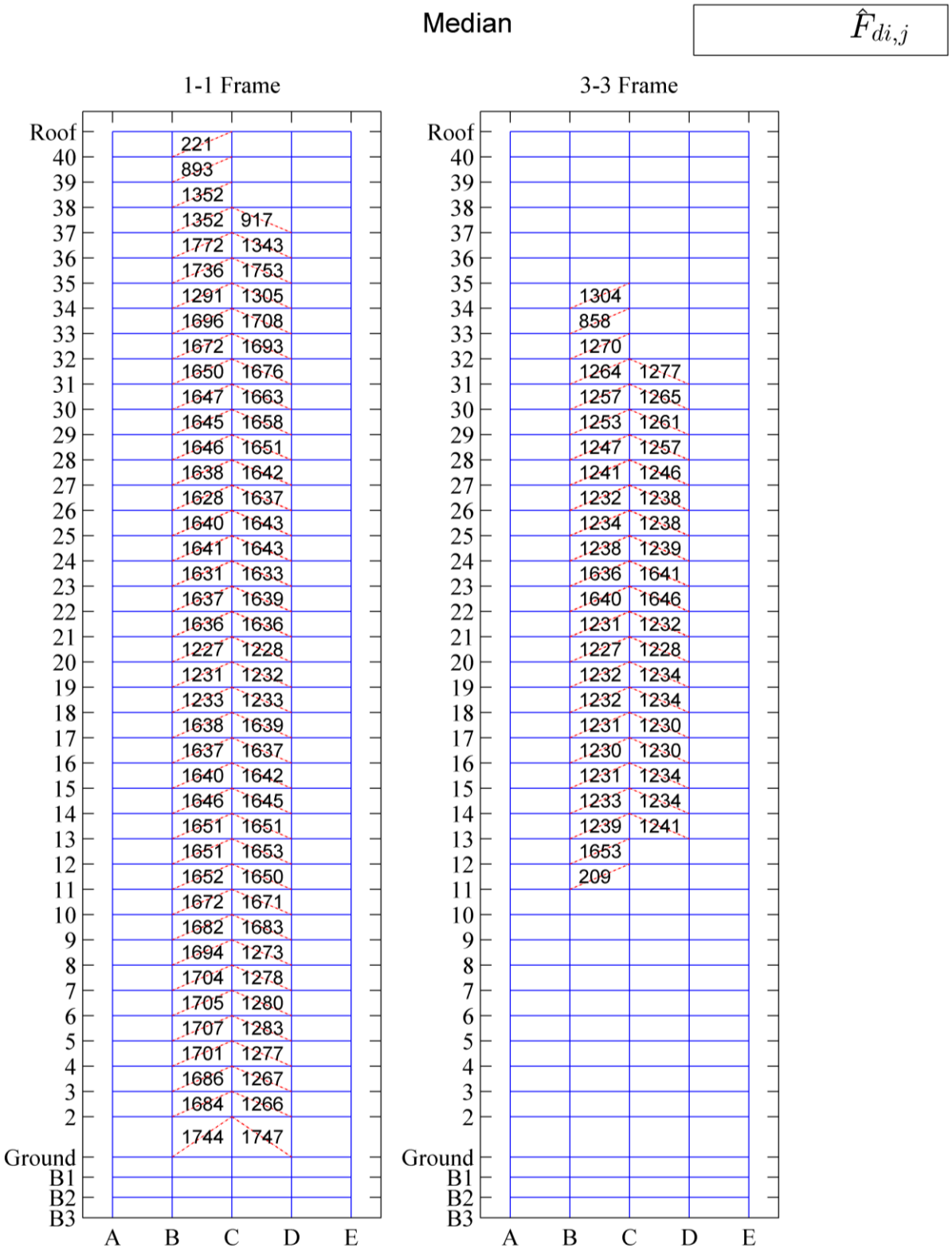

Figure 8.40: Median peak damper forces [KN] - X-loading direction (BSE-2E)

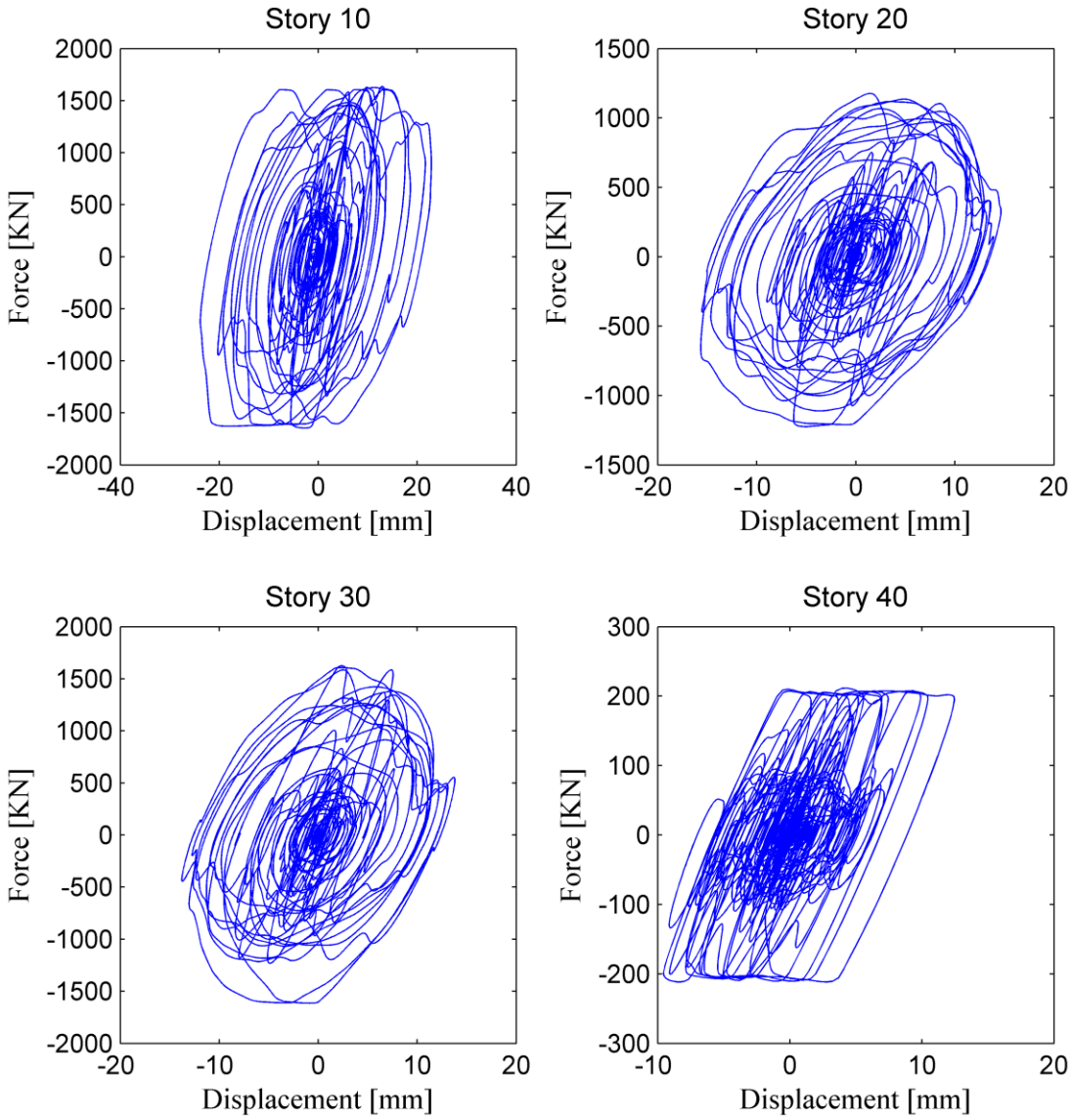

Figure 8.41: Damper force deformation relations for GM# 32, - X-loading direction (BSE-2E)

CHAPTER 9 : Summary and Conclusions

9.1 Summary

The aim of this research was to enhance the advanced and simplified seismic evaluation methodologies for steel frame buildings equipped with supplemental damping devices and provide guidance for efficient retrofit techniques of tall buildings that do not employ capacity design principles. The main accomplishments are summarized in the subsequent paragraphs.

Adaptive-step size algorithms were implemented in an open source simulation platform by for the numerical simulation of nonlinear viscous dampers (NVDs) and bilinear oil dampers (ODs). These algorithms account for the axial stiffness of the dampers. The sub-stepping within the material model was determined by the absolute relative error between 5^{th} and 4^{th} order solutions of the first order ordinary differential equation (ODE) that expresses the force equilibrium within the damper. A sensitivity study was conducted to investigate the effect of damper variables on the numerical solution. The effect of axial stiffness on the damper response was also quantified. The system level validations were carried out with experimental data obtained from full-scale shake table tests of a 5-story steel building equipped with NVDs and ODs. To this end, two new uniaxial material models were developed and implemented into the *OpenSees* platform (i.e., *ViscousDamper*, *BilinearOilDamper*).

A rate-dependent numerical model for buckling restrained braces (BRBs) was developed to improve the simulation of buildings with BRBs under dynamic excitations. The proposed model consists of a displacement-dependent asymmetric material model and a velocity-dependent bilinear oil damper model. The step-by-step calibration procedure of the input model parameters was also demonstrated. An illustrative example was shown that utilized test data from BRBs subjected to quasi-static and dynamic loading protocols. Different approaches for the nonlinear modeling of BRBs were proposed including a beam-column and a link element. The numerical model is implemented into the *OpenSees* platform.

Based on the experimental data of full-scale shake table tests of a 5-story steel building equipped with dampers, evaluation of current simplified and state-of-art assessment methods for steel buildings equipped with BRBs and NVDs was conducted. The test structure was modeled in *SAP2000* and the *OpenSees* platforms. Several simplified evaluation methods, such as linear and nonlinear static procedures per ASCE 41-13 (ASCE/SEI 2014), performance curves and P-spectra methods were implemented and compared. These methods were further refined.

A practical Multi-Degree-of-Freedom (MDF) tool was developed for the design of supplemental damping devices in tall frame buildings, which is an extension of single-degree-of-freedom (SDF) performance curves methods. Guidance on the construction of simplified models, such as the shear beam and flexural shear beam models was provided. The effectiveness of vertical damping distribution methods, such as the stiffness, the direct shear force and the effective shear force proportional distribution methods have been evaluated and discussed. A case study was presented for the design of bilinear oil dampers for the seismic retrofit of a 1970s high rise steel-frame building with space moment-resisting frames (MRFs). A comparative parametric study

was carried out with three different vertical damping distribution methods and damping levels and performance curves were developed.

A comprehensive seismic assessment of a 40-story space MRF steel building was conducted. The prototype building was designed according to UBC 1973. It represented the construction practice in early 1970s in the west coast of North America. The design of the benchmark building was conducted with a three-dimensional model. In order to carry out a rigorous seismic assessment as per ASCE 41-13 (ASCE/SEI 2014), advanced nonlinear two-dimensional (2D) model representations of the building were developed in the *OpenSees* platform. Nonlinear static analysis was conducted to preliminary explore the seismic performance of the building and to identify the influence of modelling parameters on its dynamic response. Nonlinear response history analysis were also conducted with 40 ground motions, that were selected and scaled to be compatible with the Basic Safety Earthquake Levels (BSE-1E and BSE-2E) as per ASCE 41-13 (ASCE/SEI 2014). The building seismic assessment includes both global and local engineering demand parameters.

Finally, a number of retrofit solutions were evaluated for the prototype 1970s high rise building. Supplemental damping was provided by bilinear oil dampers. The design was carried out with the aid of MDF performance curves method developed in Chapter 6. Multiple retrofit schemes were proposed and the effectiveness of various vertical damping distribution methods was discussed by means of NRHA. A newly proposed balanced shear force proportional distribution method was employed and compared with the effective and direct shear force proportional damping distribution methods. The proposed method aims to provide uniform distribution of shear deformations along the height of the building when controlled yielding is expected. Based on the final retrofit design with the balanced distribution method, NRHA was conducted for the

BSE-1E and BSE-2E hazard levels as ASCE 41-13 (ASCE/SEI 2014). A comprehensive assessment of the seismic demands in the framing members as well as the dampers was conducted.

9.2 Conclusions and Recommendations

The conclusions and recommendations of this thesis are listed as follows,

9.2.1 State-of-art Evaluation Methods for Buildings equipped with Supplemental Damping Devices

In cases that involve NVDs with large axial stiffness and small velocity exponents, a high-accuracy numerical solution of the force-displacement relations of the respective damper was achieved with relatively large integration steps and only few sub-step iterations within a solution step.

In the case of bilinear ODs with large axial stiffness, an alternative adaptive numerical integration algorithm was proposed. This integration scheme is able to provide same accuracy solutions with the adaptive Dormand-Prince iterative method but with much smaller number of sub-step iterations.

System-level validation studies indicated that the proposed integration schemes for NVDs and ODs were successful in predicting the seismic response of global engineering demand parameters of interest such as story drift ratios, story shear forces and absolute floor accelerations along the height of frame buildings with a relatively low computational cost.

When the velocity-dependency in a BRB model is neglected, the BRB local forces are significantly under estimated based on comparisons between simulated and experimental data from full-scale BRBs subjected to cyclic loading. This may be fairly critical if BRBs are utilized

as a seismic retrofit strategy in existing steel frame buildings. Depending on the frequency characteristics of the seismic excitation, similar differences may be observed in the predicted story-based engineering demand parameters such as story-drift ratios and peak absolute floor accelerations.

For relatively symmetric buildings in plan view, there is no clear advantage between 3D and 2D nonlinear response history analyses, regardless of the type of the employed passive control device (BRB or NVD). Furthermore, there is practically no difference between the 3D simulated results from commercially available (e.g., *SAP2000*) and research-oriented (e.g., *OpenSees*) software platforms that are widely used within the earthquake engineering community.

Steel frame buildings with virtually no structural damage that concentrate their inelastic behaviour into damping devices do not require the utilization of sophisticated nonlinear modeling approaches for computing various EDPs of interest for structural and non-structural damage control. Emphasis should be placed on the nonlinear modeling of the employed supplemental damping device.

9.2.2 Simplified Evaluation Methods for Buildings Equipped with Supplemental Damping Devices

The current FEMA 356 (FEMA 2000a) and ASCE 41-13 (ASCE/SEI 2014) effective damping ratio formulation for linear static procedures (LSPs) used in frame buildings equipped with BRBs and NVDs may be non-conservative. It is advisable that such formulation should consider the displacement-based ductility demand variation of BRBs. The equivalent formulation for frame buildings with NVDs should consider the damper's axial flexibility. This is consistent with current linear static procedures used in the Japanese design practice (Kasai and Ito (2005); Kasai et al. (2007).

Currently employed nonlinear static procedures (NSP) as discussed in ASCE 41-13 (ASCE/SEI 2014) and FEMA 356/FEMA 440 (FEMA 2000a) may overestimate the predicted roof displacement demands in frame buildings with BRBs for moderate and low-probability of occurrence ground motion intensities in North America. This is in part attributed (1) to the idealized bilinear approximation of the base shear-roof displacement relation of frame buildings with BRBs and (2) the effective damping formulations proposed in FEMA 273/356/440 (FEMA 1997; 2000a; 2005). A simple trilinear equivalent SDF oscillator with a versatile nonlinear SDF analysis tool retains the simplicity of NSP procedures for evaluating frame buildings with BRBs; Available full-scale experimental data suggest that the relative errors in the respective EDPs of interest are in the range of 10% or less regardless of the ground motion intensity and loading direction of interest.

The utilization of test data from shake table experiments suggest that when a performance spectra (i.e., P-Spectra) approach is employed to validate the efficiency of various damper solutions on the dynamic response of the test structure, the relative errors in predicting both the peak roof displacement and base shear of the test structure with BRBs are in general smaller than those from currently employed nonlinear static approaches. The same conclusion holds true for the test structure with NVDs when the axial flexibility of such dampers is considered for the construction of P-Spectra. This is also confirmed with rigorous nonlinear response history analysis with a 3-dimensional representation of the test structure with NVDs

A P-Spectra approach is able to provide a more realistic representation of the structural system performance including estimates of residual deformations. Traditional static approaches are not able to predict such EDP, which is essential for structural and non-structural damage control.

9.2.3 Practical Design Method for Tall Buildings Equipped with Supplemental Damping Devices

The effect of flexural deformations on the dynamic response of tall buildings is appreciable. Shear beam models (SBM-2E) predict relatively well the floor displacements of tall buildings. However, the corresponding error in predicting peak SDRs in the upper stories of the building is fairly significant when the flexural deformations are ignored. When a flexural-shear beam model (FSBM-E) is utilized the predicted response is nearly identical with the one computed from a detailed numerical representation of the building. It is recommended that shear beam models should not be considered for the seismic evaluation of new and existing tall buildings.

The effective shear force proportional damping distribution method at a low damping level (i.e. $K_d''/K_{fs} = 0.25$) suggests that dampers are only needed in few stories of a tall building. The number of stories equipped with dampers increase when with the damping level increases. On the other hand, the dampers are distributed at all levels when the shear force and stiffness proportional damping distribution methods are employed regardless of the damping level.

When a SBM-1E model is employed, the effective shear force proportional damping distribution (SFPDD) method alters the distribution of peak SDRs to be relatively uniform, particularly at high damping levels (i.e. $K_d''/K_{fs} = 1.0$). On the other hand, the direct SFPDD and stiffness proportional damping distribution methods do not alter the drift concentrations observed in the non-retrofitted building.

When a FSMB-E model is employed, the observed differences in predicted SDRs become less influenced with respect to the employed vertical damping distribution method. More importantly, the corresponding reduction factors are significantly higher than those of shear beam models.

The response reduction in the absolute floor accelerations and the corresponding base shear is less sensitive to flexural deformations than that observed in floor displacements and SDRs.

At a BSE-2E hazard level, when the MDF performance curves are employed, the base shear and maximum absolute floor accelerations are reduced by up to about 50% compared to the non-retrofitted frame; there is no reduction for $K_d''/K_{fs} > 1$.

9.2.4 Performance-Based Evaluation of a 1970s High-Rise Steel Frame Building

The steel design of existing tall buildings in the west-coast of North America may be governed by the wind load drift limitation in their lower stories. Such buildings are likely to violate the strong-column/weak-beam (SCWB) requirement of AISC (2010b) in exterior columns due to high axial load demands.

The tall building performance was evaluated through nonlinear static (pushover) analysis. The analysis suggests that differences in the dynamic response of the building are fairly small when its connections are assumed to be 'brittle' or '25% ductile'. Pushover analysis shows that at around 1% roof drift ratio the building performance was significantly compromised due to a sudden strength loss. In all cases, multiple-story mechanisms occurred in the lower half of the building. Rigorous nonlinear response history analysis indicates that the building collapsed in 29/40 ground motions at the BSE-2E level including upper story collapse mechanisms. Residual SDRs were mainly concentrated in the upper stories of the building in the rest of the cases. Almost all the beams experience flexural yielding. Notably, no yielding was observed in the panel zones.

Exterior columns in the lower stories of non-retrofitted building experience high compressive and tensile forces. In certain cases, the compressive force reached up to the expected column

yield strength. The same columns experience, on average, axial load demands ranging from $0.8P_{ye,c}$ in compression to $0.3T_{ye,c}$ in tension. The interior columns within the same stories experienced compressive axial forces up to $0.5P_{ye,c}$. No significant difference in column axial loads was obtained between BSE-1E and BSE-2E levels. This implies that unless if the peak SDR reduction is considerable, the column axial load demands are expected to remain high at the BSE-2E level even if the building would be retrofitted with supplemental damping.

About 34% of the column splices were found to be vulnerable at the BSE-2E level. On the other hand, a considerable number of interior column splices exhibited no or low tensile stresses. This indicates that the column splice upgrading may not be necessary for the entire building.

9.2.5 Seismic Retrofit of an Existing Tall Building with Bilinear Oil Dampers

The design of oil dampers according to the performance curves method utilizing different damping levels resulted in a K_b/K_d'' ratio between 4.4 to 6.3, and a K_b^*/K_d'' ratio between 1.6 and 2.4. Although the peak damper velocity ratio target was 2.0 in the initial design, it was reduced to 1.5 and 1.2 for medium and high damping levels, respectively, due to the available damper sizes for low relief velocity and reduction in damper demands.

It was found that the damper placement at internal bays of the exterior frame was more effective in reducing the story-based engineering demand parameters. This was attributed to the relatively high displacement transmission factors observed in the internal bays of the building.

The effect of vertical damping distribution on the building performance was significant. If the retrofitted frame still exhibits inelastic behaviour, the effective SFPDD is the most inefficient retrofit solution that causes damage concentration at stories where dampers are not provided,

particularly at low and medium damping levels. On the other hand, the direct SFPDD method provides the most efficient solution especially when collapse prevention is the main objective.

The peak SDRs were large in the bottom stories when the effective SFPDD method was employed, whereas in direct SFPDD the peak SDRs increased with the building height. Therefore, a refined SFPDD method was proposed and implemented to balance the peak SDR distribution along the building height. The balanced SFPDD provides supplemental damping within every story of the building. Therefore, the proposed retrofit solution is more redundant for collapse prevention than effective SFPDD. The elastic distribution and possible vertical irregularity of the frame stiffness was considered by partially accounting for the effective SFPDD method. Thus, the proposed balanced SFPDD provided an efficient retrofit solution, particularly at medium damping levels.

Based on the retrofitted building evaluation designed with the balanced SFPDD method at medium damping level, at the BSE-2E hazard level, the number of collapses was reduced from 29 to 4 and 13 to 3, in the X- and Y-loading directions, respectively. The collapse mechanisms involved bottom stories in both cases. Peak residuals SDRs were mainly concentrated in the bottom stories.

High demands in the upper story columns of the non-retrofitted building were minimized after the implementation of the retrofit solution. No reduction was observed in the bottom story exterior column compressive and tensile forces in the X-loading direction, at the BSE-2E hazard level. Furthermore, the damper installation led to an increase in the interior column forces. However, the difference in forces at mid-interior columns was minimal due to the inverted-V damper configuration. Consequently, the lower story exterior column upgrading is inevitable.

Tensile stresses at upper story column splices were reduced. The opposite was observed in the bottom story exterior columns. On average, about 27% of column splices were found vulnerable at the BSE-2E hazard level. It is recommended to strengthen the exterior column splices at the lower half of the building as well as its first story columns.

The median peak damper displacements were less than the damper stroke limit (60mm). If the 84^{th} percentile damper response is considered, then few dampers in the bottom stories of the retrofitted building may exceed their stroke limit. Although according to SDF design the post relief velocity ratio was 1.5, the median values of the post relief velocity ratio were between 2.3 to 9.8, mainly due to higher mode effects. However, the corresponding damper forces were not large, which is one of the main advantages of utilizing bilinear oil dampers.

9.3 Recommendations for Future Work

A number of future topics can be explored based on the findings of this thesis. In particular,

- Material models developed for NVDs and ODs may be improved to simulate the response at ultimate limit states, such as the behaviour of dampers after reaching stroke limits.
- The proposed BRB model capabilities may be enhanced by incorporating nonlinear rate-dependent effects of the unbonding material between the steel plate core and the mortar.
- The MDF performance curve method should be extended to yielding, viscous/viscoelastic and friction and other types of energy dissipation devices. Furthermore, the MDF performance curve method should account for potential nonlinearities that the tall building to be retrofitted may be experiencing. Thus, simplified models for existing tall buildings with supplemental damping devices should be developed to incorporate the

frame yielding. The MDF performance curve method should be also extended to include a cost-benefit analysis for the optimal design of dampers.

- In order to explore the efficiency of vertical damping distribution methods the retrofit of tall buildings with stiffness irregularities should be explored. Thus, further refinement of the proposed balanced shear force proportional damping distribution SFPDD method should be conducted.
- A hybrid implementation of passive energy dissipation devices may be interesting to be explored.
- Further numerical studies should be conducted to evaluate the seismic performance of retrofitted tall buildings equipped with various types of damping devices. A potential damper device to be explored is the inerter damper that could be efficient in mitigating absolute floor accelerations in addition to peak story drift ratios. To this end, current modeling approaches for dampers should be improved to simulate their behaviour at large deformations.

BIBLIOGRAPHY

Adams, J., and Atkinson, G. (2003). "Development of seismic hazard maps for the proposed 2005 edition of the National Building Code of Canada." *Canadian Journal of Civil Engineering*, 30(2), 255-271.

AIR (2013). "Study of impact and the insurance and economic cost of a major earthquake in British Columbia and Ontario/Québec." AIR Worlwide, Insurance Bureau of Canada, Canada.

AISC (1969). *Specification for the design, fabrication & erection of structural steel for buildings*, American Insitute of Steel Construction, New York.

AISC (2010a). "Prequalified connections for special and intermediate steel moment frames for seismic applications." *ANSI/AISC 358-10*, American Institute for Steel Construction, Chicago, IL.

AISC (2010b). "Seismic provisions for structural steel buildings." American Institute for Steel Construction, Chicago, IL.

AISC (2010c). "Specification for structural steel buildings." *ANSI/AISC 360-10*, American Institute of Steel Construction, Chicago, IL.

AISC (2016). "Specification for structural steel buildings." *ANSI/AISC 360-16*, American Institute of Steel Construction, Chicago, IL.

Akcelyan, S., Lignos, D. G., Hikino, T., and Nakashima, M. (2016). "Evaluation of simplified and state-of-the-art analysis procedures for steel frame buildings equipped with supplemental damping devices based on E-Defense full-scale shake table tests." *Journal of Structural Engineering*, 142(6), 04016024.

Almufti, I., Hutt, C. M., Willford, M., and Deierlein, G. (2012). "Seismic assessment of typical 1970s tall steel moments frame buildings in downtown San Francisco." *Proc., 15th World Conference of Earthquake Engineering*, Lisbon, Portugal.

Ancheta, T. D., Darragh, R. B., Stewart, J. P., Seyhan, E., Silva, W. J., Chiou, B. S.-J., Wooddell, K. E., Graves, R. W., Kottke, A. R., Boore, D. M., Kishida, T., and Donahue, J. L. (2014). "NGA-West2 Database." *Earthquake Spectra*, 30(3), 989-1005.

Anderson, J., and Bertero, V. (1989). "Seismic response of a 42-story steel building." *The Loma Prieta, California, Earthquake of October 17, 1989: Performance of the built environment, Building Structures, USGS*, Paper 1552-C, c113–c140.

ASCE (2010). "Minimum design loads for buildings and other structures." *ASCE/SEI 7-10*, American Society of Civil Engineers, Reston, VA.

ASCE/SEI (2014). "Seismic evaluation and retrofit of existing buildings." *ASCE/SEI 41-13*, American Society of Civil Engineers, Reston, VA.

ASTM (2016). "Standard test methods for tension testing of metallic materials." *ASTM E8/ E8M-16a,* ASTM International, West Conshohocken, PA,.

BCJ (2008). "Seismic provisions for design of building structures." The Building Center of Japan, Tokyo.

Bech, D., Tremayne, B., and Houston, J. (2015). "Proposed changes to steel column evaluation criteria for existing buildings." *Proc. Improving the Seismic Performance of Existing Buildings and Other Structures 2015*, 255-272.

BilinearOilDamper (2015). "BilinearOilDamper material." *OpenSeesWiki online manual*, <http://opensees.berkeley.edu/wiki/index.php/BilinearOilDamper_Material>. (Aug. 6, 2015).

Bjornsson, A. B. (2014). "A retrofitting framework for pre-Northridge steel moment-frame buildings." Ph.D. Dissertation, California Institute of Technology, CA.

Black, C., and Makris, N. (2007). "Viscous heating of fluiddampers under small and large amplitude motions: experimental studies and parametric modeling." *Journal of Engineering Mechanics*, 133(5), 566-577.

Black, C., Makris, N., and Aiken, I. (2004). "Component testing, seismic evaluation and characterization of buckling-restrained braces." *Journal of Structural Engineering*, 130(6), 880-894.

Bonowitz, D., and Youssef, N. (1995). "SAC survey of steel moment resisting frame buildings affected by the 1994 Northridge earthquake." *Tech. Rep. 95-06: Surveys and assessment of damage to build affected by the Northridge earthquake of January 17, 1994, SAC Joint Venture*, Federal Emergency Management Agency, Sacramento, CA., 2.1–2.169.

Boresi, A. P., Schmidt, R. J., and Sidebottom, O. M. (1993). *Advanced mechanics of materials*, Wiley New York.

Bruneau, M., and Mahin, S. (1990). "Ultimate behavior of heavy steel section welded splices and design implications." *Journal of Structural Engineering*, 116(8), 2214-2235.

BSSC (1995). "NEHRP Recommended Provisions for the Seismic Regulations for New Buildings, 1994 Edition." *FEMA 222A*, Federal Emergency Management Agency, Washington, DC.

BSSC (2001). "NEHRP recommended provisions for seismic regulations for new buildings and other structures, 2000 Edition." *FEMA 368 and FEMA 369*, Federal Emergency Management Agency, Washington, DC.

Buchanan, A., Bull, D., Dhakal, R., MacRae, G., Palermo, A., and Pampanin, S. (2011). "Base isolation and damage-resistant technologies for improved seismic performance of buildings: A report written for the Royal Commission of Inquiry into building failure caused by the Canterbury earthquakes." *Research Report 2011-02*, Department of Civil and Natural Resources Engineering, University of Canterbury, Christchurch.

Butcher, J. C. (1996). "A history of Runge-Kutta methods." *Applied Numerical Mathematics*, 20(3), 247-260.

Chang, K. C., Soong, T. T., Oh, S.-T., and Lai, M. L. (1995). "Seismic behavior of steel frame with added viscoelastic dampers." *Journal of Structural Engineering*, 121(10), 1418-1426.

Chen, C.-C., Chen, S.-Y., and Liaw, J.-J. (2001). "Application of low yield strength steel on controlled plastification ductile concentrically braced frames." *Canadian Journal of Civil Engineering*, 28(5), 823-836.

Chen, Y.-T., and Chai, Y. H. (2011). "Effects of brace stiffness on performance of structures with supplemental Maxwell model-based brace–damper systems." *Earthquake Engineering & Structural Dynamics*, 40(1), 75-92.

Chopra, A. K., and Goel, R. K. (2001). "A modal pushover analysis procedure for estimating seismic demands for buildings." Pacific Earthquake Engineering Research Center, Berkeley, CA.

Christopoulos, C., and Filiatrault, A. (2006). *Principles of supplemental damping and seismic isolation*, IUSS Press, Milan, Italy.

Chung, Y., Nagae, T., Matsumiya, T., and Nakashima, M. (2011). "Seismic resistance capacity of beam–column connections in high-rise buildings: E-Defense shaking table test." *Earthquake Engineering & Structural Dynamics*, 40(6), 605-622.

Cimellaro, G. P., Reinhorn, A. M., and Bruneau, M. (2010). "Framework for analytical quantification of disaster resilience." *Engineering Structures*, 32(11), 3639-3649.

Constantinou, M., Symans, M., Tsopelas, P., and Taylor, D. (1993). "Fluid viscous dampers in applications of seismic energy dissipation and seismic isolation." *Proc., ATC 17-1 Seminar on Seismic Isolation, Passive Energy Dissipation, and Active Control*, 2, 581-592.

Constantinou, M., Tsopelas, P., Hammel, W., and Sigaher, A. (2001). "Toggle-brace-damper seismic energy dissipation systems." *Journal of Structural Engineering*, 127(2), 105-112.

Constantinou, M. C., Soong, T. T., and Dargush, G. F. (1998). "Passive energy dissipation systems for structural design and retrofit." *MCEER-Monograh No: 1*, Multidisciplinary Center for Earthquake Engineering Research, University of Buffalo., USA.

Constantinou, M. C., and Symans, M. D. (1993a). "Experimental study of seismic response of buildings with supplemental fluid dampers." *The Structural Design of Tall Buildings*, 2(2), 93-132.

Constantinou, M. C., and Symans, M. D. (1993b). "Seimic response of the structures with supplemental damping." *The Structural Design of Tall Buildings*, 2(2), 77-92.

CSA (2009). "Design of Steel Structures."Toronto, ON.

CSA (2014). "Design of Steel Structures."Toronto, ON.

CSI. ETABS, version 9.7.4, Computer and Structures, Berkeley, CA.

CSI. SAP 2000, version 14.2.4, Computer and Structures, Berkeley, CA.

CTBUH (2008). *Recommendations for the seismic design of high-rise buildings*, Council on Tall Buildings and Urban Habitat seismic working group, Chicago, IL.

CTBUH (2016). "The Skyscraper Center: The global tall building database of the Council of Tall Buildings and Urban Habitat (CTBUH)." <http://skyscrapercenter.com/>. (May, 2, 2016).

Dao, N. D., Ryan, K. L., Sato, E., and Sasaki, T. (2013). "Predicting the displacement of triple pendulum™ bearings in a full-scale shaking experiment using a three-dimensional element." *Earthquake Engineering & Structural Dynamics*, 42(11), 1677-1695.

Dhakal, R. P., MacRae, G. A., and Hogg, K. (2011). "Performance of ceilings in the February 2011 Christchurch Earthquake." *Bulettin of the New Zealand Society for Earthquake Engineering*, 44(4), 379-389.

Diotallevi, P. P., Landi, L., and Dellavalle, A. (2012). "A methodology for the direct assessment of the damping ratio of structures equipped with nonlinear viscous dampers." *Journal of Earthquake Engineering*, 16(3), 350-373.

Dong, B., Sause, R., and Ricles, J. M. (2015). "Accurate real-time hybrid earthquake simulations on large-scale MDOF steel structure with nonlinear viscous dampers." *Earthquake Engineering & Structural Dynamics*, 44(12), 2035-2055.

Dormand, J. R., and Prince, P. J. (1980). "A family of embedded Runge-Kutta formulae." *Journal of Computational and Applied Mathematics*, 6(1), 19-26.

E-Defense (2008). "2008 blind analysis contest by E-Defense." <http://www.bosai.go.jp/hyogo/blind-analysis/2008/eng/outline/outline.html>. (Dec. 5, 2008).

Elkady, A., and Lignos, D. (2016). "Full-scale cyclic testing of deep slender wide-flange steel beam-columns under unidirectional and bidirectional lateral drift demands." *Proc., 16th World Conference on Earthquake Engineering (16WCEE)*, Shanghai, China.

Elkady, A., and Lignos, D. G. (2014). "Modeling of the composite action in fully restrained beam-to-column connections: implications in the seismic design and collapse capacity of steel special moment frames." *Earthquake Engineering & Structural Dynamics*, 43(13), 1935-1954.

Elkady, A., and Lignos, D. G. (2015). "Effect of gravity framing on the overstrength and collapse capacity of steel frame buildings with perimeter special moment frames." *Earthquake Engineering & Structural Dynamics*, 44(8), 1289-1307.

Fahnestock, L., Ricles, J., and Sause, R. (2007). "Experimental evaluation of a large-scale buckling-restrained braced frame." *Journal of Structural Engineering*, 133(9), 1205-1214.

FEMA (1997). "NEHRP provisions for the seismic rehabilitation of buildings." *FEMA 273 (Guidelines) and 274 (Commentary)*, Federal Emergency Management Agency, Washington, D.C.

FEMA (2000a). "Prestandard and commentary for the seismic rehabilitation of buildings." *FEMA-356*, Federal Emergency Management Agency, Washington, DC.

FEMA (2000b). "State of the art report on connection performance." Federal Emergency Management Agency, Washington, DC.

FEMA (2005). "Improvement of nonlinear static seismic analysis procedures." *FEMA-440,*, Federal Emergency Management Agency, Washington, D.C.

FEMA (2012). "Seismic performance assessment of buildings." *FEMA P-58-1*, Federal Emergency Management Agency, Washington, D.C.

Filippou, F. C., Popov, E. P., and Bertero, V. V. (1983). "Effects of bond deterioration on hysteretic behavior of reinforced concrete joints." *Report EERC 83-19*, Earthquake Engineering Research Center, Univ. of California, Berkeley, Calif., USA.

Folz, B., and Filiatrault, A. (2001). "SAWS - Version 1.0, A computer program for the seismic analysis of woodframe structures." *Structural Systems Research Project: SSRP-2001/09*, Department of Structural Engineering, UCSD, La Jolla, CA.

Fu, Y., and Kasai, K. (1998). "Comparative study of frames using viscoelastic and viscous dampers." *Journal of Structural Engineering*, 124(5), 513-522.

Galasso, C., Stillmaker, K., Eltit, C., and Kanvinde, A. (2015). "Probabilistic demand and fragility assessment of welded column splices in steel moment frames." *Earthquake Engineering & Structural Dynamics*, 44(11), 1823-1840.

Guo, J. W. W., and Christopoulos, C. (2013a). "Performance spectra based method for the seismic design of structures equipped with passive supplemental damping systems." *Earthquake Engineering & Structural Dynamics*, 42(6), 935-952.

Guo, J. W. W., and Christopoulos, C. (2013b). "A procedure for generating performance spectra for structures equipped with passive supplemental dampers." *Earthquake Engineering & Structural Dynamics*, 42(9), 1321-1338.

Gupta, A., and Krawinkler, H. (1999). "Seismic demands for the performance evaluation of steel moment resisting frame structures." Ph.D. Dissertation, Stanford University.

Gupta, A., and Krawinkler, H. (2000). "Estimation of seismic drift demands for frame structures." *Earthquake Engineering & Structural Dynamics*, 29(9), 1287-1305.

Hall, J. F., Heaton, T. H., Halling, M. W., and Wald, D. J. (1995). "Near-source ground motion and its effects on flexible buildings." *Earthquake Spectra*, 11(4), 569-605.

Hartloper, A. R. (2016). "Updates to the ASCE-41-13 nonlinear modelling provisions for performance-based seismic assessment of new and existing steel moment resisting frames." MSc. Dissertation, McGill University.

Hikino, T. (2012). "Full-scale shaking table test and analysis of the dynamic characteristics verification that govern the seismic behavior of steel buildings with supplemental damping." Ph.D. Dissertation, Kyoto University, Japan (in Japanese).

Hutt, C. M., Almufti, I., Willford, M., and Deierlein, G. (2016). "Seismic loss and downtime assessment of existing tall steel-framed buildings and strategies for increased resilience." *Journal of Structural Engineering*, 142(8), C4015005.

Hwang, J.-S., Lin, W.-C., and Wu, N.-J. (2013). "Comparison of distribution methods for viscous damping coefficients to buildings." *Structure and Infrastructure Engineering*, 9(1), 28-41.

Hwang, J., Huang, Y., Yi, S., and Ho, S. (2008). "Design formulations for supplemental viscous dampers to building structures." *Journal of Structural Engineering*, 134(1), 22-31.

Ibarra, L. F., and Krawinkler, H. (2005). *Global collapse of frame structures under seismic excitations*, Pacific Earthquake Engineering Research Center.

IBC (2012). "International Code Council, 2012."International Building Code. Washington, DC.

ICBO (1973). "Uniform Building Code (UBC)." International Conference of Building Officials, Washington, DC.

Ichihasi, S., Okuzono, T., Takahashi, O., Usami, M., Ninomiya, M., Tsuyuki, Y., and Ishida, Y. (2000). "Vibration test of a frame which has an oil-damper brace." *Proc., The 12th World Conference on Earthquake Engineering (WCEE)*, Auckland, New Zealand.

Ishii, M., and Kasai, K. (2010). "Shear spring model for time history analysis of multi-story passive controlled buildings." *J. Struct. Constr. Eng.*, 75(647), 103-112.

Ji, X., Hikino, T., Kasai, K., and Nakashima, M. (2013). "Damping identification of a full-scale passively controlled five-story steel building structure." *Earthquake Engineering & Structural Dynamics*, 42(2), 277-295.

Johnston, R. G. (1972). "Design methods based on stiffness: Drift criteria." *Proc. International conference on planning and design of Tall Buildings Vol II: Structural design of tall steel buildings*, American Society of Civil Engineers, Lehigh University, Bethlehem, Pennsylvania, 635-641.

JSSI (2005). "Manual for design and construction of passively-controlled buildings." Japanese Society of Seismic Isolation, 2nd Ed., Tokyo (in Japanese).

Kanno, R. (2016). "Advances in steel materials for innovative and elegant steel structures in Japan-a review." *Structural Engineering International*, 26(3), 242-253.

Kasai, K., Baba, Y., Nishizawa, K., Hikino, T., Ito, H., Ooki, Y., and Motoyui, S. (2012). "Test results for Building with steel dampers: 3D shake table tests on full scale 5-story steel building with dampers Part 2." *J. Struct. Constr. Eng.*, 77(673), 499-508 (in Japanese).

Kasai, K., Fu, Y., and Watanabe, A. (1998). "Passive control systems for seismic damage mitigation." *Journal of Structural Engineering*, 124(5), 501-512.

Kasai, K., and Ito, H. (2004). "JSSI manual for building passive control technology: Part-8 peak response evaluation and design for elasto-plastically damped system." *Proc., The 13th World Conference on Earthquake Engineering*, Vancouver, B.C., Canada.

Kasai, K., and Ito, H. (2005). "Passive control design method based on tuning of stiffness, yield strength, and ductility of elasto-plastic damper." *Journal of Structural and Construction Engineering, AIJ,* , 70(595), 45-55 (in Japanese).

Kasai, K., Ito, H., and Ogura, T. (2008a). "Passive control design method based on tuning of equivalent stiffness of bilinear oil dampers." *Journal of structural and construction engineering*, 73(630), 1281-1288.

Kasai, K., Ito, H., Ooki, Y., Hikino, T., Kajiwara, K., Motoyui, S., Ozaki, H., and Ishii, M. (2010). "Full-scale shake table tests of 5-story steel building with various dampers." *Proc., 7th International Conference on Urban Earthquake Engineering (7CUEE) & 5th International Conference on Earthquake Engineering (5ICEE)*, Tokyo Institute of Technology, Tokyo, Japan.

Kasai, K., and Iwasaki, K. (2006). "Reduced expression for various passive control systems and conversion to shear spring model." *Journal of Structural and Construction Engineering, AIJ,* (605), 37-46 (in Japanese).

Kasai, K., Lu, X., Pu, W., Yamashita, T., Arakawa, Y., and Zhou, Y. (2013). "Effective retrofit using dampers for a steel tall building shaken by 2011 East Japan Earthquake: China-Japan cooperation program (Part 2)." *Proc., 10th International Conference on Urban Earthquake Engineering (10CUEE)*, Tokyo Institute of Technology, Tokyo, Japan.

Kasai, K., and Matsuda, K. (2014). "Full-scale dynamic testing of response-controlled buildings and their components: concepts, methods, and findings." *Earthq. Engin. Engin. Vib.*, 13(1), 167-181 English.

Kasai, K., Mita, A., Kitamura, H., Matsuda, K., Morgan, T. A., and Taylor, A. W. (2013b). "Performance of seismic protection technologies during the 2011 Tohoku-Oki Earthquake." *Earthquake Spectra*, 29(S1), S265-S293.

Kasai, K., Murata, S., Kato, F., Hikino, T., and Ooki, Y. (2011). "Evaluation rule for vibration period, damping, and mode vector of buildings tested by a shake table with inevitable rocking motions." *Journal of Structural and Construction Engineering, AIJ*, 76(670), 2031-2040 (in Japanese).

Kasai, K., Nakai, M., Nakamura, Y., Asai, H., Suzuki, Y., and Ishii, M. (2008). "Current status of building passive control in Japan." *Proc., The 14th World Conference on Earthquake Engineering*, Beijing, China.

Kasai, K., and Nishimura, T. (2004). "Equivalent linearization of passive control system with oil damper bilinearly dependent on velocity." *Journal of Structural and Construction Engineering, AIJ,* (583), 47-54 (in Japanese).

Kasai, K., and Nishizawa, K. (2010). "Experiments and dynamic analysis method for buckling restrained brace." *Summaries of technical papers of Annual Meeting Architectural Institute of Japan. C-1, Structures III, Timber structures steel structures steel reinforced concrete structures*, 2010, 807-808.

Kasai, K., Ogura, T., and Suzuki, A. (2007). "Passive control desing method based on tuning equivalent stiffness of nonlinear viscous dampers." *Journal of Structural and Construction Engineering, AIJ,* , 76(618), 97-104 (in Japanese).

Kasai, K., Oohara, K., and Sekiguchi, Y. (2004). "JSSI manual for building passive control technology part-10 time-history analysis model for viscous dampers." *Proc., The 13th World Conference on Earthquake Engineering*, Vancouver, B.C., Canada.

Kasai, K., Ooki, Y., Ishii, M., Ozaki, H., Ito, H., Motoyui, S., Hikino, T., and Sato, E. (2008). "Value-added 5-story steel frame and its components: Part 1 - Full-scale damper tests and analyses." *Proc., The 14th World Conference on Earthquake Engineering*, Beijing, China.

Kasai, K., Ooki, Y., Tokori, K., Amemiya, K., and Kimura, K. (2004). "JSSI manual for building passive control technology part-9 time-history analysis model for viscoelastic dampers." *Proc., The 13th World Conference on Earthquake Engineering*, Vancouver, B.C., Canada.

Kasai, K., Suzuki, A., and Oohara, K. (2003). "Equivalent linearization of a passive control system having viscous dampers dependent on fractional power of velocity." *Journal of Structural and Construction Engineering, AIJ,*(574), 77-84 (in Japanese).

Kasai, K., Takahashi, O., and Sekiguchi, Y. (2004). "JSSI manual for building passive control technology part-10 time-history analysis model for nonlinear oil dampers." *Proc., The 13th World Conference on Earthquake Engineering*, Vancouver, B.C., Canada.

Kiggins, S., and Uang, C.-M. (2006). "Reducing residual drift of buckling-restrained braced frames as a dual system." *Engineering Structures*, 28(11), 1525-1532.

Kimura, Y., Takeda, Y., Yoshioka, K., Furuya, N., and Takemoto, Y. (1976). "An experimental study on braces encased in steel tube and mortar." *Proc. Architectural Institute of Japan Annual Meeting*, Architectural Institute of Japan, 1041–1042.

Krawinkler, H. (1978). "Shear in beam-column joints in seismic design of steel frames." *Engineering Journal*, 15(3), 82-91.

Krawinkler, H., Popov, E. P., and Bertero, V. V. (1975). "Shear behavior of steel frame joints." *Journal of the Structural Division*, 101(11), 2317-2336.

Krawinkler, H., and Seneviratna, G. D. P. K. (1998). "Pros and cons of a pushover analysis of seismic performance evaluation." *Engineering Structures*, 20(4), 452-464.

Krishnan, S., Ji, C., Komatitsch, D., and Tromp, J. (2006). "Performance of two 18-Story steel moment-frame buildings in southern California during two large simulated San Andreas earthquakes." *Earthquake Spectra*, 22(4), 1035-1061.

Kutta, W. (1901). "Beitrag zur näherungsweisen Integration totaler Differentialgleichungen." *Zeitschrift für Mathematik und Physik*, 46, 435-453.

Kyriakopoulos, N., and Christopoulos, C. (2013). "Seismic assessment and upgrade of Type 2 construction steel moment-resisting frames built in Canada between the 1960s and 1980s using passive supplemental damping." *Canadian Journal of Civil Engineering*, 40(7), 644-654.

Lai, J.-W., Schoettler, M., Wang, S., and Mahin, S. (2015). "Seismic evaluation and retrofit of existing tall buildings in California: Case study of a 35-story steel moment resisting frame building in San Francisco." *PEER 2015/14*, Pacific Earthquake Engineering Research Center Headquarters at the University of California, Berkeley.

Lai, M., Chang, K., Soong, T., Hao, D., and Yeh, Y. (1995). "Full-scale viscoelastically damped steel frame." *Journal of Structural Engineering*, 121(10), 1443-1447.

LATBSDC (2014). *An alternative procedure for seismic analysis and design of tall buildings located in the Los Angeles region*, Los Angeles Tall Buildings Structural Design Council, Los Angeles, CA.

Lavan, O., and Avishur, M. (2013). "Seismic behavior of viscously damped yielding frames under structural and damping uncertainties." *Bull Earthquake Eng*, 11(6), 2309-2332 English.

Lavan, O., Cimellaro, G., and Reinhorn, A. (2008). "Noniterative optimization procedure for seismic weakening and damping of inelastic structures." *Journal of Structural Engineering*, 134(10), 1638-1648.

Lavan, O., and Dargush, G. F. (2009). "Multi-objective evolutionary seismic design with passive energy dissipation systems." *Journal of Earthquake Engineering*, 13(6), 758-790.

Lavan, O., and Levy, R. (2006). "Optimal design of supplemental viscous dampers for linear framed structures." *Earthquake Engineering & Structural Dynamics*, 35(3), 337-356.

Lee, K., and Foutch, D. A. (2002). "Seismic performance evaluation of pre-Northridge steel frame buildings with brittle connections." *Journal of Structural Engineering*, 128(4), 546-555.

Liang, Z., Lee, G. C., and Dargush, G. F. (2011). *Structural damping: Applications in seismic response modification*, CRC Press, USA.

Lignos, D., Cravero, J., and Elkady, A. (2016). "Experimental investigation of the hysteretic behavior of wide-flange steel columns under high axial load and lateral drift demands." *Proc., 11th Pacific Structural Steel Conference (PSSC)*, Shanghai, China.

Lignos, D., Hikino, T., Matsuoka, Y., and Nakashima, M. (2013). "Collapse assessment of steel moment frames based on E-Defense full-scale shake table collapse tests." *Journal of Structural Engineering*, 139(1), 120-132.

Lignos, D., Putman, C., Zareian, F., and Krawinkler, H. (2011). "Seismic evaluation of steel moment frames and shear walls using nonlinear static analysis procedures." *Proc., Structures Congress 2011*, ASCE, Reston, VA, 2204-2215.

Lignos, D. G. (2010). "Interactive interface for incremental dynamic analysis: Theory and example applications manual, Version 1.1.5." <http://dimitrios-lignos.research.mcgill.ca/IIIDAP.html>, Department of Civil Engineering and Applied Mechanics, McGill University, Montreal, Canada.

Lignos, D. G. (2012). "Modeling and experimental validation of a full scale 5-story steel building equipped with tripple friction pendulum bearings: E-defense blind analysis competition." *Proc., 9th International Conference on Urban Earthquake Engineering (9CUEE) & 4th Asia Conference on Earthquake Engineering, Center for Urban Earthquake Engineering (CUEE)*, Tokyo Institute of Technology, Tokyo.

Lignos, D. G., and Karamanci, E. (2013). "Drift-based and dual-parameter fragility curves for concentrically braced frames in seismic regions." *Journal of Constructional Steel Research*, 90, 209-220.

Lignos, D. G., and Krawinkler, H. (2011). "Deterioration modeling of steel components in support of collapse prediction of steel moment frames under earthquake loading." *Journal of Structural Engineering*, 137(11), 1291-1302.

Lignos, D. G., and Krawinkler, H. (2013). "Development and Utilization of Structural Component Databases for Performance-Based Earthquake Engineering." *Journal of Structural Engineering*, 139(8), 1382-1394.

Lignos, D. G., Putman, C., and Krawinkler, H. (2015). "Application of simplified analysis procedures for performance-based earthquake evaluation of steel special moment frames." *Earthquake Spectra*, 31(4), 1949-1968.

Lin, W.-H., and Chopra, A. K. (2002). "Earthquake response of elastic SDF systems with non-linear fluid viscous dampers." *Earthquake Engineering & Structural Dynamics*, 31(9), 1623-1642.

Londoño, J. M., Neild, S. A., and Wagg, D. J. (2013). "A noniterative design procedure for supplemental brace–damper systems in single-degree-of-freedom systems." *Earthquake Engineering & Structural Dynamics*, 42(15), 2361-2367.

Luco, N., and Cornell, C. A. (2000). "Effects of connection fractures on SMRF seismic drift demands." *Journal of Structural Engineering*, 126(1), 127-136.

Luco, N., Valley, M., and Crouse, C. (2012). "Earthquake ground motion: Chapter 3." *2009 NEHRP Recommended Seismic Provisions: Design Examples (FEMA P-751)*, FEMA, 3-1,3-28.

Mahin, S. A. (1998). "Lessons from damage to steel buildings during the Northridge earthquake." *Engineering Structures*, 20(4), 261-270.

Maison, B. F., and Bonowitz, D. (1999). "How safe are pre-Northridge WSMFs? A case study of the SAC Los Angeles nine-story building." *Earthquake Spectra*, 15(4), 765-789.

Maison, B. F., Kasai, K., and Deierlein, G. (2009). "ASCE-41 and FEMA-351 Evaluation of E-Defense Collapse Test." *Earthquake Spectra*, 25(4), 927-953.

Makris, N., and Constantinou, M. (1991). "Fractional-derivative maxwell model for viscous dampers." *Journal of Structural Engineering*, 117(9), 2708-2724.

Makris, N., Dargush, G., and Constantinou, M. (1993). "Dynamic analysis of generalized viscoelastic fluids." *Journal of Engineering Mechanics*, 119(8), 1663-1679.

Malley, J. O., Sinclair, M., Graf, T., Blaney, C., and Ahmed, T. (2011). "Incorporation of full-scale testing and nonlinear connection analyses into the seismic upgrade of a 15-story steel moment frame building." *The Structural Design of Tall and Special Buildings*, 20(4), 472-481.

MATLAB. version R2013b, Natick, MA, MathWorks.

Maxwell, J. C. (1867). "On the dynamical theory of gases." *Philosophical Transactions of the Royal Society of London*, 157, 49-88.

McKenna, F. T. (1997). "Object-oriented finite element programming: frameworks for analysis, algorithms and parallel computing." Ph.D. Dissertation, University of California, Berkeley.

Menegotto, M., and Pinto, P. E. (1973). "Method of analysis for cyclically loaded reinforced concrete plane frames including changes in geometry and non-elastic behaviour of elements under combined normal force and bending." *Proc., IABSE, Symp. on Resistance and Ultimate Deformability of Structures Acted on by Well Defined Repeated Loads, IABSE-AIPC-IVBH*, ETH Zurich, Zurich, Switzerland, 15-22.

Merritt, S., Uang, C. M., and Benzoni, G. (2003a). "Subassemblage testing of CoreBrace buckling-restrained braces." *Rep. No. TR-2003/01*, Dept. of Structural Engineering, Univ. of California, San Diego, USA.

Merritt, S., Uang, C. M., and Benzoni, G. (2003b). "Subassemblage testing of Star Seismic buckling-restrained braces." *Rep. No. TR-2003/04*, Dept. of Structural Engineering, Univ. of California, San Diego, USA.

Miranda, E., Mosqueda, G., Retamales, R., and Pekcan, G. (2012). "Performance of nonstructural components during the 27 February 2010 Chile Earthquake." *Earthquake Spectra*, 28(S1), S453-S471.

Muto, M., and Krishnan, S. (2011). "Hope for the best, prepare for the worst: Response of tall steel buildings to the ShakeOut scenario earthquake." *Earthquake Spectra*, 27(2), 375-398.

Naeim, F. (2010). "Performance based seismic design of tall buildings." *Earthquake Engineering in Europe*, M. Garevski, and A. Ansal, eds., Springer Netherlands, 147-169.

Naeim, F., and Graves, R. W. (2005). "The case for seismic superiority of well-engineered tall buildings." *The Structural Design of Tall and Special Buildings*, 14(5), 401-416.

Nakashima, M., Matsumiya, T., Suita, K., and Zhou, F. (2007). "Full-scale test ofcomposite frame under large cyclic loading." *Journal of Structural Engineering*, 133(2), 297-304.

Nakashima, M., Roeder, C., and Maruoka, Y. (2000). "Steel moment frames for earthquakes in United States and Japan." *Journal of Structural Engineering*, 126(8), 861-868.

NBCC (2015). "National Building Code of Canada." National Research Council of Canada, Ottawa, ON.

Newmark, N. M. (1959). "A method of computation for structural dynamics." *Journal of the Engineering Mechanics Division, ASCE*, 85(3), 67-94.

NIST (2010a). "Evaluation of the FEMA P695 methadology for quantification of building seismic performance factors." NEHRP consultants Joint Venture.

NIST (2010b). "Selecting and scaling earthquake ground motions for performing response history analysis." NEHRP consultants Joint Venture, prepared by the NEHRP Consultants Joint Venture for the National Institute of Standards and Technology, Gaithersburg, Maryland.

Ohtani, K., Ogawa, N., Katayama, T., and Shibata, H. (2004). "Construction of E-Defense (3-D full-scale earthquake testing facility)." *Proc., 13th World Conference on Earthquake Engineering*, Vancouver, B.C., Canada.

Oohara, K., and Kasai, K. (2002). "Time history analysis models for nonlinear viscous dampers." *Proc., Structural Engineers World Congress (SEWC)*, Yokohama, JAPAN.

Ooki, Y., Kasai, K., Motoyui, S., Kaneko, K., Kajiwara, K., and Hikino, T. (2009). "Full-scale tests of passively-controlled 5-story steel building using E-Defense shake table part 3: full-scale tests for dampers and beam-column subassemblies." *Proc., STESSA 2009*, Philadelphia, 93-99.

Pall, A. S., and Marsh, C. (1982). "Response of friction damped braced frames." *Journal of the Structural Division, ASCE*, 108(6), 1313-1323.

PEER (2010). "Guidelines for performance-based seismic design of tall buildings." TBI Guidelines Working Group, ed., Pacific Earthquake Engineering Research Center, University of California, Berkeley, California.

PEER/ATC (2010). "Modeling and acceptance criteria for seismic design and analysis of tall buildings." Prepared for Pacific Earthquake Engineering Research Center (PEER) by Applied Technology Council (ATC), Redwood City, CA.

Pekcan, G., Mander, J. B., and Chen, S. S. (1999). "Fundamental considerations for the design of non-linear viscous dampers." *Earthquake Engineering & Structural Dynamics*, 28(11), 1405-1425.

Popov, E. P., and Stephen, R. M. (1970). "Cyclic loading of full-size steel connections." *Report EERC 70-3*, Earthquake Engineering Research Center, Univ. of California, Berkeley, Calif., USA.

Ramirez, C. M., and Miranda, E. (2012). "Significance of residual drifts in building earthquake loss estimation." *Earthquake Engineering & Structural Dynamics*, 41(11), 1477-1493.

Ramirez, O. M., Constantinou, M. C., Kircher, C. A., Whittaker, A. S., Johnson, M. W., Gomez, J. D., and Chrysostomou, C. Z. (2001). "Development and evaluation of simplified procedures for analysis and design of buildings with passive energy dissipation systems." *MCEER-00-0010 2001*, Multidisciplinary Center for Earthquake Engineering Research, University of Buffalo, USA.

Ramirez, O. M., Constantinou, M. C., Whittaker, A. S., Kircher, C. A., Johnson, M. W., and Chrysostomou, C. Z. (2003). "Validation of the 2000 NEHRP provisions' equivalent lateral force and modal analysis procedures for buildings with damping systems." *Earthquake Spectra*, 19(4), 981-999.

Reinhorn, A. M., Li, C., and Constantinou, M. C. (1995). "Experimental & analytical investigation of seismic retrofit of structures with supplemental damping, Part 1: Fluid viscous damping devices." *NCEER-95-0001*, National Center for Earthquake Engineering Research, University of Buffalo, USA.

Sabelli, R., Mahin, S., and Chang, C. (2003). "Seismic demands on steel braced frame buildings with buckling-restrained braces." *Engineering Structures*, 25(5), 655-666.

Saeki, E., Sugisawa, M., Yamaguchi, T., and Wada, A. (1998). "Mechanical properties of low yield point steels." *Journal of Materials in Civil Engineering*, 10(3), 143-152.

Scott, M., and Fenves, G. (2010). "Krylov subspace accelerated newton algorithm: Application to dynamic progressive collapse simulation of frames." *Journal of Structural Engineering*, 136(5), 473-480.

SEAOSC (2010). "Study of historical and design wind speeds in the Los Angeles area." Structural Engineers Association of Southern California, CA.

Seleemah, A., and Constantinou, M. C. (1997). "Investigation of seismic response of buildings with linear and nonlinear fluid viscous dampers." *National Center for Earthquake Engineering Research*, <http://ubir.buffalo.edu/xmlui/handle/10477/622>, State Univ. of New York at Buffalo, Buffalo, N.Y.

Singh, M., Verma, N., and Moreschi, L. (2003). "Seismic analysis and design with maxwell dampers." *Journal of Engineering Mechanics*, 129(3), 273-282.

Singh, M. P., and Moreschi, L. M. (2002). "Optimal placement of dampers for passive response control." *Earthquake Engineering & Structural Dynamics*, 31(4), 955-976.

Soong, T., and Dargush, G. (1997). *Passive energy dissipation systems in structural engineering*, John Wiley & Sons, Chichester, United Kingdom.

Stillmaker, K., Kanvinde, A., and Galasso, C. (2016). "Fracture mechanics-based design of column splices with partial joint penetration welds." *Journal of Structural Engineering*, 142(2), 04015115.

Suzuki, Y., and Lignos, D. (2016). "Collapse behavior of steel columns as part of steel frame buildings: experiments and numerical models." *Proc., 16th World Conference on Earthquake Engineering (16WCEE)*, Shanghai, China.

Symans, M., Charney, F., Whittaker, A., Constantinou, M., Kircher, C., Johnson, M., and McNamara, R. (2008). "Energy dissipation systems for seismic applications: current practice and recent developments." *Journal of Structural Engineering*, 134(1), 3-21.

Symans, M. D., and Constantinou, M. C. (1998). "Passive fluid viscous damping systems for seismic energy dissipation." *ISET Journal of Earthquake Technology*, 35(4), 185-206.

Takahashi, O., and Sekiguchi, Y. (2001). "Constitutive rule of oil damper with maxwell model and source code for analysis program." *Proc., Passively Controlled Structure Symposium 2001*, Yokohama, Japan.

Takewaki, I. (2009). *Building control with passive dampers: Optimal performance-based design for earthquakes*, John Wiley & Sons (Asia) Pte. Ltd.

Taylor Devices Inc. (2017). "Structural applications of Taylor fluid viscous dampers." <http://taylordevices.com/pdf/Yearly-updates/YearlyUpdatedStructuralApplicationChart.pdf>. (June 1, 2017).

Tremblay, R., Bolduc, P., Neville, R., and DeVall, R. (2006). "Seismic testing and performance of buckling-restrained bracing systems." *Canadian Journal of Civil Engineering*, 33(2), 183-198.

Tremblay, R., Poncet, L., Bolduc, P., Neville, R., and DeVall, R. "Testing and design of buckling restrained braces for Canadian application." *Proc., 13th World Conference on Earthquake Engineering*.

Tsai, K.-C., Hsiao, P.-C., Wang, K.-J., Weng, Y.-T., Lin, M.-L., Lin, K.-C., Chen, C.-H., Lai, J.-W., and Lin, S.-L. (2008). "Pseudo-dynamic tests of a full-scale CFT/BRB frame—Part I: Specimen design, experiment and analysis." *Earthquake Engineering & Structural Dynamics*, 37(7), 1081-1098.

Tsuyuki, Y., Gofuku, Y., Iiyama, F., and Kotake, Y. (2004). "JSSI manual for building passive control technology part-3 performance and quality control of oil damper." *Proc., The 13th World Conference on Earthquake Engineering*, Vancouver, B.C., Canada.

Uriz, P., and Whittaker, A. S. (2001). "Retrofit of pre-Northridge steel moment-resisting frames using fluid viscous dampers." *The Structural Design of Tall Buildings*, 10(5), 371-390.

ViscousDamper (2015). "ViscousDamper material." *OpenSeesWiki online manual*, <http://opensees.berkeley.edu/wiki/index.php/ViscousDamper_Material>. (Sep. 30, 2016).

Wada, A., and Huang, Y. (1995). "Preliminary seismic design of damage tolerant tall building structures." *Proc. Symp. on a New Direction in Seismic Design*, Architectural Institute of Japan Tokyo, 77-93.

Wakabayashi, M., Nakamura, T., Kashibara, A., Morizono, T., and Yokoyama, H. (1973). "Experimental study on the elasto-plastic properties of precast concrete wall with built-in insulating braces." *Summaries of Technical Papers of Annual Meeting*, Architectural Institute of Japan, 1041–1044.

Wang, S., Lai, J.-W., Schoettler, M. J., and Mahin, S. A. (2017). "Seismic assessment of existing tall buildings: A case study of a 35-story steel building with pre-Northridge connection." *Engineering Structures*, 141, 624-633.

Watanabe, A., Hitomi, Y., Saeki, E., Wada, A., and Fujimoto, M. "Properties of brace encased in buckling-restraining concrete and steel tube." *Proc., Proceedings of Ninth World Conference on Earthquake Engineering*, 719-724.

Wen, Y. K. (1976). "Method for random vibration of hysteretic systems." *Journal of Engineering Mechanics*, 102(2), 249–263.

Whittaker, A., Aiken, I., Bergman, D., Clark, P., Cohen, J., Kelly, J., and Scholl, R. (1993). "Code requirements for the design and implementation of passive energy dissipation

systems." *Proc., of ATC 17-l Seminar on Seismic Isolation, Passive Energy Dissipation, and Active Control*, 497-508.

Whittaker, A., and Constantinou, M. (2004). "Seismic energy dissipation systems for buildings: seismic energy dissipation systems for buildings. earthquake engineering: from engineering seismology to oerformance-based engineering." *Earthquake Engineering*, Y. Bozorgnia, and V. V. Bertero, eds., CRC Press, New York.

Whittle, J. K., Williams, M. S., Karavasilis, T. L., and Blakeborough, A. (2012). "A comparison of viscous damper placement methods for improving seismic building design." *Journal of Earthquake Engineering*, 16(4), 540-560.

Yamada, S., Yamaguchi, M., Takeuchi, T., and Wada, A. "Hysteresis model of steel material for the buckling restrained brace considering the strain rate dependency." *Proc., 13th World Conference on Earthquake Engineering*.

Yamamoto, M., Minewaki, S., Nakahara, M., and Tsuyuki, Y. (2016). "Concept and performance testing of a high-capacity oil damper comprising multiple damper units." *Earthquake Engineering & Structural Dynamics*, 45(12), 1919-1933.

Yamashita, T., Kawabata, J., Ninomiya, M., Sakaba, N., and Yanagawa, Y. (2010). "2- and 3-D blind analyses of full-scale 5-story building with viscous dampers." *Proc., 7th International Conference on Urban Earthquake Engineering (7CUEE) &5th International Conference on Earthquake Engineering (5ICEE)*, Tokyo Institute of Technology, Tokyo, Japan.

Yassin, M. H. M. (1994). "Nonlinear analysis of prestressed concrete structures under monotonic and cycling loads." Ph.D. Dissertation, University of California, Berkeley.

Youssef, N. F., Bonowitz, D., and Gross, J. L. (1995). "A survey of steel moment-resisting frame buildings affected by the 1994 Northridge earthquake." *Rep. No. NISTIR 5625*, US National Institute of Standards and Technology.

Yu, Y., Tsai, K., Li, C., Weng, Y., and Tsai, C. (2013). "Earthquake response analyses of a full-scale five-story steel frame equipped with two types of dampers." *Earthquake Engineering & Structural Dynamics*, 42(9), 1301-1320.

Zareian, F., and Krawinkler, H. (2006). "Simplified performance-based earthquake engineering." Stanford University Stanford, CA, USA.

Zona, A., and Dall'Asta, A. (2012). "Elastoplastic model for steel buckling-restrained braces." *Journal of Constructional Steel Research*, 68(1), 118-125.

Zsarnóczay, Á. (2013). "Experimental and numerical analysis of buckling restrained braced frames for Eurocode conform design procedure evaluation." Ph.D. Dissertation, BME Department of Structural Engineering, Budapest.

APPENDIX A

Figure A1 illustrates two available types of oil dampers produced by KAYABA System Machinery in Japan. Type A is composed of the damper portion (cylinder) only with the connection segments in both ends. This damper type used mainly in shorter dimensions, such as a V-brace and stud-type configurations. In this case, dampers are placed horizontally. Type B is composed of the damper portion and supporting brace. This damper type is mainly used in diagonal brace configurations, where the distance between the connection points require longer braces. Table A1 summarizes the available oil damper dimensions, such as the stroke, length and diameter, the damper weight and brace portions of these two types. The table provides the internal damper stiffness $\widehat{K}_d$ as well, which can be used to compute the stiffness-to-damping coefficient ratio of the internal damper β_k. Table A2 provides the available linear and bilinear oil damper properties, such as the maximum damper velocity, initial and post relief damping coefficient, relief load and relief velocity. Table A3 summarizes the properties and scale factors of selected records from NGA-West2 database.

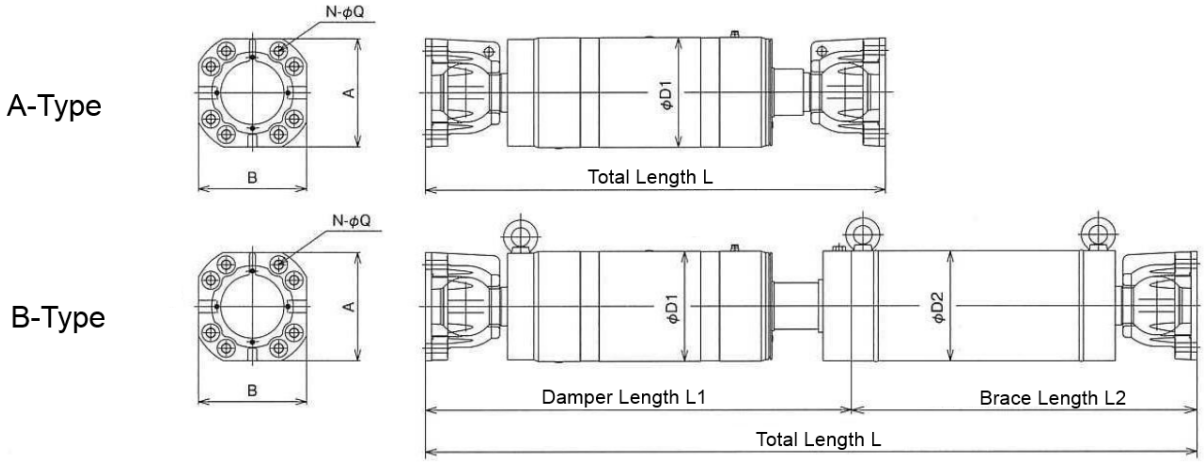

Figure A.1: Damper types and dimensions (image courtesy of KAYABA System Machinery)

Table A.1: Dimensions of oil dampers (KAYABA System Machinery)

Model	Maximum Damper Force $\hat{F}_{dmax}$ [KN]	Stroke [mm]	ϕD1 [mm]	ϕD2 [mm]	t_2* [mm]	Cross-section Area A_2* [mm^2]	A-Type L [mm]	B-Type L1 [mm]	Internal Damper Stiffness K_d [KN/cm]
BDH250120	250	±60	139.8	139.8	9.5	3889	840	780	900
BDH250160	250	±80	139.8	139.8	9.5	3889	940	860	750
BDH500120	500	±60	190	216.3	10.5	6789	1020	980	1600
BDH500160	500	±80	190	216.3	10.5	6789	1120	1060	1400
BDH500200	500	±100	190	216.3	10.5	6789	1220	1140	1100
BDH1000120	1000	±60	274	267.4	13	10390	1230	1160	3500
BDH1000160	1000	±80	274	267.4	13	10390	1330	1240	3000
BDH1000200	1000	±100	274	267.4	13	10390	1430	1320	2400
BDH1500120	1500	±60	310	318.5	17.4	16459	1350	1260	5200
BDH1500160	1500	±80	310	318.5	17.4	16459	1450	1340	4600
BDH1500200	1500	±100	310	318.5	17.4	16459	1550	1420	4000
BDH1500240	1500	±120	310	318.5	17.4	16459	1650	1500	3400
BDH2000120	2000	±60	355.6	355.6	19	20092	1390	1300	6200
BDH2000160	2000	±80	355.6	355.6	19	20092	1490	1380	5500
BDH2000200	2000	±100	355.6	355.6	19	20092	1590	1460	4700
BDH2000240	2000	±120	355.6	355.6	19	20092	1690	1540	4000

*Thickness and cross-section area of supporting steel brace are derived from the weight formulation

Table A.2: Properties of oil dampers (KAYABA System Machinery)

Size	Model*	Maximum Damper Force $\hat{F}_{dmax}$ [KN]	Maximum Velocity $\hat{v}_{dmax}$ [cm/s]	Initial Damping Coefficient $\hat{C}_d$ [KN/(cm/s)]	Post-relief Damping Coefficient $\hat{C}_{d2}$ [KN/(cm/s)]	Relief Load $\hat{F}_{dr}$ [KN]	Relief Velocity $\hat{v}_{dr}$ [cm/s]
250	BDH250-B1	250	30	15.6	2.9	200	12.8
	BDH250-B2	250	30	31.3	2.1	200	6.4
	BDH250-B3	250	30	46.9	1.9	200	4.3
	BDH250-B4	250	30	62.5	1.9	200	3.2
	BDH250-B5	250	30	78.1	1.8	200	2.6
	BDH250-B6	250	30	93.8	1.8	200	2.1
	BDH250-B7	250	30	109.2	1.8	200	1.8
	BDH250-L	250	30	8.3			
500	BDH500-B1	500	30	31.3	5.8	400	12.8
	BDH500-B2	500	30	62.5	4.2	400	6.4
	BDH500-B3	500	30	93.8	3.9	400	4.3
	BDH500-B4	500	30	125.0	3.7	400	3.2
	BDH500-B5	500	30	156.3	3.6	400	2.6
	BDH500-B6	500	30	187.5	3.6	400	2.1
	BDH500-B7	500	30	218.8	3.6	400	1.8
	BDH500-L	500	30	16.7			
1000	BDH1000-B1	1000	30	62.5	11.6	800	12.8
	BDH1000-B2	1000	30	125.0	8.5	800	6.4
	BDH1000-B3	1000	30	187.5	7.8	800	4.3
	BDH1000-B4	1000	30	250.0	7.5	800	3.2
	BDH1000-B5	1000	30	312.5	7.3	800	2.6
	BDH1000-B6	1000	30	375.0	7.2	800	2.1
	BDH1000-B7	1000	30	437.5	7.1	800	1.8
	BDH1000-L	1000	30	33.3			
1500	BDH1500-B1	1500	30	93.8	17.4	1200	12.8
	BDH1500-B2	1500	30	187.5	12.7	1200	6.4
	BDH1500-B3	1500	30	281.3	11.7	1200	4.3
	BDH1500-B4	1500	30	375.0	11.2	1200	3.2
	BDH1500-B5	1500	30	468.8	10.9	1200	2.6
	BDH1500-B6	1500	30	562.5	10.8	1200	2.1
	BDH1500-B7	1500	30	656.0	10.7	1200	1.8
	BDH1500-L	1500	30	60.0			
2000	BDH2000-B1	2000	25	125.0	32.8	1600	12.8
	BDH2000-B2	2000	30	250.0	16.9	1600	6.4
	BDH2000-B3	2000	30	375.0	15.5	1600	4.3
	BDH2000-B4	2000	30	500.0	14.9	1600	3.2
	BDH2000-B5	2000	30	625.0	14.6	1600	2.6
	BDH2000-B6	2000	30	750.0	14.4	1600	2.1
	BDH2000-B7	2000	30	875.0	14.2	1600	1.8
	BDH2000-L	2000	25	80.0			

*B represents bilinear dampers, while L stands for linear dampers

Table A.3: Properties of selected ground motions

Result ID	Record Sequence Number	Earthquake Name	Year	Station Name	Magnitude	Mechanism	Rjb (km)	Rrup (km)	Vs30 (m/sec)	Horizontal-1 Acc. Filename	Scale Factor BSE-2E	Scale Factor BSE-1E
1	20	"Northern Calif-03"	1954	"Ferndale City Hall"	6.5	strike slip	26.7	27.0	219.3	RSN20_NCALIF.FH_H-FRN044.AT2	3.43	2.22
2	36	"Borrego Mtn"	1968	"El Centro Array #9"	6.63	strike slip	45.1	45.7	213.4	RSN36_BORREGO_A-ELC180.AT2	4.95	3.21
3	169	"Imperial Valley-06"	1979	"Delta"	6.53	strike slip	22.0	22.0	242.1	RSN169_IMPVALL.H_H-DLT262.AT2	3.16	2.05
4	174	"Imperial Valley-06"	1979	"El Centro Array #11"	6.53	strike slip	12.6	12.6	196.3	RSN174_IMPVALL.H_H-E11140.AT2	1.51	0.98
5	175	"Imperial Valley-06"	1979	"El Centro Array #12"	6.53	strike slip	17.9	17.9	196.9	RSN175_IMPVALL.H_H-E12140.AT2	5.00	3.24
6	187	"Imperial Valley-06"	1979	"Parachute Test Site"	6.53	strike slip	12.7	12.7	348.7	RSN187_IMPVALL.H_H-PTS225.AT2	4.98	3.23
7	192	"Imperial Valley-06"	1979	"Westmorland Fire Sta"	6.53	strike slip	14.8	15.3	193.7	RSN192_IMPVALL.H_H-WSM090.AT2	3.81	2.47
8	266	"Victoria_ Mexico"	1980	"Chihuahua"	6.33	strike slip	18.5	19.0	242.1	RSN266_VICT_CHI102.AT2	4.92	3.19
9	721	"Superstition Hills-02"	1987	"El Centro Imp. Co. Cent"	6.54	strike slip	18.2	18.2	192.1	RSN721_SUPER.B_B-ICC000.AT2	2.64	1.72
10	728	"Superstition Hills-02"	1987	"Westmorland Fire Sta"	6.54	strike slip	13.0	13.0	193.7	RSN728_SUPER.B_B-WSM090.AT2	3.18	2.06
11	838	"Landers"	1992	"Barstow"	7.28	strike slip	34.9	34.9	370.1	RSN838_LANDERS_BRS000.AT2	4.55	2.96
12	848	"Landers"	1992	"Coolwater"	7.28	strike slip	19.7	19.7	353.0	RSN848_LANDERS_CLW-LN.AT2	2.89	1.87
13	900	"Landers"	1992	"Yermo Fire Station"	7.28	strike slip	23.6	23.6	353.6	RSN900_LANDERS_YER270.AT2	2.96	1.92
14	1101	"Kobe_ Japan"	1995	"Amagasaki"	6.9	strike slip	11.3	11.3	256.0	RSN1101_KOBE_AMA000.AT2	2.68	1.74
15	1104	"Kobe_ Japan"	1995	"Fukushima"	6.9	strike slip	17.9	17.9	256.0	RSN1104_KOBE_FKS000.AT2	2.94	1.90
16	1110	"Kobe_ Japan"	1995	"Morigawachi"	6.9	strike slip	24.8	24.8	256.0	RSN1110_KOBE_MRG000.AT2	3.18	2.07
17	1115	"Kobe_ Japan"	1995	"Sakai"	6.9	strike slip	28.1	28.1	256.0	RSN1115_KOBE_SKI000.AT2	4.62	2.99
18	1121	"Kobe_ Japan"	1995	"Yae"	6.9	strike slip	27.8	27.8	256.0	RSN1121_KOBE_YAE000.AT2	2.26	1.46
19	1158	"Kocaeli_ Turkey"	1999	"Duzce"	7.51	strike slip	13.6	15.4	281.9	RSN1158_KOCAELI_DZC180.AT2	2.27	1.47
20	1180	"Chi-Chi_ Taiwan"	1999	"CHY002"	7.62	Reverse Oblique	25.0	25.0	235.1	RSN1180_CHICHI_CHY002-N.AT2	1.91	1.24
21	1246	"Chi-Chi_ Taiwan"	1999	"CHY104"	7.62	Reverse Oblique	18.0	18.0	223.2	RSN1246_CHICHI_CHY104-N.AT2	1.42	0.92
22	1478	"Chi-Chi_ Taiwan"	1999	"TCU033"	7.62	Reverse Oblique	40.9	40.9	423.4	RSN1478_CHICHI_TCU033-E.AT2	3.36	2.18
23	1496	"Chi-Chi_ Taiwan"	1999	"TCU056"	7.62	Reverse Oblique	10.5	10.5	403.2	RSN1496_CHICHI_TCU056-E.AT2	3.79	2.46
24	1602	"Duzce_ Turkey"	1999	"Bolu"	7.14	strike slip	12.0	12.0	293.6	RSN1602_DUZCE_BOL000.AT2	1.42	0.92
25	1762	"Hector Mine"	1999	"Amboy"	7.13	strike slip	41.8	43.1	382.9	RSN1762_HECTOR_ABY090.AT2	3.75	2.43
26	3754	"Landers"	1992	"Indio - Jackson Road"	7.28	strike slip	48.8	48.8	292.1	RSN3754_LANDERS_INJ090.AT2	2.96	1.92
27	3758	"Landers"	1992	"Thousand Palms Post Office"	7.28	strike slip	36.9	36.9	333.9	RSN3758_LANDERS_TPP045.AT2	4.93	3.20
28	3852	"Chi-Chi_ Taiwan-04"	1999	"CHY006"	6.2	strike slip	24.6	24.6	438.2	RSN3852_CHICHI.04_CHY006N.AT2	2.81	1.82
29	5823	"El Mayor-Cucapah_ Mexico"	2010	"Chihuahua"	7.2	strike slip	18.2	19.5	242.1	RSN5823_SIERRA.MEX_CHI000.AT2	1.39	0.90
30	5827	"El Mayor-Cucapah_ Mexico"	2010	"MICHOACAN DE OCAMPO"	7.2	strike slip	13.2	15.9	242.1	RSN5827_SIERRA.MEX_MDO000.AT2	1.82	1.18
31	5832	"El Mayor-Cucapah_ Mexico"	2010	"TAMAULIPAS"	7.2	strike slip	25.3	26.6	242.1	RSN5832_SIERRA.MEX_TAM000.AT2	3.16	2.05
32	5859	"El Mayor-Cucapah_ Mexico"	2010	"Westmorland Fire Sta"	7.2	strike slip	42.3	42.6	193.7	RSN5859_SIERRA.MEX_WSM360.AT2	4.00	2.59
33	5988	"El Mayor-Cucapah_ Mexico"	2010	"Meloland_ E Holton Rd."	7.2	strike slip	30.2	30.6	196.0	RSN5988_SIERRA.MEX_DRE360.AT2	3.14	2.04
34	6887	"Darfield_ New Zealand"	2010	"Christchurch Botanical Gardens"	7	strike slip	18.1	18.1	187.0	RSN6887_DARFIELD_CBGSN89W.AT2	3.26	2.11
35	6889	"Darfield_ New Zealand"	2010	"Christchurch Hospital"	7	strike slip	18.4	18.4	194.0	RSN6889_DARFIELD_CHHCN01W.AT2	1.62	1.05
36	6942	"Darfield_ New Zealand"	2010	'NNBS North New Brighton School	7	strike slip	26.8	26.8	211.0	RSN6942_DARFIELD_NNBSS13E.AT2	2.19	1.42
37	6952	"Darfield_ New Zealand"	2010	"Papanui High School "	7	strike slip	18.7	18.7	263.2	RSN6952_DARFIELD_PPHSS33W.AT2	1.94	1.26
38	6960	"Darfield_ New Zealand"	2010	"Riccarton High School "	7	strike slip	13.6	13.6	293.0	RSN6960_DARFIELD_RHSCN86W.AT2	2.59	1.68
39	6969	"Darfield_ New Zealand"	2010	"Styx Mill Transfer Station "	7	strike slip	20.9	20.9	247.5	RSN6969_DARFIELD_SMTCN88W.AT2	2.60	1.69
40	8606	"El Mayor-Cucapah_ Mexico"	2010	"Westside Elementary School"	7.2	strike slip	10.3	11.4	242.0	RSN8606_SIERRA.MEX_CIWESHNN.AT2	2.61	1.70
				MAX	7.6		48.8	48.8	438.2		5.00	3.24
				MIN	6.2		10.3	10.5	187.0		1.39	0.90
				MEDIAN	7.0		19.2	19.6	244.8		2.96	1.92